Robotic Technology to Aid and Assess Recovery and Learning in Stroke Patients

by

Jerome J. Palazzolo

M.S., Mechanical Engineering, Michigan State University (1994)
B.S., Mechanical Engineering, Michigan State University (1992)

Submitted to the Department of Mechanical Engineering
in partial fulfillment of the requirements for the degree of

Doctor of Philosophy in Mechanical Engineering

at the

MASSACHUSETTS INSTITUTE OF TECHNOLOGY

June 2005

Author ..... Signature redacted
Department of Mechanical Engineering
May 16, 2005

Certified by ..... Signature redacted
Neville Hogan
Professor, Department of Mechanical Engineering
Professor, Department of Brain and Cognitive Sciences
Thesis Supervisor

Accepted by ..... Signature redacted
Lallit Anand
Professor, Department of Mechanical Engineering
Chairman, Committee on Graduate Students

Robotic Technology to Aid and Assess Recovery and Learning in Stroke Patients

by

Jerome J. Palazzolo

Submitted to the Department of Mechanical Engineering
in partial fulfillment of the requirements for the degree of

Doctor of Philosophy in Mechanical Engineering

Abstract

Each year, about 700,000 people in the United States have a stroke, making it a leading cause of serious, long-term disability. Modalities of therapy often assume the processes underlying motor recovery and motor learning are similar because both exhibit activity-dependent neural plasticity. However, the impact of other factors unique to recovery such as re-acquisition of muscle strength and resolution of abnormal muscle tone confounds the validity of this assumption. By implementing an adaptive impedance controller that collapses from a "virtual slot" between two targets to a "virtual spring" at the desired target, a new performance-based progressive therapy (PBPT) algorithm was developed to test whether recovery would be enhanced by incorporating learning strategies like repetition, goal specification, and positive reinforcement.

A study of chronic stroke patients (8 to 95 months post-stroke) who were in a clinically verified "stable" phase of recovery was conducted with the PBPT protocol, in which patients made over 12,000 visually guided, point-to-point movements. Though prior clinical results suggested that recovery would plateau 6 months post-stroke, two studies using sensorimotor (SM) and progressive resistance (PR) therapy protocols achieved significant, though modest, reductions in impairment. The new PBPT protocol produced significantly larger impairment reductions with over 6,000 fewer movements than SM and PR.

By design, the adapting PBPT parameters, namely, the time allotted to move between targets and the virtual slot sidewall stiffness, serve as indicators of patients' abilities to move and aim (as parameters decrease (increase), patients move faster (slower) and require less (more) aiming assistance). By analyzing the parameters' evolution throughout the PBPT protocol, it was shown that motor recovery follows an exponential progression similar to a motor learning "law of practice". In addition, a serendipitous

benefit of the PBPT protocol occurred – a sustained reduction in abnormal muscle tone, a factor unrelated to learning. A spectral impedance estimation method suitable for a clinical setting was developed and validated by identifying known mechanical systems. In addition, preliminary data was collected on unimpaired subjects and stroke patients.

Thesis Supervisor: Neville Hogan
Title: Professor, Department of Mechanical Engineering
Professor, Department of Brain and Cognitive Sciences

Acknowledgements

This thesis marks the culmination of my research at the MIT Newman Lab and the end of my "good ole college days" (yes, I know, it's about time ☺). The work reported in this thesis is the result of the ideas, support, and encouragement of many people. If I forget to mention anyone who has helped me along the way, I apologize.

First, I would like to thank my advisor, Professor Neville Hogan. When I arrived at MIT, his intellect and intuition on all things engineering were somewhat humbling, but, more importantly, they were also inspiring. Indeed, I will continue to emulate his abilities as an engineer and a researcher for years to come. In addition, I would not have made it this far without his support, encouragement, and understanding nature. I also admire his recognition of the importance of family and friends despite pressure from course work and research deadlines. My dear Grams passed away my second semester at MIT, and, without hesitation, he told me to go home because that was where I needed to be. He was right. Thank you for everything Neville.

Next, I would like to thank the members of my Ph.D. committee for their advice and support. Dr. Igo Krebs has been a great help to me throughout my years at MIT. His firsthand knowledge of rehabilitation and engineering was a valuable resource and his many contributions to this work are appreciated. Professor Dava Newman is an outstanding engineer and person. Although she was on sabbatical sailing around the world when I asked her to join my committee, she responded quickly and provided very insightful comments regarding my thesis proposal (via ship-to-shore email from Tahiti, I might add!). I am grateful for her many suggestions and for her words of encouragement. As a neurologist, Dr. Bruce Volpe provided much insight into the nature of stroke and its effects on patients. In addition, his support, suggestions, and encouragement throughout my doctoral studies are much appreciated.

Being a member of the Newman Lab has been a great experience. I consider myself lucky to have worked with so many intelligent and talented people. Steve Buerger and I began working in the lab at the same time, and I have been impressed by his technical knowledge and skill since day one. In addition to being a talented engineer who helped me get past several of my research stumbling blocks, he is also a down-to-earth guy. As an occupational therapist/post-doc, Sue Fasoli has been a valuable clinical resource for my research, but, just as important, she has been a good friend to me. Our chats about family and friends gave me much-needed breaks from research. James Celestino, a proud Yankee fan in a Red Sox land, helped keep me sane at times and he was always the first to volunteer a helping hand as an engineer, as a friend, and as a softball coach. Brandon Rohrer was a pleasure to work with and his ability to make progress at MIT while staying dedicated to his family and church was admirable. As well

as being productive researchers and nice guys, Steven Charles and Josh Young are doing a fine job as the group's sys admins. The unique contributions of Ryan, Lorenzo, Shelly, Jooeun, Nevan, and Laura help make the Hogan group a special and prosperous one. Marj Joss is a pleasure to work with and really knows how to get things done.

I am also very grateful for the friends I've met at MIT who are not part of the Newman Lab: Katy, Heidi, Lori, David, Margaret, Robert, Bethany, Marcia, Brett, Natalia, and Christiane, just to name a few. God bless you all.

Leslie Regan has made me feel at home at MIT ever since my first campus visit. In addition to being a great graduate administrator, she has gone out of her way many times to help me. Leslie and Joan Kravit make the ME Graduate Office the BEST graduate office at MIT. To them, I give special thanks.

Some of my most special and lasting friendships developed when I was at MSU. Don Pilon and I met in Statics class and spent the next three years taking ME classes and cheering Spartan sports together. Don, his wife Amy, his son & my Godson Alec, his daughter Victoria, and his mother Louise are family to me. John Hermann, DVM, and I were roommates for five years and kept each other sane despite living on floors filled with many eccentric Honors College cuckoos. Philip FitzSimons, PhD, was a great UG honors project & master's thesis advisor, and an even better friend. His wife Kathy, daughter Laure, and son Peter are dear to me. Professor Ron Rosenberg was the best undergraduate advisor I could have ever hoped for. His introductory class on bond graphs, which began "$\dot{\mathbf{x}} = \mathbf{Ax} + \mathbf{Bu}$ happy, happy, joy, joy", got me excited about dynamic systems and control theory, and the rest is history.

The amount of gratitude that I have for my mother and father, Linda and Jerry, is immeasurable. They have always been there for me with plenty of love, encouragement, and support. My sisters, brothers-in-law, nieces, and nephews have always been supportive and they are all very special to me – my sister Beth, her daughters Nicole & Andrea, Nicole's son Athier, Andrea's daughter DeAnna, my sister Mary & brother-in-law Jim, their sons Edward, Thomas & Robert, my sister Kathi & brother-in-law Joe, their daughter Diana & son Joseph, my sister Paula, and her sons Dennis & Jeremy. In addition, I have countless wonderful aunts, uncles, and cousins. I love you all!

Last, but certainly not least, I thank Amy Badley. We met in the autumn of 2002 and she has been waiting patiently for me to finish this thesis and come home for many, many months. Despite my imperfections and sometimes-crabby mood, she has stood firmly by me and has been a plentiful source of joy in my life. Thank you again, darling.

This work was supported by National Institutes of Health grant #R01-HD37397, by the Burke Medical Research Institute, and by a N.Y. State Score Award.

Table of Contents

List of Figures

List of Tables

Chapter 1

Introduction

Each year, about 700,000 people suffer a new or recurrent stroke; about 500,000 of these are first attacks and 200,000 recurrent attacks [5]. Research to date has shown that repetitive, task-specific, goal-directed, robot-assisted therapy is effective in reducing motor impairments in the affected arm after stroke [3,55,60,97]. However, there is no reason to believe that a "one-size-fits-all" optimal treatment exists. Instead, therapy should be tailored to each patient's needs and abilities. Improvements in motor recovery of stroke survivors would promote more functional use of the impaired limb and would increase the efficiency of robot-based neuro-rehabilitation. The overarching goal of this work is to aid and assess human stroke rehabilitation by exploring the nature of recovery.

1.1. Motivation

Stroke is a leading cause of serious, long-term disability in the United States, and it is estimated that the direct healthcare costs (i.e., costs of 1. services provided by physicians and other healthcare professionals; 2. hospitals and nursing homes; 3. medications, home health care, and other medical durables) associated with stroke in 2005 will be $35 billion [5]. Due to these staggering numbers, a need to study the recovery of damaged nervous systems exists. A prominent theme of current research into recovery from brain injury posits that activity-dependent plasticity underlies neuro-recovery. If this were true, motor recovery would exhibit behavioral characteristics commonly associated with motor learning in unimpaired subjects.

A number of studies have shown that robotic devices can increase the motor recovery of stroke survivors [3,55,60,97]. They can also be used to quantify motor learning of unimpaired subjects [29,30,36,37,63,72,73,82,83,90,103]. With this

knowledge, one goal of this research from the onset was to investigate the nature of motor learning to determine if an algorithm could be developed to increase both the rate and extent of motor recovery. These improvements would increase the efficiency of robot-assisted neuro-rehabilitation. In addition to contributing to a broader understanding of motor recovery, this research will also provide evidence whether mathematical theories of motor learning [19,48,67,102,104] may be adapted to serve as a basis for building a scientific theory of stroke rehabilitation.

1.2. Types of strokes and their effects

Strokes are caused by an interruption of the blood supply to the brain resulting in necrosis of brain tissue. Ischemic strokes are due to a blockage in the arteries supplying blood to the brain while hemorrhagic strokes are due to burst blood vessels within the brain. Of all strokes, 88 percent are ischemic, 9 percent are intracerebral hemorrhagic, and 3 percent are subarachnoid hemorrhagic [5]. In the National Heart, Lung, and Blood Institute's (NHLBI) Framingham Heart Study (FHS), the following disabilities were observed at 6 months post-stroke among ischemic stroke survivors who were at least 65 years old [5]:

- Fifty percent had some hemiparesis (i.e., paralysis on one side of the body)
- Thirty percent were unable to walk without some assistance
- Twenty-six percent were dependent in activities of daily living (e.g. feeding, dressing, bathing, moving from a bed to a chair, etc.)
- Nineteen percent had aphasia (i.e., loss or impairment of the power to use or comprehend words)
- Thirty-five percent had depressive symptoms
- Twenty-six percent were institutionalized in a nursing home

Also reported in the NHLBI FHS study, 50 to 70 percent of stroke survivors regain functional independence, but 15 to 30 percent are permanently disabled [5].

1.3. Stroke rehabilitation

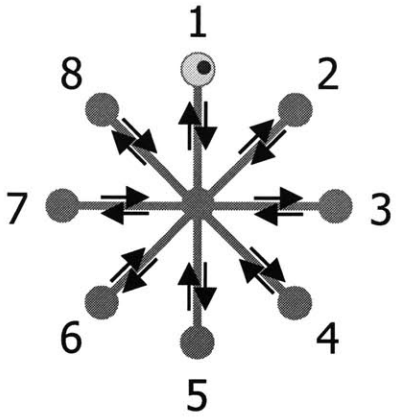

Figure 1.1. Sketch of target locations during planar robot therapy. Patients are directed to move towards the target when its color goes from blue to red (depicted by medium gray and light gray). The smaller circle in target 1 represents the location of the patient's arm.

In addition to traditional rehabilitation methods, robots and computers can support and enhance a clinician's productivity as they facilitate a disabled person's functional recovery. MIT-MANUS is a two-degree-of-freedom (2-DOF), planar, direct-drive robot [46]. During previous studies, MIT-MANUS either used impedance control to guide a stroke patient's arm through a desired trajectory or simply supported the patient's arm against gravity [3,55,60,97]. During both cases, kinematic data and the x-y-z components of the interaction force between the subject and the robot were recorded. A typical therapeutic "game" is displayed in Figure 1. A computer monitor was placed in front of the subject displaying a center target and eight equally spaced radial targets similar to a compass pattern (1-N, 2-NE, 3-E, etc.). A cursor, currently inside target 1, depicted where the end of the robot arm was relative to the targets. The clinician positioned the subject's arm at the center target and started the first trial. During the trial, a desired target changed from blue to red to cue the subject to move to target 1 (as shown with dark gray and light gray), back to center, to target 2, back to center, etc. The therapy session consisted of 3 blocks of 20 trials (in addition, a trial consisting of 16 unassisted movements to/from each target took place before and after each of the 3 blocks). An impedance controller with constant stiffness and damping was used to guide the patient's arm along a minimum jerk "virtual" trajectory of constant duration from the initial target to the desired target.

Reinkensmeyer et al. are also investigating therapy and performance measurement using a 1-DOF robotic device called ARM ("Assisted Rehabilitation and Measurement guide"; orientation in vertical and horizontal planes can be adjusted manually resulting in multiple degrees of freedom) [79,80]. Another robotic device being developed is called MIME ("Mirror Image Movement Enabler") [16]. MIME utilizes a PUMA robot and moves the impaired limb to mirror movements of the contralateral limb. Although MIME is a 3-DOF robot, it is not back-drivable so active force feedback is needed to make the robot respond, although slowly, to subjects' movements.

1.4. Overview of remaining chapters

- Chapter 2. Using a conceptual framework, the processes underlying human motor learning will be introduced as intuitive building blocks for the development of the performance-based progressive algorithm.
- Chapter 3. A novel adaptive impedance control system will be introduced. Different metrics to characterize the performance of patients during therapy will be investigated and related to motor learning. Numerical simulations of a robot arm model interacting with a patient arm model will be used to define performance measures that quantify performance at the human-machine port of interaction. Based on these performance measures, a progressive algorithm will be introduced that is intended to challenge patients to improve while keeping them motivated by changing the difficulty of the task and providing positive reinforcement.
- Chapter 4. Results from chronic stroke patients who underwent the performance-based progressive therapy (PBPT) protocol will be discussed. Clinical results will show a significant enhancement of motor recovery relative to the sensorimotor and progressive resistance protocols. Performance indicators from the chronic stroke patients who participated in the PBPT protocol will be analyzed and the results will provide an empirical link between motor recovery and motor learning.
- Chapter 5. An experimental method to estimate arm mechanical impedance will be introduced and implemented in a manner suitable for clinical use with patients

(specifically, on the robot used during therapy, MIT-MANUS). Simulations of the man-machine interaction will identify shortfalls of the experimental and analytical methods. Compensation techniques will be proposed to minimize the effect of the shortfalls on the impedance estimate.

- Chapter 6. The reliability and accuracy of the spectral estimation method described in Chapter 5 will be evaluated by connecting the end-effector of the robot to a mechanical spring array. Results of arm impedance measurements conducted on unimpaired subjects will be compared to previously published data of the arm during maintained posture. The sensitivity of the estimate to the spectral analysis parameters and the material properties of the arm trough that supports the subject's forearm during testing will be discussed. Then, preliminary results from patient testing will be presented.
- Chapter 7. The final chapter summarizes the major conclusions and contributions from this work and suggests future research directions that might benefit from the PBPT protocol and the arm endpoint impedance spectral estimate.

Chapter 2

Human motor learning

2.1. Summary

This chapter provides background on topics related to human motor learning, such as appropriateness of task difficulty, practice scheduling, and knowledge of performance or results, mainly from a behavioral or experimental psychologist's perspective. Although the experimental results and conceptual framework for motor learning and motivation are not as mathematically intensive as other approaches (e.g., self-organization/dynamic patterns theory [52] and neural network models of learning that utilize forward/inverse models [48,104]), they do provide insight related to what methods have (and have not) aided human subjects who were learning motor tasks. Although several aspects of the performance-based progressive therapy algorithm and protocol were influenced by the topics discussed in this chapter, they are not guaranteed to enhance recovery.

2.2. Motor learning

Before discussing models of motor learning, definitions and characteristics related to motor learning will be introduced. Similar to most abstract concepts, learning has been defined in a variety of ways. The Oxford English Dictionary defines learning as "the action of receiving instruction or acquiring knowledge; in psychology, a process which leads to the modification of behavior or the acquisition of new abilities or responses, and which is additional to natural development by growth or maturation" [71]. In addition, relative to anatomy and physiology, it also defines motor as "designating the neural structures (nerves, neurons, etc.) that initiate and coordinate movement, especially those that cause contraction of skeletal muscle or other effector activity, such as glandular secretion; of or relating to such structures of the nervous system" [71].

Therefore, motor learning can be defined as the acquisition of capabilities to coordinate movement of the musculoskeletal system to complete a novel task. Although this definition may be a step in the right direction, notice that it also contains several abstract concepts. For instance, how does one determine that a "capability to coordinate movement" has truly been "acquired" (i.e., the skill becomes internalized in the subject)? Must the subject exceed a certain level of performance ad infinitum? For that matter, how does one measure performance? How does one determine whether the task being learned by a subject is "novel"? Researchers may be able to guarantee task novelty with infants, but this becomes more difficult as subjects grow older and their repertoire of motor skills becomes more refined. The following sections will address these issues.

2.2.1. Measuring performance

One difficulty associated with quantifying motor learning is that the underlying processes in the central nervous system (CNS) that allow human beings to learn are not easily observed or measured. Several methods do exist that quantify electrical and biochemical activity in the brain as well as structural information about brain tissue, e.g. electroencephalography, magnetic resonance imaging (MRI), positron emission tomography (PET). The electrical activity in a brain can be measured with an electroencephalograph (whose output is an electroencephalogram, termed an EEG). Computer images generated by MRI provide structural and biochemical information about brain tissue by graphically displaying the response of a magnetic field to short bursts of radio waves. In comparison, PET can measure the metabolic activity of the brain, i.e., oxygen consumption, by analyzing gamma rays that are released when radioisotopes inhaled by the subject decay. Despite these technical achievements, the brain is exquisitely complex and the data is difficult to interpret. This requires one to infer that learning has occurred by measuring changes at the behavioral level [85].

With this in mind, it is important to select a measure that accurately and reliably reflects the task being learned. Due to the nature of motor skills, kinematic variables related to displacement, velocity, and higher-order derivatives, and kinetic variables related to force and torque are commonly used. Temporal variables may also be used, i.e., timing of a sequence of movements, total duration to complete movement, total time

on target during a tracking task, etc. With some tasks, the nature of the goal may be coarse-grained. For example, when learning to make free throws in basketball, the two possible outcomes are either making a basket or missing one. When playing horseshoes, the ultimate goal is to have the horseshoe ring a steel pole that has been hammered into the ground, but a secondary more-refined goal is for the horseshoe to land close to the pole. Once the performance measure is identified, its evolution throughout the learning trials provides one indication that the task is being learned during practice. However, for reasons to be discussed in the following sections, interpreting performance gains during training as motor learning is oversimplifying the complex processes that occur in the CNS [52,69,86].

2.2.2. Effect of practice on performance

One fundamental concept that is used to quantify motor learning is the "law of practice" [85]. Performance curves that characterize learning are usually negatively accelerated functions such that the rate of improvement tends towards zero with practice. Depending on how the performance measure is defined, the subject could start at a large value and approach a smaller one (e.g. mean distance between the subject's position and the center of a circular target during a tracking task) or start at a small value and approach a larger one (e.g. total time within circular target during the same task). A common formula used to describe the law of practice is a power function such as

$$L = aP^b \tag{2.1}$$

where L is a measure of performance, P is a measure of the amount of practice, a is a constant multiplier, and b is a constant exponent.

Although performance curves are sometimes called learning curves, behavioral scientists are wary about interpreting changes in performance curves as a reflection of learning [85]. Recall, motor learning was defined as the acquisition of capabilities to coordinate movement of the musculoskeletal system to complete a novel task. The performance curve gives an indication of how well a subject is performing the task during a particular range of trials, but it does not necessarily give an indication of whether the capability for movement has been internalized by the CNS [85]. The following section

reviews two methods that are commonly used to quantify whether motor learning has occurred (retention of skills) or whether learning one task has an influence on learning another task (transfer of skills).

2.2.3. Quantifying motor learning with retention or transfer tests

Although performance measures are usually related to the amount of practice by power functions, the goal for training a motor skill is not only to improve performance during the learning trials, but also to enable subjects to perform the skill whenever the need arises in the future. After a skill is learned (i.e., a capability for movement is acquired via practice), an abstraction of the skill called a "motor memory" develops in the CNS during a process called consolidation. Brashers-Krug et al. [10] provided psychophysical evidence that a rest period of four hours was sufficient for the CNS to consolidate the motor memory of producing point-to-point movements in a novel force field that was generated by a two-link planar robot. In a later study, Shadmehr and Holcomb [89] used PET to investigate the brain activity of subjects after they had completed a motor task similar to the one in [10]. Specifically, the regional cerebral blood flow (an indirect marker of neural activity) was monitored to infer that the motor memory had shifted from the prefrontal regions of the cortex to the premotor, posterior parietal, and cerebellar cortex structures within six hours [89]. However, recent work by Caithness, et al. [17] has challenged the idea of consolidation because four tests from three different laboratories were unable to replicate the results from Brashers-Krug et al. [10]. Instead, their experimental results support another hypothesis of memory formation that proposes memories can shift between active and inactive states [10].

Because humans tend to learn motor skills quickly, novel tasks used to investigate the processes involved in motor learning are often contrived. However, humans who take time to learn a motor skill for personal reasons most likely expect to use that acquired capability in the future. In addition, employers who train their employees to complete a particular task, e.g. assemble manufactured parts, are interested in evaluating how that training impacts employee performance and their investment in human capital. Based on these concerns, subjects that participate in learning studies are commonly called back at prespecified time intervals to determine whether their performance has degraded over

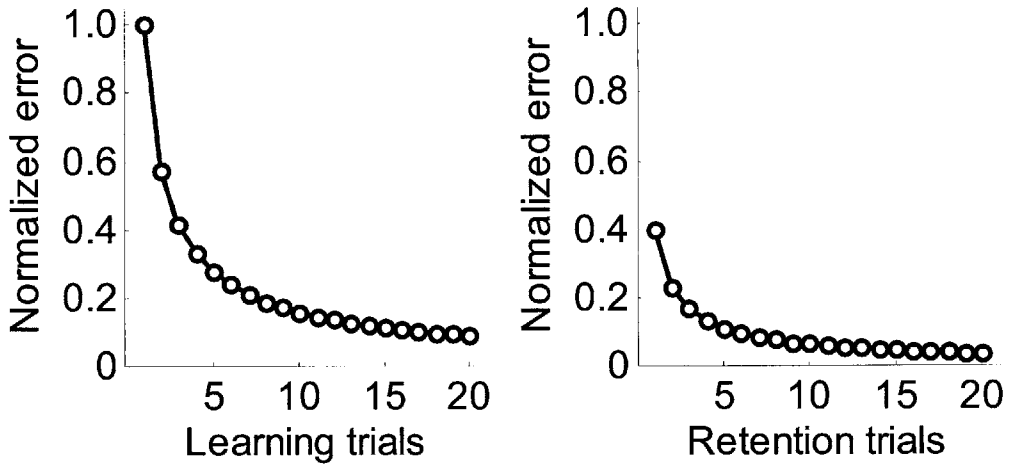

Figure 2.1. Hypothetical practice curves to demonstrate the ability to learn a task and the ability to retain the ability to perform the task after a retention interval.

time [85,86]. If the performance measures during their early callback trials are worse than the performance measures during their late learning trials, the callback trials could be used to determine how long it takes them to perform the skill as well as they did during the latter part of their original learning trials. This information might suggest improvements in training techniques to increase the longevity of the acquired skill.

Schmidt and Lee [85] discuss the concept of motor forgetting which refers to losing capabilities for movement that have been acquired via motor learning. At the theoretical level, motor forgetting is a term used to indicate the opposite of motor learning, i.e., the loss of a motor memory. At the behavioral level, motor forgetting pertains to decreases in performance that occur between the original learning trials and trials conducted after the skill is acquired. In this context, motor skills are evaluated at the behavioral level to infer the state of motor memory at the theoretical level.

Retention is defined as the persistence of the gains in performance that had occurred while practicing a motor task (or the lack of persistence if total motor forgetting occurred) [85]. In order to measure retention, time must pass between the learning trials and the retention trials (this passage of time is referred to as a retention interval; its length depends on the task being learned and the design/purpose of the experiment). Figure 2.1 displays hypothetical performance curves of normalized error for a session of 20 learning trials and a session of 20 retention trials. The curves in Figure 2.1 were generated with

power functions that had a common exponent. Several different measures to quantify retention have been proposed in past studies of motor learning. Absolute retention measures are based on the performance measures of the subject during the retention trials, but not during the learning trials; relative retention measures are based on the performance measures of the subject during the learning and retention trials [85].

Absolute retention is simply defined as the value of the performance measure from the first retention trial (Figure 2.1, retention trial 1: 0.14). Relative retention measures, such as difference scores and percentage scores, are defined by mathematically comparing the absolute retention score with performance measures from the learning trials. The difference score is defined as the absolute retention score minus the value of the performance measure at the last learning trial (Figure 2.1, learning trial 20: 0.09; 0.14-0.09=0.05). The percentage score describes the difference score as a percentage of the amount that the performance measure improved during the learning trials, e.g. in Figure 2.1, performance measure from learning trial 1 minus that from trial 20 (100%*0.05/(1-0.09) equals 5.5%). Schmidt and Lee [85] also discuss a "savings score" that is meant to quantify the "savings" in relearning the task relative to the performance level reached during the learning trials. The savings score is defined as the number of retention trials needed by a subject to perform the task as well as he/she did during the last learning trial. For the hypothetical case shown in Figure 2.1, this occurs between retention trials 6 and 7 so the savings score would be 7. In general, experimental results will appear to be a power function superimposed with a random function. This might make absolute and relative retention measures more difficult to calculate and interpret because data from the learning and retention trials will not be monotonically decreasing from trial to trial.

Although these estimates of retention are widely used, they exhibit the same drawbacks that performance measures did relative to motor learning. That is, the true quantity of interest is an internal memory state that cannot be observed directly. Since retention measures are based on performance measures, they can only be used to infer the state of the motor memory and the process of motor forgetting. Schmidt and Lee [85] recommend using the absolute retention measure because it is the simplest and most straightforward one to interpret, whereas the relative retention measures are based on two

or more values of the performance measures which may cloud their interpretation. Despite their recommendation, it seems as though the absolute retention measure would still have to be compared to the performance measures during the learning trials in order to infer whether any retention occurred during the retention interval.

Transfer tests provide an indication whether learning one coordinated movement task influences the performance of subjects when they learn a different task [85]. Similar to the retention trials, time must pass between the learning trials and the transfer trials. Therefore, retention trials and transfer trials are similar; the only difference is that retention trials retest the subjects on the same task that they practiced during the learning trials, whereas transfer trials evaluate the performance of the subjects on a different task. One experimental method to test for transfer involves two groups of subjects. While the first group learns a transfer task (A) and then learns the desired task (B), the second group only learns task B. The performance curves of both groups completing task B are then compared. If group 1 performs task B better than group 2, then practicing task A has also increased the capability of group 1 to perform task B and "positive transfer" has occurred from task A to task B. To the contrary, if group 1 performs worse than group 2, then practicing task A has decreased the capability of group 1 to perform task B and "negative transfer" has occurred.

Figure 2.2 displays hypothetical cases of positive and negative transfer where the circles depict the performance curve of the group that only practiced the desired task and the squares depict the performance curve of the group that learned the transfer task beforehand (adapted from Figure 14.2 in [85]). If the performance of groups 1 and 2 is indistinguishable, then "zero transfer" has occurred, i.e., learning task A had no impact on the capability of group 1 to learn task B. One caveat of this experimental method is that groups 1 and 2 are assumed to have the same "capability" to complete task B at the onset. That is, if both groups were to learn **only** task B, then their performance curves would be indistinguishable. If this assumption were not made, then any number of factors could have caused the differences seen in Figure 2.2. This section has demonstrated how retention and transfer tests can be used to determine whether a practiced capability for movement has been retained and whether learning one motor task can affect the performance and retention on another task. In the following section,

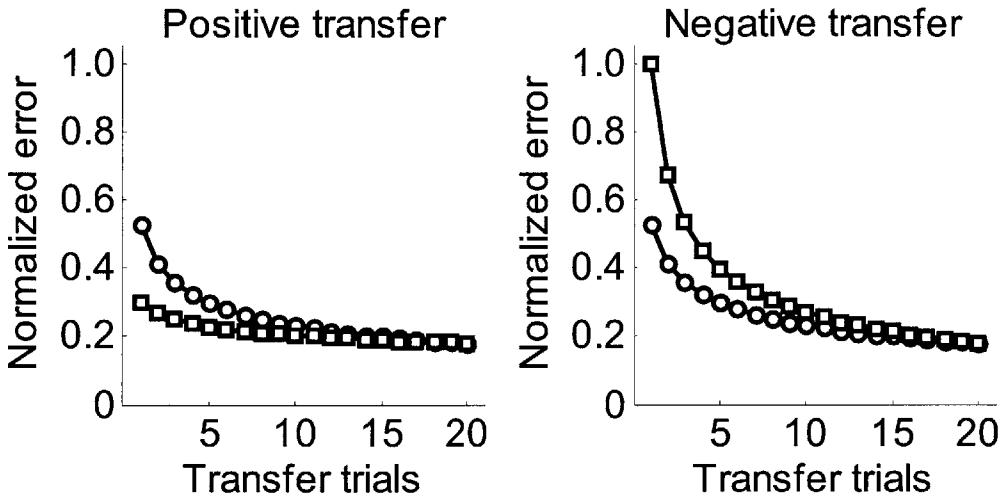

Figure 2.2. Hypothetical practice curves during transfer trials to demonstrate the concepts of positive and negative transfer.

different ways to structure practice will be introduced and evidence from past retention and transfer experiments will be summarized.

2.2.4. Structuring practice sessions to enhance motor learning

As the proverb "practice makes perfect" suggests, the amount of time practicing a task leads to better performance. However, another proverb "nobody is perfect" suggests that perfection is unattainable. Indeed, the law of practice represented by a power function in Equation (2.1) asymptotically approaches a value, but as the amount of practice increases, the rate at which it approaches that value becomes slower and slower. For many tasks, a variety of practice techniques can be used to improve performance both during the original practice trials and during the retention (and/or transfer) trials. One might wonder if better performance while the skill is being acquired using a particular practice technique will always lead to better performance during the retention session. This section will discuss several different methods to structure practice and address how these techniques tend to affect performance during the practice and retention/transfer trials.

Two common practice techniques used during motor learning studies are blocked practice and random practice. During a blocked practice session, the task objectives remain fixed during a block of practice trials and the practice session may consist of several blocks of different tasks. For example, if A, B, and C are different tasks to be

completed 3 times each during a practice session, AAABBBCCC and CCCAAABBB are two possible blocked practice orders. Random practice sessions, on the other hand, consist of a randomly or quasi-randomly ordered set of the different tasks, e.g., CBAACBCAB, BACABCBAC. The first question to be addressed is what are the effects of blocked and random practice orders on the acquisition, retention, and transfer of motor skills.

Shea and Morgan [91] were the first to investigate the effects of blocked and random practice orders on motor skill acquisition and learning by utilizing a double-retention/transfer experimental design. In order to prescribe practice sessions with blocked and random orders, all subjects learned to complete three different movement patterns (e.g. A, B, and C) during a practice session. Each movement pattern was illustrated on a card located above a colored stimulus light. After a stimulus light came on, subjects picked up a tennis ball from the ball's starting position, knocked over three wooden blocks in the order depicted on the card above the stimulus light, and then placed the ball at its final position. Subjects in the blocked group completed 18 trials of each movement pattern (total of 54 trials) and subgroups were formed to counterbalance the practice order, i.e., not all subjects practiced the movement pattern corresponding to stimulus A first, B second, and C third. Subjects in the random group also completed 18 trials of each of the three movement patterns, but the order of their trials was quasi-random such that the same movement pattern could be performed in no more than two consecutive trials. The double-retention design was constructed by splitting the blocked and random practice groups in two subgroups to investigate the immediate (10 minutes after practice) and delayed (10 days after practice) retention. Although the groups also performed additional transfer tasks (knocking down 3 blocks in a new order and knocking down 5 blocks) after the retention trials, the primary interest of this discussion is retention. By splitting the groups in two, Shea and Morgan eliminated the possibility that the immediate retention test might influence the delayed retention test. During the retention tests, subjects completed three trials of each of the three movement patterns specified in both random order and blocked order. This was done to eliminate either group from having an unfair advantage during the retention trials. That is, if only a random order were used, the blocked group would be at a disadvantage because they did

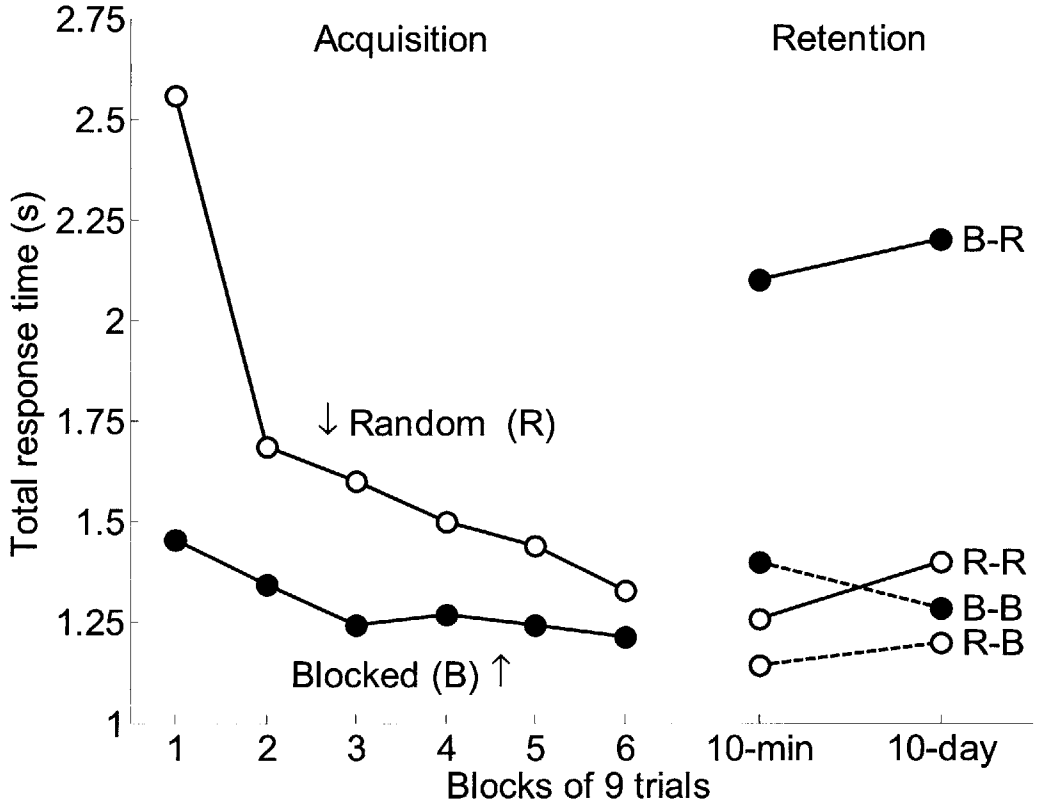

Figure 2.3. Double-retention experimental design revealed that random practice orders result in poorer performance during acquisition, but superior performance during retention (Shea and Morgan [91]).

not have prior experience with random ordering. A similar argument could be made if only a blocked order were used.

Figure 2.3 displays results from the acquisition and retention trials (adapted from Figure 10.9 from [85], which Schmidt and Lee adapted from [91]). The results presented during the acquisition session were the average total movement times, measured in seconds, from the blocked and random practice groups. Total response time was defined as the sum of the reaction time (RT) and the movement time (MT), where RT was the time from the stimulus to the initial movement and MT was the time from the initial movement to the final ball placement. The 54 acquisition trials were divided into 6 blocks of 9 trials. Because the blocked and random practice groups completed blocked and random retention trials, the results for retention shown in Figure 2.3 consist of four acquisition-retention combinations, namely, random-random (R-R), random-blocked (R-B), blocked-random (B-R), blocked-blocked (B-B). Similar to the results from the

acquisition trials, the results from the nine retention trials were averaged together. Although a line connects the immediate and delayed retention subgroups, recall that these subgroups were evaluated during the immediate or delayed retention session, not both. Results for subgroups that completed random (blocked) retention trials are depicted with solid (dashed) lines.

The results from this study exemplify the fact that the performance during practice trials may not be indicative of how well subjects learned the motor skill being practiced. Notice, although the performance of the blocked practice group was better the performance of the random practice group during the acquisition trials, there was a complete reversal of performance between the two groups (B-R relative to R-R and B-B relative to R-B) during the retention tests. That is, despite performing worse during the acquisition trials, the subjects who practiced using random task orders performed better than those who practiced using blocked task orders on the random retention trials AND the blocked retention trials. This finding is commonly referred to as the contextual interference effect [85,91].

Blocked practice, in which all trials of a common task must be practiced consecutively before changing tasks, and random practice, in which no consecutive trials can consist of a common task, are the two extremes of practice scheduling. Several researchers have investigated various practice orders using combinations of these two extremes to determine whether an optimum practice order exists. In this context, the optimum order would be the one that improves performance during acquisition trials by decreasing (but not eliminating) the amount of contextual interference and that retains (or exceeds) the performance advantage exhibited by random practice orders during retention trials. Two studies that examined this research area and proved to be insightful will be discussed next.

Lee and Magill [62] used a "serial" practice order that was similar to a random practice order because no two consecutive trials were the same. However, the tasks were always presented in the same order so subjects could predict which task would be next. For instance, if three tasks A, B, and C were to be practiced, examples of serial practice orders would be ABCABC..., CABCAB..., BACBAC..., etc. They also tested groups of

subjects with blocked and random practice orders. The experimental results of their blocked and random groups were very similar to the results reported by Shea and Morgan [91]. In addition, the results of the group that used serial practice orders were indistinguishable from the group that used random practice orders both during the practice trials and during the retention trials [62]. This suggests that the repetitiveness of blocked practice may be what causes better performance during the acquisition trials and worse performance during the retention trials [85].

Al-Ameer and Toole [4] conducted an experiment similar to Shea and Morgan [91] to determine whether a compromise between repetitiveness and randomness of practice orders would be beneficial to motor skill learning. In two of their subject groups, blocks of two and three trials were randomly ordered. Similar to the two studies discussed previously, groups of subjects with blocked and random practice orders were also included. Instead of using the sum of reaction time (RT) and movement time (MT) as the performance measure, they considered RT and MT separately. The contextual interference effect was observed in the groups with blocked and random practice orders for both RT and MT (reinforcing the results from [62,91]). Al-Ameer and Toole also reported that the randomized blocks of two and three trials resulted in better performance during the acquisition trials and similar or improved performance during the retention trials as the random group [4]. In fact, using randomized blocks of three trials resulted in RT and MT values that were significantly faster than the groups with random practice trials and randomized blocks of two trials [4].

Guidance is another method used to structure practice sessions, but it is somewhat different from the order in which the task is practiced. Although guidance can be administered during practice in a variety of ways, its primary intent is not to allow the subject to make errors during practice sessions. For example, a form of extreme guidance could be to conduct a motor learning study where the experimental apparatus follows a desired trajectory exactly. To lesser degrees, an experimenter could manually make corrections to a subject's movement by using a hand-over-hand technique or simply use verbal commands to eliminate deviations from the desired movement pattern. Many of the initial studies that utilized guidance reported that it had a significant positive effect on subject performance during acquisition [85]. However, this is not very surprising

because the role of guidance is to minimize errors made by subjects. As demonstrated by contextual interference, improved performance during acquisition does not always lead to improved performance during retention and transfer trials. So, does a similar observation apply to guidance as well?

Schmidt and Lee [85] discuss a study conducted by Armstrong [6] that compared three different forms of guidance as subjects learned a complex spatiotemporal elbow movement pattern. Specifically, one group of subjects practiced the movement pattern while the mechanically controlled experimental apparatus minimized their deviations from the desired trajectory (Figure 2.4). Another group practiced the movement pattern with visual feedback from a monitor that displayed traces of the current elbow position and the desired position. Subjects in the last group were told how they performed after each trial and were shown a plot after each block of 15 trials with the desired trajectory and their movement during the previous trial. Practice trials were distributed over three days with 5 blocks of 15 trials on the first and second days and 4 blocks of 15 trials on the third day. Armstrong also conducted two blocks of 15 transfer trials on the third day to quantify motor learning. During the transfer trials, subjects were told to reproduce the elbow movement pattern without any form of guidance.

Figure 2.4 displays the "average integrated absolute error" for each group in the study (adapted from Figure 11.12 in [85], which was reprinted from [6]). Graphically, the effects of guidance on learning (as quantified by retention and/or transfer trials) are similar to the effects that contextual interference had on learning. As more guidance was provided to the subjects during the acquisition trials, their integrated error decreased, as expected. However, the transfer trials revealed that the capability to reproduce the movement pattern decreased as the amount of guidance increased. Although providing an excessive amount of physical guidance tends to impede learning, some forms of extrinsic feedback may be beneficial. Notice, subjects who received feedback after each movement and a summary graph after each block of 15 movements retained their capability to make the complex elbow movement when this feedback was withheld during their transfer trials.

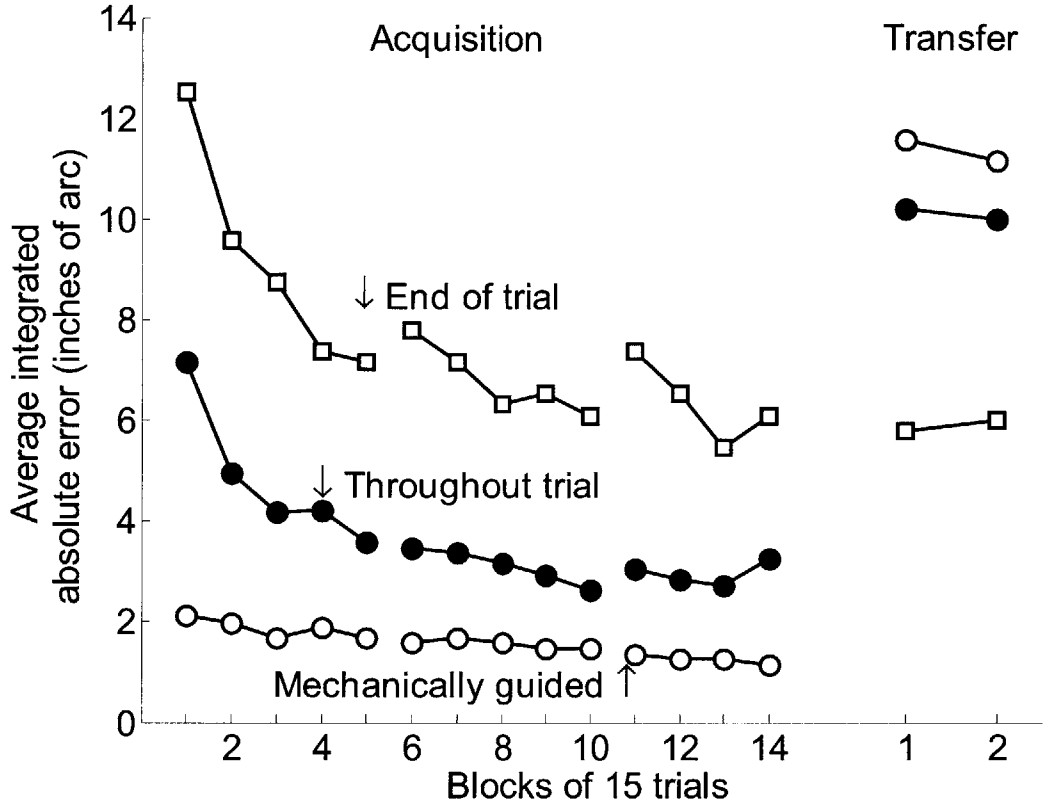

Figure 2.4. Mechanical guidance results in superior performance during practice trials than other forms of feedback, but lackluster performance during retention – performance of mechanically-guided group during retention is similar to end-of-trial group's initial performance (Armstrong [6]).

Schmidt and Lee [85] discussed two additional aspects of guidance that are rarely studied, namely, reduction of fear and prevention of injury. Psychologically, these aspects allow subjects to concentrate on the task that is being learned instead of being preoccupied with anxiety. One example of this form of guidance is a child learning to ride a bike. Initially, frequent guidance can be provided by installing training wheels on the bike. After the child develops more skill and feels more comfortable on the bike, the training wheels can be removed and an adult can run alongside the child on the bike until the child feels comfortable riding the bike without any guidance. The results from the guidance study conducted by Armstrong suggest that providing some forms of extrinsic feedback during motor learning may be beneficial. The following section discusses methods used to structure extrinsic feedback that can enhance motor learning.

2.2.5. Structuring extrinsic feedback to enhance motor learning

With some simple tasks, the outcome of a practice trial might be obvious to the subject. Recall the examples of shooting free throws (hit or miss) and playing horseshoes (ring or closeness to pole) mentioned in section 2.2.1. As tasks become more complex, subjects may require more feedback to evaluate how successful their practice attempts were. The sensory system receives both intrinsic and extrinsic feedback. Intrinsic feedback is composed of both proprioceptive and exteroceptive feedback [85]. Sources of proprioceptive feedback come from within the subject, e.g., muscle lengths, muscle forces, joint displacements, balance, pain. Sources of exteroceptive feedback, on the other hand, occur outside of the body, e.g., focal vision, hearing. Extrinsic feedback, or augmented feedback, is any information provided about the task that is supplemental to intrinsic feedback [85]. Two sources of extrinsic feedback that are used in motor learning studies will be discussed next, namely, knowledge of performance (KP) and knowledge of results (KR).

As defined by Schmidt and Lee [85], KP is "augmented feedback related to the nature of the movement produced" and KR is "augmented feedback related to the nature of the result produced in terms of the environmental goal." KP is feedback related to the movement made by a subject and can refer to aspects of the movement that the subject is either vaguely aware of, e.g., exact kinematics of limbs (as measured by sensors or viewed with videotapes), or cannot be aware of, e.g. blood pressure or variations in muscle electrical potential (i.e., an electromyogram/EMG) [85]. For example, when practicing free throws, players might be instructed by their coaches to bend their knees more or to follow through the throwing motion of their arms. KP can be presented to the learner while the movement is being made, which is called concurrent KP, or after the movement is complete, which is called terminal KP. The experimental study by Armstrong [6] discussed in the previous section involved both types of KP. Subjects in the first group were given terminal KP after each trial and subjects in the second group saw a graph with their current elbow position and the desired elbow position while they practiced, i.e., concurrent KP.

Although KP can be presented to subjects concurrently or terminally, KR, by definition, can only be presented terminally because it is feedback related to the outcome of a movement. KR can be information that is provided to subjects on Boolean scales (such as "hit" and "miss"), coarse scales (such as "very short", "short", "good", "long", and "very long"), and fine scales that usually consist of physical measurements (such as "low by 1 cm" while playing darts or "far right by 3 meters" when kicking field goals). As mentioned earlier, KR feedback can also be based on combinations of these scales (i.e., the ultimate goal of horseshoes is to ring the pole, but the closeness to the pole after the horseshoe is thrown also matters).

In addition to selecting the KR parameter and defining its scale, an experimenter specifies how often the feedback will be given to subjects and how the results will be presented, e.g. verbal, graphical, multi-colored lights. All four of these experimental design specifications may impact the performance during the acquisition and retention trials (to quantify learning, the acquisition task is usually performed during the retention trials without any KR). Although KR is intended to have a beneficial impact on skill learning, several experimental studies have shown that the effects of some forms of KR can also be detrimental [87,93,101,106,107]. An overview of these results will follow.

Motor learning literature usually classifies how often feedback is given in terms of "absolute frequency of KR" or "relative frequency of KR". Absolute frequency of KR is the number of trials during the experimental session that KR is presented to the subject and relative frequency of KR is the percentage of trials during the session that the subject is provided KR (i.e., 100% times absolute frequency divided by total number of trials) [85]. As mentioned earlier, although KR provides subjects with a measure of how well they performed the task being learned, it is not always beneficial to provide KR on every acquisition trial.

In general, practice curves for acquisition and retention performance with a relative frequency of 100% appear similar to the mechanically guided case in Figure 2.4. That is, subjects that are provided 100% KR tend to perform well during acquisition trials and poorly during retention trials. By nature, KR provides information that supplements a subject's intrinsic sensory feedback. If subjects become more dependent on extrinsic

feedback, they may become less dependent on intrinsic feedback and rely less on how it felt to complete the movement (similar to the subjects who received mechanical guidance during their acquisition trials). When KR is removed during the retention trials, their only source of feedback will be intrinsic feedback, and, since the impact of this information on the CNS was minimized during acquisition, they will not have an intrinsic reference of how completing the task was supposed to feel [85,86].

Swinnen, et al. [93] conducted an experiment that suggested another reason why 100% KR might have a detrimental effect on learning. In this study, two groups of subjects received 100% KR during two days of training (6 blocks of 15 trials on each day). The first group received KR instantaneously, whereas the second group received KR after a delay of 3.2 seconds. Although both groups had similar trends (i.e., their performance scores approximately followed the same exponential progression) during the acquisition trials on the first day, the delayed KR group outperformed the instantaneous KR group throughout the second day of acquisition trials and the retention trials (no KR during retention trials; retention intervals of 10 minutes, 2 days, and 4 months) [93]. The authors suggested that instantaneously providing KR after the trial was complete blocked the subjects' brains from processing alternative sources of information (i.e., intrinsic feedback) and thereby reduced the effectiveness of the practice sessions to train the subject [85,93]. Notice, both explanations are related to losing sensory information, either by the subject becoming dependent on extrinsic feedback or by the extrinsic feedback interrupting the subject's neural processing of intrinsic feedback.

Another observation can be made relative to the Swinnen et al. study [93]. Although 100% KR presented instantaneously impeded motor learning for one group of subjects, 100% KR delayed by 3.2 seconds enhanced learning for another group. That is, providing 100% KR does not always impede learning and, depending on the skill being learned and the experimental design, could potentially enhance learning. Other methods related to scheduling KR have also been investigated and will be discussed next.

"Summary KR" presents environmental outcomes for all of the trials to the subject, but only after a certain number of trials have passed [85]. For example, consider a practice session that consists of 20 trials of a timing task with a "5-trial summary KR"

feedback schedule. The absolute timing error will be the KR measure. Subjects do not receive any feedback about their performance until after trial 5, at which time they are given a graph that displays the absolute timing error for trials 1-5. Similarly, after trial 10, they are given a graph that displays the absolute timing error for trials 6-10, and so on. This method allows subjects to concentrate on their intrinsic feedback during a group of trials and then receive extrinsic feedback about their performance during those trials. A variation of this method called "Average KR" is structured in the same manner as summary KR, but subjects are simply told the average value of the performance measure during a group of trials [85].

Yao, et al. [107] conducted a motor learning study with five different groups of subjects: every-trial KR, 5-trial summary KR, 5-trial average KR, 15-trial summary KR, and 15-trial average KR. The skill being learned was an aiming task that required both spatial and temporal accuracy. The skill acquisition phase consisted of 4 blocks of 15 trials and 1 block of 15 no-KR retention trials were conducted 10 minutes and 2 days after the practice trials were complete. Figure 2.5 displays the absolute timing error from this study (adapted from Figure 12.11 in [85], which was reprinted from [107]). The results for the spatial measure of their aiming task were similar to the results for the temporal measure [107]. Although the group with every-trial KR performed better than the other four groups during the practice session, they performed the worst on the retention trials. The 5-trial average KR group performed the best on the retention trials. For both the 5- and 15- trial cases, the acquisition and retention trials of the summary KR and average KR groups were similar to each other. These data might suggest that the subjects interpreted the summary KR and average KR methods in a similar way, perhaps simply taking a mental average of the graphical data [85].

Another method of presenting KR called the "fading procedure" [85] also has some appeal. Instead of providing feedback to the subject every trial or after a fixed number of trials, this method provides feedback more often during the early trials when the subject is trying to become accustomed to the task. As the practice session continues, the KR information is provided less often. However, once again, it is difficult to know a priori which schedules of fading will enhance learning for different subjects and different tasks.

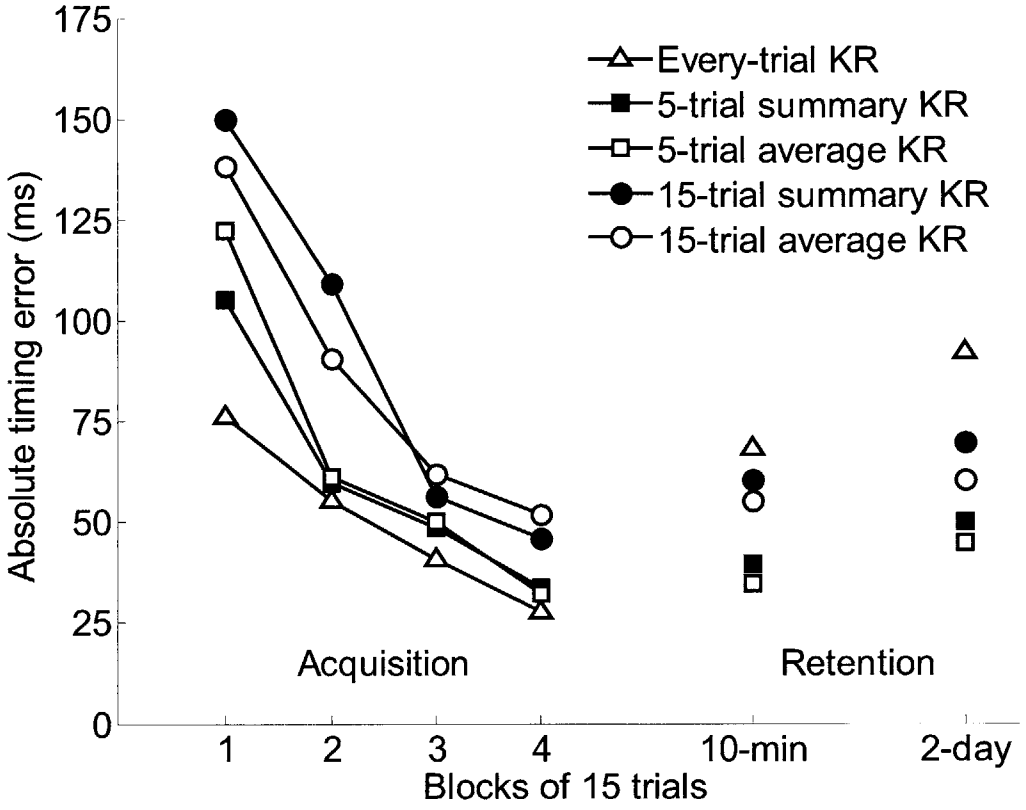

Figure 2.5. Frequency of KR can impede or enhance learning depending on the task. Providing KR too often acts similar to guidance in that subjects depend on feedback; low frequency KR might delay the ability of the subject to make corrective actions (Yao, et al. [107]).

Unfortunately, there does not seem to be a universal method to structure feedback that maximizes performance during the acquisition and retention trials for all motor skills. In section 2.2, several concepts related to behavioral studies of motor learning, such as defining performance measures, quantifying the effects of practice, quantifying learning with retention and transfer trials, structuring practice sessions, and structuring extrinsic feedback, were discussed. The following section will introduce several early conceptual models of motor learning that were devised from empirical results and then will expound upon the schema theory of motor learning [84].

2.3. Conceptual models of motor learning

Although the schema theory proposed by Schmidt [28,85,86] is arguably the most widely used conceptual model of how humans learn motor skills, it was certainly not the first

conceptual model of motor learning. In the late 1800s, Bryan and Harter conducted experiments with telegraphers to study the perceptual and motor changes that occur during the acquisition of the motor skill of telegraphy [11,12]. Their view of skill learning was that it was a hierarchy of habits. The first skill required to become a proficient telegrapher using Morse code was the ability to discriminate units of time. Morse code consists of dots ('.': one unit of time of an auditory signal), dashes ('-': three units), and intervals of time with no signal (one unit between dots and dashes of a letter, three units between letters, and six units between words). Next, telegraphers would learn the various sequences of dots and dashes that represent alphanumeric characters (e.g., letters: a '-.', b '-...', c '-.-.'; numbers 0 '-----', 1 '.----', 2 '..---'). After these first two skills were learned, Bryan and Harter noted plateaus in some subjects' practice curves that were followed by rapid improvements in performance [85]. They proposed that the plateaus persisted until a higher order habit was formed, i.e., instead of hearing dots and dashes, the telegraphers would start "hearing" letters, then words, and perhaps even larger units of a sentence [85].

Fitts and Posner discussed learning of perceptual-motor skills in terms of three distinct phases of practice – the cognitive phase, the associative phase, and the autonomous phase [28]. The cognitive phase of practice occurs when the learner is first introduced to the task. Instructions on what the task is and how performance is measured allows the learner to use and evaluate different strategies to accomplish the desired motor task. The associative phase is characterized by subtle changes in motor performance once the learner has selected the most effective strategy to complete the task, i.e., fine-tuning. The autonomous phase of practice is characterized by lower cognitive requirements because the skill has become ingrained in the motor skills repertoire of the learner after many practice trials [85].

Adams developed his closed-loop theory of motor learning based on empirical laws developed for slow, linear-positioning movements and assumed that these empirical relationships would pertain to all types of movement skills that are learned [2]. The crux of Adams' theory was that all movements are made by comparing ongoing feedback from the limbs to a sensory reference signal that is learned during practice. The reference signal was called the "perceptual trace" because inherent feedback from the limb was

assumed to be stored in the CNS during each move. During correctly made movements, proprioceptive and exteroceptive sensory feedback would reinforce a desired trace of sensations for the CNS to follow. In addition to the perceptual trace, a "memory trace" was needed to produce the movement to allow the motor control system to have the capability to detect errors between the actual movement and the desired movement [85].

According to Schmidt, the primary reason why he developed his schema theory for motor learning was that the closed-loop theory proposed by Adams did not address open-loop motor control processes [85]. Although the closed-loop theory was empirically based, it was based on experimental evidence of slow, linear-positioning movements. Since the range of voluntary reaction times to proprioceptive stimuli for the human neuromuscular system is 80-120 ms, the perceptual trace cannot be used to guide the limb when making rapid movements [51]. (The range of voluntary reaction times to visual stimuli is 150-250 ms and can increase significantly if the human has to decide between several movement patterns, i.e., the choice effect [39,51].) In addition, the existence of central pattern generators in the spinal cord enables complex coordinated motions of limbs in the absence of feedback, e.g. walking and running [64]. However, Despite the drawbacks relative to open-loop processes, it should become obvious throughout the discussion of the schema theory that Schmidt did find some of Adams' concepts appealing.

2.3.1. Schema theory

The primary concept from the closed-loop theory that was incorporated by the schema theory was the need for two states of memory in the motor control system, termed the recall and recognition memory states. The purpose of the recall memory state was movement production whereas the purpose of the recognition memory state was movement evaluation [85]. The recall memory state addressed open-loop motor control processes such as rapid movements. It was responsible for storing the motor commands necessary to complete rapid movements without relying on proprioceptive and exteroceptive feedback. On the contrary, the recognition memory state was more involved with the production of slow movements and was similar to the perceptual trace in the closed-loop theory of motor learning. With slow movements, the recognition

memory state evaluates the magnitude and the direction of errors between the desired and actual movements while the recall memory state attempts to minimize this error by moving the limb along the desired path with "small bursts" of motor commands [85].

Central to Schmidt's schema theory of motor learning was the existence of generalized motor programs (GMPs). After discussing past work that introduced the notion that the motor control system uses prestructured sets of commands to make movements in an open-loop manner [47,61], Schmidt defined a motor program as an "abstract representation that, when initiated, results in the production of a coordinated movement sequence" [85]. One line of evidence was mentioned previously. Specifically, closed-loop feedback cannot be used to guide the limb when making rapid movements because the range of voluntary reaction times for the human neuromuscular system is 150-250 ms [86]. In addition, deafferentation studies, where the afferent sensory signals into the spinal cord were either cut surgically or numbed with anesthesia while the efferent signals were left intact, have shown that close to normal movements can be achieved without feedback from limbs in both humans and monkeys [75-77]. The time it takes for a subject to begin moving after a stimulus is presented (i.e., reaction time) also suggests movement planning is taking place. In 1960, Henry and Rogers designed an experiment where subjects were asked to make a different movement during three sets of trials while using the same stimulus (a gong sound) [39]. Since the subjects received the same stimulus for the three sets of movement responses of increasing complexity, namely,

a. lift finger off of reaction key
b. lift finger off of reaction key-reach forward-grasp ball suspended by string
c. lift finger off of reaction key-reach forward-strike suspended ball with back of hand-reach back-push dummy key next to reaction key-reach forward-strike different ball with back of hand

the only difference from trial to trial was in the nature of the movement [85]. Henry and Rogers found that the reaction time for subjects to begin moving increased as the complexity of the desired response increased (a: 159 ms, b: 195 ms, c: 208 ms) [39]. This result suggests that the increase in reaction time was due to an increase in the time required for the motor control system to plan the response once the stimulus was delivered, i.e., to generate a motor program to complete the task.

Schmidt also assumed that motor programs were generalized, meaning each program contained an abstract code about the order of the events, the temporal structure of the events, and the relative force required during each event [85]. Parameters, such as the duration of the movement, the muscles to be used, and the muscle loads that are required, enable the same GMP to produce many different movements [85]. Assuming motor programs are generalized also helps to reduce the storage and novelty problems encountered in the fields of motor control and motor learning. If motor programs were not generalized, each movement would not only have to be stored separately in the brain but also be accessible on demand (thereby, creating a storage problem). In addition, novel movements can be made simply by selecting parameters for GMPs that have not been used before.

Schmidt assumed that after a movement is made with a GMP, the individual briefly stores the following four types of information [85]:

- initial conditions, e.g. bodily positions, muscle tensions, weight of thrown objects
- parameters assigned to the GMP when the movement was planned, e.g. movement duration, muscles used, muscle exertions
- outcome of the movement in the environment in terms of knowledge of results, e.g. distance object was thrown, closeness of object relative to target
- sensory consequences of the movement, i.e., how the movement felt, looked, etc.

With this information, the individual can develop the recall schema and the recognition schema that are the building blocks of the schema theory of motor learning. The following paragraphs will describe how Schmidt envisioned schema development in the CNS.

The recall schema, like the recall memory state, is related to the production of movement. Figure 2.6 displays a hypothetical relationship between the individual movement outcomes and the parameters used to produce them (circles) along with the recall schema (line) that is formed (adapted from Figure 13.7 in [85]). As an example, consider an individual throwing a baseball. The abscissa of the graph designates an outcome of the movement, e.g. the distance thrown, whereas the ordinate designates a parameter that the individual used in the GMP, e.g. speed of joint rotations, amount of body weight shifted during throw, position at which individual lets go of ball. Each dot

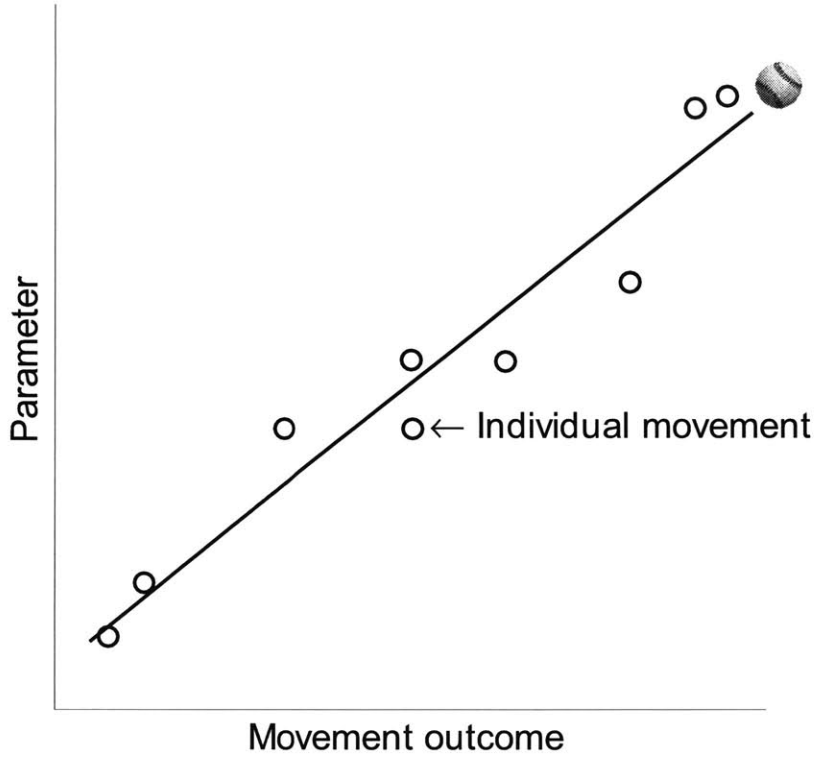

Figure 2.6. Hypothetical formulation of recall schema occurs when an association develops between the prescribed motor control plan and the movement outcome.

on the graph represents a practice trial of throwing the baseball. The regression line represents the learned relationship between movement outcomes and the parameter values used, and is defined as the recall schema by Schmidt [85]. After each throw of the baseball, the movement outcome and parameters used are noted and the recall schema is refined. As learning continues, Schmidt assumed that the motor control system would only have to store the recall schema, not the individual results of all practice throws (thereby, avoiding a storage problem).

After making a movement using a GMP, the individual also stores the initial conditions and the sensory consequences of the movement. In Figure 2.7, the graph on the left side displays three hypothetical recall schemas that were formed from three different initial conditions, e.g. throwing baseballs, softballs, and footballs (adapted from Figure 13.8 in [85]). The recognition schemas used for movement evaluation are formed in a similar manner as the recall schemas, but the learned relationships are now between

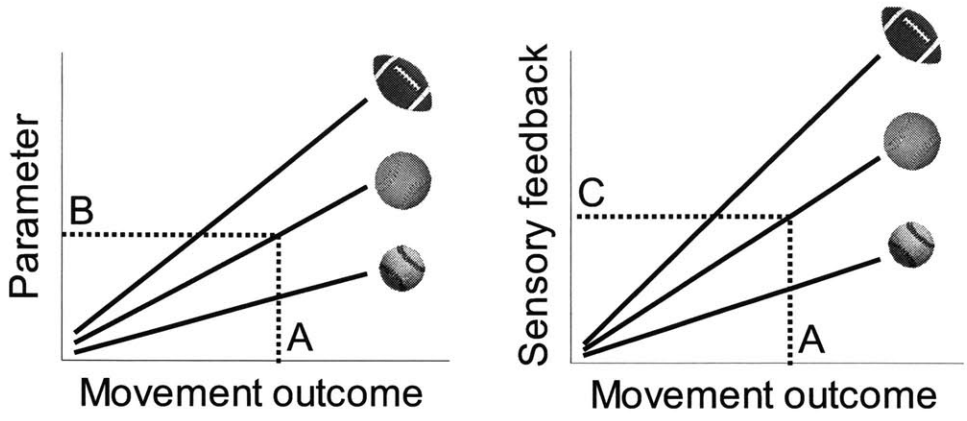

Figure 2.7. Hypothetical formulation of recognition schema occurs when an association develops between the sensory feedback that was experienced and the movement outcome. Once the schemata are developed, a subject can complete a desired outcome (A) by selecting the motor control parameters to complete the movement (B) and evaluating the sensory feedback during and after the movement execution.

the movement outcomes and the sensory consequences of the practice trials. The hypothetical recognition schemas for throwing baseballs, softballs, and footballs that correspond to the hypothetical recall schemas are shown in the graph on the right side of Figure 2.7 (adapted from Figure 13.9 in [85]).

After the recall and recognition schemas are established via practice trials, they are used by the individual to complete future movements in the following manner. First, the initial conditions and desired outcome are identified, e.g. the task is to throw a softball a certain distance A (depicted by point A in Figure 2.7). Second, the recall schema for throwing softballs is cross-referenced at point A to identify the parameters that should be used in the GMP (depicted by point B in Figure 2.7). Third, the recognition schema for throwing softballs is cross-referenced at point A to provide the individual with an estimate of what the sensory consequences should feel like for the desired movement outcome to be produced (depicted by point C in Figure 2.7). Finally, the individual can generate the appropriate motor program to throw the softball, observe how far the ball was thrown (relative to expectations form the recall schema), and evaluate whether the expected sensory consequences were experienced (relative to expectations form the recognition schema) [85]. In this manner, learning never truly ends because each new trial can influence the recall and recognition schemas.

2.3.2. Schema learning of motor skills

Recall, the primary reason that Schmidt developed the schema theory was that the closed-loop theory was unable to explain how rapid movements were made because it depended on feedback from the perceptual trace that experienced delays greater than the duration of many rapid movements. The schema theory accounts for both fast and novel movements by using the GMP as its foundation. Rapid movements are made by selecting appropriate parameters for the GMP prior to executing the GMP, whereas slow movements are made using closed-loop feedback. Novel movements are made by simply using parameters that have not been used before. Although Schmidt strongly believes that experimental evidence supports GMPs, he also points out that its structure is somewhat vague. For example, how are motor programs formed in the first place and how do humans make movements before any schemas exist [85]? There is also uncertainty surrounding the physiological mechanisms that the CNS would use to develop and use the recall and recognition schemas [85].

Although Schmidt's recognition schema is similar to Adams' perceptual trace, the primary difference is the underlying assumptions of how each is acquired. While Adams assumed that intrinsic feedback from both proprioceptive and exteroceptive senses reinforces the perceptual trace **only** when the movement pattern and its outcome are correct (i.e., incorrect movements can degrade perceptual trace), Schmidt assumed that intrinsic feedback from **every** movement contributes to the formation of the recall and recognition schema. That is, the initial conditions, parameters, sensory consequences, and outcome of every movement are still used by the CNS to refine the schema even when the movement and its outcome do not match the expectations of the subject [85]. Experimental results support the schema theory. In section 2.2.4, several examples were provided that demonstrated random practice orders resulted in poorer performance during the acquisition trials, but better performance during the retention trials.

The schema theory provides a good conceptual framework for the macro-processes that underlie motor learning. Although Schmidt does not delve much into the neurological and physiological aspects of the CNS (i.e., micro-processes), the schema theory emphasizes the collective roles of the CNS, the musculoskeletal system, and the

sensory system that enable humans to learn motor skills. In essence, we humans learn motor skills by learning rules about how our bodies function [85]. Since the development of schema depends on the CNS storing information about initial conditions, parameters of GMPs, sensory consequences, and environmental outcomes, Schmidt and Lee pointed out that, if any of these items were missing, a degradation in learning would occur [85]. They also pointed out KR can be the most crucial piece of information for some motor skills. For example, Trowbridge and Cason [94] conducted a motor learning study in which blindfolded subjects were instructed to draw 100 lines that were 3 inches long. Without vision, subjects needed supplemental feedback (KR) to learn to complete the task effectively. As another example, passive movements do not affect recall schema because only active movements require parameter specification and execution of GMPs. Similarly, if proprioceptive feedback is missing, either permanently with spinal deafferentation or temporarily with anesthesia, then no recognition schema associated with the missing feedback can be updated (although degraded forms of learning might occur via intact senses such as vision) [85].

2.4. Conclusions

Although this chapter provides insight into how humans learn motor tasks and how to develop practice sessions to enhance learning, the topics discussed are not guaranteed to aid recovery. However, the working hypothesis to be introduced in the following chapter will be that the processes that underlie motor recovery are similar to the processes that underlie motor learning. Therefore, incorporating methods that enhance learning into rehabilitation therapy could be informative, depending on the outcome of patient trials. The remaining chapters of this thesis will discuss the development and the effectiveness of the performance-based progressive therapy protocol.

Chapter 3

Performance-based progressive algorithm and therapy protocol

3.1. Summary

This chapter discusses the development of performance-based progressive robot therapy that was based on methods that enhance human motor learning and motivation such as practice scheduling, practice variability, positive reinforcement, etc. Research to date has shown that repetitive task-specific, goal-directed, robot-assisted therapy is effective in reducing motor impairments in the affected arm after stroke. One research goal is to determine the optimal therapy tailored to each stroke patient that will maximize his/her recovery. A component of the proposed method to achieve this goal is a novel performance-based impedance control algorithm, which is triggered via a speed threshold to guarantee proper timing between efferent motor commands and afferent sensory signals. The algorithm first identifies the ability of patients to move and aim, and then independently adjusts the time allotted for patients to complete their movements and the level of stiffness that assists patients to aim their movements. Knowledge of performance via verbal comments of the clinician and knowledge of results via a visual display after every five trials are used to challenge patients to improve their performance or, at the very least, maintain it.

3.2. Robotic and information technology – assist, quantify, and enhance rehabilitation

The use of robotics to assist, quantify, and enhance rehabilitation is a growing field whose clinical application was pioneered in the 1990s via a collaboration between MIT and the Burke Medical Research Institute. Unlike predecessors who used robotics as an

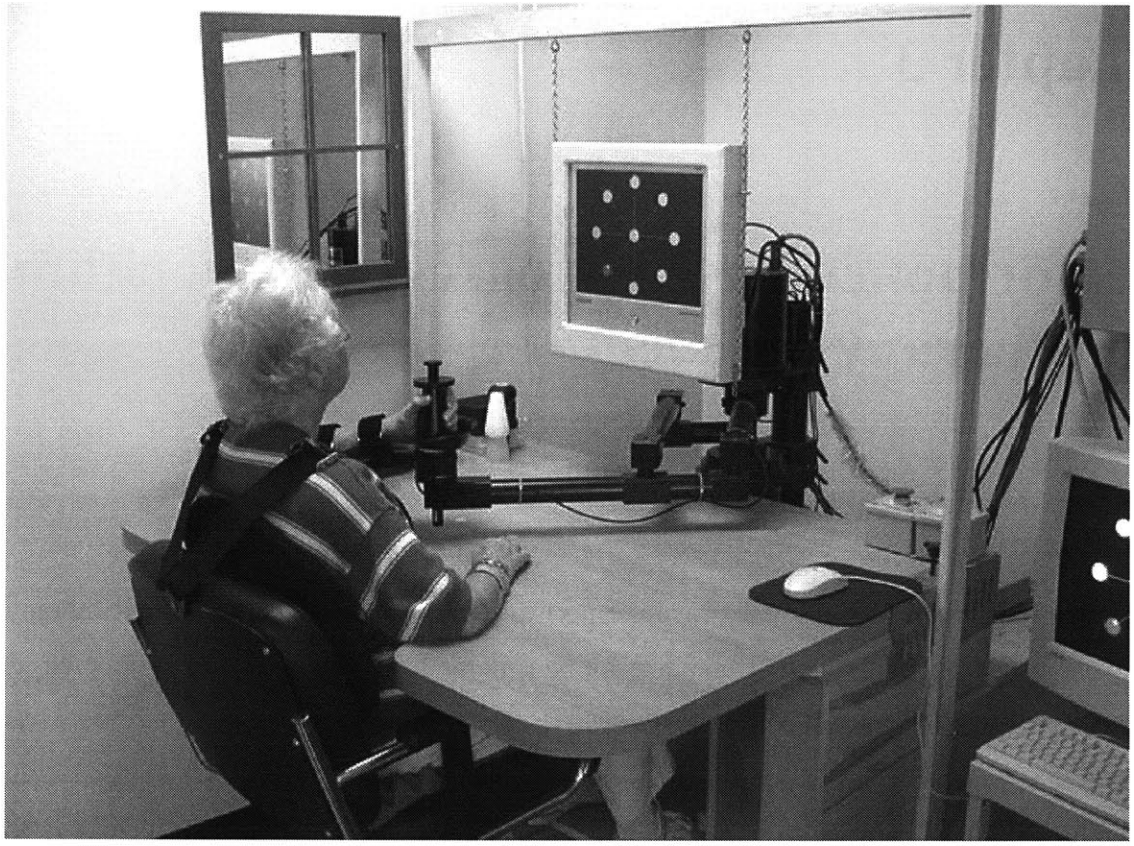

Figure 3.1. Stroke patient participating in a robot-aided therapy session.

assistive technology for the disabled, their approach used robotics to support and enhance the productivity of clinicians who facilitate the functional recovery of stroke patients. Robot-aids not only are more efficient in delivering certain routine physical and occupational therapy activities to patients, but also provide a rich stream of kinematic and kinetic data that quantifies the interaction between the patient and the robot. The initial patient study used fixed-duration, repetitive, goal-directed therapy and was able to clearly demonstrate that using robotics in a rehabilitation setting was effective in reducing motor impairments in the hemiplegic arm after stroke [3].

The centerpiece of our ongoing research and development program is MIT-MANUS, a robot specifically designed for clinical, neurological applications [46,55]. InMotion^2 is a descendent of MIT-MANUS that is commercially available through Interactive Motion Technologies, Inc. under license to MIT (Figure 3.1). Because the mechanical system was designed to have low intrinsic end-point impedance, with extremely low inertia and friction (i.e. it is highly "back-drivable"), MIT-MANUS is able

to move smoothly and can rapidly comply with a patient's motor actions [53,56]. Industrial robots can be programmed to follow different paths or exert different forces, but not both simultaneously. Robots designed to be back-drivable can be programmed to deliver interactive therapy and different force field patterns (active, semi-active, passive, resistive) including patterns that are non-existent in nature [57,72,73]. The robot sensors permit accurate and essentially continuous measurement of the key variables relevant to motor behavior, namely position, velocity, and interaction forces. MIT-MANUS has two degrees-of-freedom (DOF) that can move a patient's shoulder, elbow, and hand in a horizontal, gravity-eliminated plane. During a therapy session, the patient's hemiplegic arm is placed in a customized arm support that is attached to the end-effector (i.e. handle) of the robot arm. A trial consists of moves to and from each of the 8 targets that are oriented like a compass, starting with the north target and proceeding clockwise, i.e., N, NE, E, SE, etc. As shown in Figure 3.1, a LCD monitor in front of the patient provides visual feedback of the current location of the patient's hand and the desired target location (stimulus – target changes color from light blue to red). If the patient is unable to move, the robot guides the hand to the target in a similar manner as a therapist provides hand-over-hand assistance during conventional therapy. The following section will discuss why the neurological processes underlying motor recovery are thought to be similar to the processes underlying motor learning and why these processes might not be similar. Then, the performance-based progressive algorithm will be developed using concepts that enhance motor learning (e.g. repetition, active participation, goal specification, positive reinforcement; detailed examples of these concepts were provided in chapter 2).

3.3. Development of the performance-based progressive algorithm

A prominent theme of current research into recovery from brain injury posits that activity-dependent plasticity underlies neuro-recovery. This plasticity may be due to the unmasking of pre-existing connections, activity-dependent synaptic changes, or the growth of new synapses. Experimental support for this idea derives primarily from measurements of synaptic branching and cortical thickness in rats raised in enriched and derived environments [20-23,38] and in monkeys recovering from ischemic injury [70].

Li, et al. [63] also identified populations of neurons in the brain of the monkey (specifically, primary motor cortex) that exhibited learning-dependent activity. Although both motor learning and recovery exhibit activity-dependent plasticity, several other factors affect recovery such as re-acquisition of muscle strength, resolution of abnormal tone, etc. These recovery phenomena are not related to learning so it is unclear to what extent, if any, motor recovery resembles motor learning.

Research to date has shown that repetitive, task-specific, goal-directed, robot-assisted therapy can be effective in reducing motor impairments in the hemiplegic arm after stroke; results of initial studies showed statistically significant differences between the experimental and control groups for the shoulder and elbow, but not for the wrist and fingers [3,25,58,98]. This result for motor recovery is similar to specificity of motor learning. Schmidt and Wrisberg [86] define the specificity of learning as "the notion that the best learning experiences are those that most closely approximate the movement components and environmental condition of the target skill and target context." Since the focus of the robotic exercise was training the muscles in the shoulder and elbow to make planar movements, the gains achieved at the wrist and fingers in the robot therapy group were not statistically significant.

There is no reason to believe that a "one-size-fits-all" optimal treatment exists. Instead, therapy should be tailored to each patient's needs and abilities. Robot-assisted therapy can be delivered in a variety of ways to reduce motor impairment and enhance functional motor outcomes. Goal-directed therapeutic "games" can be designed to address motor impairments including poor coordination, impaired motor speed or accuracy, decreased grasp or dexterity, and diminished strength, as well as addressing cognitive or perceptual impairments. Recall, robotic aids can provide passive, active-assistive, active, and active-resistive exercises as well as therapeutic approaches that do not exist in nature [57,72]. The understanding of what constitutes the most appropriate therapy has already become an intensively active topic of research.

Recall, the stroke rehabilitation therapy administered during the initial clinical trials was a fixed-duration, repetitive, goal-directed exercise cued by a video display. It consisted of a series of assisted point-to-point moves, which appeared to be well suited

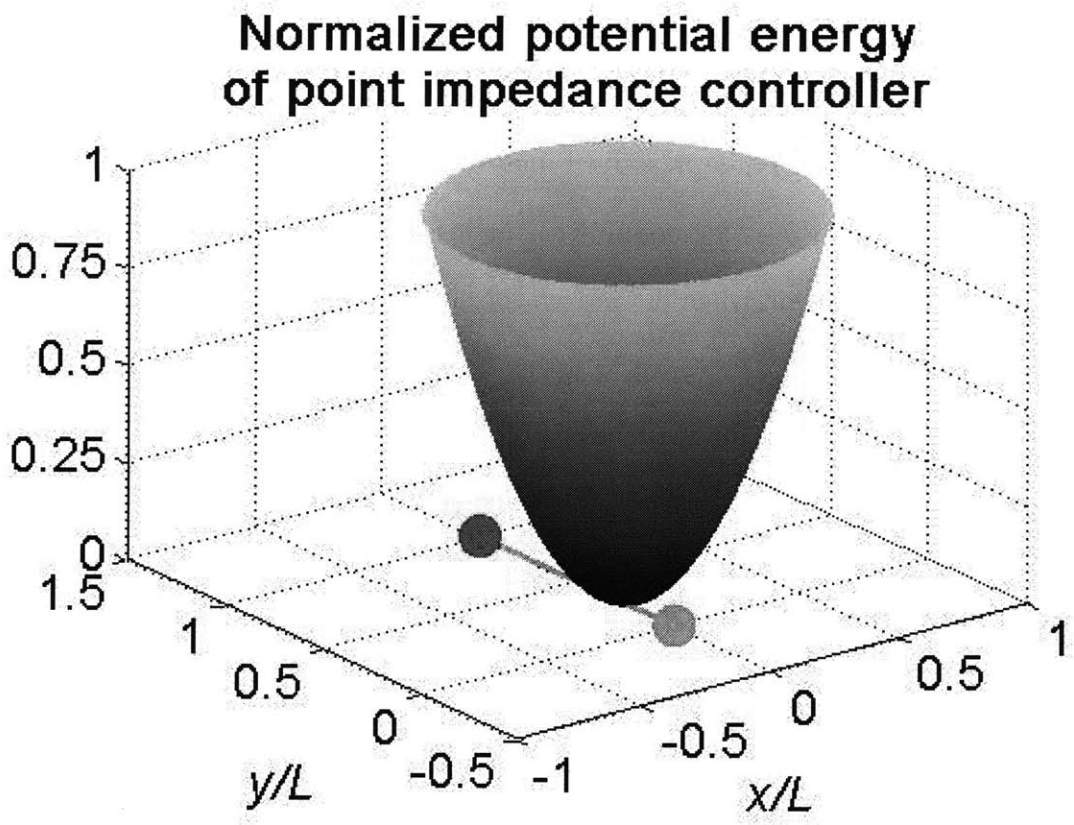

Figure 3.2. Point impedance controller assists stroke patient while moving from the center target to an outer target (currently $y = 0.25L$), but might impede capable patients from moving ahead of the commanded trajectory.

for patients with very limited movement ability. During therapy, an impedance controller [41-43] with constant stiffness and damping was used to guide the patient's arm with a minimum-jerk movement of fixed duration from the starting position ($y = 0$) to the end position ($y = L$) as shown in Figure 3.2. A minimum-jerk trajectory was selected because it describes experimental data of primates making large-amplitude, voluntary movements at intermediate speeds [31,40]. The effect of the stiffness of the controller can be visualized as a potential energy field about a moving desired position that limits deviation along the target axis, y, and its normal axis, x. Specifically, the command forces along these axes are given by

$$F_{c,x} = -kx - b\dot{x} \tag{3.1}$$

$$F_{c,y} = -k(y - y_{m.j.}) - b\dot{y} \tag{3.2}$$

$$y_{m.j.} = l_m\left[10\left(\frac{t-t_s}{t_m}\right)^3 - 15\left(\frac{t-t_s}{t_m}\right)^4 + 6\left(\frac{t-t_s}{t_m}\right)^5\right] \tag{3.3}$$

where $y_{m.j.}$ is the control system's prescribed minimum jerk displacement (m), k is the controller stiffness (N/m), b is the controller damping (Ns/m), $l_m(\equiv L)$ is the length of movement (m), t_s is the time when the movement begins (s), and t_m is the duration of the movement (s).

Assume the time when the movement to the north target commences is specified as $t_s = t_{s,1}$. If a patient is unable to complete the movement from the center target to the north target, MIT-MANUS will assist the patient by generating the forces defined in (3.1) and (3.2). During the move from the north target back to the center target, the equation defining $F_{c,x}$ remains the same, whereas $F_{c,y}$ becomes

$$F_{c,y} = -k\left(y - \left(l_m - y_{m.j.}\right)\right) - b\dot{y} \tag{3.4}$$

with $t_s = t_{s,2} = t_{s,1} + t_m$. Note, the duration between consecutive movements is t_m, i.e., $t_{s,j+1} - t_{s,j} = t_m$ and odd subscripts from 1 to 15 designate movements to the 8 outer targets whereas even subscripts from 2 to 16 designate movements back to the center target. The calculation of the forces defined by (3.1) and (3.2) or (3.4) that allow the robot to assist patients making movements to and from the 7 other targets (i.e., NE, E, SE, S, SW, W, NW) is enabled by coordinate transformations to and from the north target axis (i.e., the y–axis). First, the measured displacement and velocity vectors are rotated from the desired target axis to the north target axis via (3.5) and (3.6). Second, the controller forces that would assist movements to or from the north target are calculated via (3.1) and (3.2) or (3.4). Finally, the force vector defined relative to the north target axis is rotated back to the appropriate target axis via (3.7).

$$\begin{bmatrix} x' \\ y' \end{bmatrix} = \begin{bmatrix} \cos\theta_t & -\sin\theta_t \\ \sin\theta_t & \cos\theta_t \end{bmatrix} \begin{bmatrix} x \\ y \end{bmatrix} \tag{3.5}$$

$$\begin{bmatrix} \dot{x}' \\ \dot{y}' \end{bmatrix} = \begin{bmatrix} \cos\theta_t & -\sin\theta_t \\ \sin\theta_t & \cos\theta_t \end{bmatrix} \begin{bmatrix} \dot{x} \\ \dot{y} \end{bmatrix} \tag{3.6}$$

$$\begin{bmatrix} F_{c,x} \\ F_{c,y} \end{bmatrix} = \begin{bmatrix} \cos\theta_t & \sin\theta_t \\ -\sin\theta_t & \cos\theta_t \end{bmatrix} \begin{bmatrix} F_{c,x'} \\ F_{c,y'} \end{bmatrix} \tag{3.7}$$

where $\theta_t = 45°$ for the northeast target, $\theta_t = 90°$ for the east target, $\theta_t = 135°$ for the southeast target, etc. Note, the transformation equations (3.5)-(3.7) also apply to the north target ($\theta_t = 0°$) because the three transformation matrices simply become identity matrices.

In chapter 2, section 2.2.4, the outcomes of blocked and random orders during motor learning trials were discussed and the concept of contextual interference was introduced. Specifically, despite performing worse during the acquisition trials, the subjects who practiced using random task orders performed better than those who practiced using blocked task orders on the random retention trials and the blocked retention trials [85,91]. Recall, the initial rehabilitation therapy consisted of a fixed-duration, repetitive, goal-directed exercise cued by a video display, i.e., therapy sessions followed a blocked schedule throughout the entire therapy protocol. One approach to introduce more variability into a therapy session could be to present the eight targets in a random order, i.e., S, NE, SW, N, E, NW, SE during trial 1, NW, S, N, SW, SE, E, NE during trial 2, etc. However, due to the physical and cognitive impairments that result from stroke, this approach might cause patients to become unduly frustrated and eventually discourage them from actively participating. Another approach could be to present the targets in the same order during all trials, but tailor the assistance provided by the robot from trial to trial based on each patient's abilities in an effort to encourage the patient to actively participate throughout the therapy session. With this in mind, a novel impedance controller that allowed a wider range of interactions between the patient and the robot was developed. This controller will be discussed next.

3.3.1. Novel impedance controller

The potential energy field of the novel impedance controller is also shown in Figure 3.3. While the stiffness of the point impedance controller tends to impede the patient from moving ahead of the desired trajectory, the proposed controller allows capable patients to reach the target unassisted because $F_{c,y} = 0\text{N}$ in between the target location and the

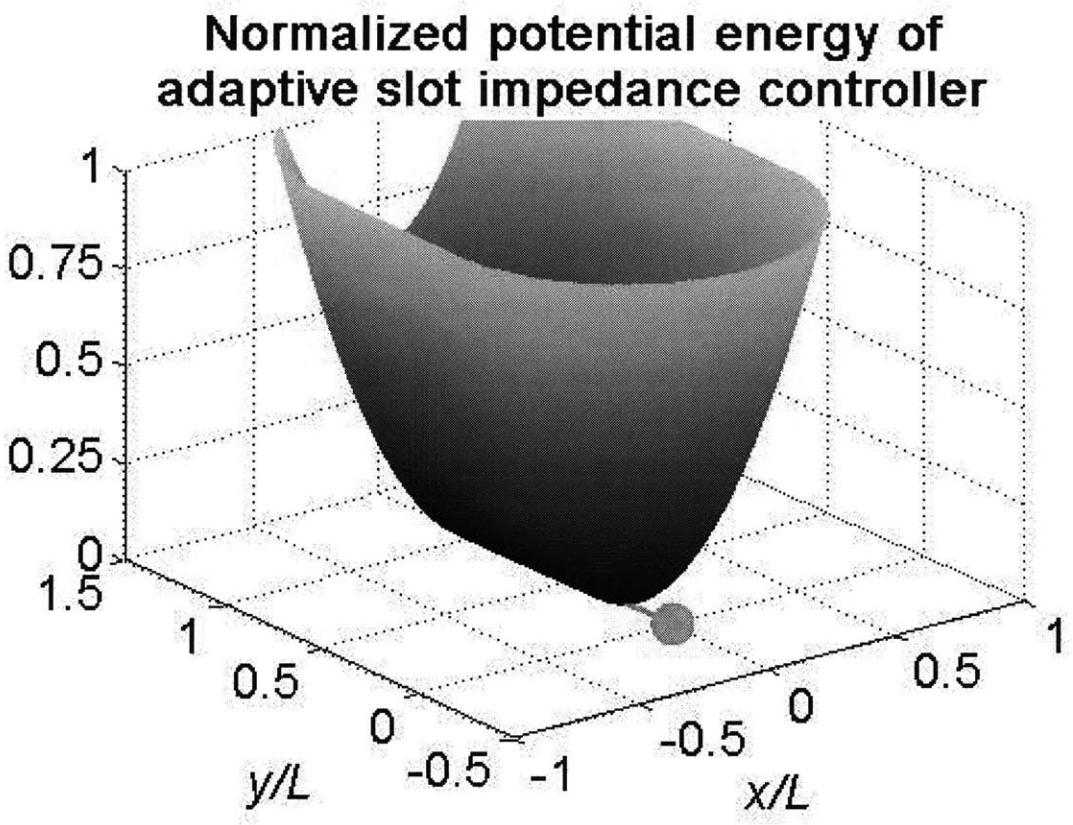

Figure 3.3. Slot impedance controller assists stroke patient while moving from the center target to an outer target (currently $y = 0.25L$) and allows capable patients to move ahead of the commanded trajectory.

position of minimum jerk trajectory specified in the control law, i.e., $y_{m.j.} \le y \le l_m$. The command forces that correspond to the potential energy field of the novel impedance controller for movements to the north target are

$$F_{c,x} = -k_{sw}x - b\dot{x} \tag{3.8}$$

$$F_{c,y} = \begin{cases} -k_{bw}\left(y - y_{m.j.}\right) - b\dot{y} & y < y_{m.j.} \\ 0 & y_{m.j.} \le y \le l_m \\ -k_{sw}\left(y - l_m\right) - b\dot{y} & y > l_m \end{cases} \tag{3.9}$$

The rotational transformations defined in (3.5)-(3.7) can also used with this controller to specify assist forces along the target axes. During performance-based progressive therapy sessions, the time allotted for the patient to make the move, t_m, and the primary stiffness of the impedance controller, termed the "sidewall" stiffness, k_{sw}, are specified

by a yet-to-be-defined algorithm that attempts to challenge patients to improve their performance. The "back wall" stiffness, k_{bw}, assists patient motion along the target axis and is held constant throughout therapy trials.

Similar to (3.1) defined for the point impedance controller, (3.8) is valid for movements to and from the outer targets. The equation used to specify $F_{c,y}$ for the movement back to the center target is defined as

$$F_{c,y} = \begin{cases} -k_{sw}y - b\dot{y} & y < 0 \\ 0 & 0 \le y \le (l_m - y_{m.j.}) \\ -k_{bw}(y - (l_m - y_{m.j.})) - b\dot{y} & y > (l_m - y_{m.j.}) \end{cases} \tag{3.10}$$

Although the point impedance controller defined by (3.1) and (3.2) or (3.4) operates robustly when the movement switches from going out to the outer target to coming back to the center target, the novel impedance control laws for $F_{c,y}$ will command a discontinuous force along the target axis if the patient did not reach the outer target. For example, if the patient required assistance during the movement and still was not able to reach the desired target location, e.g. $y = 0.95 \cdot l_m$, the controller force along the target axis would be $F_{c,y} = +0.05 \cdot k_{bw}(\mathrm{N})$ assuming the viscous damping force, $b\dot{y}$, is negligible. When the desired target switches from the outer target to the center target, the patient's location will lie within the "dead-zone" of novel impedance controller, i.e., $0 < 0.95 \cdot l_m < l_m$ so $F_{c,y} = 0$ N. Therefore, when this occurs, the commanded force will drop suddenly from $0.05 \cdot k_{bw}$ to 0 N.

Although this sudden decrease in assistance does not affect the stability or performance of MIT-MANUS, it might distract or seem harsh to the patient depending on the value of k_{bw} and by how much the patient missed the target. For this reason, dwell periods that last t_{dw}-seconds were added at the outer targets ($y' = l_m$) and center target ($y' = 0$). The desired trajectory along the y'-target axis including the two dwell periods and the initialization period (i.e., t_s) is shown in Figure 3.4.

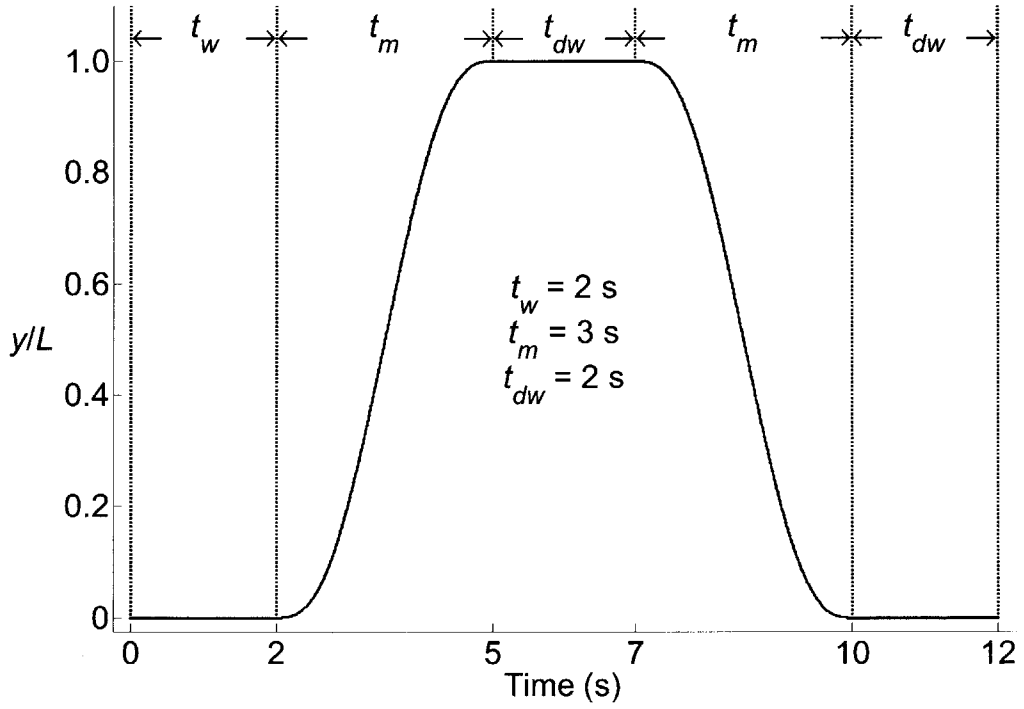

Figure 3.4. Desired trajectory of the slot's "back wall": an initialization period at the center target (at most t_w, smaller if velocity threshold is exceeded); a minimum-jerk profile from the center target to the outer target (t_m); a dwell period at the outer target (t_{dw}); a minimum-jerk profile from the outer target back to the center target (t_m); a dwell period at the center target (t_{dw}).

During the first quarter of the dwell period at the outer target, the linear shape function, $\alpha(t)$ as shown in Figure 3.5, is used to transition the control law for $F_{c,y}$ from (3.9) to a point impedance control law at the target (i.e., $F_{c,l_m} = -k_{sw}(y - l_m) - b\dot{y}$), which operates for the next $0.5 \cdot t_{dw}$-seconds. Then, during the last quarter of the dwell period, the linear shape function is used to transition the control law from the point impedance controller to $F_{c,y}$ as defined by (3.10). Specifically, the command force along the target axis during the dwell period is defined as $\alpha(t)F_{c,l_m} + (1 - \alpha(t))F_{c,y}$ where $F_{c,y}$ is defined by (3.9) during the first quarter of the dwell period and by (3.10) during the last quarter. A similar transition was prescribed at the center target. Now that the novel impedance controller has been defined, the next topic to be discussed is modeling the interaction

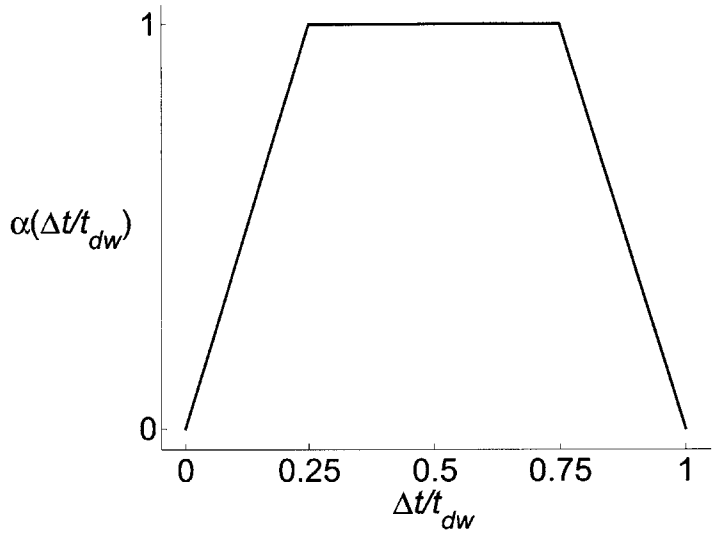

Figure 3.5. Linear scaling function used during dwell times to transition the slot impedance controller from the outer target to the center target or from the center target to the next outer target.

between the patient and MIT-MANUS. In turn, this model will be used to develop the performance-based progressive algorithm.

3.3.2. Model of patient and robot interaction

To gain a deeper understanding of the coupled dynamics of the patient and MIT-MANUS operating under novel impedance control, a state-space model of the human-machine interaction was defined by connecting a nonlinear two-link model of the robot with a nonlinear two-link model of the human arm through a virtual force transducer as shown in Figure 3.6. The nonlinear equations of motion for the robot are

$$\begin{bmatrix} H_{11}\ddot{\theta}_s + H_{12}\cos(\theta_e - \theta_s)\ddot{\theta}_s - H_{12}\sin(\theta_e - \theta_s)\dot{\theta}_e^2 + b_1\dot{\theta}_s \\ H_{12}\cos(\theta_e - \theta_s)\ddot{\theta}_s + H_{22}\ddot{\theta}_e - H_{12}\sin(\theta_e - \theta_s)\dot{\theta}_s^2 + b_2\dot{\theta}_e \end{bmatrix} = \begin{bmatrix} \tau_{c,1} + \tau_{i,1} \\ \tau_{c,2} + \tau_{i,2} \end{bmatrix} \tag{3.11}$$

where (θ_s, θ_e) are the absolute angular displacements of the robot's shoulder and elbow joints, H_{ij} with $i, j \in 1,2$ are the inertial characteristics of the robot arms, b_1 and b_2 are the viscous damping coefficients for the shoulder and elbow joints, $(\tau_{c,1}, \tau_{c,2})$ are the commanded shoulder and elbow torques, and $(\tau_{i,1}, \tau_{i,2})$ are torques equivalent to the

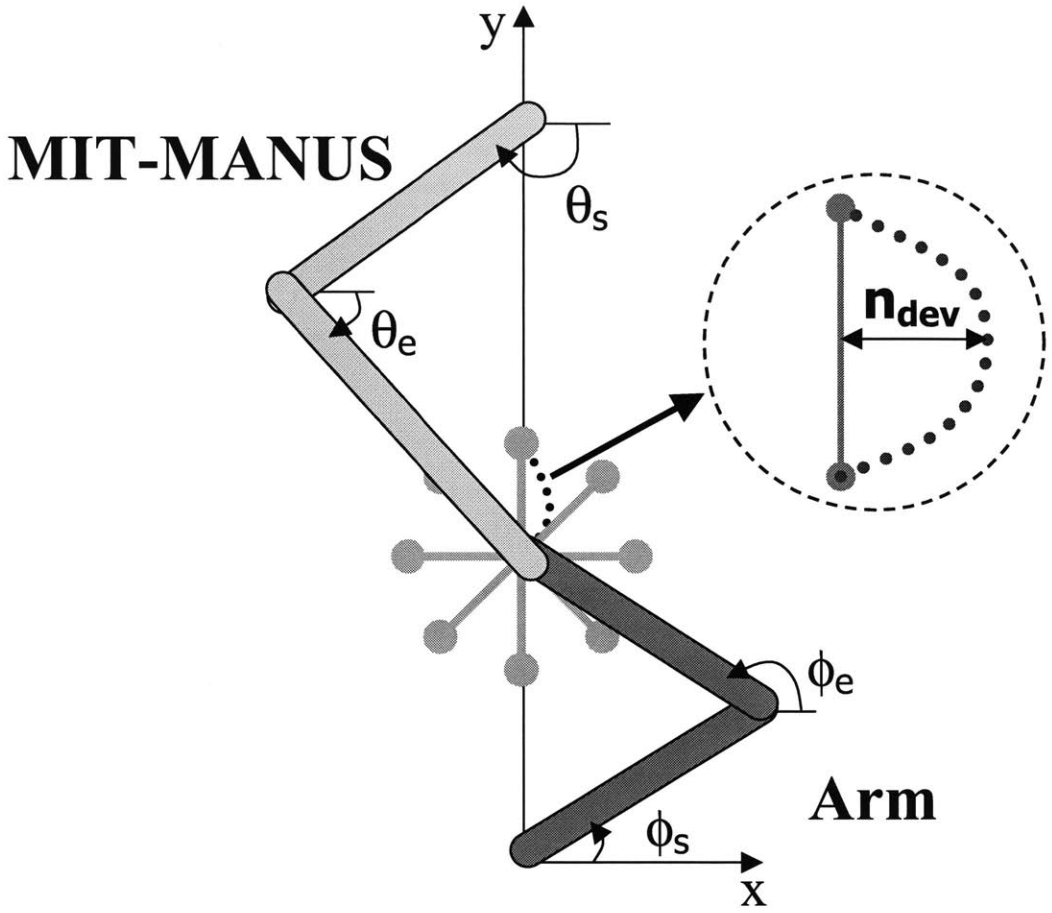

Figure 3.6. Schematic used to model the dynamic interaction between MIT-MANUS and the human arm. Both were modeled as two-link mechanisms with torque inputs at their shoulder and elbow joints. MIT-MANUS was simulated under slot impedance control. The human arm model generated torques that corresponded to a virtual trajectory to move between targets with a maximum deviation normal to the target axis of n_{dev}.

human-machine interaction forces. The command torques, $\boldsymbol{\tau}_{\mathbf{c}} = \begin{bmatrix} \tau_{c,1} & \tau_{c,2} \end{bmatrix}^{\mathrm{T}}$, are related to the command forces $\mathbf{F}_{\mathbf{c}} = \begin{bmatrix} F_{c,x} & F_{c,y} \end{bmatrix}^{\mathrm{T}}$ by

$$\boldsymbol{\tau}_{\mathbf{c}} = \mathbf{J}_{\theta}{}^{\mathrm{T}} \mathbf{F}_{\mathbf{c}} \tag{3.12}$$

Similarly, the interaction torques, $\boldsymbol{\tau}_{\mathbf{i}} = \begin{bmatrix} \tau_{i,1} & \tau_{i,2} \end{bmatrix}^{\mathrm{T}}$, are related to the interaction forces, $\mathbf{F}_{i} = \begin{bmatrix} F_{i,x} & F_{i,y} \end{bmatrix}^{\mathrm{T}}$ by

$$\boldsymbol{\tau}_{\mathbf{i}} = -\mathbf{J}_{\theta}{}^{\mathrm{T}} \mathbf{F}_{i} \tag{3.13}$$

where $\mathbf{J}_\theta = \begin{bmatrix} -l_1 \sin(\theta_s) & -l_2 \sin(\theta_e) \\ l_1 \cos(\theta_s) & l_2 \cos(\theta_e) \end{bmatrix}$ is the Jacobian matrix relating absolute joint speeds to the endpoint velocity, l_1 is the length of the link from the robot's shoulder joint to elbow joint, l_2 is the length of the link from the robot's elbow joint to the manipulandum, and the negative sign reflects the force the human exerts on the robot is equal and opposite in sign to the force the robot exerts on the human.

As mentioned earlier, the arm of the patient is also modeled as a nonlinear two-link mechanism and the equations of motion are given by

$$\begin{bmatrix} H_{ss}\ddot{\phi}_s + H_{se}\ddot{\phi}_e - C_{se}\dot{\phi}_e^2 + b_{ss}\dot{\phi}_s + b_{se}\dot{\phi}_e + k_{ss}\phi_s + k_{se}\phi_e \\ H_{se}\ddot{\phi}_s + H_{ee}\ddot{\phi}_e + C_{se}\dot{\phi}_s^2 + b_{se}\dot{\phi}_s + b_{ee}\dot{\phi}_e + k_{se}\phi_s + k_{ee}\phi_e \end{bmatrix} = \begin{bmatrix} \tau_{i,s} + \tau_{vt,s} \\ \tau_{i,e} + \tau_{vt,e} \end{bmatrix} \tag{3.14}$$

where (ϕ_s, ϕ_e) are the absolute shoulder and elbow angles in the patient arm model, $H_{ss} = m_{1a} l_{c1a}^2 + I_{1a} + m_{2a} l_{1a}^2$, $H_{se} = m_{2a} l_{1a} l_{c2a} \cos(\phi_e - \phi_s)$, $H_{ee} = m_{2a} l_{c2a}^2 + I_{2a}$, $C_{se} = m_{2a} l_{1a} l_{c2a} \sin(\phi_e - \phi_s)$, $\mathbf{B}_{\mathbf{jnt}} = \begin{bmatrix} b_{ss} & b_{se} \\ b_{se} & b_{ee} \end{bmatrix}$ is the joint viscous damping matrix, $\mathbf{K}_{\mathbf{jnt}} = \begin{bmatrix} k_{ss} & k_{se} \\ k_{es} & k_{ee} \end{bmatrix}$ is the joint stiffness matrix, $\boldsymbol{\tau}_{\mathbf{if}} = \begin{bmatrix} \tau_{i,s} \\ \tau_{i,e} \end{bmatrix} = \mathbf{J}_\phi{}^{\mathrm{T}} \mathbf{F}_{\mathrm{i}}$ are the torques caused by the interaction forces with the robot that are transmitted to the arm, $\mathbf{J}_\phi = \begin{bmatrix} -l_{1a} \sin(\phi_s) & -l_{2a} \sin(\phi_e) \\ l_{1a} \cos(\phi_s) & l_{2a} \cos(\phi_e) \end{bmatrix}$ is the Jacobian matrix of the patient arm model, $\boldsymbol{\tau}_{\mathbf{vt}} = \begin{bmatrix} \tau_{vt,s} \\ \tau_{vt,e} \end{bmatrix} = \begin{bmatrix} H_{ss}\ddot{\phi}_{vt,s} + H_{se}\ddot{\phi}_{vt,e} - C_{se}\dot{\phi}_{vt,e}^2 + b_{ss}\dot{\phi}_{vt,s} + b_{se}\dot{\phi}_{vt,e} + k_{ss}\phi_{vt,s} + k_{se}\phi_{vt,e} \\ H_{se}\ddot{\phi}_{vt,s} + H_{ee}\ddot{\phi}_{vt,e} + C_{se}\dot{\phi}_{vt,s}^2 + b_{se}\dot{\phi}_{vt,s} + b_{ee}\dot{\phi}_{vt,e} + k_{se}\phi_{vt,s} + k_{ee}\phi_{vt,e} \end{bmatrix}$ are the joint torques necessary to complete a desired movement when the subject is not connected to the robot (i.e., the virtual trajectory in joint coordinates corresponding to the desired movement in joint coordinates is $\boldsymbol{\varphi}_{\mathbf{vt}} = \begin{bmatrix} \phi_{vt,s} \\ \phi_{vt,e} \end{bmatrix} = \mathbf{K}_{\mathbf{jnt}}^{-1} \boldsymbol{\tau}_{\mathbf{vt}}$ [31,40]), and m_{ia}, I_{ia}, l_{ia}, and l_{cia} are the mass, rotational inertia about the center of mass, total link length, and distance to the center of mass of the arm ($i = 1$) and forearm ($i = 2$) specified in the patient model. The combination of virtual trajectories and muscular impedance control

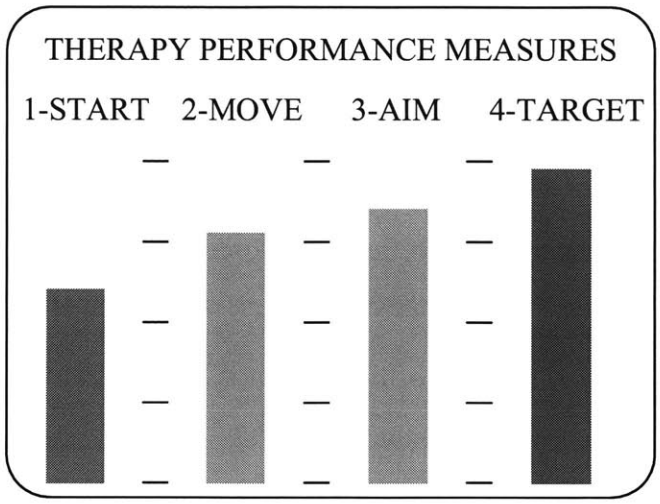

Figure 3.7. Screen layout for knowledge of results provided to stroke patients during their therapy sessions.

have been shown to experimentally describe both single-joint movements [40] and multi-joint movements [31] where the virtual trajectory appears to maximize the smoothness by minimizing the mean square jerk of the movement.

The nonlinear state-space equations of the coupled system were defined by using the robot parameter estimates determined experimentally by Foster [32] and estimates of the inertia, damping, and stiffness matrices of the human arm while maintaining posture from the unimpaired subject testing reported by Tsuji, et al. [95]. The next section will investigate several metrics based on kinematic and kinetic variables that will be used to quantify how well the patient is performing during a therapy session.

3.3.3. Development of measures to quantify patient performance

In an effort to keep patients motivated during therapy sessions, a video display provides the patient with positive reinforcement during the session (Figure 3.7). The height and color of the four bars in the display reflect patient performance. The four performance measures grade patients' ability to initiate movement (PM_1), to move from the starting position to the target (PM_2), to aim their movement along the target axis (PM_3), and to reach the target position (PM_4) [59,60]. PM_1 is the percentage of times that the patient initiated a movement towards each outer target by moving faster than a speed threshold. PM_2 and PM_3 enable the performance-based progressive algorithm to adjust t_m and k_{sw}

during a therapy session and will be described in detail later. PM_4 is the average maximum distance that the patient moved along each of the target axes.

PM_1 quantifies how many times the patient initiated movement toward the eight outer targets by moving the robot above a modest velocity threshold. If the tangential velocity of the patient $\left(V_t = \sqrt{\dot{x}^2 + \dot{y}^2} \right)$ fails to exceed the threshold within two seconds, the assisted movement to the outer target commences. To avoid discontinuous command forces when the robot begins to assist a patient (similar to discontinuity discussed earlier), the control system ramps the stiffnesses to the prescribed values of k_{bw} and k_{sw} over the initial $0.1 \cdot t_m$ s of the movement. As mentioned earlier, the impedance controller's desired trajectory has a minimum-jerk profile whose duration, t_m, will be specified by the yet-to-be-defined, performance-based, progressive algorithm. The velocity threshold is defined to be 10% of the maximum speed of this minimum-jerk trajectory, namely,

$$V_{th} = 0.10\left[1.875\left(\frac{l_m}{t_m}\right)\right] \tag{3.15}$$

Since the duration of the minimum jerk trajectory will vary depending on patient performance, success in initiating movement will also be redefined. That is, as t_m increases, V_{th} decreases, and vice versa.

Recall, PM_2 and PM_3 evaluate a patient's ability to move and aim during each trial, which consists of moves to and from eight equally spaced radial targets. These metrics are calculated from data during the move to the outer target axis and back to the center target, not during the initialization time or the two dwell times (recall Figure 3.4). The most promising candidates for PM_2 – the ability to move (top row) and PM_3 – the ability to aim (bottom row) are shown in Figure 3.8. The measures were calculated from data that was collected before and after treatment of an outpatient who participated in a sensorimotor protocol at Spaulding Rehabilitation Hospital (SRH) in Boston, MA [25,26]. The measures in the first column are derived from kinetic variables and the measures in the second column are derived from kinematic variables.

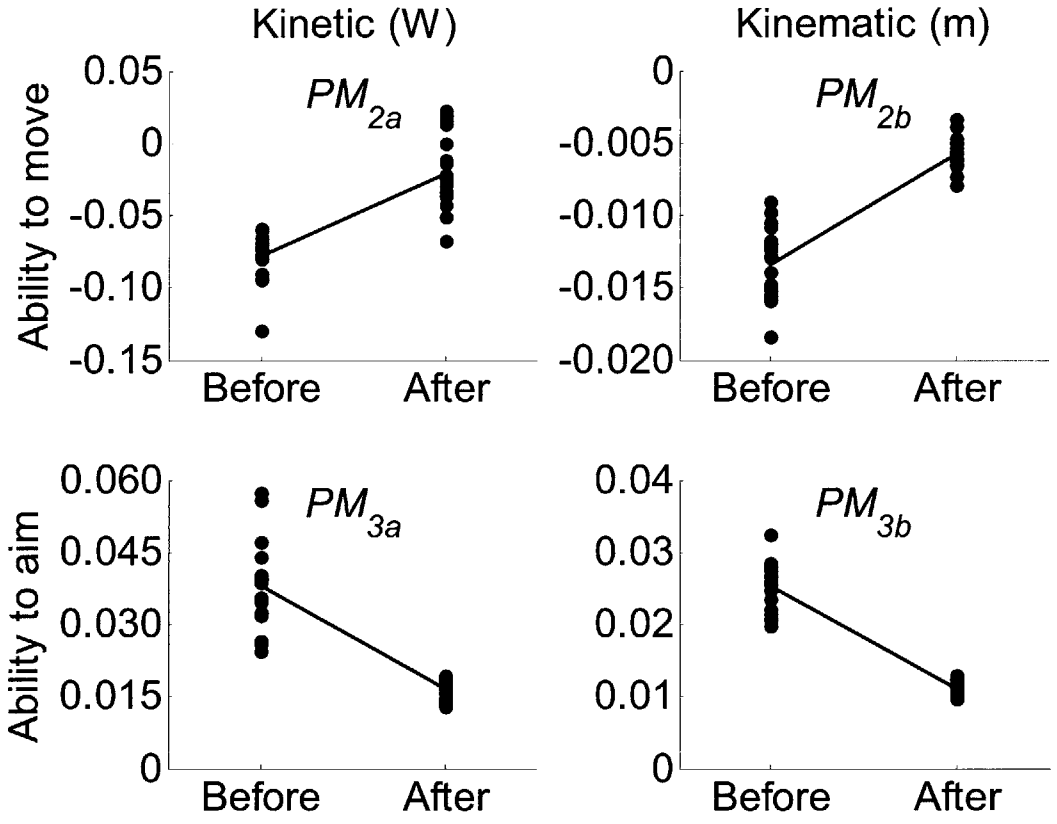

Figure 3.8. Promising kinetic and kinematic performance measure candidates that quantify how well patients can move their arm along a target axis, i.e., abilities to move and to aim. Results are from first and last therapy sessions of an outpatient who participated in the sensorimotor protocol at SRH (assistance was provided by the point impedance controller).

The kinetic measurement used to define PM_2 is the average power along the target axis (PM_{2a}), whereas the kinematic measurement is the average deviation from the robot control system's minimum-jerk trajectory (PM_{2b}).

$$PM_{2a} = \frac{1}{N}\sum_{k=1}^{N}\left(F_{i,y}[k]\dot{y}[k]\right) \tag{3.16}$$

$$PM_{2b} = \frac{1}{N}\sum_{k=1}^{N}\left(y[k] - y_{m.j.}[k]\right) \tag{3.17}$$

where N is the number of data points sampled during the movement. The rotational transformations discussed earlier are also useful to calculate the measures along (and normal to) the target axes. Note that the representative patient data shows that from

admission to discharge these numbers become less negative, indicating that the patient contributed more force and motion to complete the task.

The kinetic measurement used to define PM_3 is the average absolute power normal to the target axis (PM_{3a}), whereas the kinematic measurement is the root-mean-square deviation normal to the target axis (PM_{3b}).

$$PM_{3a} = \frac{1}{N}\sum_{k=1}^{N}\left|F_{i,x}[k]\dot{x}[k]\right| \tag{3.18}$$

$$PM_{3b} = \sqrt{\frac{1}{N}\sum_{k=1}^{N}x[k]^2} \tag{3.19}$$

Although PM_2 is based on signed power to quantify whether the robot provided assistance during the movement (or vice versa), PM_3 is based on absolute power to reflect that any movement normal to the target access will degrade the aiming performance metric. Similar to the patient's ability to move, both measures for PM_3 indicate the patient's ability to aim improved between admission and discharge.

Simulations of a model of a two-link human arm interacting with a two-link robot arm operating under novel impedance control were conducted to determine how the performance measures used to quantify the ability of the patient to move and aim would vary within the assumed domains of the robot control parameters and the patient capabilities. The adaptive parameters of the novel impedance controller were allowed to vary in the following domains: $t_m \in [1.5, 4.5]$ s and $k_{sw} \in [50, 350]$ N/m. It was assumed that patients would be able to complete a movement between two targets separated by 0.14 m within the interval $t_a \in [1.5, 4.5]$ s and their maximum deviation along the axis normal to the target axis along a curved trajectory would lie within the interval $n_{dev} \in [0.01, 0.07]$ m.

Before presenting the simulation results, an additional detail related to the calculation of performance measures will be discussed. In order to more accurately reflect the performance of the patient (in the simulations and the robot implementation),

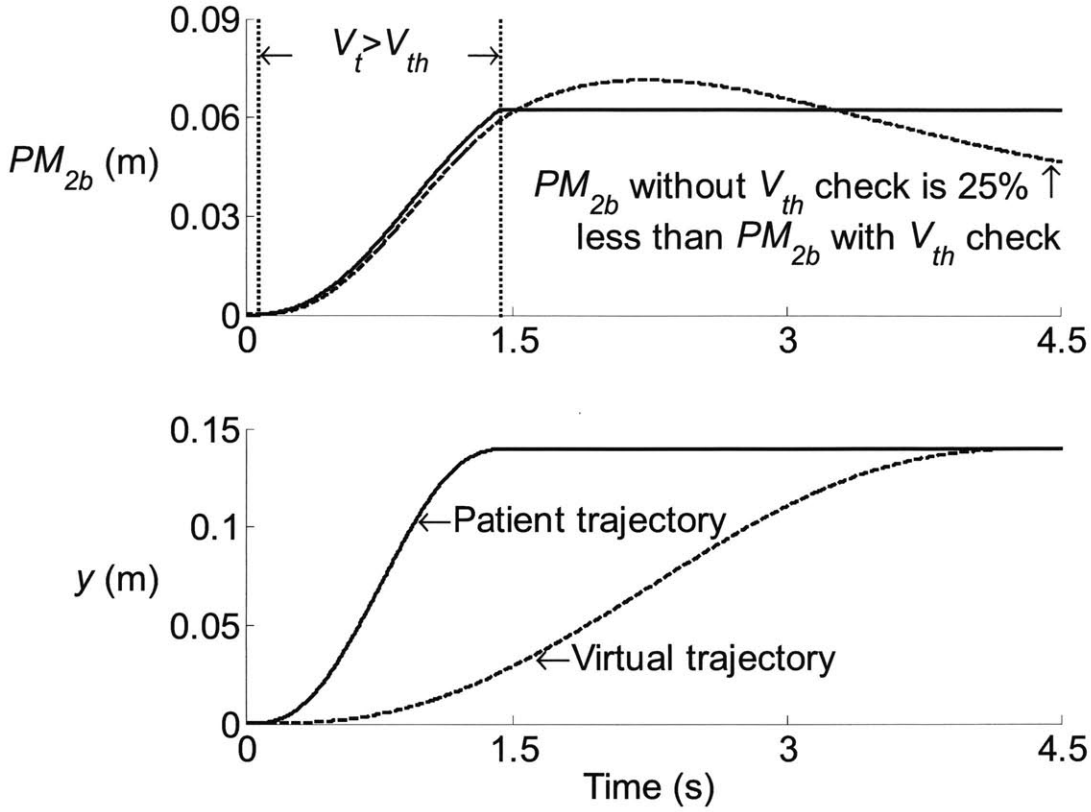

Figure 3.9. Simulation with $t_a = 1.5$ s and $t_m = 4.5$ s that demonstrates a velocity threshold condition is needed while calculating performance measures.

data points were included in the calculations of PM_2 and PM_3 only when the patient's tangential velocity exceeded V_{th}. The reason for this will be demonstrated by Figure 3.9.

Consider a hypothetical situation where $t_a = 1.5$ s and $t_m = 4.5$ s, that is, the patient reached the target in 1.5 s while the allotted time for the robot to complete the movement was 4.5 s (both depicted by minimum jerk trajectories along y-axis with zero x-axis components for simplicity). The top graph contains the values of PM_{2b} at each instant in time, where the solid line depicts PM_{2b} calculated only with the data points that satisfy $V_t > V_{th}$ and the dashed line depicts PM_{2b} calculated with all data points. The bottom graph depicts the trajectory of the patient (and robot end-effector) with a solid line and the virtual trajectory defined by the robot controller with a dashed line. If the velocity threshold were not used, the resulting PM_{2b} value would be 25% less than it

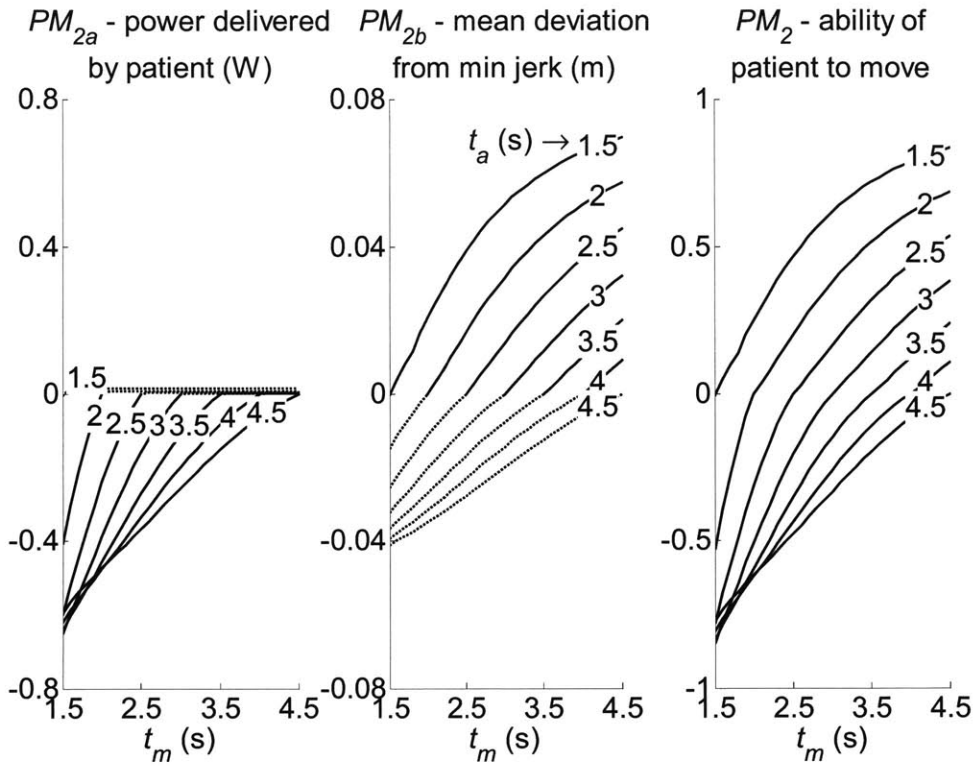

Figure 3.10. Ability of the patient to move (PM_2) is defined to be a weighted sum of a kinetic measure (PM_{2a}) and a kinematic measure (PM_{2b}). The family of curves was defined by varying the movement durations of the simulated patient and the desired trajectory of the slot impedance controller – $t_{a,m} \in [1.5, 4.5]$ s.

was when the patient reached the target. This analysis was repeated over the interval $t_m \in [1.505, 4.5]$ s (with $t_a = 1.5$ s). The percent difference starts at –17% falls to –30%, and then rises back to –25%.

The final selections for PM_2 and PM_3 are displayed in Figures 3.10 and 3.11. The performance measure PM_2, which quantifies the ability to move, was defined as a weighted sum of PM_{2a} and PM_{2b}. Namely,

$$PM_2 = \begin{cases} 1.95 \cdot PM_{2a} & PM_{2a} \le 0 \\ 0 & PM_{2a} > 0 \end{cases} + \begin{cases} 0 & PM_{2b} \le 0 \\ 12 \cdot PM_{2b} & PM_{2b} > 0 \end{cases} \tag{3.20}$$

Thus, both kinetic and kinematic information of the patient's movement comprise this performance measure. In particular, the negative values correspond to the average power delivered from MIT-MANUS to the patient during assisted moves and the positive values correspond to the average deviation from the commanded minimum jerk trajectory when

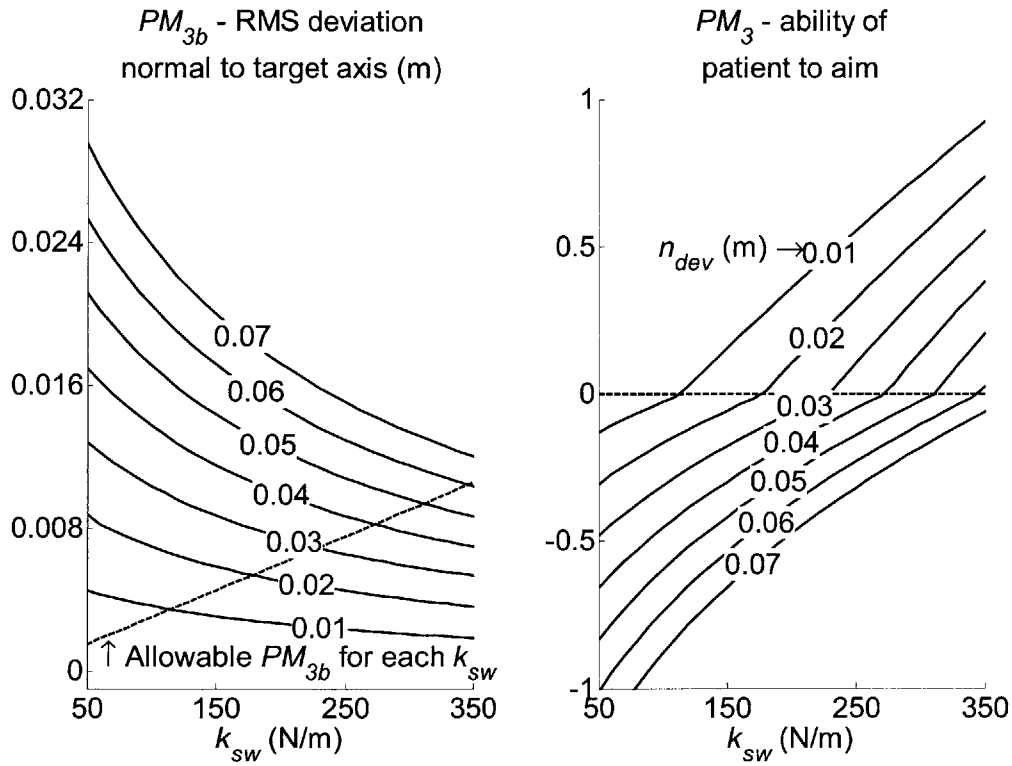

Figure 3.11. Ability of the patient to aim (PM_3) is defined to be a function of the RMS deviation of displacement normal to the target axis (PM_{3b}). The family of curves was defined by varying k_{sw} and n_{dev}.

the patient is moving ahead of the assist. By design, this composite performance measure was able to distinguish patients who were capable of moving to the target in the specified time from those who were not. A purely kinetic metric was unable to discriminate between subjects who moved ahead of the robot assist because the robot was back-drivable. Similarly, a purely kinematic metric was unable to discriminate between patients who required assistance because the back wall stiffness of the novel impedance controller, k_{bw}, kept patients relatively close to the minimum jerk trajectory.

To the contrary, PM_3 was defined solely as a function of the kinematic measure PM_{3b}, the RMS deviation of the patient on the axis normal to the target axis. The line shown in the graph on the left side of Figure 3.11 is used to map the measured value of PM_{3b} to the results shown in the graph on the right side and is given by

$$x_{RMS} = 3.02 \times 10^{-5} k_{sw} \tag{3.21}$$

Notice, each value of sidewall stiffness, k_{sw}, is uniquely associated with a value of RMS deviation normal to the target axis, x_{RMS}. Then, PM_{3b} is mapped to the desired performance metric PM_3 by

$$PM_3 = \begin{cases} 42.4 \cdot (x_{RMS} - PM_{3b}) & (x_{RMS} - PM_{3b}) \leq 0 \\ 106 \cdot (x_{RMS} - PM_{3b}) & (x_{RMS} - PM_{3b}) > 0 \end{cases} \tag{3.22}$$

The constant multipliers in (3.20) and (3.22) were selected to provide a smooth transition from positive to negative PM_2 and PM_3 values (i.e., provide similar slopes for lines of constant patient parameters as $PM_{2,3} \rightarrow 0^-$ and $PM_{2,3} \rightarrow 0^+$) while trying to keep the range of $PM_{2,3}$ values close to $|PM_{2,3}| \leq 1$ in Figures 3.10 and 3.11.

The last of the performance measures is PM_4. It records the maximum distance reached along the target axis during a particular move. Its complement is the distance from the robot position to the target position at the maximum distance reached. Now that the performance measures (PM_2 and PM_3 in particular) have been defined, the performance-based progressive algorithm can be developed.

3.3.4. Development of tracking-mode and adaptive-mode control strategies that comprise performance-based progressive algorithm

Several observations can be made concerning PM_2 and PM_3. As the control parameters increase, the performance measures also increase monotonically along each line of constant patient parameters. Note, when PM_2 equals zero, on average the patient trajectory equals the commanded robot trajectory and no power is exchanged between the patient and robot. As mentioned in the previous section, when PM_3 equals zero, each controller stiffness is uniquely associated with a value of RMS deviation normal to the target axis. By considering the aforementioned properties of the performance measures, MIT-MANUS is able to track the patient's move time by using a simple control law such as:

$$t_m[k+1] = t_m[k] + \lambda_t \cdot PM_2[k] \tag{3.23}$$

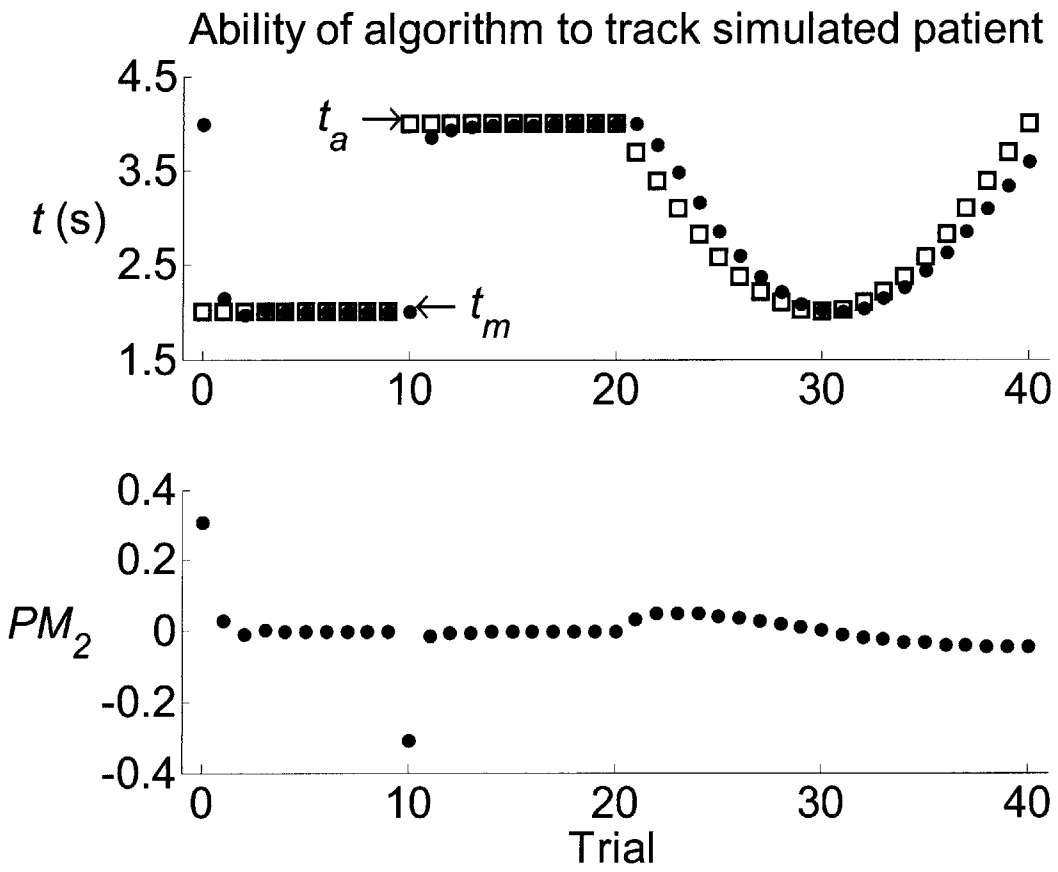

Figure 3.12. Simulation where the robot's control system converges to a patient's movement duration (t_a) and then tracks an abrupt change and a sinusoidal variation in the movement duration.

where $t_m[k]$ is the controller move time during the k^{th} trial, and λ_t is the gain from PM_2 to t_m, namely $(t_{m,\min} - t_{m,\max}) = (1.5 - 4.5) = -3.0$ s per unit PM_2. The negative sign of λ_t reflects that, as the patient's ability to move improves, the time allotted for the movement decreases. An example of the ability of (3.23) to track the performance of a simulated patient is shown in Figure 3.12.

This tracking algorithm is a good first step, but we are not simply interested in tracking the performance of patients, but intend to challenge them to improve their performance or, at the very least, motivate them to maintain it. During the initial 5 (out of 20) trials, the control system operates in a tracking mode to identify how well the patient is able to complete the task. Recall, when the controller parameters are changed, the zero PM values occur at different levels of patient performance. In order to help

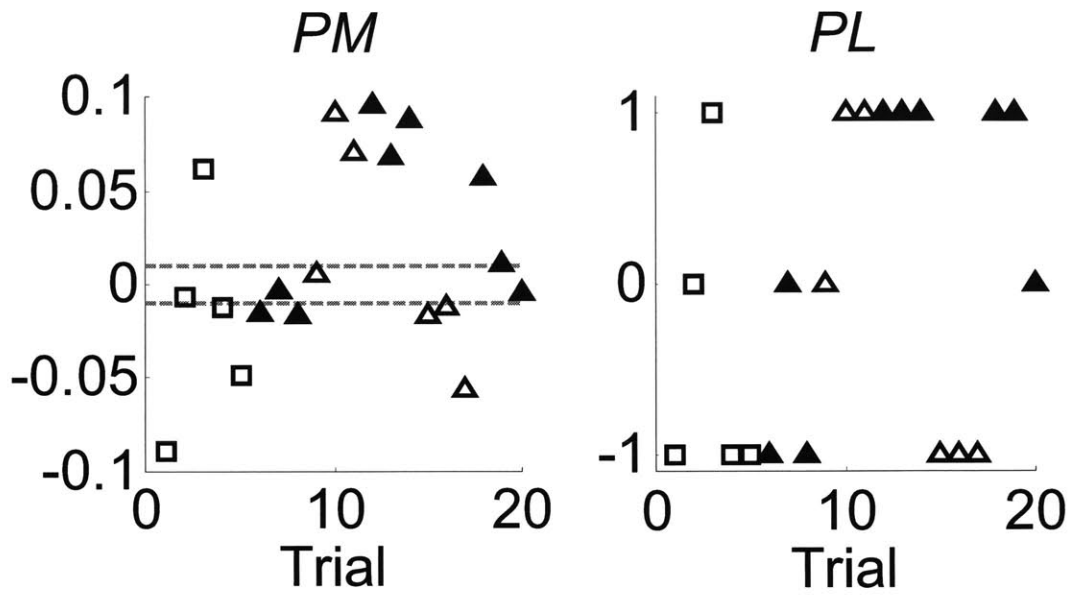

Figure 3.13. Performance level (PL) evaluates the variability in a patient's performance, particularly during the last 15 trials in a session (tracking during trials 1-5 □). The impedance control parameters are held constant in 5 blocks of 3 trials. The sum of the PL values in a block of 3 trials determines to what extent the control parameters will change in the block of 3 trials that follows.

account for this, a secondary performance measure will be introduced that serves as an indicator of patient variability. The performance level (PL) is defined to be

$$PL(PM) = \begin{cases} -1 & PM < -0.01 \\ 0 & |PM| \le +0.01 \\ +1 & PM > +0.01 \end{cases} \tag{3.24}$$

The value of PL indicates whether patients perform worse ($PL = -1$) or better ($PL = +1$) than their expected ability at $PM = 0$. $PL = 0$ denotes when patients perform approximately the same. A hypothetical case that displays the variation of PL is shown in Figure 3.13.

The last 15 trials in a session are grouped into 5 sections of 3 trials. During each of these sections, the desired controller move time and the controller stiffness remain constant. Although this method results in blocks of 3 therapy trials, Al-Ameer and Toole conducted a motor learning experiment where randomized blocks of 3 practice trials resulted in better performance in acquisition and retention than random practice trials and randomized blocks of 2 trials ([4]; discussed in chapter 2, section 2.2.4). Although the

blocks of three trials will not be randomly ordered per se, it was hoped that keeping the controller parameters fixed over three trials would be beneficial to the motor recovery of the patient. By utilizing the average of the PM values ($PM_{ave} = \frac{1}{3}\sum_{j=0}^{2} PM[k-j]$) and the sum of the PL values ($-3 \le PL_{sum} \le +3$) from the prior block of three trials to define t_m for the next block, the control algorithm adapts to patients' performance and variability, and challenges them to continue to improve. The performance-based progressive algorithm is stated as follows:

$$t_m|_{k+1,k+2,k+3} = t_m[k] + \alpha(PL_{2,sum}) \cdot \lambda_t \cdot PM_{2,ave} \tag{3.25}$$

$$\alpha(PL_{sum}) = \begin{cases} 0.5 & PL_{sum} = -3 \\ 0.25 & PL_{sum} = -2 \\ 0.125 & PL_{sum} = -1 \\ 0.125 & PL_{sum} = 0 \\ 0.25 & PL_{sum} = +1 \\ 0.5 & PL_{sum} = +2 \\ 1 & PL_{sum} = +3 \end{cases} \tag{3.26}$$

The desired effect of challenging patients to improve while keeping them motivated is accomplished, in part, by the asymmetry in the definition of $\alpha(PL_{sum})$. When patients do consistently better than their previous performance, $\alpha(+3) = 1$, and when patients do consistently worse, $\alpha(-3) = 0.5$. Thus, the algorithm uses information related to patient variability to dictate by how much the parameter will increase or decrease during the next 3 trials. The asymmetry challenges improving patients to improve further, but makes the task easier, to a lesser extent, when patient performance is worsening.

So far, we have only discussed the approach to modify t_m. An analogous approach is used to alter k_{sw}, i.e.,

$$k_{sw}[k+1] = k_{sw}[k] + \lambda_k \cdot PM_3[k] \tag{3.27}$$

specifies k_{sw} during the first 5 trials and, thereafter,

$$k_{sw}|_{k+1,k+2,k+3} = k_{sw}[k] + \alpha(PL_{3,sum}) \cdot \lambda_k \cdot PM_{3,ave} \tag{3.28}$$

That is, k_{sw}, PM_3, and λ_k are simply substituted for t_m, PM_2, and λ_t. The performance measures were intentionally scaled over similar ranges so that λ_k and λ_t could be defined in a similar manner, i.e., $\lambda_k = (k_{sw,\min} - k_{sw,\max}) = (50 - 350) = -300$ N/m per unit PM_3. The negative sign reflects that k_{sw} decreases as the patient's ability to aim improves. Conversely, if a patient aims poorly, k_{sw} increases and provides more guidance to the patient. Although some excessive forms of guidance have shown to be detrimental to motor learning [6], other forms of guidance can be beneficial [85]. Guidance is usually detrimental to motor learning when subjects are unable to make any errors. This causes them to become dependent on the guidance to complete the task so they tend to perform poorly when the guidance is removed during retention or transfer trials.

One important feature of impedance control is that it does not force subjects to follow a specific trajectory. Rather, it specifies the dynamics of interaction between the patient and the robot. During therapy, the range of stiffnesses prescribed by the performance-based progressive algorithm, i.e., $k_{bw} \equiv 350$ and $k_{sw} \in [50, 350]$ N/m, are relatively low in magnitude. Figure 3.14 displays four graphs of trajectories generated by the same patient. The top row of graphs took place on the first day of therapy, whereas the second row took place on the last day of therapy. The first column of graphs displays the first trial from the therapy session (during the first trial of all therapy sessions, $t_m = 3$ s and $k_{sw} = 200$ N/m) and the second column displays the last trial during each of the two sessions. The novel impedance control parameters on the last trial of first day of therapy were $t_m = 2.17$ s and $k_{sw} = 191$ N/m, whereas $t_m = 2.01$ s and $k_{sw} = 115$ N/m on the last trial of the last day of therapy. Notice, during the first trial of the first therapy session, the patient was unable to reach the north, northeast, and east targets with $k_{bw} = 350$ N/m, i.e., the guidance should not be characterized as excessive because large errors were permitted. Although k_{sw} initially increased during the first therapy session (not shown), it had decreased to $k_{sw} = 191$ N/m by the end of the session. The results from the last session are also informative. During most of the first trial, the patient's trajectory was

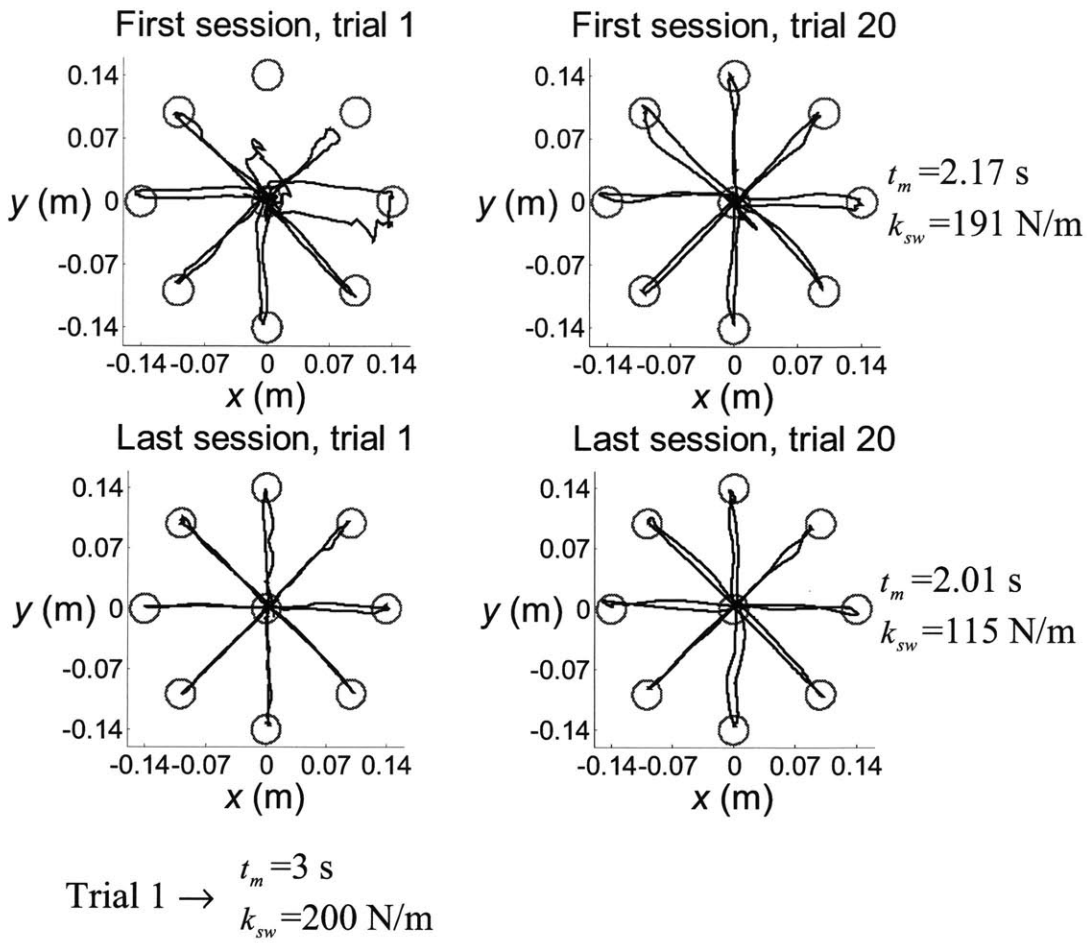

Figure 3.14. Comparison of a patient's movements during the first and last trials of the first and last PBPT sessions. Impedance control guides the patient during therapy, but does not dictate "errorless" performance. During last session, k_{sw} is reduced from 200 N/m to 115 N/m to challenge the patient to improve.

along the target axis and had very little aiming error. By the end of the last session, the stiffness k_{sw} had decreased from 200 N/m to 115 N/m providing less assistance to the patient and allowing more aiming error to occur, i.e., the performance-based progressive algorithm was challenging the patient to improve by providing less guidance.

Figure 3.15 depicts the changes in t_m (top row) and k_{sw} (bottom row) during an early (first column) and late (second column) therapy session for an outpatient who participated in the PBPT protocol. Similar to Figure 3.13, squares are used to depict the controller parameters during the tracking trials and triangles are used during the PBPT trials (alternating filled and unfilled triangles accentuate 5 blocks of 3 trials). This figure demonstrates how the PBPT algorithm adjusts the difficulty of the task based on the

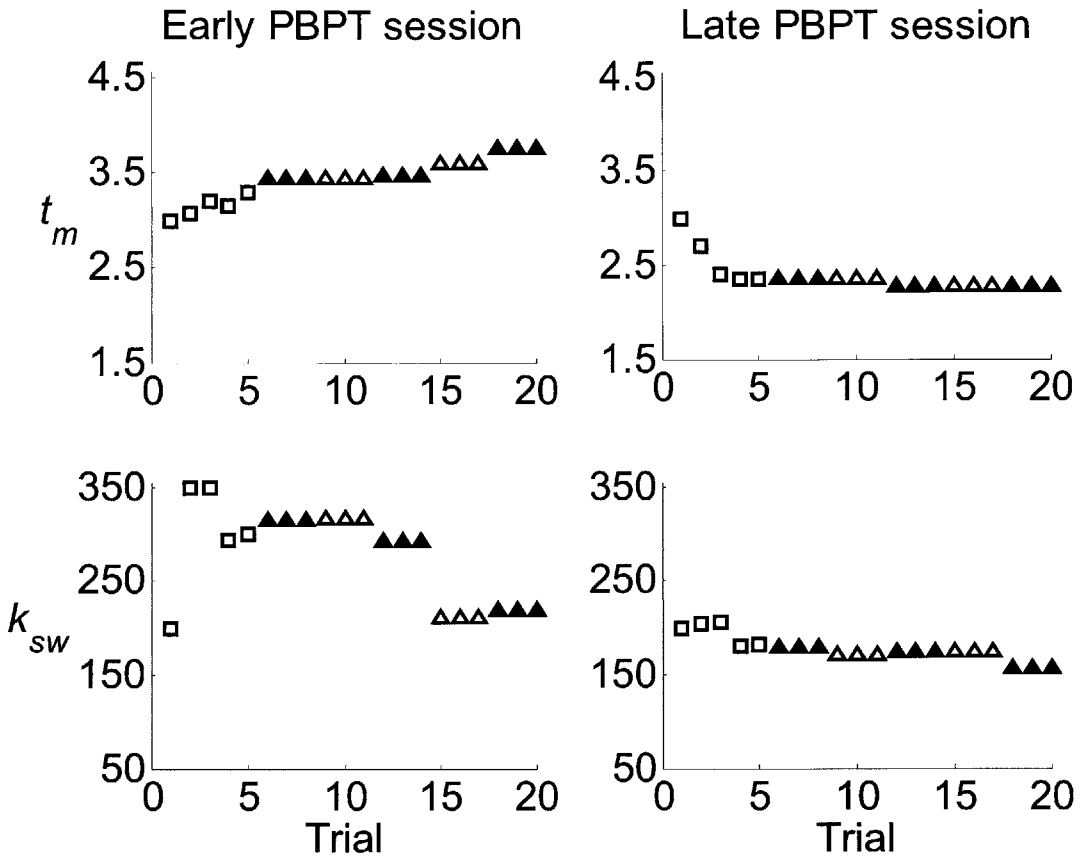

Figure 3.15. Evolution of t_m and k_{sw} during early and late PBPT sessions for a chronic outpatient. In the early session, the patient's ability to move degrades while the ability to aim improves. In the late session, the abilities of the patient to move and aim improve.

patient's abilities to move and aim. Throughout the early therapy session, t_m increased, i.e., the patient moved slower. Although k_{sw} increased to its maximum value during trials 2 and 3, it approached the initial value of k_{sw} towards the end of the session, i.e., the patient's ability to aim improved during the session. Therefore, during the early PBPT session, the patient moved slower but aimed better throughout the session. In the late therapy session, both t_m and k_{sw} tended to decrease so the patient was making faster movements with less aiming assistance.

Although the performance-based progressive algorithm was inherently designed to challenge patients to improve their performance during each therapy session, extrinsic feedback in the forms of knowledge of performance (KP) and knowledge of results (KR) was also used to motivate patients by keeping them informed on how well they were

performing the task during each therapy session. This will be discussed further in the next section.

3.4. Methods to keep patients motivated

Two methods of keeping patients motivated were used. First, the clinician administering the PBPT protocol would provide patients with knowledge of performance. Comments that provide positive reinforcement to patients help motivate them to continue to be active participants in the robotic therapy. A simple comment such as "good job" will help patients stay focused on the task. Clinicians also provide detailed assessments to the patients concerning their movement patterns. For instance, patients might use their trunk to initiate movement or to reach a target (a shoulder strap helps to secure patients, but there is still some "wiggle room"). However, if clinicians feel that patients are relying too much on their trunks to generate movement, they can remind patients of the importance of posture or tell them that they are doing great and don't need to reach the target every time.

The second method to keep patients motivated was the use of a visual display to provide patients with knowledge of results, i.e., a summary of the outcome of their efforts. The visual display (introduced earlier in Figure 3.7) is a bar graph that is presented to patients after trials 5, 10, 15, and 20. The following four performance measures that range from 0% to 100% were used to inform patients (and their clinicians) how patients were doing:

- PM1-START: There is a 2 s delay before the robot moves from the center to each of the 8 targets. If the patient is able to move the robot above a specified velocity threshold, the robot begins moving and PM1 is incremented by 12.5% (i.e., 100%/8). Otherwise, the robot waits until the delay time has elapsed and nothing is added to PM1.
- PM2-MOVE: The robot moves with a prescribed minimum jerk trajectory. If the patient moves faster (slower) than the robot's command trajectory is moving, PM2 increases (decreases).
- PM3-AIM: Each sidewall stiffness is associated with an allowable RMS deviation normal to the target axis. If the patients "aims" better (worse) than this level, the stiffness decreases (increases).
- PM4-TARGET: During each, the computer keeps track of the maximum distance the patient moves radially from the center of the workspace along the target axis.

PM4 is this distance divided by the target distance times 100% (if the patient overshoots the target, they are given the max score of 100%).

PM2-MOVE depends on the performance measure, PM_2, and the performance level, PL_2, whereas PM3-AIM depends on the performance measure, PM_3, and the performance level, PL_3. The height of the bar graph displays for PM_2 and PM_3 are defined as:

$$PM\% = \begin{Bmatrix} 80 \text{ After Game 5} \\ 80 + c_1 \sum PL + c_2 PM_{ave} \end{Bmatrix} \tag{3.24}$$

In this expression, c_1 and c_2 are scaled to limit patient display between approximately 70 and 90% as the robot parameters are changed. Recall that the purpose of the visual display is to provide positive reinforcement to the patient throughout the session.

The PBPT algorithm provides a mechanism for patients to evolve from hemiplegic to normal arm movement. Like a line integral[1], it specifies the initial and final conditions (PM1-START and PM4-TARGET) and the path between these conditions (PM2-MOVE and PM3-AIM). PM1-START is particularly useful for hemiplegic or severe hemiparetic patients as they recover some movement. It requires the patient to actively participate in the initiation of movement and facilitates proper timing between afferent-efferent signals to induce increase in the excitability of the corticospinal projections. It might be also used to train the recruitment of a particular muscle group by requiring the threshold to be in a particular direction. PM4-TARGET is useful for patients with severe or moderate hemiparesis. It rewards patients for relaxing their arms, which might allow the impedance controller to drive their hands closer to the target (reduce tone – severe case), or it measures patients' ability to move to the target ahead of the controller. For patients with moderate or mild hemiparesis PM2-MOVE and PM3-AIM provide a speed-accuracy tradeoff.

[1] If I remember correctly, Igo Krebs was the person who described this excellent analogy to me.

3.5. Conclusions

The performance-based progressive robot therapy was based on methods that enhance human motor learning and motivation such as practice scheduling, practice variability, positive reinforcement, etc. One area of active research is to determine the optimal therapy tailored to each stroke patient that will maximize his/her recovery. A novel performance-based impedance control algorithm, which is triggered via a speed threshold to guarantee proper timing between efferent motor commands and afferent sensory signals, was designed with this goal in mind. The algorithm first identifies the ability of the patient to move and aim, and then independently adjusts the time allotted for the patient to complete movements and the level of stiffness that assists patients to aim movements. Knowledge of performance via verbal comments of the clinician and knowledge of results via a visual display after every five trials are used to challenge patients to improve their performance or, at the very least, maintain it.

Chapter 4

Clinical and robot-based results from patients treated with the performance-based progressive therapy protocol

4.1. Summary

Chapter 3 described the development of a performance-based progressive algorithm that uses specific movement-related feedback to specify the time allotted for the patient to move from one target to another and the "side wall" stiffness of a novel adaptive impedance controller [57]. This chapter will present clinical results to demonstrate that the performance-based progressive therapy protocol enhanced motor recovery of moderate-to-severe chronic stroke patients (time post-stroke for patient population > 7 months) in comparison to the sensorimotor and progressive resistance protocols conducted with outpatients [27].

This chapter will also present robot-based evidence from very severe and moderate-to-severe patient groups to demonstrate that motor recovery can be modeled similar to a motor learning "law of practice," i.e., an amount of practice is related to a performance level via a power function. Least squares regressions will demonstrate that the relation between the trial number and the adaptive impedance controller parameters can be quantified with power functions throughout the entire therapy protocol for both patient groups and within individual therapy sessions except for the time allotted for movement of the very severe group. In addition, a phenomenon similar to the concept of retention (or forgetting) in motor learning will be shown to occur with the moderate-to-severe patient group, but not with the very severe patient group. Further study is needed to conclusively establish the differences in the recovery of very severe and moderate-to-

severe patients. These findings could allow researchers to develop improved rehabilitation methods and to predict the effect of more treatment sessions for stroke patients, thereby providing justification to extend inpatient hospital stays or to develop more outpatient rehabilitation programs.

4.2. Motor recovery – Plasticity and the performance-based progressive algorithm

A prominent theme of current research into recovery from brain injury posits that activity-dependent plasticity underlies neuro-recovery. This plasticity may be due to the unmasking of pre-existing connections, activity-dependent synaptic changes, or the growth of new synapses. Experimental support for this idea derives primarily from measurements of synaptic branching and cortical thickness in rats raised in enriched and derived environments [20-23,38] and in monkeys recovering from ischemic injury [70]. Li, et al. [63] also identified populations of neurons in the brain of the monkey (specifically, primary motor cortex) that exhibited learning-dependent activity. Although both motor learning and recovery exhibit activity-dependent plasticity, several other factors affect recovery such as re-acquisition of muscle strength, resolution of abnormal tone, etc. These recovery phenomena are not related to learning so it is unclear to what extent, if any, motor recovery resembles motor learning.

Research to date has shown that repetitive, task-specific, goal-directed, robot-assisted therapy can be effective in reducing motor impairments in the affected arm after stroke; results of initial studies showed statistically significant differences between the experimental and control groups for the shoulder and elbow, but not for the wrist and fingers [3,25,58,96,98]. This result for motor recovery is similar to specificity of motor learning. Schmidt and Wrisberg [86] define the specificity of learning as "the notion that the best learning experiences are those that most closely approximate the movement components and environmental condition of the target skill and target context." Although the mean improvement in the Motor Status Wrist-Hand Score of the experimental group was larger than that of the control group (4.16 ± 1.16 versus 2.64 ± 0.78 [3]), it was not significantly different, because the focus of the robotic therapy was to train the muscles in the shoulder and elbow to make planar movements.

By assuming motor recovery is similar to motor learning, the performance-based progressive therapy (PBPT) protocol was developed to implement motor learning concepts such as repetition, active participation, and goal specification. Studies of human motivation have revealed that providing positive reinforcement, knowledge of performance, and knowledge of results can also stimulate the learning process [65,85,86,100,101,105,106,108]. The performance-based algorithm specifies two distinct parameters that are related to each patient's motor ability, namely, the time allotted for movement, t_m, and the sidewall stiffness of the impedance controller, k_{sw}. Although t_m and k_{sw} are parameters determined by the robot control algorithm, because that algorithm adapts to the patient's current performance, these parameters also serve as summary measures of the patient's recovery. Specifically, t_m is an indicator of patients' overall motor ability to move from one target to another and k_{sw} is an indicator of their ability to direct their movements from the initial to the final target, i.e. to aim. During the first five "tracking" trials of a session, the control system determines the patient's ability to move and aim by driving the kinetic/kinematic performance measures to zero, thereby matching the patient's performance. Control parameter specification during the last fifteen trials in a session is dictated by the performance-based progressive algorithm that intends to challenge patients to improve or at least maintain their performance.

This approach appears to be particularly well suited if we consider typical examples of unassisted patient movements shown in Figure 4.1. This figure illustrates quite well that different stroke lesions can lead to very different kinematic behavior during movements. The first patient (109.9 cm^3 lesion of the corpus striatum and cortex) makes fast movements but aims poorly, whereas the second patient (8.9 cm^3 lesion of the corpus striatum) aims well but moves slowly [57]. The novel modality of the PBPT guides the hand of patients who aim poorly without holding them back and assists slow-moving patients to make faster movements.

By examining the evolution of the controller parameters that serve as summary measures of the ability of the patients to move and aim their movements, motor recovery will be shown to be similar to motor learning. Namely, the evolution of parameters will follow a decreasing exponential progression relative to the amount of therapy delivered to

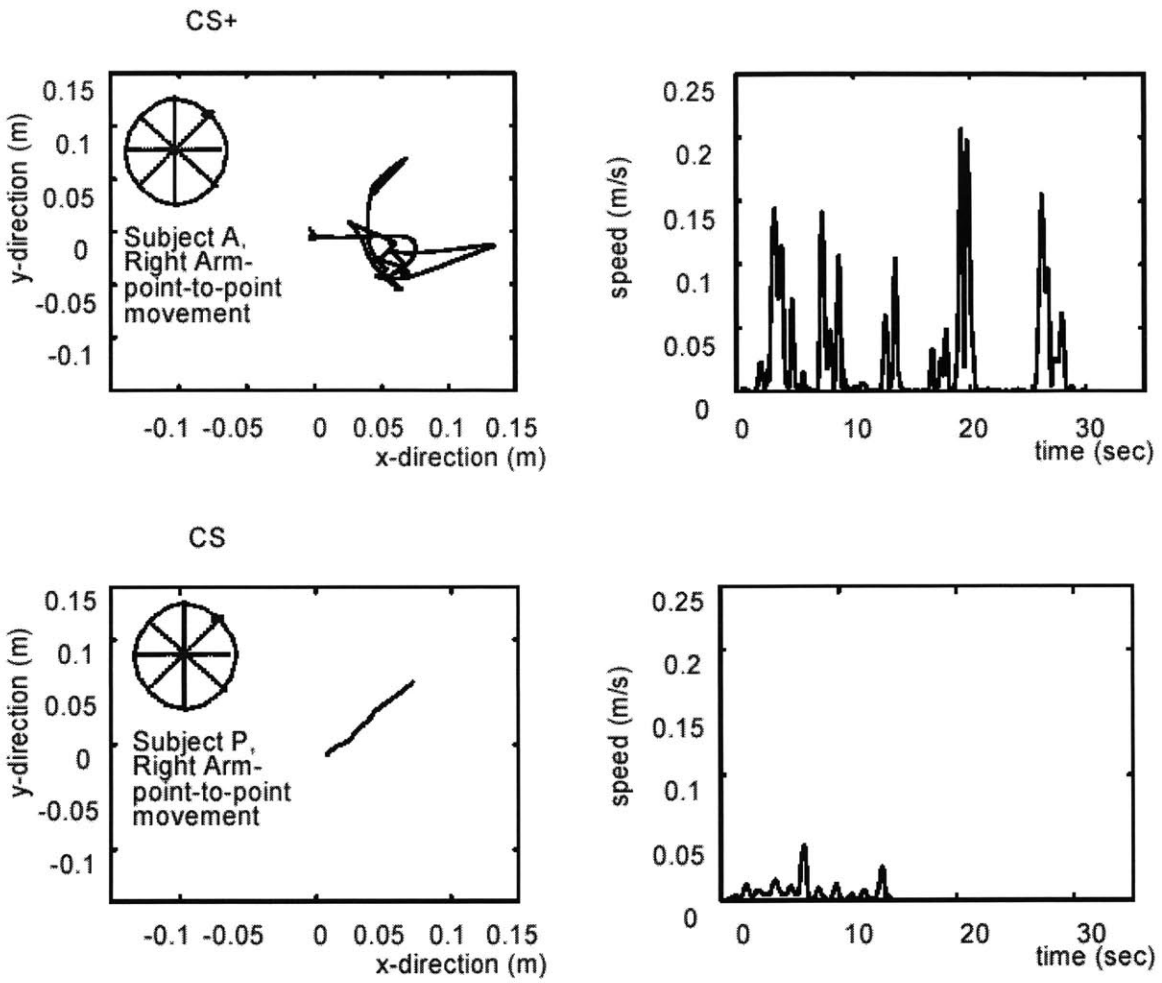

Figure 4.1. Reaching movements made by patients with corpus striatum plus cortex lesion – CS+ (109.9 cm^3) and corpus striatum lesion – CS (8.9 cm^3). The left column shows a plan view of the patients' hand path attempting a point-to-point movement. The right column shows tangential hand speed [57].

the patient. The following section will introduce concepts of motor learning and then demonstrate the similarities between motor learning and recovery.

4.3. Clinically based metric: Upper Extremity Fugl-Meyer scores indicate PBPT protocol outperforms sensorimotor and progressive resistance protocols

The Upper Extremity Fugl-Meyer evaluation is a standardized and reliable scale [81] that clinicians use to assess the motor impairment of stroke patients (see Appendix A for list of criteria and score classifications; maximum score of 66 [33]). As such, it will be used to measure the effect of three distinct robot therapy protocols that were conducted with

chronic stroke patients, namely, the PBPT protocol described in Chapter 3, the sensorimotor (SM) protocol, and the progressive resistance (PR) protocol. Each therapy protocol consisted of 18 hours of training with a planar robot (MIT-MANUS [46] or InMotion^2, a commercial version of MIT-MANUS manufactured by Interactive Motion Technologies, Inc.). During the training sessions of all three protocols, eight targets were radially spaced along a circle of radius 0.14 m and were oriented like a compass, i.e., N, NE, E, SE, S, SW, W, and NW. The SM and PR protocols [92] were designed to answer the research question – will addressing upper limb weakness permit greater recovery than an active-assisted exercise alone?

The SM protocol consisted of a repetitive task-specific, goal-directed, robot-assisted training. A point impedance controller was used to assist patients to make visually cued fixed duration movements from one target to another. The values of robot stiffness and damping approximated the mechanical impedance of a human arm to mimic the "hand-over-hand" movement assistance approach used by therapists (stiffness of 200 N/m and damping of 10 Ns/m) [55].

The PR protocol used a strength-training exercise to reduce shoulder and elbow muscle weakness of patients who were able to reach all eight targets without robot assistance. Patients in the PR protocol were required to make the same series of point-to-point movements as patients in the SM protocol while the robot provided varying degrees of resistance. The controller used in PR therapy was the same impedance controller used in SM therapy (with viscous damping of 10 Ns/m), but the desired reference trajectory was fixed at the origin throughout the PR trial and the stiffness was assigned four different values depending on how close the patient came to reaching the targets during the previous treatment session. Specifically, if the mean value of the radial distance moved in the previous session was less than 0.035 m, the stiffness was set equal to 100 N/m in the current session. If it was greater than 0.035 m and less than 0.07 m, the stiffness was set equal to 133 N/m. Similarly, mean displacement values of 0.10 m and 0.14 m corresponded to stiffness values of 166 N/m and 200 N/m. Therefore, the maximum forces exerted by the robot that the patient had to overcome to reach the targets for the four stiffness values were 14, 18.6, 23.2, and 28 N.

At the onset of robotic therapy, chronic outpatients who were able to reach all eight targets were randomly assigned to the SM and PR therapy protocols [92]. Patients who were unable to reach all eight targets were assigned to the SM therapy protocol. After participating in the SM protocol for 3 weeks, patients who were able to reach all eight targets were again randomly assigned to the SM and PR therapy protocols for another 3 weeks of therapy. Patients who were unable to reach the targets unassisted participated in the SM protocol for another 3 weeks.

Although the three protocols used the same basic task, i.e., 20 trials of 16 point-to-point movements to and from 8 targets located 0.14 m away from the center of the robot workspace, the number of moves made during the PBPT protocol was less than the number of moves made in the SM and PR protocols. This was necessary because the performance-based progressive algorithm allowed the allotted time for the patient to move, t_m, to vary from 1.5 s to 4.5 s. The initialization time of (up to) 2 s and the two dwell times of 2 s added 48 s to each trial (assuming patient was not able to exceed the velocity threshold to initiate the trial), resulting in a total trial time that ranged from 72-120 s (24-40 minutes for 20 trials). In comparison, the SM and PR therapy protocols had the same allotted move time of 1.5 s, resulting in a total trial time of 24 s (8 minutes for 20 trials).

For this reason, robot-assisted trials in the PBPT protocol consisted of a set of 20 PBPT trials and a set of 20 robot-assisted SM trials. The SM and PR protocols consisted of 3 sets of 20 robot-assisted or resistive trials. In addition to the robot-assisted (or resistive) trials, patients also made a series of 16 unassisted point-to-point movements before and after each set of 20 robot-assisted trials. Specifically, a PBPT session consisted of 16 unassisted movements, 20*16 SM movements, 16 unassisted movements, 20*16 PBPT movements, and 16 unassisted movements (total of 688 movements per session), whereas the SM and PR protocols had an additional 20*16 robot-assisted (or resistive) movements and 16 unassisted movements (total of 1024 movements per session). Since each protocol consisted of 18 sessions, patients participating in the PBPT protocol would make 12,384 movements, whereas patients participating in the SM and PR protocols would make 18,432 movements (PBPT+6,048).

Patient group	Fugl-Meyer Upper Extremity: UE F-M (max 66)	
	Burke PBPT protocol	Spaulding SM & PR protocols
Very severe (UE F-M < 14)	8.59±0.58 (n=21)	N/A (n=0)
Moderate-to-severe (UE F-M ≥ 14)	26.86±2.51 (n=15)	27.37±1.48 (n=47)

Table 4.1. Fugl-Meyer Upper Extremity clinical evaluations at admission (mean of 3 to verify stable phase of motor impairment) grouped by rehabilitation hospital. PBPT protocol was administered at Burke Rehabilitation Hospital, whereas SM and PR protocols were administered at Spaulding Rehabilitation Hospital.

Before patients began robot therapy in the PBPT, SM, or PR protocols, three clinical evaluations were conducted over a two-month period to verify that their level of impairment was stable. In order to make valid comparisons between the three protocols, the patients were divided into two groups: very severe (UE F-M < 14) and moderate-to-severe (UE F-M ≥ 14). This was necessary because all patients in the SM and PR groups were classified as moderate-to-severe. The mean values of the three UE F-M clinical evaluations for the chronic outpatients treated at the Burke Rehabilitation Hospital (BRH) in White Plains, NY and the Spaulding Rehabilitation Hospital (SRH) in Boston, MA are given in Table 4.1. Demographic information concerning these patients (e.g., age, gender, type of stroke) is included in Appendix B. In addition, a within group comparison of the patients treated at SRH revealed that patients who were unable to reach all 8 targets (S3, n=18) were significantly different than patients in the PR (n=15, p <0.001) and SM (n=14, p =0.001) protocols who were able to reach all 8 targets, and is included in Appendix B.

The results of the group comparisons (ANOVA/multiple comparisons) of PBPT (n=15), PR (n=15), and SM (n=14) are given in Table 4.2. Patients in the PBPT moderate-to-severe group exhibited a larger increase in impairment reduction than in the SM group (p =0.046) and in the PR group (p =0.047). There were no significant differences between the SM and PR groups (p =0.97). This analysis has shown that a therapy protocol based on intuitive concepts of motor learning (practice variability, define tasks that challenge subjects while keeping them motivated, positive reinforcement

Moderate-to-severe patient group – Upper Extremity Fugl-Meyer (max 66) ≥ 14		
Therapy protocol	Number of subjects	Change in UE F-M from admission to discharge
PBPT	15	7.28±1.29
PR	15	4.53±0.81
SM	14	4.48±0.91
ANOVA p-value comparison of protocols	**PBPT** vs PR	**0.047***
	PBPT vs SM	**0.046***
	PR vs SM	0.967

Table 4.2. Comparison of the impairment reductions exhibited by moderate-to-severe chronic stroke patients participating in the PBPT, SM, and PR protocols.

via knowledge of results, etc.) resulted in larger impairment reductions than therapy protocols based on goal-directed robot-assisted and robot-resistive tasks. One significant aspect of this result is patients in the PBPT protocol completed 33% fewer movements during their therapy, but still exhibited a significantly better outcome (↑ 62%). This is contrary to the common assumption that more practice will result in better performance.

4.4. Robot-based metric: evolution of controller parameters during therapy protocol

One fundamental concept that is used to quantify motor learning is the law of practice [85]. Performance curves that characterize learning are usually negatively accelerated functions such that the rate of improvement tends towards zero with practice. A common formula used to describe the law of practice is a power function such as

$$L = aP^b \tag{4.1}$$

where L is a measure of performance, P is a measure of the amount of practice, a is a constant multiplier, and b is a constant exponent.

4.4.1. Does motor recovery from stroke follow a similar trend as motor learning, i.e., can a power function be used to quantify recovery?

The performance-based progressive algorithm was designed to challenge patients to improve, while not making the challenge so difficult that patients would become

discouraged. In general, as therapy progressed and the patients regained some ability to move their arms, the movement became quicker, i.e. t_m decreased. Similarly, as the patients' ability to aim their movements improved, less guidance normal to the target axis was provided by the robot, i.e. k_{sw} decreased. Although these trends in patient data were in the expected direction (i.e. quicker, better-aimed movements), it was of interest to determine whether a power function could model these aspects of the evolution of patient recovery. If yes, the PBPT protocol based on motor learning concepts enhanced recovery in a similar manner that these concepts enhance learning, i.e., motor recovery is similar to motor learning in this respect. This finding could allow researchers to predict the effect of more treatment sessions, thereby providing justification to extend inpatient hospital stays or to develop more outpatient rehabilitation programs. It could also lead to improved rehabilitation methods that are based on concepts that have enhanced motor learning [65,85,86,100,101,105,106,108]. If not, other trends might exist that could provide insight to understand motor recovery.

During this initial investigation of the process of motor recovery, the amount of practice, P, was simply the trials ordered consecutively from 1 to 360 (20 trials/session for 18 sessions). The measures of performance were defined to be t_m and k_{sw}. To define a least-squares optimization problem that is linear in its parameters, take the logarithm on both sides of (4.1) and simplify the result

$$\log(L) = b\log(P) + \log(a) \tag{4.2}$$

Thus, the abscissa of the line is $\log(P)$, its ordinate is $\log(L)$, its slope is b, and its y-intercept is $\log(a)$. Graphically, if two parameters are related by a power function, then their relationship appears linear on a plot with logarithmic scaling of its axes.

Using the least-squares formulation afforded by (4.2), multiplier and exponent parameters were defined for the power functions that were attempting to quantify the evolution of t_m and k_{sw} during the therapy protocol. The optimum parameters were calculated for the mean values of t_m and k_{sw} for 10 patients in the very severe group and 10 patients in the moderate-to-severe group. Only the last 15 trials of each therapy

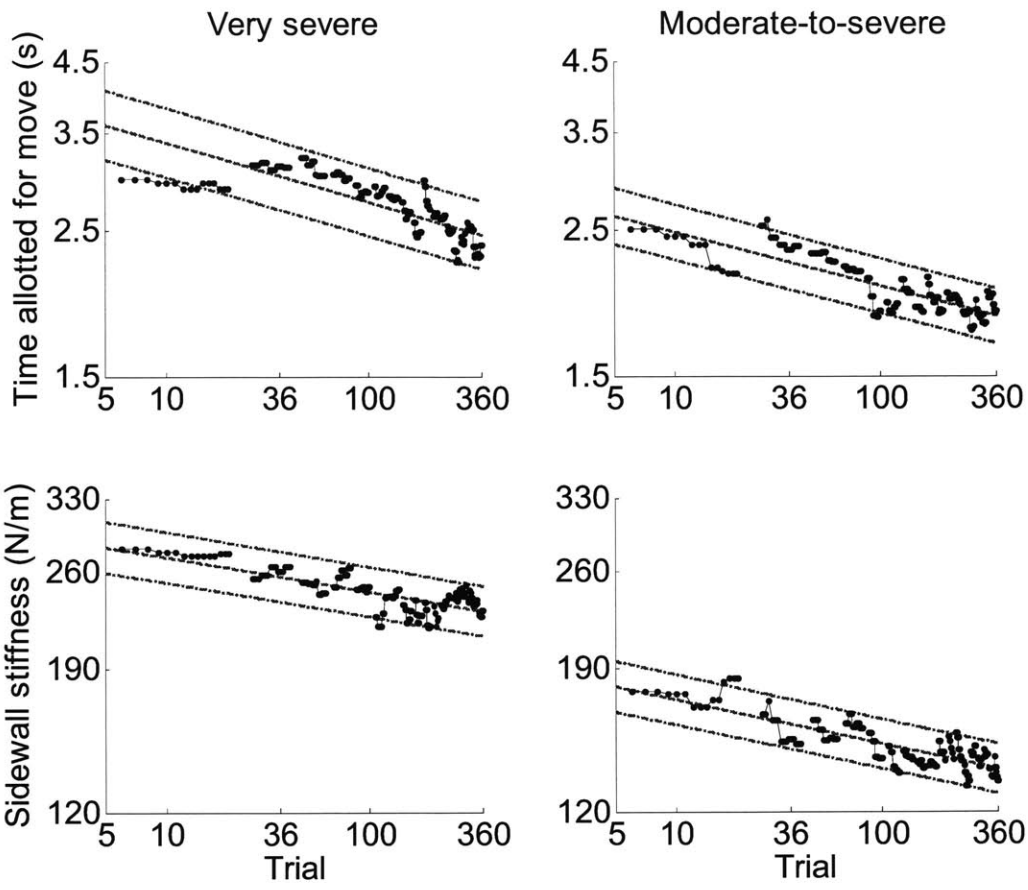

Figure 4.2. Evolution of the mean values of the control parameters specified by the performance-based progressive algorithm, namely, time allotted for movement (t_m) and sidewall stiffness (k_{sw}), for groups of 10 very severe patients and 10 moderate-to-severe patients.

session are included in this optimization because the first 5 trials of each session allow the controller to determine the ability of the patient to move and aim.

The results for both patient groups are displayed in Figure 4.2 (results for the individual patients are included in Appendix C). The results for the very severe group are given in the first column of graphs and the results for the moderate-to-severe group are given in the second. The first row displays the evolution of t_m during the PBPT protocol and the second displays the evolution of k_{sw}. The mean values of t_m and k_{sw} are depicted by circles (sessions are depicted by solid lines). The optimum parameters from

	Group	Multiplier	Multiplier 95%CI	Exponent	Exponent 95%CI	R^2	F	p
t_m	Very severe	4.17	4.34 4.00	-0.090	-0.082 -0.098	0.62	474.5	<0.0001
	Moderate-to-severe	2.99	3.09 2.89	-0.081	-0.075 -0.088	0.71	600.6	<0.0001
k_{sw}	Very severe	304.8	313.4 296.5	-0.048	-0.043 -0.054	0.56	295.5	<0.0001
	Moderate-to-severe	198.6	204.2 193.2	-0.062	-0.057 -0.068	0.67	499.9	<0.0001

Table 4.3. Least-squares regression results from mean values of controller parameters specified by the performance-based progressive algorithm for the very severe and moderate-to-severe patient groups.

the least-squares regressions were used to generate the dashed lines and the 95% confidence intervals[2] (CI) of the predictions were used to generate the dash-dotted lines.

The optimization results are displayed in Table 4.3. The optimum multipliers and exponents are given as well as their confidence intervals. The correlation coefficient squared (R^2), F-statistic, and p-statistic are also given in the table [66]. R^2 is the fraction of variability of in the data explained by the regression model. The F-distribution is the quotient of two chi-square distributions with N_1 and N_2 degrees of freedom. The probability that the regression parameters are equal to zero is given by p. Specifically,

$$R^2 = \frac{\left(\mathrm{cov}\left(L,\hat{L}\right)\right)^2}{\sigma^2(L)\,\sigma^2\left(\hat{L}\right)} \tag{4.3}$$

$$F = \frac{\sum_1^N \left(\log\left(\hat{L}\right) - \frac{1}{N}\sum_1^N \log(L)\right)^2 \Big/ \left(N_p - 1\right)}{\sum_1^N \left(\log\left(\hat{L}\right) - \log(L)\right)^2 \Big/ \left(N - N_p\right)} \tag{4.4}$$

$$p = 1 - \mathrm{fcdf}\left(F, N_p - 1, N - N_p\right) \tag{4.5}$$

where cov is the covariance between L and $\hat{L}$, σ^2 is the variance, N is the number of observations, N_p is the number of parameters in the least-squares regression, and fcdf is

[2] Unless otherwise noted, confidence intervals in this chapter will calculated at the 95% confidence level.

the F-cumulative distribution function with $N_p - 1$ and $N - N_p$ degrees of freedom at the value F. It is obvious from the low probability values in Table 4.3 that the multiplier and exponent parameters are non-zero.

The optimum exponent values of each group are close to one another for both summary measures, whereas the multiplier values are quite different. The confidence intervals of the optimum multipliers for the summary measures that describe the progression of therapy for the very severe and moderate-to-severe groups do not overlap (i.e., upper bounds of the moderate-to-severe group, $t_m \to 3.09$ and $k_{sw} \to 204.2$, are less than lower bounds of the very severe group, $t_m \to 4.0$ and $k_{sw} \to 296.5$). On the contrary, the confidence intervals of the optimum exponents that describe the evolution of t_m for the very severe and moderate-to-severe groups do overlap over the range $[-0.088, -0.082]$. Although the confidence intervals of the optimum exponents for k_{sw} do not overlap, their separation is relatively small; overlapping does occur at a 99% confidence level. In contrast, the optimum multipliers for both performance indicators remain substantially separated at the 99% confidence level: t_m (moderate-to-severe: [2.86, 3.12]; very severe: [3.95, 4.4]) and k_{sw} (moderate-to-severe: [191.5, 205.9]; very severe: [293.9, 316.2]).

Due to the separation of multipliers and closeness of exponents, it almost appears as though the moderate-to-severe patients began their therapy where the very severe patients ended. In addition, it does not appear that the process of motor recovery had reached a plateau after 6 weeks of therapy for either group, i.e., extending therapy past 6 weeks may further benefit patients. This is encouraging because previous outcome results from stroke recovery suggest that most gains occur within the first three months after stroke and no substantial gains occur five months post-stroke [49]. Recall, the patients recruited for this study were outpatients whose brain injuries had occurred much earlier than three months prior to entering the study (participants ranged from 8 months to 95 months post stroke).

The means of the controller parameters for both patient groups undergo a near linear decline on a logarithmically scaled graph over the duration of therapy, some

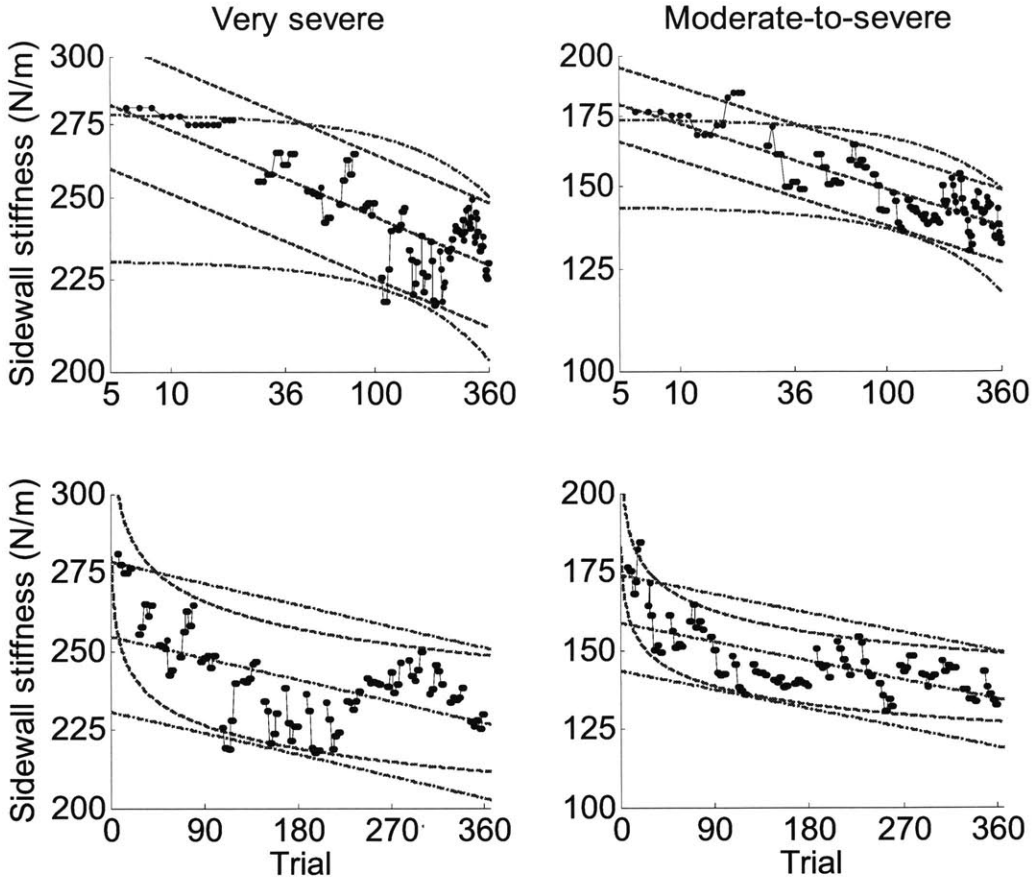

Figure 4.3. Evolution of the mean values of the sidewall stiffness (k_{sw}) for groups of 10 very severe patients and 10 moderate-to-severe patients plotted on logarithmically scaled graphs (top row) and linearly scaled graphs (bottom row).

departures notwithstanding. As comparison, the mean values of the sidewall stiffness data were also fitted with a linear function. Although the parameters of the power function formulation were statistically different from zero, it might be useful to compare the previous result to a linear fit to determine whether a power function is necessary to capture the decreasing trend in the data. The sidewall stiffness was chosen because its optimum exponents were less negative than the exponents from the time allotted for movement, i.e., the slower rate of decay might be indicative of a simpler decreasing trend.

The results of this analysis are shown in Figure 4.3. Similar to Figure 4.2, the very severe patient results are given in the first column and the moderate-to-severe patient results in the second. The second row of graphs contains the same data from the

	Group	R^2		F	
		Power	Linear	Power	Linear
k_{sw}	Very severe	0.56	0.31	295.5	117.7
	Moderate-to-severe	0.67	0.46	499.9	224.2

Table 4.4. Statistical comparison between least-squares regressions of k_{sw} using a power function and a linear function for the very severe and moderate-to-severe patient groups.

first row, but the data are plotted on a linear scale instead of a logarithmic scale. Each trial result is represented by a dot and each session by a solid line. The optimum power function and its confidence intervals on the prediction are represented by dashed lines and the optimum linear results by dash-dotted lines. Table 4.4 contains the statistical measures R^2 and F for the least-squares regressions shown in Figure 4.3. Although the decreasing trend of the sidewall stiffness for the moderate-to-severe group resembles a simple power function, the trend for the very severe group appears more complex (initially decreases, then increases, and finally decreases again). Regardless, the power function does a better job capturing the response for both patient groups.

Notice, the confidence intervals of the predictions for the power function are smaller than for the linear function. Although most of the data are enclosed by the confidence intervals of both functions, the quality of fit of the power functions exceeds the quality of fit of the linear functions by 0.23 on average. The F-statistic for the power function regression and for the linear function regression has $N_p - 1$ and $N - N_p$ degrees of freedom since both use two parameters and the same data sets. In both the very severe and moderate-to-severe groups, the F-statistic for the power function is more than twice that of the linear function. This provides another indication that motor recovery follows a power-law/exponential progression similar to motor learning.

	Group	Multiplier 95% CI		Exponent 95% CI	
		Mean	All	Mean	All
t_m	Very severe	4.34 4.00	4.06 3.50	-0.082 -0.098	-0.066 -0.096
	Moderate-to-severe	3.09 2.89	3.00 2.62	-0.075 -0.088	-0.066 -0.093
k_{sw}	Very severe	313.4 296.5	324.6 285.9	-0.043 -0.054	-0.044 -0.069
	Moderate-to-severe	204.2 193.2	217.3 173.8	-0.057 -0.068	-0.062 -0.106

Table 4.5. Comparison of the ranges of controller parameter values from optimizations done with the mean of the patient data and with all of the data.

4.4.2. Variability within patients/trials – comparison of optimization results from mean of the patient data and from all of the patient data

Although the R^2 values range from 0.56 to 0.71 for the mean values of each parameter and group, it is evident from the SEM bounds shown in Figure 4.2 that the data is variable within patients and trials. To test whether the previous power function least-squares regression results were an artifact of only considering the mean values of the parameters for each trial, the optimizations were repeated using data from all of the patients in the problem formulation. Data from all 10 patients in each group for the controller parameters along with traces of the optimum parameters are shown in Appendix C, Figure C.1. The results are also summarized in Appendix C, Table C.1, which is formatted similar to Table 4.3. Although the R^2 and F-statistic values have decreased due to the wide range of controller parameters encountered during patient therapy, the probability that the regression coefficients are nonzero remains the same, i.e., $p < 0.0001$ for all cases.

Table 4.5 compares the confidence intervals of the multiplier and exponent parameters for the optimization that used the mean of the patient data (Table 4.3) and the optimization that used all of the data (Table C.1). Without exception, the confidence intervals of t_m and k_{sw} for the optimization with all patient data overlap with a portion of the confidence intervals for the optimization with just the mean of the patient data (18-100% for multipliers, 55-100% for exponents; percentages defined relative to range of optimum parameters determined with the mean values). Thus, the results from both

	Group	Multiplier	Multiplier 95%CI	Exponent	Exponent 95%CI	R^2	F	p
t_m	Very severe	2.86	2.93 2.79	-0.024	-0.015 -0.034	0.71	31.5	0.0001
	Moderate-to-severe	2.26	2.31 2.22	-0.048	-0.048 -0.056	0.92	158.1	<0.0001
k_{sw}	Very severe	241.5	247.3 235.8	-0.001	0.008 -0.011	0.01	0.1	0.78
	Moderate-to-severe	162.2	166.7 157.8	-0.041	-0.030 -0.052	0.84	67.3	<0.0001

Table 4.6. Least-squares regression results from mean values of t_m and k_{sw} over trials 6-20 for the very severe and moderate-to-severe patient groups.

optimizations, both patient groups, and both controller parameters are consistent with a model describing recovery as learning.

4.4.3. Variability within sessions

The previous results are based on the evolution of patients' summary measures during their entire PBPT protocol (18 sessions). Another area of interest is the evolution of the summary measures during a single session (particularly adapting trials 6-20). Although it is clear that summary parameters t_m and k_{sw} of both groups follow an exponential progression throughout recovery, can a similar statement be made about the evolution of these parameters during an individual therapy session? This question was addressed by calculating the mean values of both summary measures for both groups over trials 6-20 of all sessions (18 sessions x 10 patients = 180 sessions) and fitting the result with a power function similar to the method discussed earlier. The results are summarized in Table 4.6 and are shown in Figure 4.4.

The confidence intervals for the multipliers and exponents of t_m of the two patient groups did not overlap, but were statistically different from zero. The least-squares regression results for t_m described 71% of the variation of the mean values for the very severe group and 92% of the variation of the mean values for the moderate-to-severe group. At first glance, the exponents for t_m seem to imply that the two groups had different recovery rates than each other during sessions and that these rates were lower

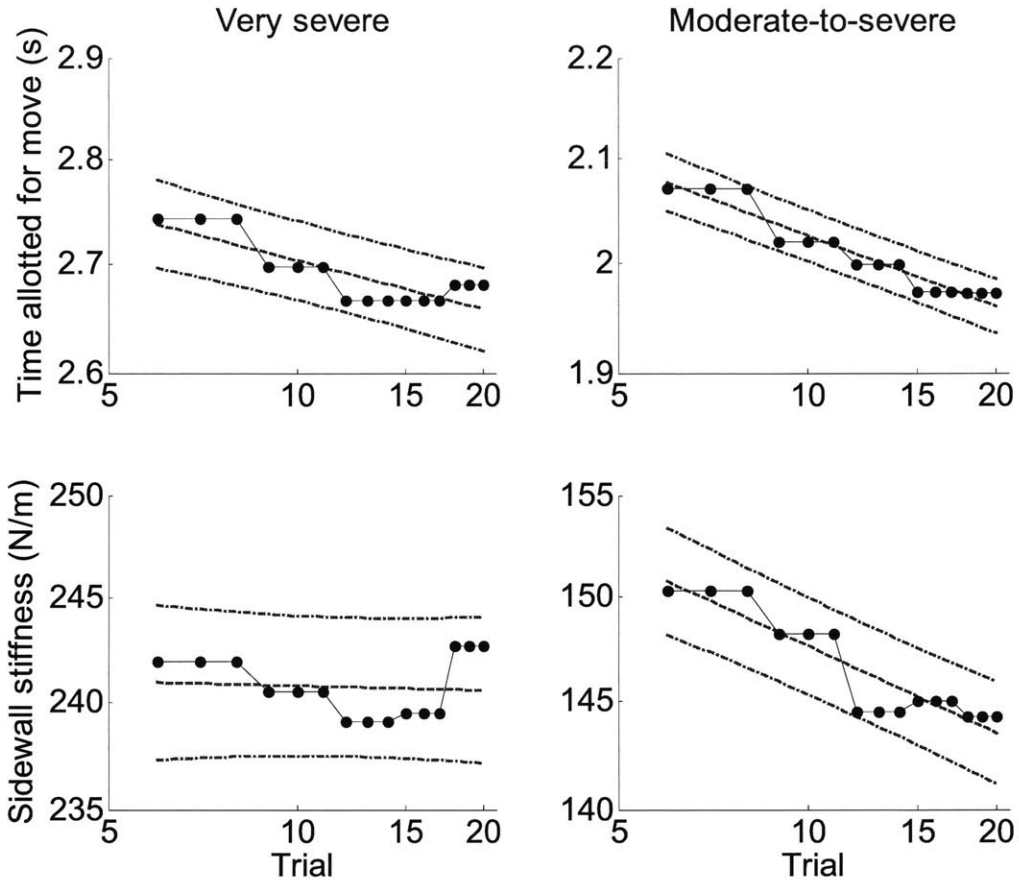

Figure 4.4. Evolution of the mean values of the time allotted for movement (t_m) and the sidewall stiffness (k_{sw}) over the last 15 trials of all sessions of the PBPT protocol.

than their overall recovery rates throughout the therapy protocol. To investigate further, least-squares regressions were also conducted on all of the data points (Appendix C, Table C.2). The confidence intervals for the exponents derived from the mean and all of the data throughout the therapy protocol and within a session are summarized in Table 4.7.

Although the regression parameters for t_m of the very severe group were not statistically different from 0 at the prescribed 0.05 level, the probability was close ($p = 0.061$). The resulting within-session exponents for t_m when all of the data is included in the regression of the very severe and moderate-to-severe patient groups were comparable to each other and to the exponents for the entire therapy protocol. As shown in Figure 4.5, although the CI's of the mean parameters throughout the protocol (dash-

	Group	95% CI for exponents			
		Trials 6-360 Mean	Trials 6-360 All	Trials 6-20 Mean	Trials 6-20 All
t_m	Very severe	-0.082 -0.098	-0.066 -0.096	-0.015 -0.034	0.002 -0.072
	Moderate-to-severe	-0.075 -0.088	-0.066 -0.093	-0.048 -0.056	-0.017 -0.084
k_{sw}	Very severe	-0.043 -0.054	-0.044 -0.069	0.008 -0.011	0.018 -0.044
	Moderate-to-severe	-0.057 -0.068	-0.062 -0.106	-0.030 -0.052	-0.028 -0.137

Table 4.7. Least-squares regression 95% CI for the exponents derived from the mean and all of the data for t_m and k_{sw} throughout the therapy protocol and within a session for the very severe and moderate-to-severe patient groups.

dotted gray lines) appear to have a steeper slope than those within a session (dash-dotted black lines), the wide range of data (light gray circles and lines) does not permit discrimination between the exponents for the throughout-protocol and within-session regressions.

The optimum parameters for k_{sw} of the very severe patient group were not statistically different from zero ($p = 0.78 \rightarrow$CI for exponent contained 0), whereas the parameters for the moderate-to-severe group were statistically different from zero with a quality of fit of $R^2 = 0.84$ at $p < 0.0001$. The confidence intervals for the exponent of the regression that included all of the moderate-to-severe patient k_{sw} data (Table C.2) contain the confidence intervals for the previous least-squares regressions of k_{sw} for the moderate-to-severe patient group (Table 4.7). Similar to t_m, the wide range of data in Figure 4.5 does not permit discrimination between the exponents for the throughout-protocol and within-session regressions.

Although a power function was unnecessary to capture the evolution of k_{sw} for the very severe patient group (i.e., exponent might equal 0), the evolution of t_m of both patient groups and k_{sw} of the moderate-to-severe patient group did follow an exponential progression similar to motor learning. Therefore, for three out of the four performance

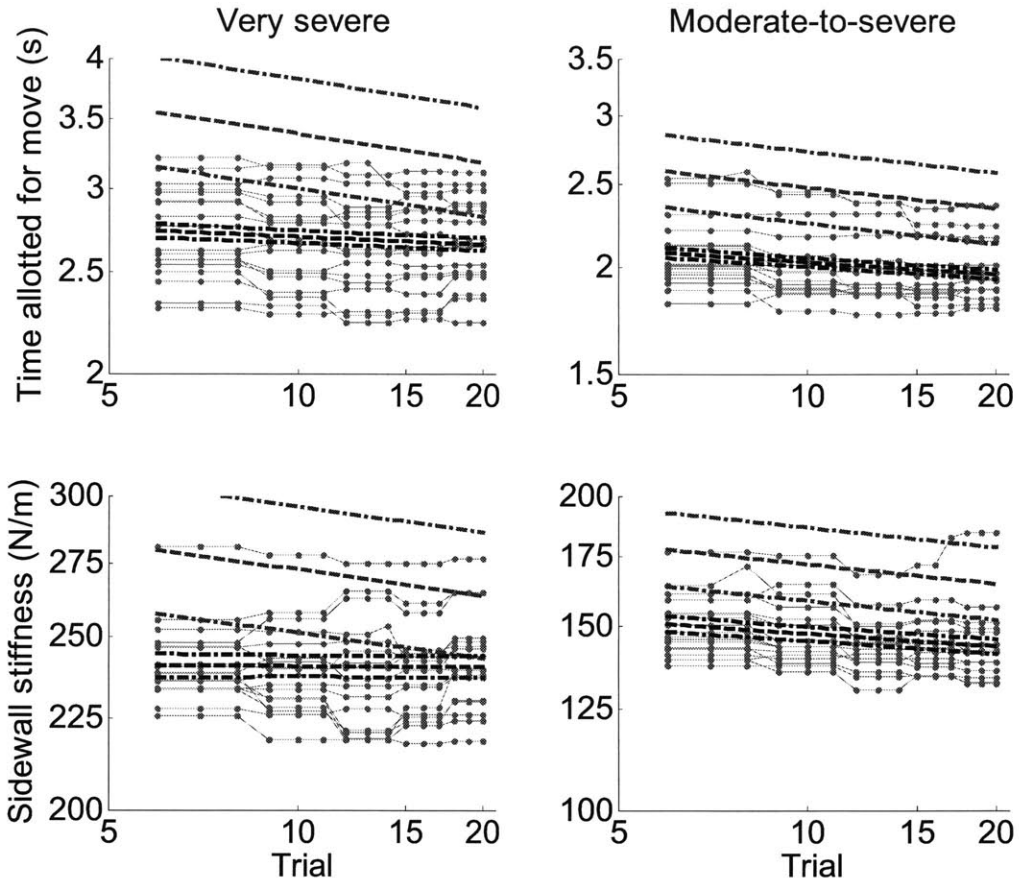

Figure 4.5. Data contributing to means (light gray) does not permit discrimination between the throughout-protocol and within-session regression exponents. Least-squares regression lines and 95% CI for the mean values of summary parameters throughout protocol are depicted with gray dashed and dash-dotted lines, whereas those for within a session are depicted with black dashed and dash-dotted lines.

measures considered in this study, motor recovery follows a power-law similar to motor learning throughout an individual therapy session as well as the entire therapy protocol.

4.4.4. Variability from the end of one session to the beginning of the next – is phenomenon similar to retention in motor learning also present in motor recovery?

Schmidt and Lee [85] discuss the concept of motor forgetting which refers to losing capabilities for movement. At the theoretical level, motor forgetting is a term used to indicate the opposite of motor learning, i.e., the loss of a motor memory (here, motor memory refers to an "acquired capability for movement" via practice). At the behavioral level, decreases in performance level from the end of one training session to the

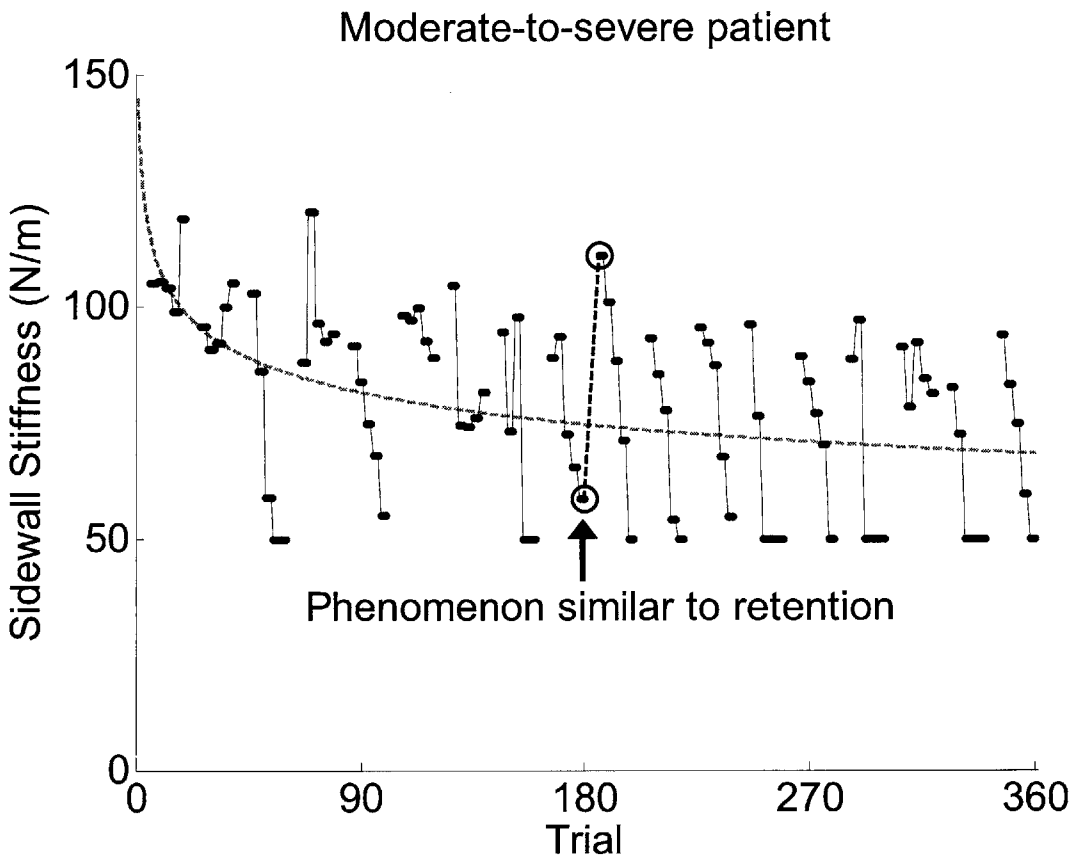

Figure 4.6. Evolution of k_{sw} through 18 therapy sessions for a moderate-to-severe patient. A decrease in stiffness corresponds to an improvement in aiming performance. Retention-like phenomena occur when the stiffness at the end of one session is less than the stiffness at the beginning of the next, i.e., performance gains from one session do not carry through to the next session (in some cases, total motor forgetting occurred).

beginning of the next are associated with motor forgetting. Retention is defined as the persistence of the gains in performance that resulted from practice (or lack of persistence if total motor forgetting occurred) [85]. In order to measure retention, time must pass between the learning trials and the retention test trials (referred to as the retention interval).

Figure 4.6 demonstrates what is proposed to be a phenomenon of motor forgetting at the behavioral level for one of the moderate-to-severe patient's ability to aim movements from one target to another. The controller parameters from the performance-based progressive algorithm act as summary measures of performance at the behavioral level. Recall, as patients' movements become quicker, t_m decreases, and as their

movements become better aimed, k_{sw} decreases. Therapy is delivered to the patient three times a week for 6 weeks, usually on Monday, Wednesday, and Friday. The day or two breaks between therapy sessions can act as the retention interval. During most sessions, the stiffness starts at a high level and then decreases (as expected from Figure 4.4). Likewise, from the end of most therapy sessions to the beginning of the next, the patient's ability to aim declines, as depicted by the increase in k_{sw}.

Although the moderate-to-severe patient results shown in Figure 4.6 were selected specifically to demonstrate the concept of retention relative to the ability to aim, instances where the sidewall stiffness decreased or remained constant from one therapy session to the next also occurred. Therefore, it was desirable to determine the extent to which the very severe and moderate-to-severe patient groups exhibit retention. A statistical test to determine whether retention is a reliable characteristic of motor recovery will be developed next.

One measure to quantify relative retention is the change in performance from the end of one session to the beginning of the next, referred to as a difference score by Schmidt and Lee [85]. Since increases in t_m and k_{sw} from one therapy session to the next represent a decrease in performance, i.e., a loss of an ability gained through practice, the metrics used to develop the statistical tests of interest were defined as

$$\Delta_{1,t_m}[k] = t_m[k+1, 6] - t_m[k, 20] \tag{4.6a}$$

$$\Delta_{1,k_{sw}}[k] = k_{sw}[k+1, 6] - k_{sw}[k, 20] \tag{4.6b}$$

where $k \in [1, 17]$ denotes the session number and each difference is computed between trial 6 of session $k+1$ and trial 20 of session k.

Three other metrics that are related to changes in performance will also be defined and are shown in Figure 4.7 (graphical example using sessions 9 and 10 from Figure 4.6). The change in a parameter during a session, i.e., the difference between trials 20 and 6, is given by Δ_2.

$$\Delta_{2,t_m}[k] = t_m[k, 20] - t_m[k, 6] \tag{4.7a}$$

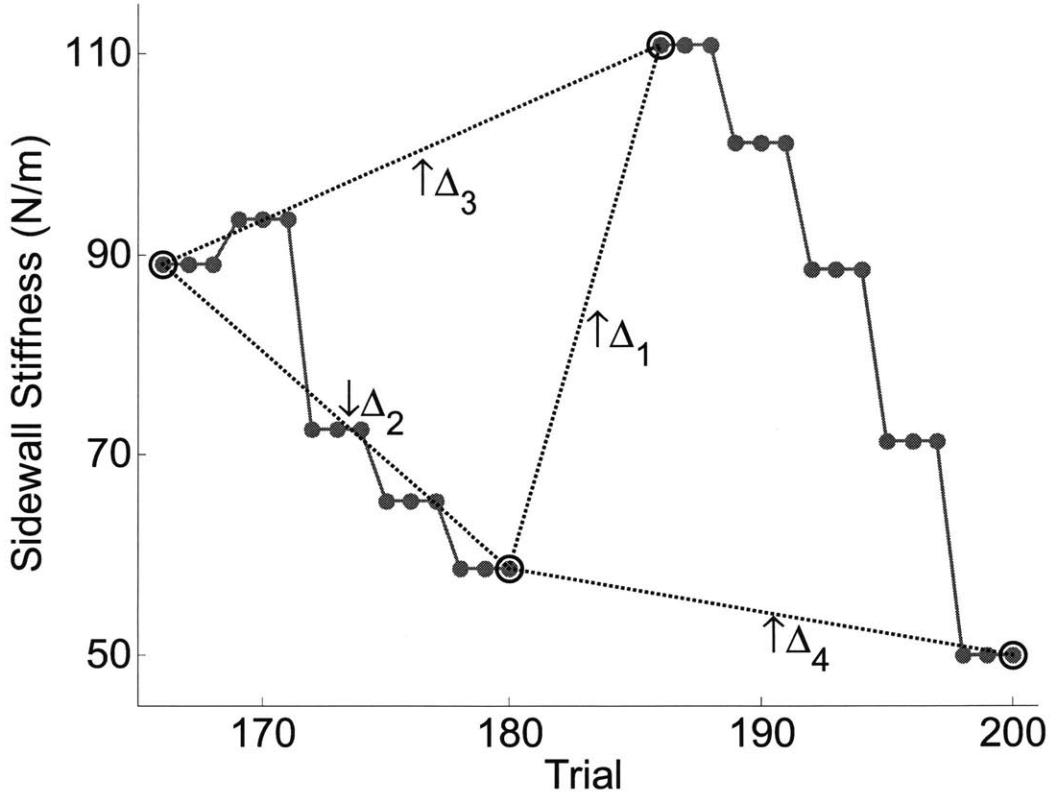

Figure 4.7. Four difference metrics used to investigate between-session Δ_1, within-session Δ_2, and session-to-session $\Delta_{3,4}$ trends in the PBPT controller parameters.

$$\Delta_{2,k_{sw}}[k] = k_{sw}[k, 20] - k_{sw}[k, 6] \tag{4.7b}$$

where $k \in [1, 18]$. This metric quantifies trends similar to the within-session least-squares regressions in section 4.4.3 (domain: trials 6-20), but only considers the parameter values at trials 6 and 20 of each session. In Figure 4.6, there are several instances where total forgetting occurs (i.e., the stiffness at trial 6 of a session is greater than the stiffness at trials 6 and 20 of the previous session). Metric Δ_3 is defined to examine whether trends exist between the initial PBPT algorithm trials of two consecutive sessions,

$$\Delta_{3,t_m}[k] = t_m[k+1, 6] - t_m[k, 6] \tag{4.8a}$$

$$\Delta_{3,k_{sw}}[k] = k_{sw}[k+1, 6] - k_{sw}[k, 6] \tag{4.8b}$$

whereas Δ_4 is defined to examine whether trends exist between the final PBPT algorithm trials of two consecutive sessions

$$\Delta_{4,t_m}[k] = t_m[k+1, 20] - t_m[k, 20] \tag{4.9a}$$

$$\Delta_{4,k_{sw}}[k] = k_{sw}[k+1, 20] - k_{sw}[k, 20] \tag{4.9b}$$

and $k \in [1, 17]$ for both Δ_3 and Δ_4. Notice, if is Δ_2 consistently greater than zero, the phenomenon is similar to retention if Δ_3 is consistently less than zero or it is similar to total motor forgetting if Δ_3 is consistently greater than zero.

The metrics defined in (4.6)-(4.9) were calculated over 18 therapy sessions for each group of 10 patients, resulting in $N_\Delta = 170$ data points ($N_\Delta = 180$ for Δ_2). A hypothesis test was then conducted on the mean of each set. The test statistic $(\overline{X} - \mu_0)/(s_x/\sqrt{N_\Delta})$ was used to construct the hypothesis test on the mean value of the sample distribution. $\overline{X}$ is the mean value of the sample set, μ_0 is mean value used to define the null hypothesis, and s_x is the standard deviation of the sample set. Although the given test statistic follows a $T_{N_\Delta - 1}$ distribution if $\overline{X}$ is normal, it has been found that violating this assumption does not seriously affect the distribution of the test statistic for samples of moderate to large sizes $(N_\Delta \geq 25)$ [66]. Therefore, it does not appreciably change the probability of making a Type I error (reject null hypothesis when it is true) or Type II error (fail to reject the null hypothesis when it is false) [66].

To determine whether any trends might exist, a two-tailed t-test was conducted on each sample set with $\mu_0 = 0$ [66]. Specifically, the null hypothesis (H_0) and the alternative hypothesis (H_1) were defined to be

$$H_0: \quad \mu = 0 \tag{4.10a}$$

$$H_1: \quad \mu \neq 0 \tag{4.10b}$$

The alternative hypothesis is true when a decreasing trend occurs, $\mu < 0$, or when an increasing trend occurs, $\mu > 0$. The probabilities that the null hypothesis is true for each metric are given in Table 4.8. The asterisk in the table (*) denotes where $p < 0.10$. The hypothesis tests for Δ_1 reveal that a retention-like phenomenon might exist in t_m and k_{sw} for the moderate-to-severe group. Similarly, the hypothesis tests for Δ_2 reveal that a

	Group	Probability that $\mu = 0$			
		Δ_1	Δ_2	Δ_3	Δ_4
t_m	Very severe	0.684	0.039*	0.331	0.346
	Moderate-to-severe	0.057*	<0.001*	0.374	0.426
k_{sw}	Very severe	0.357	0.804	0.338	0.464
	Moderate-to-severe	0.029*	<0.001*	0.213	0.248

Table 4.8. Summary of two-tailed hypothesis tests conducted on four difference metrics for both patient groups and both PBPT controller parameters to identify where trends in data might exist (* denotes $p < 0.10$).

within-session trend might exist in t_m and k_{sw} for the moderate-to-severe group and in t_m for the very severe group. The hypothesis tests for Δ_3 and Δ_4 reveal that the null hypothesis cannot be rejected for any of the test cases and, therefore, no clear session-to-session trends exist.

Left-tailed t-tests ($H_1: \ \mu < 0$) and right-tailed t-tests ($H_1: \ \mu > 0$) were then conducted on the five cases designated with (*) in Table 4.8 to determine whether the corresponding trends present in the difference metric were decreasing or increasing. If retention were a property of the entire group, the mean value of the retention metric should be greater than zero. Indeed, the alternative hypothesis of the right-tailed hypothesis tests was accepted for both of the moderate-to-severe group's retention metrics (Δ_1). Specifically, the probabilities supporting the null hypothesis for the metrics derived from the moderate-to-severe group's data were $p = 0.029$ for t_m and $p = 0.014$ for k_{sw}. Consistent with the decreasing trends shown in Figure 4.4, the alternative hypothesis of the left-tailed hypothesis tests was accepted for t_m ($p = 0.019$) of the very severe group, and for t_m ($p < 0.001$) and k_{sw} ($p < 0.001$) of the moderate-to-severe group.

This section investigated the variation of the summary measures from session to session. A phenomenon similar to retention (or forgetting) from motor learning studies

was observed in the evolution of k_{sw} of a moderate-to-severe patient and its prevalence in the recovery of the moderate-to-severe patient group was demonstrated by hypothesis tests that were conducted on proposed retention metrics for t_m and k_{sw}. However, similar hypothesis tests conducted on the same metrics for the very severe patient group could not reject the null hypothesis. Therefore, the moderate-to-severe patient group exhibited another similarity with motor learning, but the very severe group did not.

4.5. Conclusions

Chapter 4 has provided clinical evidence that the PBPT protocol, which was based on concepts that enhance motor learning (e.g. repetition, active participation, goal specification, positive reinforcement), enhanced the motor recovery of moderate-to-severe chronic stroke patients in comparison to the sensorimotor and progressive resistance protocols. Robot-based performance summary measures from the same patient groups were analyzed to demonstrate that motor recovery could be modeled similar to motor learning, where an amount of practice is related to a performance level via a power function. Least-squares regressions were used to demonstrate that the relation between the trial number and the summary measures could be quantified with power functions. Specifically, the time allotted for movement and the sidewall stiffness exhibited a power-law/exponential progression throughout the therapy protocol of both patient groups. With the exception of the sidewall stiffness data from the very severe patient group, the summary measures also followed an exponential progression within individual therapy sessions. In addition, a phenomenon similar to retention in motor learning occurred in the evolution of both summary measures of the moderate-to-severe patient group, but was not a prevalent characteristic of the recovery of the very severe patient group.

Motor recovery of the moderate-to-severe patient group exhibited several characteristics that are commonly associated with motor learning. Motor recovery of the very severe patient group exhibited some, but not all, of these characteristics. Although further study is needed to conclusively establish the origins of the differences between the recovery characteristics of very severe and moderate-to-severe patients, perhaps the differences were due to the heightened neurological and musculoskeletal deficits of the very severe patients. To test this hypothesis, some of these deficits, such as abnormal

tone, could be addressed prior to or concurrently with robotic therapy. These findings could allow researchers to develop improved rehabilitation methods and to predict the effect of more treatment sessions for very severe and moderate-to-severe patients, thereby providing justification to extend inpatient hospital stays or to develop more outpatient rehabilitation programs.

Chapter 5

Spectral estimation of arm mechanical impedance during robotic stroke therapy

5.1. Summary

This chapter presents a spectral method to estimate the multi-joint mechanical impedance of the human arm that is suitable for use in a clinical setting, e.g., with stroke patients undergoing robotic rehabilitation for a paralyzed arm. In this context, special circumstances such as hypertonicity and tissue atrophy due to disuse of the hemiplegic limb must be considered. A low-impedance robot was used to bring the upper limb of a stroke patient to a test location, generate force perturbations, and measure the resulting motion. Data was analyzed both by assuming a known model structure and by spectral procedures that make no assumption about model structure. Methods to compensate for input signal coupling at low frequencies were developed. Analysis of stroke patient data showed that this method improved numerical conditioning of the estimates.

5.2. Introduction

Patients with stroke who had robotic therapy using a performance-based, progressive protocol experienced a marked change in tone – a muscle's resistance to passive elongation or stretch [27,57]. Although clinicians judge muscle tone subjectively, an objective measure would provide valuable insight about the effect of stroke on a hemiplegic limb and better characterize the effect of rehabilitation therapy. Robots such as MIT-MANUS [46] or InMotion^2 (Interactive Motion Technologies, Inc.) are able to deliver forces to a patient's limb and measure the position, velocity, and interaction forces between the robot and that limb. Therefore, these robots are well suited to

measure motion of the human arm resulting from applied forces, and thereby objectively quantify at least one aspect of patient tone.

The physical quantity corresponding to clinical assessment of muscle tone is mechanical impedance, which characterizes the dynamic relation between motion and force. Considered a dynamic generalization of stiffness, impedance plays an important role in the control of complex multi-joint movements. Past reasons for measuring impedance[3] range from understanding basic physiological properties of muscle [68] to testing different hypotheses concerning the maintenance of posture or the control of movement [35,44]. Psychophysical studies have also investigated how impedance properties vary with motor learning [14]. Although several methods have been developed to measure impedance of unimpaired subjects' limbs, its measurement in patients with stroke is complicated by their special circumstances, which may include hypertonicity, profound muscle weakness due to central denervation, or tissue atrophy due to disuse of the hemiplegic limb. Nevertheless, because of the clinical importance of muscle tone and because recovery from brain injury appears to share some features of unimpaired motor learning, we have developed a new method to measure impedance of stroke patient's limbs during rehabilitation treatment.

Several different methods have been developed to estimate impedance properties of the multi-joint human arm. An initial attempt to measure human arm stiffness used a series of displacement perturbations in eight different directions in a horizontal plane [68]. While the subject's hand was held at the perturbation location, the restoring forces were measured. The force and displacement vectors were then used to characterize stiffness. Since the authors were interested in measuring biomechanical properties subserving arm posture, the measurement procedure was designed to increase the duration of the subject reaction time in order to reduce the occurrence of voluntary movement. The results of this study showed that the neuromuscular impedance of the arm during posture is predominantly spring-like.

Later studies were extended to include the estimation of dynamic parameters commonly used to quantify arm impedance, such as inertia and viscous damping. For

[3] The term "impedance" is used synonymously with "mechanical impedance" for brevity.

example, Dolan et al. [24] applied several rapidly rising, underdamped position perturbations. By assuming a linear model structure, they were able to estimate the arm's inertial, damping, and stiffness properties using the force and displacement time histories in a Cartesian reference frame. Again, the experimental procedure attempted to limit voluntary responses to the applied perturbations. Tsuji et al. [95] conducted a similar experiment to estimate impedance properties and also transformed the property matrices from Cartesian coordinates at the hand to joint coordinates at the shoulder and elbow. In a later experiment by Gomi and Kawato [35], static stiffness was estimated by applying trapezoidal positional perturbations in eight randomly ordered directions. Dynamic inertia, viscosity, and stiffness parameters were estimated during movement by applying a small, randomized force perturbation. As with previous experiments, the subjects were given instructions not to intervene voluntarily during perturbations.

Burdet et al. [15] developed a different method to estimate endpoint stiffness during multi-joint arm movements by using displacement perturbations instead of force perturbations. This was accomplished by displacing the hand relative to a **prediction** of the unperturbed trajectory estimated by observing that trajectories of repeated movements under the same conditions were similar. The commanded trajectory was constructed by adding the perturbation trajectory to the predicted unperturbed trajectory. Although useful for unimpaired subjects, implementing this method with stroke patients would be difficult because of the inherent variability of their movements.

The method described by Perreault et al. [74] used small stochastic force perturbations to estimate the dynamic compliance transfer function matrix and subsystem impulse response functions in the presence of output measurement noise and input coupling (via linear and nonlinear numerical simulations). Unlike the previous methods, a model structure was not assumed, although the system was assumed to behave linearly for small perturbations. The stochastic input is desirable because its random nature in magnitude and direction avoids the need for separate measurements in individual directions and minimizes the likelihood of voluntary reactions (however, compensatory muscle activations such as co-contraction or relaxation may still occur). This provides a frequency-rich input to the subject in a relatively short time frame, rendering it more attractive for use with patients. This research group later modified their method and

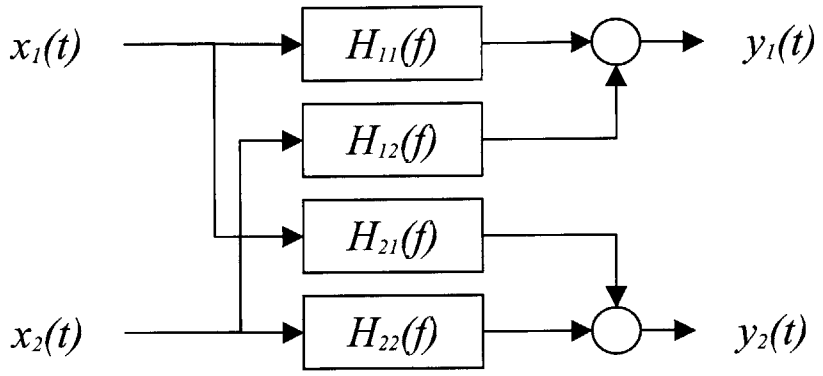

Figure 5.1. Block diagram of linear MIMO system identification structure: H_{11} and H_{12} are the transfer functions from the inputs, x_1 and x_2, to output y_1; H_{21} and H_{22} are the transfer functions from the same inputs to output y_2.

applied stochastic position perturbations instead of force perturbations [1]. System properties were estimated by using a previously developed multiple-input, single-output (MISO) system identification technique [8] applied to each output simultaneously, resulting in a multiple-input, multiple-output (MIMO) methodology.

In this chapter, we present an impedance measurement methodology that is tailored for clinical use. In addition to the application of force perturbations, a simple Proportional-Derivative (PD) controller is used to gently bring the patient's arm to a test location and limit large-scale deviations from that location. Although unimpaired subjects are able to relax their arm at a given location, the hemiplegic arms of patients often exhibit hypertonicity, causing their arms to substantially drift in the workspace. Data is analyzed both by assuming a known model structure and by spectral procedures that make no assumption about model structure. Two methods to reduce input signal coupling are considered – an experimental method that modifies the commanded perturbation and an analytical method that improves the numerical conditioning of the estimate. Stroke patient data is used to illustrate the effectiveness of the method.

5.3. Methods to estimate human arm impedance

5.3.1. Impedance estimate with assumed model structure

Figure 5.1 displays the block diagram of the structure used to represent a linear MIMO system with two inputs $x_{1,2}$ and two outputs $y_{1,2}$. For instance, the inputs to the system

could be forces and the outputs displacements or vice versa. One method of estimating arm impedance properties is to assume a known structure for the system model (e.g. constant stiffness like Mussa-Ivaldi et al. [68], or inertia, damping, and stiffness like Dolan et al. [24]) and determine an optimal set of parameter values that minimize the error between the predicted output and the measured output. For example, assuming that a linear arm model in hand space with second-order dynamics in each degree of freedom is sufficient to characterize arm impedance,

$$\begin{bmatrix} m_{11} & m_{12} \\ m_{21} & m_{22} \end{bmatrix}\begin{bmatrix} \ddot{x} \\ \ddot{y} \end{bmatrix}+\begin{bmatrix} b_{11} & b_{12} \\ b_{21} & b_{22} \end{bmatrix}\begin{bmatrix} \dot{x} \\ \dot{y} \end{bmatrix}+\begin{bmatrix} k_{11} & k_{12} \\ k_{21} & k_{22} \end{bmatrix}\begin{bmatrix} x \\ y \end{bmatrix}=\mathbf{F}=\begin{bmatrix} F_x \\ F_y \end{bmatrix} \tag{5.1}$$

where (x,y) are the Cartesian hand coordinates, m_{ij}, b_{ij}, and k_{ij} with $i,j\in 1,2$ are components of the endpoint inertia, damping, and stiffness matrices, and $\mathbf{F}$ is a vector of applied forces. The interaction force between the robot and patient, and the patient's equilibrium arm position contribute to the applied forces. Specifically,

$$\begin{bmatrix} F_x \\ F_y \end{bmatrix}=\begin{bmatrix} F_{i,x} \\ F_{i,y} \end{bmatrix}+\begin{bmatrix} k_{11} & k_{12} \\ k_{21} & k_{22} \end{bmatrix}\begin{bmatrix} x_o \\ y_o \end{bmatrix} \tag{5.2}$$

where $(F_{i,x}, F_{i,y})$ are the Cartesian interaction forces and (x_o, y_o) is the equilibrium position of the arm. To formulate the parameter identification problem in a least-squares optimal manner, the second term on the right-hand side of (5.2) is moved to the left-hand side of (5.1) and defined to be an unknown offset force $(F_{o,x}, F_{o,y})$, i.e.,

$$\begin{bmatrix} m_{11} & m_{12} \\ m_{21} & m_{22} \end{bmatrix}\begin{bmatrix} \ddot{x} \\ \ddot{y} \end{bmatrix}+\begin{bmatrix} b_{11} & b_{12} \\ b_{21} & b_{22} \end{bmatrix}\begin{bmatrix} \dot{x} \\ \dot{y} \end{bmatrix}+\begin{bmatrix} k_{11} & k_{12} \\ k_{21} & k_{22} \end{bmatrix}\begin{bmatrix} x \\ y \end{bmatrix}+\begin{bmatrix} F_{o,x} \\ F_{o,y} \end{bmatrix}=\begin{bmatrix} F_{i,x} \\ F_{i,y} \end{bmatrix} \tag{5.3}$$

The least-squares optimal solution can be found by rearranging the previous equation into the form

$$\mathbf{Ap}=\mathbf{F}_i \tag{5.4}$$

where $\mathbf{p}=[m_{11}, m_{12}, m_{21}, m_{22}, b_{11}, b_{12}, b_{21}, b_{22}, k_{11}, k_{12}, k_{21}, k_{22}, F_{o,x}, F_{o,y}]^{\mathrm{T}}$ is a 14×1 vector of parameters to be estimated, $\mathbf{A}$ is a $2N\times 14$ matrix that contains displacement, velocity, and acceleration data at each point in time along with zero and unity column

vectors, and $\mathbf{F}_i$ is a $2N \times 1$ vector that contains the interaction forces at each point in time (N is the length of the experimental record). Specifically,

$$\begin{bmatrix} \ddot{\mathbf{x}} & \ddot{\mathbf{y}} & \mathbf{0} & \mathbf{0} & \dot{\mathbf{x}} & \dot{\mathbf{y}} & \mathbf{0} & \mathbf{0} & \mathbf{x} & \mathbf{y} & \mathbf{0} & \mathbf{0} & \mathbf{1} & \mathbf{0} \\ \mathbf{0} & \mathbf{0} & \ddot{\mathbf{x}} & \ddot{\mathbf{y}} & \mathbf{0} & \mathbf{0} & \dot{\mathbf{x}} & \dot{\mathbf{y}} & \mathbf{0} & \mathbf{0} & \mathbf{x} & \mathbf{y} & \mathbf{0} & \mathbf{1} \end{bmatrix} \cdot \mathbf{p} = \begin{bmatrix} \mathbf{F}_{i,x} \\ \mathbf{F}_{i,y} \end{bmatrix} \tag{5.5}$$

The least-squares optimal solution is defined as

$$\mathbf{p} = \left(\mathbf{A}^{\mathrm{T}}\mathbf{A}\right)^{-1}\mathbf{A}^{\mathrm{T}}\mathbf{F}_{\mathrm{i}} \tag{5.6}$$

Note, once the optimal parameters are found, it is possible to estimate the equilibrium position of the arm in the following manner:

$$\begin{bmatrix} x_o \\ y_o \end{bmatrix} = -\begin{bmatrix} k_{11} & k_{12} \\ k_{21} & k_{22} \end{bmatrix}^{-1} \begin{bmatrix} F_{o,x} \\ F_{o,y} \end{bmatrix} \tag{5.7}$$

With the asymmetric linear structure developed, it is straightforward to define other linear model structures with second-order dynamics in each Cartesian coordinate. For instance, assuming the inertial, damping, and stiffness matrices are all symmetric – $m_{21} = m_{12}$, $b_{21} = b_{12}$, and $k_{21} = k_{12}$, the least squares formulation becomes

$$\begin{bmatrix} \ddot{\mathbf{x}} & \ddot{\mathbf{y}} & \mathbf{0} & \dot{\mathbf{x}} & \dot{\mathbf{y}} & \mathbf{0} & \mathbf{x} & \mathbf{y} & \mathbf{0} & \mathbf{1} & \mathbf{0} \\ \mathbf{0} & \ddot{\mathbf{x}} & \ddot{\mathbf{y}} & \mathbf{0} & \dot{\mathbf{x}} & \dot{\mathbf{y}} & \mathbf{0} & \mathbf{x} & \mathbf{y} & \mathbf{0} & \mathbf{1} \end{bmatrix} \cdot \mathbf{p}' = \begin{bmatrix} \mathbf{F}_{i,x} \\ \mathbf{F}_{i,y} \end{bmatrix}$$

where $\mathbf{p}' = \left[m_{11}, m_{12}, m_{22}, b_{11}, b_{12}, b_{22}, k_{11}, k_{12}, k_{22}, F_{o,x}, F_{o,y}\right]^{\mathrm{T}}$.

5.3.2. Impedance estimate without assumed model structure

Although assuming a linear structure with second-order dynamics in each degree of freedom is appealing from intuitive and pedagogical standpoints, it is not physiologically plausible with respect to the biological system being modeled. This assumption ignores the dynamics of neuro-muscular excitation, reflex action, and excitation-contraction coupling [45]. Frequency-domain MIMO system-identification algorithms assume the system behaves linearly for small perturbations, but otherwise do not assume any explicit structure.

The input/output cross-spectra for a general MIMO system is related to the input autospectra and cross-spectra by the following equation [8]:

$$G_{x_i y_j}(f) = \sum_{k=1}^{N} H_{y_j x_k}(f) \cdot G_{x_i x_k}(f) \tag{5.8}$$

where $G_{x_i x_k}$ is the one-sided input cross-spectrum between inputs x_i and x_k (input autospectrum when $i = k$), $G_{x_i y_j}$ is the one-sided input/output cross-spectrum between input x_i and output y_j, and $H_{y_j x_k}$ is the transfer function relating input x_k to output y_j. For the system of interest, there are two inputs and two outputs. If a force perturbation is used ($x_1 = F_x$, $x_2 = F_y$, $y_1 = x$, and $y_2 = y$), the dynamic compliance (or admittance) is estimated. Similarly, if a displacement perturbation is used ($x_1 = x$, $x_2 = y$, $y_1 = F_x$, and $y_2 = F_y$), the dynamic stiffness (or impedance) is estimated. To simplify notation, the dependence of the power spectra and transfer functions on f will be implied. The solution for the two-input, two-output system is given by the following set of equations (with $i \in 1, 2$):

$$H_{y_i x_1} = \frac{G_{x_1 y_i}\left[1 - \dfrac{G_{x_1 x_2} G_{x_2 y_i}}{G_{x_2 x_2} G_{x_1 y_i}}\right]}{G_{x_1 x_1}\left(1 - \gamma^2_{x_1 x_2}\right)} \tag{5.9a}$$

$$H_{y_i x_2} = \frac{G_{x_2 y_i}\left[1 - \dfrac{G_{x_2 x_1} G_{x_1 y_i}}{G_{x_1 x_1} G_{x_2 y_i}}\right]}{G_{x_2 x_2}\left(1 - \gamma^2_{x_1 x_2}\right)} \tag{5.9b}$$

where $\gamma^2_{x_1 x_2}(f)$ is the ordinary coherence between inputs x_1 and x_2, and is defined to be

$$\gamma^2_{x_1 x_2} = \frac{\left|G_{x_1 x_2}\right|^2}{G_{x_1 x_1} G_{x_2 x_2}} \tag{5.10}$$

Coherence is a measure of linear dependency of the inputs (a value of 0 corresponds to mutually independent inputs whereas 1 corresponds to perfectly linearly dependent inputs). By examining (5.9), it is obvious that this method will fail if the inputs are perfectly linearly dependent on one another because all of the denominator values will go

to zero causing the transfer function estimates to go to infinity. Although mutually independent inputs are desirable, in practice the ordinary coherence will lie between 0 and 1.

Partial and multiple coherence functions are used to assess the performance of the spectral method [8]. Partial coherence measures the linear dependency of one input to a particular output and is equivalent to ordinary coherence after the effect of the other input has been removed (i.e., ordinary coherence of conditioned multiple inputs). The partial coherence functions are given by

$$\gamma^2_{x_1y_i\cdot x_2} = \frac{\left|G_{x_1y_i}G_{x_2x_2} - G_{x_2y_i}G_{x_1x_2}\right|^2}{G^2_{x_2x_2}G_{x_1x_1}G_{y_iy_i}\left(1-\gamma^2_{x_2x_1}\right)\left(1-\gamma^2_{x_2y_i}\right)} \tag{5.11a}$$

$$\gamma^2_{x_2y_i\cdot x_1} = \frac{\left|G_{x_2y_i}G_{x_1x_1} - G_{x_1y_i}G_{x_2x_1}\right|^2}{G^2_{x_1x_1}G_{x_2x_2}G_{y_iy_i}\left(1-\gamma^2_{x_1x_2}\right)\left(1-\gamma^2_{x_1y_i}\right)} \tag{5.11b}$$

where $\gamma^2_{x_jy_i} = \dfrac{\left|G_{x_jy_i}\right|^2}{G_{x_jx_j}G_{y_iy_i}}$ is the ordinary coherence between input x_j and output y_i with $i, j \in 1, 2$.

Multiple coherence functions measure how well a given output can be predicted from both of the inputs. They can also determine over what frequency range a linear model can accurately describe the system dynamics. Low multiple coherence values indicate insufficient input power in a frequency range, system nonlinearities, noise, and/or contributions from unmeasured inputs [74]. The multiple coherence functions for 2-input, 2-output case are given by

$$\gamma^2_{y_i\cdot x} = \frac{\overline{H}_{y_ix_1}G_{x_1y_i} + \overline{H}_{y_ix_2}G_{x_2y_i}}{G_{y_iy_i}} \tag{5.12}$$

where $i \in 1, 2$ and $\overline{H}$ denotes the complex conjugate of H.

5.4. Pilot study and importance of human-machine interaction

5.4.1. Implementation of clinical stochastic test

A pilot study was conducted with three stroke patients at The Burke Medical Research Institute in White Plains, NY. The institutional review boards of the Burke Rehabilitation Hospital and the Massachusetts Institute of Technology approved the protocol. Written informed consent was obtained from all patients. Although accepted into a robotic study[4], the patients had not yet begun their protocol and had no prior experience with the robot or robotic therapy.

During the measurement, the patients were instructed to "simply relax and allow the robot to shake their arm." One difficulty that often arises with stroke patients that usually doesn't arise with unimpaired subjects is their inability to relax at a given position. The hemiplegic arms of patients exhibiting hypertonicity may curl towards the fetal position because their flexors contract more than their extensors. Although a patient's arm can usually be brought to a desired position in the workspace, it often drifts from that position. For example, 18 trials (3 patients, 6 trials each) were conducted in which the clinician manually moved the patient's arm to the desired test location, released it, and the robot controller applied perturbations but did not attempt to prevent drift. On average, patients drifted 7.8 cm (standard deviation of 2.9 cm, minimum of 4.4 cm, maximum of 12.3 cm) during the test. Since arm impedance parameters vary significantly throughout the workspace, this could result in significant nonlinear dynamics or a non-stationary process, either (or both) of which would invalidate assumptions underlying the spectral methods to be used. To prevent this, a simple PD controller was added to the robot control:

$$F_{c,x} = \Delta F_x - k_p(x - x_{des}) - k_d \dot{x} \tag{5.13a}$$

$$F_{c,y} = \Delta F_y - k_p(y - y_{des}) - k_d \dot{y} \tag{5.13b}$$

[4] Selection criteria: Patients had hemiparesis or hemiplegia of the upper and lower extremity after a single stroke (identified by neuroimaging) that had occurred at least 8 months prior to the initial assessment. Sensory or visual field impairment, aphasia, and cognitive impairment were not exclusion criteria, but the patients needed to be able to follow simple instructions.

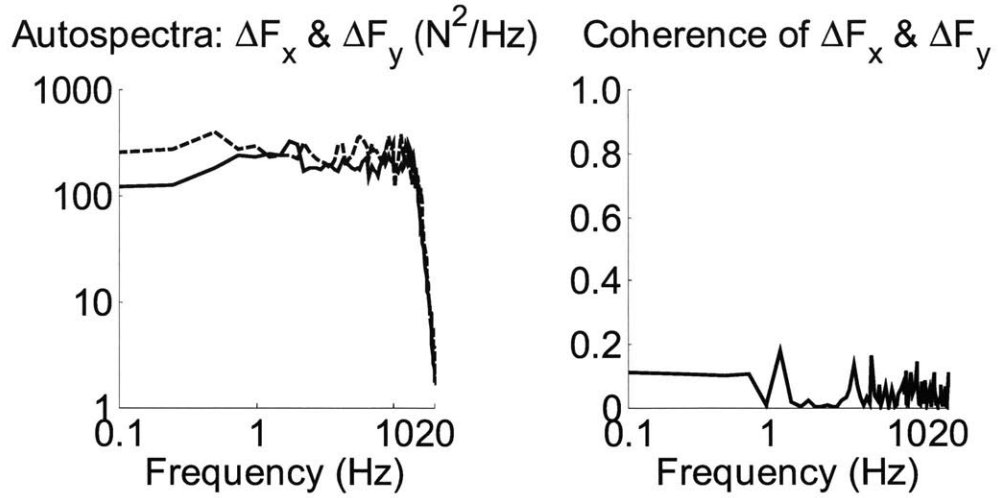

Figure 5.2. Autospectra of commanded force perturbations, ΔF_x (solid line) and ΔF_y (dashed line), as well as their coherence (solid line).

where $(F_{c,x}, F_{c,y})$ are the commanded forces at the robot manipulandum, $(\Delta F_x, \Delta F_y)$ are the commanded force perturbations, (x_{des}, y_{des}) are the desired Cartesian coordinates of the test in the robot workspace, k_p is the controller proportional gain, and k_d is the derivative gain.

An example result from one patient will be discussed to compare the time-domain and frequency-domain methods. After the PD controller brought the patient's hand to the center target location used during therapy, a force perturbation was applied to the patient's hemiplegic arm for 50 seconds while the PD controller resisted the patient's natural tendency to drift. Perturbation commands were generated at a sampling rate of 500 Hz by filtering a set of uniformly distributed random numbers with an eighth-order Butterworth filter that had a cut-off frequency of 15 Hz (selected to exceed the natural frequency of the human arm, ~ 2 to 3 Hz). The seed of the random number generator was varied to find a pair of signals with low coherence (Figure 5.2). A portion of the time responses for the three repeatability tests is shown in Figure 5.3. This data was post-processed by using the MATLAB function filtfilt function with a fourth-order Butterworth filter that had a cut-off frequency of 25 Hz (significantly above perturbation bandwidth). The asymmetric and symmetric least-squares optimal parameter values for the three repeatability test runs result in the following means and standard errors of parameter values:

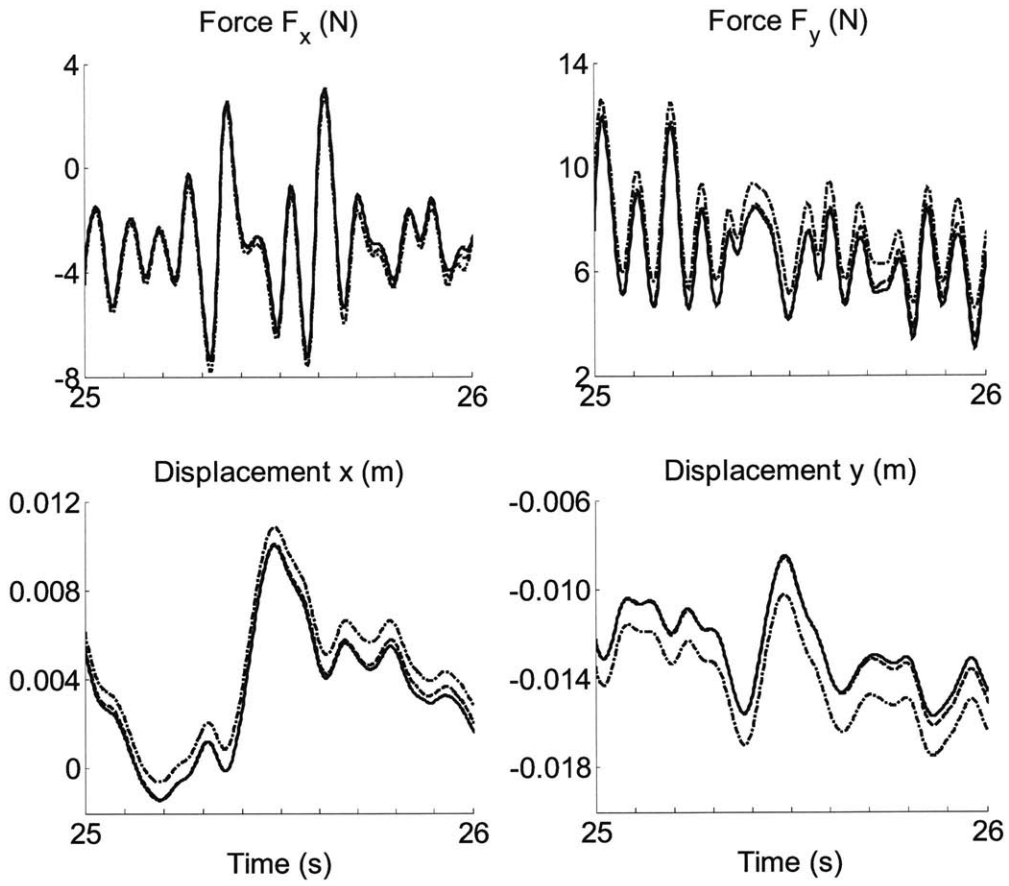

Figure 5.3. Repeatability of patient data (1 second shown of three 50-second tests): mean of standard deviations from each test – $\overline{\sigma}_{F_x} = 2.06$ N, $\overline{\sigma}_{F_y} = 2.14$ N, $\overline{\sigma}_x = 3.1$ mm, and $\overline{\sigma}_y = 2.4$ mm.

$$\mathbf{M}_{\text{asym}} = \begin{bmatrix} 0.894 \pm 0.007 & -0.050 \pm 0.016 \\ -0.117 \pm 0.031 & 0.834 \pm 0.016 \end{bmatrix} \text{kg} \quad \mathbf{M}_{\text{sym}} = \begin{bmatrix} 0.901 \pm 0.016 & -0.078 \pm 0.008 \\ -0.078 \pm 0.008 & 0.813 \pm 0.016 \end{bmatrix} \text{kg}$$

$$\mathbf{B}_{\text{asym}} = \begin{bmatrix} 10.82 \pm 0.34 & -9.63 \pm 0.18 \\ -4.12 \pm 0.20 & 17.53 \pm 0.31 \end{bmatrix} \text{N} \cdot \text{s/m} \quad \mathbf{B}_{\text{sym}} = \begin{bmatrix} 9.66 \pm 0.33 & -6.90 \pm 0.11 \\ -6.90 \pm 0.11 & 18.49 \pm 0.46 \end{bmatrix} \text{N} \cdot \text{s/m}$$

$$\mathbf{K}_{\text{asym}} = \begin{bmatrix} 31.4 \pm 9.6 & -26.9 \pm 3.1 \\ -56.0 \pm 12.5 & 293.1 \pm 13.7 \end{bmatrix} \text{N/m} \quad \mathbf{K}_{\text{sym}} = \begin{bmatrix} 33.7 \pm 7.8 & -43.4 \pm 7.8 \\ -43.4 \pm 7.8 & 290.2 \pm 11.9 \end{bmatrix} \text{N/m}$$

These values are comparable in magnitude to those reported in Tsuji et al. [95]. The squared correlation coefficients for the least-squares optimal parameters (comparing the right-hand side of (5.3) to the left-hand side) from each of the repeatability tests were 0.71 in the x-coordinate and 0.75 in the y-coordinate. The results from the time-domain optimization problem can be compared to the spectral transfer function estimates by

computing the transfer function matrix of the linear model. The transfer function matrix that describes the dynamic stiffness (or impedance) of the system, i.e.,

$$\mathbf{H}_{\mathrm{K}}(s)=\begin{bmatrix} m_{11}s^2+b_{11}s+k_{11} & m_{12}s^2+b_{12}s+k_{12} \\ m_{21}s^2+b_{21}s+k_{21} & m_{22}s^2+b_{22}s+k_{22} \end{bmatrix} \tag{5.14}$$

has a corresponding dynamic compliance (or admittance) $\equiv \mathbf{H}_{\mathrm{K}}^{-1}$, namely,

$$\mathbf{H}_{\mathrm{C}}(s)=\frac{\begin{bmatrix} m_{22}s^2+b_{22}s+k_{22} & -\left(m_{12}s^2+b_{12}s+k_{12}\right) \\ -\left(m_{21}s^2+b_{21}s+k_{21}\right) & m_{11}s^2+b_{11}s+k_{11} \end{bmatrix}}{\left(m_{11}s^2+b_{11}s+k_{11}\right)\left(m_{22}s^2+b_{22}s+k_{22}\right)-\left(m_{12}s^2+b_{12}s+k_{12}\right)\left(m_{21}s^2+b_{21}s+k_{21}\right)} \tag{5.15}$$

Although the frequency response of each element of the dynamic stiffness consists of a pair of underdamped zeros, the dynamic compliance has a relative order of two with a fourth-order characteristic polynomial (due to coupling of x- and y-axes). This difference is displayed graphically in Figure 5.4 with parameter values from Tsuji et al.: Table 1. Subject A, Position 1 [95].

Using the frequency-domain, system-identification method defined in (5.9) with force inputs and displacement outputs, the dynamic compliance estimates for three repeatability tests were calculated. The results are displayed in Figure 5.5. The frequency response of the transfer function matrix of the average asymmetric and symmetric least-squares optimal solutions for the three test runs are also included in Figure 5.5. The systems defined by the least-squares optimal parameters are close to the frequency-domain estimates, especially in the frequency range from 1 to 10 Hz.

The partial and multiple coherence functions, defined in (5.11) and (5.12), are displayed in Figure 5.6. The multiple coherence values are close to unity from 2 to 15 Hz for both outputs x and y. However, the partial and multiple coherence values below 2 Hz are substantially below 1, implying insufficient input power, coupled inputs, system nonlinearities, noise, and/or contributions from unmeasured inputs in that frequency range. In Figure 5.7, the autospectra and coherence of x and y interaction forces reveal that the most likely cause was a combination of insufficient input power (compare with autospectra magnitude in Figure 5.2) and input coupling (coherence values around 0.8).

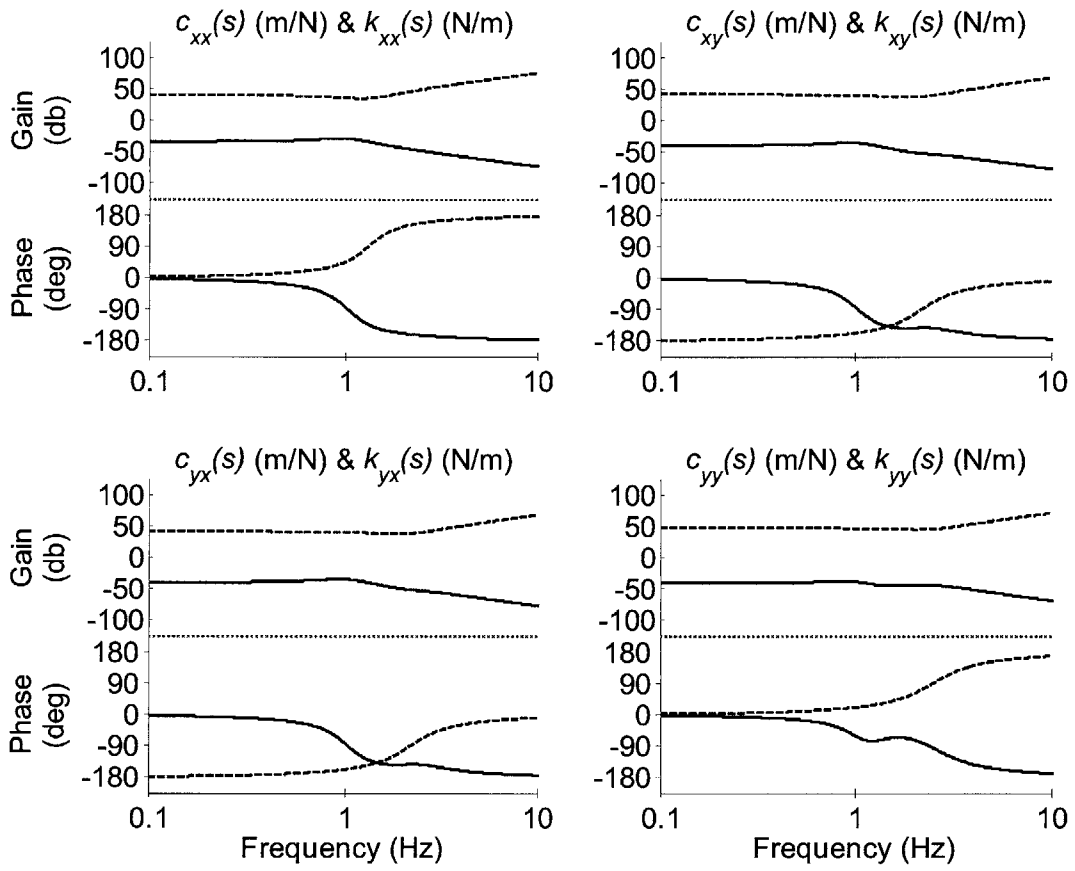

Figure 5.4. Transfer function matrix elements of dynamic stiffness (dashed line) are characterized by a pair of second-order zeros, whereas the transfer function matrix elements of dynamic compliance (solid line), i.e. the matrix inverse of dynamic stiffness, are characterized by a fourth-order characteristic polynomial with relative degree of two.

5.4.2. Human-machine interaction

In order to understand this phenomenon, one must first recognize that the robot delivered the desired force perturbations in an open-loop manner (i.e., without feedback on the interaction force). This avoids the difficult coupled instability problems that accompany the use of force feedback, an important consideration for patient safety. In addition, the PD controller that was necessary to eliminate patient drift in the robot workspace also affected how much of the commanded perturbation was transmitted to the patient's arm. Notice, as the PD controller gains increase, the allowable deviation from (x_{des}, y_{des}), along with the magnitude of the transmitted force, will decrease. Since the

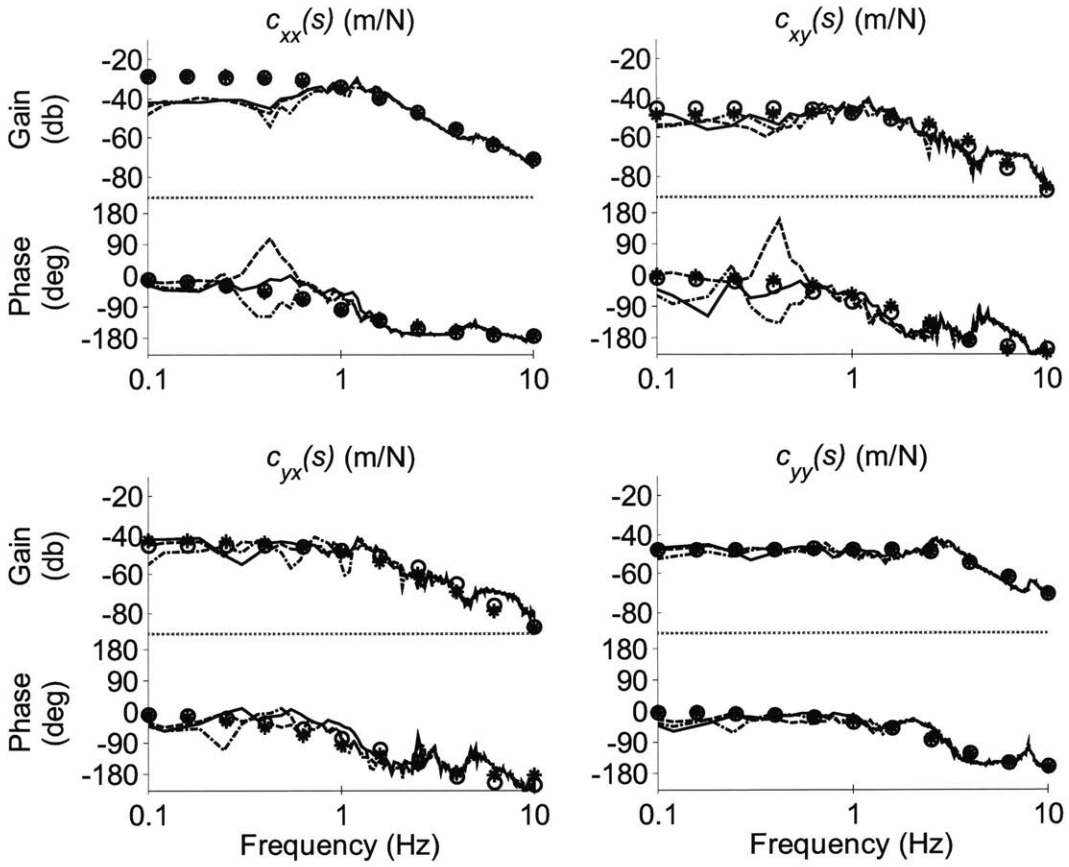

Figure 5.5. Dynamic compliance spectral estimates of three test runs (solid, dashed, and dash-dotted lines) along with linear model estimates from least-squares optimal asymmetric (* symbols) and symmetric (o symbols) parameters.

command perturbations are known and the interaction forces are measured, it is possible to estimate the transfer function matrix from $(\Delta F_x, \Delta F_y)$ to $(F_{i,x}, F_{i,y})$ using (5.9).

To gain a deeper understanding of this transfer function matrix, a state-space model of the human-machine interaction was defined by linearizing a nonlinear model of the robot interacting with a linear model of the human arm through a virtual force transducer (see Appendix D). The state space system relating the commanded perturbations to the measured interaction forces is defined as

$$\begin{aligned} \dot{\mathbf{x}} &= \mathbf{A}\mathbf{x} + \mathbf{B}\mathbf{u} \\ \mathbf{y} &= \mathbf{C}\mathbf{x} + \mathbf{D}\mathbf{u} \end{aligned} \tag{5.16}$$

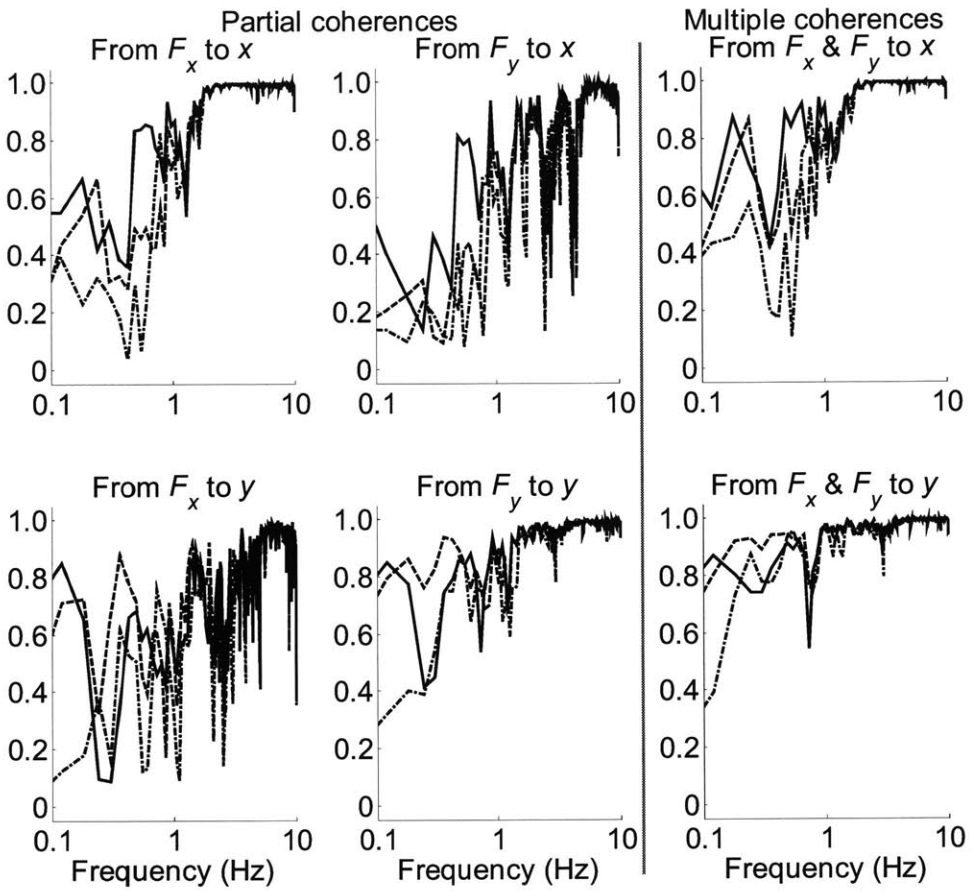

Figure 5.6. Partial and multiple coherences for dynamic compliance spectral estimates of three test runs (solid, dashed, and dash-dotted lines).

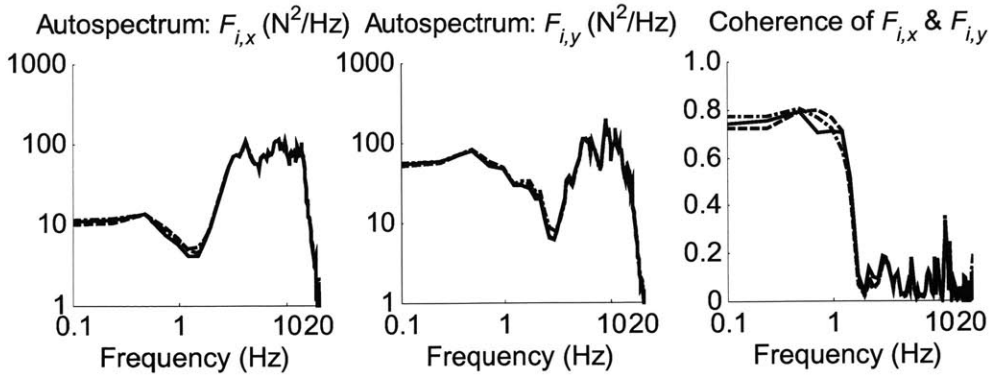

Figure 5.7. Autospectra of interaction force perturbations, F_x and F_y, of three test runs, as well as their coherences (solid, dashed, and dash-dotted lines).

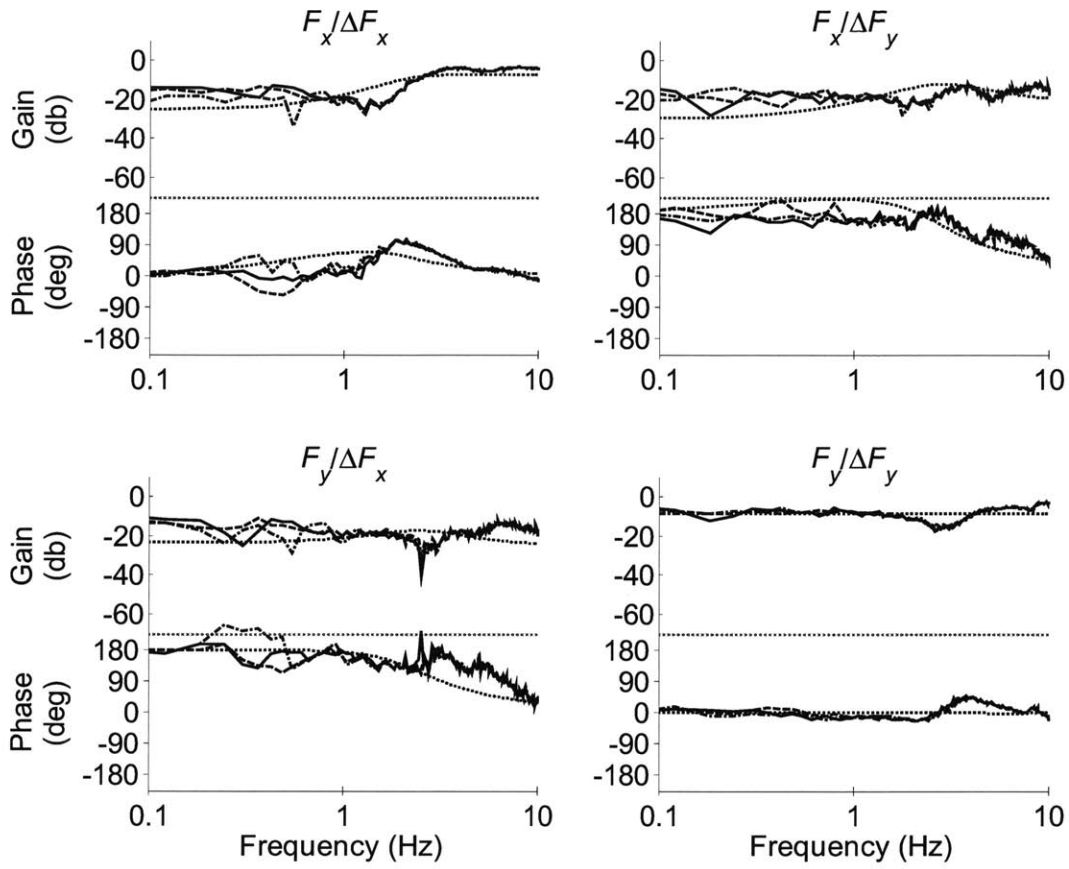

Figure 5.8. Transfer function matrix from commanded force perturbations, ΔF_x and ΔF_y, to interaction force perturbations, F_x and F_y, from linearized model of human-machine interaction (short-dashed line) and from spectral estimates of three test runs (solid, long-dashed, and dash-dotted lines).

where $\mathbf{x} = \left[\theta_s, \theta_e, \dot{\theta}_s, \dot{\theta}_e, x_a, y_a, \dot{x}_a, \dot{y}_a\right]^{\mathrm{T}}$ is the state vector of absolute robot joint angles (θ_s, θ_e) and Cartesian hand coordinates (x_a, y_a) along with their first derivatives, $\mathbf{u} = \left[\Delta F_x, \Delta F_y\right]^{\mathrm{T}}$ is the input vector, and $\mathbf{y} = \mathbf{F_i}$ is the output vector.

The frequency response of the state-space system was defined by using robot parameters from [32] and the human arm estimates of the asymmetric inertia, damping, and stiffness matrices from the patient data. The linearized system is shown in Figure 5.8 as a short-dashed line and the transfer function estimates of the three test runs are shown as a solid, long-dashed, and dash-dotted line. Figure 5.9 displays the partial and multiple coherence functions of the estimates.

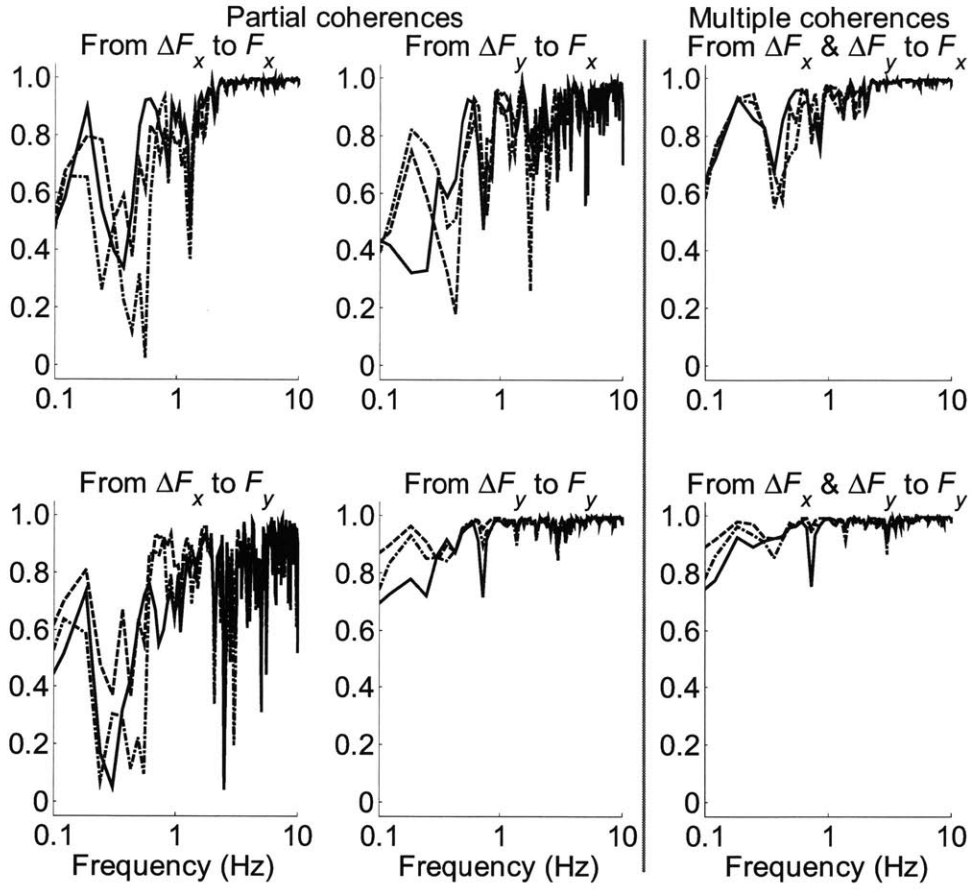

Figure 5.9. Partial and multiple coherences for spectral estimates from commanded force perturbations, ΔF_x and ΔF_y, to interaction force perturbations, F_x and F_y, of three test runs (solid, dashed, and dash-dotted lines).

The estimate from $(\Delta F_x, \Delta F_y)$ to (F_x, F_y) provides one explanation of why the coherence of the interaction forces was high. At frequencies lower than 2 Hz, the gains of the matrix elements $F_x / \Delta F_x$ and $F_x / \Delta F_y$ are approximately equal and are significantly below unity gain. Therefore, although the desired perturbations ΔF_x and ΔF_y have low coherence, they contribute approximately the same amount of input energy to F_x (and to F_y, though to a lesser degree) causing F_x and F_y to become more linearly dependent.

5.5. Compensating for inputs coupled by human-machine interaction

5.5.1. Experimental compensation – modified perturbation commands

The ideal transfer function matrix from the commanded perturbations to the interaction forces is the identity matrix. In an attempt to achieve this, one could define a new set of experimental perturbations by pre-multiplying the commanded perturbations by the inverse of the linearized transfer function matrix described by (5.16):

$$\mathbf{\Delta F_{new}} = \mathbf{T_{model}^{-1}} \mathbf{\Delta F_{old}} \tag{5.17}$$

When the modified perturbations are commanded, the intended set of perturbations will be delivered to the patient,

$$\mathbf{F} = \mathbf{T_{system}} \left(\mathbf{T_{model}^{-1}} \mathbf{\Delta F_{old}} \right) \cong \mathbf{\Delta F_{old}} \tag{5.18}$$

Notice, since the linearized model depends on the operating condition, (5.17) must be applied at each test location individually. A more problematic aspect of this approach is that the linearized model depends on the human arm impedance properties that are being estimated. It may be practical to use parameters representing an average of a wide range of patients and unimpaired subjects in the model. However, at a minimum, a sensitivity analysis would be required to determine whether this would adversely affect the estimates. An alternative approach that avoids this difficulty is presented below.

5.5.2. Analytical compensation – derived estimate

In the previous section, it was shown that a set of commanded inputs that had low coherence resulted in interaction forces with higher coherence because of the dynamics of the human-machine interaction. An alternative estimate of the transfer function matrix of interest (namely, from interaction forces to displacement) can be derived based on the subsystems shown in Figures 5.10. Since the commanded perturbations, interaction forces, and displacements are known at the same instant in time, we can define the MIMO structures in Figure 5.10 as

$$\begin{bmatrix} F_{i,x} \\ F_{i,y} \end{bmatrix} = \begin{bmatrix} T_{xx} & T_{xy} \\ T_{yx} & T_{yy} \end{bmatrix} \begin{bmatrix} \Delta F_x \\ \Delta F_y \end{bmatrix} \tag{5.19}$$

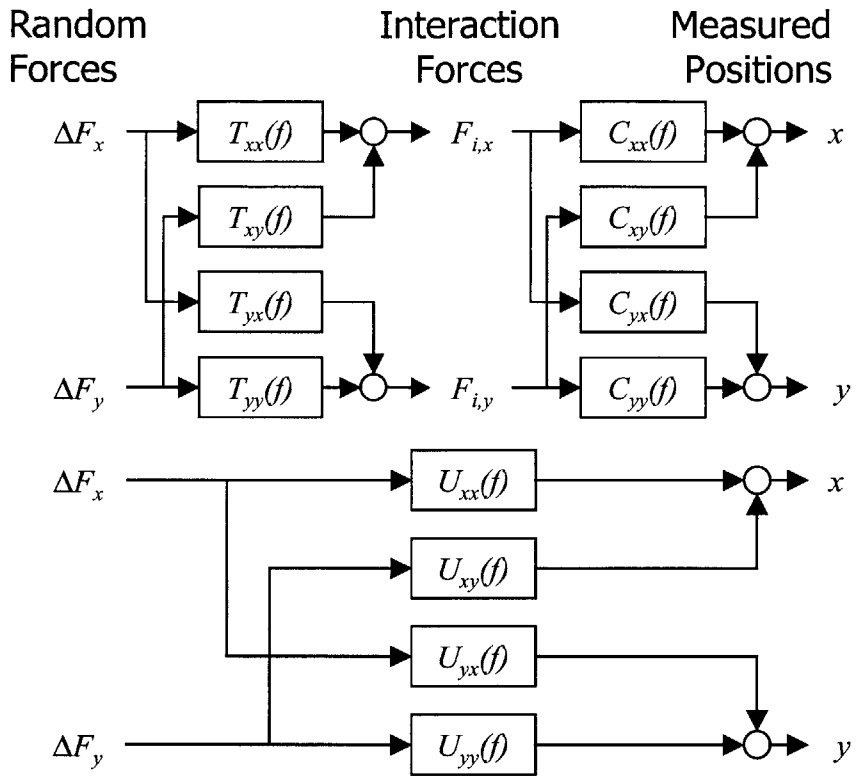

Figure 5.10. Linear MIMO structures: $\mathbf{T}(f)$ is transfer function matrix from commanded force perturbations, ΔF_x and ΔF_y, to interaction forces, $F_{i,x}$ and $F_{i,y}$; $\mathbf{C}(f)$ is transfer function matrix from same interaction forces to displacements, x and y. Linear MIMO structure: $\mathbf{U}(f)$ is transfer function matrix from commanded perturbations, ΔF_x and ΔF_y, to displacements, x and y.

$$\begin{bmatrix} x \\ y \end{bmatrix} = \begin{bmatrix} C_{xx} & C_{xy} \\ C_{yx} & C_{yy} \end{bmatrix} \begin{bmatrix} F_{i,x} \\ F_{i,y} \end{bmatrix} \tag{5.20}$$

$$\begin{bmatrix} x \\ y \end{bmatrix} = \begin{bmatrix} U_{xx} & U_{xy} \\ U_{yx} & U_{yy} \end{bmatrix} \begin{bmatrix} \Delta F_x \\ \Delta F_y \end{bmatrix} \tag{5.21}$$

where (5.19) defines the transfer function matrix that results from the human-machine interaction, (5.20) defines the human arm dynamic compliance, and (5.21) defines the transfer function matrix from the commanded perturbation to the displacements. Notice, the inputs for the estimates in (5.19) and (5.21) are the commanded perturbations that have relatively low coherence, whereas the inputs for the estimate in (5.20) are the interaction forces that have relatively high coherence at low frequencies. By computing

the estimates for (5.19) and (5.21), a "derived" estimate for the human arm impedance can be defined as the product of $\mathbf{U}(f)(\mathbf{T}(f))^{-1}$ at each corresponding frequency point f.

$$\begin{bmatrix} x \\ y \end{bmatrix} = \begin{bmatrix} U_{xx} & U_{xy} \\ U_{yx} & U_{yy} \end{bmatrix} \begin{bmatrix} T_{xx} & T_{xy} \\ T_{yx} & T_{yy} \end{bmatrix}^{-1} \begin{bmatrix} F_{i,x} \\ F_{i,y} \end{bmatrix} \tag{5.22}$$

An alternative approach to calculating the inverse of the estimate, i.e. $(\mathbf{T}(f))^{-1}$, would be to estimate that transfer function matrix $(\mathbf{T}'(f))$ directly,

$$\begin{bmatrix} \Delta F_x \\ \Delta F_y \end{bmatrix} = \begin{bmatrix} T'_{xx} & T'_{xy} \\ T'_{yx} & T'_{yy} \end{bmatrix} \begin{bmatrix} F_{i,x} \\ F_{i,y} \end{bmatrix} \tag{5.23}$$

However, this estimate suffers from the same limitation as the one in (5.20) – inputs that have relatively high coherence at low frequencies.

To quantify how well the derived estimate describes the transfer function matrix from interaction forces to displacements, the partial and multiple coherence functions were defined in terms of the derived estimate. As stated in [8],

$$G_{y_i y_i} = G_{v_i v_i} + G_{n_i n_i} \tag{5.24}$$

$$G_{v_i v_i} = \left|H_{y_i x_1}\right|^2 G_{x_1 x_1} + \overline{H}_{y_i x_1} H_{y_i x_2} G_{x_1 x_2} + \overline{H}_{y_i x_2} H_{y_i x_1} G_{x_2 x_1} + \left|H_{y_i x_2}\right|^2 G_{x_2 x_2} \tag{5.25}$$

where $G_{y_i y_i}$ is the total output power spectrum, $G_{v_i v_i}$ is ideal predicted linear output power spectrum, and $G_{n_i n_i}$ is the output noise power spectrum. By definition,

$$G_{n_i n_i} = \left(1 - \gamma^2_{y_i \cdot x}\right) G_{y_i y_i} \tag{5.26}$$

Based on the above definitions with $i \in 1, 2$, if it is assumed that the noise output spectrum for the derived estimate (to be denoted with "hat" symbol) is equal to the noise output spectrum of the direct estimate, $\hat{G}_{n_i n_i} = G_{n_i n_i}$, then the total output spectrum of the derived transfer function matrix will be

$$\hat{G}_{y_i y_i} = \left|\hat{H}_{y_i x_1}\right|^2 G_{x_1 x_1} + \overline{\hat{H}}_{y_i x_1} \hat{H}_{y_i x_2} G_{x_1 x_2} + \overline{\hat{H}}_{y_i x_2} \hat{H}_{y_i x_1} G_{x_2 x_1} + \left|\hat{H}_{y_i x_2}\right|^2 G_{x_2 x_2} + G_{n_i n_i} \tag{5.27}$$

the input/output cross-spectra will be

$$\hat{G}_{x_1y_i} = \hat{H}_{y_ix_1} G_{x_1x_1} + \hat{H}_{y_ix_2} G_{x_1x_2} \tag{5.28a}$$

$$\hat{G}_{x_2y_i} = \hat{H}_{y_ix_1} G_{x_2x_1} + \hat{H}_{y_ix_2} G_{x_2x_2} \tag{5.28b}$$

and the ordinary coherence functions will be

$$\hat{\gamma}^2_{x_1y_i} = \frac{\left|\hat{G}_{x_1y_i}\right|^2}{G_{x_1x_1}\hat{G}_{y_iy_i}} \tag{5.29a}$$

$$\hat{\gamma}^2_{x_2y_i} = \frac{\left|\hat{G}_{x_2y_i}\right|^2}{G_{x_2x_2}\hat{G}_{y_iy_i}} \tag{5.29b}$$

Using (5.27)-(5.29), the partial and multiple coherence functions for each output of the derived estimate can be defined as

$$\hat{\gamma}^2_{x_1y_i \cdot x_2} = \frac{\left|\hat{G}_{x_1y_i} G_{x_2x_2} - \hat{G}_{x_2y_i} G_{x_1x_2}\right|^2}{G^2_{x_2x_2} G_{x_1x_1} \hat{G}_{y_iy_i} \left(1-\gamma^2_{x_2x_1}\right)\left(1-\hat{\gamma}^2_{x_2y_i}\right)} \tag{5.30a}$$

$$\hat{\gamma}^2_{x_2y_i \cdot x_1} = \frac{\left|\hat{G}_{x_2y_i} G_{x_1x_1} - \hat{G}_{x_1y_i} G_{x_2x_1}\right|^2}{G^2_{x_1x_1} G_{x_2x_2} \hat{G}_{y_iy_i} \left(1-\gamma^2_{x_1x_2}\right)\left(1-\hat{\gamma}^2_{x_1y_i}\right)} \tag{5.30b}$$

$$\hat{\gamma}^2_{y_i \cdot x} = \frac{\overline{\hat{H}}_{y_ix_1} \hat{G}_{x_1y_i} + \overline{\hat{H}}_{y_ix_2} \hat{G}_{x_2y_i}}{\hat{G}_{y_iy_i}} \tag{5.30c}$$

The derived estimate and its partial and multiple coherence functions are shown in Figures 5.11 and 5.12. Notice, the low-frequency gains for x/F_x and x/F_y from the derived estimate are closer to the asymmetric and symmetric least-squares optimal frequency responses than those from the direct estimate. A similar observation can be made with respect to the partial coherence values at low frequencies. There are substantial improvements in the partial coherences from F_x to x and from F_y to x. The multiple coherence of the derived estimate from F_x and F_y to x has also improved when compared to the direct estimate, with only some modest improvements in the multiple coherence from F_x and F_y to y. Thus, by deriving the desired estimate from two

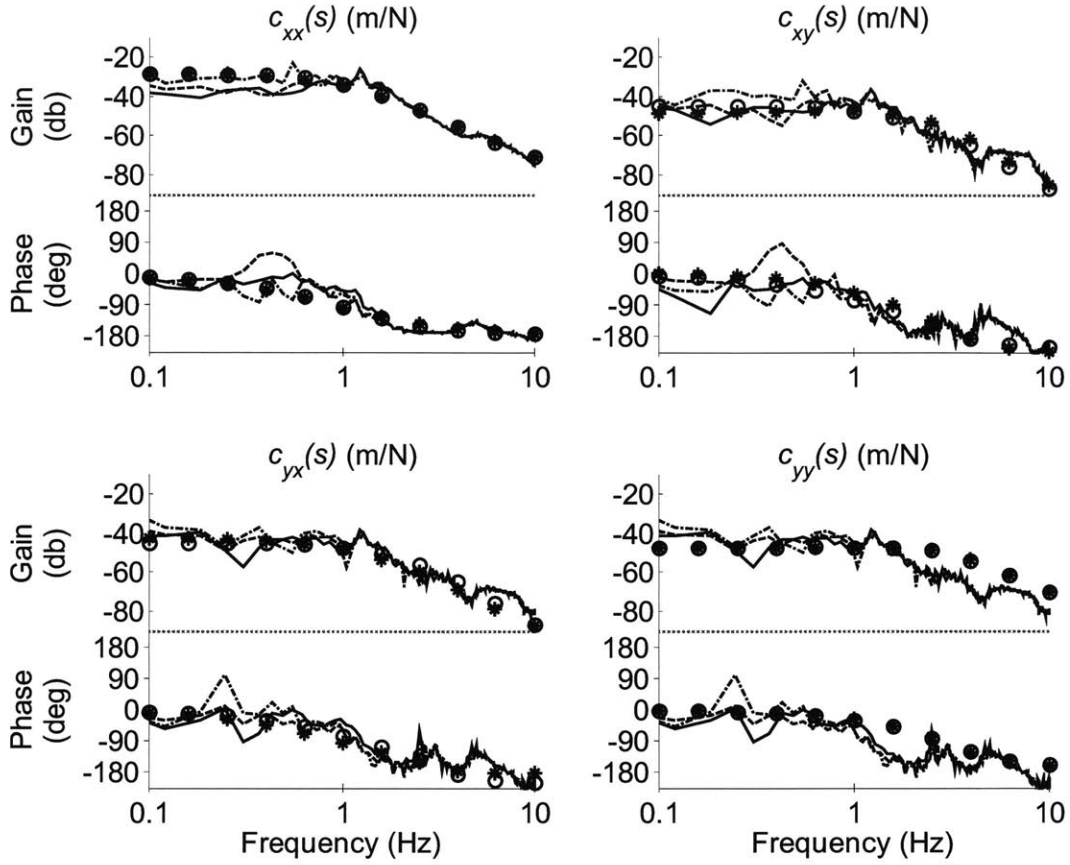

Figure 5.11. Derived dynamic compliance spectral estimates of three test runs (solid, dashed, and dash-dotted lines) along with linear model estimates from least-squares optimal asymmetric (* symbols) and symmetric (o symbols) parameters.

estimates with better-conditioned inputs, an estimate with improved partial and multiple coherence characteristics was found.

5.6. Discussion

The work presented here provides a basis for a reliable test that can be used in a clinical setting. After considering several experimental procedures, the stochastic method was selected because the random nature of its inputs in both magnitude and direction not only minimizes the likelihood of voluntary reactions, but also avoids the need for separate measurements in individual directions. The duration of the test (50 seconds) is short enough that clinicians can measure patients both during robot evaluation sessions and during treatment sessions. An important aspect of providing therapy to patients and taking measurements with patients is that the patients feel comfortable. Not only have

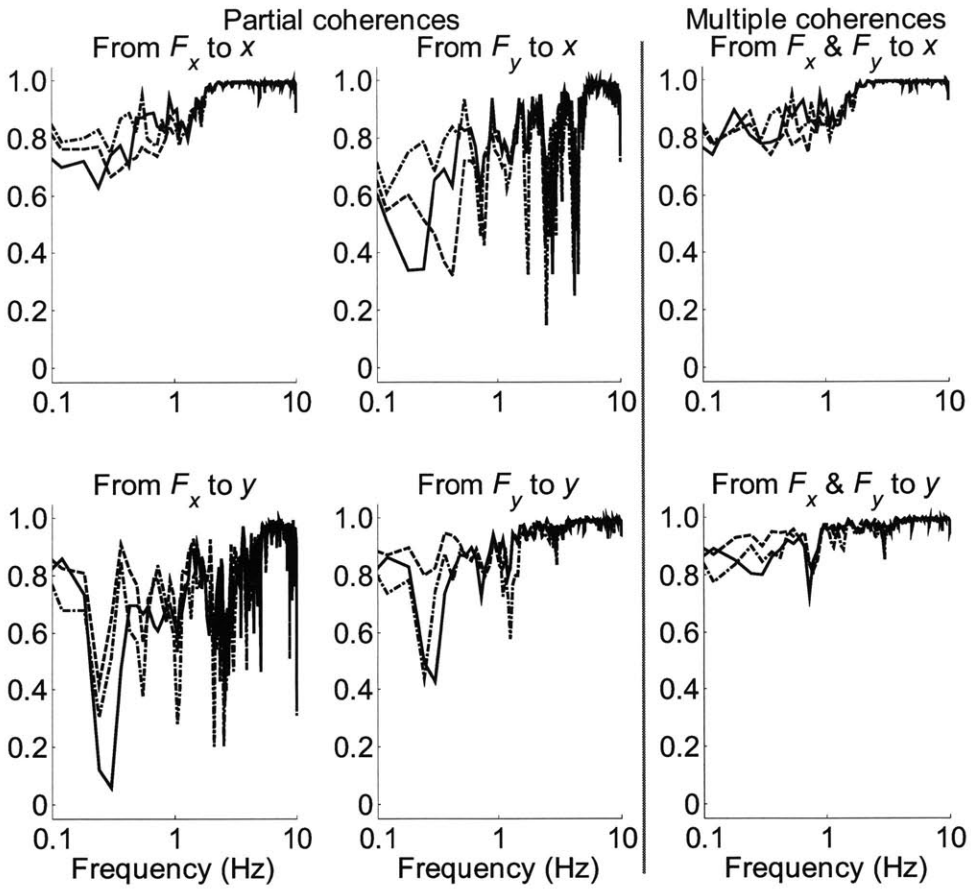

Figure 5.12. Partial and multiple coherences for derived dynamic compliance spectral estimates of three test runs (solid, dashed, and dash-dotted lines).

the patients who have been exposed to the measurement tolerated it, but they also seem to like the random nature of the test and liken it to a vibrating massage.

Although voluntary reactions to random inputs are unlikely, patients could still exhibit compensatory muscle activations, e.g. tensing up or relaxing. However, a close examination of the data indicated that these patients did not change their muscle activation levels significantly during the three test runs. To check for stationarity, mean square values of the commanded perturbations and the interaction forces (minus their mean values) were calculated over equal time intervals [8]. The variation of the mean square values between $F_{i,y}$ and ΔF_y were similar, but the input coupling along the x-axis caused the variation $F_{i,x}$ to be influenced by the variation of both ΔF_x and ΔF_y. However, differences in the variation of $F_{i,x}$ between the three tests were small

($R^2_{F_1F_2} = R^2_{F_1F_3} = R^2_{F_2F_3} = 0.96$) implying those variations were from input coupling and not patient compensatory muscle activations. The normalized instantaneous values (e.g. $(\Delta F_x - \mu)/\sigma$, where μ and σ are the mean and standard deviation of ΔF_x) of the commanded and interaction perturbation force data were also checked for normality by using the MATLAB function normplot. Deviations from a normal distribution were small throughout the probability range 0.05 to 0.95 with the largest deviations below 0.01 and above 0.99. Finally, the force and displacement time histories for the three experimental test runs were similar throughout the test ($\overline{R}^2_{F_x} = 0.96$, $\overline{R}^2_{F_y} = 0.95$, $\overline{R}^2_x = 0.98$, $\overline{R}^2_y = 0.96$, where $\overline{R}^2$ is the average correlation coefficient between signals 1 & 2, 1 & 3, and 2 & 3), as were the resulting impedance estimates.

Time-domain, least-squares optimization problems assuming asymmetric and symmetric linear system structure with second-order dynamics in each degree of freedom displayed that the random data method, which assumes no model structure, resulted in a remarkably similar estimate for the arm's dynamic compliance. Although the dynamics of neuro-muscular excitation, reflex action, and excitation-contraction coupling were not accounted for in the time-domain approach, their effects may not be significant over certain frequency ranges. Thus, depending on the intended use of the model, a linear system structure with second-order dynamics in each degree of freedom may adequately describe the dynamics of the system. Although random data methods do not assume a model structure, they do assume that the system behaves linearly for small perturbations, i.e., that the quantity being measured is a smooth function in the Lipschitz sense. However, nonlinearities abound in biological systems. When active wrist muscles were cyclically stretched and shortened, Gillard et al. [34] showed that hysteresis in angle-torque curves was caused by short-range stiffness effects [50]. Within this range, actin-myosin cross-bridges are thought to remain attached and deform elastically; outside of this range, the cross-bridges detach and the stiffness decreases as the muscle lengthens [78]. Due to the cyclical nature of stochastic perturbations, a similar hysteresis may occur within the hypertonic arm muscles of patients.

By considering the human-machine interaction, the likely cause of low input coherence during testing was uncovered. Although a set of force perturbation inputs with low coherence was commanded, the resulting interaction forces were linearly dependent on one another (i.e., F_x was composed of ΔF_x and ΔF_y, whereas F_y was composed mostly of ΔF_y). The method of inverting the human-machine interaction model ($\mathbf{F} = \mathbf{T}_{\text{system}}\left(\mathbf{T}_{\text{model}}^{-1}\Delta\mathbf{F}\right) \cong \Delta\mathbf{F}$) in order to improve input signal coherence was proposed. Another alternative would be to use a high-impedance robot and deliver position perturbations to the subject. In a clinical setting, however, one must take special care so that high forces are not delivered to a patient whose musculoskeletal system is not as robust as an unimpaired subject's. Common afflictions among stroke patients are joint and tendon pain in the shoulder, wrist, and hand, as well as shoulder-hand syndrome. Shoulder-hand syndrome is characterized by burning pain and swelling of the fingers and hand with skin atrophy that occur with a painful, stiff shoulder. Past clinical trials with MIT-MANUS and InMotion^2 have resulted in a reduction of these afflictions [25,55,57,96]. In this respect, force perturbations with a low-impedance robot are advantageous, if not required, for this application.

Despite high input signal coherence for the desired transfer function estimate, a method of deriving an improved estimate from two other direct estimates was developed. The inputs to the direct estimates were the commanded perturbations, which were specified with low coherence. The improvement in the estimate can be quantified simply by assuming that the output noise power spectrum for the derived estimate is the same as the direct estimate and by calculating the partial and multiple coherence functions. Although there were significant improvements in the multiple coherence functions at low frequencies, they did not reach the levels (~1.0) that occurred in the frequency range of 2 to 15 Hz because the derived estimate cannot change the fact that the input power delivered to the arm was lower than expected.

Although the present study focused on estimating dynamic compliance along two coordinate axes, the stochastic method can be easily generalized to any number of inputs and outputs [8]. For example, our research group has also developed a robot for wrist rehabilitation [18,99] that senses and actuates the wrist in pronation/supination,

abduction/adduction, and flexion/extension. Thus, by commanding three stochastic perturbations with low coherence, the dynamic compliance of the wrist can be estimated.

5.7. Conclusion

An arm impedance test suitable for clinical use was developed by adapting previous methods to the special requirements of this application. By carefully considering the human-machine interaction, a plausible explanation for input coupling was identified and a potential way of de-coupling the coupled inputs was introduced. This is important in a clinical setting where a low-impedance robot is preferred. Furthermore, an alternative method to derive a desired estimate by using two better-conditioned estimates was introduced. Improvements in the derived transfer function matrix estimate were verified by the partial and multiple coherence functions.

Chapter 6

Experimental results using spectral estimation method

6.1. Summary

The spectral estimation method developed in Chapter 5 arose from a serendipitous effect of the performance-based progressive therapy protocol that was unrelated to motor learning. Patients undergoing this therapy protocol exhibited a sustained reduction in abnormal muscle tone [54]. This chapter evaluates the new spectral estimation method by identifying mechanical systems with known inertial and stiffness properties. Counter-intuitive results from an unimpaired subject study of both arms revealed the method was sensitive to the hardware that was used to attach the subject to the end-effector of the robot. Despite the counter-intuitive phenomena present in the spectral estimates, properties of a linear second-order model whose parameters were found with a nonlinear least-squares regression were consistent with previously reported properties of unimpaired subjects. Results from a preliminary study of the hemiplegic and less-impaired arms of a group of chronic stroke patients were also presented. Although the counter-intuitive phenomena were present in the spectral estimates of the patient trials (due to the aforementioned hardware sensitivity), the impedance properties were shown to be consistent with past results.

6.2. Introduction

While the performance-based progressive therapy (PBPT) was designed to increase the extent and rate of motor recovery exhibited by stroke patients, another serendipitous benefit was noted by the clinicians administering the robot therapy, namely a sustained

reduction in arm abnormal muscle tone – a muscle's resistance to passive elongation or stretch [27,57]. Although clinicians judge muscle tone subjectively, an objective measure would provide valuable insight about the effect of stroke on a hemiplegic limb and better characterize the effect of rehabilitation therapy.

Chapter 5 described the experimental and analytical development of an arm mechanical impedance[5] estimation technique that is suitable for a clinical setting. During a preliminary study, MIT-MANUS [46] (or InMotion^2) was used to bring the upper limb of a stroke patient to the center of the robot workspace using Proportional-Derivative (PD) control, generate stochastic force perturbations, and measure the resulting motion. The kinematic linkage used in the mechanical design of MIT-MANUS is referred to as a Selective Compliance Assembly Robot Arm (SCARA) because its in-plane impedance is low (i.e., back-drivable) while its out-of-plane impedance is high. This feature allows the robot to support the weight of the patient's arm and the control system to specify the impedance of the human-machine interaction [41-43].

Although an alternative method would be to simply use a position controller to apply displacement perturbations and measure the resulting interaction forces between the patient and robot, this approach may result in excessive forces being transmitted from the robot to the arm of the patient. In general, the musculoskeletal systems of stroke patients are not as robust as the musculoskeletal systems of unimpaired humans so ensuring lower interaction forces is desirable, if not essential. In addition, although back-drivability is a desirable property for robots that operate under impedance control to generate an interaction force [13], this property makes it more difficult to implement position control systems. For this reason, robots used for position control tasks generally have high endpoint impedance.

This chapter will evaluate whether the experimental method introduced in Chapter 5 can successfully be implemented in a clinical setting. Before presenting experimental results for unimpaired subjects or stroke patients, a mechanical system consisting of inertial and stiffness components will be examined to validate the experimental method and the programs that analyze the test data. An experimental test bed termed a spring

[5] The term "impedance" is used synonymously with "mechanical impedance" for brevity.

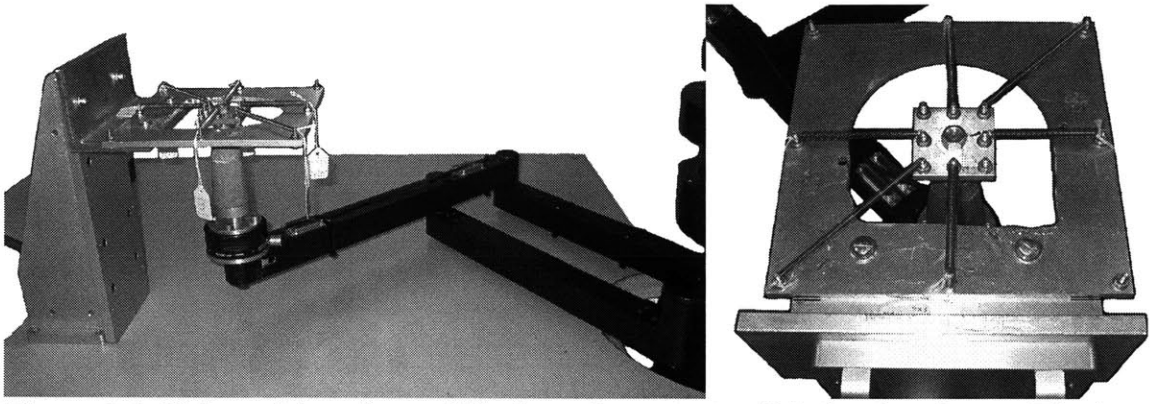

Figure 6.1. Side and top views of the impedance test validation hardware. The inner spring array fixture was attached to the end-effector of the robot used to generate the random force perturbations. The outer fixture was clamped to ground. A variety of stiffness fields was realized by mounting extension springs between the posts on the inner and outer fixtures.

array will be used to demonstrate the ability of the spectral method to identify inertial loads and various stiffness fields. Results from tests conducted on six unimpaired subjects will demonstrate that MIT-MANUS can be used to characterize arm's impedance. Although the results were sensitive to the spectral analysis parameters (i.e., the known trade-off between the variance of the spectral estimate and the frequency resolution) and to the hardware that was used to attach the subject's arm to the robot's end-effector, ways to reduce the sensitivities that affect the spectral estimate were introduced and evaluated. Impedance tests were conducted with both arms of six stroke patients to demonstrate that the method can be used in a clinical setting.

6.3. Validation results using mechanical systems

Although using stochastic inputs to estimate the frequency response of a system is an established technology [7,8], tests were conducted on mechanical systems to validate the experimental procedures and spectral analysis MATLAB programs that were written. The mechanical apparatus used during the validation tests is shown in Figure 6.1. The robot was mounted on a patient workstation in the Newman Lab and part of the mechanical assembly was clamped to the workstation table. The top view displays the mechanical spring array that was used to generate various stiffness fields. The outer fixture was bolted to the bracket that was clamped to the table. The inner fixture was bolted to the top of a handle used for patient therapy, which was bolted to the force

a. 1 steel nut
b. 1 inner spring array fixture
c. 1 rubber washer & 5 steel washers
d. 1 Delrin hollow cylinder
e. 1 tall wood cone
f. 1 aluminum collar
g. 1 aluminum post handle
h. 4 steel metric bolts (to ATI)

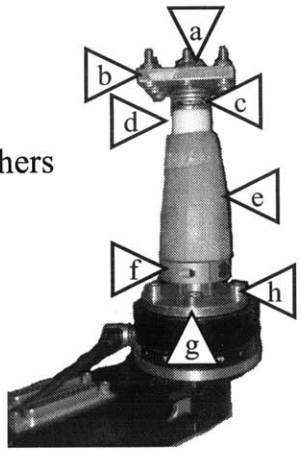

Figure 6.2. Inner spring array fixture mounted on the end-effector of MIT-MANUS. Combinations of labeled components were used to validate spectral estimate of pure inertial loads.

transducer (ATI Industrial Automation Gamma) on the end effector of the robot. Both the square outer fixture and the square inner fixture have four bolts located at their corners and four bolts at the midpoints of their sides to mount extension springs that generate a stiffness field at the end-effector of the robot. The following sections will describe the tests that were conducted to demonstrate the ability of the spectral method to characterize the impedance of mechanical systems.

6.3.1. Isotropic inertial loads

The ability of the spectral estimation method to characterize isotropic inertial loads (e.g., "point" masses comprised of material that is distributed symmetrically) was evaluated by running six trials on four different combinations of the various components that contribute to the inner fixture mass (Figure 6.2): sm1, sm2, sm3, and sm4 (Table 6.1). Although the masses of the mechanical components attached to the force transducer could be measured using a digital scale, the mass of the tool side of the force transducer could not because it is an integral component of the transducer. To estimate this inertia, six impedance measurement trials were run with nothing bolted to tool side of the transducer. Although the spectral analysis of a system with force perturbation inputs and displacement outputs results in a dynamic compliance frequency response estimate (admittance), the matrix can be inverted at each frequency to describe a corresponding dynamic stiffness (impedance). The mean of the six complex-valued dynamic stiffness

Test ID	Components from Figure 6.2 contributing to mass	Measured Mass (kg)
sm1	steel hex nut, inner spring array fixture, 1 rubber washer, 5 steel washers, wood cone, Delrin cylinder, aluminum collar, aluminum handle, 4 bolts	0.3334
sm2	steel hex nut, 2 steel washers, wood cone, Delrin cylinder, aluminum collar, aluminum handle, 4 bolts	0.2483
sm3	Delrin cylinder, aluminum collar, aluminum handle, 4 bolts	0.2096
sm4	aluminum handle, 4 bolts	0.1375

Table 6.1. Mass measurements of the components in Figure 6.2 used to determine the ability of the spectral estimation method to characterize isotropic inertial loads.

estimates was calculated so that it could be subtracted from the dynamic stiffness estimates of sm1-sm4. The resulting dynamic stiffness estimate was then compared to the dynamic stiffness of the measured mass of the components, i.e. $\left(ms^2\right)\cdot \mathbf{I}_{2x2}$ where m corresponds to the mass listed in Table 6.1. Alternatively, one can estimate the mass of the tool side of the transducer by subtracting the measured masses from the corresponding mass estimates of the 24 experimental trials (4 masses $\times$ 6 trials; to be discussed in following paragraph) and then averaging the differences. This resulted in an inboard force transducer mass of $m_{ift} = 0.0962$ kg.

Validation tests were run for the four different combinations of components given in Table 6.1. To demonstrate the repeatability of the experimental procedure with this simple mechanical system, the lower and upper bounds of the dynamic compliance spectral estimate for the six trials of "sm1" are depicted in Figure 6.3. Each trial lasted 50 seconds and the data was sampled at 500 Hz, i.e., each trial consisted of 25,000 samples. Welch's periodogram method was used to estimate the power spectral density and coherence functions [8]. The number of data points included in the FFT calculation, N_{FFT}, was equal to 8192, the length of the Hanning windowing function, N_{WND}, was equal to 8192, and the number of overlapped samples, N_{OVL}, was equal to 4096. With these parameters, the spectral density functions of five overlapping data segments ($N_{MNS} = 5$) are averaged to produce the estimate. The magnitude of the random error depends on N_{MNS} and the partial coherences ($\gamma_{x_i y_k \cdot x_j}$, defined in Equation (5.11) where $x_1 = F_x$, $x_2 = F_y$, $y_1 = x$, and $y_2 = y$), specifically [8],

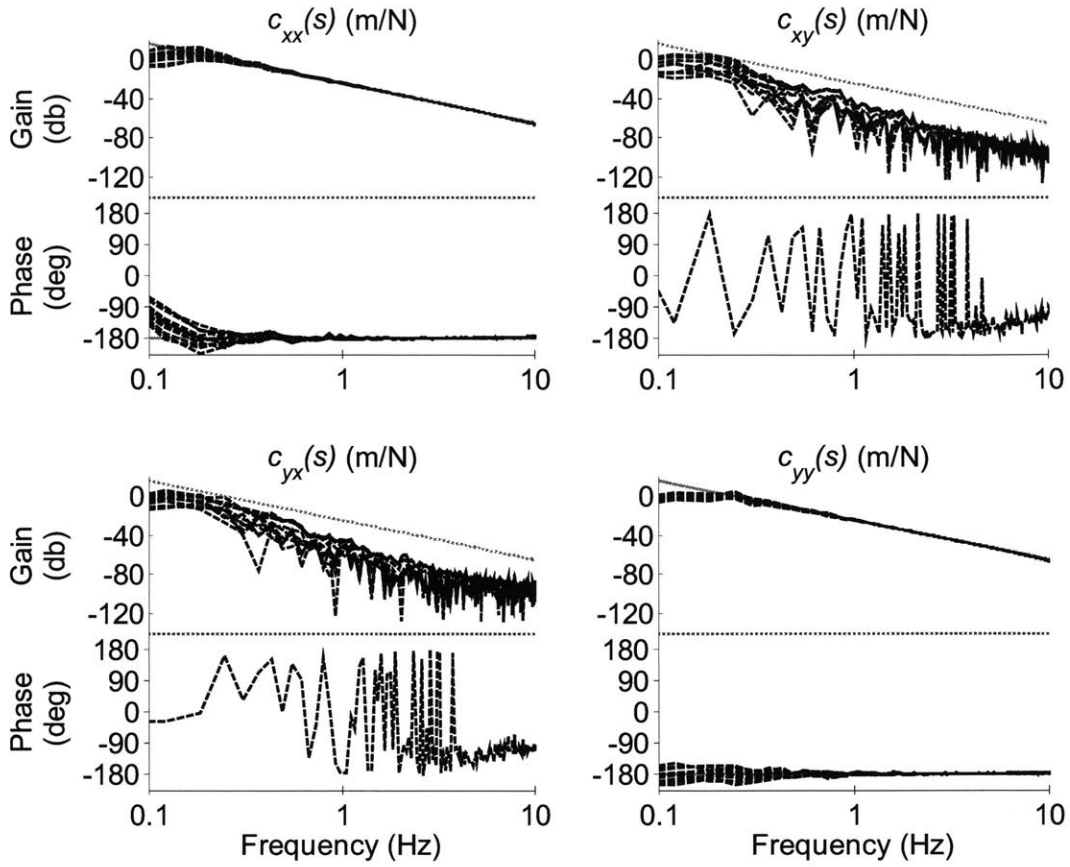

Figure 6.3. Lower and upper bounds of the dynamic compliance spectral estimates with 5 overlapping data segments for 6 tests with the inertial load sm1. Solid gray lines are the expected frequency response, whereas dotted gray line in gain of $c_{xy}(s)$ and $c_{yx}(s)$ is provided as reference.

$$e_{y_k x_i} = \sqrt{\frac{1-\gamma_{x_i y_k \cdot x_j}}{2(N_{MNS}-1)\gamma_{x_i y_k \cdot x_j}}} \tag{6.1}$$

The lower and upper bounds on the magnitude and phase are then defined as

$$\left|H_{y_k x_i}\right| \in \left[\left|H_{y_k x_i}\right|\left(1-2e_{y_k x_i}\right), \left|H_{y_k x_i}\right|\left(1+2e_{y_k x_i}\right)\right] \tag{6.2}$$

$$\angle H_{y_k x_i} \in \left[\left(\angle H_{y_k x_i} - 2e_{y_k x_i}\right), \left(\angle H_{y_k x_i} + 2e_{y_k x_i}\right)\right] \tag{6.3}$$

where the magnitude of the dynamic compliance has units of (m/N) and the phase has units of (rad/s) [8].

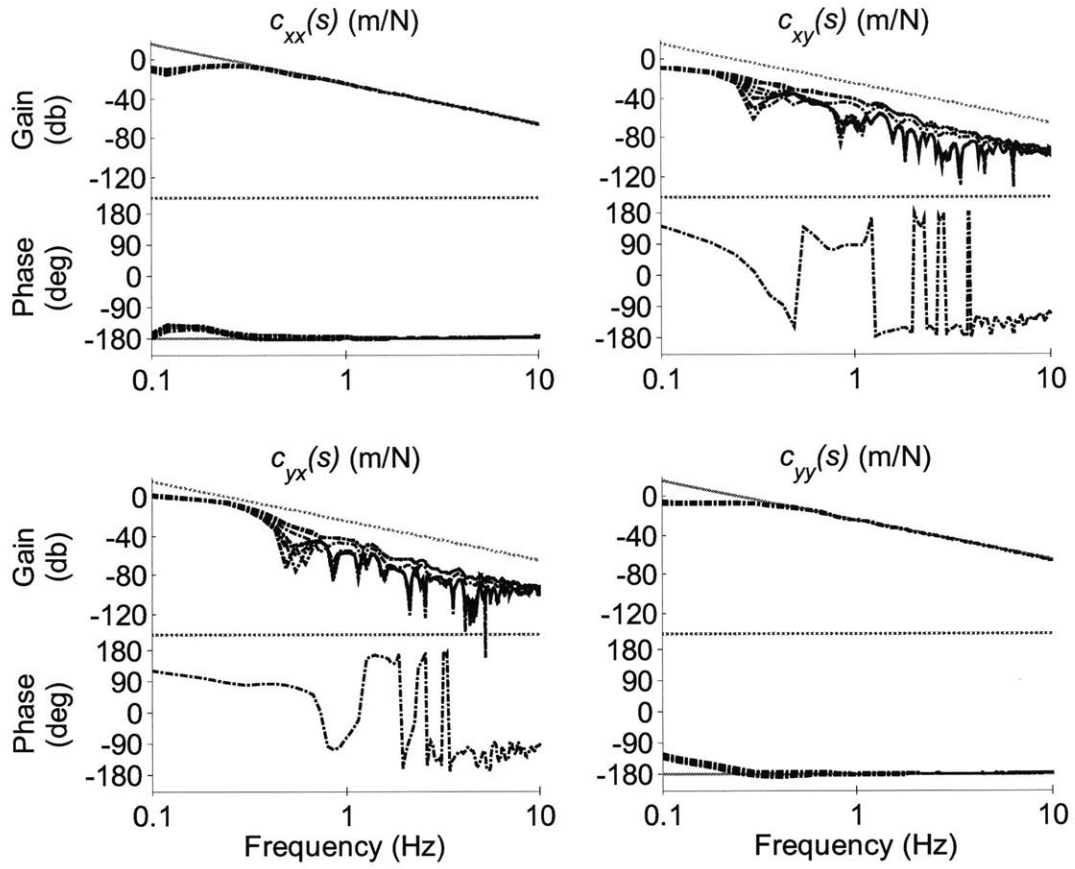

Figure 6.4. Lower and upper bounds of the dynamic compliance spectral estimates with 45 overlapping data segments for 6 tests with the inertial load sm1. Solid gray lines are the expected frequency response, whereas dotted gray line in gain of $c_{xy}(s)$ and $c_{yx}(s)$ is provided as reference.

In Figure 6.3, the dashed lines depict the lower and upper bounds of the estimate, the solid gray lines depict the expected values of the magnitude and phase of the diagonal components ($c_{xx}(s)$ and $c_{yy}(s)$), and the dashed gray lines are provided as a reference for the magnitude of the off-diagonal components ($c_{xy}(s)$ and $c_{yx}(s)$). Since the inertia is isotropic, the diagonal elements should be equal to each other and the off-diagonal components should be zero. Notice, in the mid to high frequency ranges, inertial effects dominate the dynamic compliance and the magnitude of the off-diagonal terms is significantly lower than the actual mass. Only the average phase is shown for the off-diagonal terms because the lower and upper bounds overlap, i.e., $\angle H_{y_k x_i} \in [-180°, 180°]$. Figure 6.4 also depicts dynamic compliance estimates for the sm1 trials with

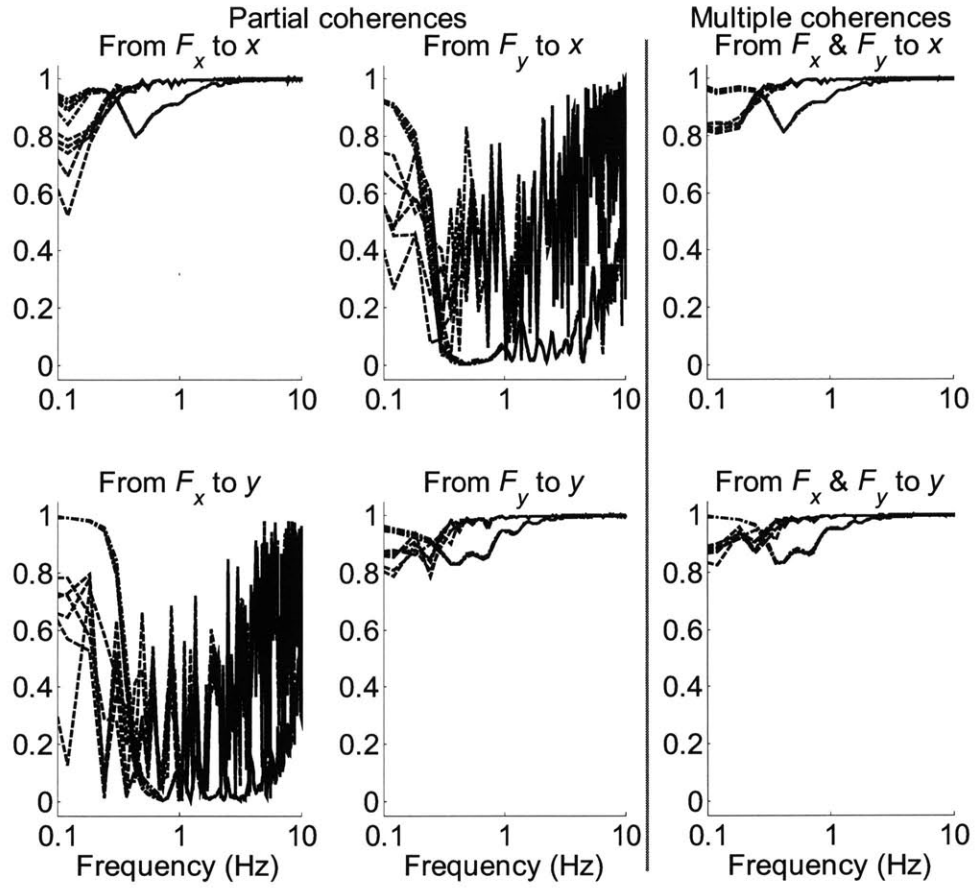

Figure 6.5. Partial and multiple coherence functions for the dynamic compliance spectral estimates with 5 (dashed) and 45 (dash-dotted) overlapping data segments for 6 tests with the inertial load sm1.

$N_{FFT} = 8192$, $N_{WND} = 2048$, and $N_{OVL} = 1536$, resulting in 45 overlapping segments of data during the calculation of the power spectral density and coherence functions (dash-dotted lines). As expected, increasing the number of averages reduced the variance of the estimate.

Figure 6.5 contains the partial and multiple coherence functions for these estimates. Although the increased number of overlaps decreased the variance of the spectral estimate, it also decreased the spectral resolution from 0.061 Hz to 0.244 Hz (because N_{WND} decreased from 8192 to 2048) and resulted in lower partial and multiple coherence function values (coherence values at frequencies less than the spectral resolution should be disregarded). As expected, the partial coherence values are best in

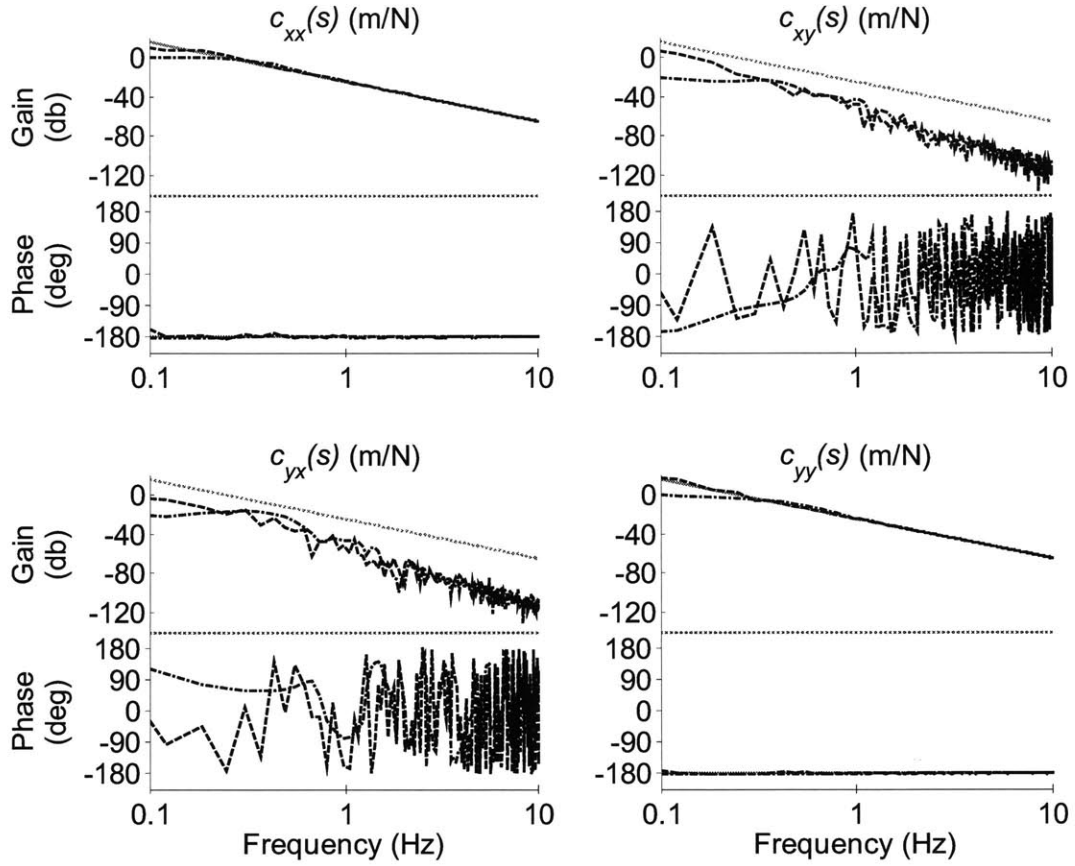

Figure 6.6. Dynamic compliance spectral estimates with 5 (dashed) and 45 (dash-dotted) overlapping data segments for a time-domain simulation of sm1 (solid gray).

the diagonal elements in the frequency range where the dynamic compliance is dominated by inertia.

Numerical simulations of a point mass were conducted and analyzed to compare this ideal test case with the experimental dynamic compliance and the partial and multiple coherence functions (Figures 6.6 and 6.7). The experimental and ideal case results are very similar. It might be possible to improve the spectral estimates of $c_{xy}(s)$ and $c_{yx}(s)$ by increasing the duration of the trial (50 s), but the occurrence of non-zero frequency responses is simply a numerical artifact arising from the calculation of the spectral estimate and the resolutions of the force and displacement sensors.

Two different measures will be used to evaluate the quality of the dynamic compliance (or stiffness) estimates from the isotropic inertia tests. Variance Accounted

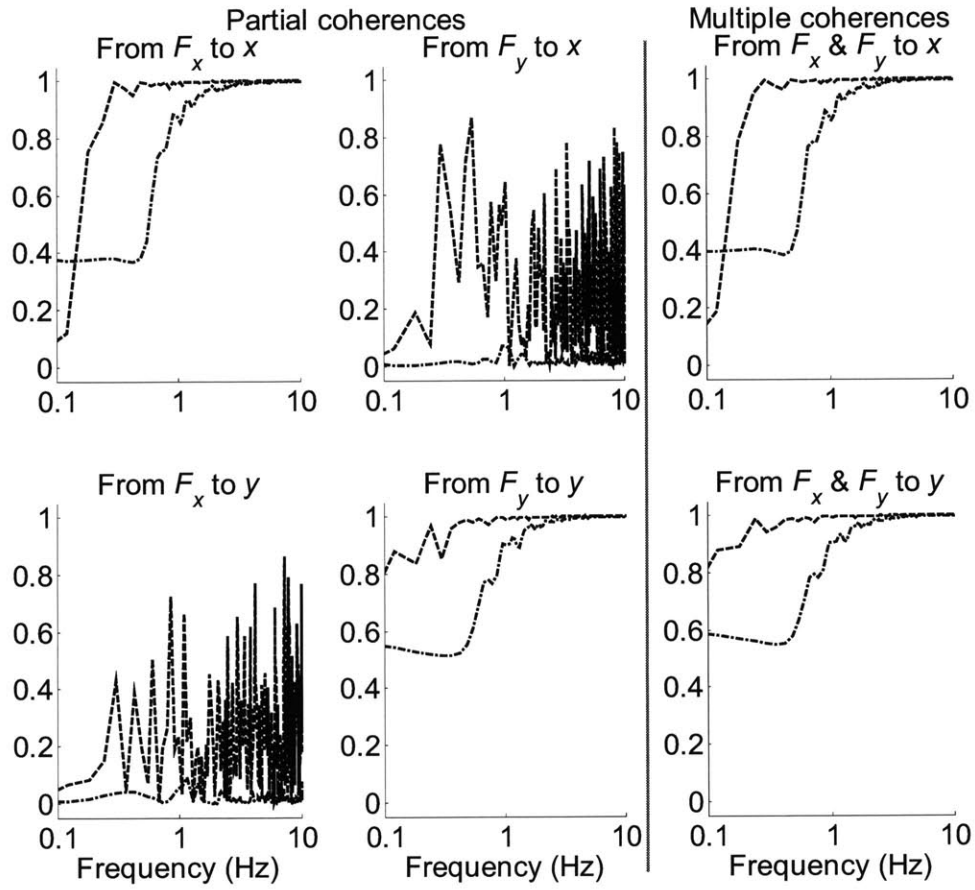

Figure 6.7. Partial and multiple coherence functions for the dynamic compliance spectral estimates with 5 (dashed) and 45 (dash-dotted) overlapping data segments for a time-domain simulation of sm1.

For ($VAF \in [0\%, 100\%]$) describes how close each of the four estimated frequency responses come to their corresponding expected frequency responses. The correlation coefficient squared ($R^2 \in [0, 1]$) is defined as a composite measure of the goodness of fit of all four elements of the transfer function matrix. These measures are based on the quadratic frequency-domain cost functions that were defined to find the optimum second-order linear model parameters that quantify the spectral estimates.

In an attempt to weight the inertial and stiffness properties equally, optimizations were conducted on the impedance (input velocity, output force) rather than dynamic stiffness (input displacement, output force). Instead of a frequency response that is constant at low frequencies and has a slope of +40 db/decade at high frequencies, the

frequency response for impedance has slopes of –20 and +20 db/decade at low (stiffness-dominated) and high (inertia-dominated) frequencies.

The quadratic cost function was defined in terms of the impedance gain and phase as

$$\psi_z = \mathbf{z}_{\mathbf{g,w}}^{\mathbf{T}}\mathbf{z}_{\mathbf{g,w}} + \mathbf{z}_{\mathbf{p,w}}^{\mathbf{T}}\mathbf{z}_{\mathbf{p,w}} \tag{6.4}$$

where $\mathbf{z}_{\mathbf{g,w}}$ and $\mathbf{z}_{\mathbf{p,w}}$ are vectors of differences between the estimated (subscript e in (6.5)) and measured (subscript m in (6.5)) impedance gains (db) and phases (deg) that are weighted (subscript w in (6.4) and (6.5)) by the corresponding partial coherence function at each frequency data point, i.e.,

$$z_{g,w} = 10\gamma_e\left(z_{g,e} - z_{g,m}\right) \tag{6.5a}$$

$$z_{p,w} = \gamma_e\left(z_{p,e} - z_{p,m}\right) \tag{6.5b}$$

Since partial coherence functions indicate whether the relationship between the input and output is linear, weighting by this function will de-value differences between the estimated and expected frequency responses when $\gamma_{x_i y_k \cdot x_j}$ is close to zero. An additional factor of 10 was used in (6.5a) to weight differences in gain higher than differences in phase (the MATLAB function lsqnonlin uses the vector $\left[\mathbf{z}_{\mathbf{g,w}}^{\mathbf{T}} \quad \mathbf{z}_{\mathbf{p,w}}^{\mathbf{T}}\right]^{\mathbf{T}}$ to define ψ_z and to search for the optimum parameter values). Although the differences defined in (6.5) are between the estimated and expected frequency responses instead of the estimated and modeled responses used in the optimization problem, VAF and R^2 will be defined similarly for both. The gain and phase of the impedance of the measured mass, i.e., $(ms)\cdot\mathbf{I}_{\mathbf{2x2}}$, were used to normalize the value of ψ_z in order to define VAF and R^2. Specifically,

$$\psi_n = \mathbf{z}_{\mathbf{g,w'}}^{\mathbf{T}}\mathbf{z}_{\mathbf{g,w'}} + \mathbf{z}_{\mathbf{p,w'}}^{\mathbf{T}}\mathbf{z}_{\mathbf{p,w'}} \tag{6.6}$$

$$z_{g,w'} = 10\gamma_e z_{g,m} \tag{6.7a}$$

$$z_{p,w'} = \gamma_e z_{p,m} \tag{6.7b}$$

Next, the VAF matrix and R^2 were defined as

$$\mathbf{VAF} = 100\%\left(1-\begin{bmatrix} \psi_{xx,z}/\psi_{xx,n} & \psi_{xy,z}/\psi_{xy,n} \\ \psi_{yx,z}/\psi_{yx,n} & \psi_{yy,z}/\psi_{yy,n} \end{bmatrix}\right) \tag{6.8}$$

$$R^2 = 1-\frac{\psi_{xx,z}+\psi_{xy,z}+\psi_{yx,z}+\psi_{yy,z}}{\psi_{xx,n}+\psi_{xy,n}+\psi_{yx,n}+\psi_{yy,n}} \tag{6.9}$$

Since the off-diagonal elements of the impedance matrix of an isotropic inertia are identically equal to zero, $\psi_{xy,n}=\psi_{yx,n}\equiv 0$, the off-diagonal quotients in **VAF** have denominators that are equal to zero. Therefore, for this validation test case of an isotropic inertia,

$$\mathbf{VAF_{iso}} = 100\%\left(1-\begin{bmatrix} \psi_{xx,z}/\psi_{xx,n} & \psi_{yy,z}/\psi_{yy,n} \end{bmatrix}\right) \tag{6.10}$$

$$R^2_{iso} = 1-\frac{\psi_{xx,z}+\psi_{yy,z}}{\psi_{xx,n}+\psi_{yy,n}} \tag{6.11}$$

The $\mathbf{VAF_{iso}}$ and R^2_{iso} values for the six reliability trials of the four mass configurations were very close to 100% and 1. The mean and standard error of the mean (SEM) values for VAF_{xx} were equal to 99.1±0.03% for $N_{MNS}=5$ and 99.6±0.05% for $N_{MNS}=45$. The mean and SEM values for VAF_{yy} were equal to 99.99±0.06% for $N_{MNS}=5$ and 99.3±0.05% for $N_{MNS}=45$. The values for R^2_{iso} were equal to 0.991±0.001 for $N_{MNS}=5$ and 0.994±0.001 for $N_{MNS}=45$.

Results from this section have shown that the impedance test is capable of identifying inertial loads reliably and accurately. The next mechanical system to be considered will consist of the inertial components in sm1 and various stiffness fields generated by using different combinations of paired springs in the spring array fixture.

6.3.2. Stiffness fields generated by spring array

The spring array was discussed earlier and is shown in Figure 6.1. As sketched in Figure 6.8, eight springs can be mounted between bolts on the inner and outer spring array

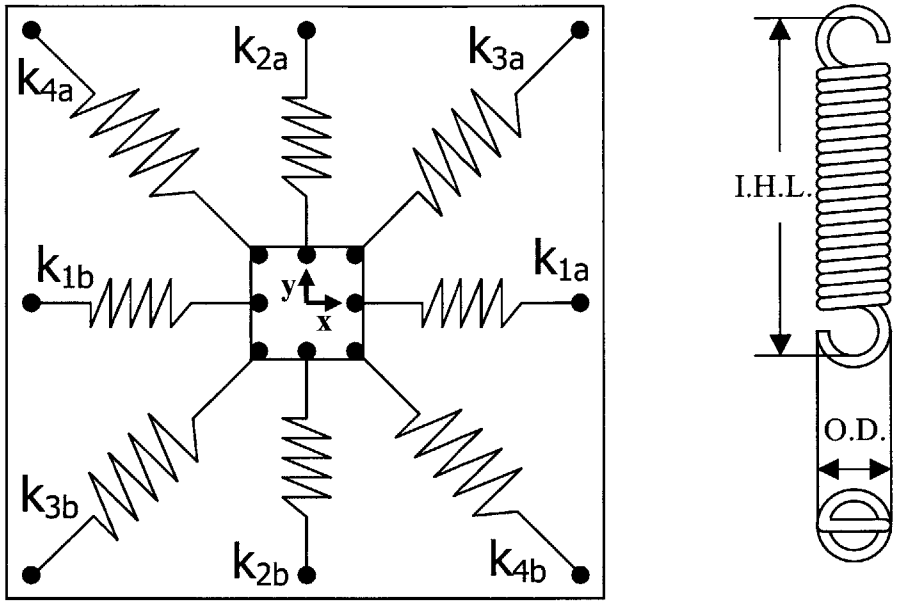

Figure 6.8. Sketch of the spring array inner and outer test fixtures to identify the 8 possible mounting locations for up to 4 pairs of matched springs (i.e., stiffness $k_{ia} \cong k_{ib}$) relative to the MIT-MANUS coordinate system whose origin is at the center of the outer test fixture (left) as well as an extension spring with Inner-Hoop Length and Outer Diameter (right).

fixtures. The type of extension springs that were chosen is also depicted in Figure 6.8 where I.H.L. stands for inner-hoop length and O.D. stands for outer diameter. During the validation testing, it was assumed that $k_{ia} = k_{ib} = k_i$ and $l_{ia} = l_{ib} = l_i$ where k_i and l_i are the nominal stiffness and free length of each spring. The locations of the spring mounts along the perimeter of the inner and outer fixtures were specified to ensure the springs would always be in tension during testing. This pairing of springs allows the equilibrium point of the spring array to remain at the center of the outer fixture. The nonlinear restoring forces generated by the spring array are given by

$$\begin{aligned} F_x = {} & 2k_1x + \frac{k_1 l_1 (l-x)}{\sqrt{(l-x)^2 + y^2}} - \frac{k_1 l_1 (l+x)}{\sqrt{(l+x)^2 + y^2}} + 2k_2x - \frac{2k_2 l_2 x}{\sqrt{x^2 + (l-y)^2}} \\ & - \frac{2k_2 l_2 x}{\sqrt{x^2 + (l+y)^2}} + 2k_3x + \frac{k_3 l_3 (l-x)}{\sqrt{(l-x)^2 + (l-y)^2}} + \frac{k_3 l_3 (l+x)}{\sqrt{(l+x)^2 + (l+y)^2}} \\ & + 2k_4x - \frac{k_4 l_4 (l+x)}{\sqrt{(l+x)^2 + (l-y)^2}} + \frac{k_4 l_4 (l-x)}{\sqrt{(l-x)^2 + (l+y)^2}} \end{aligned} \quad (6.12a)$$

$$F_y = 2k_1 y - \frac{k_1 l_1 y}{\sqrt{(l-x)^2 + y^2}} - \frac{k_1 l_1 y}{\sqrt{(l+x)^2 + y^2}} + 2k_2 y + \frac{2k_2 l_2 (l-y)}{\sqrt{x^2 + (l-y)^2}}$$
$$- \frac{2k_2 l_2 (l+y)}{\sqrt{x^2 + (l+y)^2}} + 2k_3 y + \frac{k_3 l_3 (l-y)}{\sqrt{(l-x)^2 + (l-y)^2}} - \frac{k_3 l_3 (l+y)}{\sqrt{(l+x)^2 + (l+y)^2}} \quad (6.12b)$$
$$+ 2k_4 y + \frac{k_4 l_4 (l-y)}{\sqrt{(l+x)^2 + (l-y)^2}} - \frac{k_4 l_4 (l+y)}{\sqrt{(l-x)^2 + (l+y)^2}}$$

where l is the length between any two adjacent mounting points on the outer fixture of the spring array. Equations (6.12a) and (6.12b) were linearized to determine the nominal endpoint stiffness matrix of the spring array:

$$\mathbf{K}_{sa} = \begin{bmatrix} k_{11,sa} & k_{12,sa} \\ k_{21,sa} & k_{22,sa} \end{bmatrix} \quad (6.13a)$$

$$k_{11,sa} = 2k_1 + 2k_2\left(1 - \frac{l_2}{l}\right) + 2k_3\left(1 - \frac{l_3}{2\sqrt{2}l}\right) + 2k_4\left(1 - \frac{l_4}{2\sqrt{2}l}\right)$$
$$k_{12,sa} = k_{21,sa} = \frac{k_3 l_3 - k_4 l_4}{\sqrt{2}l} \quad (6.13b)$$
$$k_{22,sa} = 2k_1\left(1 - \frac{l_1}{l}\right) + 2k_2 + 2k_3\left(1 - \frac{l_3}{2\sqrt{2}l}\right) + 2k_4\left(1 - \frac{l_4}{2\sqrt{2}l}\right)$$

Notice, springs k_3 and k_4 enable the specification of the off-diagonal elements in the stiffness matrix as well as contribute to the diagonal elements of the stiffness matrix. Another method to specify the properties of the stiffness matrix is to rotate the spring array fixture. For example, rotating the fixture 45° in a clockwise direction would align the k_3 springs along the x-axis, whereas rotating the fixture 45° in a counterclockwise direction would align them along the y-axis.

The springs used during these experiments were "Ultra-Precision Extension Springs" distributed by the MSC Industrial Supply Company. Several properties of interest are included in Table 6.2 (English units; as listed in MSC catalog). Tolerance information was provided for stiffness, I.H.L., and O.D., but not for music wire diameter and initial tension. However, "initial tension is for reference only and may vary" was noted in the MSC catalog. In total, nine different spring array configurations were tested using the PD plus force perturbation control system (Table 6.3). Before conducting

Stiffness (lb/in)	Initial tension (lb)	Inner hoop length (in)	Outer diameter (in)	Music wire diameter (in)
0.2±0.02	0.11	1.50±0.010	0.240±0.003	0.018
0.4±0.04	0.14	2.00±0.015	0.180±0.002	0.018
0.6±0.06	0.19	1.75±0.010	0.240±0.003	0.022

Table 6.2. Material properties and dimensions of extension springs used with spring array to validate spectral estimates of combined inertial and stiffness loads.

Test ID	Nominal k_1 (lb/in.)	Nominal k_2 (lb/in.)	Nominal k_3 (lb/in.)	Nominal k_4 (lb/in.)
sa1	0.2	0.2	0.4	
sa2	0.2	0.2		0.4
sa3	0.2	0.2	0.4	
sa4	0.2	0.2		
sa5			0.2	0.2
sa6	0.2		0.6	
sa7		0.2		0.6
sa8	0.2		0.4	
sa9		0.2		0.4

Table 6.3. Spring array locations and stiffness values used to determine the ability of the spectral estimation method to characterize stiffness fields. Shading indicates no springs were mounted at that location.

impedance measurements on each spring array, a quasi-static calibration was completed to verify the linear relationships in (6.5) and to determine the impact of the parameter variations of the extension springs. This was done by slowly tracing a circle about the origin of the workspace to limit the influence of inertia (and damping) on the measured force. After ramping up the PD control gains to bring the spring array inner fixture to the desired starting point, the control system followed a desired trajectory, namely, a circle with a radius of $r = 0.005$ m with a period of $T = 50$ s,

$$\begin{aligned} x_c &= r\cos(2\pi t/T) \\ y_c &= r\sin(2\pi t/T) \end{aligned} \tag{6.14}$$

which results in a tangential velocity of magnitude $(2\pi/T)\cdot r = 0.63$ mm/s and a tangential acceleration of magnitude $(2\pi/T)^2 \cdot r = 0.079$ mm^2/s. The test was repeated

with $r = 0.010$ m and $r = 0.015$ m to check how well the nonlinear forces generated by the spring array could be characterized by the linearized model in (6.13) as the displacement was increased.

The stiffness matrices from the quasi-static tests were determined via a least-squares optimization. Although it was assumed $k_{ia} = k_{ib} = k_i$ and $l_{ia} = l_{ib} = l_i$ (another source of variation could be different initial tensions in the paired springs), there might have been small differences because the equilibrium point of the stiffness field varied slightly for the different spring configurations. For this reason, offset forces were also included in the least-squares formulation. The terms on the left side of (6.15) are the forces generated by the spring array whereas the term on right side is the interaction forces measured by the force transducer.

$$\begin{bmatrix} k_{11} & k_{12} \\ k_{21} & k_{22} \end{bmatrix} \begin{bmatrix} x \\ y \end{bmatrix} + \begin{bmatrix} F_{o,x} \\ F_{o,y} \end{bmatrix} = \begin{bmatrix} F_{i,x} \\ F_{i,y} \end{bmatrix} \tag{6.15}$$

The least-squares optimal solution can be found by rearranging the previous equation into the form

$$\mathbf{Ap} = \mathbf{F}_i \tag{6.16}$$

where $\mathbf{p} = \left[k_{11}, k_{12}, k_{21}, k_{22}, F_{o,x}, F_{o,y}\right]^{\mathrm{T}}$ is a 6×1 vector of parameters to be estimated, $\mathbf{A}$ is a $2N \times 6$ matrix that contains displacement data at each point in time along with zero and unity column vectors, and $\mathbf{F}_i$ is a $2N \times 1$ vector that contains the interaction forces at each point in time (N is the length of the experimental record). Specifically,

$$\begin{bmatrix} \mathbf{x} & \mathbf{y} & \mathbf{0} & \mathbf{0} & \mathbf{1} & \mathbf{0} \\ \mathbf{0} & \mathbf{0} & \mathbf{x} & \mathbf{y} & \mathbf{0} & \mathbf{1} \end{bmatrix} \cdot \mathbf{p} = \begin{bmatrix} \mathbf{F}_{i,x} \\ \mathbf{F}_{i,y} \end{bmatrix} \tag{6.17}$$

The least-squares optimal solution is defined as

$$\mathbf{p} = \left(\mathbf{A}^{\mathrm{T}}\mathbf{A}\right)^{-1}\mathbf{A}^{\mathrm{T}}\mathbf{F}_{\mathrm{i}} \tag{6.18}$$

Note, once the optimal parameters are found, it is possible to estimate the equilibrium position of the spring array in the following manner:

$$\begin{bmatrix} x_o \\ y_o \end{bmatrix} = -\begin{bmatrix} k_{11} & k_{12} \\ k_{21} & k_{22} \end{bmatrix}^{-1} \begin{bmatrix} F_{o,x} \\ F_{o,y} \end{bmatrix} \tag{6.19}$$

With the asymmetric linear structure developed, it is straightforward to define the symmetric case, i.e., $k_{21} = k_{12}$. The least squares formulation becomes

$$\begin{bmatrix} \mathbf{x} & \mathbf{y} & \mathbf{0} & \mathbf{1} & \mathbf{0} \\ \mathbf{0} & \mathbf{x} & \mathbf{y} & \mathbf{0} & \mathbf{1} \end{bmatrix} \cdot \mathbf{p}' = \begin{bmatrix} \mathbf{F}_{i,x} \\ \mathbf{F}_{i,y} \end{bmatrix}$$

where $\mathbf{p} = \left[k_{11}, k_{12}, k_{22}, F_{o,x}, F_{o,y}\right]^{\mathrm{T}}$.

Similar to the quasi-static test, one method to visualize a stiffness matrix is to multiply the symmetric component of the matrix by a unit displacement vector that rotates from 0-360°. The resulting shape, circular or elliptical, represents the conservative portion of the stiffness field. Indeed, because the spring array is composed of mechanical springs, one would expect the stiffness matrix to be symmetric (some asymmetry may arise due to numerical artifacts, but the stiffness matrix should be symmetric since the mechanical components are passive). Figure 6.9 compares the stiffness ellipses of the linearized spring array forces (depicted with gray solid lines) to ellipses generated with the mean asymmetric (dashed lines) and symmetric (dash-dotted lines) least-squares optimal stiffness matrices from the three quasi-static trials. Although the spring array configurations of sa4 and sa5 are slightly larger than predicted and sa6 and sa7 are slightly smaller, the size and orientation of the other five stiffness ellipses are very close to the predictions. In order to quantify how close the least-squares optimal parameters are to the linearized prediction, the geometric mean of the minor and major axis stiffness values was calculated for each and the following percent difference metric was calculated.

$$\%\Delta = 100\% \cdot \sqrt{\frac{\left(\alpha_{minor}\alpha_{major}\right)_{LSQ}}{\left(\alpha_{minor}\alpha_{major}\right)_{pred}}} - 100\% \tag{6.12}$$

$$\begin{aligned} \alpha_{minor} &= \sqrt{\lambda_{min}\left(\mathbf{K}^{\mathrm{T}}\mathbf{K}\right)} \\ \alpha_{major} &= \sqrt{\lambda_{max}\left(\mathbf{K}^{\mathrm{T}}\mathbf{K}\right)} \end{aligned} \tag{6.13}$$

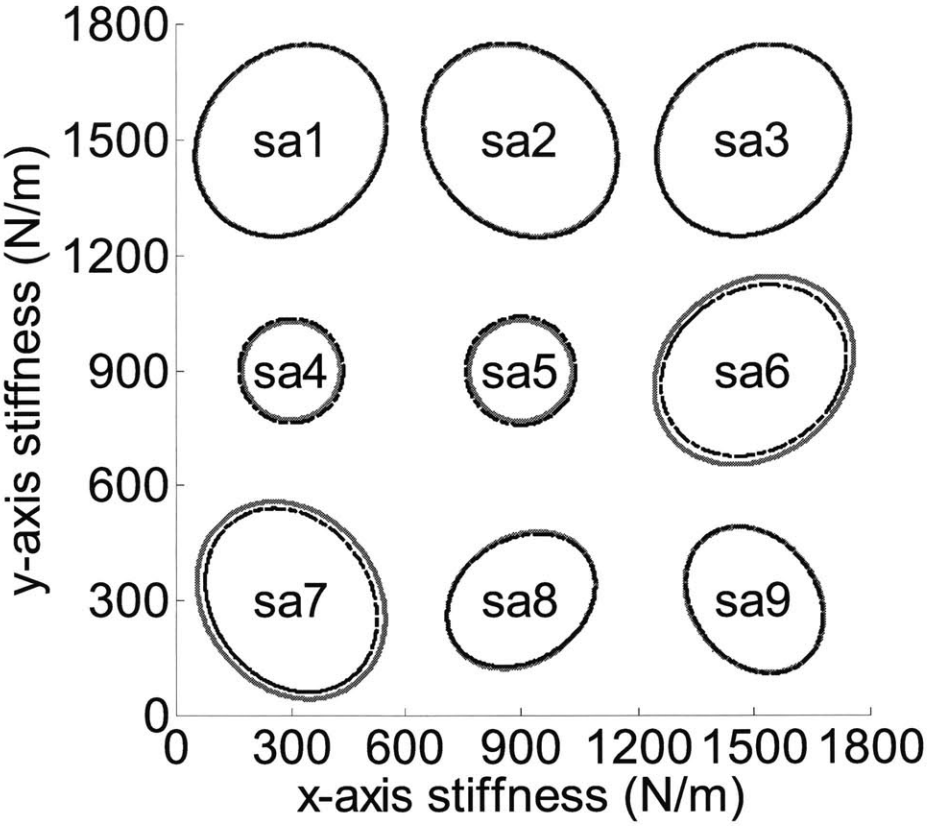

Figure 6.9. Spring array quasi-static calibration test results depicted by stiffness ellipses. Comparison of the analytical prediction (solid gray), and the asymmetric (dashed) and symmetric (dash-dotted) stiffness matrix parameters obtained via linear regression.

where $\lambda(\cdot)$ is the minimum or maximum eigenvalue of the matrix $\mathbf{K}^{\mathrm{T}}\mathbf{K}$. In addition, another metric was calculated to quantify the non-conservative component (i.e., curl) of the asymmetric least-squares optimal stiffness matrix [68]. Namely,

$$\%\,\mathrm{C} = \frac{100\%\left|\left(k_{12} - k_{21}\right)/2\right|}{\sqrt{\left(\alpha_{minor}\alpha_{major}\right)_{LSQ}}} \tag{6.14}$$

Figure 6.10 displays the percent difference metrics for the symmetric and asymmetric least-squares optimum parameters ($\%\Delta_s$ and $\%\Delta_a$) as well as the percent curl metric for the asymmetric case ($\%\,\mathrm{C}$). Metrics for the three trials are depicted with the symbols □, ◇, and ○. The values of $\%\Delta_s$ and $\%\Delta_a$ for the three repeatability trials are close to each other for each spring array configuration and lie within the interval $[-8.1\%, 7.5\%]$.

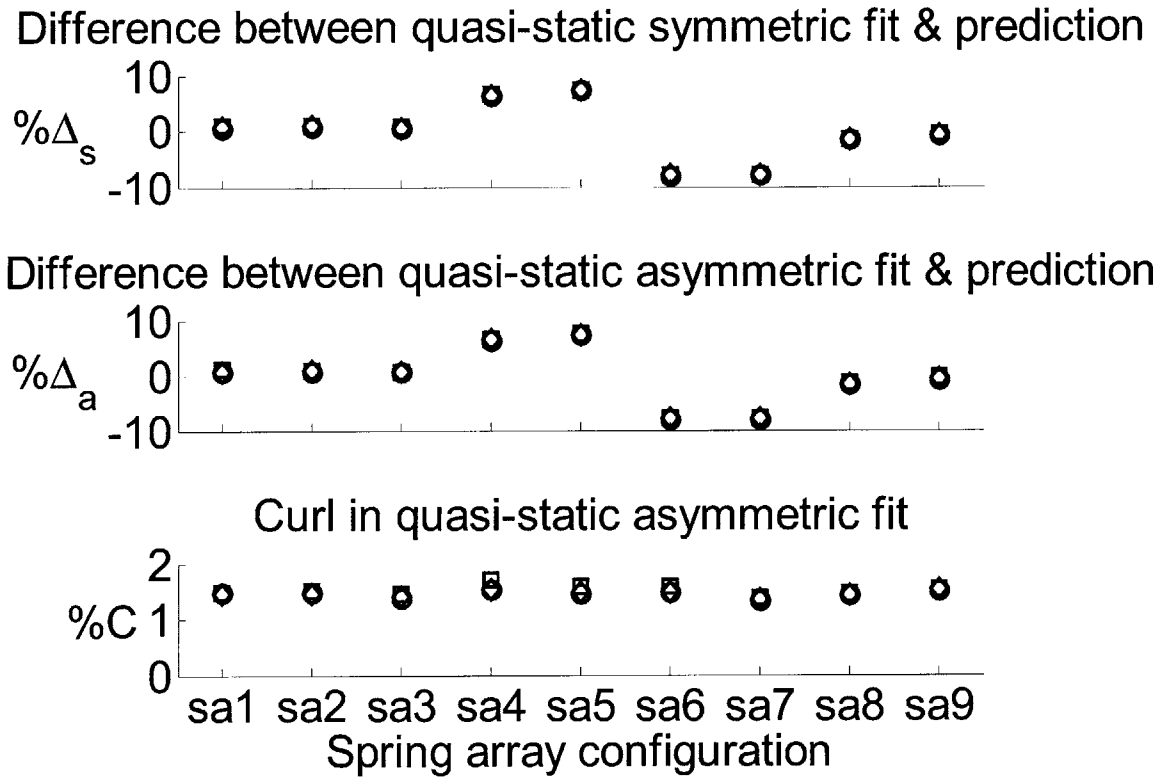

Figure 6.10. Quasi-static results are within 10% tolerance on extension spring stiffness. Curl of mechanical spring array should equal zero; non-zero curl must be a numerical artifact.

Since %C is relatively small 1.48±0.02% (mean ± SEM) as expected, the symmetric and asymmetric percent difference values are close to each other. Therefore, these metrics have verified the stiffness matrices from the quasi-static trials were in agreement with the predicted values of these matrices from the linearized spring array equation. Recall, although the tolerances on the dimensions of the spring were quite small, the tolerance on the spring constant was ±10% and the spring preloads were not controlled during the manufacturing process.

Since the stiffness matrices of the spring array configurations and the inertia matrix of the components that comprise the spring array inner fixture have been verified, the spectral estimates can now be compared to the transfer function matrix of each linear system. Prior to doing this, a couple observations will be made. First, although modeled as an ideal spring (no mass, purely restorative stiffness), the springs used during testing are not massless. However, the masses of the springs ($m_{k=0.2} = 1.8\,\text{g}$, $m_{k=0.4} = 1.0\,\text{g}$, and

$m_{k=0.6} = 1.3$ g; measurements included string and labels) are negligible compared to the mass of the inner fixture ($m_{sm1} + m_{ift} = 429.6$ g). Second, although mechanical springs are close to ideal energy storage devices, some energy is dissipated during this process, e.g., internal damping present in the springs and aerodynamic drag on the components of the handle between the tool side mount of the force transducer and the springs. Therefore, when comparing the frequency responses of the dynamic stiffness spectral estimates and the linear model, viscous damping was included in the model. The parameters along the diagonal of the viscous damping matrix were defined such that the damping coefficient for both elements $\zeta = 0.01$ and the off-diagonal parameters were set equal to zero, i.e., $b_{ii} = 2\zeta\sqrt{k_{ii}m_{ii}}\Big|_{\zeta=0.01}$ for $i = 1, 2$ and $b_{12} = b_{21} = 0$ Ns/m.

Figure 6.11 displays the spectral estimate of the dynamic stiffness for configuration sa1 and Figure 6.12 displays the corresponding partial and multiple coherence function values. In Figure 6.11, the symmetric linear model prediction is depicted by a gray solid line. In Figures 6.11 and 6.12, the spectral analysis results for $N_{MNS} = 5$ are depicted by dashed lines, whereas the results for $N_{MNS} = 45$ are depicted by dash-dotted lines. Recall from Figures 6.4 and 6.5 that the lower and upper bounds of the transfer functions are tightest when the corresponding partial coherences are close to 1. Because the mean partial coherences from the six trials are close to 1 throughout most of the frequency range (Figure 6.12), only the mean spectral estimates from 6 trials have been plotted for each element of the transfer function matrix in Figure 6.11. Although the partial coherence values corresponding to the diagonal elements of dynamic stiffness are similar, the partial coherence values corresponding to the off-diagonal elements with $N_{MNS} = 45$ are significantly lower than those with $N_{MNS} = 5$. Despite the drop in coherence values, the dynamic stiffness estimates remain close with $N_{MNS} = 5$ and $N_{MNS} = 45$. Lower partial coherences are expected at frequencies close to and below 0.244 Hz (spectral resolution of Hanning window), but not in the mid-frequency range (0.5 to 3 Hz) where the transfer function is still dominated by the spring array stiffness, i.e., the frequency range below the natural frequency of system.

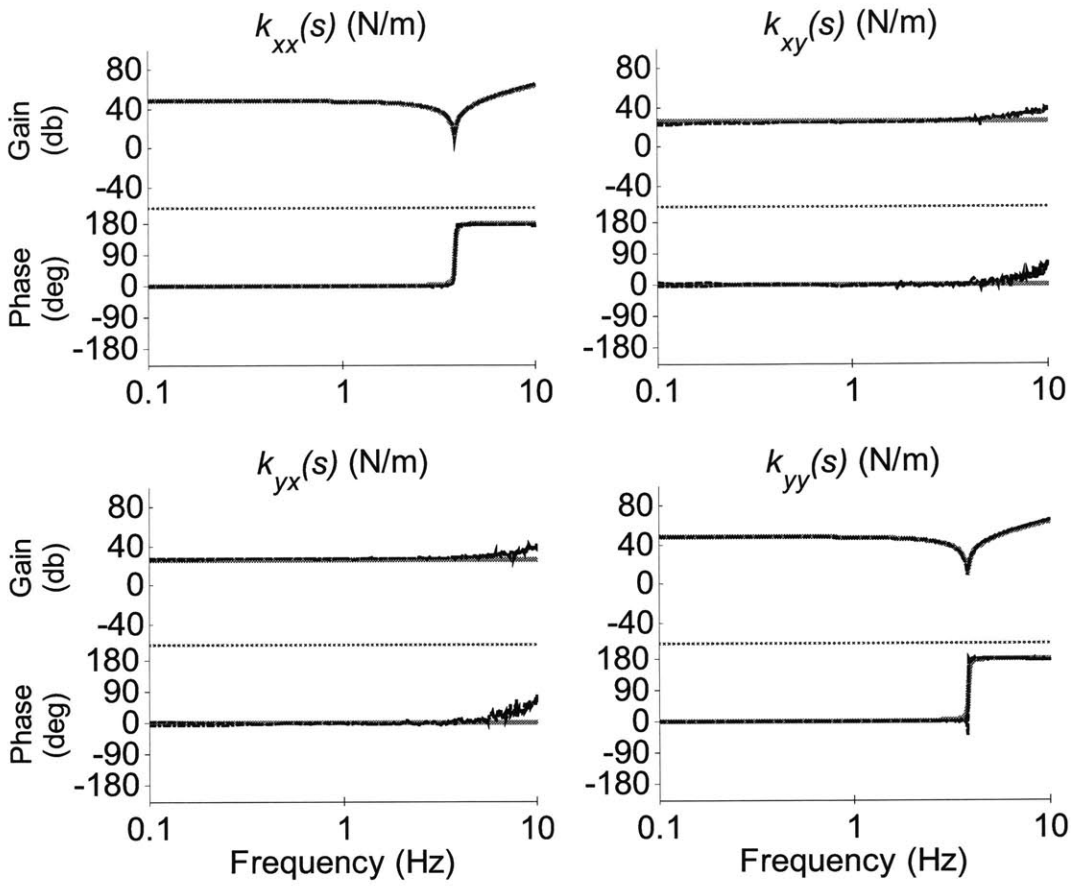

Figure 6.11. Dynamic stiffness spectral estimates of sa1: expected (solid gray), with 5 overlaps (dashed), and 45 overlaps (dash-dotted).

The dynamic stiffness spectral estimates and partial/multiple coherence function values for configurations sa2-sa9 are included in Appendix E. Figure 6.13 displays the values of the VAF matrix and R^2 defined in (6.8)-(6.9) for sa1-sa9 with $N_{MNS} = 5$ and $N_{MNS} = 45$ over the frequency ranges of 0-5 Hz and 0-10 Hz. The off-diagonal VAF values and R^2 for sa4 and sa5 were lower than the values for the other configurations because the ideal frequency responses of the off-diagonal elements were identically equal to zero (inertia matrix has zero-valued off-diagonal terms due to symmetry and stiffness ellipse is circular). Although the number of overlaps had little impact on VAF_{xx} and VAF_{yy}, increasing the number of overlaps improves VAF_{xy} and VAF_{yx} over the frequency range 0-10 Hz. In general, when the frequency range used in the VAF and R^2 calculations was reduced from 0-10 Hz to 0-5 Hz, VAF_{xy} and VAF_{yx} approached 100%

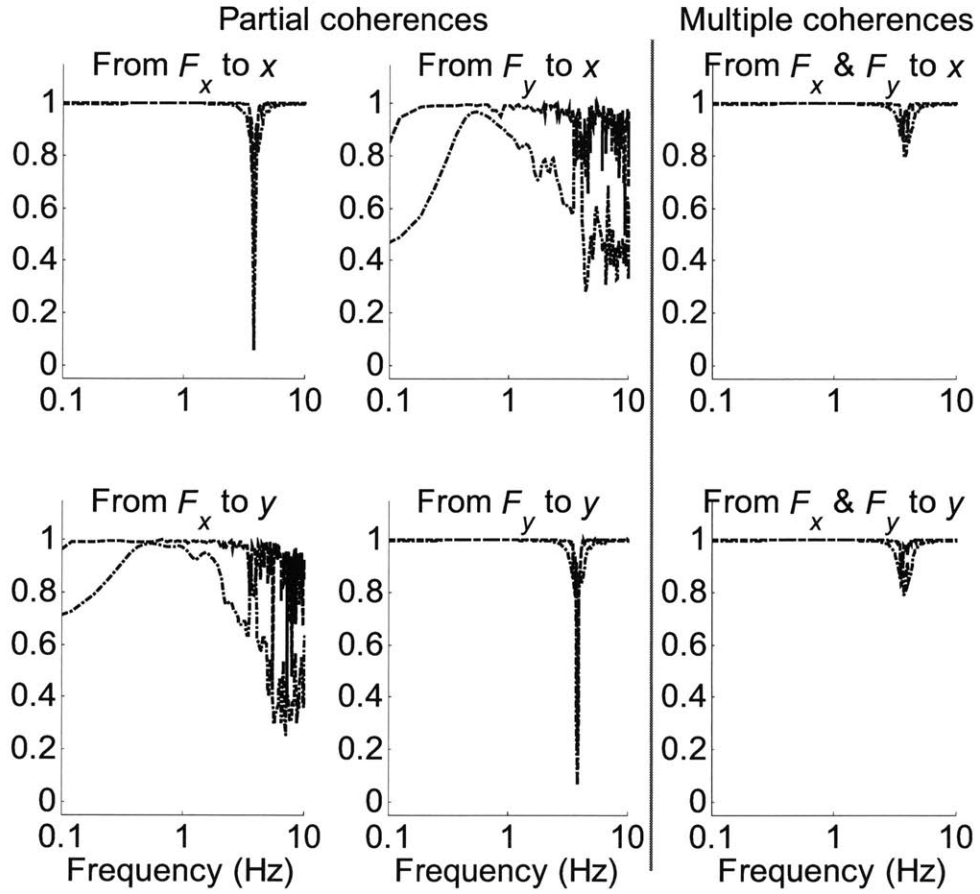

Figure 6.12. Partial and multiple coherence functions for dynamic compliance spectral estimate of sa1 with 5 (dashed) and 45 (dash-dotted) overlaps.

for both $N_{MNS} = 5$ and 45. Note, the increases in gain and phase of the spectral estimates for $k_{xy}(s)$ and $k_{yx}(s)$ over the frequency range 5-10 Hz must be a numerical artifact since the off-diagonal elements in the inertia matrix were equal to zero. Based on the reliability and accuracy of the spectral estimates for purely mechanical systems, tests were conducted with unimpaired subjects to verify the resulting spectral estimates were consistent with past studies of human arm impedance.

6.4. Unimpaired subject study

Unimpaired subject testing was completed in the MIT Newman Laboratory for Biomechanics and Human Rehabilitation with approval from the MIT Committee on the Use of Humans as Experimental Subjects (COUHES). MIT-MANUS was mounted on the same patient workstation as the mechanical system testing (Figure 6.1) and an arm

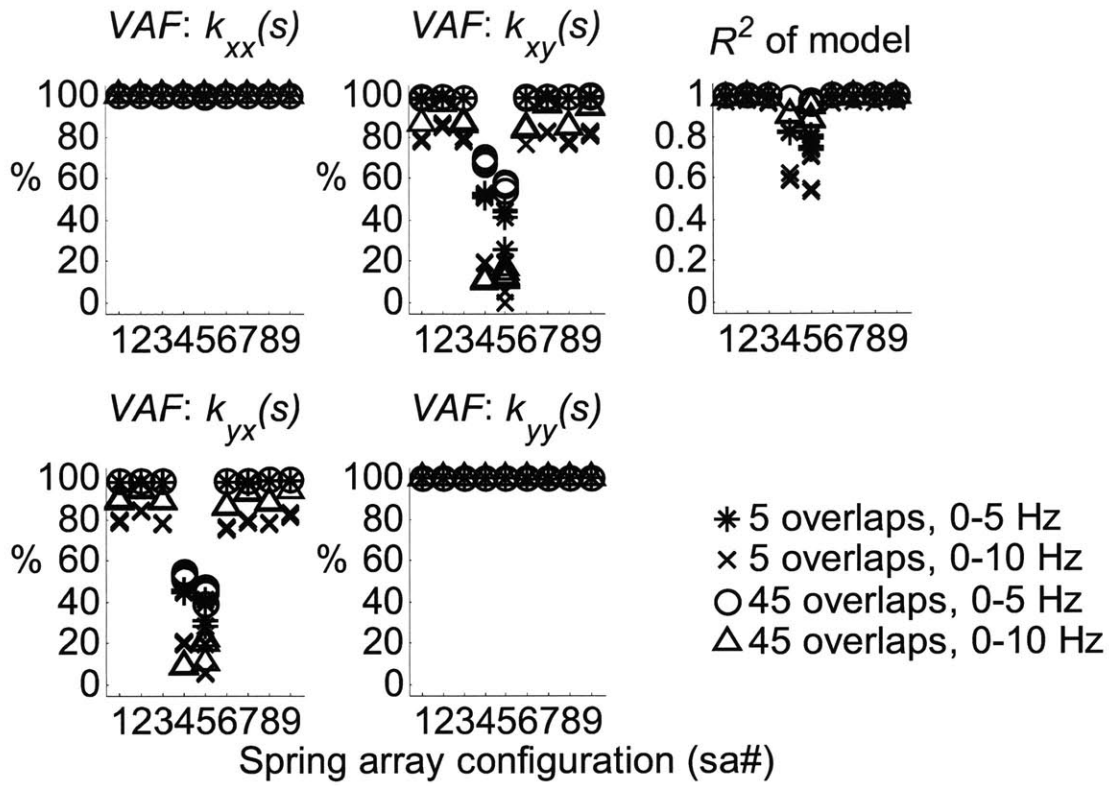

Figure 6.13. Summary of VAF values for the dynamic stiffness spectral estimates and for R^2 of the entire model for sa1-sa9.

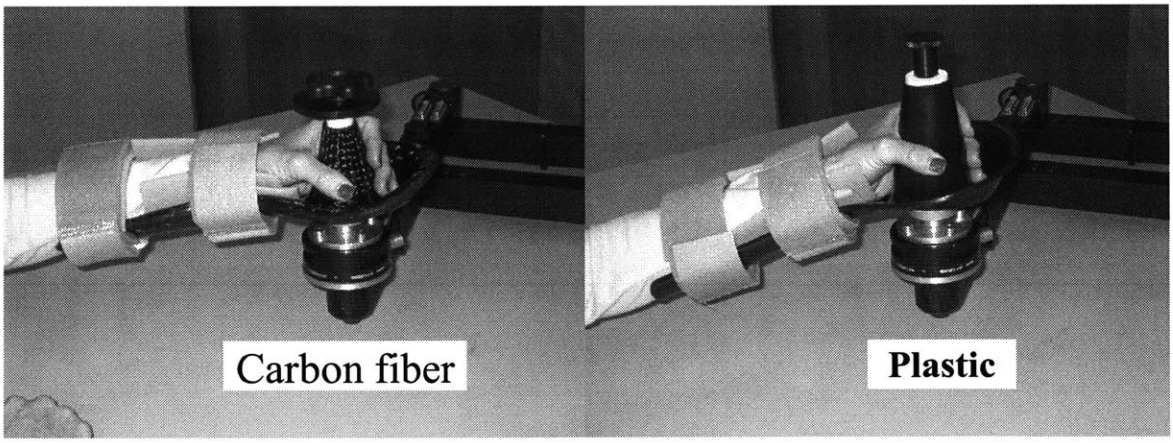

Figure 6.14. Comparison of the carbon-fiber arm trough and plastic arm trough that were used to support the left arms of unimpaired subjects.

trough with Velcro straps at the robot's end-effector was used to support and secure subjects' arms during testing (Figure 6.14 displays carbon fiber and plastic arm troughs for the left arm).

Analysis of preliminary test data from an unimpaired subject revealed counter-intuitive phase transitions in the dynamic stiffness frequency response. The phase in all four elements of the dynamic stiffness matrix from tests of the left arm should be 0° at low frequencies and increase to 180° at higher frequencies. However, in several trials the estimated phase of $k_{xy}(s)$ and $k_{yx}(s)$ began at 0° and decreased to −180° (other counter-intuitive transitions occurred, but this was most common). Similar transitions occurred in the phase estimates of $k_{xy}(s)$ and $k_{yx}(s)$ with right arm tests (instead of −180° to 0°, 180° to 0° was observed). The counter-intuitive phase transitions will be investigated in the following section to determine the cause of this unexpected result.

6.4.1. Preliminary results suggest estimate is sensitive to test hardware, stochastic perturbation level, and spectral analysis parameters

Further testing and analysis suggested that several factors contribute to the occurrence of the counter-intuitive phase transitions, namely, the magnitude of the force perturbations, the material properties of the arm troughs that support the subject's arm, and the spectral analysis parameters (i.e., N_{FFT}, N_{WND}, N_{OVL}, and N_{MNS}). Therefore, tests were conducted at five command perturbation levels (1.5, 2.25, 3.0, 3.75, 4.5 N) on the right and left arms of six subjects with carbon fiber and plastic arm troughs. Three tests at each perturbation level were conducted by repeating the low to high block of perturbation levels three times. The trade-off between spectral estimate variance and frequency resolution was investigated by considering the same two sets of spectral analysis parameters that were used to analyze the mechanical system tests, i.e., ($N_{WND} = 8192$, $N_{OVL} = 4096$, $N_{MNS} = 5$) or ($N_{WND} = 2048$, $N_{OVL} = 1536$, $N_{MNS} = 45$) with $N_{FFT} = 8192$.

Figure 6.15 demonstrates the effects that the spectral analysis parameters, the arm trough material, and the force perturbation levels have on $k_{xy}(s)$ and $k_{yx}(s)$ for the left arm of an unimpaired subject. The top row of graphs contains the gain and phase plots of $k_{xy}(s)$, whereas the bottom row contains $k_{yx}(s)$. The first column of graphs contains the results for a plastic arm trough with $N_{MNS} = 5$. The phase of $k_{xy}(s)$ near the resonance

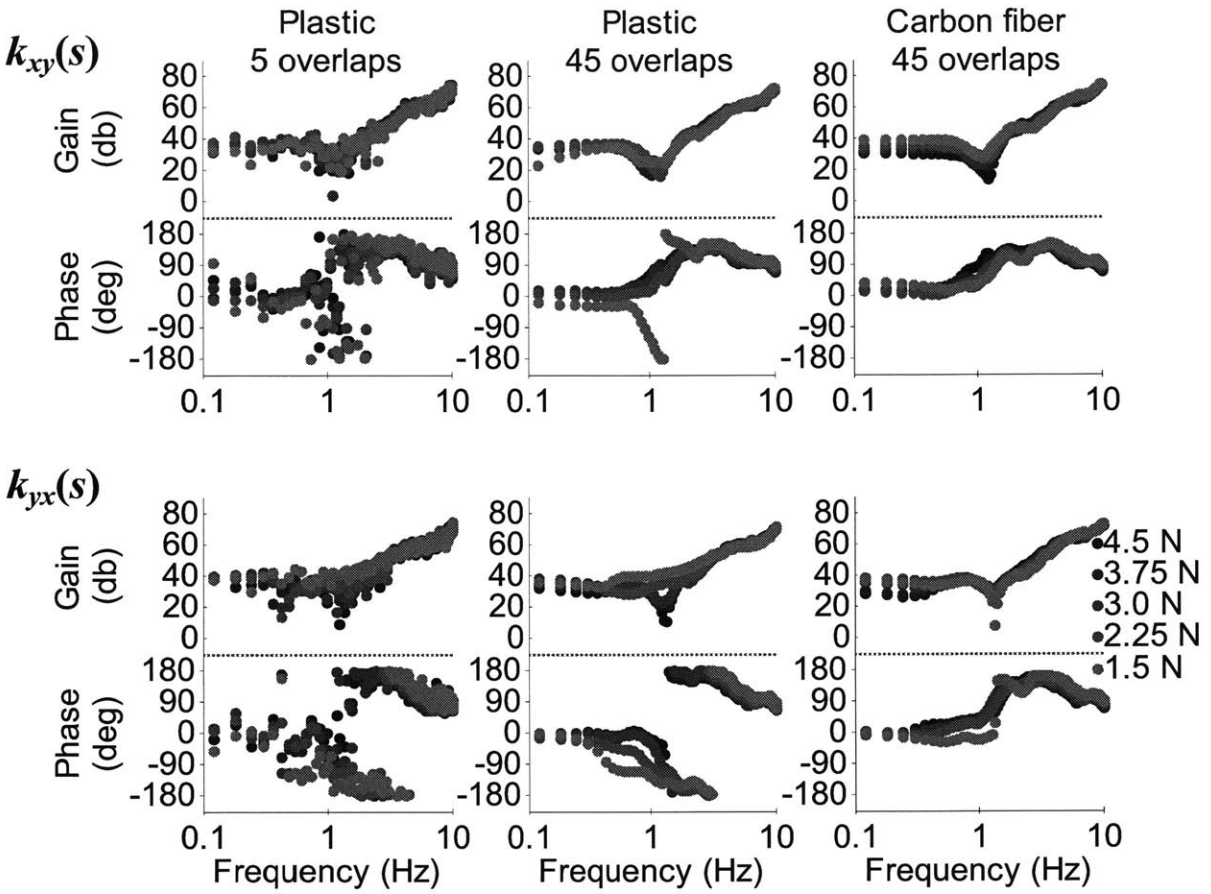

Figure 6.15. Occurrences of a counter-intuitive phase transition from 0° to -180° instead of 0° to +180° (first column) were lessened by increasing the number of overlaps from 5 to 45 (second column) and changing from a plastic to a carbon fiber arm trough (third column).

frequency undergoes a phase transition from 0° to 180° in some cases as expected, but 0° to –180° in others (note, transfer function phase has been defined from –180° to 180°, i.e., it has not been "unwrapped"), whereas the phase of $k_{yx}(s)$ for most test cases undergoes a phase transition from 0° to –180°.

The second column of graphs contains the analysis results of the plastic arm trough with $N_{MNS} = 45$. As expected, increasing the number of averages used to calculate the auto/cross-spectra and ordinary coherence functions decreases the variance of the resulting estimate. The phase of $k_{xy}(s)$ undergoes the expected transition of 0° to 180° for all of the force perturbation levels except $\Delta F = 1.5$ N. However, $k_{yx}(s)$ still

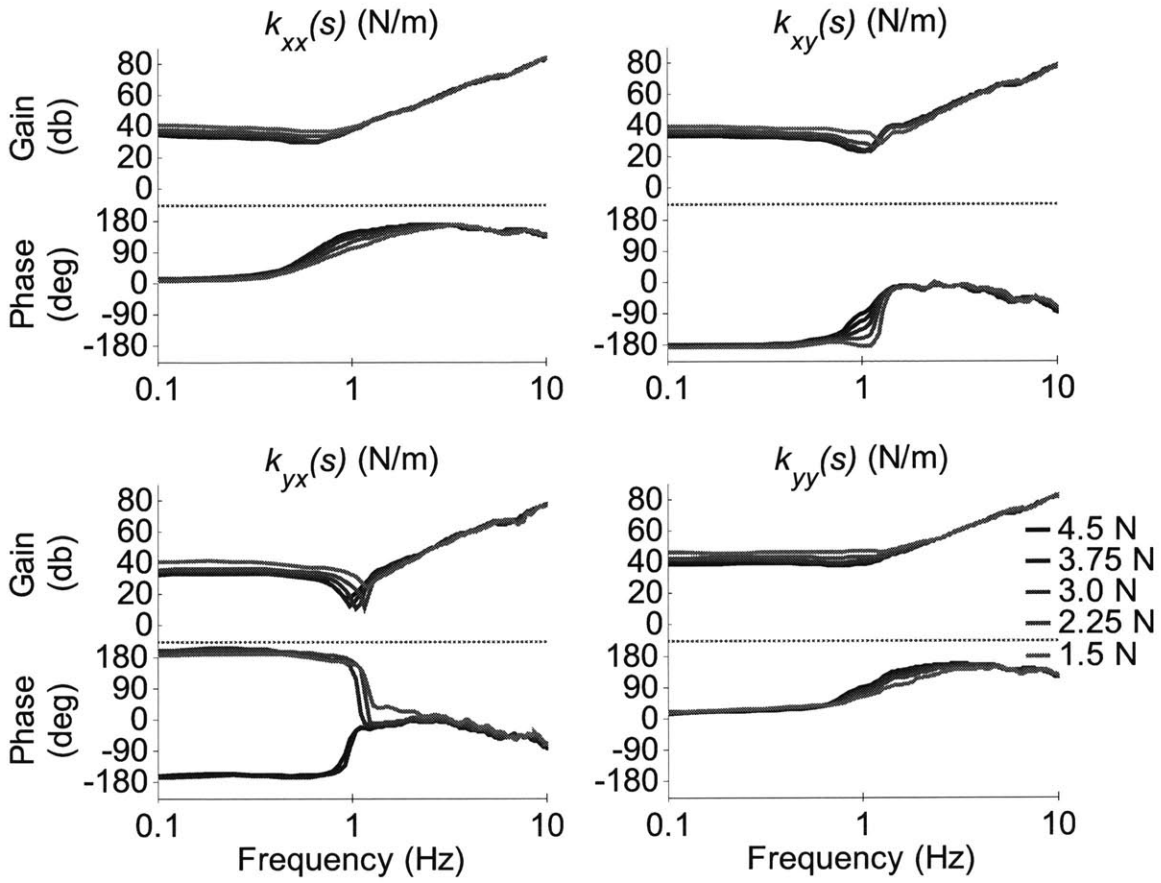

Figure 6.16. Dynamic stiffness estimates exhibit counter-intuitive phase behavior at the three lowest force perturbation amplitudes, but not the two highest (right arm, carbon fiber arm trough, 45 overlaps).

undergoes a counter-intuitive phase transition from 0° to -180° regardless of the force perturbation level.

The third column of graphs contains $k_{xy}(s)$ and $k_{yx}(s)$ estimates for the subject when a carbon fiber arm trough was used and the spectral analysis was completed with $N_{MNS} = 45$. By using an arm trough that is stiffer, the phase of $k_{xy}(s)$ and the phase of $k_{yx}(s)$ undergo the expected transition from 0° to 180°. Although the estimate for $k_{yx}(s)$ with $\Delta F = 1.5$ N undergoes a rapid change in magnitude and phase that is characteristic of a lightly damped resonance, it could be an artifact similar to the one that occurred with the plastic arm trough, $\Delta F = 1.5$ N, and $N_{MNS} = 45$.

Figure 6.16 displays the dynamic stiffness of the right arm of an unimpaired subject. Each line depicts the mean of three tests for each force perturbation level with

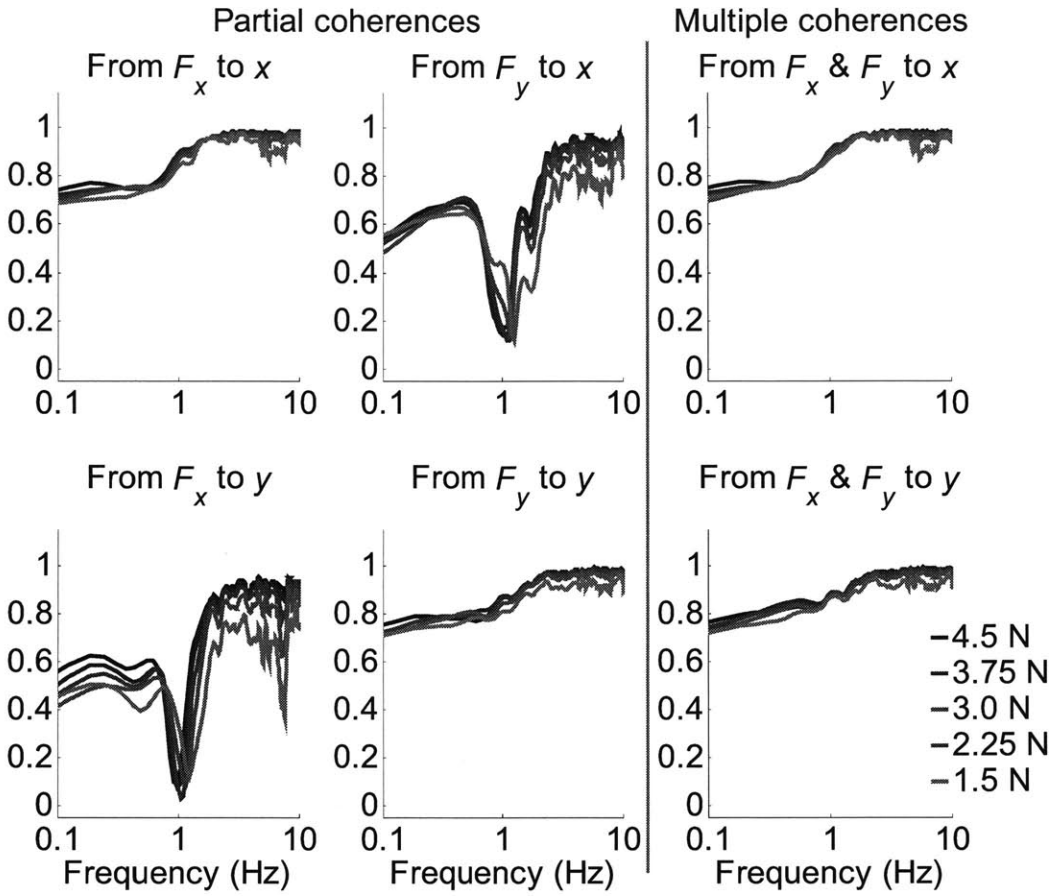

Figure 6.17. Partial coherences are near their smallest values in the frequency range where the counter-intuitive phase transitions occurred.

$N_{MNS} = 45$ and a carbon fiber arm trough. As noted earlier, the phase of $k_{xy}(s)$ and $k_{yx}(s)$ for the right arm is expected to increase from –180° to 0°. Despite using the carbon fiber arm trough during the experiment and $N_{MNS} = 45$ for the analysis, the phase estimates of $k_{yx}(s)$ for the three smallest perturbation levels (i.e., 1.5 N, 2.25 N, 3.0 N) begin at 180° and decrease to 0°.

Figure 6.17 displays the corresponding partial and multiple coherence functions. In a neighborhood about the resonance frequency, the partial coherence functions from F_y to x and from F_x to y are at their lowest values and, from (6.1), the magnitudes of the random errors are at their highest values. Although the partial and multiple coherences are below 0.8 at 0.1 Hz, the spectral resolution of the estimate is only 0.244 Hz (because $N_{WND} = 2048$). The dynamic stiffnesses and partial/multiple coherence

functions calculated with $N_{MNS} = 5$ and $N_{MNS} = 45$ for the right and left arms of six unimpaired subjects are included in Appendix F.

Based on the results from this section, in order to reduce the likelihood of numerical artifacts arising when calculating the spectral estimate, use an arm trough that is comprised of a stiff material like carbon fiber. In addition, carefully select the spectral analysis parameters and the force perturbation level used. The next section will further examine the sensitivity of the dynamic stiffness spectral estimates of six unimpaired subjects.

6.4.2. Summary of dynamic stiffness spectral estimates for a group of unimpaired subjects

Although the spectral estimation method worked very well with a purely mechanical system, the previous section demonstrated a need for careful implementation of the test and analysis of the data gathered. The next step was to compare the dynamic stiffness estimates from the group of unimpaired subjects to previously reported properties of human arm impedance. The results from Tsuji et al. [95] were selected for comparison simply because they estimated arm impedance during maintained posture of 4 male subjects (21-23 years old) at 4 test locations. However, the unimpaired subjects who participated in this study consisted of 2 female and 4 male subjects (over a wider range of ages) so the results from [95] are intended to provide a "ballpark" estimate of property values, not to set hard limits. By applying a series of step displacement inputs in 8 different directions, measuring the interaction forces, and fitting the data to a second-order linear system model, they were able to estimate the inertia, damping, and stiffness matrices. In order to compare the unimpaired subjects' frequency response estimates to the results from [95], a nonlinear least-squares regression was used to determine the optimum second-order linear system model parameters for each dynamic stiffness estimate. Recall, the optimization problem was defined in terms of impedance in an attempt to weight stiffness and inertia equally (see (6.4)-(6.5)). Two model structures were used for the mass, damping, and stiffness matrices: 1. symmetric mass, asymmetric damping and stiffness; 2. symmetric mass, damping, and stiffness.

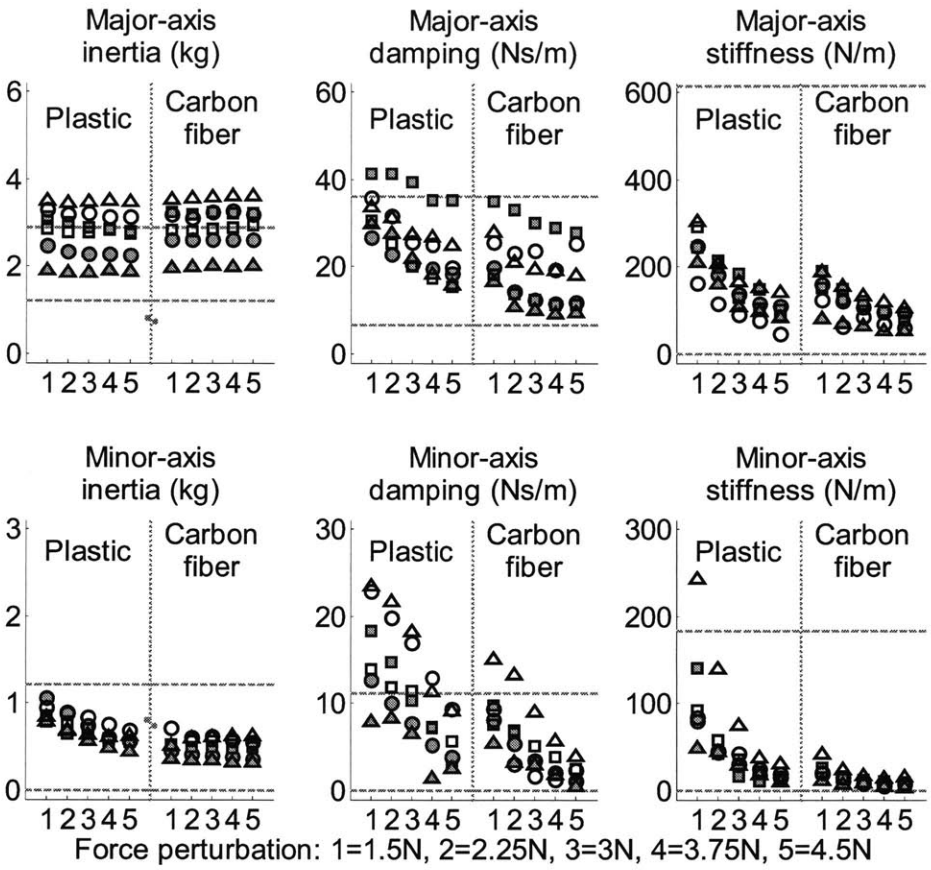

Figure 6.18. Major and minor-axis properties of the least-squares optimum mass, damping, and stiffness matrices for the left arms of 6 unimpaired subjects with plastic and carbon fiber arm troughs (spectral analysis: 45 overlapping data segments).

The major and minor-axis properties of the mass, damping, and stiffness matrices of the left arm trials with the plastic and carbon fiber arm troughs ($N_{MNS} = 45$, symmetric mass, asymmetric damping and stiffness) are shown in Figure 6.18. Recall, the major and minor-axis properties in equation (6.13) are the eigenvalues of the transpose of the matrix post-multiplied by itself, e.g., $\lambda\left(\mathbf{K}^{\mathrm{T}}\mathbf{K}\right)$. The dashed lines are the 95% confidence intervals for the four male subjects reported in [95]. The symbols correspond to the mean value of the major or minor-axis property of an unimpaired subject for three trials at each perturbation level. The results of the tests with the plastic arm trough are shown on the right side of each plot and the results for the carbon fiber arm trough are shown on the left. The gray dots on each side of the dividing line in the major and minor-axis inertia graphs depict the mass of the arm trough, Velcro straps, and other end-effector hardware

used to attach the subject to the robot. The mass of these components was assumed to be lumped at the handle and was subtracted from the subjects' estimated inertial properties. As shown in Figure 6.18, the majority of the minor-axis and major-axis properties of the mass, damping, and stiffness matrices fall within the confidence intervals from [95].

Although the minor-axis inertia decreases as the perturbation level increases for tests with the plastic arm trough, the values for tests with the carbon fiber arm trough remain nearly constant. In general, the trends for the damping and stiffness properties with plastic and carbon fiber arm troughs are similar to the trend uncovered for minor-axis inertia tests with the plastic arm trough. That is, as the perturbation level increases, the major and minor-axis damping and stiffness decrease. However, properties from tests with the plastic arm trough and low perturbation levels are larger than the properties from tests with the carbon fiber arm trough.

As shown in Figure 6.19, the VAF values (as defined in (6.8)) for $k_{xx}(s)$ and $k_{yy}(s)$ remain close to 100% for the five perturbation levels. The VAF values for $k_{xy}(s)$ and $k_{yx}(s)$ are lower than the values for $k_{xx}(s)$ and $k_{yy}(s)$, but most of the second-order linear system models still explain more than 95% of the variation that is present in the nonparametric spectral estimates. In addition, the R^2 values for the dynamic stiffness matrix lie in the range of 0.98 and 0.995. The results of this analysis for both the left-arm and right-arm tests, for both $N_{MNS} = 5$ and $N_{MNS} = 45$, and for both model structures (symmetric mass, asymmetric damping and stiffness; symmetric mass, damping, and stiffness) are similar to the results presented in Figures 6.18-6.19 and have been included in Appendix F.

Although using a plastic arm trough was shown to make the spectral estimate prone to the counter-intuitive phase transitions, the variation of the inertial, damping, and stiffness properties as the force perturbation increases shown in Figure 6.18 is remarkably well structured. Due to this, it might be possible to quantify the nature of the counter-intuitive behavior by comparing the results from trials with the plastic arm trough to the results from trials with the carbon fiber arm trough. If successful, the counter-intuitive

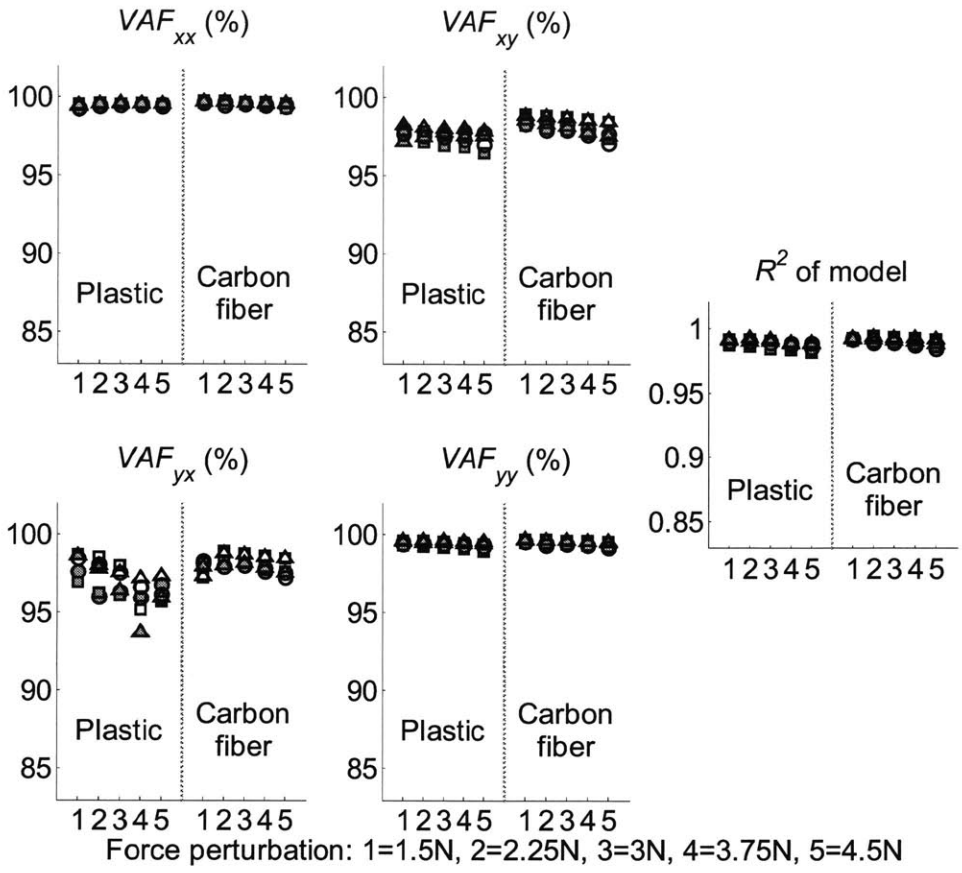

Figure 6.19. Summary of VAF values for the dynamic stiffness spectral estimates and for R^2 of the entire model for the left arms of 6 unimpaired subjects.

behavior could be mathematically compensated for in the spectral estimates derived from past and current trials where plastic arm troughs were used.

Based on the results from section 6.3, the spectral estimation method developed in Chapter 5 is a reliable and accurate method for identifying impedance properties of mechanical systems. Although sensitive to experimental and analytical factors, it can still identify the arm mechanical impedance of unimpaired subjects. The compliance of the hardware that is used to attach the subject to the end-effector contributed to the counter-intuitive phase behavior present in some spectral estimates. Using a carbon fiber arm trough instead of a plastic one reduced the occurrence of counter-intuitive phase transitions in the spectral estimates. The next section will discuss results of a pilot study with stroke patients using the spectral estimation method to demonstrate that the method is suitable for a clinical setting.

6.5. Stroke patient pilot study

A pilot study with three left and three right hemiplegic stroke patients was conducted at the Burke Medical Research Center in White Plains, NY with approval from MIT COUHES and the institutional review board of the Burke Rehabilitation Hospital. This study was completed prior to the unimpaired subject study and the only force perturbation level considered was $\Delta F = 2.25$ N (which was the second lowest perturbation in the unimpaired subject study). The tests were conducted using an InMotion^2 planar robot with plastic arm troughs similar to the ones used during the unimpaired subject study (Figure 6.14).

As in the unimpaired subject study, the dynamic stiffness frequency responses of both arms of the stroke patients were estimated. Ten trials on each arm were completed in six blocks – 3 trials with the right arm, 3 trials with the left arm, 4 trials with the right arm, 4 trials with the left arm, 3 trials with the right arm, and 3 trials with the left arm. This test sequence was used for a couple of reasons. First, rather than running two successive blocks of 10 trials, the test sequence allowed patients to take short breaks during the test session while the therapist switched from one arm trough to the other. Since it was uncertain whether the patients would tolerate the stochastic forces that were being delivered by the robot, switching arms would help split up the monotony of the test session. Second, switching the patient from one arm trough to the other might reveal if the estimate was sensitive to the manner in which a patient's arm was positioned and secured before the test.

In addition to the robot measurements, the clinician administering the trials also evaluated muscle tone across nine muscle groups from the hemiplegic arm using the Modified Ashworth Scale (MAS). This was done before and after the 20 trials. Clinicians grade muscle tone on an ordinal scale by the amount of resistance to passive movement [9]. Specifically, the ratings are

0 - no increase in tone

1 - slight increase in tone, manifested by a catch and release or by minimal resistance at the end of the range of motion

2 - slight increase in tone, manifested by a catch, followed by minimal resistance throughout the remainder (less than half) of the range of motion (ROM)

Muscle group	1		2		3		4		5		6	
	a	b	a	b	a	b	a	b	a	b	a	b
Shoulder internal rotator	2	2	3	2	2	1	2	1	1	1	2	2
Elbow extensor	0	1	2	1	0	0	2	2	0	0	3	3
Elbow flexor	3	3	3	2	3	3	0	0	3	3	0	0
Forearm pronator	0	0	0	0	0	0	3	3	1	1	0	0
Forearm supinator	3	3	1	1	0	0	0	0	0	0	0	0
Wrist flexor	2	2	3	3	2	2	4	4	2	2	1	1
Wrist extensor	0	0	0	0	0	0	0	0	0	0	0	0
Digit flexor	2	2	3	3	2	2	4	4	3	3	3	3
Digit extensor	0	0	0	0	0	0	0	0	0	0	0	0
MAS-S/E	5	6	8	5	5	4	4	3	4	4	5	5
MAS-Total	12	13	15	12	9	8	15	14	10	10	9	9

Table 6.4. Modified Ashworth Scale (MAS) evaluations for stroke patients who participated in impedance measurement trials (10 trials/arm). Patients 1-3 were left hemiplegic and patients 4-6 were right hemiplegic. Evaluation was completed by clinician before and after robot trials. An increase in a MAS muscle group was denoted by dark shading and a decrease by light shading.

3 - more marked increase in tone through most of the ROM, but affected parts easily moved

4 - considerable increase in tone and passive movement difficult

5 - affected part(s) rigid in flexion or extension

MAS Total is the sum of the nine individual ratings (maximum of 45). This was done to determine whether the stochastic inputs had an effect on the property that they were intended to estimate.

The MAS clinical evaluations are given in Table 6.4. MAS S/E is a subset of the nine muscle groups used to define MAS Total that pertain to the shoulder and elbow, i.e., the shoulder internal rotator, the elbow flexors, and the elbow extensors (MAS S/E maximum of 15). Patients 1-3 are left hemiplegic, whereas patients 4-6 are right hemiplegic. MAS ratings in the "a" columns were the pre-session evaluations and the ratings in the "b" columns were the post-session evaluations. Although there was one instance of a MAS rating for a muscle group increasing (dark gray shading), there were five instances of MAS ratings decreasing (light gray shading). In addition, the only muscle groups that were affected were those in the MAS S/E subset. This implies running 10 trials of the test could be causing a decrease in patient muscle tone. However,

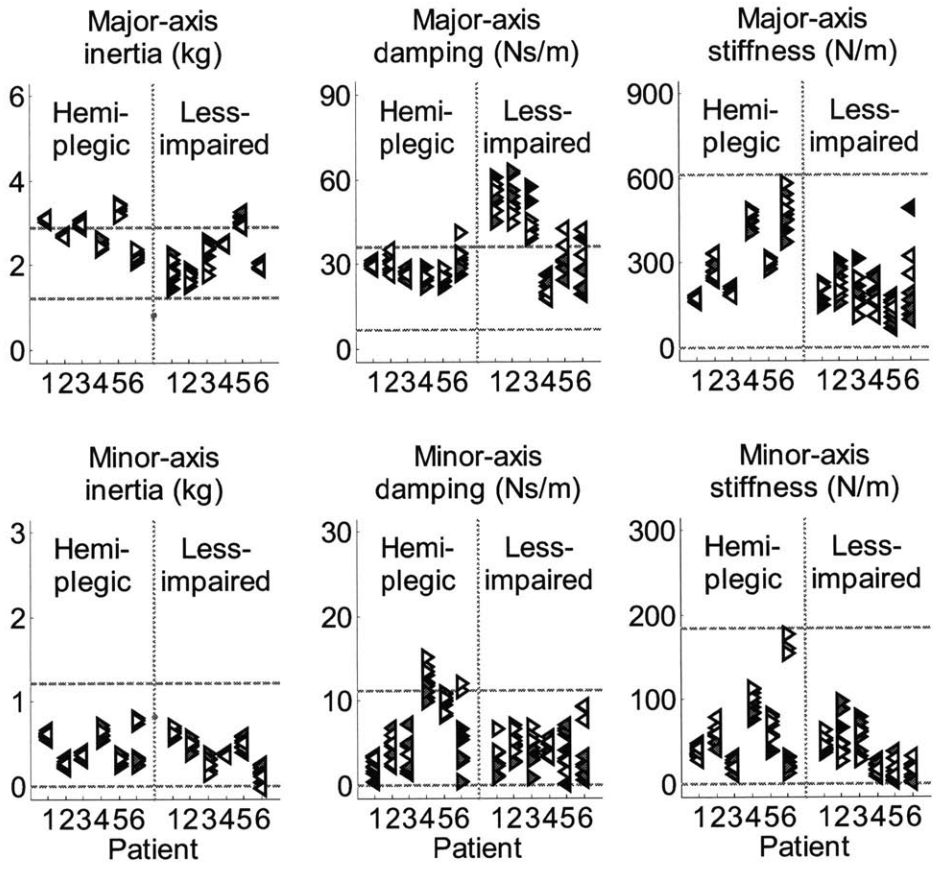

Figure 6.20. Major and minor-axis properties of the least-squares optimum mass, damping, and stiffness matrices for both arms of 6 stroke patients (spectral analysis using 45 overlapping data segments).

in the modified PBPT protocol, it will only be run three times during a PBPT session (once before sensorimotor game, once before PBPT game, and once after PBPT game: games are described in Chapter 4, section 4.3)

The major and minor-axis properties of the symmetric mass matrix and asymmetric damping and stiffness matrices and $N_{MNS} = 45$ are given in Figure 6.20 and the corresponding VAF and R^2 values are given in Figure 6.21. The dynamic stiffness frequency responses with $N_{MNS} = 5$ and $N_{MNS} = 45$, and the optimization results for a second-order linear model with symmetric mass, damping, and stiffness matrices are given in Appendix G. The results for patients' left arms are depicted with triangles pointing to the left (◀ for trials 1-3, ◀ for trials 4-7, and ◁ for trials 8-10) and the results for the patients' right arms are depicted with triangles pointing to the right (▶ for trials 1-

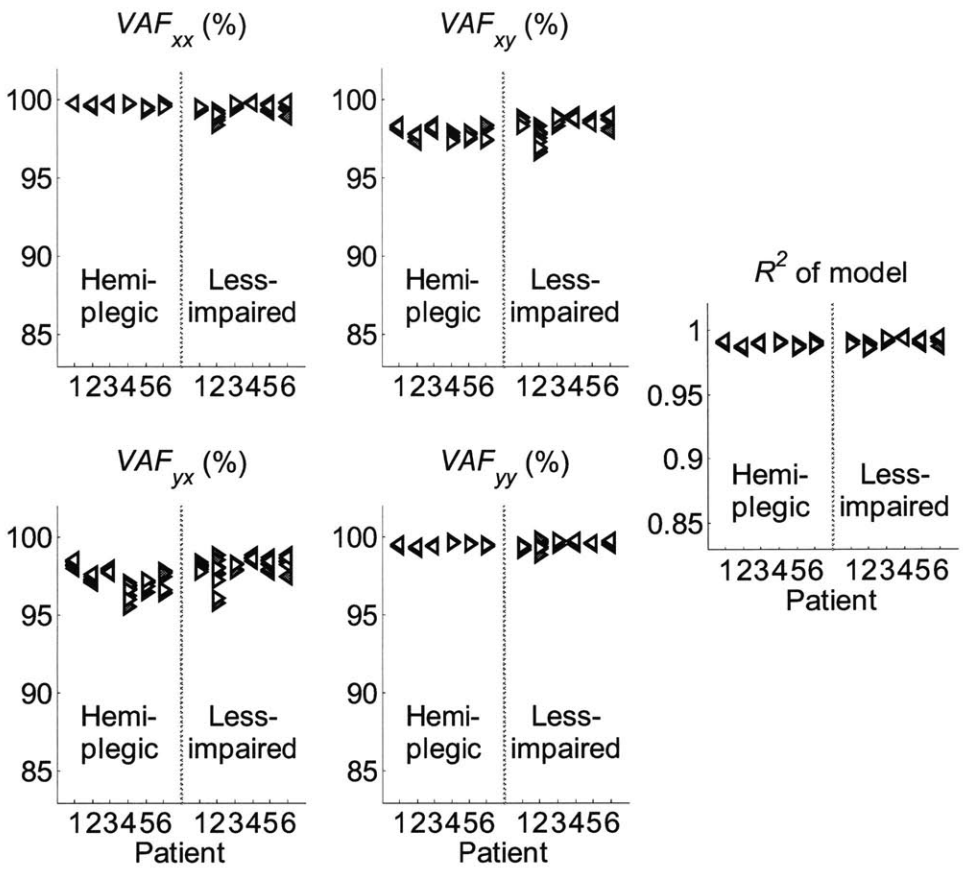

Figure 6.21. Summary of VAF values for the dynamic stiffness spectral estimates and for R^2 of the entire model for the right and left arms of 6 stroke patients.

3, ▶ for trials 4-7, and ▷ for trials 8-10). The shading in the symbols may be informative if patterns emerge, e.g., stiffness or damping properties change uniformly as the trials progress. Ideally, the symbols would lie in a small cluster to demonstrate the estimate is precise.

Although major-axis inertial properties for the hemiplegic left arms of patients 1-3 are arranged in clusters, the properties for their less-impaired right arms are more dispersed. To the contrary, the properties for both arms of patients 4-6 are clustered and the results for the less-impaired left arms are relatively close to the results for their hemiplegic right arms. With the exception of the last 3 trials testing the right arm of patient 6, the minor-axis inertial properties are also clustered and the results for both arms of each patient are close in proximity.

The major-axis damping parameters for patients with left hemiplegic arms are substantially different between the hemiplegic and less-impaired arms. The parameters for the hemiplegic arms are clustered and lie within the bounds calculated from [95] whereas the parameters for the less-impaired arms are dispersed over a wider range and are all greater than the upper bound from [95]. The major-axis damping parameters for both arms of the right hemiplegic patients lie almost entirely within the bound from [95], but the results for the patients' hemiplegic arms are less variable than the results for their less-impaired arms. In general, the minor-axis damping parameters for the patients' hemiplegic and less-impaired arms are clustered in close proximity. With the exception of the properties from 7 trials of patient 4's hemiplegic right arm and 3 trials of patient 6's hemiplegic right arm, the minor-axis damping parameters lie almost entirely within the bounds from [95].

The major and minor-axis stiffness properties for the left hemiplegic patients are clustered, but the variability between estimates present with their left hemiplegic arms is less than with their right less-impaired arms. Although the stiffness properties of both arms of the left hemiplegic patients lie near each other, the stiffness properties of the right arms of right hemiplegic patients are greater than the stiffness properties of their less-impaired arms with the exception of patient 6 (note overlap of left and right arm minor-axis stiffness properties).

Despite the known issues related to the plastic arm troughs and low force perturbation level, an attempt to correlate the changes in the impedance properties with the changes in the MAS ratings will be made. Although the MAS elbow extensor rating for patient 1 increased by 1, results from a linear regression of each of the six parameters shown in Figure 6.20 demonstrated that the slopes of the lines passing through the parameters were indistinguishable from a slope of zero. The dynamic stiffness properties of patient 2, who exhibited a MAS reduction of 1 in all three components of the MAS S/E score, are nearly constant over the 10 trials (p-values for hypothesis that the linear regression coefficients equal zero: 0.07 and 0.26 for the major and minor-axis inertia; 0.63 and 0.57 for damping; 0.25 and 0.41 for stiffness). The rating for the MAS shoulder internal rotator for patient 3 decreased by 1. Three of the six properties for patient 3 had

regression coefficients with $p < 0.05$: major-axis stiffness (0.005, slope of –4.45), minor-axis inertia (0.02, slope of +0.01), and minor-axis damping (0.02, slope of +0.66). Although the MAS shoulder internal rotator rating for patient 4 decreased by 1, the slopes of the linear regressions were all indistinguishable from zero. Although the minor-axis properties for the last three trials of patient 6's right arm are elevated compared to the results from the seven other trials, the MAS evaluations before and after the trials are identical. From this analysis, only the slope of –4.45 ($p = 0.005$) for the major-axis stiffness of patient 3 concurs with the decrease in the MAS Total evaluation.

6.6. Conclusions

Patients undergoing the PBPT protocol exhibited a sustained reduction in abnormal muscle tone, an unexpected benefit unrelated to learning. First, the ability of the new spectral estimation method to identify inertial and stiffness properties of mechanical system components was evaluated. Second, counter-intuitive results from an unimpaired subject study resulted from the method's sensitivity to how the subject or patient was attached to the end-effector of the robot. Specifically, the sensitivity was related to the material properties of the arm troughs that were used. Based on the test results, the spectral estimates for the carbon fiber arm trough trials were less affected by the counter-intuitive phase transition artifact than the plastic arm trough. However, the inertial, damping, and stiffness properties of the subjects were still similar to past results. The well-structured variation of the properties as the perturbation level increased could provide a means to assess to what extent results from trials using the plastic arm trough are affected by the artifact. Third, the results from a preliminary study of the hemiplegic and less-impaired arms of six chronic stroke patients whose arms were supported by plastic troughs were also shown to be comparable to past results.

Chapter 7

Conclusions and future work

7.1. Motor recovery is similar but not identical to motor learning

The performance-based progressive therapy (PBPT) algorithm and protocol were motivated by the working hypothesis that the processes that underlie motor recovery are similar to the processes that underlie motor learning. Although both motor learning and motor recovery exhibit activity-dependent plasticity (changes in synapses or growth of new synapses), several other factors are unique to motor recovery, e.g. re-acquisition of muscle strength, resolution of abnormal tone.

Clinical evidence presented in Chapter 4 supported the working hypothesis. Specifically, clinical evidence of impairment reductions demonstrated that the PBPT protocol enhanced the recovery of chronic stroke patients relative to two other groups of chronic stroke patients who participated in progressive resistance (PR) and sensorimotor (SM) therapy protocols. The SM protocol was intended to enhance the motor recovery of patients with a repetitive, goal-directed, robot-assisted task, whereas the PR protocol was intended to determine if addressing upper limb weakness with a strength-training exercise would enhance motor recovery of patients who could reach the 8 targets in the SM protocol unassisted. Though prior clinical results suggested that recovery would plateau 6 months post-stroke, chronic patients who were in a clinically verified "stable" phase of recovery prior to participating in the SM and PR therapy protocols achieved significant, though modest, reductions in impairment. The new PBPT protocol produced significantly larger impairment reductions with over 6,000 fewer movements than SM and PR. Although making repetitive goal-directed movements is beneficial, customizing the robot-assisted task to the patient's ability and keeping the patient actively involved

can result in larger reductions in impairment than delivering a larger number of fixed repetitive movements.

In addition to the clinical evidence that supported the working hypothesis in Chapter 4, robot-based evidence related to the time course of recovery was presented. By design, the adapting PBPT control system parameters, namely, the time allotted to move between targets and the virtual slot sidewall stiffness, serve as indicators of patients' abilities to move and aim (as parameters decrease (increase), patients move faster (slower) and require less (more) aiming assistance). By analyzing the parameters' evolution throughout the PBPT protocol, it was shown that motor recovery follows an exponential progression similar to a motor learning "law of practice".

Although the PBPT algorithm was based on methods that tend to enhance human motor learning (appropriate levels of task difficulty, practice scheduling and variability, positive reinforcement, etc.), chronic stroke patients participating in the PBPT protocol also exhibited a significant reduction in abnormal muscle tone. This reduction was quantified by the Modified Ashworth Scale (MAS) evaluations performed by clinicians before and after the PBPT protocol [54]. These evaluations revealed a portion of the reduction in abnormal muscle tone that clinicians observed during individual PBPT sessions was sustained over the 18-session therapy protocol. Schmit, et al. [88] reported that reductions in muscle tone occurred with passive movements of the hemiplegic elbow of stroke patients, but the beneficial effect was short-term and not sustained, unlike the effects of the PBPT protocol. Therefore, the PBPT protocol enhanced aspects of recovery that are both related and unrelated to motor learning. This suggests that the processes underlying motor recovery are more complex than the processes underlying motor learning.

7.2. Estimating mechanical impedance with back-drivable robots

Chapters 5 and 6 discussed the development and experimental validation of a spectral estimation method suitable for a clinical setting, namely, robot-assisted neuro-rehabilitation with MIT-MANUS or InMotion^2. Although the spectral estimation method works well with both force perturbations (admittance estimate) and displacement

perturbations (impedance estimate), force perturbations were used for several reasons. To take advantage of the desirable stability and performance characteristics of impedance control during robot-assisted therapy [41-43], MIT-MANUS was designed to be back-drivable [46]. Applications that require position control ordinarily use robots with high endpoint impedance (i.e., robots that are not back-drivable) and large interaction forces may occur. In general, the musculoskeletal system of a stroke patient is not as robust as the musculoskeletal system of an unimpaired subject. Therefore, it is desirable to limit the magnitude of the force that is delivered to the patient. For these reasons, a Proportional-Derivative position controller with relatively low gains was used to gently bring the arm of the patient to a test location and then force perturbations were superimposed on the command signal while the resulting displacements and interaction forces were recorded.

Since the human-machine interaction affects the forces delivered to the patient's arm, experimental and analytical compensation methods were devised to improve the quality of the spectral estimate. Tests conducted on a mechanical system composed of a variety of inertial and stiffness loads were used to validate the robot control system and the analysis programs. In addition to the trade-off between the variance of the spectral estimate and the spectral frequency resolution, an unimpaired subject study revealed the spectral estimate was sensitive to the type of arm trough that was used to support the subject's arm and attach the patient's arm to the robot. Specifically, impedance properties from tests using a carbon fiber arm trough were less variable than tests using a plastic arm trough. By carefully selecting the spectral analysis parameters and the hardware that is used to attach the patient's arm to the robot end-effector, a mechanical impedance spectral estimation method suitable for a clinical setting was developed.

7.3. Suggestions for future work

This research has demonstrated that the PBPT protocol, which was designed using methods that tend to enhance motor learning (appropriate levels of task difficulty, practice scheduling and variability, positive reinforcement, etc.), enhanced the motor recovery of chronic stroke patients via reductions in motor impairment and abnormal muscle tone. These results are encouraging, especially because the algorithm was

intended to be a proof of concept and was not optimized. The evolution of the time allotted for movement and sidewall stiffness can provide an empirical model of patients' recovery of their abilities to move and aim. The empirical model could then guide the development of a mathematical model of motor recovery similar to mathematical models of motor learning (e.g., self-organization/dynamic patterns theory [52] and neural network models of learning that utilize forward/inverse models [48,104]). After incorporating this model of recovery into the patient arm model, the algorithm could be optimized to increase the rate and/or extent of motor recovery.

Although the performance measures defined in this thesis were specific to planar robotic therapy of the shoulder and elbow, the PBPT algorithm could be generalized by defining similar performance measures for robotic therapy involving other limbs/muscle groups (e.g., wrist, ankle, gait). In addition, the performance-based progressive algorithm could be used to train unimpaired subjects in virtual and haptic environments. Since it was motivated by methods that tend to enhance motor learning and it has been shown to enhance motor recovery, it should also enhance motor learning. For example, surgeons learning to perform operations on haptic/robotic simulators could be provided a variable amount of assistance to complete a procedure, eventually achieving satisfactory performance without any assistance.

Having identified the engineering obstacles of the spectral estimation method of arm mechanical impedance (material properties of the arm trough and spectral analysis parameters), experimental trials can be conducted with another group of patients participating in the PBPT protocol to determine whether the spectral estimate can discriminate a reduction in tone (correlating to the MAS clinical evaluations). Similar to the PBPT protocol, the spectral estimation method could also be extended to the other back-drivable robots used by our research group for stroke rehabilitation. For example, the impedance of the wrist along the abduction/adduction and flexion/extension axes could be estimated by scaling the random force perturbations appropriately and delivering them via the wrist robot while keeping the pronation/supination axis fixed at a desired location. Alternatively, three random inputs with low coherence could be defined to excite the pronation/supination, abduction/adduction, and flexion/extension axes of the

wrist simultaneously. However, unless the transmission was assumed ideal, an additional sensor would be needed to measure the forces (torques) delivered to the wrist of the subject or patient.

Appendix A

Fugl-Meyer assessment of motor function – upper extremity

In 1975, Fugl-Meyer et al. [33] developed "a system for evaluation of motor function, balance, some sensation qualities, and joint function in hemiplegic patients." Although the clinical system includes evaluations of the upper extremity, lower extremity, sensation (touch/position), and passive joint motion/pain, this appendix will concentrate on the upper extremity components because the robotic therapy was designed to rehabilitate the shoulder and elbow muscles using a goal-directed task that consisted of gravity-eliminated, point-to-point movements. Tables A.1-A.4 include the categories, components, and descriptions of scoring for the four portions of what is now commonly known as the Fugl-Meyer Upper Extremity (F-M UE) evaluation. In particular,

A. Shoulder, elbow, and forearm (18 evaluations on an ordinal scale of 0, 1, and 2; maximum score of 36)
B. Wrist (5 evaluations on an ordinal scale of 0, 1, and 2; maximum score of 10)
C. Hand (7 evaluations on an ordinal scale of 0, 1, and 2; maximum score of 14)
D. Coordination and speed (3 evaluations on an ordinal scale of 0, 1, and 2; maximum score of 6)

The F-M UE overall score is the sum of the scores for sections A-D (maximum score of 66).

Fugl-Meyer assessment of motor function – Upper Extremity A. Shoulder, elbow, and forearm (maximum score of 36)		
Category	**Component**	**Description of scoring**
1. Reflexes	Biceps or finger flexors	0 – no reflex elicited 2 – reflex elicited
	Triceps	
2. Flexor synergy (forearm supinated, bring affected arm to ipsilateral ear)	Retraction	0 – cannot perform at all 1 – performed partly 2 – performed faultlessly
	Elevation	
	Abduction ≥ 90°	
	External rotation	
	Elbow flexion	
	Forearm supination	
3. Extensor synergy (forearm pronated and hand to contralateral knee)	Adduction and internal rotation	0 – cannot perform at all 1 – performed partly 2 – performed faultlessly
	Elbow extension	
	Forearm pronation	
4. Mixed synergy patterns	Hand to lumbar spine	0 – synergy components begin with the onset of movement 1 – synergy components begin later in movement 2 – no synergy components
	Shoulder flexion to 90°, elbow at 0°, forearm neutral	
	Forearm pronation – supination, shoulder at 0°, elbow flexed at 90°	
5. Isolated movements without synergy	Shoulder abduction to 90°, elbow at 0°, forearm pronated	0 – synergy components begin with the onset of movement 1 – synergy components begin later in movement 2 – no synergy components
	Shoulder flexion 90°-180°, elbow at 0°, forearm neutral	
	Forearm pronation – supination, shoulder flexion between 30°-90°, elbow at 0°	0 – cannot perform at all 1 – performed partly 2 – performed faultlessly
6. If all 3 components in category 5 received 2/2, evaluate normal reflex activity	Biceps, finger flexors, triceps	0 – two-thirds of reflexes are markedly hyperactive 1 – 1 reflex is hyperactive or 2 are lively 2 – no more than 1 reflex is lively, none are hyperactive

Table A.1. Category, component, and description of scoring for shoulder, elbow, and forearm F-M UE evaluations.

Fugl-Meyer assessment of motor function – Upper Extremity B. Wrist, all tests with forearm pronated (maximum score of 10)		
Category	**Component**	**Description of scoring**
1. Wrist flexion/ extension	Elbow at 90°, shoulder at 0°	0 – no volitional movement 1 – wrist flexion/extension through partial range 2 – controlled movement through full range
	Elbow and shoulder at 0°	
2. Wrist stability	Elbow at 90°, shoulder at 0°	0 – unable to extend wrist 15° 1 – wrist extension to 15°, unable to take resistance 2 – able to maintain wrist extension to 15° against minimal resistance
	Elbow and shoulder at 0°	
3. Wrist circumduction	Elbow at 90°, shoulder at 0° **or** elbow and shoulder at 0°	0 – unable to perform 1 – incomplete or uncontrolled motion 2 – complete, controlled motion

Table A.2. Category, component, and description of scoring for wrist F-M UE evaluations.

Fugl-Meyer assessment of motor function – Upper Extremity C. Hand (maximum score of 14)		
Category	**Component**	**Description of scoring**
1. Fingers	Mass flexion	0 – cannot perform 1 – performs partly 2 – performs flawlessly
	Mass extension	
2. Proximal interphalangeal (PIP) – distal interphalangeal (DIP) hook grasp	Metacarpophalangeal joints are extended, PIP and DIP joints are flexed	0 – unable 1 – performed weakly without resistance 2 – performed with great resistance
3. Object grasping	Thumb adduction with paper, all other joints at 0°	0 – unable to perform 1 – able to hold with slight tug 2 – hold firmly with tug
	Pincer grasp with pencil	
	Cylinder grasp with can	
	Spherical grasp with tennis ball	

Table A.3. Category, component, and description of scoring for hand F-M UE evaluations.

Fugl-Meyer assessment of motor function – Upper Extremity D. Coordination and speed (maximum score of 6)		
Category	**Component**	**Description of scoring**
1. Coordination – finger to nose 5 times with eyes closed	Tremor Dysmetria	0 – marked tremor or dysmetria 1 – slight tremor or dysmetria 2 – no tremor or dysmetria
2. Speed – finger to nose 5 times with eyes closed	Time	0 – more than 6 seconds difference between hands 1 – 2 to 5 seconds difference between hands 2 – less than 2 seconds difference between hands

Table A.4. Category, component, and description of scoring for coordination and speed F-M UE evaluations.

Appendix B

Clinical characteristics of stroke patients participating in the performance-based progressive, sensorimotor, and progressive resistance therapy protocols

The clinical characteristics of the stroke patients who participated in the Performance-Based Progressive Therapy (PBPT) protocol at the Burke Rehabilitation Hospital (BRH) in White Plains, NY, and in the Progressive Resistance (PR) and Sensorimotor (SM) therapy protocols at Spaulding Rehabilitation Hospital (SRH) in Boston, MA are given in Table B.1. The effectiveness of the therapy protocols was evaluated using the Fugl-Meyer Upper Extremity (F-M UE, see Appendix A) clinical scores of groups of patients. The clinical outcome of the protocols could only be compared with moderate-to-severe patient groups (F-M UE$\geq$14) since no patients participating in the PR and SM protocols had FM UE $<$ 14. Table B.2 revealed that there were no significant differences in the FM UE scores for patients treated at BRH and SRH. Table B.3 revealed that the outcomes of the PR and SM protocols were similar, but the PBPT protocol resulted in a significantly larger decrease in motor impairments. A subgroup of SM patients (SM3) was unable to reach all eight targets at the end of treatment. Table B.4 investigates the between-protocol differences when the SM3 patients are excluded from the SM group. Table B.5 revealed that the outcomes of the PR and SM (minus SM3) protocols were similar, but the PBPT protocol still resulted in a significantly larger decrease in motor impairments.

Characteristics	Burke PBPT			Spaulding PR & SM		
Age (y)	64.2±2.0			57.5±1.9		
Gender	16 M	20 F		33 M	15 F	
Incidence of stroke to initial evaluation (d)	1296±140			830±62		
Disabled limb	17 L	19 R		29 L	19 R	
Type of stroke: hemorrhagic | ischemic | unknown	6	24	6	5	32	11
Subcortex alone	7			13		
Cortex alone	1			4		
Subcortex and cortex	22			20		
Unknown location	6			11		

Table B.1. Clinical characteristics of outpatients who participated in the Performance-Based Progressive Therapy (PBPT) protocol at the Burke Rehabilitation Hospital, and in the Progressive Resistance (PR) and Sensorimotor (SM) protocols at the Spaulding Rehabilitation Hospital.

Patient group	Fugl-Meyer Upper Extremity: F-M UE (max 66)	
	Burke PBPT protocol	Spaulding PR & SM protocols
Very severe (F-M UE < 14)	8.59±0.58 (n=21)	N/A (n=0)
Moderate-to-severe (F-M UE ≥ 14)	26.86±2.51 (n=15)	27.37±1.48 (n=47)

Table B.2. Fugl-Meyer Upper Extremity clinical evaluations at admission (mean of 3 to verify stable phase of motor impairment) grouped by rehabilitation hospital.

Moderate-to-severe patient group – Fugl-Meyer Upper Extremity (max 66) ≥ 14		
Therapy protocol	Number of subjects	Change in F-M UE from admission to discharge
PBPT	15	7.28±1.29
PR	15	4.53±0.81
SM	32	3.42±0.62
ANOVA *p*-value comparison of protocols	**PBPT** vs PR	**0.04***
	PBPT vs SM	**0.02***
	PR vs SM	0.34

Table B.3. Comparison of the impairment reductions exhibited by moderate-to-severe stroke patients participating in the PBPT, PR, and SM protocols.

Moderate-to-severe patient group – Fugl-Meyer Upper Extremity (max 66) ≥ 14				
Protocol	PBPT	PR	SM (SM1, SM2)	SM3
F-M UE at admission	26.86±2.51 (n=15)	33.13±2.51 (n=15)	31.45±3.01 (n=14)	19.91±0.66 (n=18)
ANOVA *p*-value comparison of protocols	PBPT vs PR		0.038*	
	PBPT vs SM		0.113	
	PBPT vs SM3		0.080	
	PR vs SM		0.634	
	PR vs SM3		<0.001*	
	SM vs SM3		0.001*	

Table B.4. Fugl-Meyer Upper Extremity clinical evaluations at admission (mean of 3 to verify stable phase of motor impairment) grouped by protocol while excluding SM3 patients (who were unable to reach all eight targets).

Moderate-to-severe patient group – Fugl-Meyer Upper Extremity (max 66) ≥ 14		
Therapy protocol	Number of subjects	Change in F-M UE from admission to discharge
PBPT	15	7.28±1.29
PR	15	4.53±0.81
SM	14	4.48±0.91
ANOVA *p*-value comparison of protocols	**PBPT** vs PR	**0.047***
	PBPT vs SM	**0.046***
	PR vs SM	0.967

Table B.5. Comparison of the impairment reductions exhibited by moderate-to-severe stroke patients participating in the PBPT, PR, and SM protocols while excluding SM3 patients.

Appendix C

Evolution of controller parameters during the performance-based progressive therapy protocol

In Figure C.1, the results of the least-squares regression problems formulated with data from all patients in the very severe and moderate-to-severe groups (as opposed to the mean) are depicted by dashed lines and the 95% confidence intervals of the prediction by dash-dotted lines. The individual patients' trial data are depicted by dots and session data by solid lines. The optimum multiplier and exponent values for the cases shown in Figure C.1 are given in Table C.1. The optimum multiplier and exponent values for the within-session cases shown in Figure 4.5 are given in Table C.2. Each patient's trial data (dots and solid lines) are also depicted with the least-squares regression lines (dashed) and 95% confidence intervals of the prediction (dash-dotted lines) of the mean value of the group in Figures C.2 through C.21 (10 very severe patients followed by 10 moderate-to-severe patients). The time allotted for movement is shown in the top row of graphs, whereas the sidewall stiffness is shown in the bottom. The results are plotted on linearly (left column) and logarithmically (right column) scaled graphs.

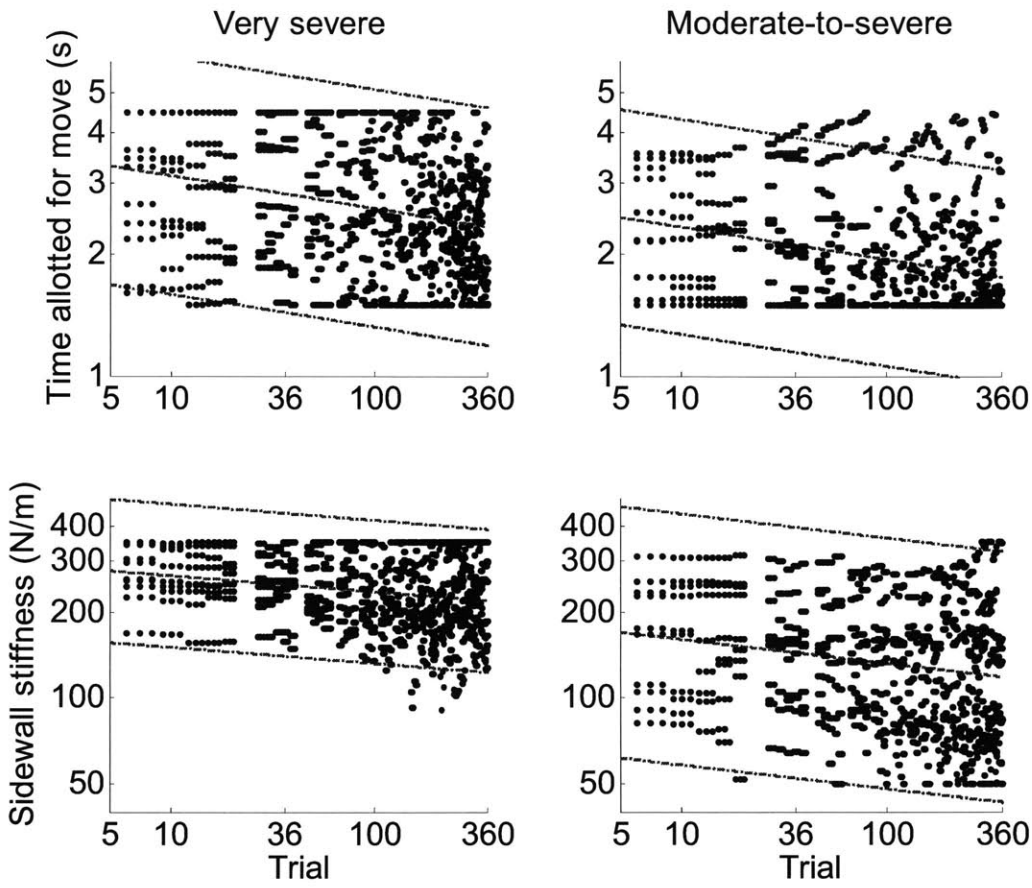

Figure C.1. Evolution of ALL values of the control parameters specified by the performance-based progressive algorithm, namely, time allotted for movement (t_m) and sidewall stiffness (k_{sw}), for groups of 10 very severe patients and 10 moderate-to-severe patients.

	Group	Multiplier	Multiplier 95%CI	Exponent	Exponent 95%CI	R^2	F	p
t_m	Very severe	3.76	4.06 3.50	-0.081	-0.066 -0.096	0.05	113.8	<0.0001
	Moderate-to-severe	2.80	3.00 2.62	-0.079	-0.066 -0.093	0.04	133.4	<0.0001
k_{sw}	Very severe	304.7	324.6 285.9	-0.056	-0.044 -0.069	0.02	76.48	<0.0001
	Moderate-to-severe	194.3	217.3 173.8	-0.084	-0.062 -0.106	0.01	54.86	<0.0001

Table C.1. Least-squares regression results from ALL values of controller parameters specified by the performance-based progressive algorithm for the very severe and moderate-to-severe patient groups.

	Group	Multiplier	Multiplier 95%CI	Exponent	Exponent 95%CI	R^2	F	p
t_m	Very severe	2.76	3.03 2.52	-0.035	0.002 -0.072	<0.01	3.5	0.061
	Moderate-to-severe	2.15	2.34 1.98	-0.050	-0.017 -0.084	<0.01	8.8	0.003
k_{sw}	Very severe	238.2	257.8 220.2	-0.013	0.018 -0.044	<0.01	0.7	0.42
	Moderate-to-severe	157.7	180.9 137.4	-0.082	-0.028 -0.137	<0.01	8.8	0.003

Table C.2. Least-squares regression results from ALL values of the PBPT controller parameters over trials 6-20 for the very severe and moderate-to-severe patient groups.

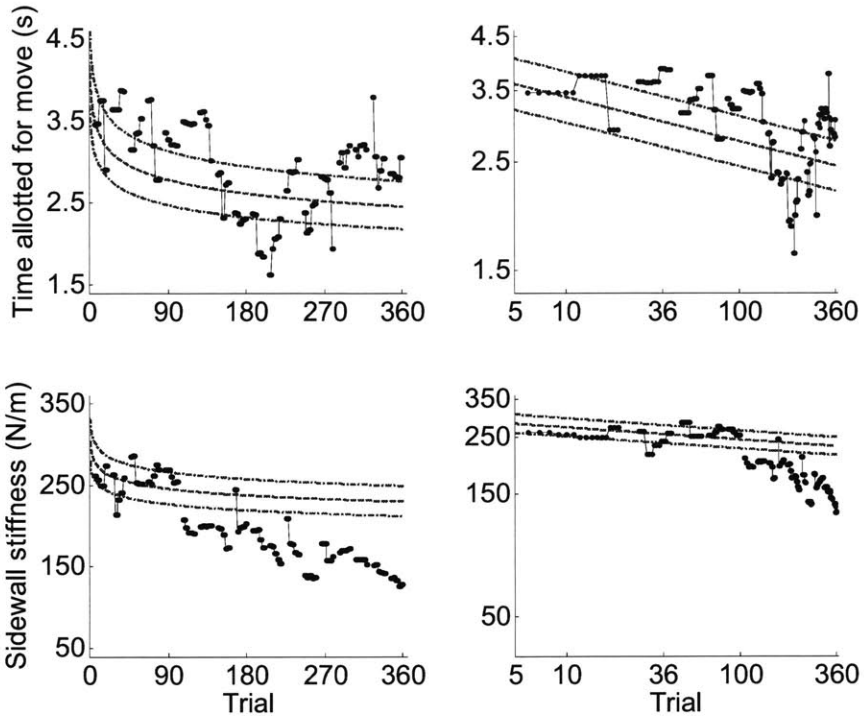

Figure C.2. Evolution of controller parameters during the PBPT protocol for patient 01 in the very severe patient group.

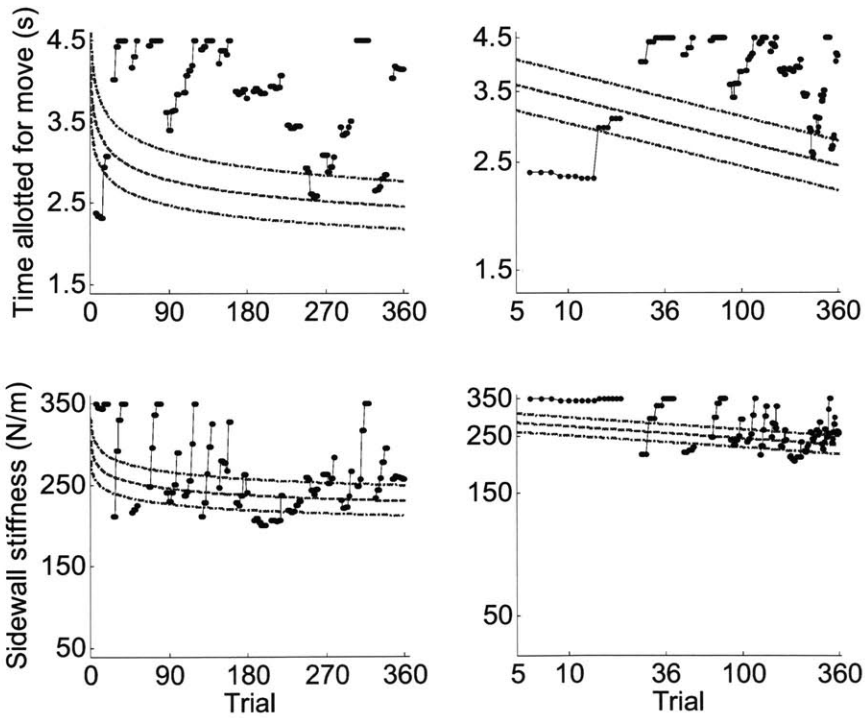

Figure C.3. Evolution of controller parameters during the PBPT protocol for patient 02 in the very severe patient group.

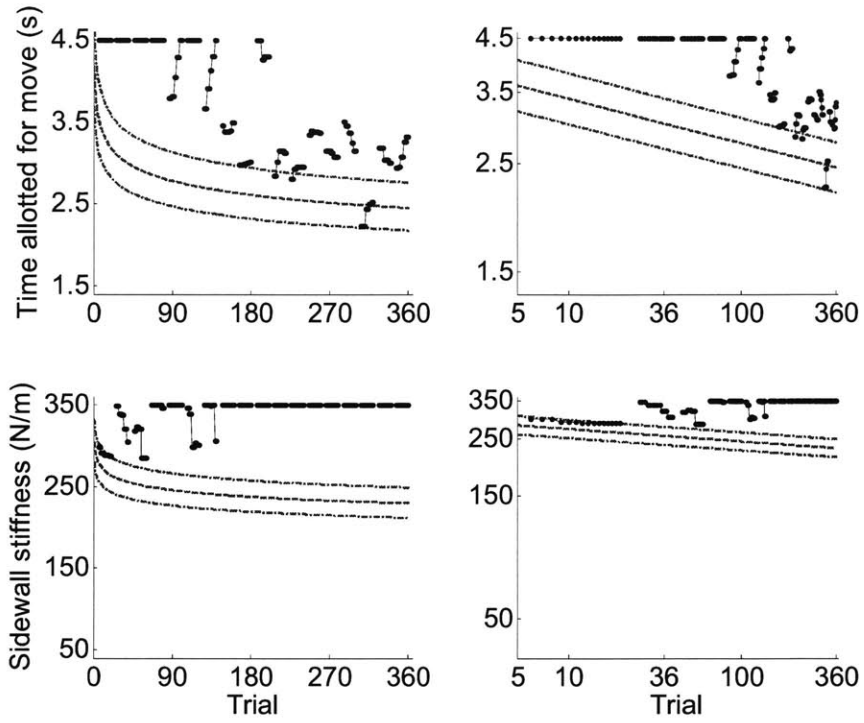

Figure C.4. Evolution of controller parameters during the PBPT protocol for patient 03 in the very severe patient group.

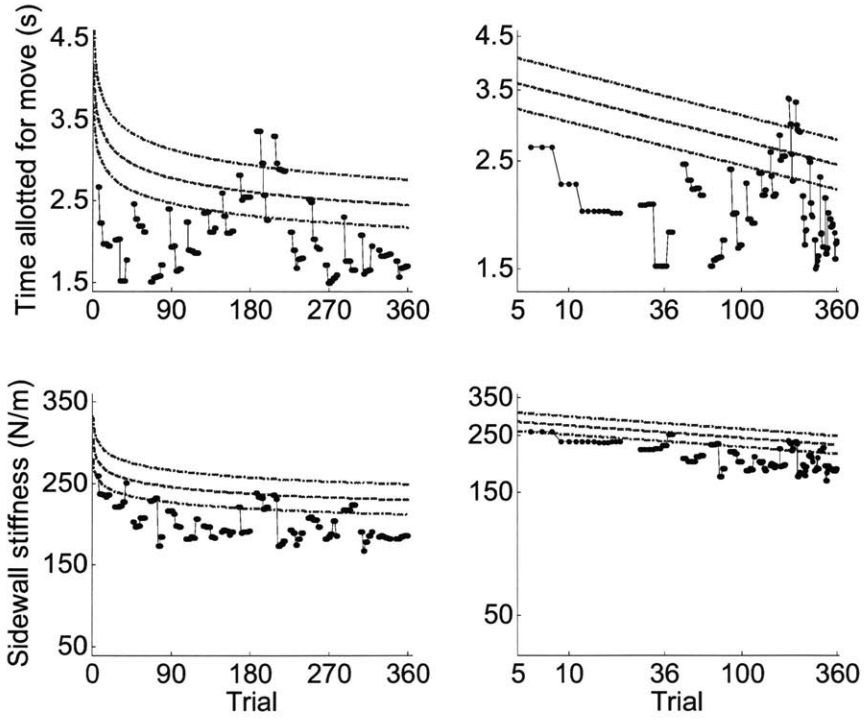

Figure C.5. Evolution of controller parameters during the PBPT protocol for patient 04 in the very severe patient group.

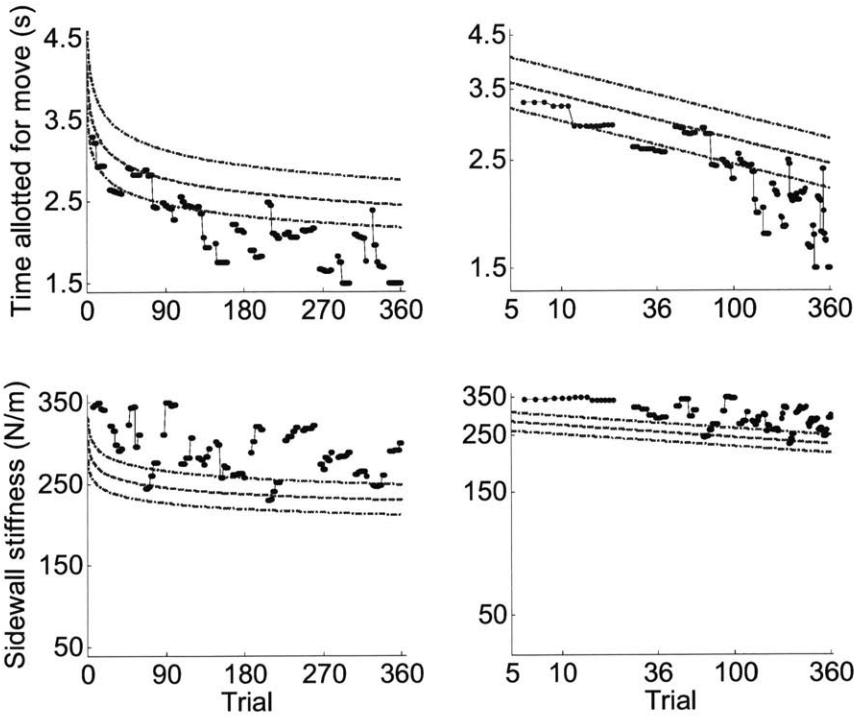

Figure C.6. Evolution of controller parameters during the PBPT protocol for patient 05 in the very severe patient group.

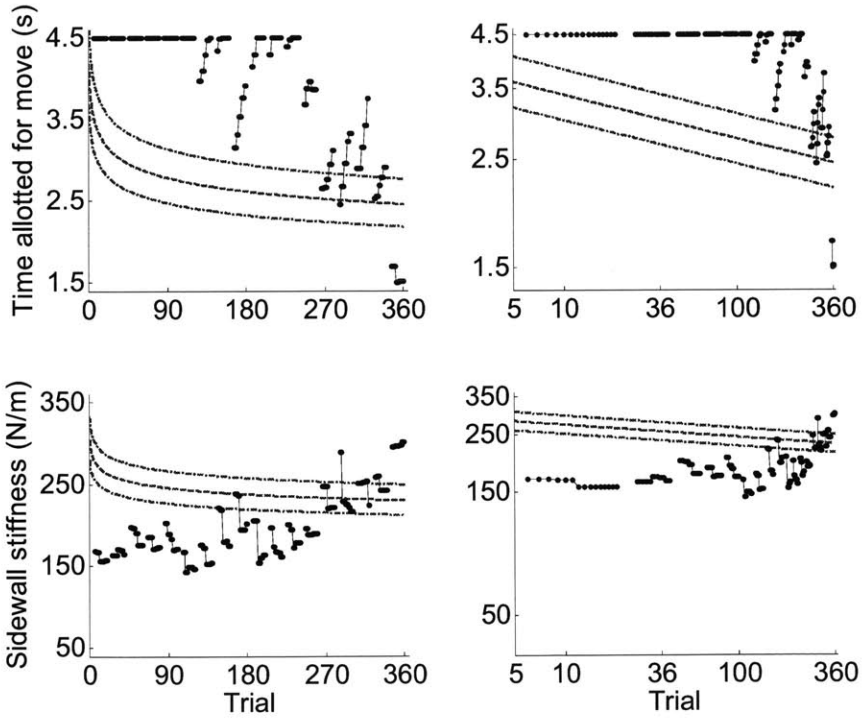

Figure C.7. Evolution of controller parameters during the PBPT protocol for patient 06 in the very severe patient group.

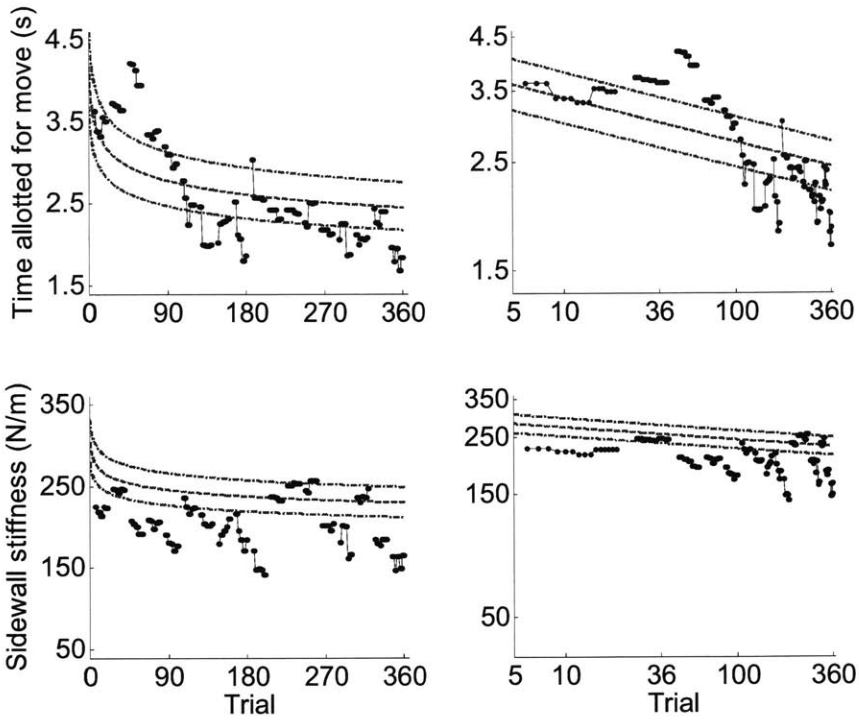

Figure C.8. Evolution of controller parameters during the PBPT protocol for patient 07 in the very severe patient group.

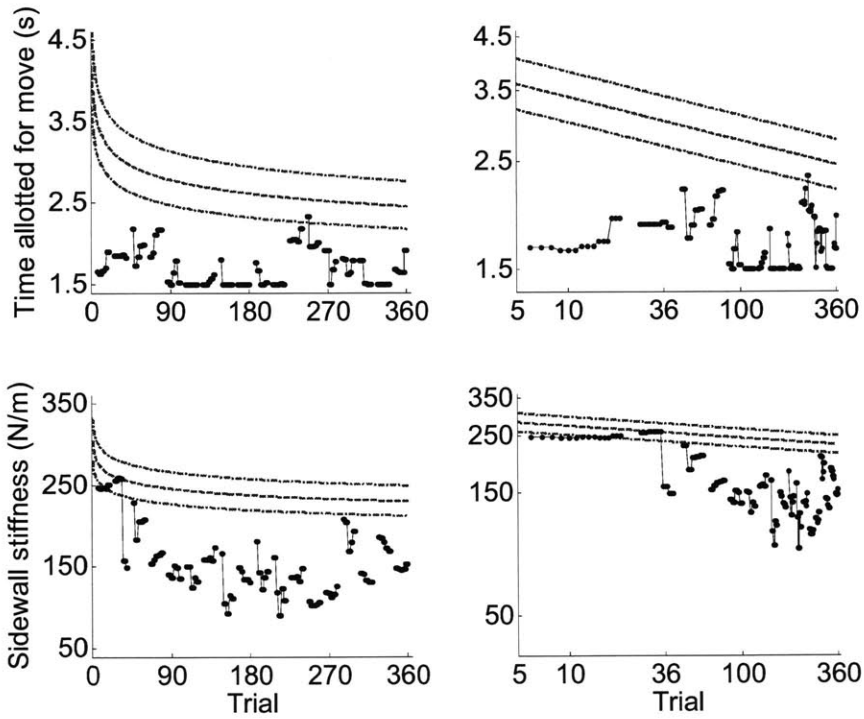

Figure C.9. Evolution of controller parameters during the PBPT protocol for patient 08 in the very severe patient group.

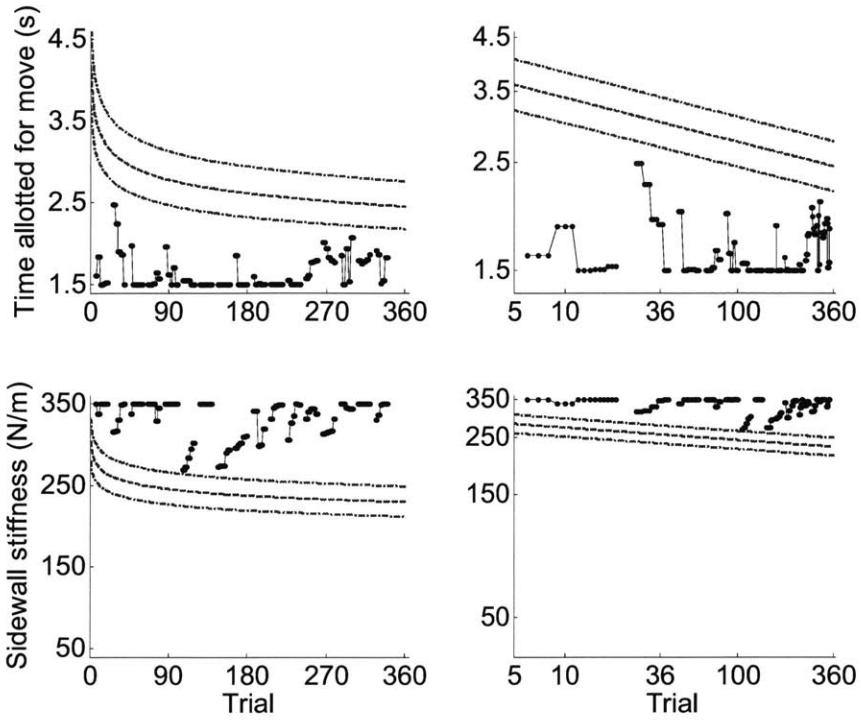

Figure C.10. Evolution of controller parameters during the PBPT protocol for patient 09 in the very severe patient group.

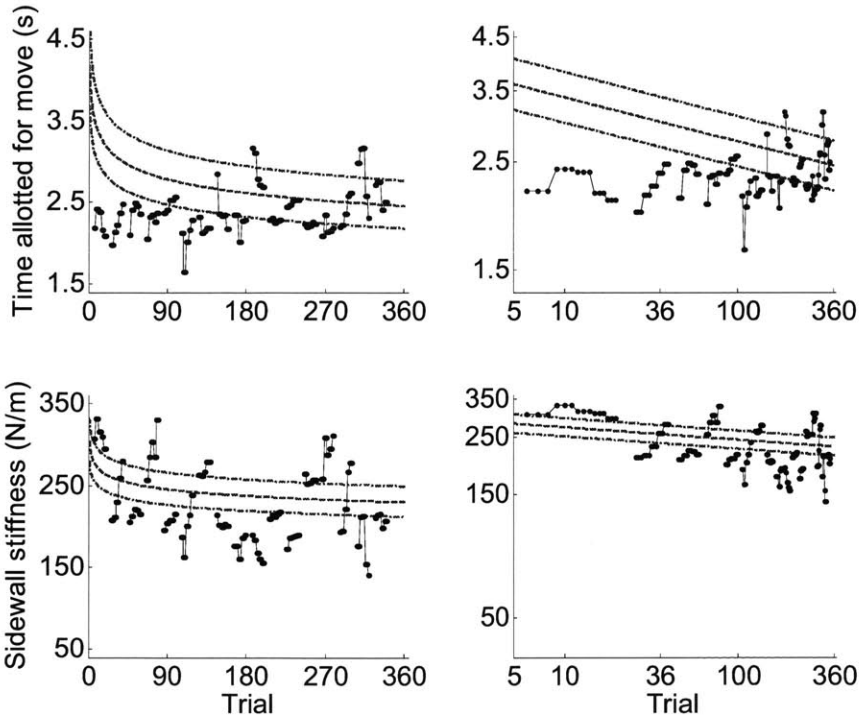

Figure C.11. Evolution of controller parameters during the PBPT protocol for patient 10 in the very severe patient group.

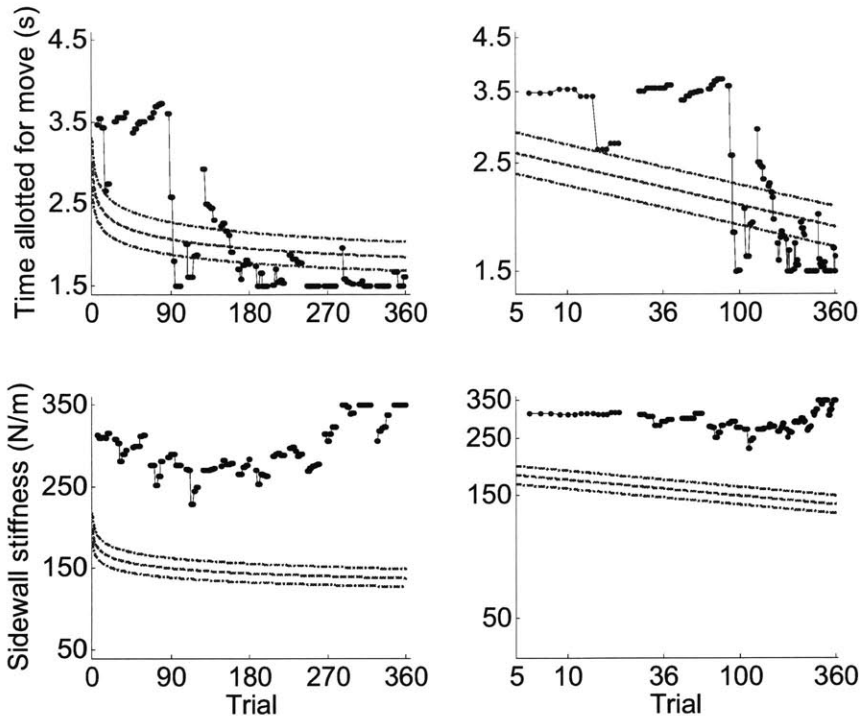

Figure C.12. Evolution of controller parameters during the PBPT protocol for patient 01 in the moderate-to-severe patient group.

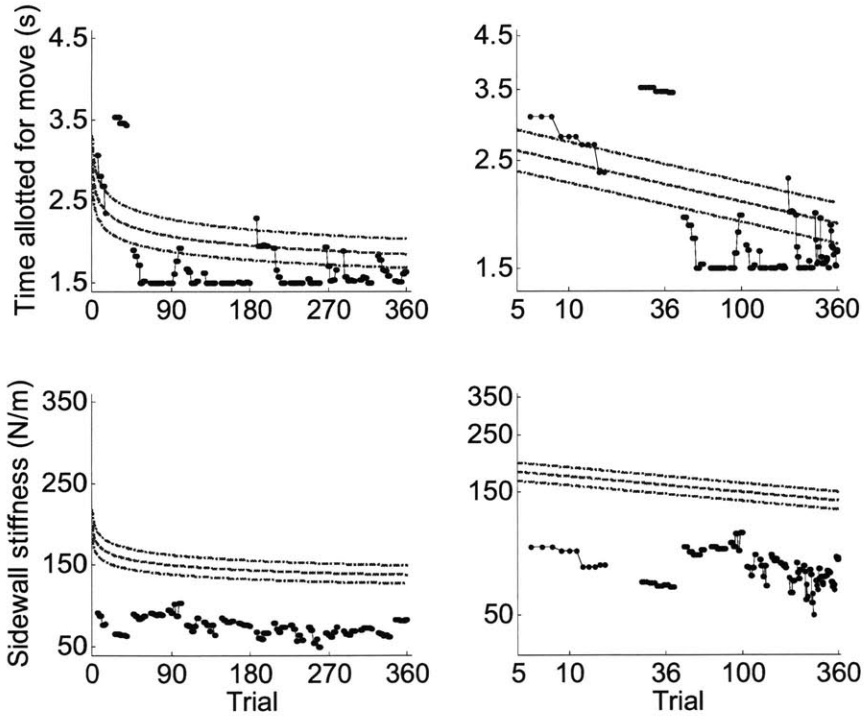

Figure C.13. Evolution of controller parameters during the PBPT protocol for patient 02 in the moderate-to-severe patient group.

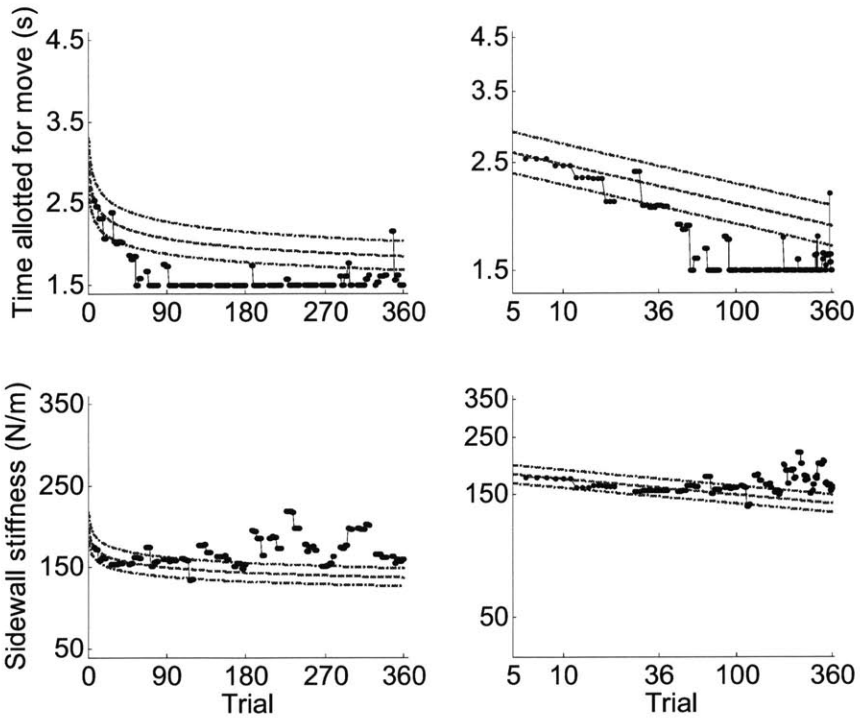

Figure C.14. Evolution of controller parameters during the PBPT protocol for patient 03 in the moderate-to-severe patient group.

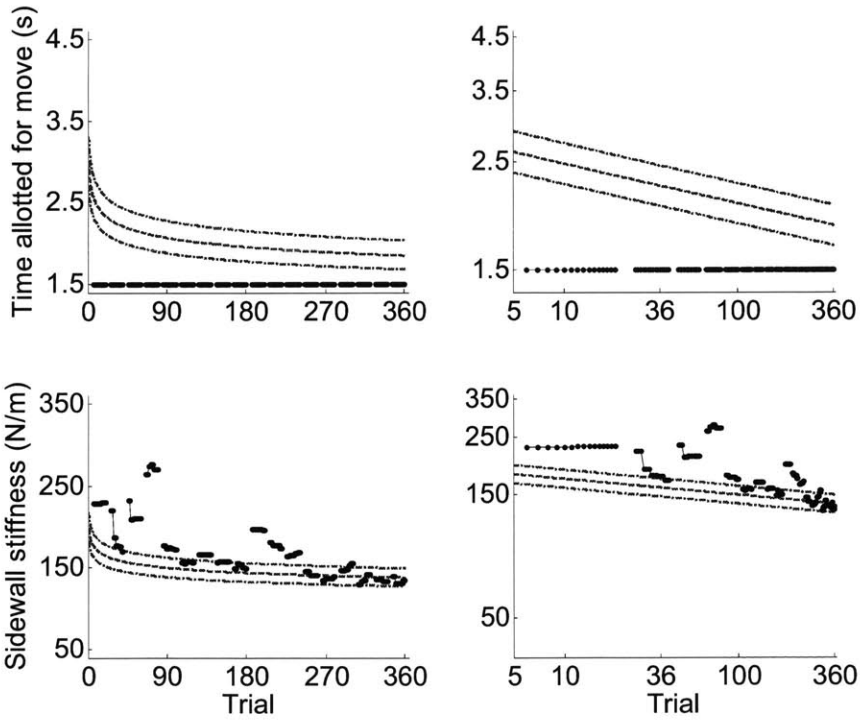

Figure C.15. Evolution of controller parameters during the PBPT protocol for patient 04 in the moderate-to-severe patient group.

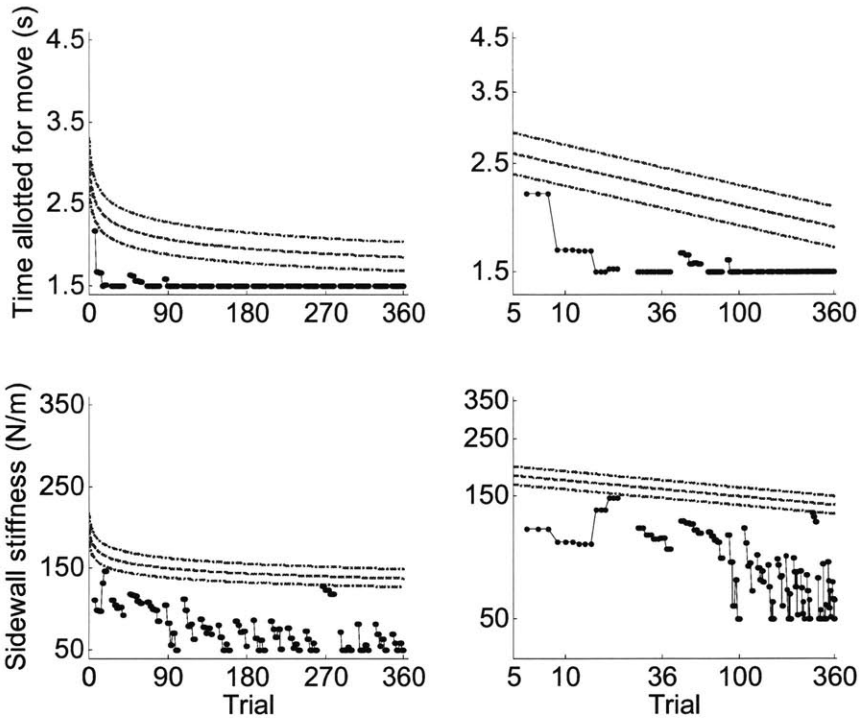

Figure C.16. Evolution of controller parameters during the PBPT protocol for patient 05 in the moderate-to-severe patient group.

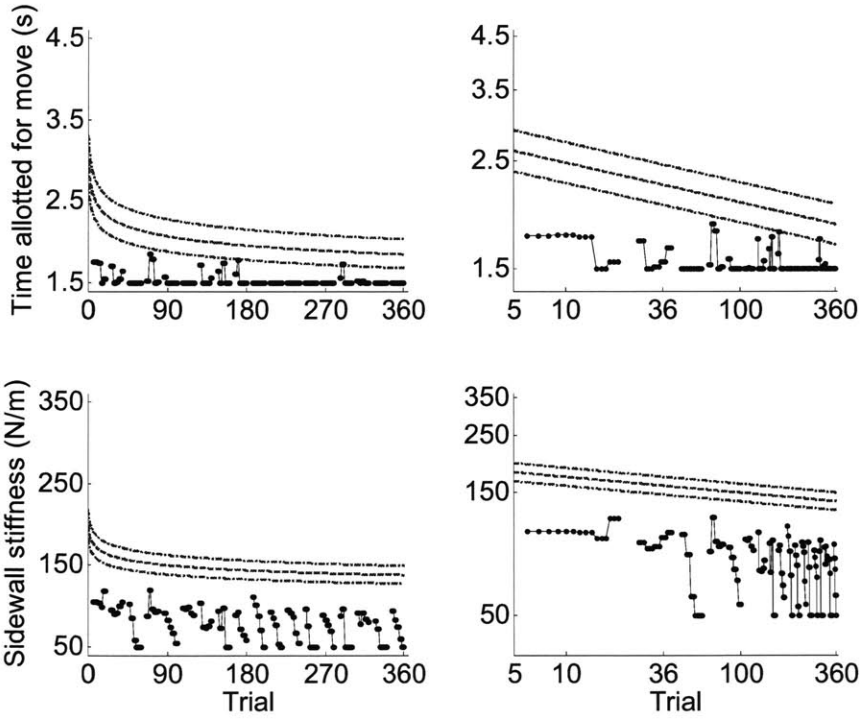

Figure C.17. Evolution of controller parameters during the PBPT protocol for patient 06 in the moderate-to-severe patient group.

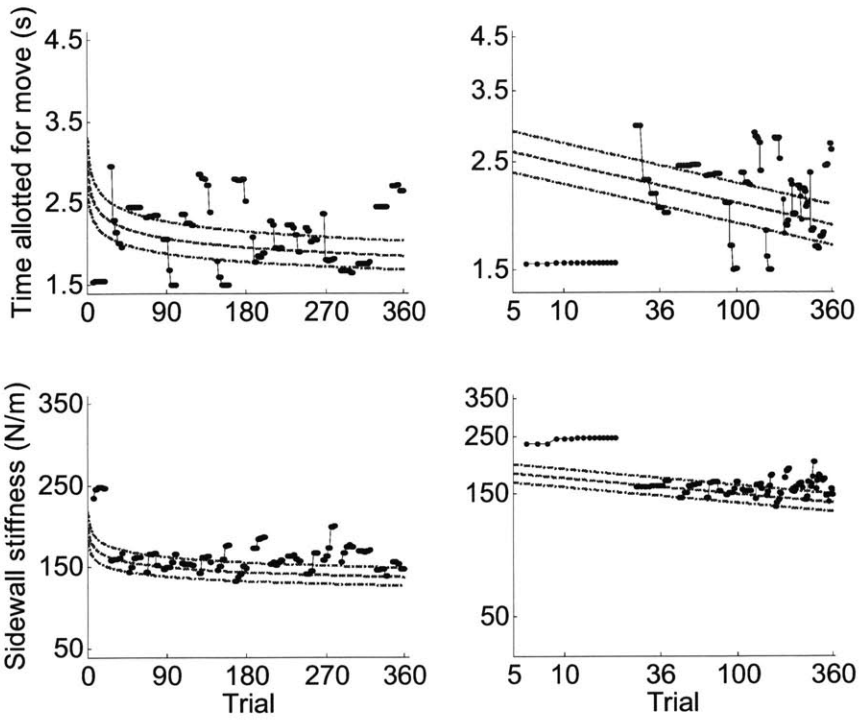

Figure C.18. Evolution of controller parameters during the PBPT protocol for patient 07 in the moderate-to-severe patient group.

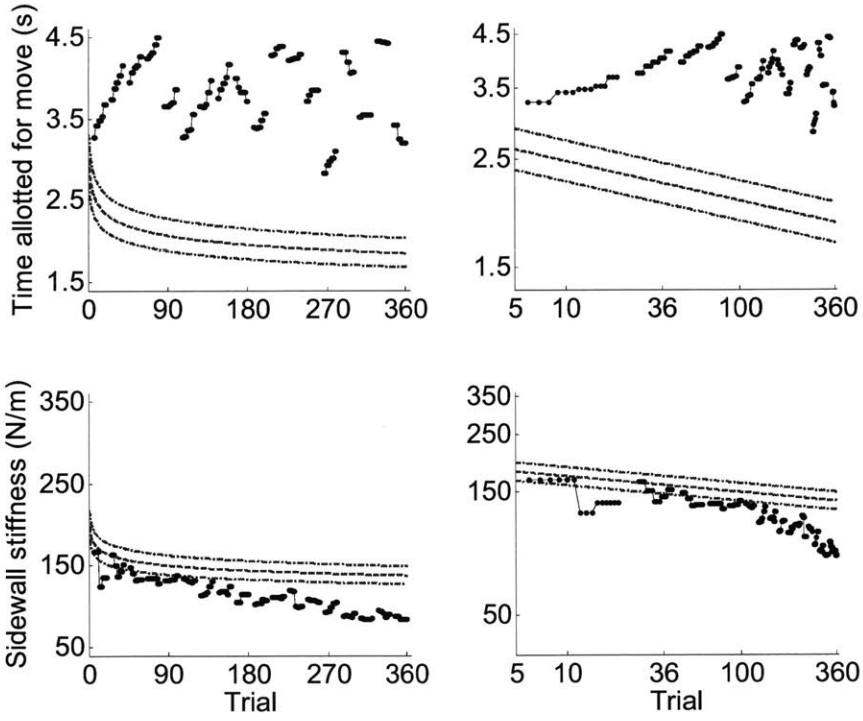

Figure C.19. Evolution of controller parameters during the PBPT protocol for patient 08 in the moderate-to-severe patient group.

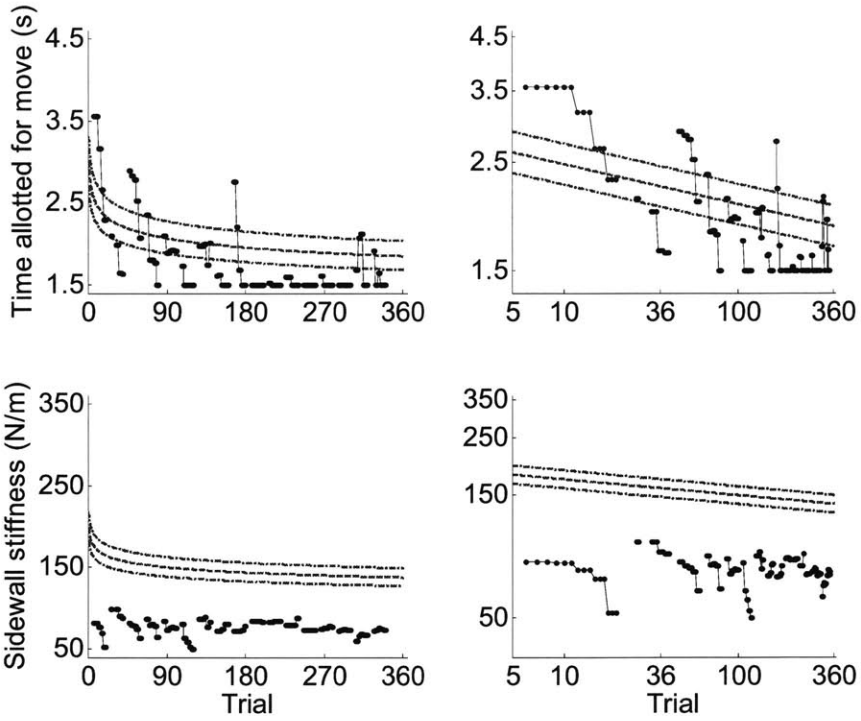

Figure C.20. Evolution of controller parameters during the PBPT protocol for patient 09 in the moderate-to-severe patient group.

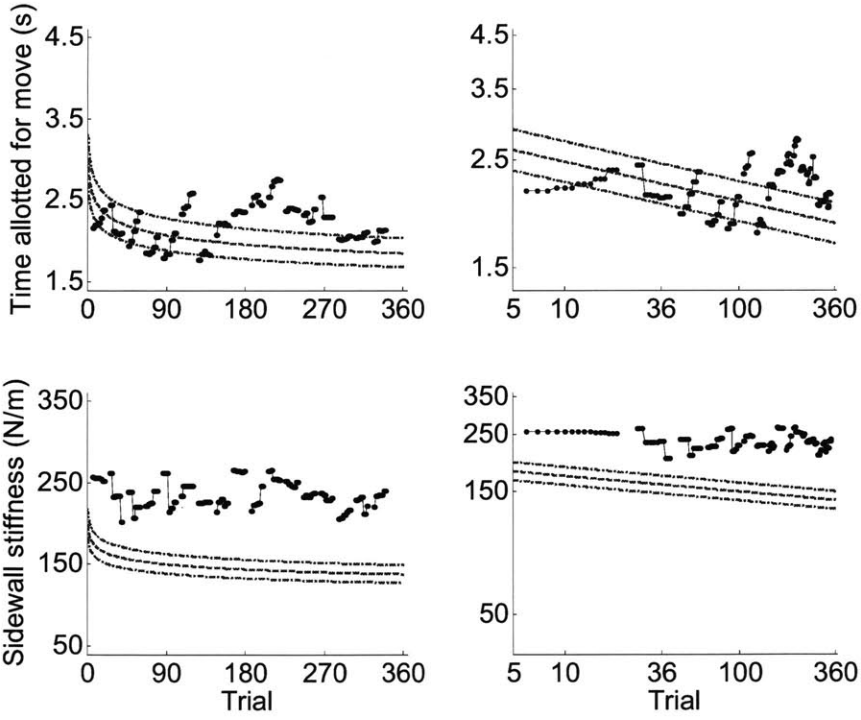

Figure C.21. Evolution of controller parameters during the PBPT protocol for patient 10 in the moderate-to-severe patient group.

Appendix D

Linearized model of human-machine interaction

The nonlinear equations of motion for the robot are

$$\begin{bmatrix} H_{11}\ddot{\theta}_s + H_{12}\cos(\theta_e - \theta_s)\ddot{\theta}_s - H_{12}\sin(\theta_e - \theta_s)\dot{\theta}_e^2 + b_s\dot{\theta}_s \\ H_{12}\cos(\theta_e - \theta_s)\ddot{\theta}_s + H_{22}\ddot{\theta}_e - H_{12}\sin(\theta_e - \theta_s)\dot{\theta}_s^2 + b_e\dot{\theta}_e \end{bmatrix} = \begin{bmatrix} \tau_{c,s} + \tau_{i,s} \\ \tau_{c,e} + \tau_{i,e} \end{bmatrix} \tag{D.1}$$

where (θ_s, θ_e) are the absolute angular displacements of the robot's shoulder and elbow joints, H_{ij} with $i, j \in 1, 2$ are the inertial characteristics of the robot arms, b_s and b_e are the viscous damping coefficients for the shoulder and elbow joints, $(\tau_{c,s}, \tau_{c,e})$ are the commanded shoulder and elbow torques, and $(\tau_{i,s}, \tau_{i,e})$ are torques equivalent to the human-machine interaction forces. The command torques, $\boldsymbol{\tau}_c = [\tau_{c,s}, \tau_{c,e}]^T$, are related to the command forces in (5.13), $\mathbf{F}_c = [F_{c,x}, F_{c,y}]^T$, by

$$\boldsymbol{\tau}_c = \mathbf{J}^T\mathbf{F}_c \tag{D.2}$$

and the interaction torques, $\boldsymbol{\tau}_i = [\tau_{i,s}, \tau_{i,e}]^T$, are related to the interaction forces, $\mathbf{F}_i = [F_{i,x}, F_{i,y}]^T$, in a similar manner,

$$\boldsymbol{\tau}_i = -\mathbf{J}^T\mathbf{F}_i \tag{D.3}$$

where $\mathbf{J} = \begin{bmatrix} -l_s\sin(\theta_s) & -l_e\sin(\theta_e) \\ l_s\cos(\theta_s) & l_e\cos(\theta_e) \end{bmatrix}$ is the Jacobian matrix relating absolute joint speeds to the endpoint velocity, l_s is the length of the link from the robot's shoulder joint to elbow joint, l_e is the length of the link from the robot's elbow joint to the manipulandum,

and the negative sign reflects the force the human exerts on the robot is equal and opposite to the force the robot exerts on the human.

The arm dynamics were simply modeled as a linear system because this information was readily available from the time-domain, least-squares estimate. Specifically,

$$\begin{bmatrix} m_{11} & m_{12} \\ m_{21} & m_{22} \end{bmatrix}\begin{bmatrix} \ddot{x}_a \\ \ddot{y}_a \end{bmatrix}+\begin{bmatrix} b_{11} & b_{12} \\ b_{21} & b_{22} \end{bmatrix}\begin{bmatrix} \dot{x}_a \\ \dot{y}_a \end{bmatrix}+\begin{bmatrix} k_{11} & k_{12} \\ k_{21} & k_{22} \end{bmatrix}\begin{bmatrix} x_a \\ y_a \end{bmatrix}=\begin{bmatrix} F_{i,x} \\ F_{i,y} \end{bmatrix} \tag{D.4}$$

where (x_a, y_a) is the location of the subject's hand and the port of human-machine interaction was modeled as an ideal virtual force transducer, namely,

$$\begin{bmatrix} F_{i,x} \\ F_{i,y} \end{bmatrix}=\begin{bmatrix} k_f & 0 \\ 0 & k_f \end{bmatrix}\begin{bmatrix} x_r - x_a \\ y_r - y_a \end{bmatrix} \tag{D.5}$$

where $x_r = l_s\cos(\theta_s)+l_e\cos(\theta_e)$ and $y_r = l_s\sin(\theta_s)+l_e\sin(\theta_e)$ are the x- and y-coordinates of the robot manipulandum, and k_f is the force transducer stiffness.

The linearized state space equations relating the commanded perturbations, $\mathbf{u}=[\Delta F_x, \Delta F_y]^{\mathrm{T}}$, to the measured interaction forces, $\mathbf{y}=\mathbf{F_i}$, is defined as

$$\begin{aligned} \dot{\mathbf{x}} &= \mathbf{Ax}+\mathbf{Bu} \\ \mathbf{y} &= \mathbf{Cx}+\mathbf{Du} \end{aligned} \tag{D.6}$$

where $\mathbf{x}=[\theta_s, \theta_e, \dot{\theta}_s, \dot{\theta}_e, x_a, y_a, \dot{x}_a, \dot{y}_a]^{\mathrm{T}}$ is the state vector of absolute robot joint angles (θ_s, θ_e) and Cartesian hand coordinates (x_a, y_a) along with their first derivatives. After linearizing the nonlinear robot dynamic equations at the nominal test location at equilibrium, $\mathbf{x}_o=[\theta_{s,o}, \theta_{e,o}, 0, 0, x_{a,o}, y_{a,o}, 0, 0]^{\mathrm{T}}$, the state space matrices were found to be

$$\mathbf{A}=\begin{bmatrix} \mathbf{0_{2x2}} & \mathbf{I_{2x2}} & \mathbf{0_{2x2}} & \mathbf{0_{2x2}} \\ -\mathbf{M}_{\theta\theta}^{-1}\mathbf{K}_{\theta\theta} & -\mathbf{M}_{\theta\theta}^{-1}\mathbf{B}_{\theta\theta} & -k_f\mathbf{M}_{\theta\theta}^{-1}\mathbf{J}^{\mathrm{T}} & \mathbf{0_{2x2}} \\ \mathbf{0_{2x2}} & \mathbf{0_{2x2}} & \mathbf{0_{2x2}} & \mathbf{I_{2x2}} \\ -k_f\mathbf{M}_{xx}^{-1}\mathbf{J}^{\mathrm{T}} & \mathbf{0_{2x2}} & -\mathbf{M}_{xx}^{-1}\mathbf{K}_{xx} & -\mathbf{M}_{xx}^{-1}\mathbf{B}_{xx} \end{bmatrix} \tag{D.7a}$$

$$\mathbf{B} = \begin{bmatrix} \mathbf{0}_{2x2} & \left(\mathbf{M}_{\theta\theta}^{-1}\mathbf{J}^{T}\right)^{T} & \mathbf{0}_{2x2} & \mathbf{0}_{2x2} \end{bmatrix}^{T} \tag{D.7b}$$

$$\mathbf{C} = \begin{bmatrix} k_f\mathbf{J}^{T} & \mathbf{0}_{2x2} & -k_f\mathbf{I}_{2x2} & \mathbf{0}_{2x2} \end{bmatrix} \tag{D.7c}$$

$$\mathbf{D} = \mathbf{0}_{2x2} \tag{D.7d}$$

where $\mathbf{M}_{\theta\theta} = \begin{bmatrix} H_{11} & H_{12}\cos\left(\theta_{e,o} - \theta_{s,o}\right) \\ H_{12}\cos\left(\theta_{e,o} - \theta_{s,o}\right) & H_{22} \end{bmatrix}$,

$$\mathbf{K}_{\theta\theta} = \left(k_p + k_f\right)\begin{bmatrix} l_s\left(x_{a,o}\cos\left(\theta_{s,o}\right) + y_{a,o}\sin\left(\theta_{s,o}\right)\right) & 0 \\ 0 & l_e\left(x_{a,o}\cos\left(\theta_{e,o}\right) + y_{a,o}\sin\left(\theta_{e,o}\right)\right) \end{bmatrix} +$$

$$\left(k_p + k_f\right)l_s l_e\cos\left(\theta_{e,o} - \theta_{s,o}\right)\begin{bmatrix} -1 & 1 \\ 1 & -1 \end{bmatrix},$$

$$\mathbf{B}_{\theta\theta} = \begin{bmatrix} b_s + k_d l_s^2 & k_d l_s l_e\cos\left(\theta_{e,o} - \theta_{s,o}\right) \\ k_d l_s l_e\cos\left(\theta_{e,o} - \theta_{s,o}\right) & b_e + k_d l_e^2 \end{bmatrix},\ \mathbf{M}_{xx} = \begin{bmatrix} m_{11} & m_{12} \\ m_{21} & m_{22} \end{bmatrix},$$

$$\mathbf{K}_{xx} = \begin{bmatrix} k_{11} + k_f & k_{12} \\ k_{21} & k_{22} + k_f \end{bmatrix},\ \text{and}\ \mathbf{B}_{xx} = \begin{bmatrix} b_{11} & b_{12} \\ b_{21} & b_{22} \end{bmatrix}.$$

Appendix E

Experimental results of spring array mechanical impedance testing

Spectral analysis results from the mass-only test configurations (sm1-sm4) and from the spring array test configurations (sa1-sa9) are included in this appendix as Figures E.1-E.26. The dynamic stiffness spectral estimates (top graph), and the partial and multiple coherences of the derived dynamic compliance estimate (bottom graph) are included in each figure. Welch's periodogram method was used to estimate the power spectral density and coherence functions [8]. In Chapter 6, the number of data points included in the FFT calculation was defined as N_{FFT}, the length of the Hanning windowing function as N_{WND}, and the number of overlapped samples as N_{OVL}. The odd numbered figures contain the spectral analysis results with $N_{FFT} = 8192$, $N_{WND} = 8192$, and $N_{OVL} = 4096$ ($N_{MNS} = 5$ overlapping data segments), whereas the even numbered figures contain the results with $N_{FFT} = 8192$, $N_{WND} = 2048$, and $N_{OVL} = 1536$ ($N_{MNS} = 45$). The six trials of each test configuration are depicted by dots with different gray shading. The expected dynamic stiffness frequency responses are depicted with black solid lines. For the mass-only configurations, a gray dashed line is included in the off-diagonal gain terms of the dynamic stiffness to provide a reference to the gain of the observed mass, $k_{xx}(s) = k_{yy}(s) = ms^2$, because the object being tested is isotropic and $k_{xy}(s) = k_{yx}(s) = 0$.

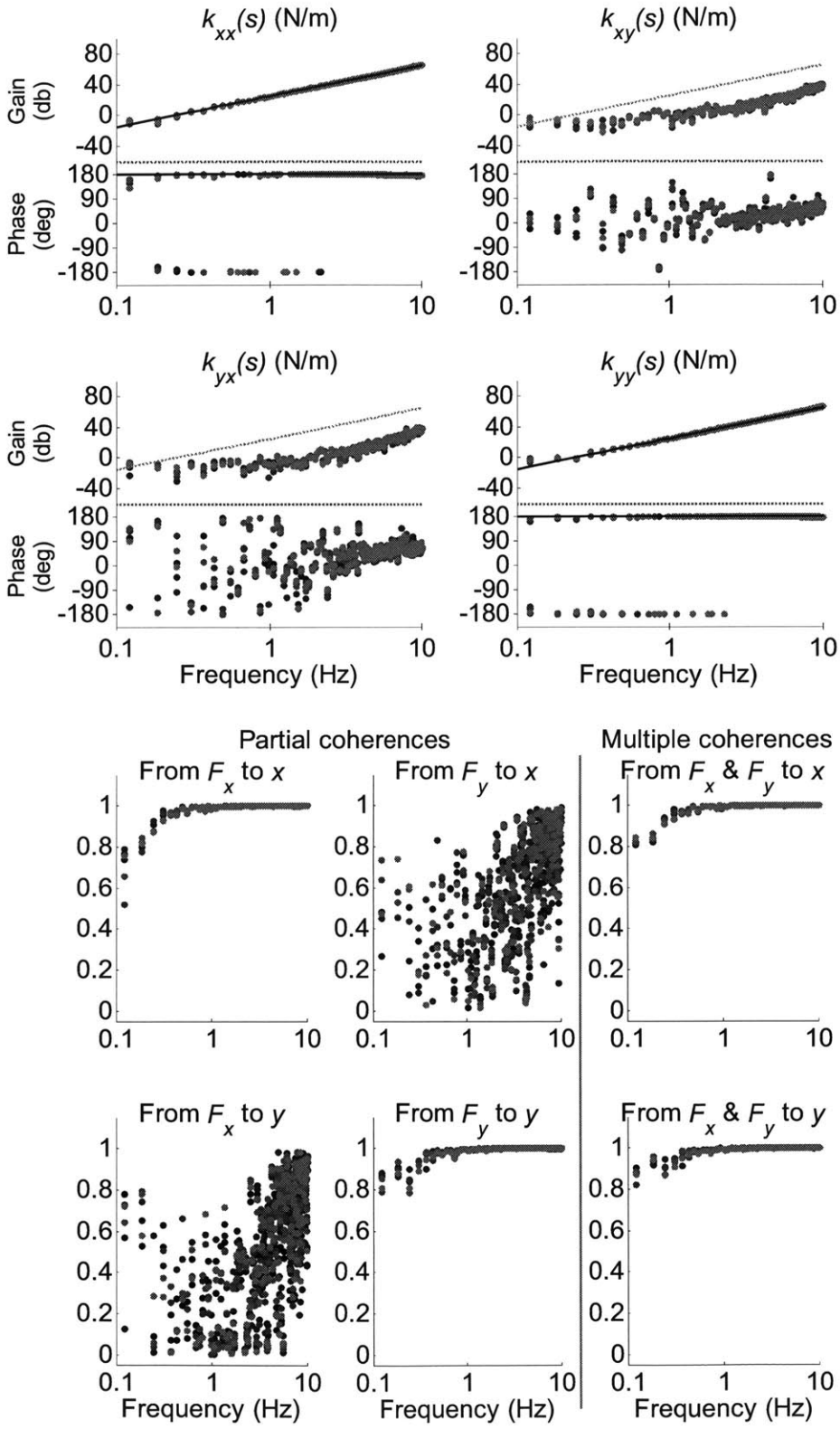

Figure E.1. Mass only configuration sm1, 5 overlaps: dynamic stiffness spectral estimates (top), and partial and multiple coherences (bottom)

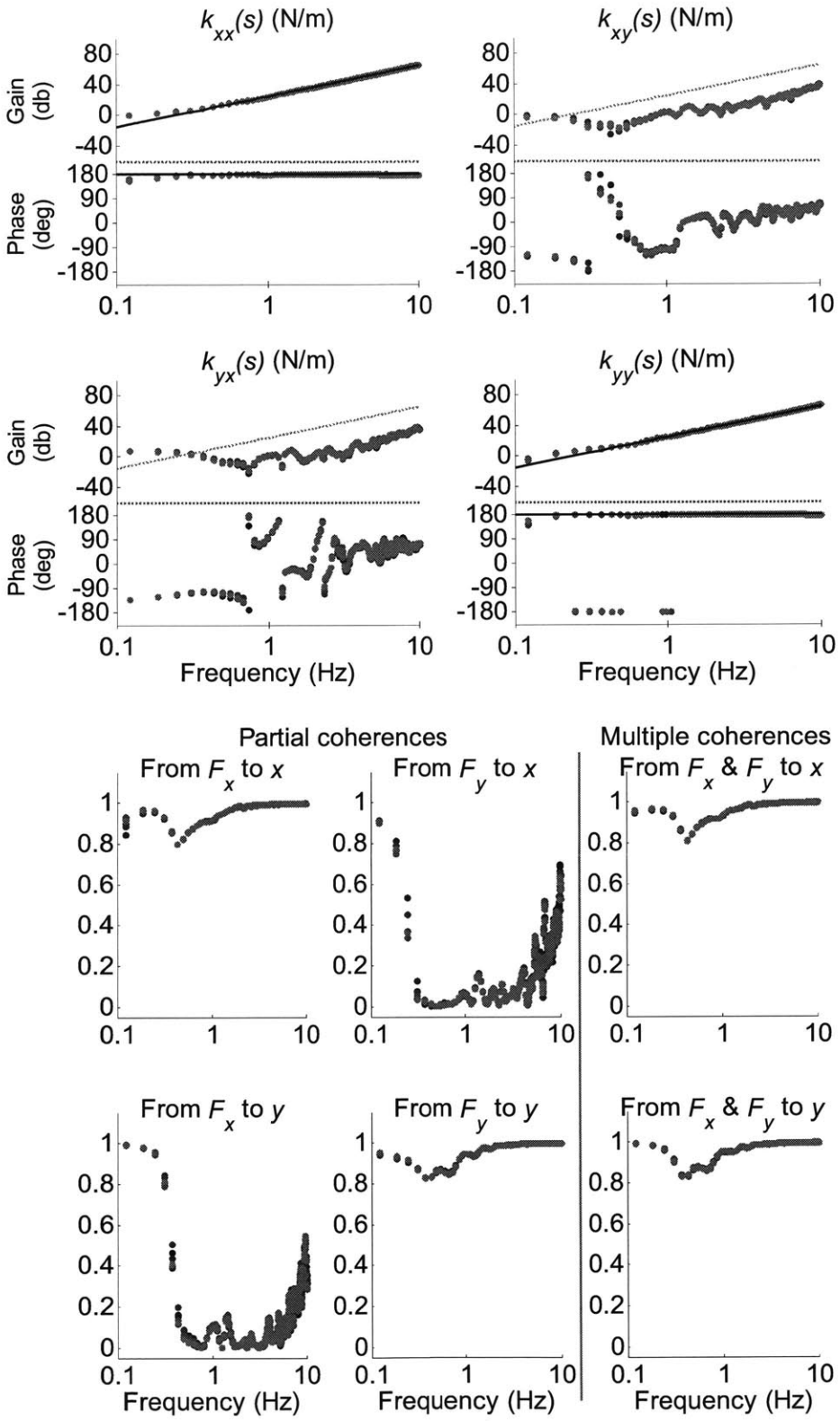

Figure E.2. Mass only configuration sm1, 45 overlaps: dynamic stiffness spectral estimates (top), and partial and multiple coherences (bottom)

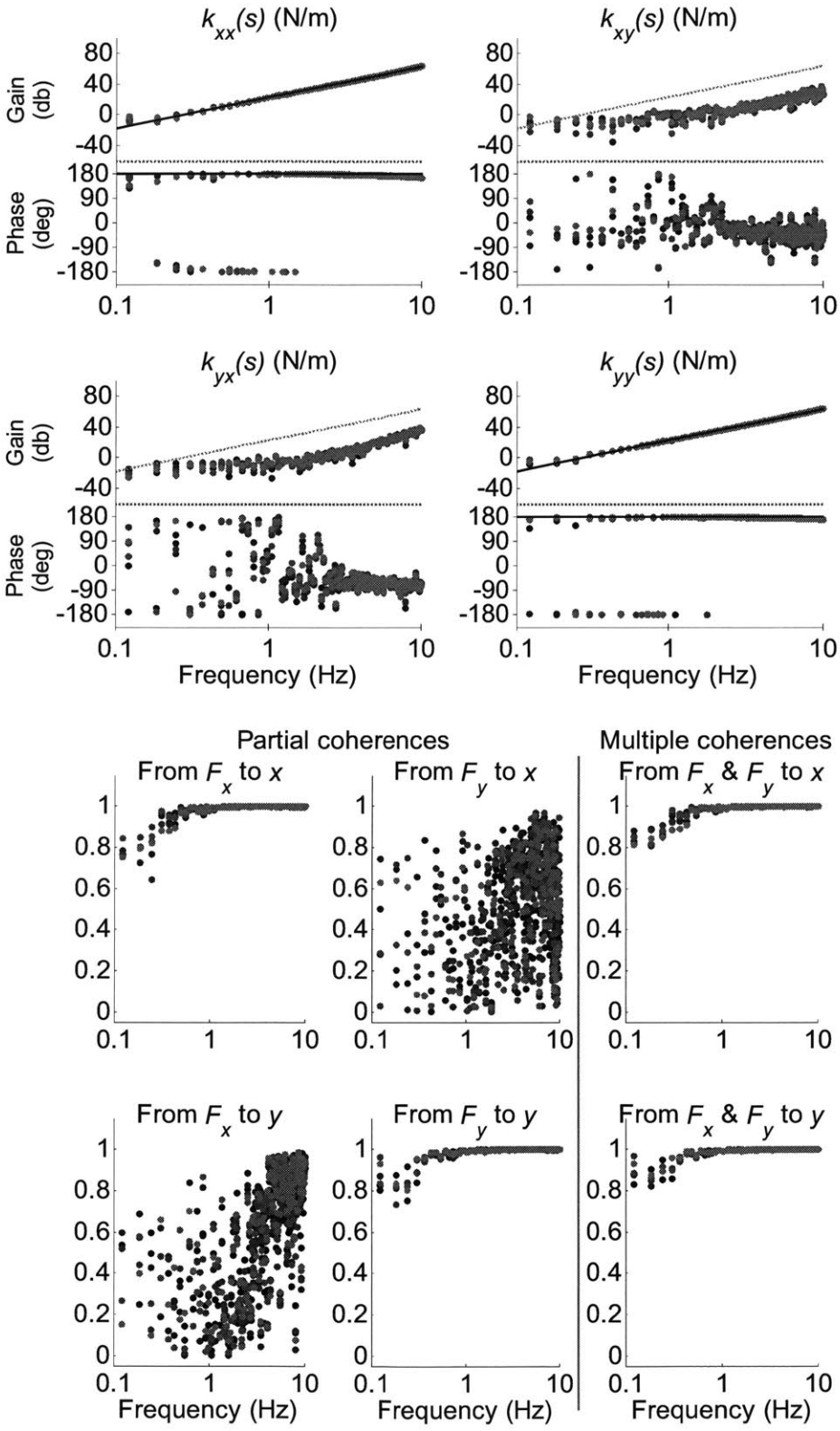

Figure E.3. Mass only configuration sm2, 5 overlaps: dynamic stiffness spectral estimates (top), and partial and multiple coherences (bottom)

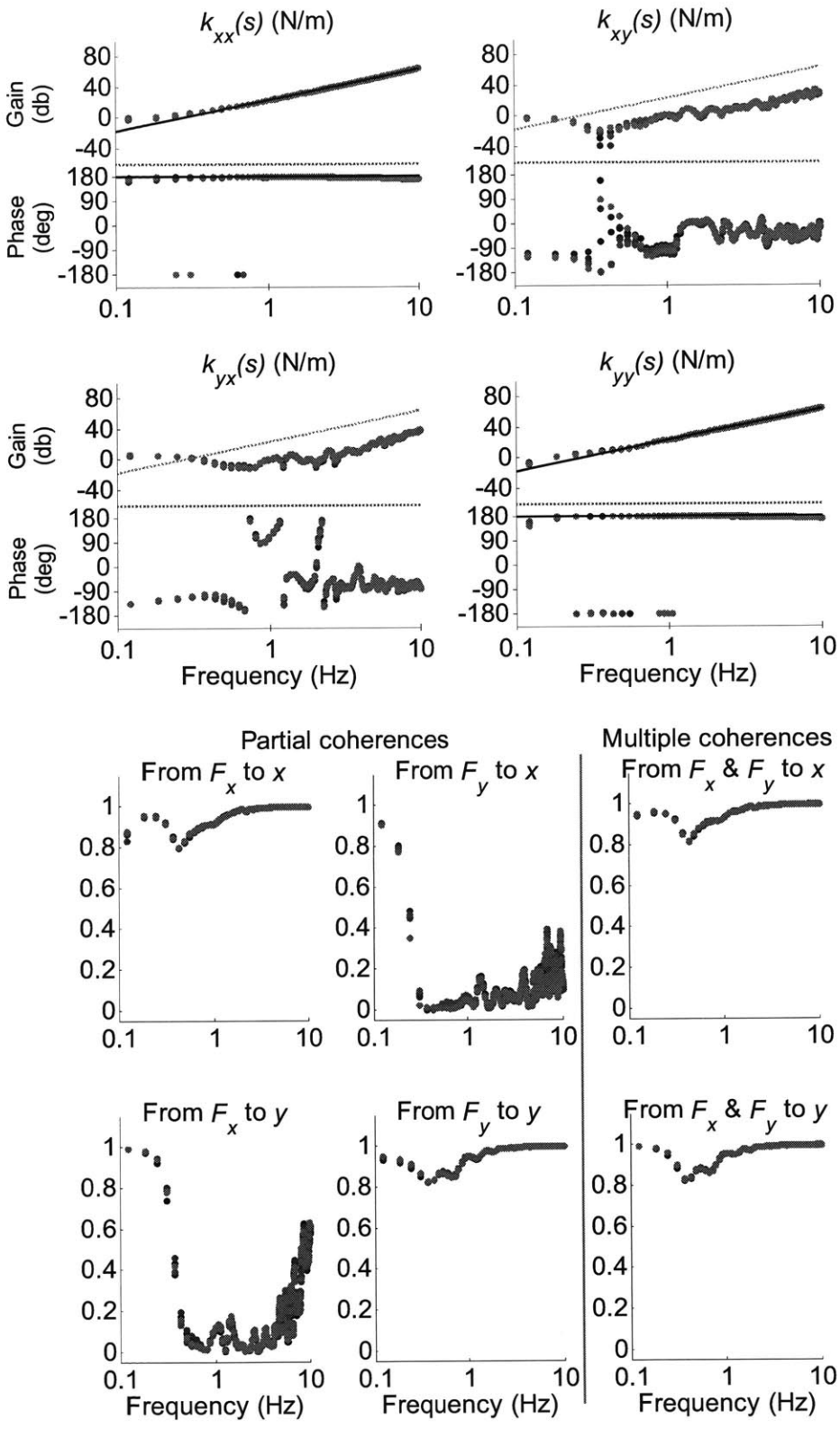

Figure E.4. Mass only configuration sm2, 45 overlaps: dynamic stiffness spectral estimates (top), and partial and multiple coherences (bottom)

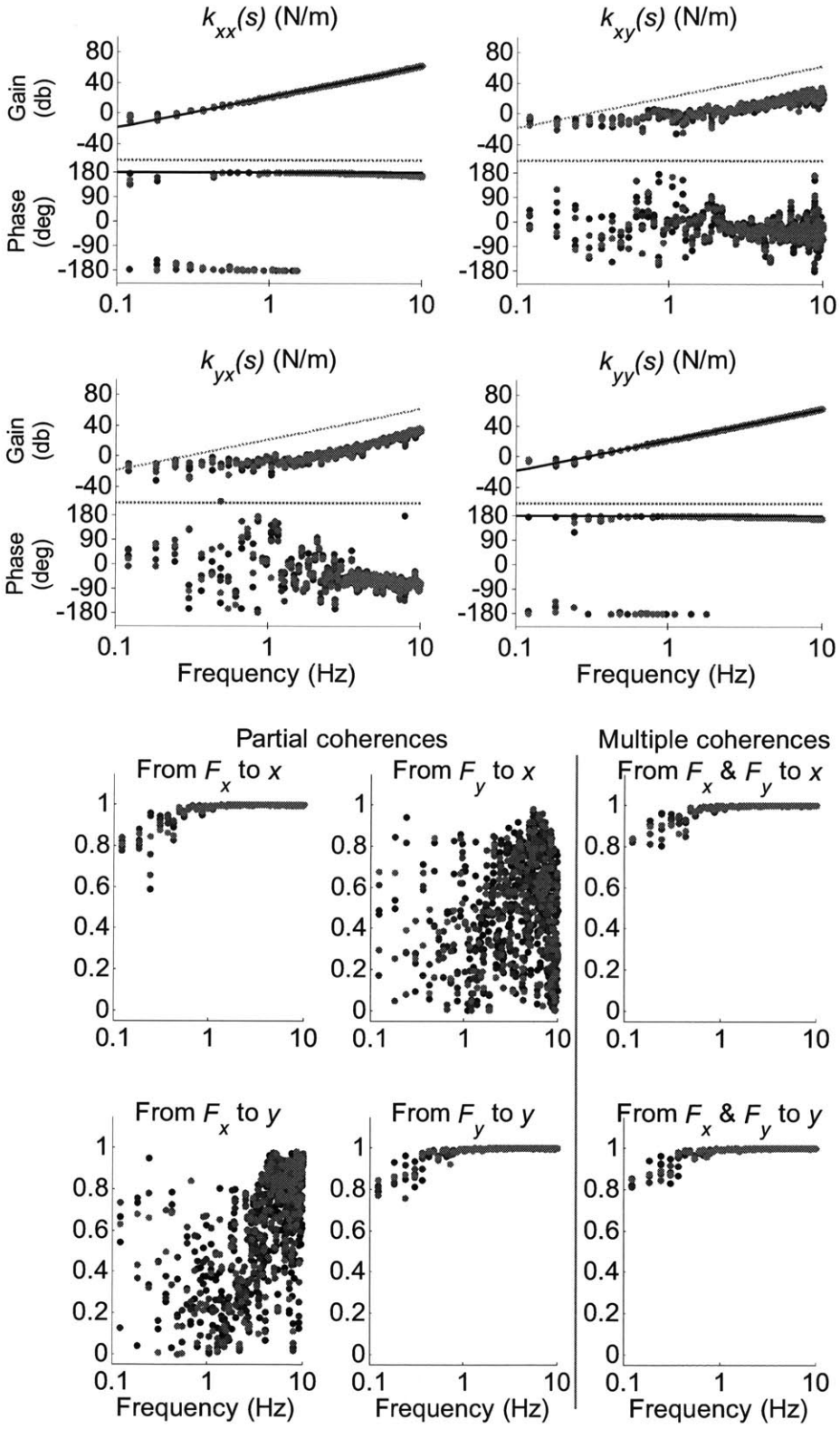

Figure E.5. Mass only configuration sm3, 5 overlaps: dynamic stiffness spectral estimates (top), and partial and multiple coherences (bottom)

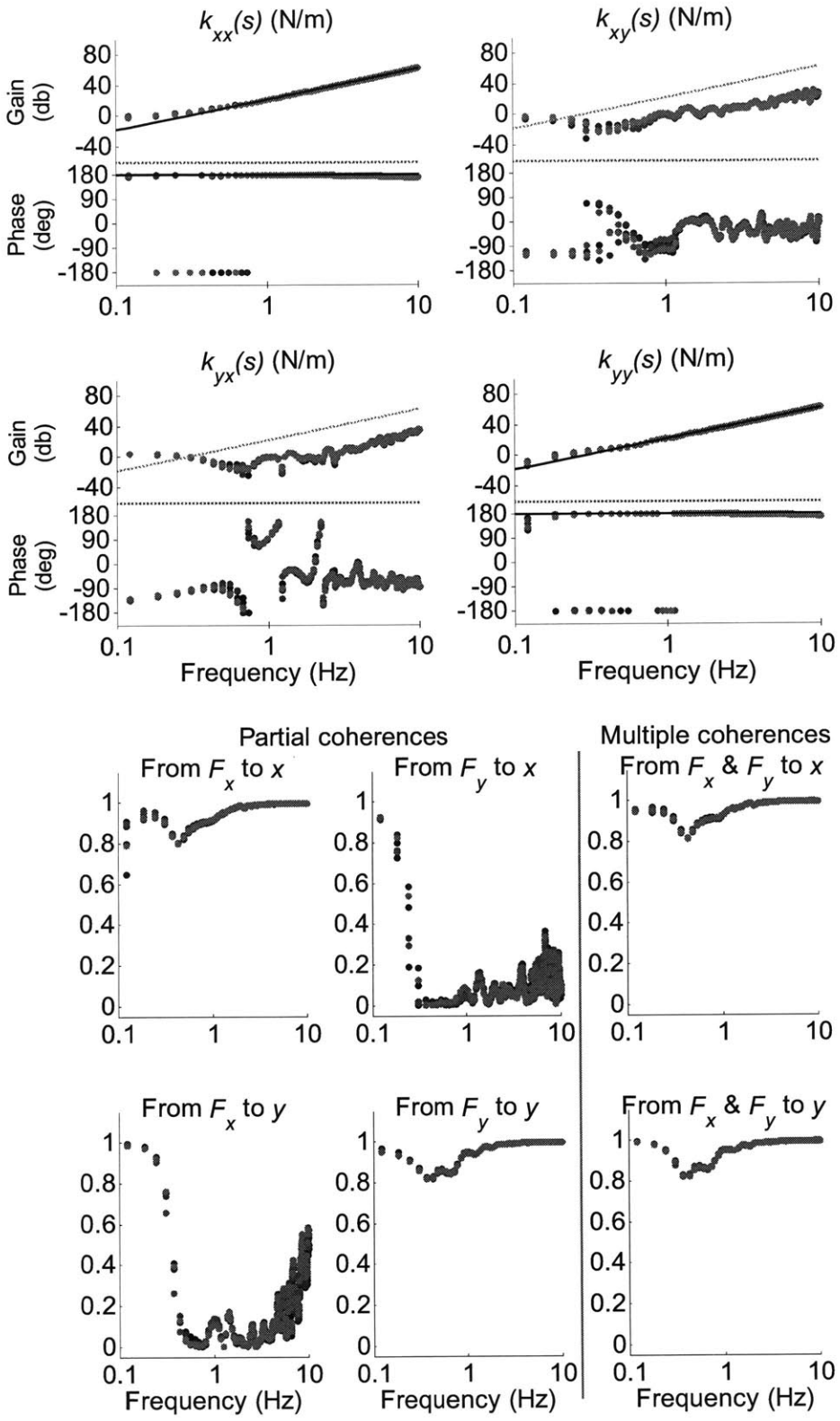

Figure E.6. Mass only configuration sm3, 45 overlaps: dynamic stiffness spectral estimates (top), and partial and multiple coherences (bottom)

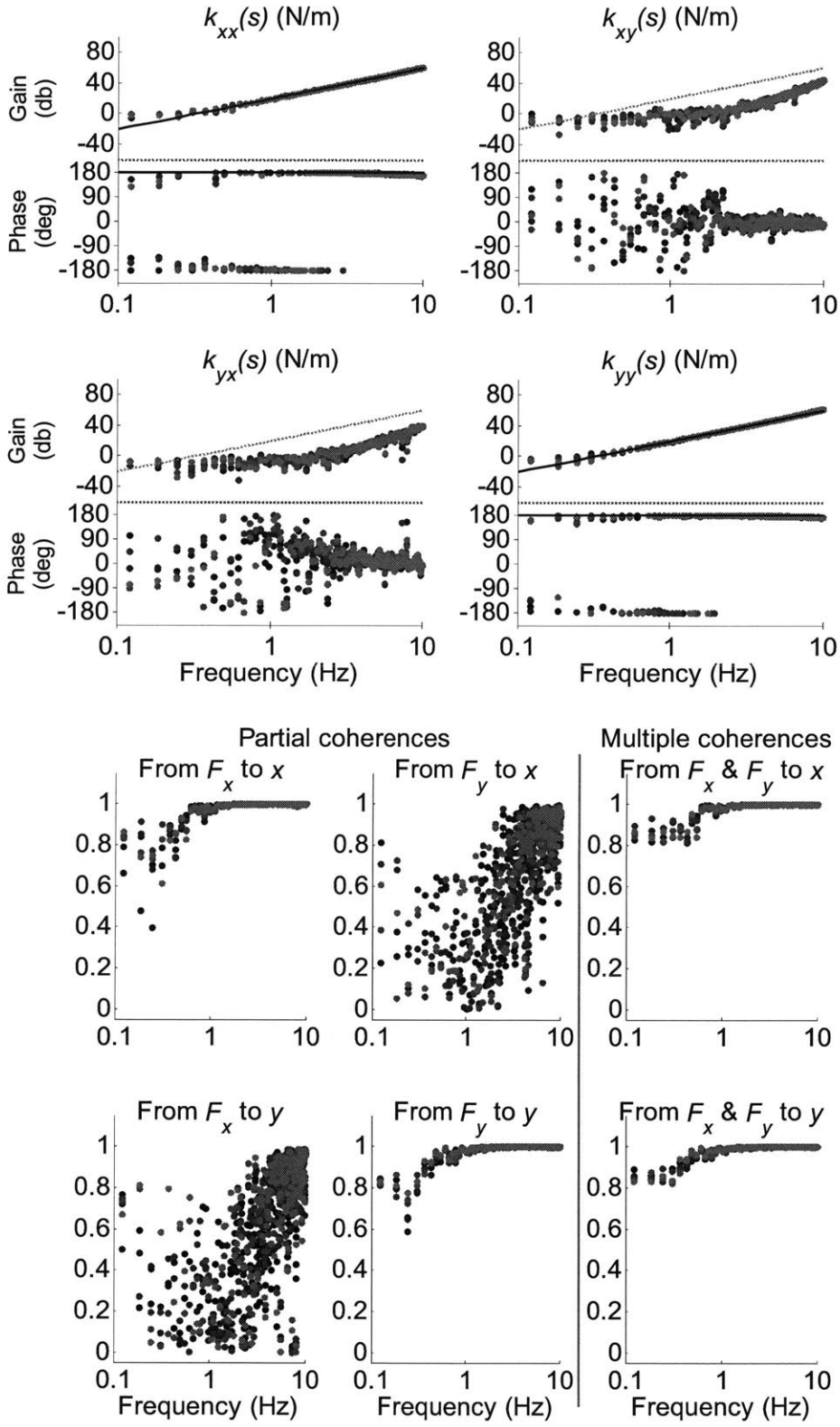

Figure E.7. Mass only configuration sm4, 5 overlaps: dynamic stiffness spectral estimates (top), and partial and multiple coherences (bottom)

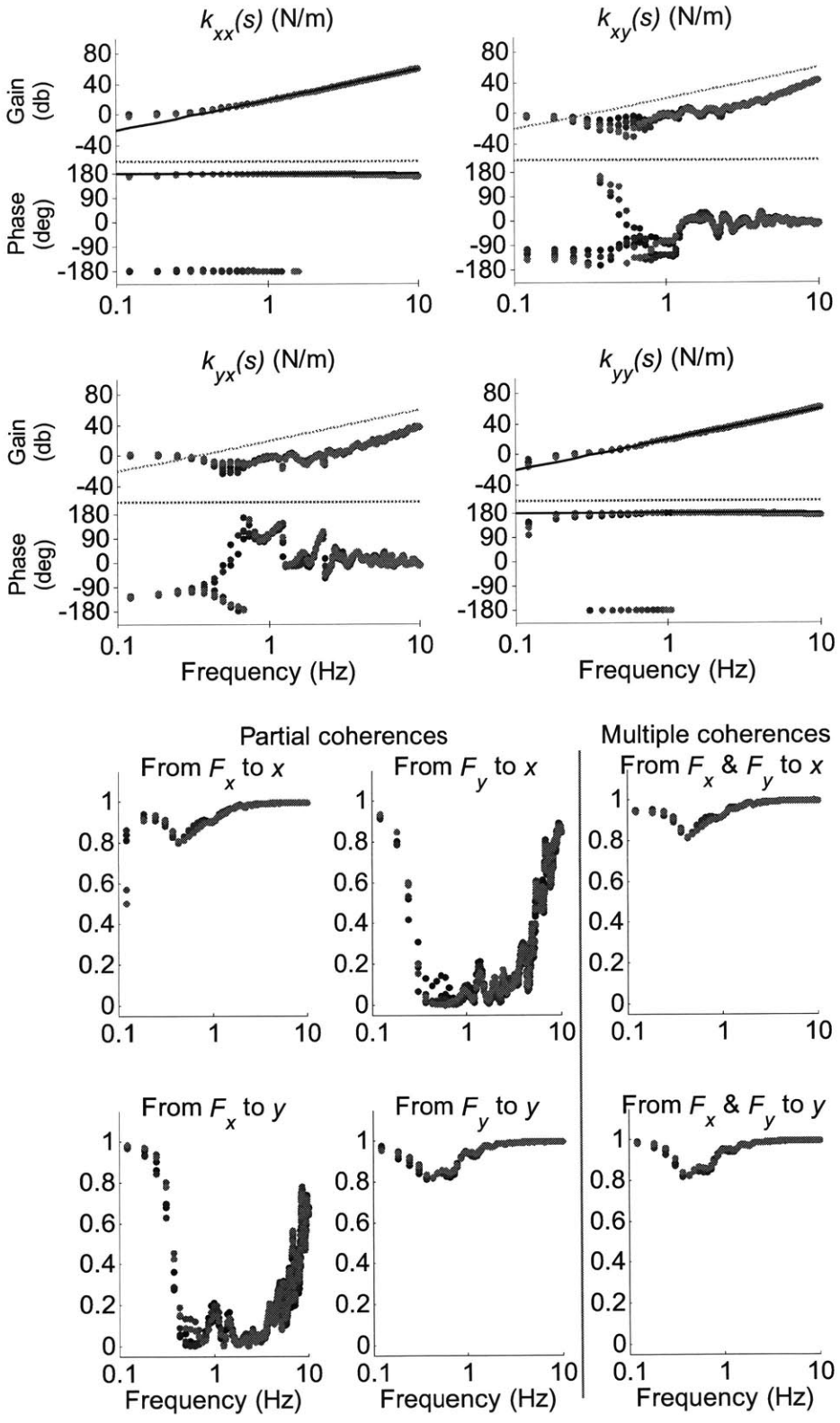

Figure E.8. Mass only configuration sm4, 45 overlaps: dynamic stiffness spectral estimates (top), and partial and multiple coherences (bottom)

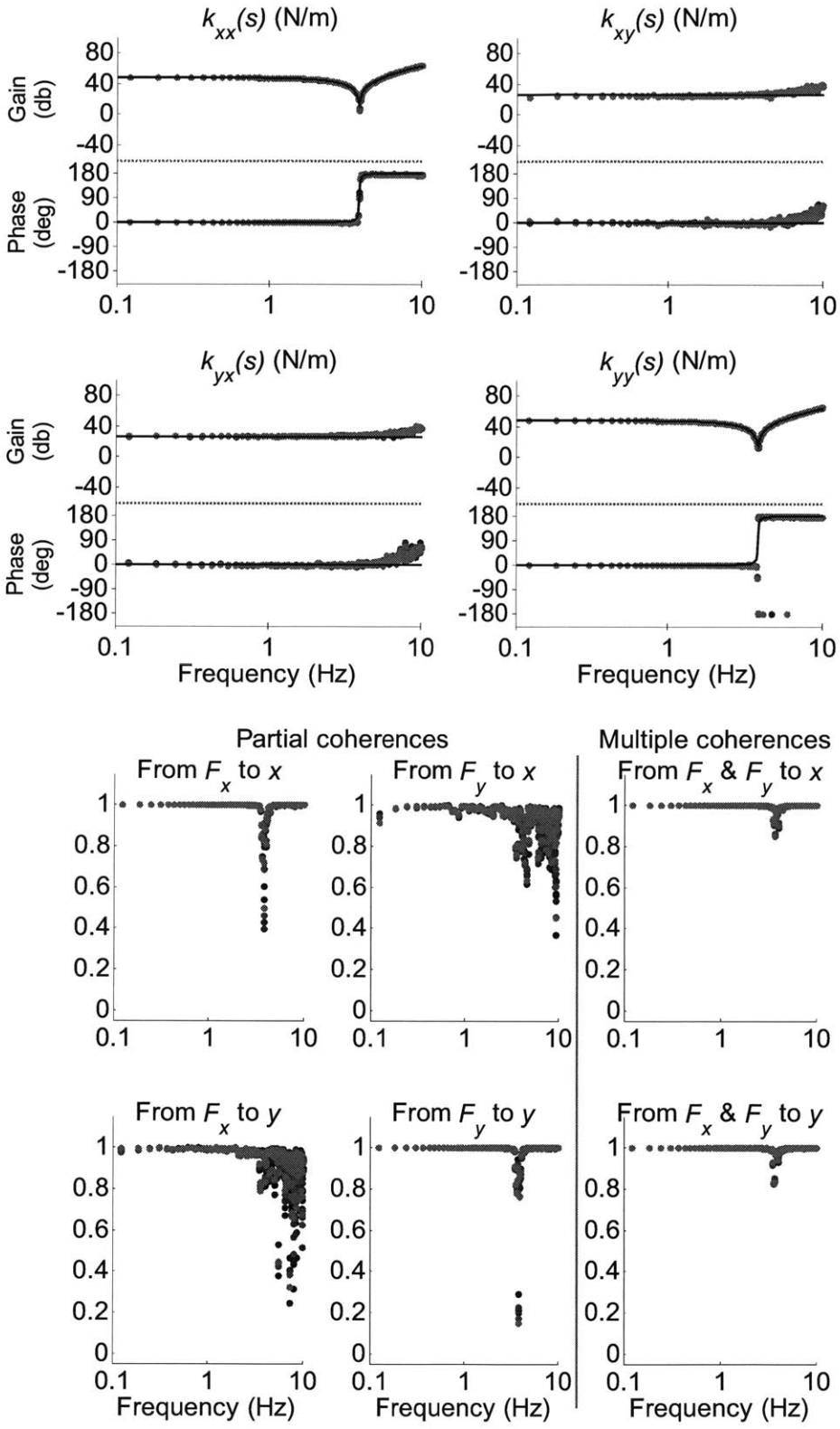

Figure E.9. Spring array configuration sa1, 5 overlaps: dynamic stiffness spectral estimates (top), and partial and multiple coherences (bottom)

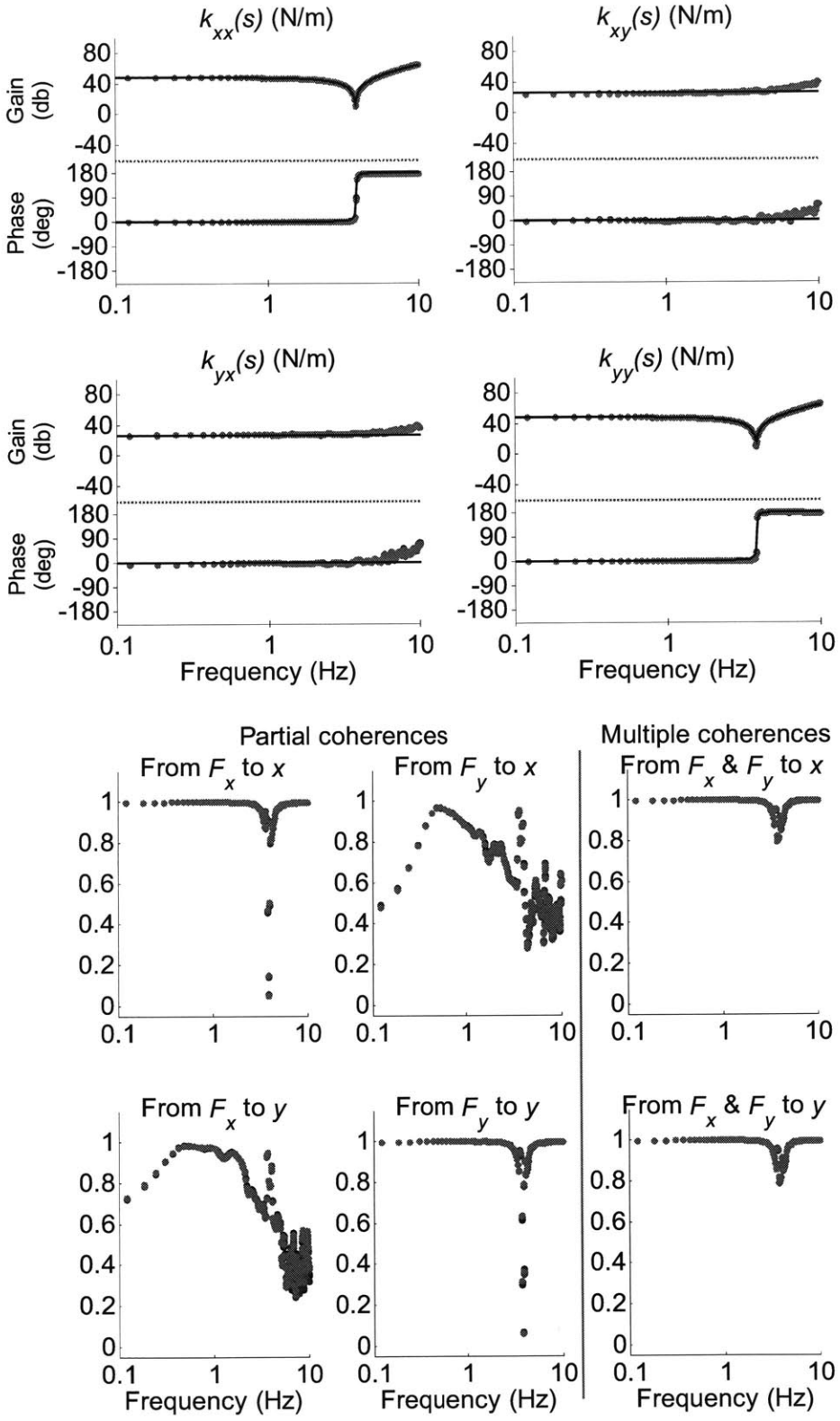

Figure E.10. Spring array configuration sa1, 45 overlaps: dynamic stiffness spectral estimates (top), and partial and multiple coherences (bottom)

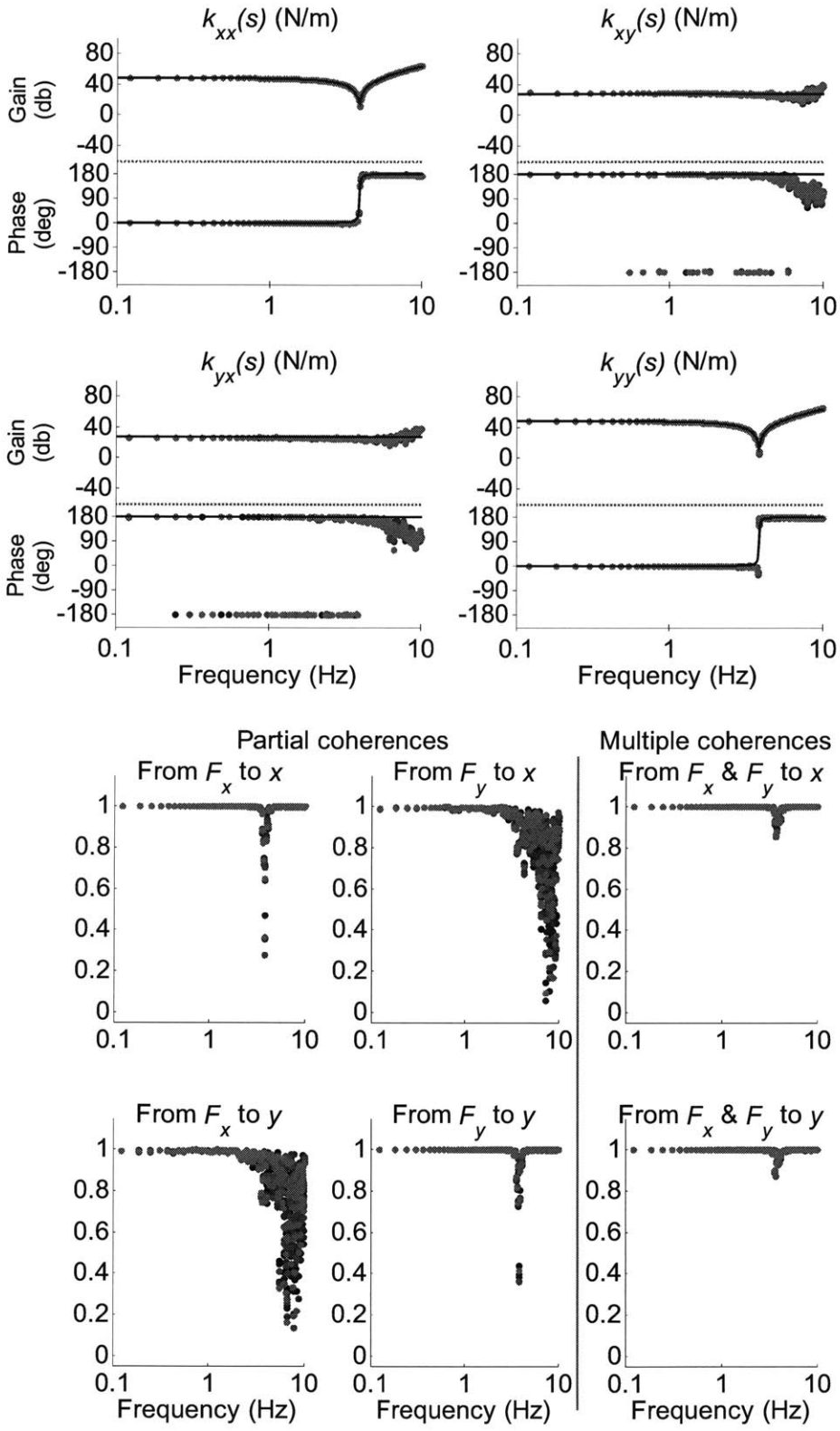

Figure E.11. Spring array configuration sa2, 5 overlaps: dynamic stiffness spectral estimates (top), and partial and multiple coherences (bottom)

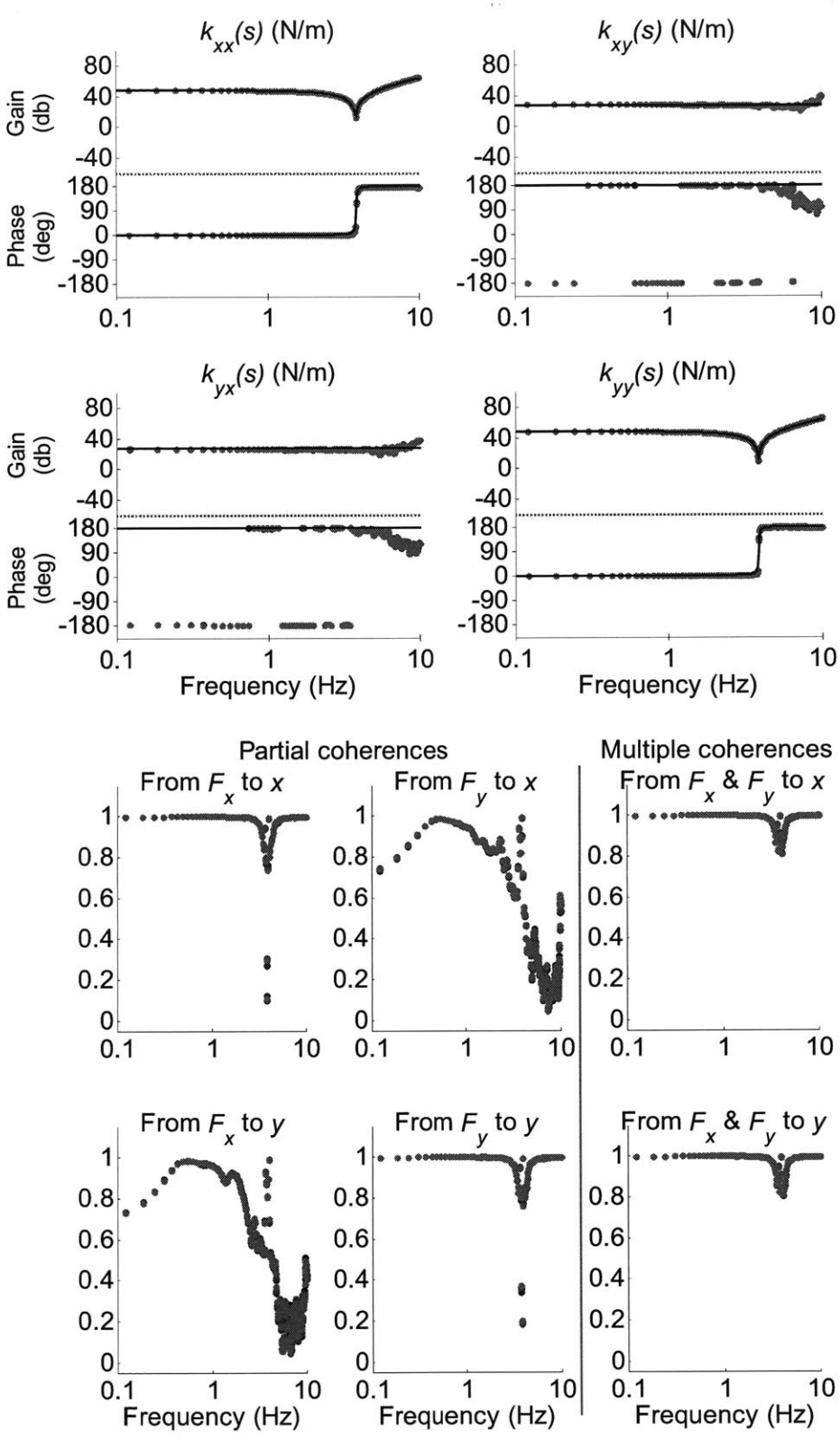

Figure E.12. Spring array configuration sa2, 45 overlaps: dynamic stiffness spectral estimates (top), and partial and multiple coherences (bottom)

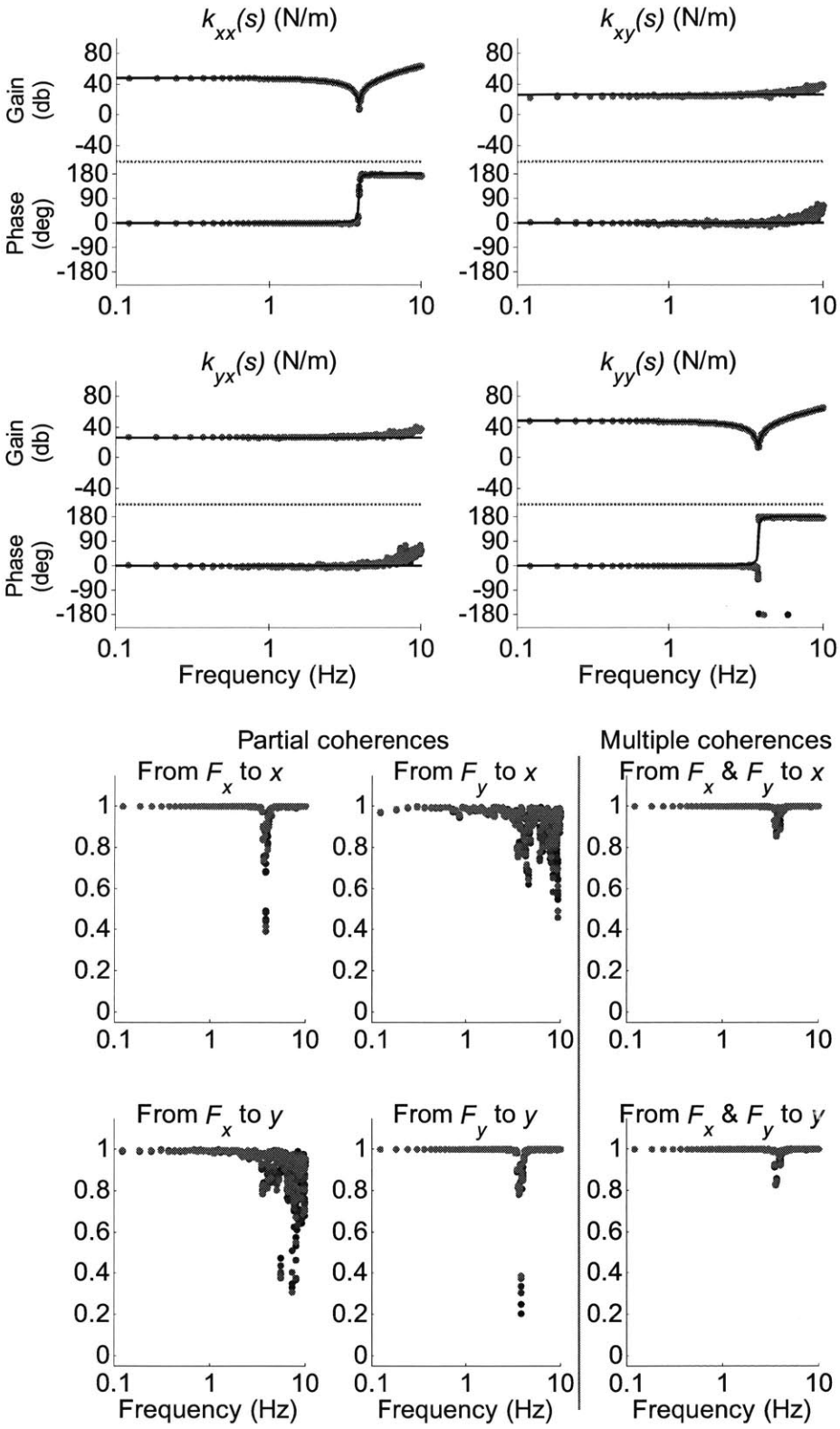

Figure E.13. Spring array configuration sa3, 5 overlaps: dynamic stiffness spectral estimates (top), and partial and multiple coherences (bottom)

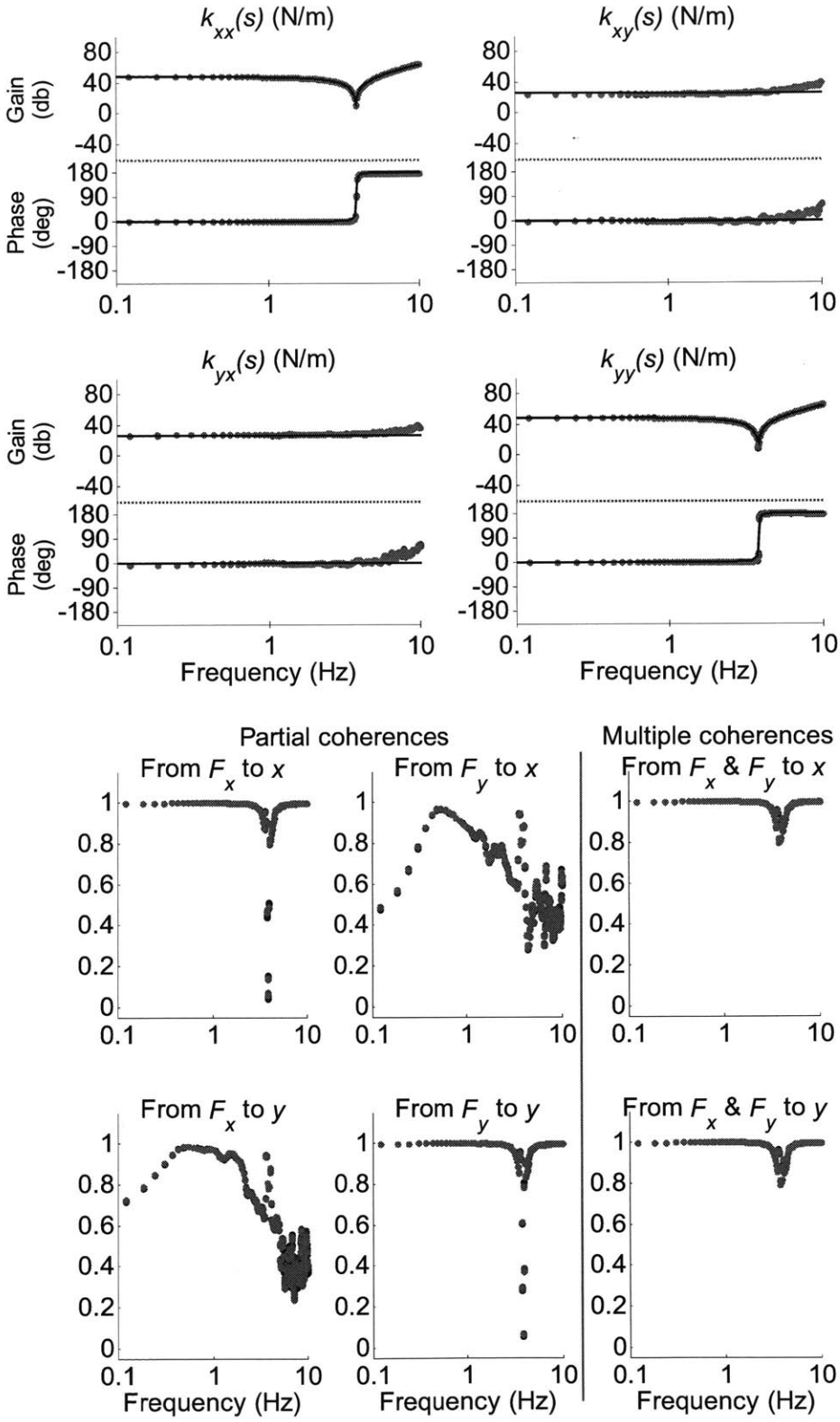

Figure E.14. Spring array configuration sa3, 45 overlaps: dynamic stiffness spectral estimates (top), and partial and multiple coherences (bottom)

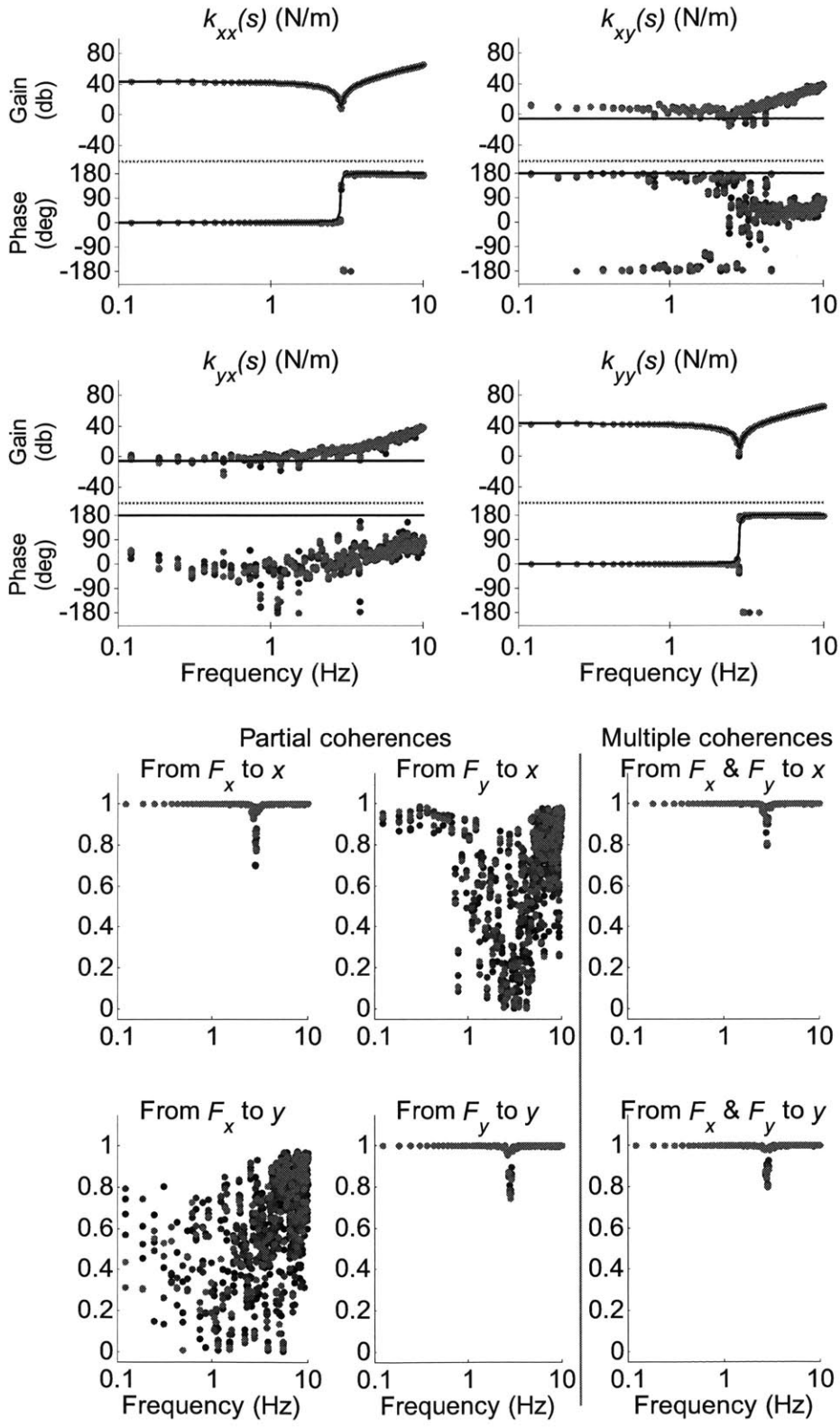

Figure E.15. Spring array configuration sa4, 5 overlaps: dynamic stiffness spectral estimates (top), and partial and multiple coherences (bottom)

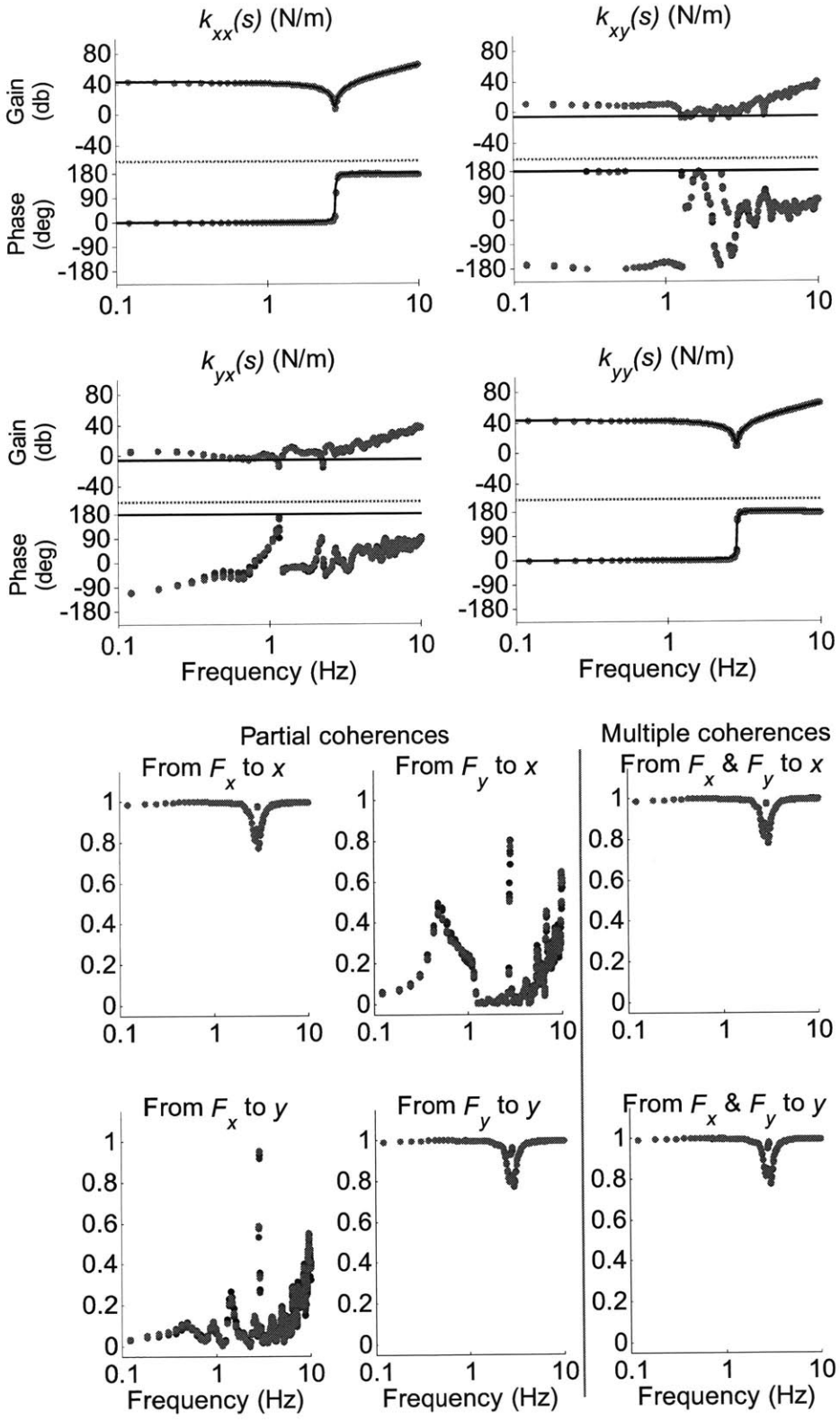

Figure E.16. Spring array configuration sa4, 45 overlaps: dynamic stiffness spectral estimates (top), and partial and multiple coherences (bottom)

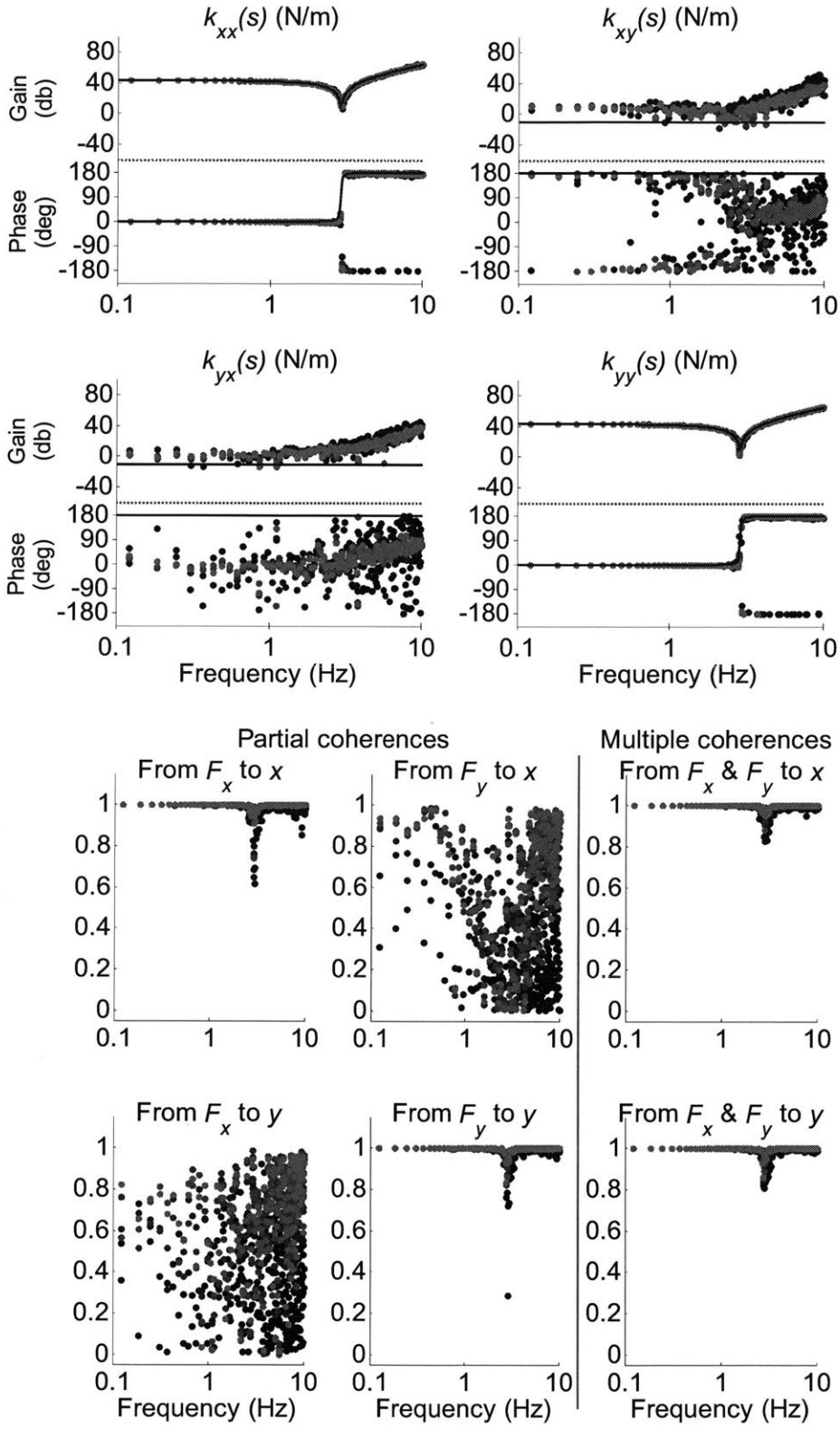

Figure E.17. Spring array configuration sa5, 5 overlaps: dynamic stiffness spectral estimates (top), and partial and multiple coherences (bottom)

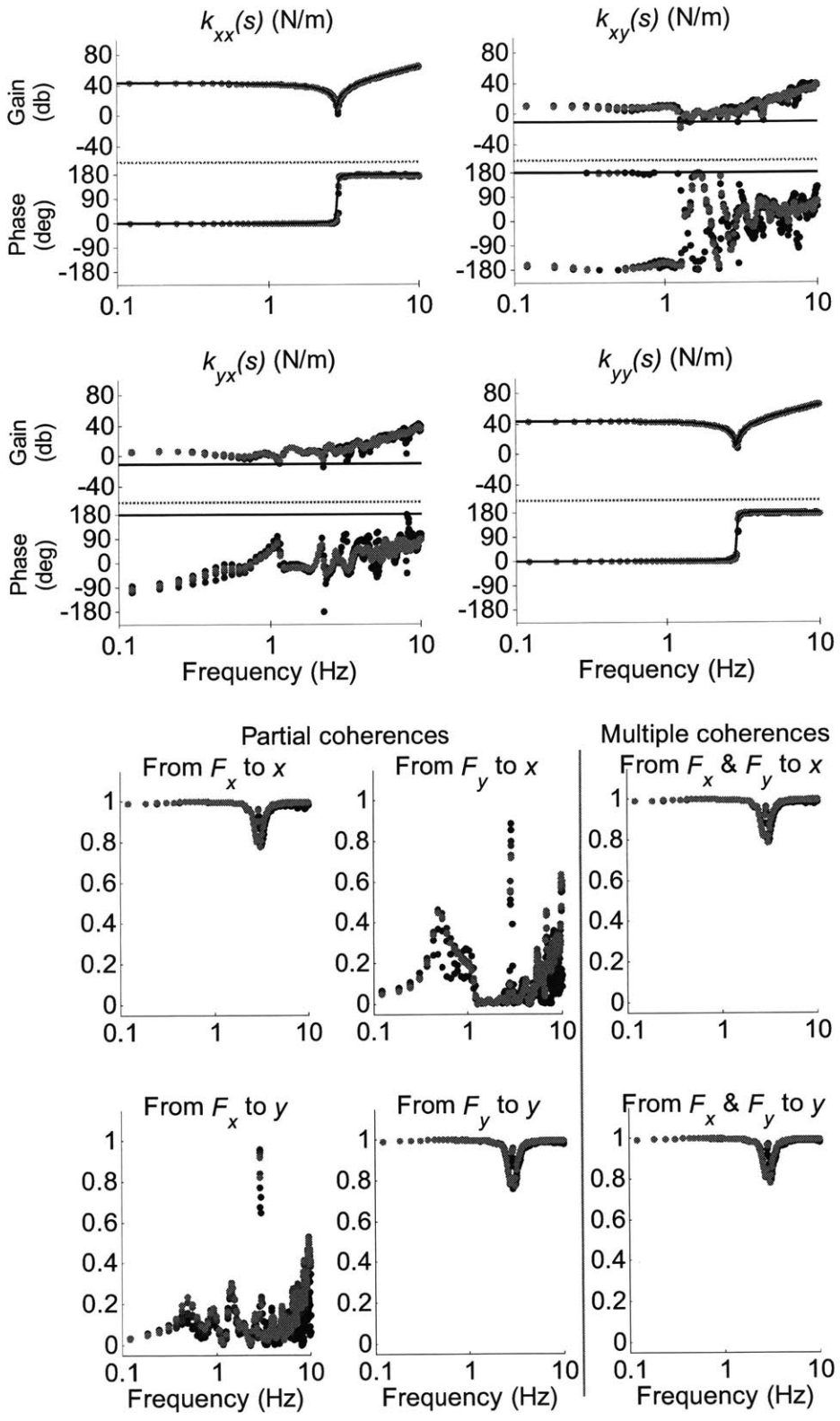

Figure E.18. Spring array configuration sa5, 45 overlaps: dynamic stiffness spectral estimates (top), and partial and multiple coherences (bottom)

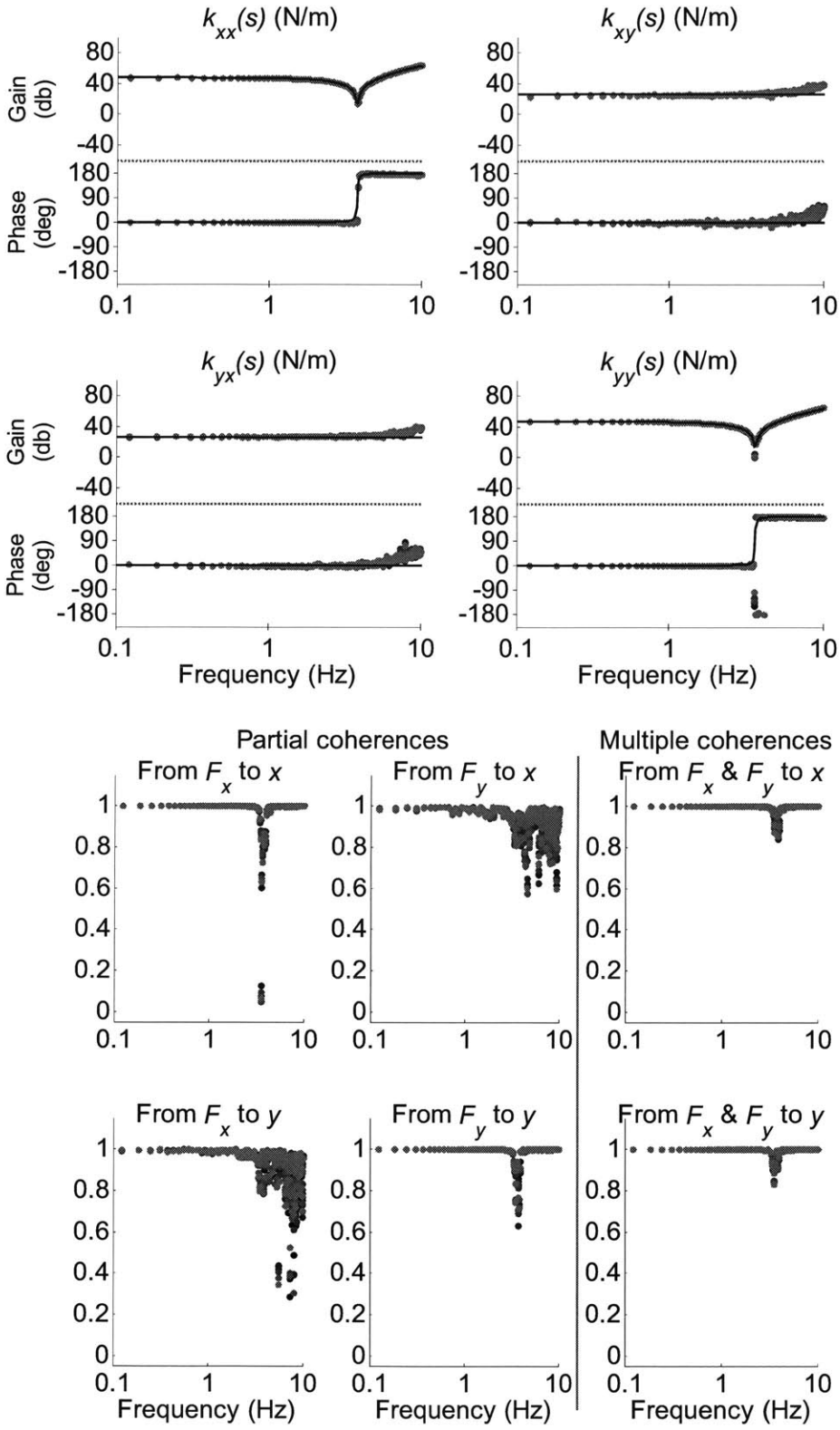

Figure E.19. Spring array configuration sa6, 5 overlaps: dynamic stiffness spectral estimates (top), and partial and multiple coherences (bottom)

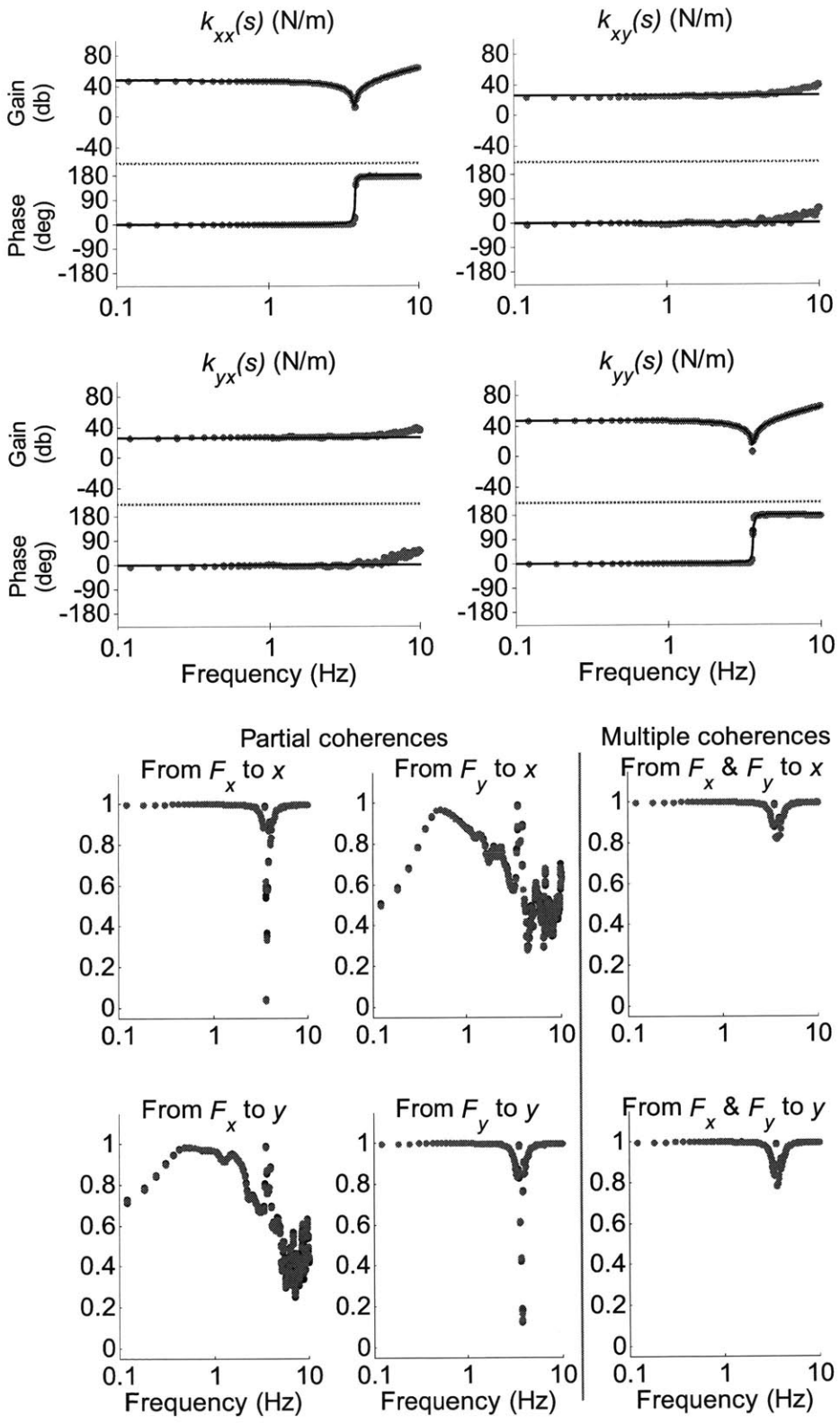

Figure E.20. Spring array configuration sa6, 45 overlaps: dynamic stiffness spectral estimates (top), and partial and multiple coherences (bottom)

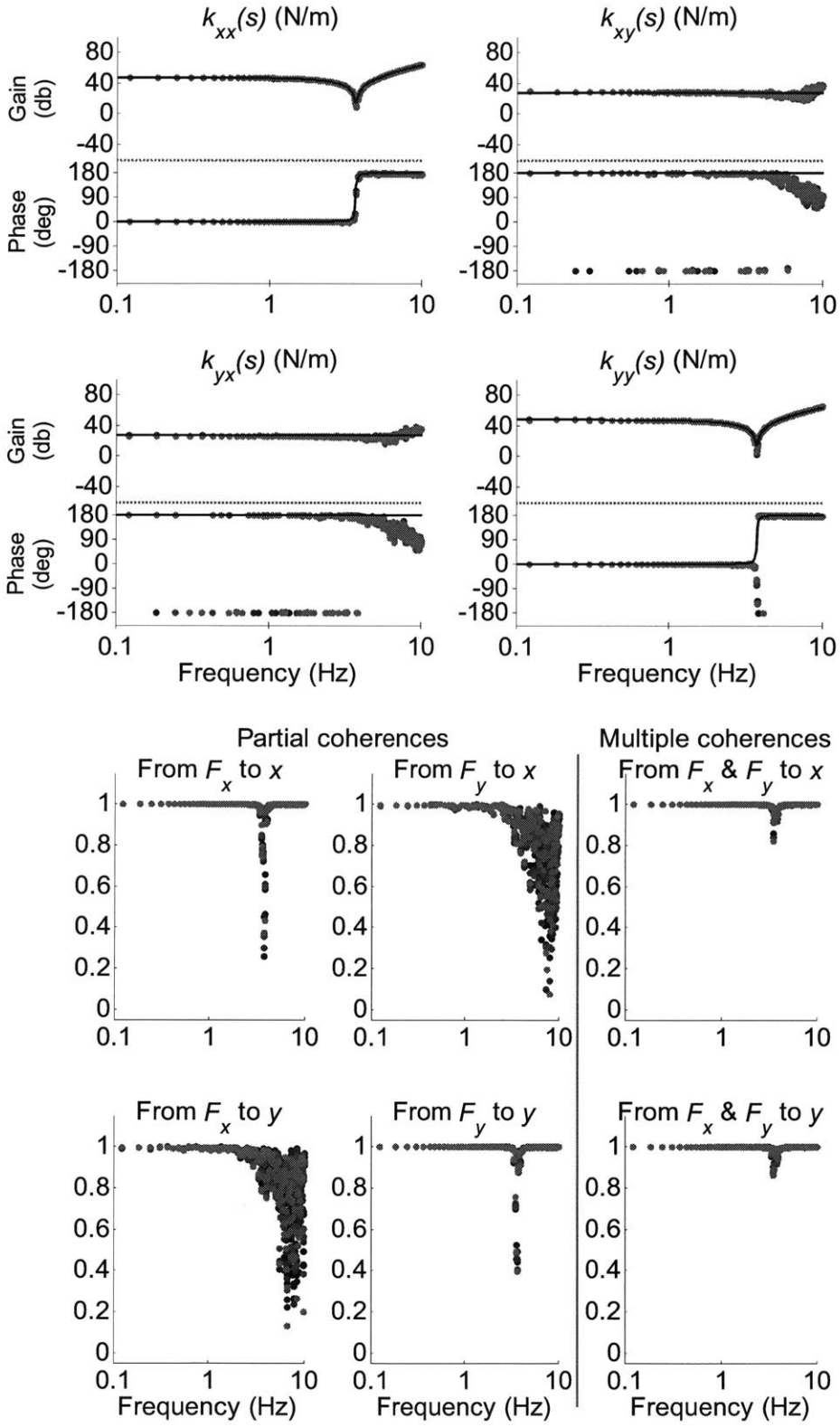

Figure E.21. Spring array configuration sa7, 5 overlaps: dynamic stiffness spectral estimates (top), and partial and multiple coherences (bottom)

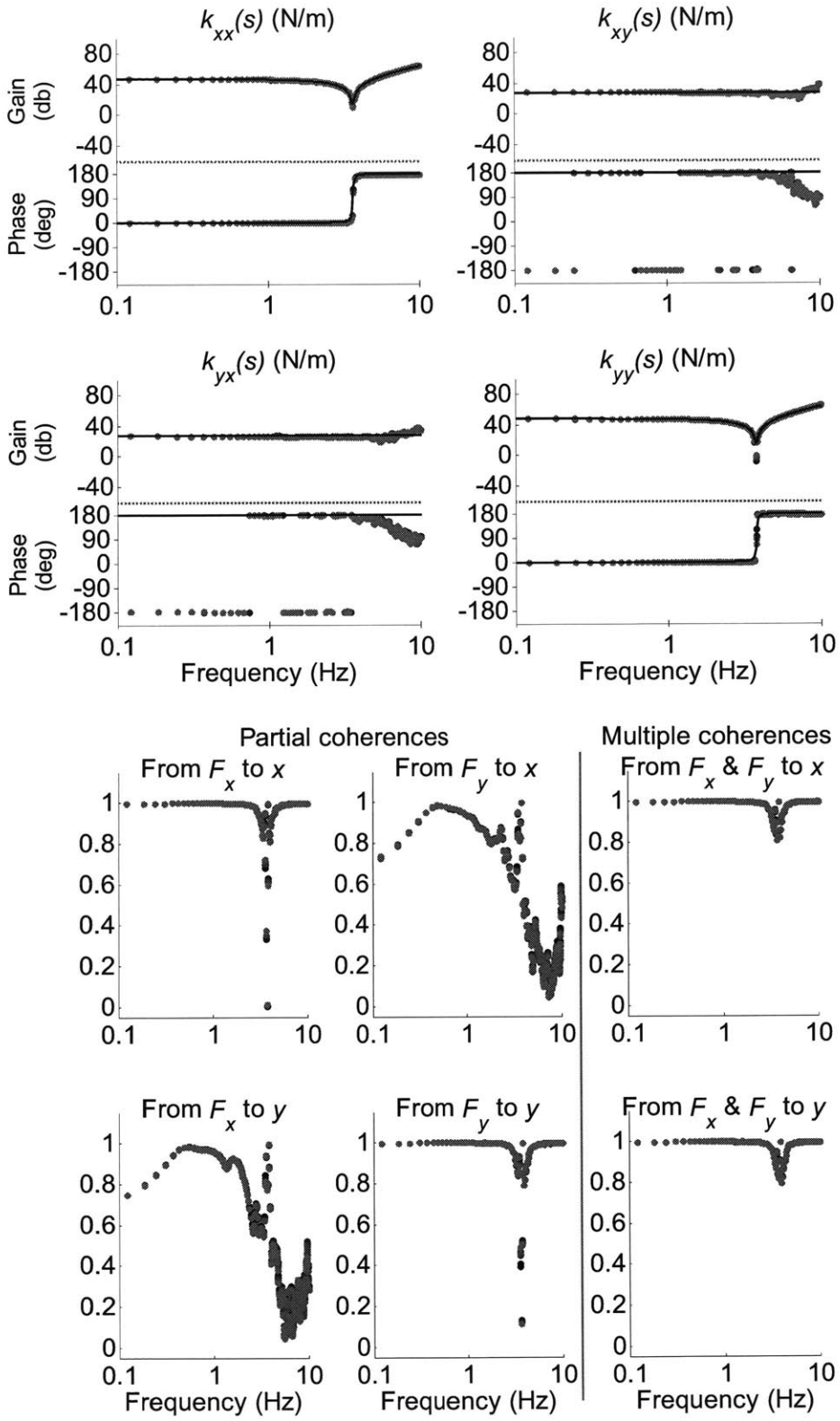

Figure E.22. Spring array configuration sa7, 45 overlaps: dynamic stiffness spectral estimates (top), and partial and multiple coherences (bottom)

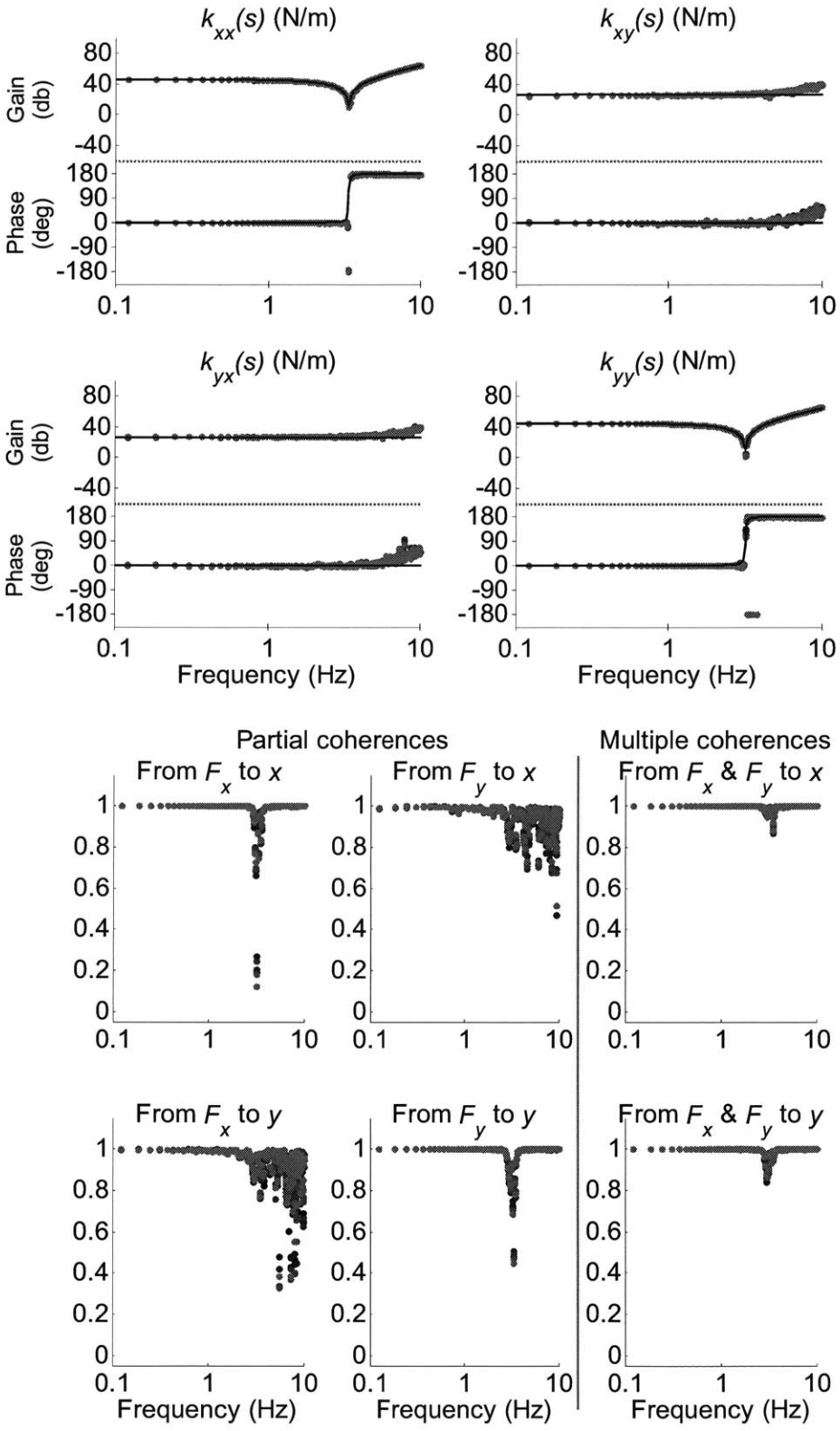

Figure E.23. Spring array configuration sa8, 5 overlaps: dynamic stiffness spectral estimates (top), and partial and multiple coherences (bottom)

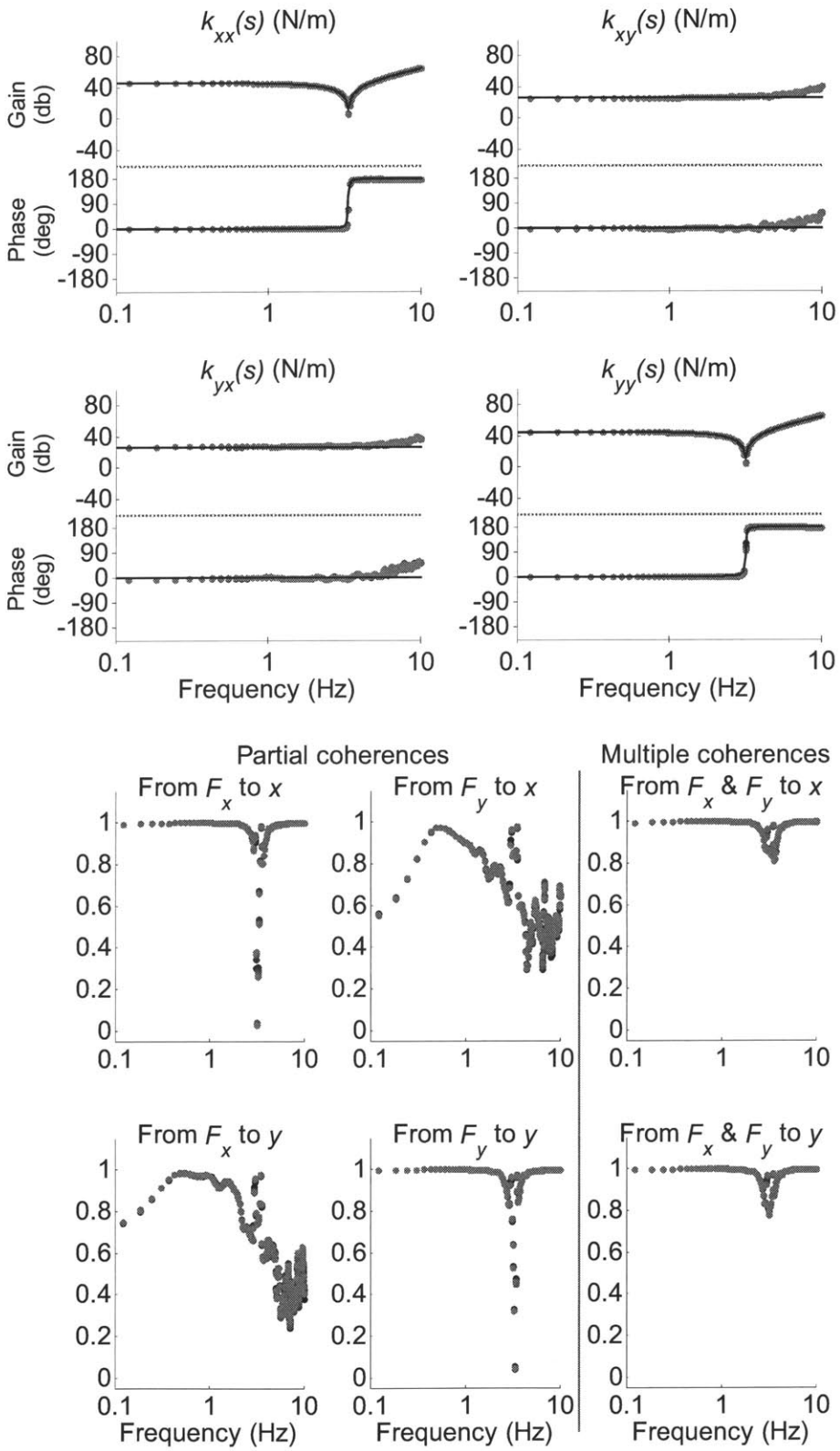

Figure E.24. Spring array configuration sa8, 45 overlaps: dynamic stiffness spectral estimates (top), and partial and multiple coherences (bottom)

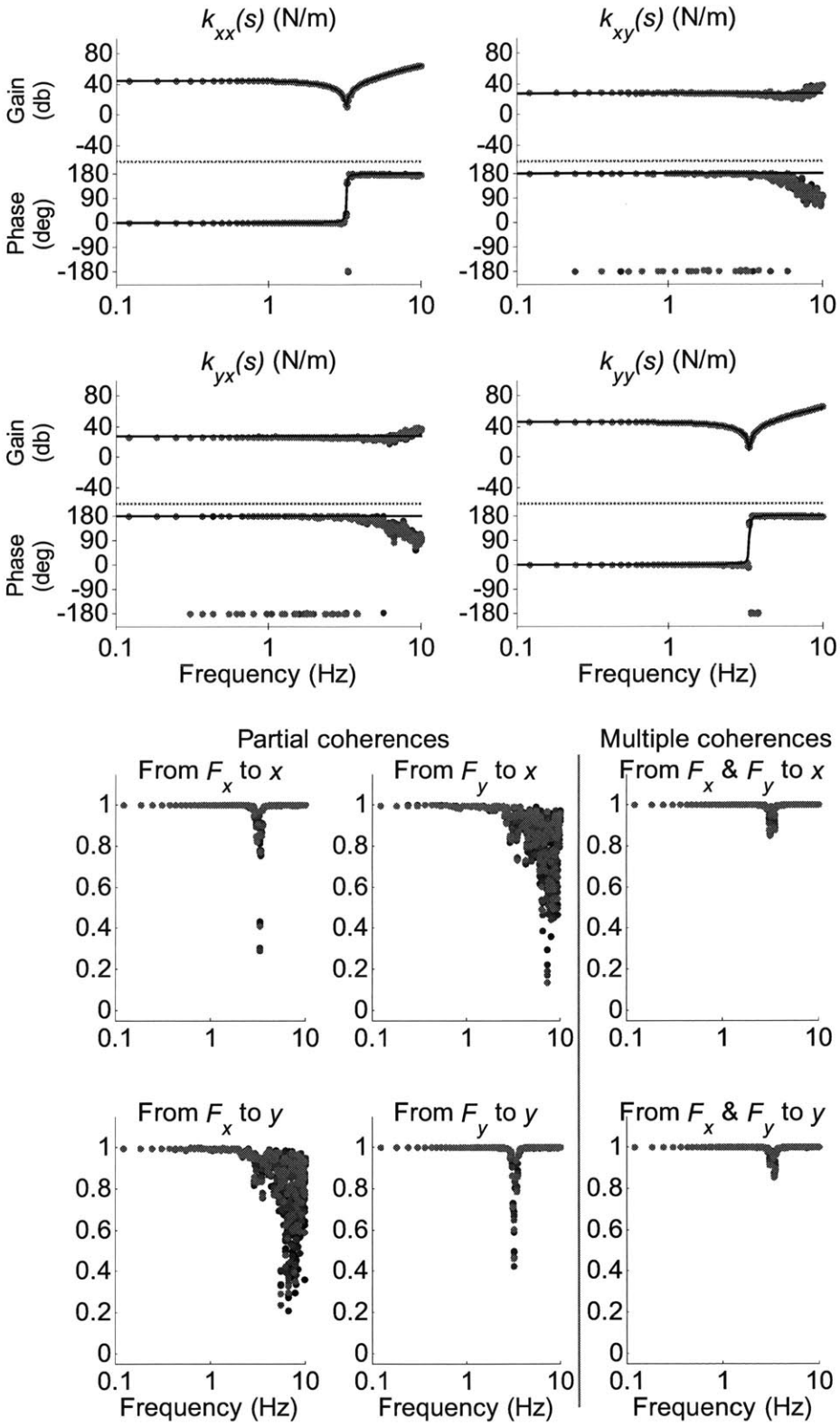

Figure E.25. Spring array configuration sa9, 5 overlaps: dynamic stiffness spectral estimates (top), and partial and multiple coherences (bottom)

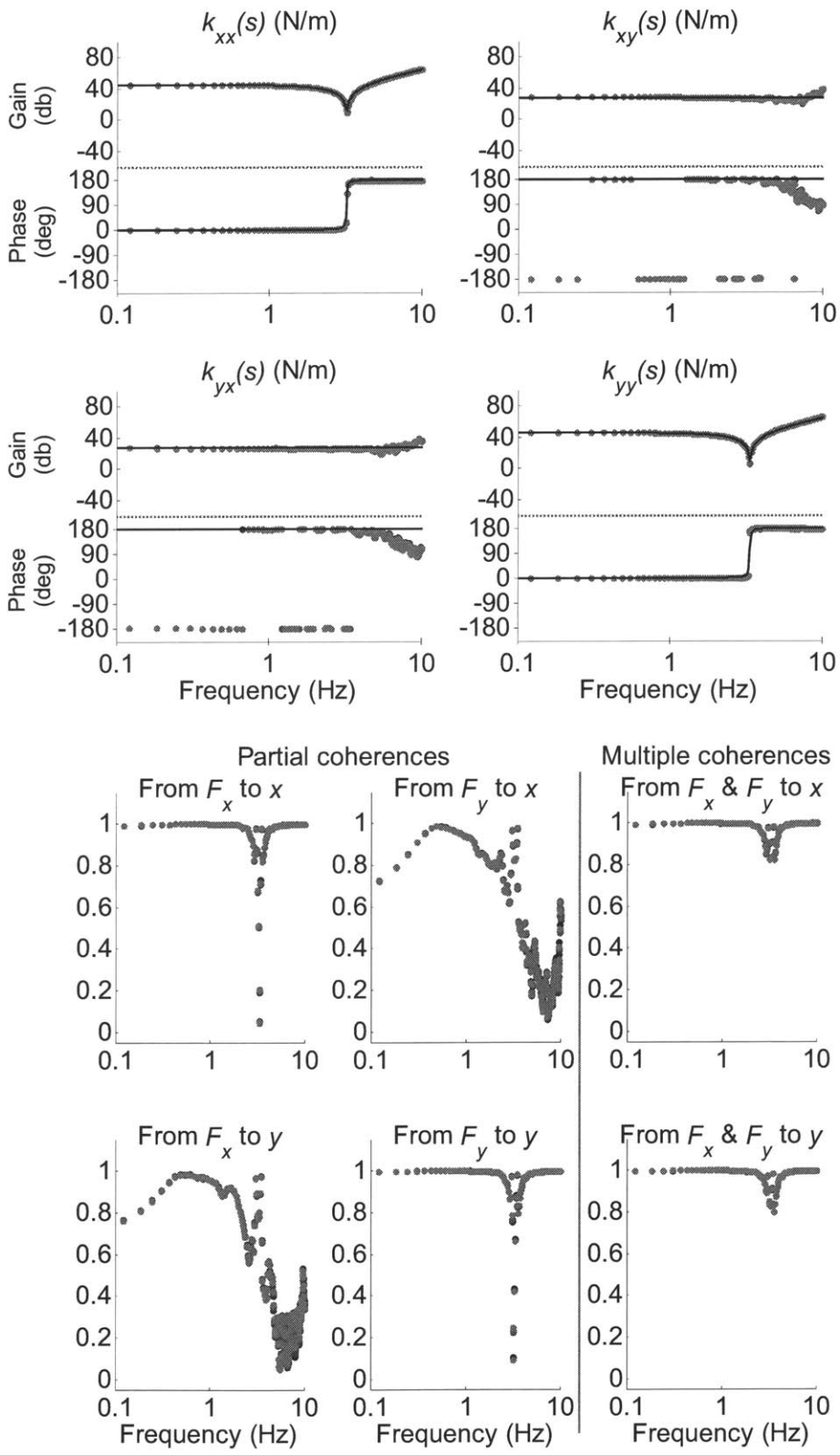

Figure E.26. Spring array configuration sa9, 45 overlaps: dynamic stiffness spectral estimates (top), and partial and multiple coherences (bottom)

Appendix F

Experimental results of arm mechanical impedance testing of unimpaired subjects

Spectral analysis results from both arms of the unimpaired subjects using plastic and carbon fiber arm troughs are included in this appendix as Figures F.1-F.56. The dynamic stiffness spectral estimates (top graph), and the partial and multiple coherences of the derived dynamic compliance estimate (bottom graph) are included in each figure. Welch's periodogram method was used to estimate the power spectral density and coherence functions [8]. In Chapter 6, the number of data points included in the FFT calculation was defined as N_{FFT}, the length of the Hanning windowing function as N_{WND}, and the number of overlapped samples as N_{OVL}. The odd numbered figures contain the spectral analysis results with $N_{FFT} = 8192$, $N_{WND} = 8192$, and $N_{OVL} = 4096$ ($N_{MNS} = 5$ overlapping data segments), whereas the even numbered figures contain the results with $N_{FFT} = 8192$, $N_{WND} = 2048$, and $N_{OVL} = 1536$ ($N_{MNS} = 45$). Each line shown in the graph is the mean value of three estimates taken with different perturbation levels, 1.5N, 2.25N, 3.0N, 3.75N, and 4.5N (as described in Chapter 6, this sequence was repeated three times at each test condition). Nonlinear least-squares optimizations were used to define inertial, damping, and stiffness parameters for a linear second-order model of the dynamic stiffness spectral estimates. Two model structures were considered: 1. symmetric mass matrix, asymmetric damping and stiffness matrices; 2. symmetric mass, damping, and stiffness matrices. The results for both $N_{MNS} = 5$ and $N_{MNS} = 45$ are given in Figures F.57-F.64, which display the major and minor-axis properties (top graph), and the Variance Accounted For and R^2 of the model (bottom graph).

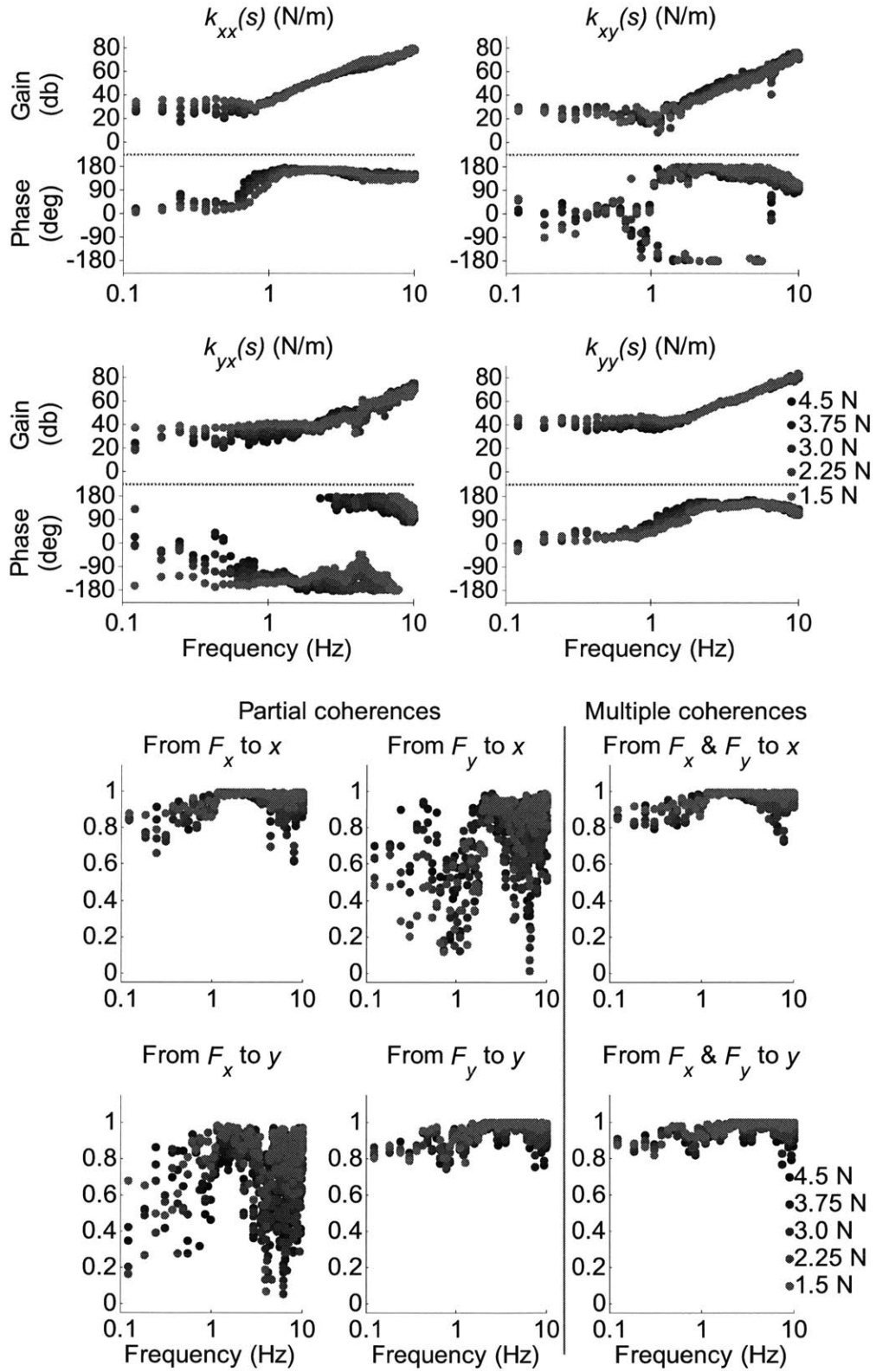

Figure F.1. Subject A, left arm, plastic arm trough, 5 overlaps: dynamic stiffness spectral estimates (top), and partial and multiple coherences (bottom)

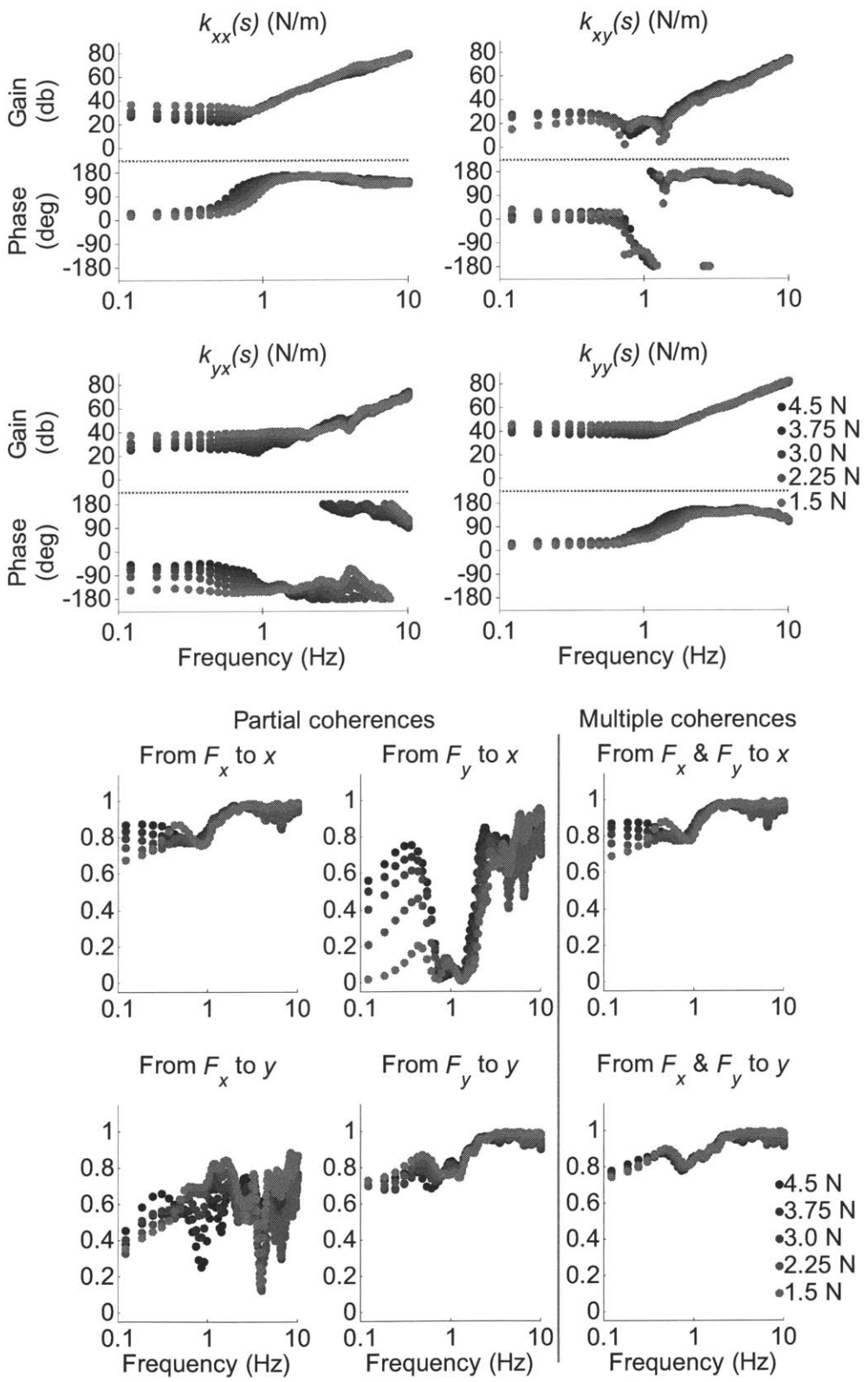

Figure F.2. Subject A, left arm, plastic arm trough, 45 overlaps: dynamic stiffness spectral estimates (top), and partial and multiple coherences (bottom)

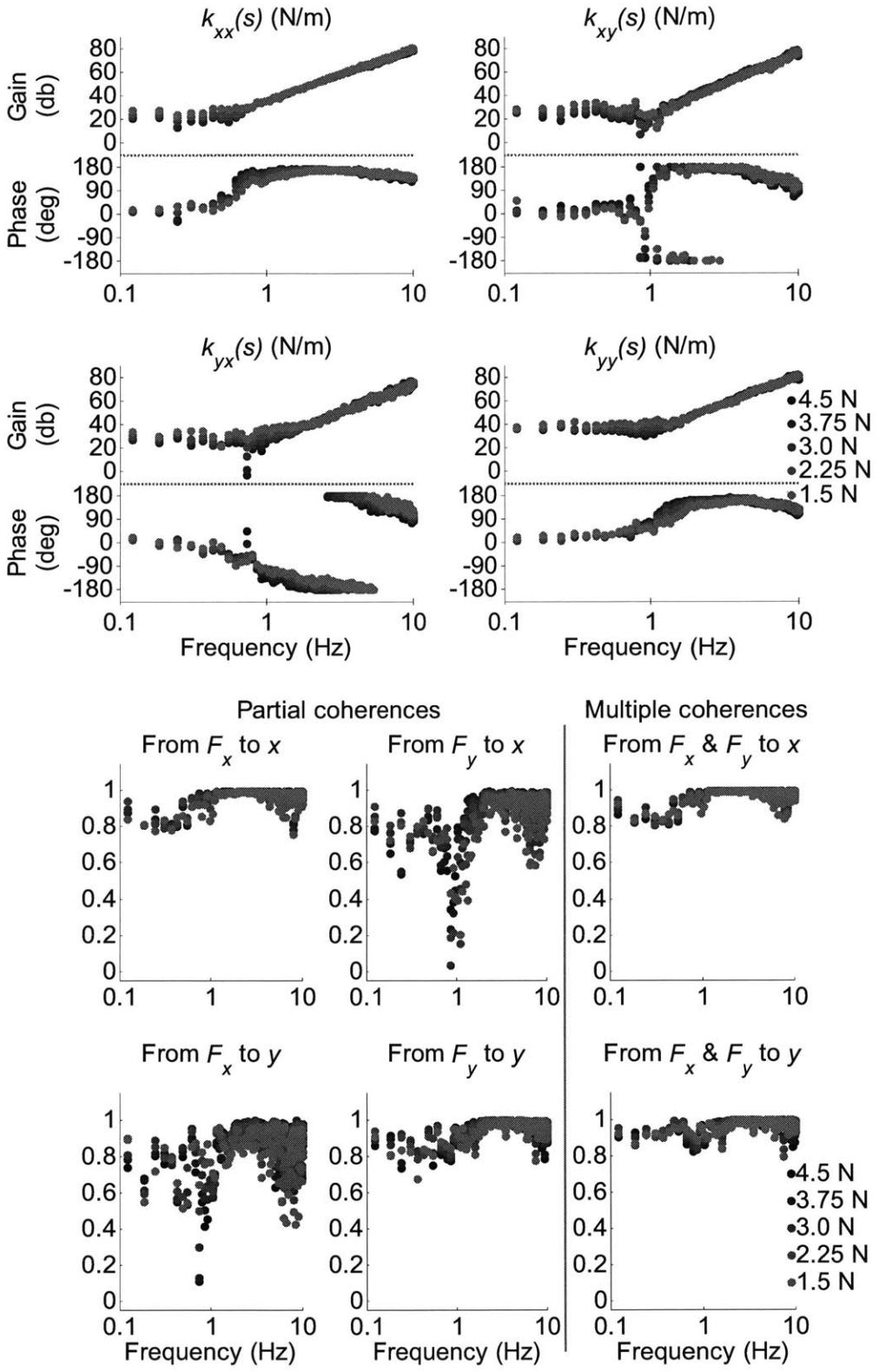

Figure F.3. Subject A, left arm, carbon-fiber arm trough, 5 overlaps: dynamic stiffness spectral estimates (top), and partial and multiple coherences (bottom)

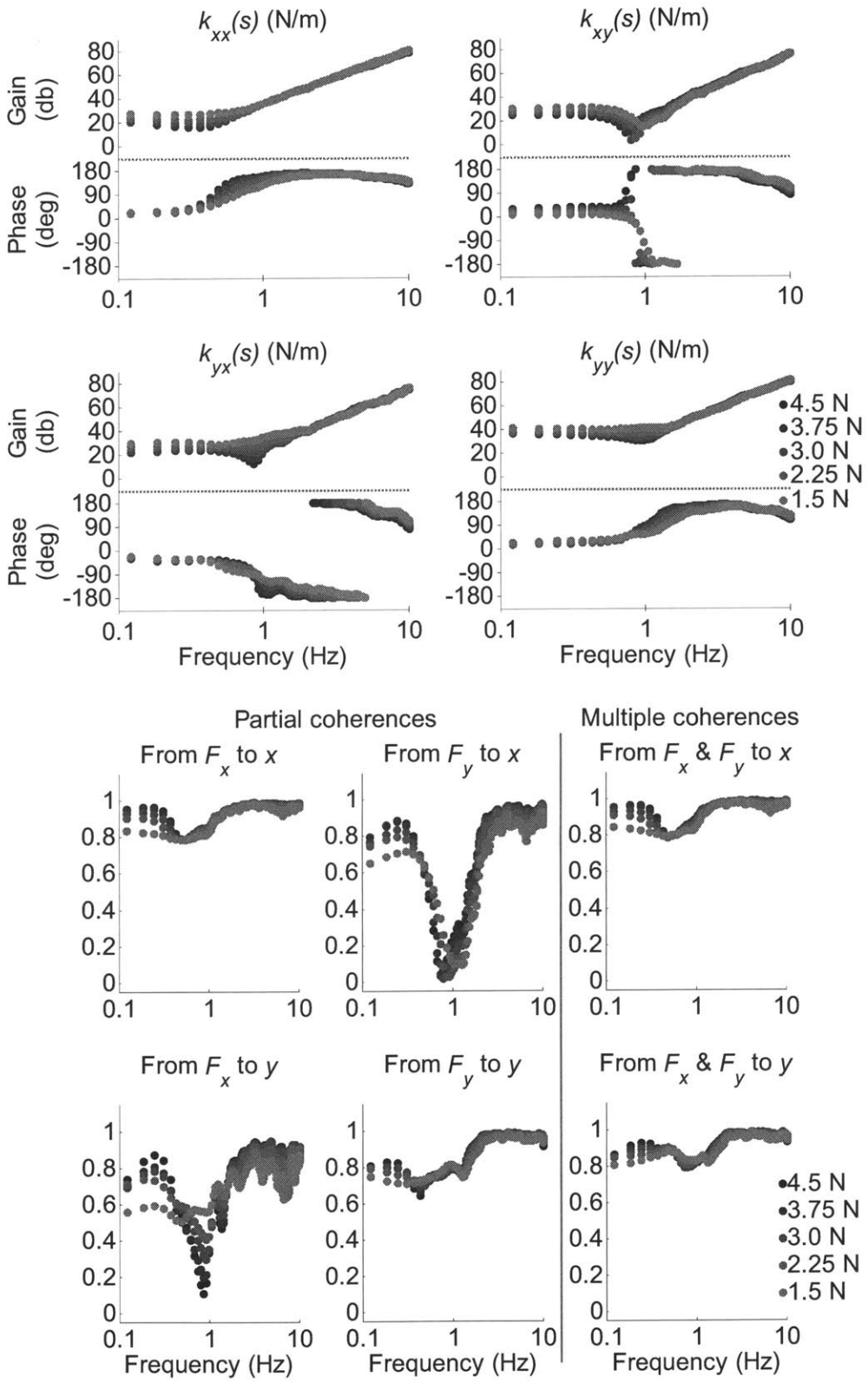

Figure F.4. Subject A, left arm, carbon-fiber arm trough, 45 overlaps: dynamic stiffness spectral estimates (top), and partial and multiple coherences (bottom)

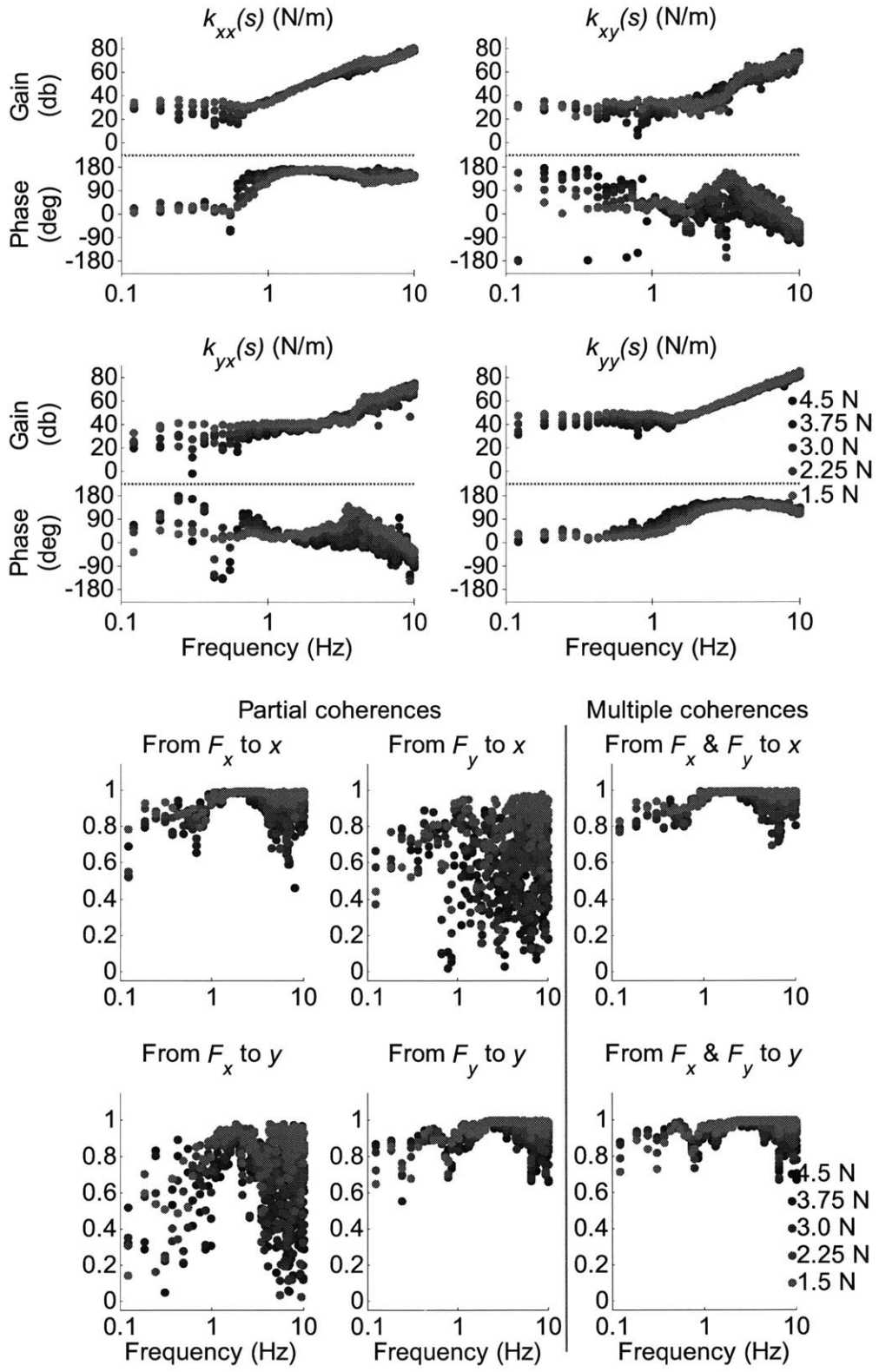

Figure F.5. Subject A, right arm, plastic arm trough, 5 overlaps: dynamic stiffness spectral estimates (top), and partial and multiple coherences (bottom)

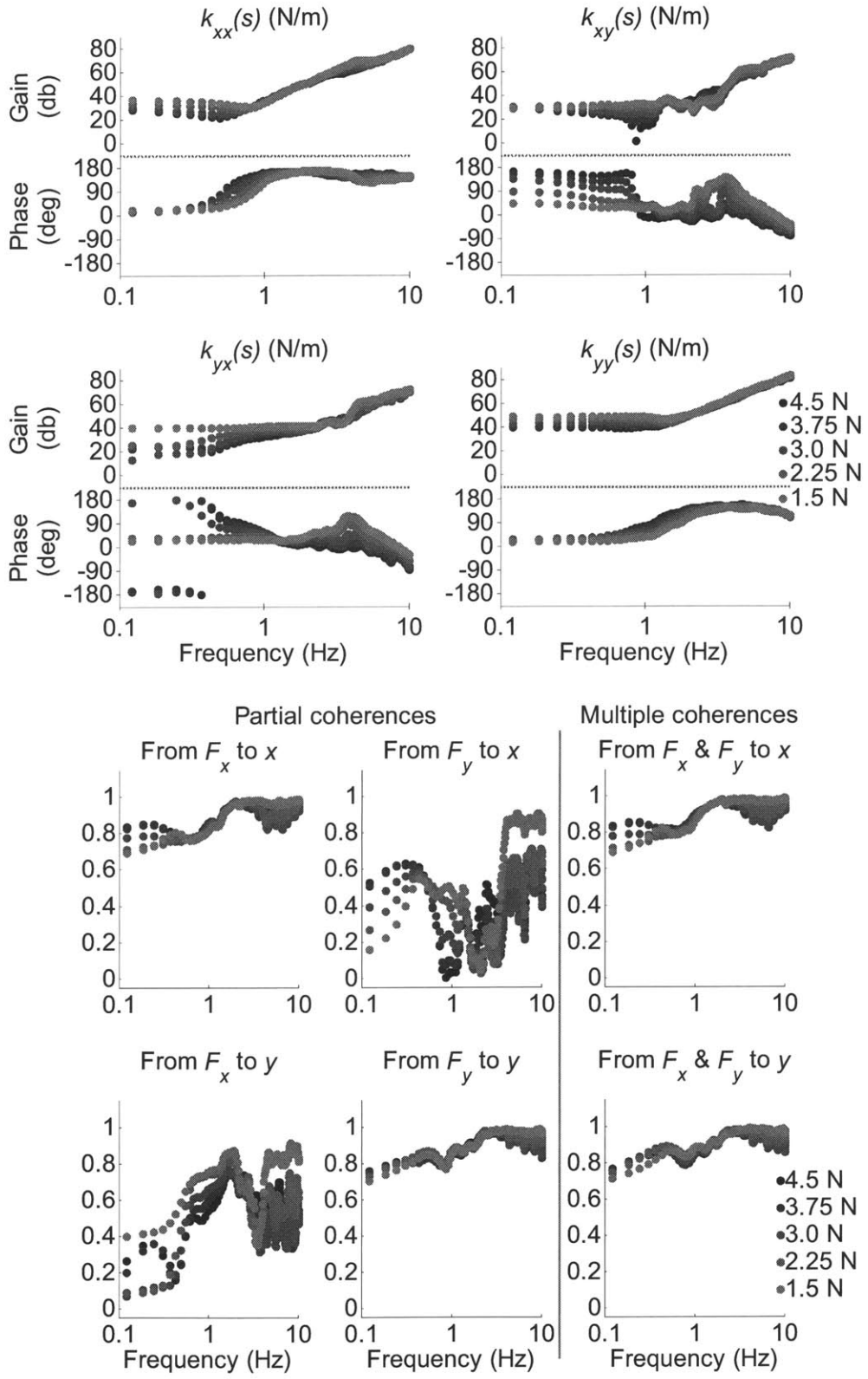

Figure F.6. Subject A, right arm, plastic arm trough, 45 overlaps: dynamic stiffness spectral estimates (top), and partial and multiple coherences (bottom)

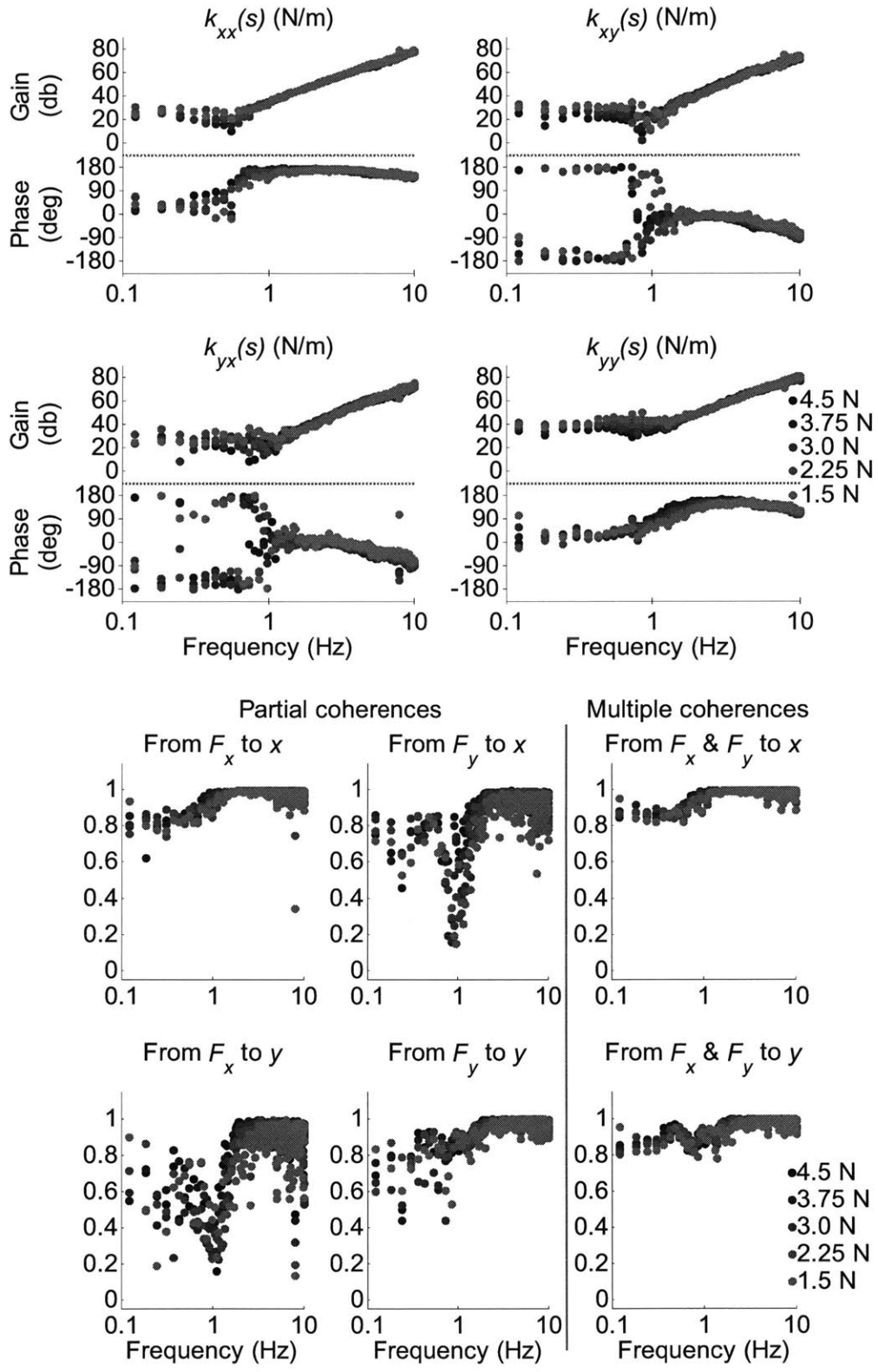

Figure F.7. Subject A, right arm, carbon-fiber arm trough, 5 overlaps: dynamic stiffness spectral estimates (top), and partial and multiple coherences (bottom)

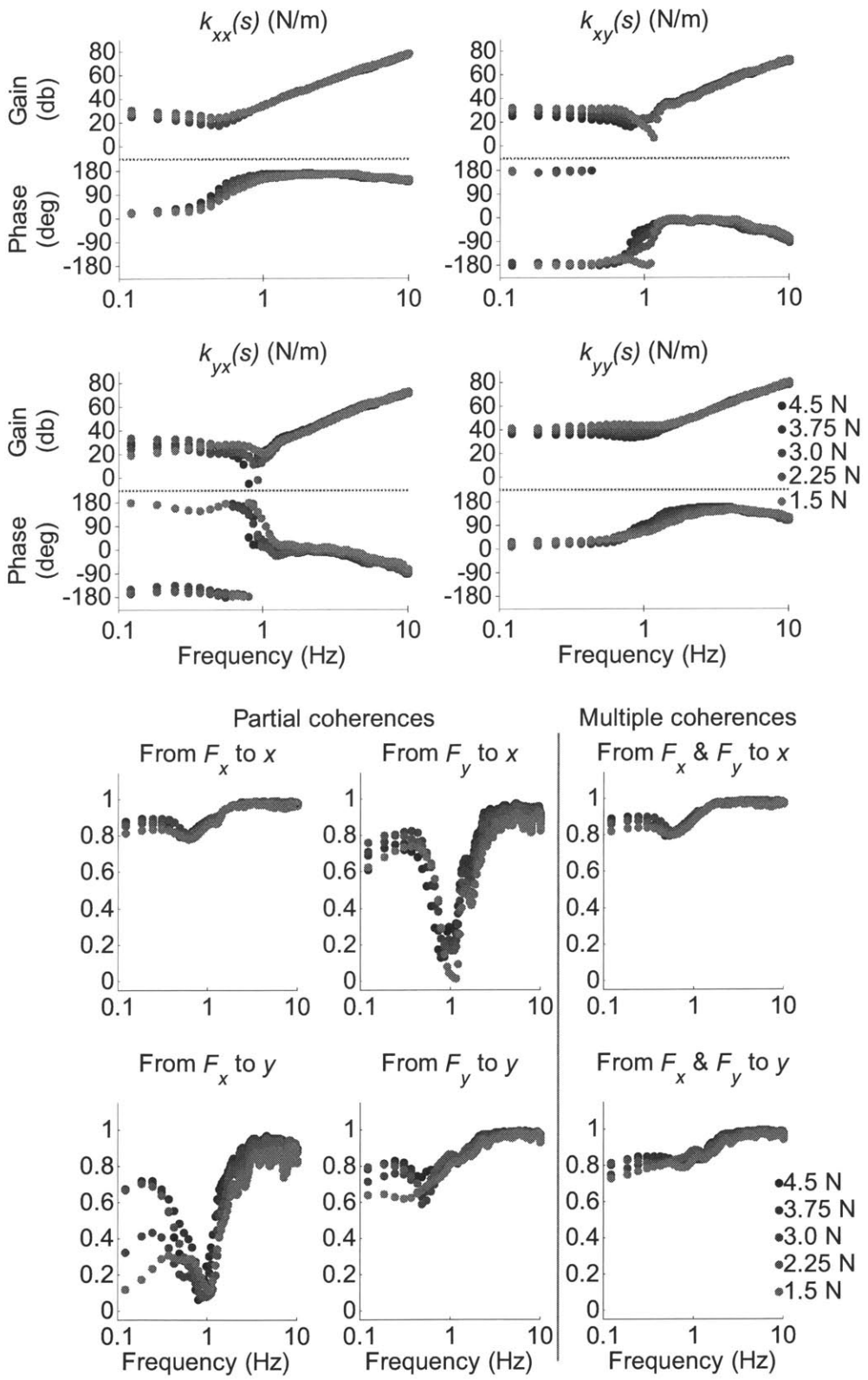

Figure F.8. Subject A, right arm, carbon-fiber arm trough, 45 overlaps: dynamic stiffness spectral estimates (top), and partial and multiple coherences (bottom)

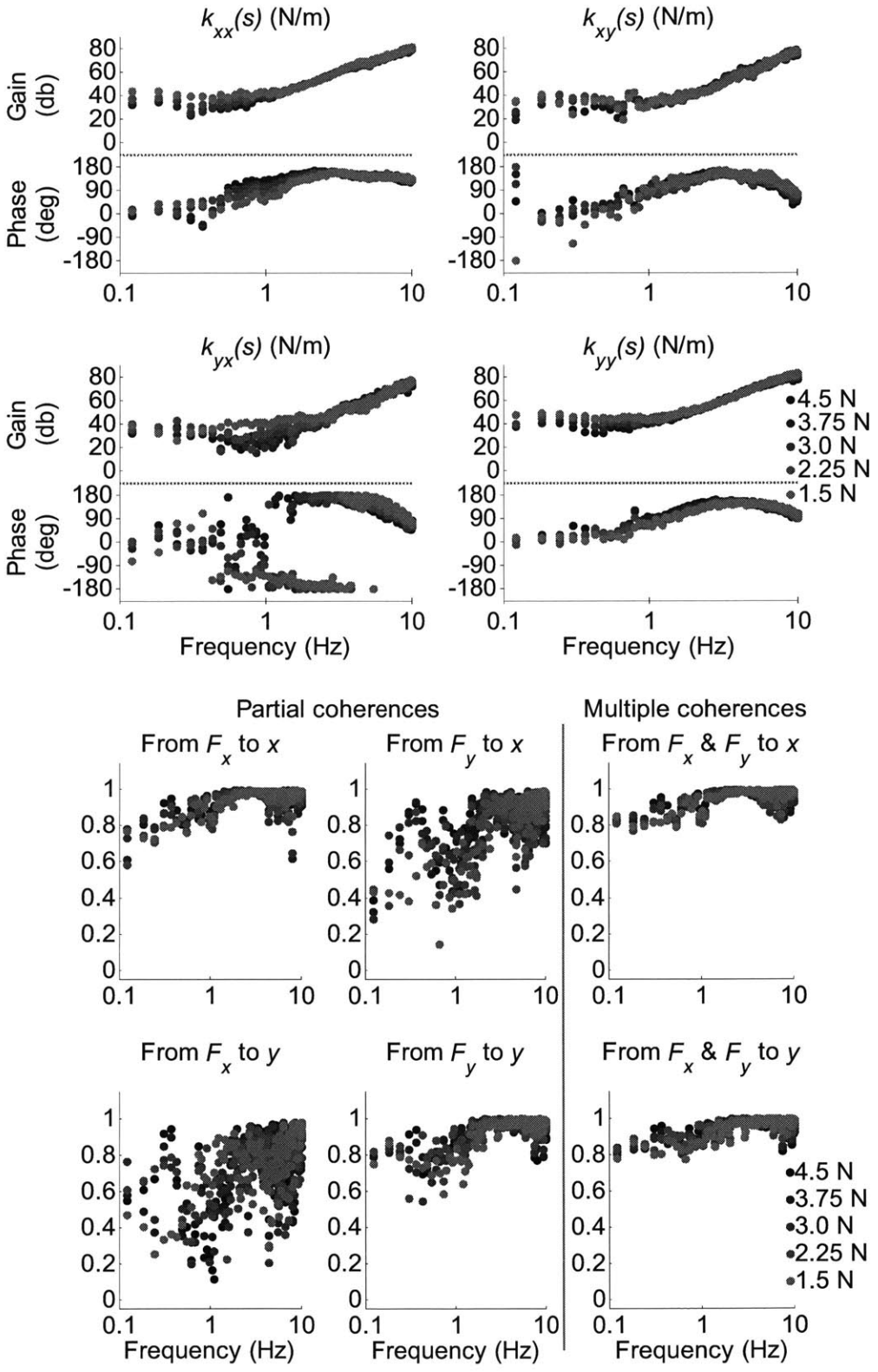

Figure F.9. Subject B, left arm, plastic arm trough, 5 overlaps: dynamic stiffness spectral estimates (top), and partial and multiple coherences (bottom)

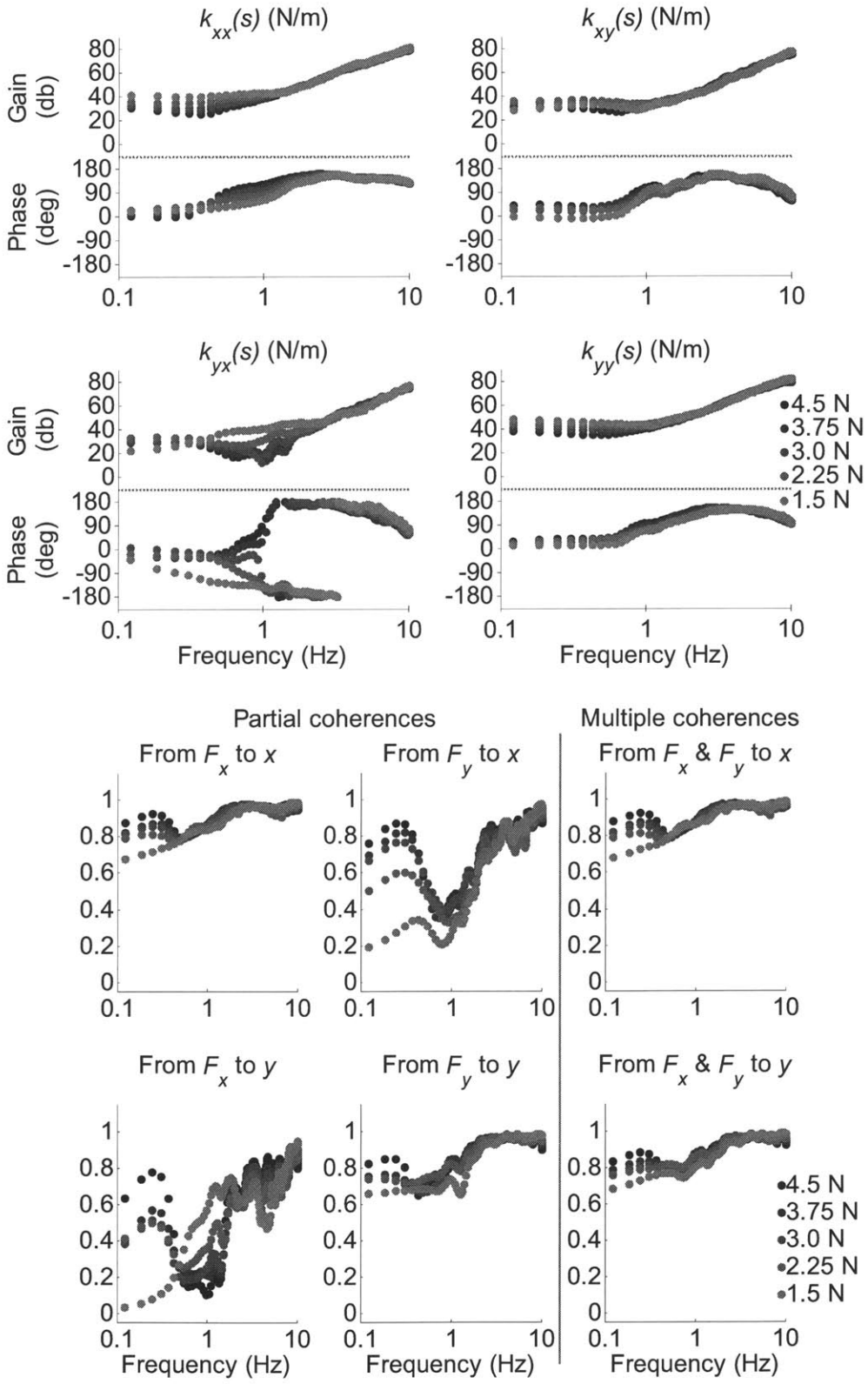

Figure F.10. Subject B, left arm, plastic arm trough, 45 overlaps: dynamic stiffness spectral estimates (top), and partial and multiple coherences (bottom)

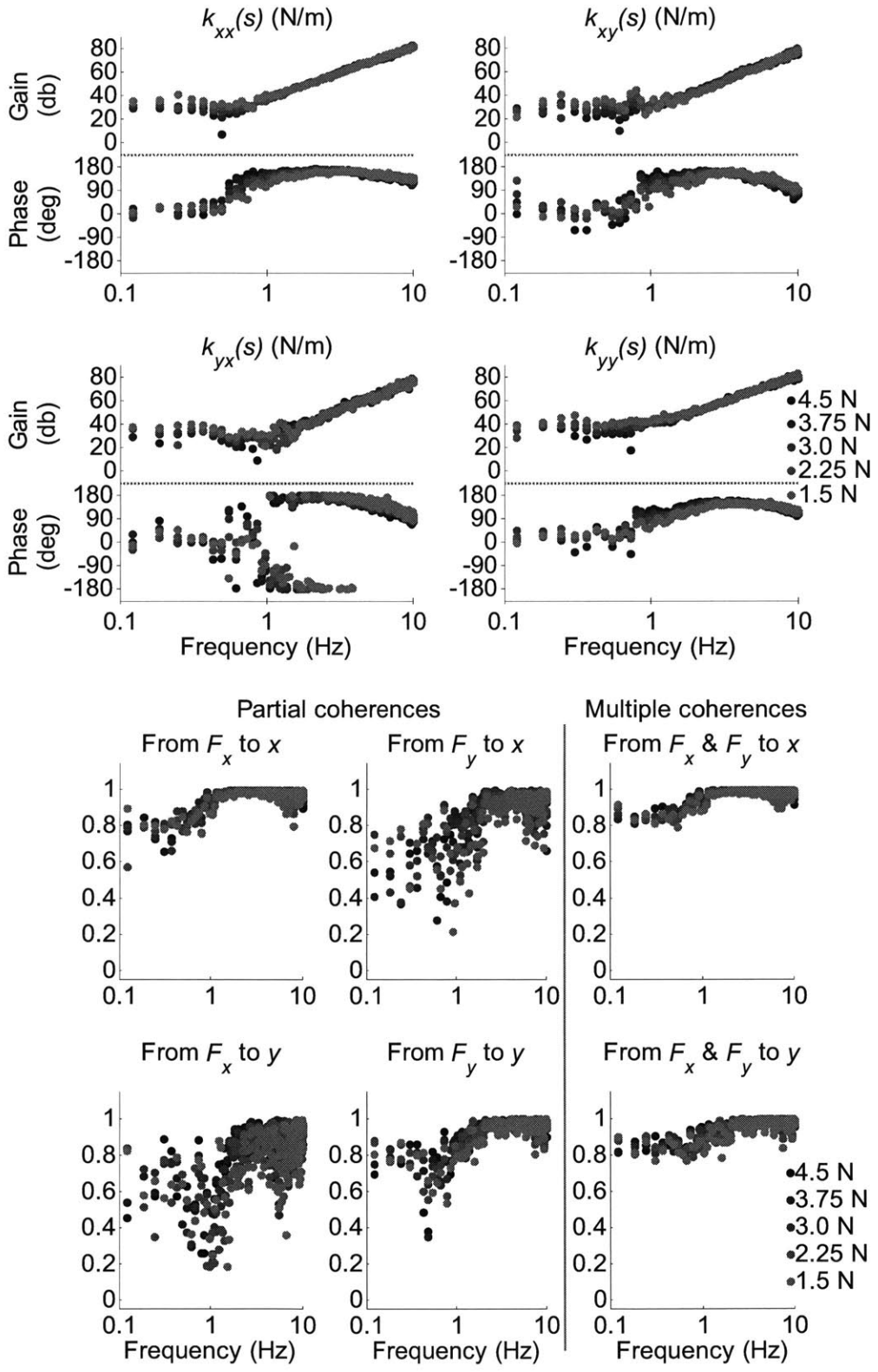

Figure F.11. Subject B, left arm, carbon-fiber arm trough, 5 overlaps: dynamic stiffness spectral estimates (top), and partial and multiple coherences (bottom)

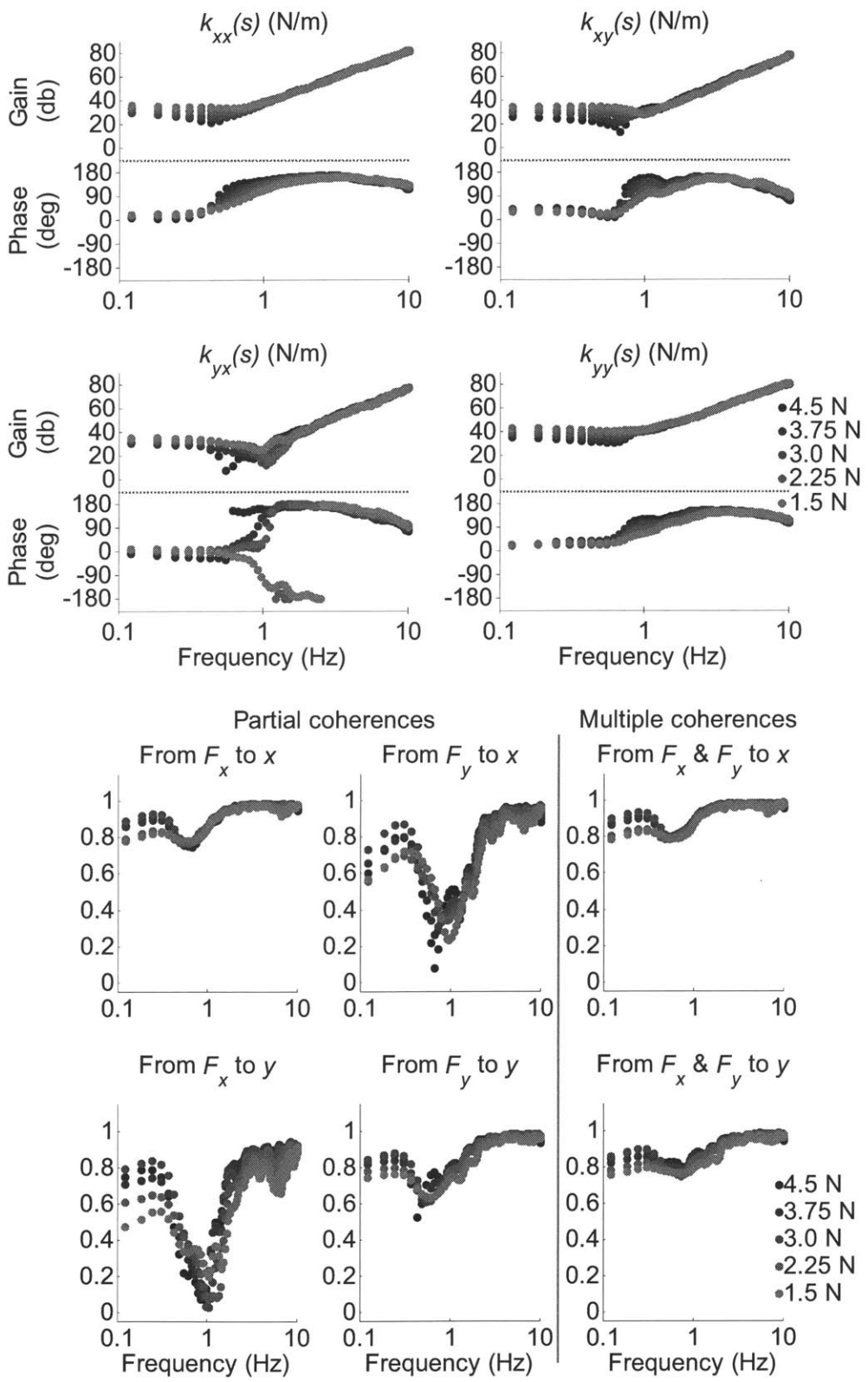

Figure F.12. Subject B, left arm, carbon-fiber arm trough, 45 overlaps: dynamic stiffness spectral estimates (top), and partial and multiple coherences (bottom)

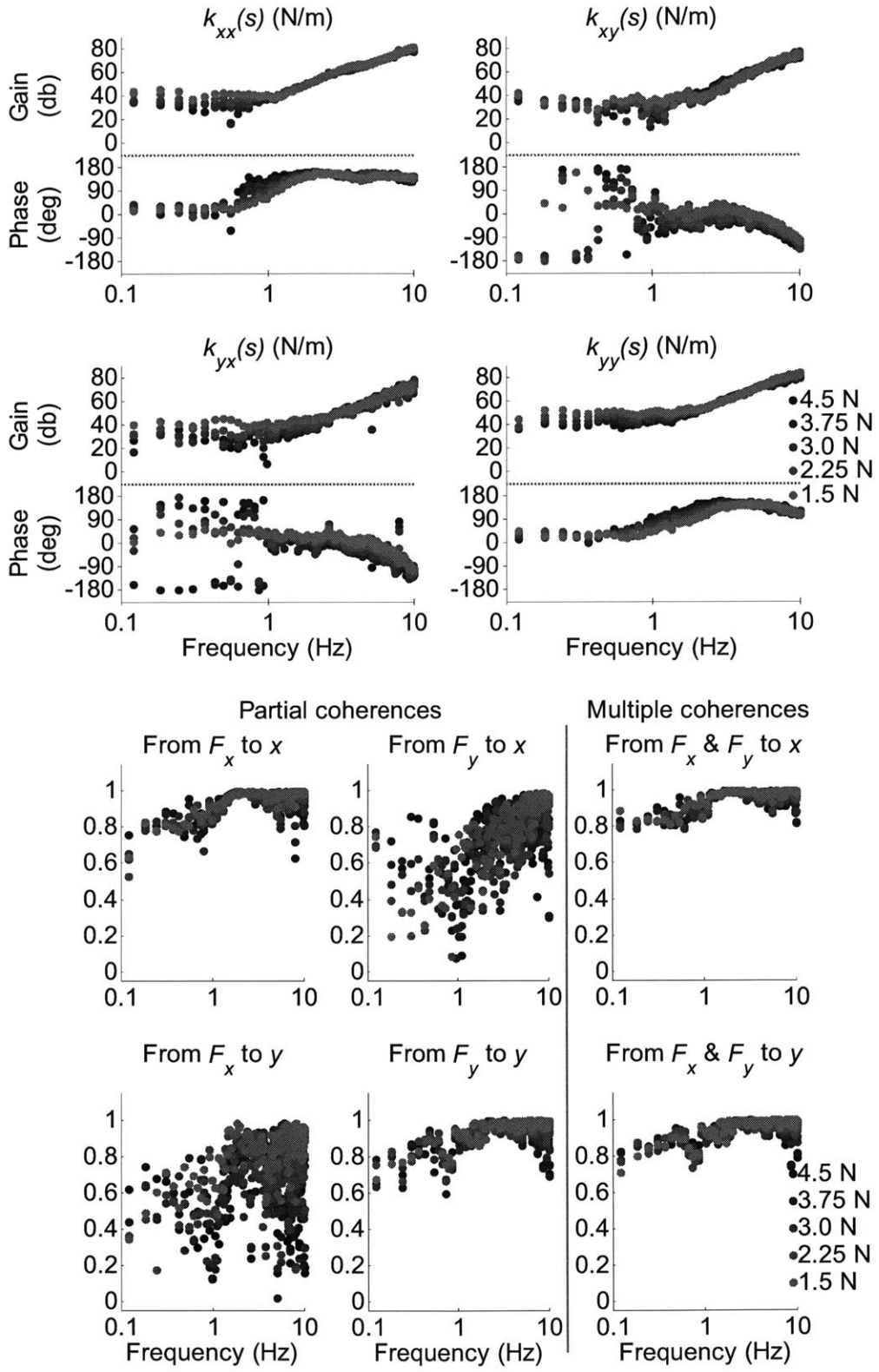

Figure F.13. Subject B, right arm, plastic arm trough, 5 overlaps: dynamic stiffness spectral estimates (top), and partial and multiple coherences (bottom)

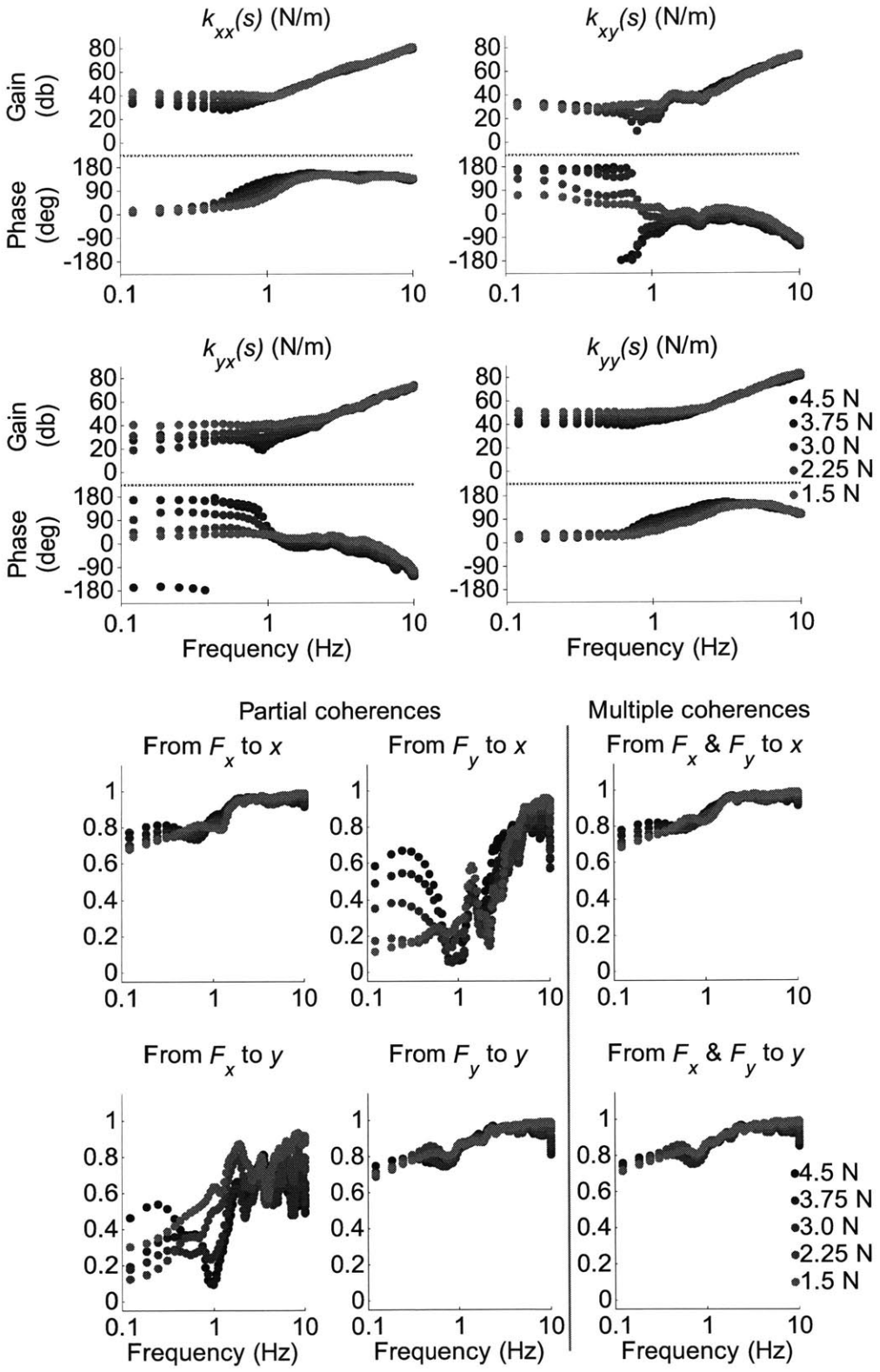

Figure F.14. Subject B, right arm, plastic arm trough, 45 overlaps: dynamic stiffness spectral estimates (top), and partial and multiple coherences (bottom)

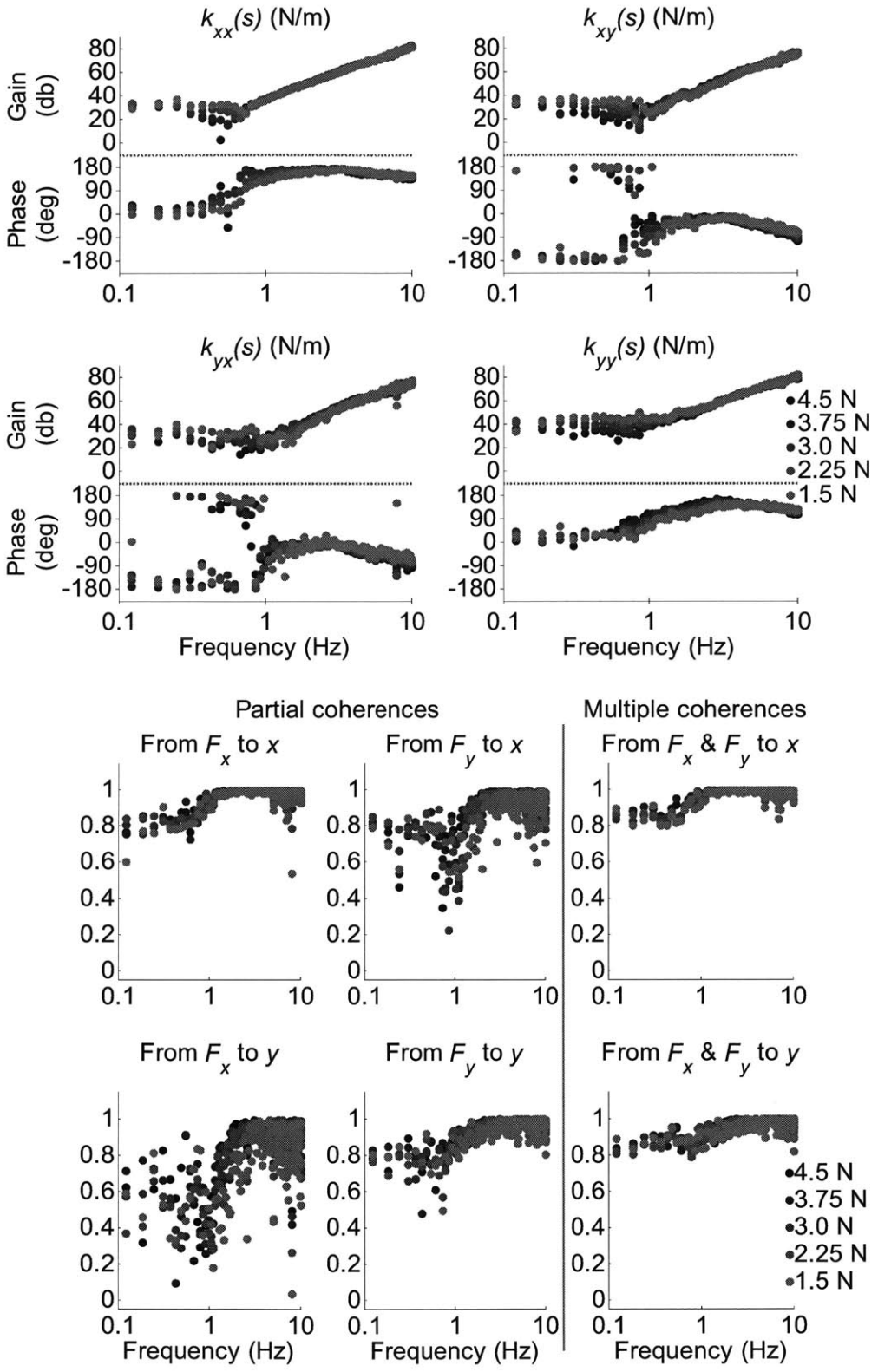

Figure F.15. Subject B, right arm, carbon-fiber arm trough, 5 overlaps: dynamic stiffness spectral estimates (top), and partial and multiple coherences (bottom)

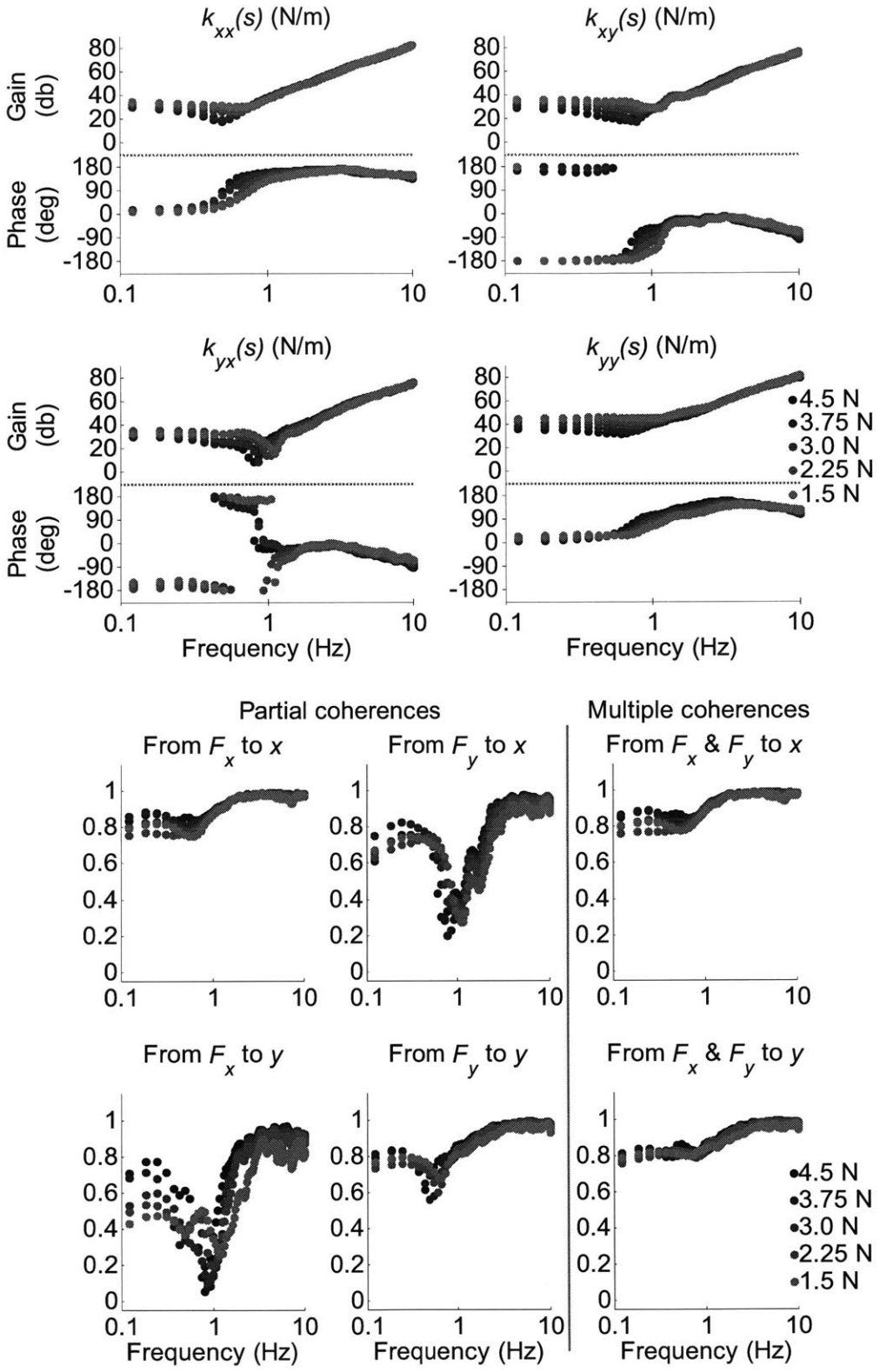

Figure F.16. Subject B, right arm, carbon-fiber arm trough, 45 overlaps: dynamic stiffness spectral estimates (top), and partial and multiple coherences (bottom)

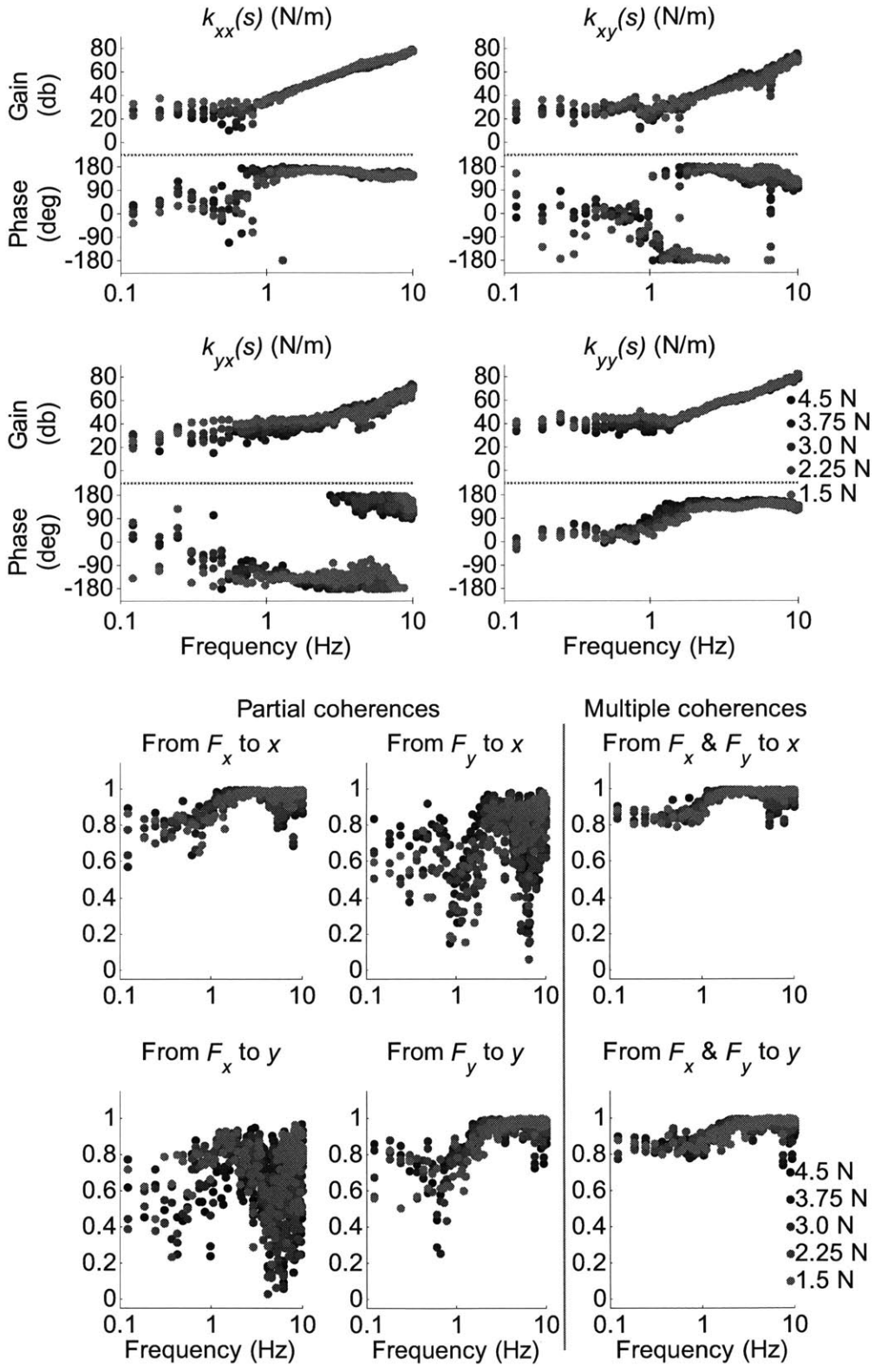

Figure F.17. Subject C, left arm, plastic arm trough, 5 overlaps: dynamic stiffness spectral estimates (top), and partial and multiple coherences (bottom)

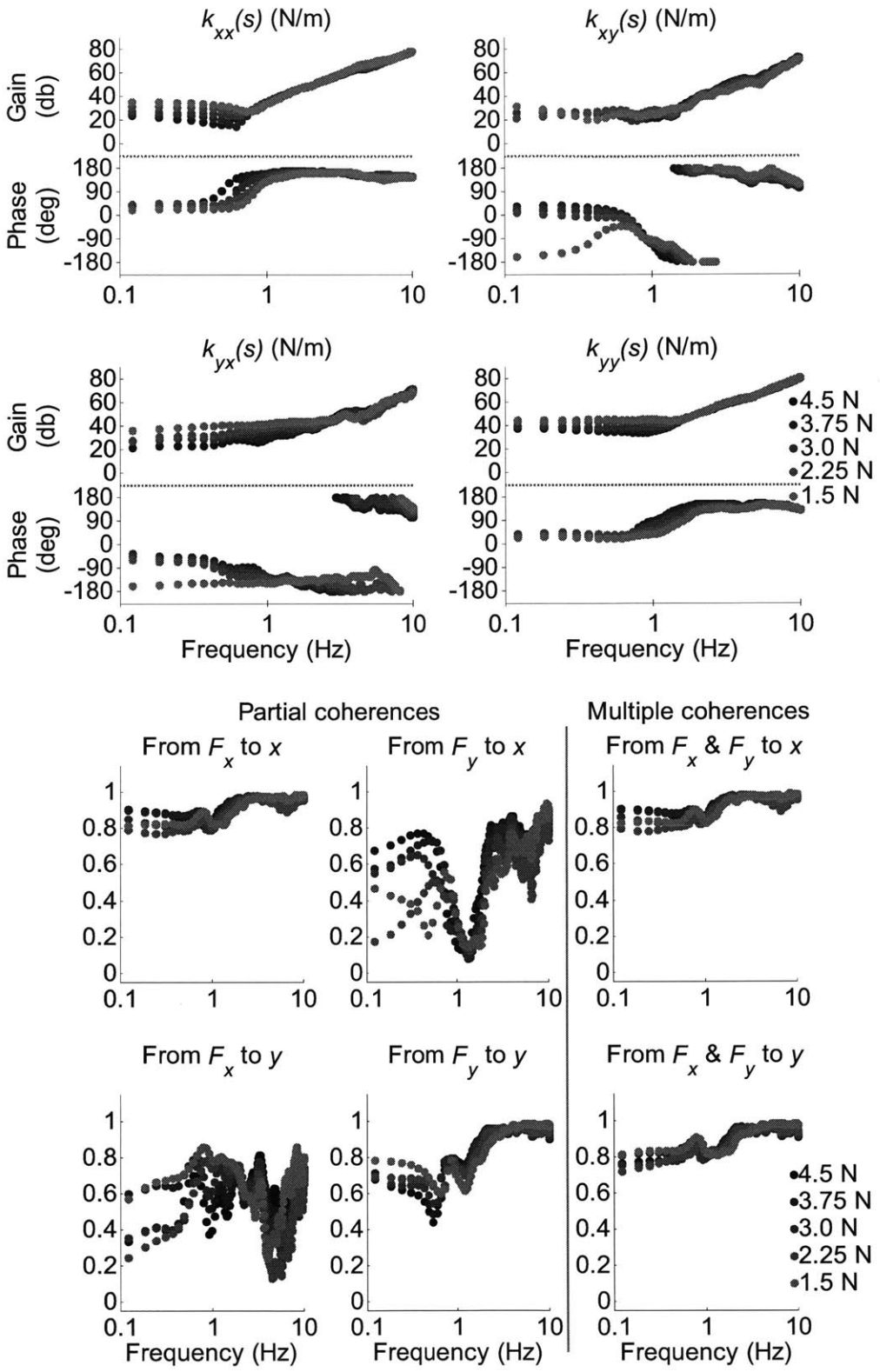

Figure F.18. Subject C, left arm, plastic arm trough, 45 overlaps: dynamic stiffness spectral estimates (top), and partial and multiple coherences (bottom)

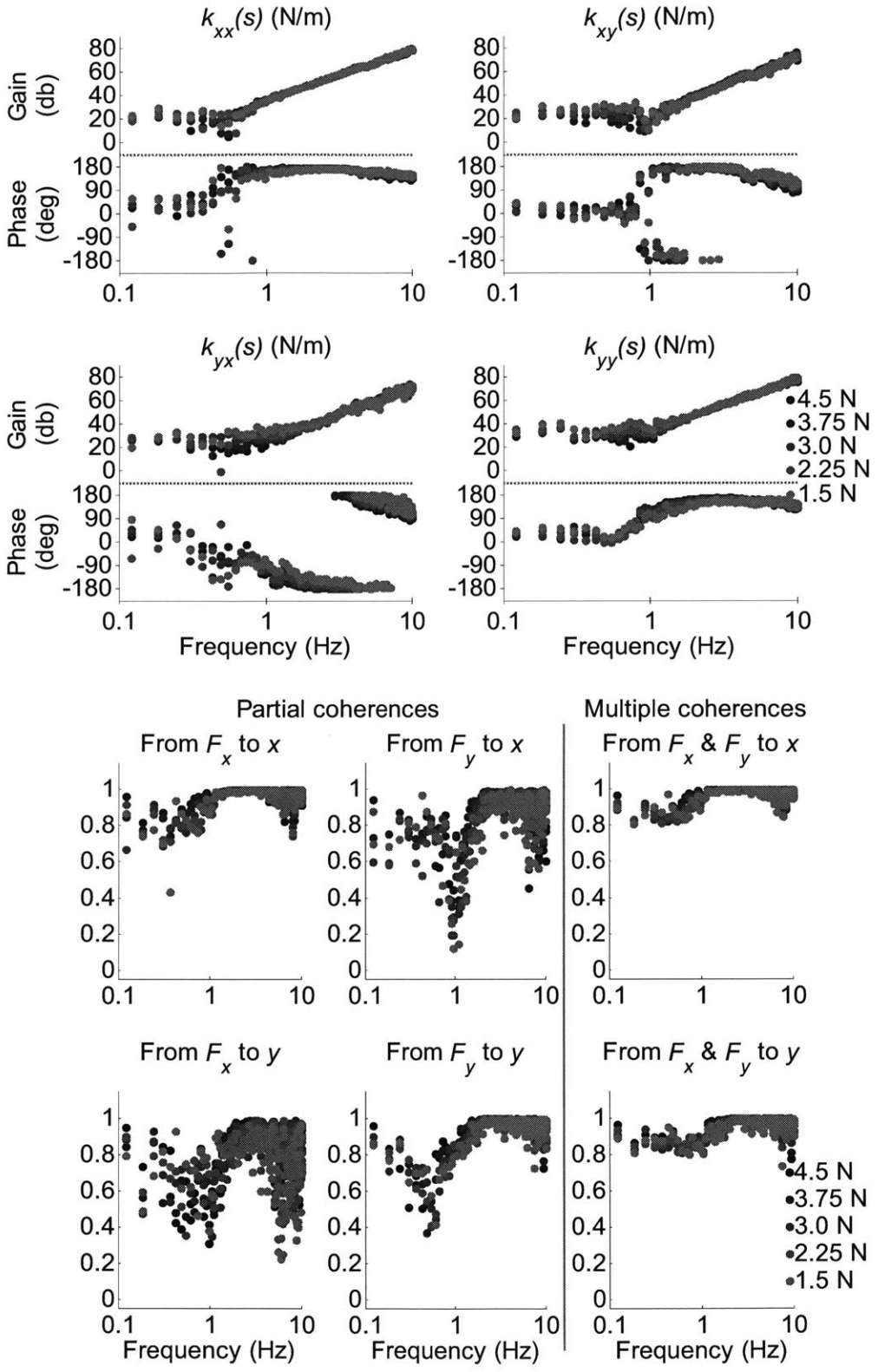

Figure F.19. Subject C, left arm, carbon-fiber arm trough, 5 overlaps: dynamic stiffness spectral estimates (top), and partial and multiple coherences (bottom)

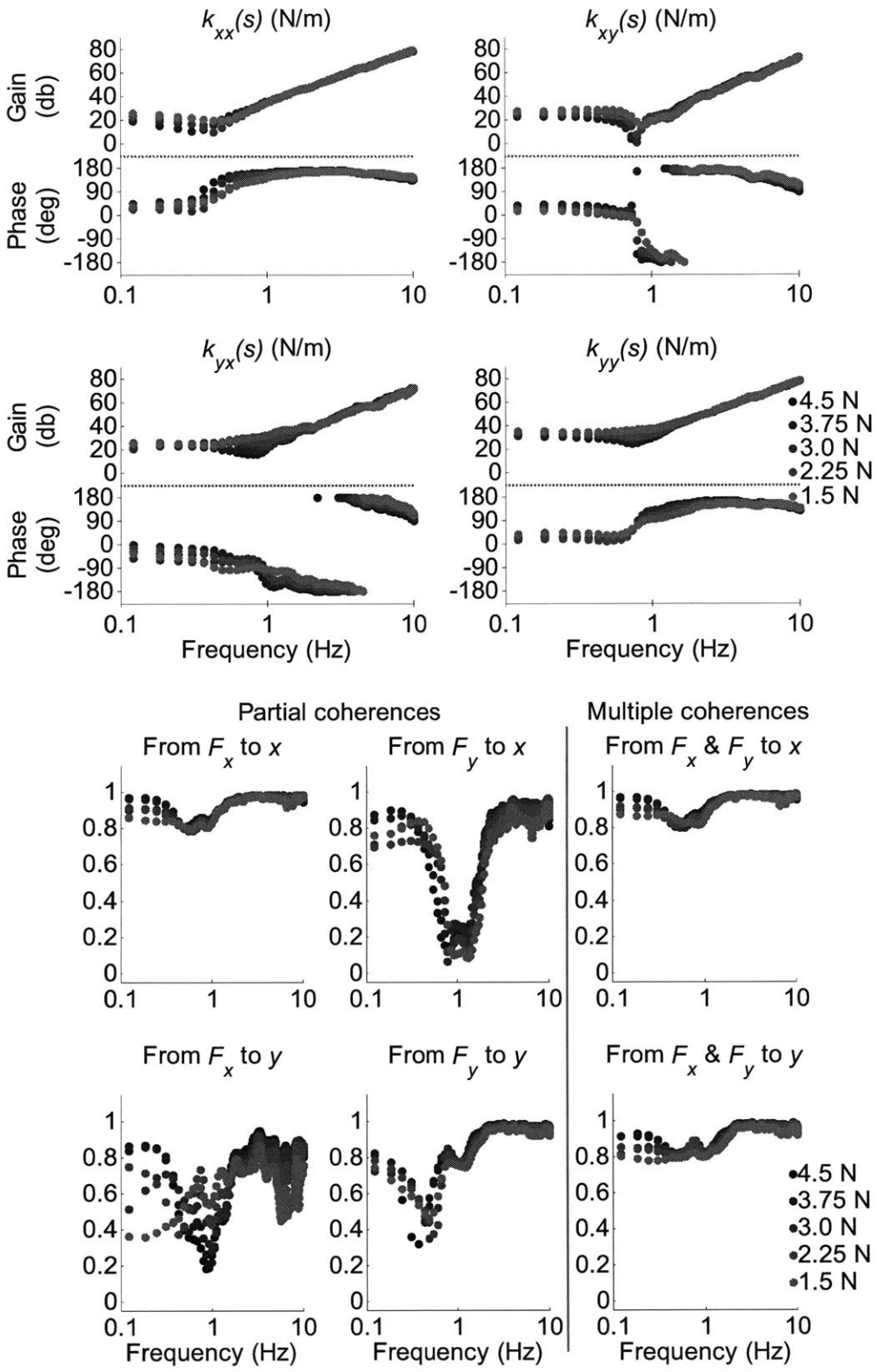

Figure F.20. Subject C, left arm, carbon-fiber arm trough, 45 overlaps: dynamic stiffness spectral estimates (top), and partial and multiple coherences (bottom)

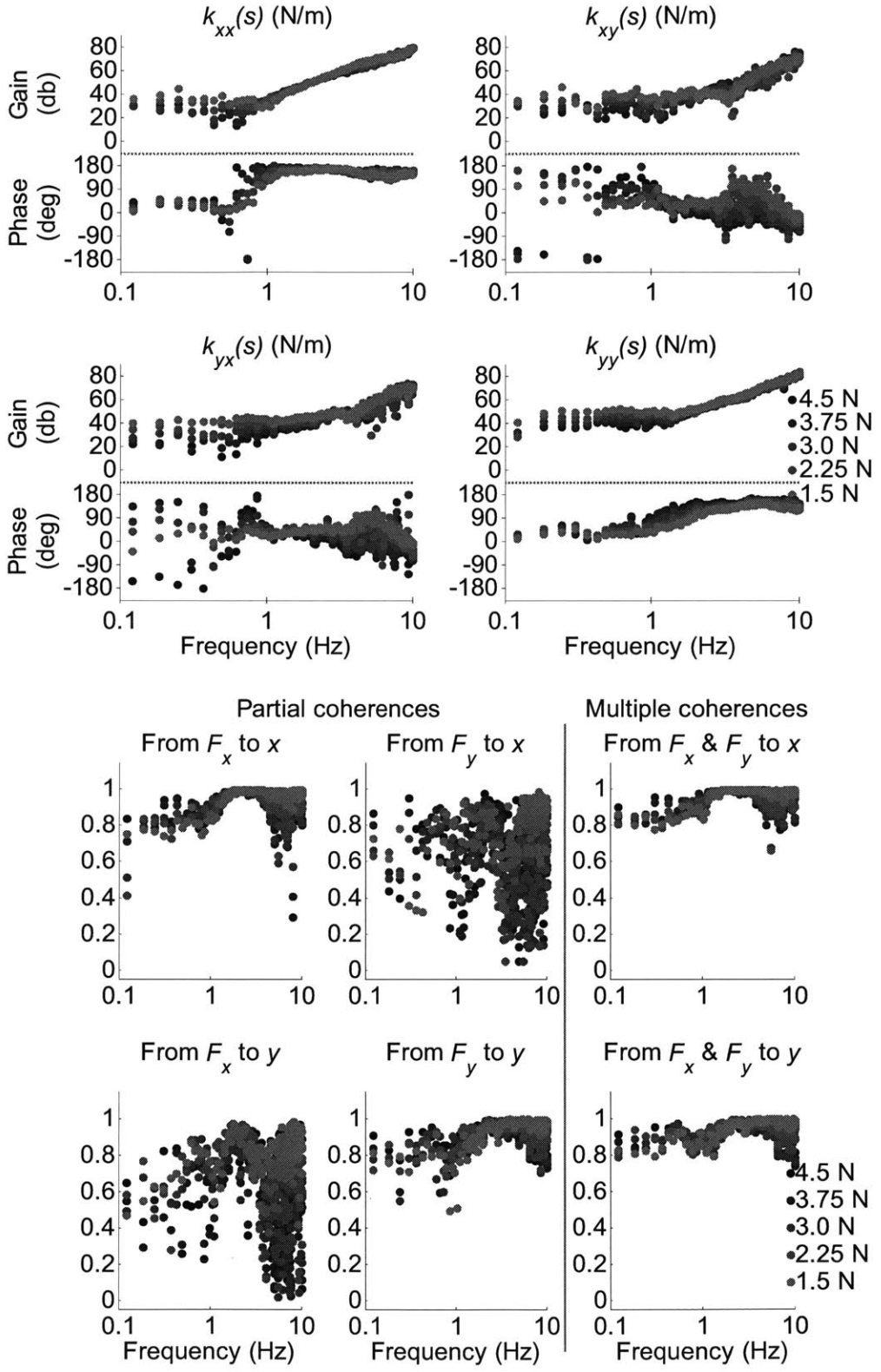

Figure F.21. Subject C, right arm, plastic arm trough, 5 overlaps: dynamic stiffness spectral estimates (top), and partial and multiple coherences (bottom)

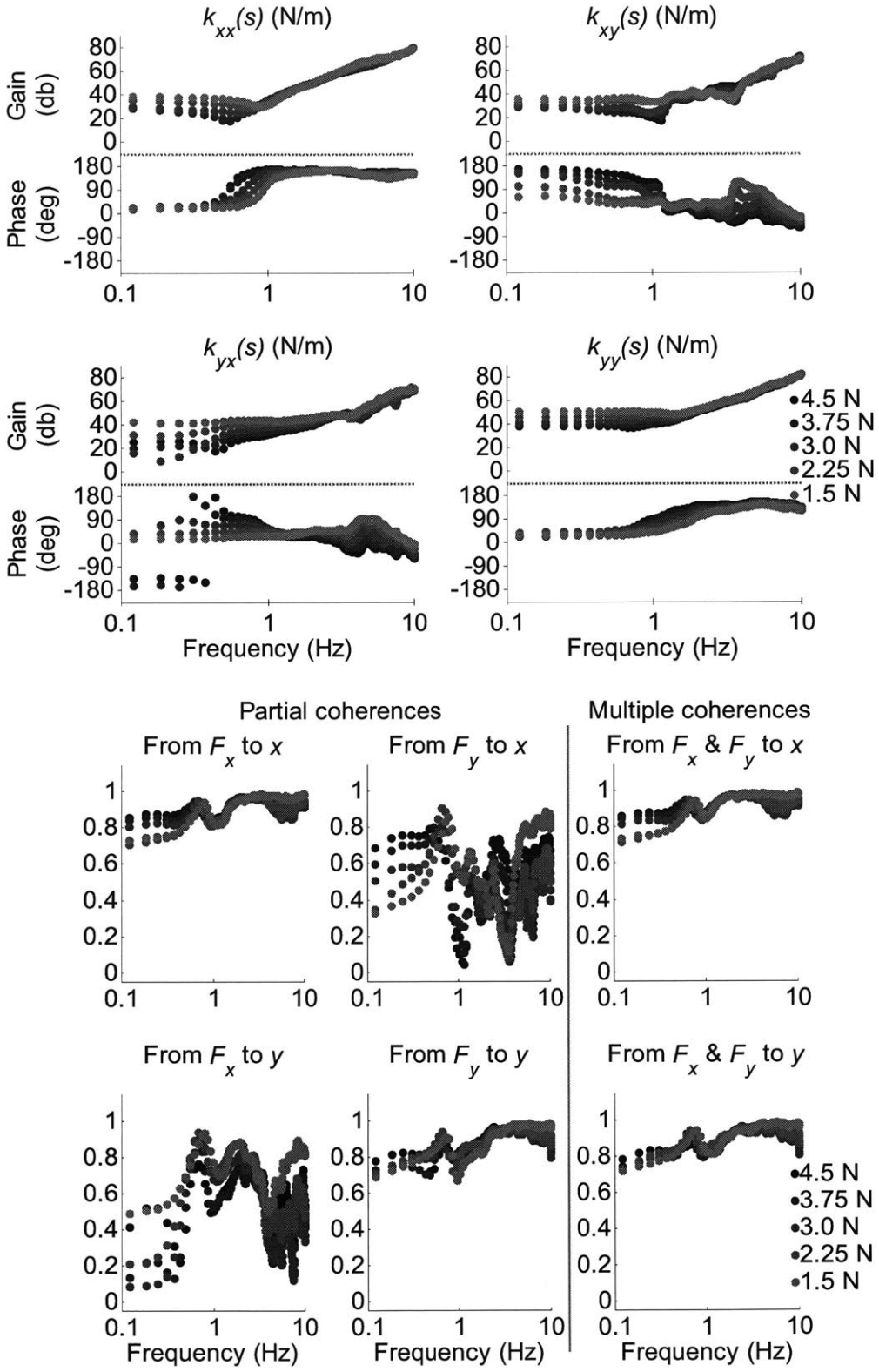

Figure F.22. Subject C, right arm, plastic arm trough, 45 overlaps: dynamic stiffness spectral estimates (top), and partial and multiple coherences (bottom)

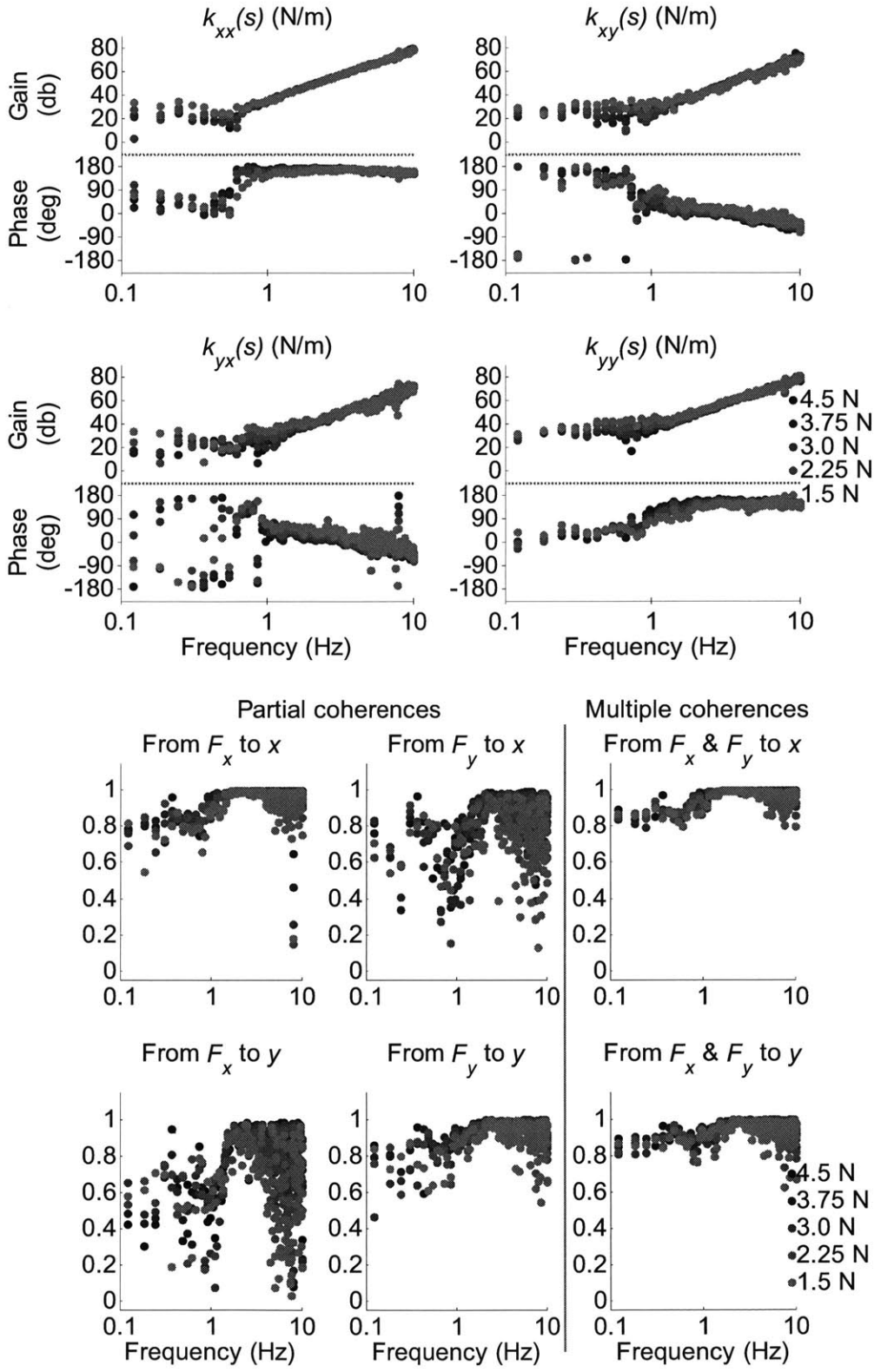

Figure F.23. Subject C, right arm, carbon-fiber arm trough, 5 overlaps: dynamic stiffness spectral estimates (top), and partial and multiple coherences (bottom)

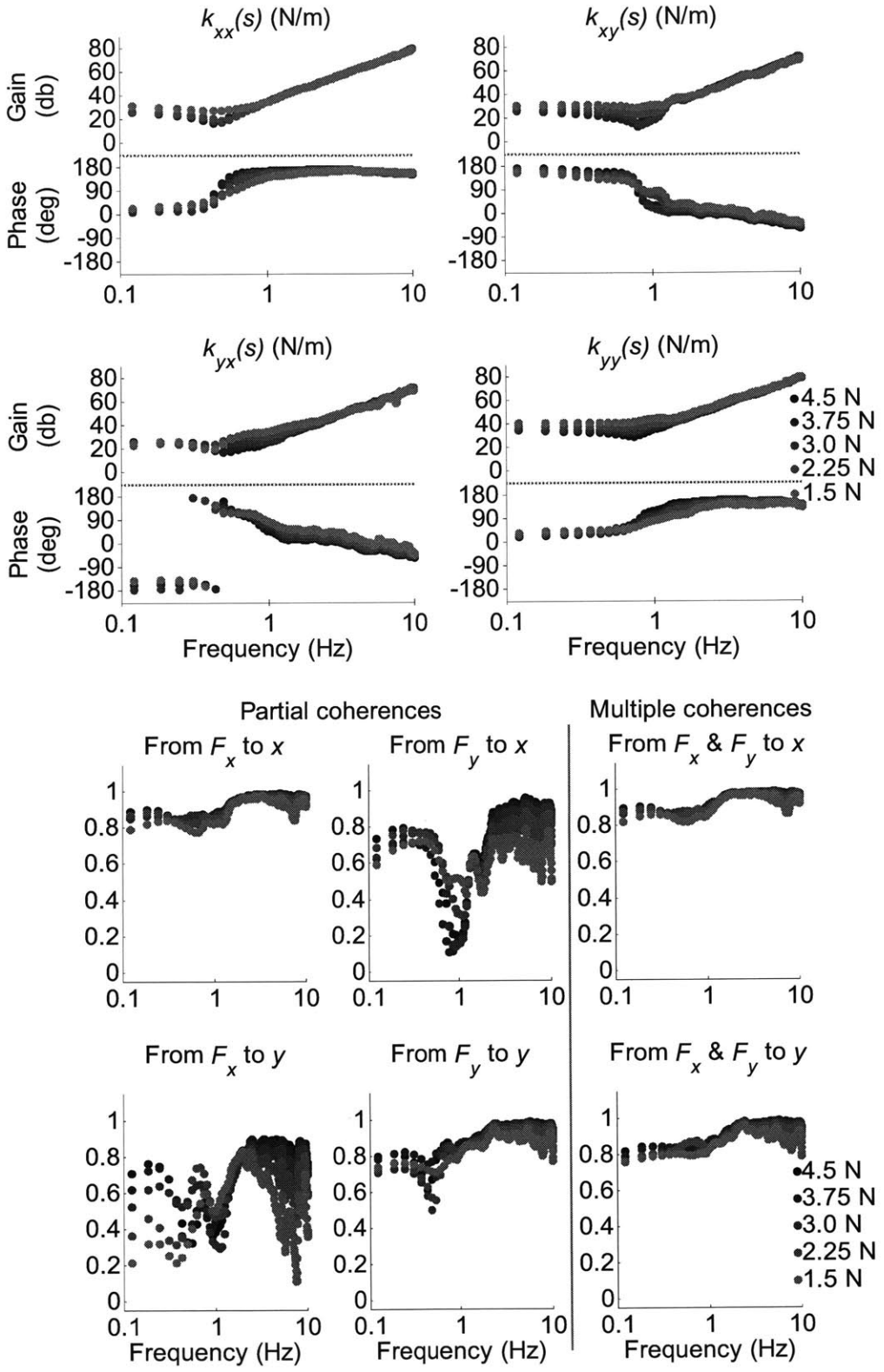

Figure F.24. Subject C, right arm, carbon-fiber arm trough, 45 overlaps: dynamic stiffness spectral estimates (top), and partial and multiple coherences (bottom)

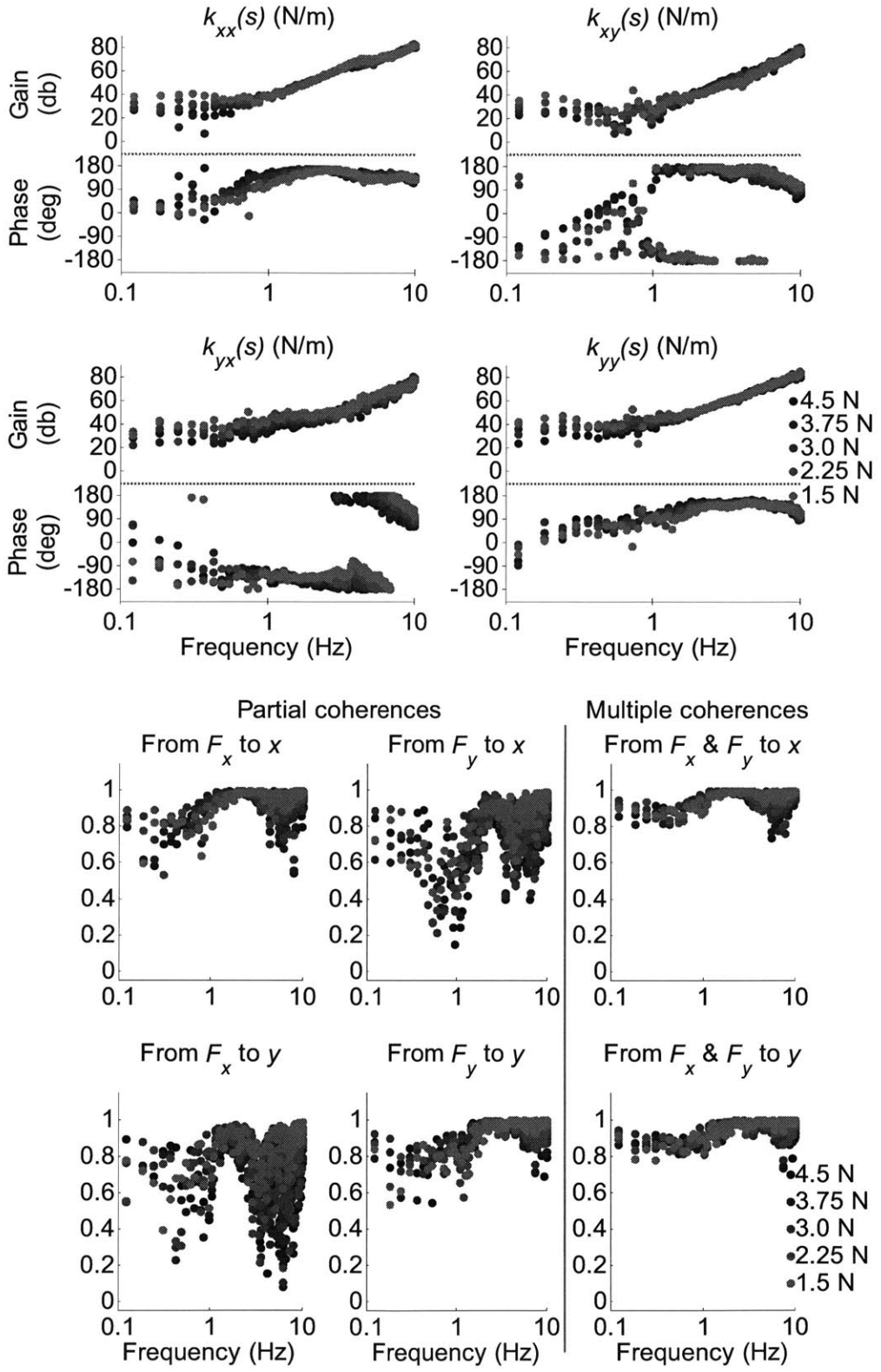

Figure F.25. Subject D, left arm, plastic arm trough, 5 overlaps: dynamic stiffness spectral estimates (top), and partial and multiple coherences (bottom)

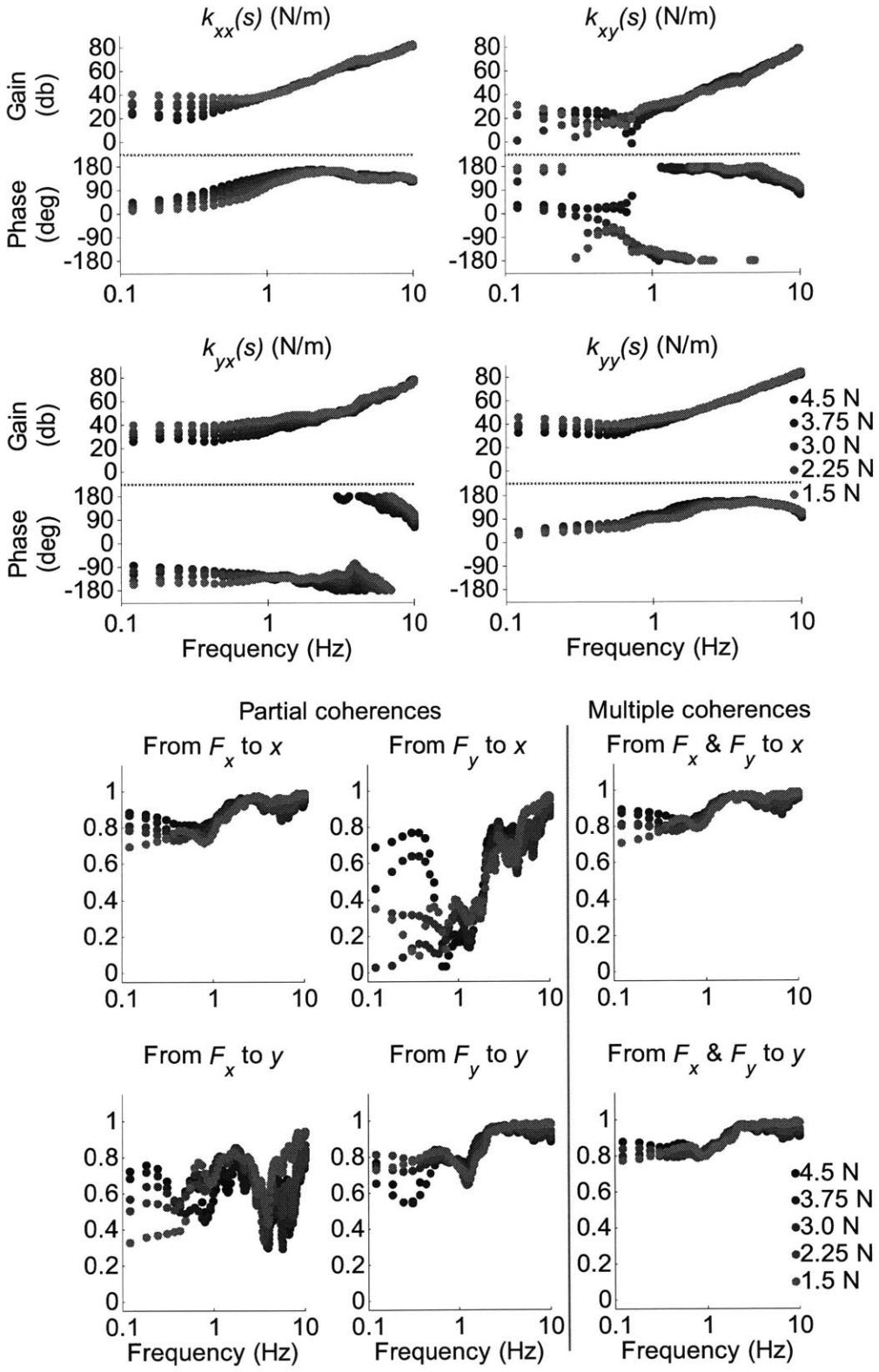

Figure F.26. Subject D, left arm, plastic arm trough, 45 overlaps: dynamic stiffness spectral estimates (top), and partial and multiple coherences (bottom)

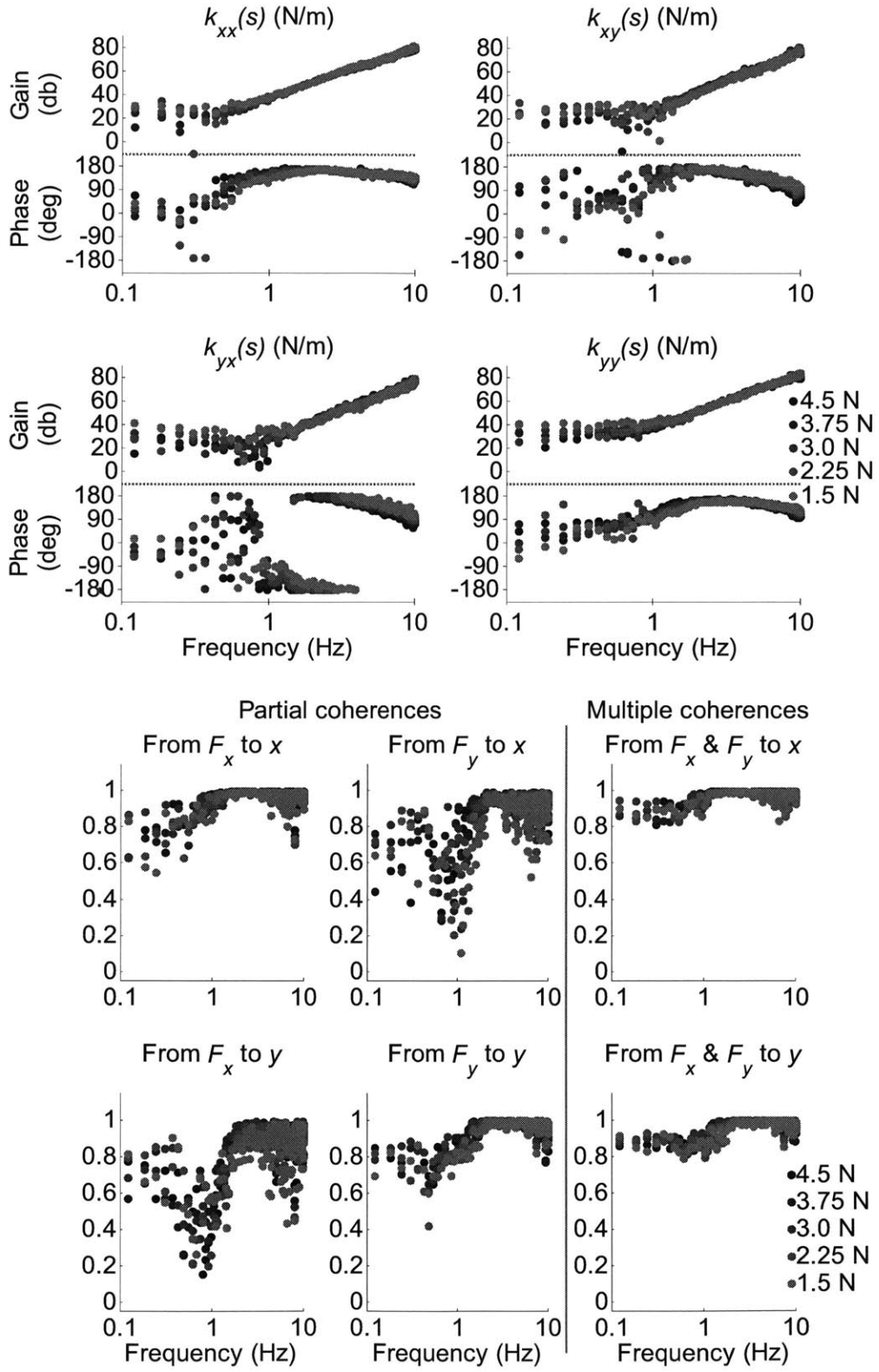

Figure F.27. Subject D, left arm, carbon-fiber arm trough, 5 overlaps: dynamic stiffness spectral estimates (top), and partial and multiple coherences (bottom)

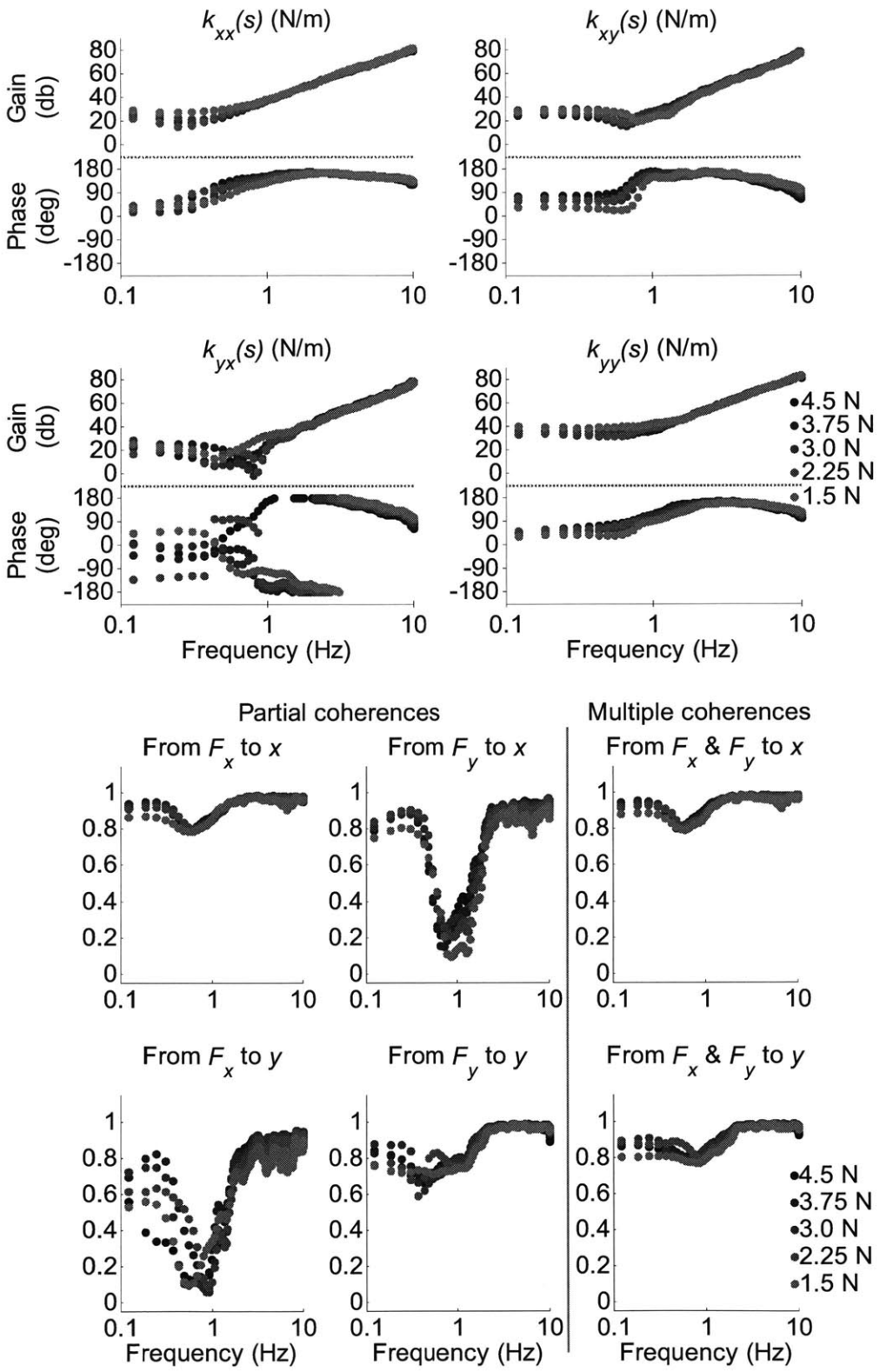

Figure F.28. Subject D, left arm, carbon-fiber arm trough, 45 overlaps: dynamic stiffness spectral estimates (top), and partial and multiple coherences (bottom)

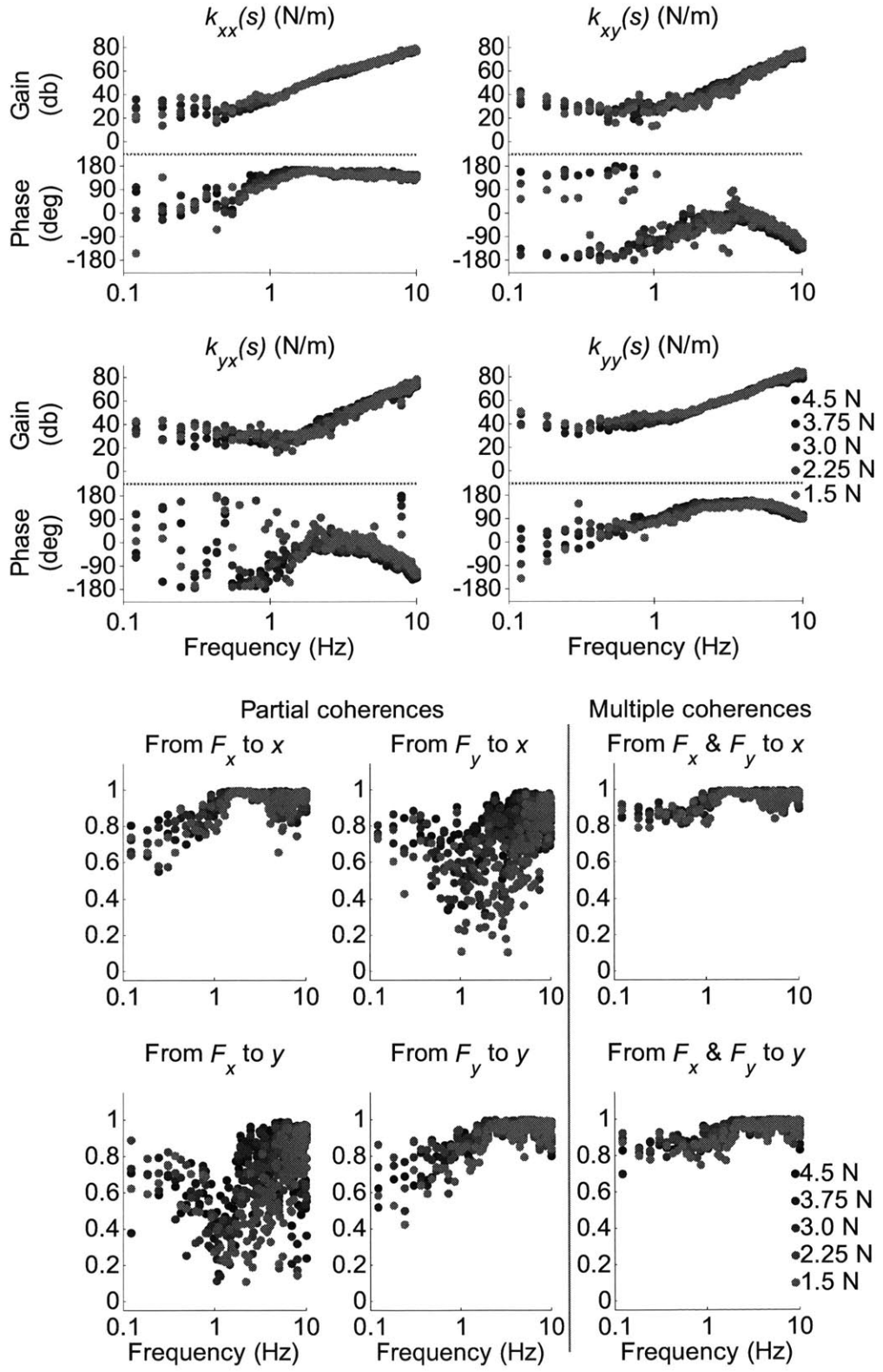

Figure F.29. Subject D, right arm, plastic arm trough, 5 overlaps: dynamic stiffness spectral estimates (top), and partial and multiple coherences (bottom)

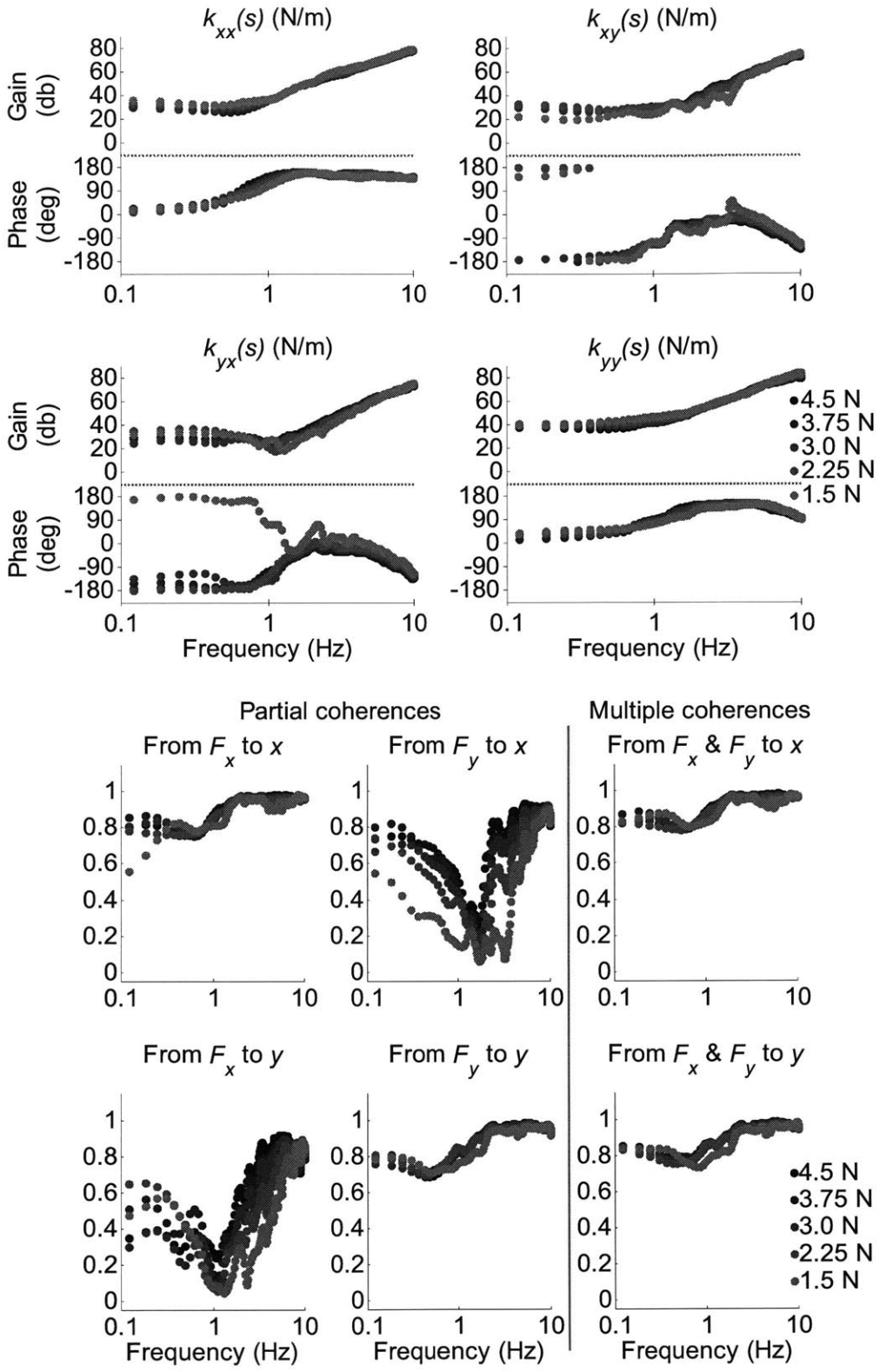

Figure F.30. Subject D, right arm, plastic arm trough, 45 overlaps: dynamic stiffness spectral estimates (top), and partial and multiple coherences (bottom)

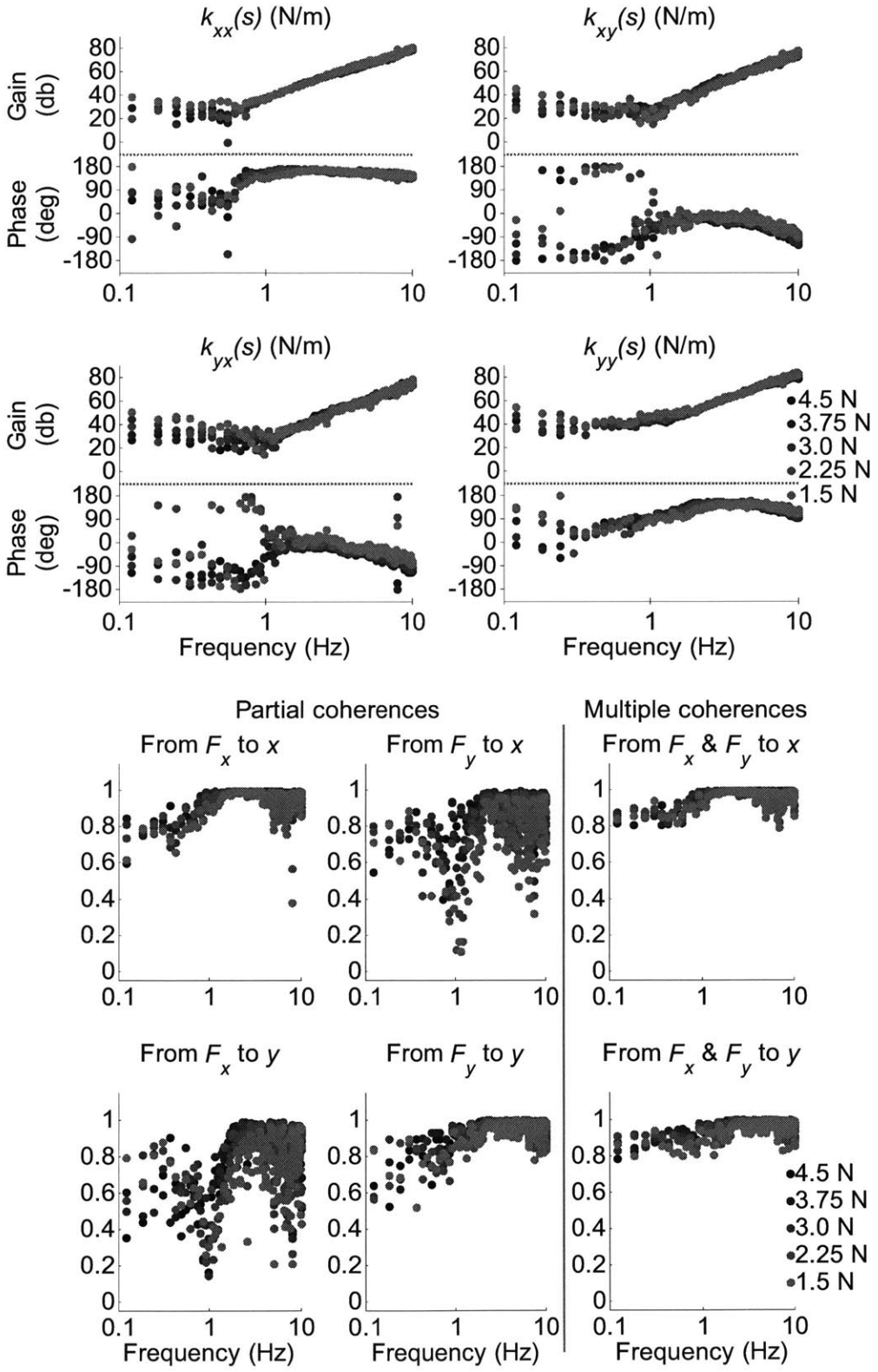

Figure F.31. Subject D, right arm, carbon-fiber arm trough, 5 overlaps: dynamic stiffness spectral estimates (top), and partial and multiple coherences (bottom)

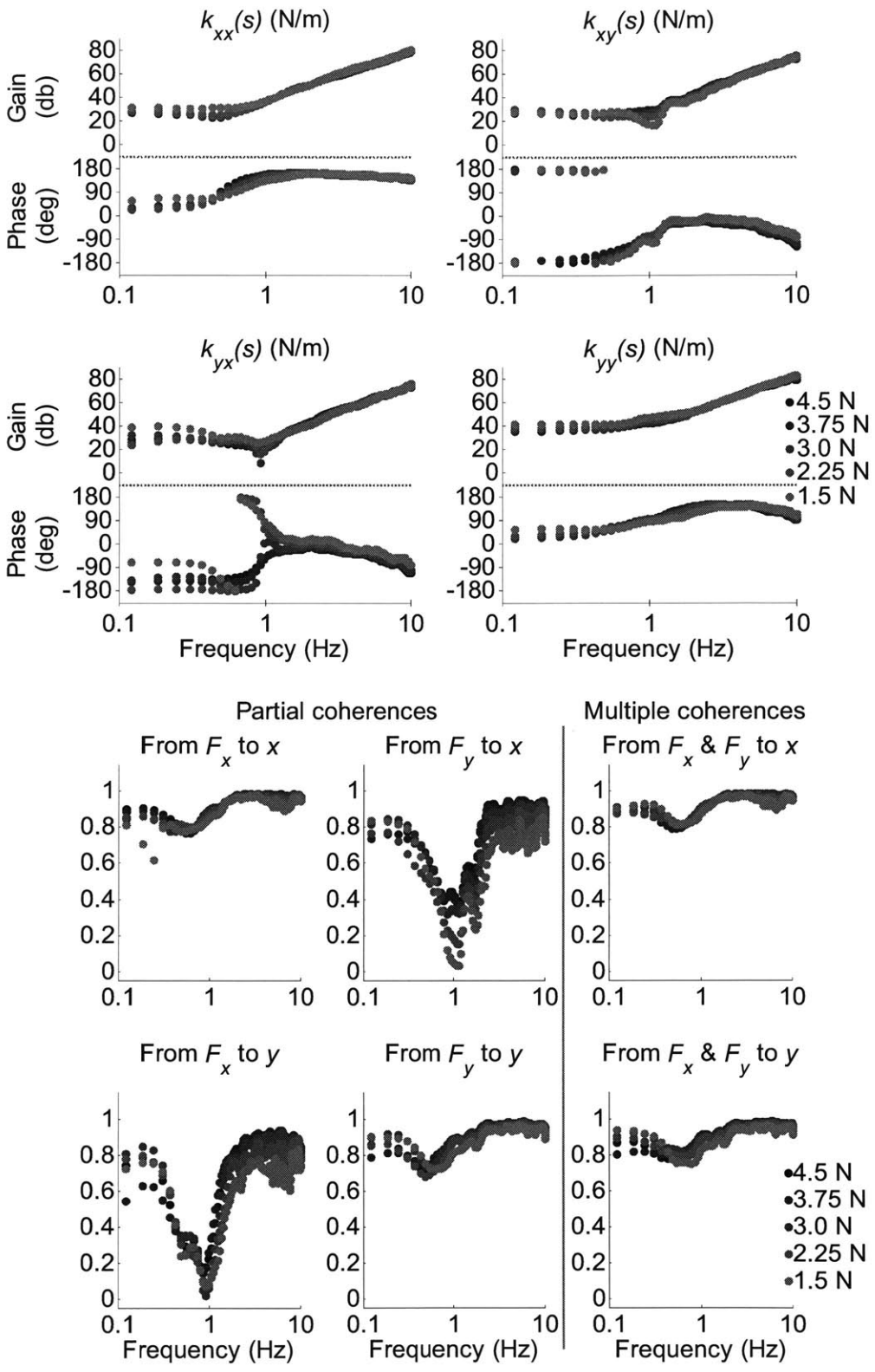

Figure F.32. Subject D, right arm, carbon-fiber arm trough, 45 overlaps: dynamic stiffness spectral estimates (top), and partial and multiple coherences (bottom)

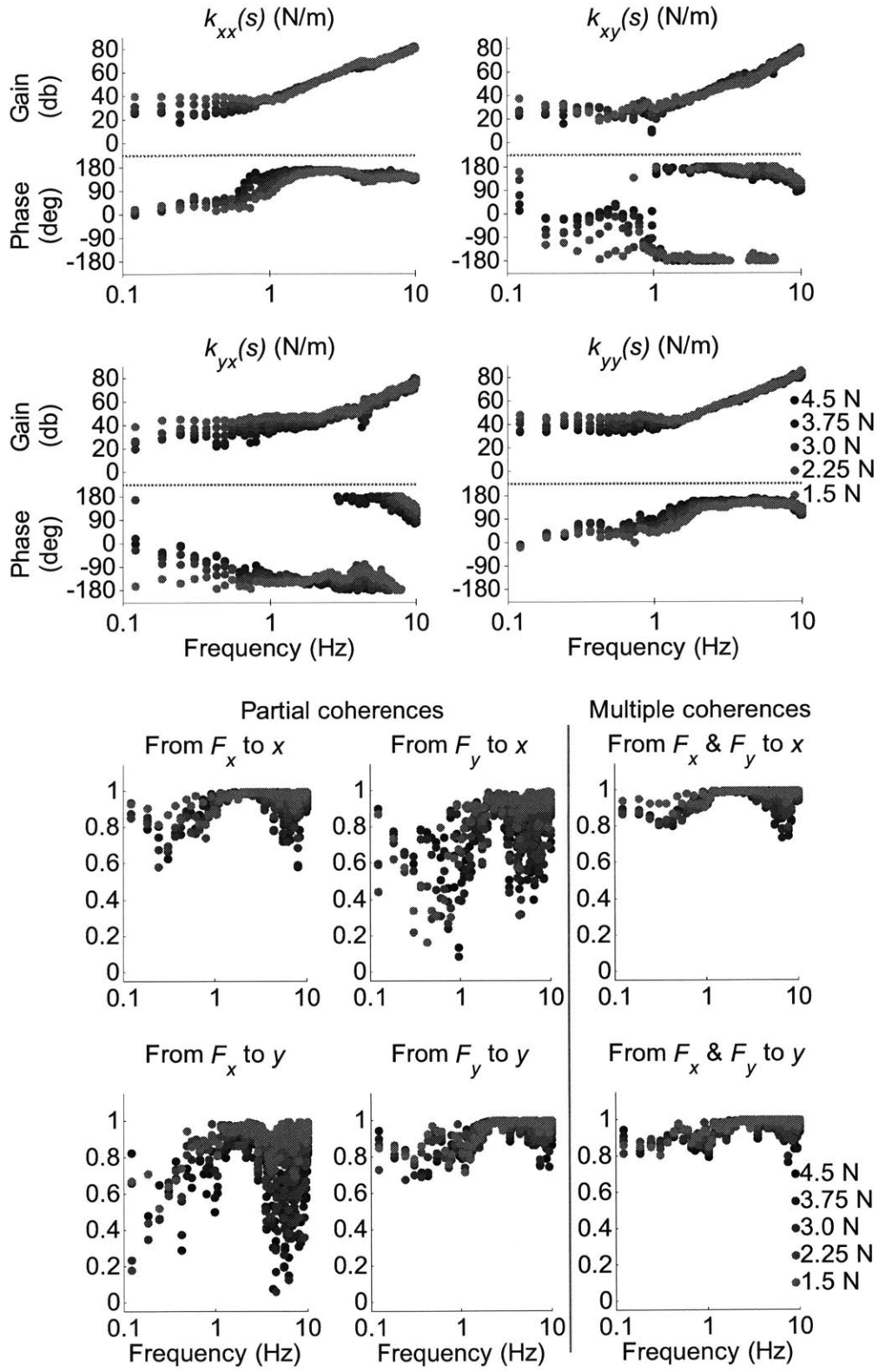

Figure F.33. Subject E, left arm, plastic arm trough, 5 overlaps: dynamic stiffness spectral estimates (top), and partial and multiple coherences (bottom)

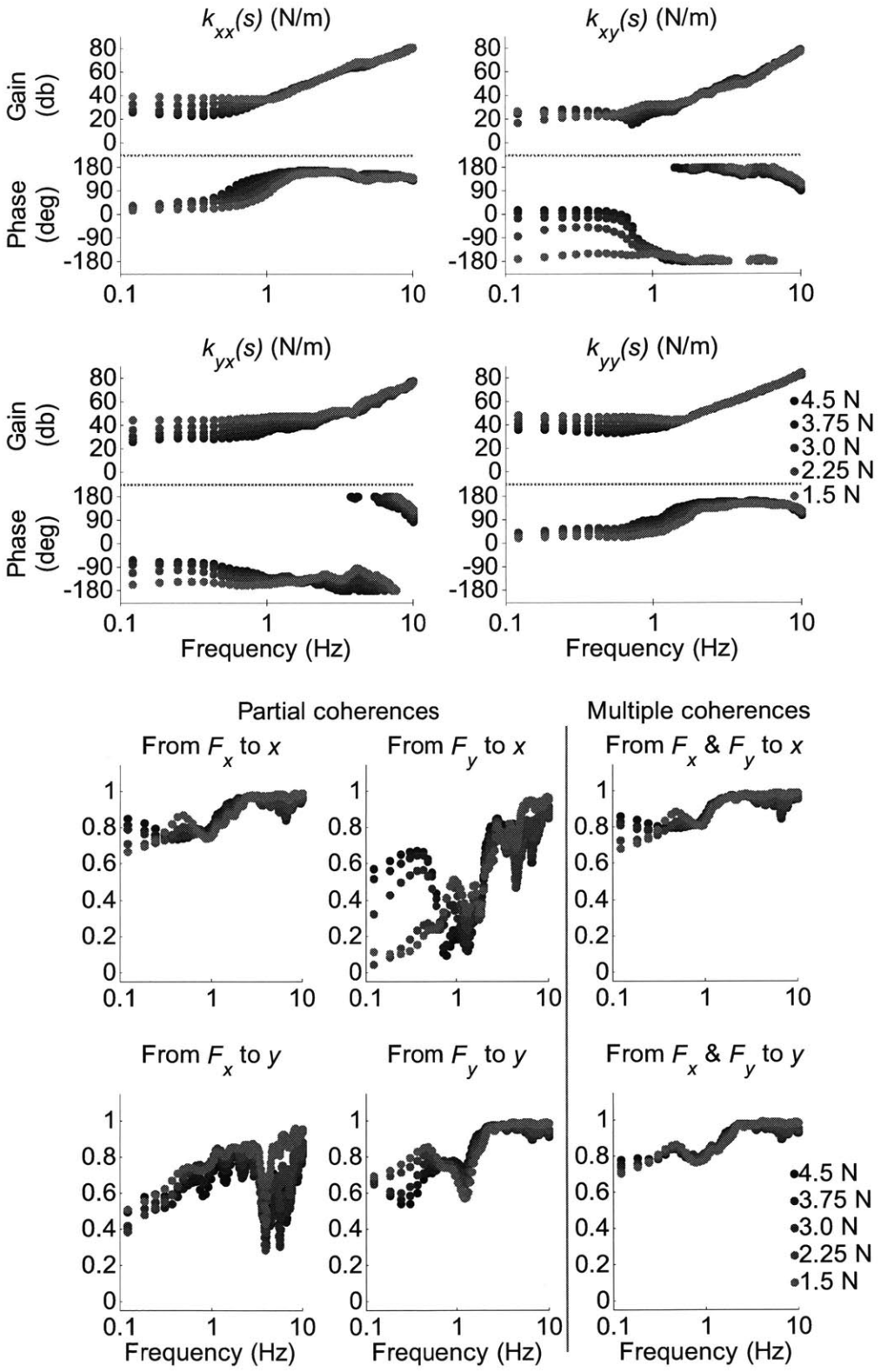

Figure F.34. Subject E, left arm, plastic arm trough, 45 overlaps: dynamic stiffness spectral estimates (top), and partial and multiple coherences (bottom)

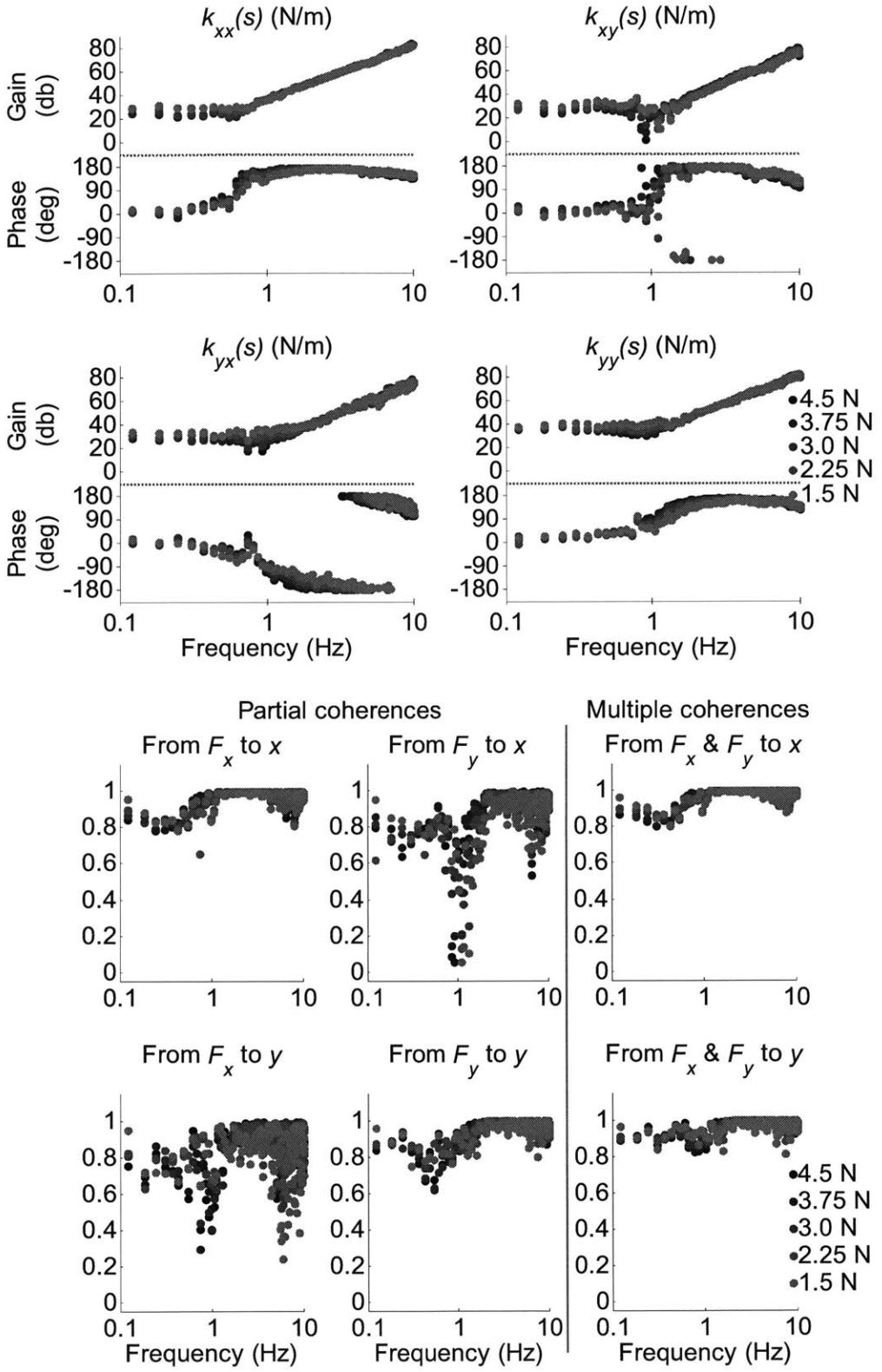

Figure F.35. Subject E, left arm, carbon-fiber arm trough, 5 overlaps: dynamic stiffness spectral estimates (top), and partial and multiple coherences (bottom)

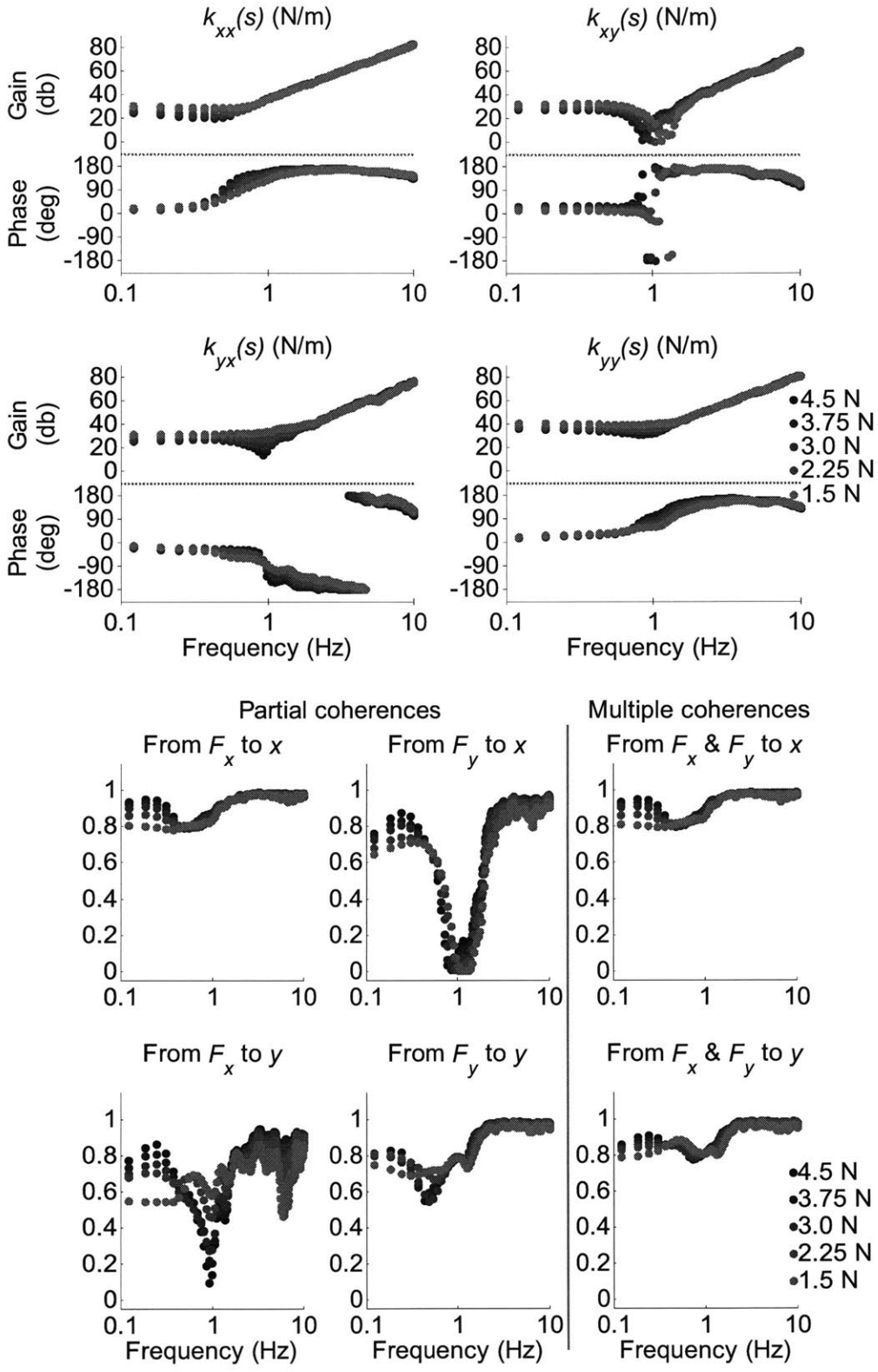

Figure F.36. Subject E, left arm, carbon-fiber arm trough, 45 overlaps: dynamic stiffness spectral estimates (top), and partial and multiple coherences (bottom)

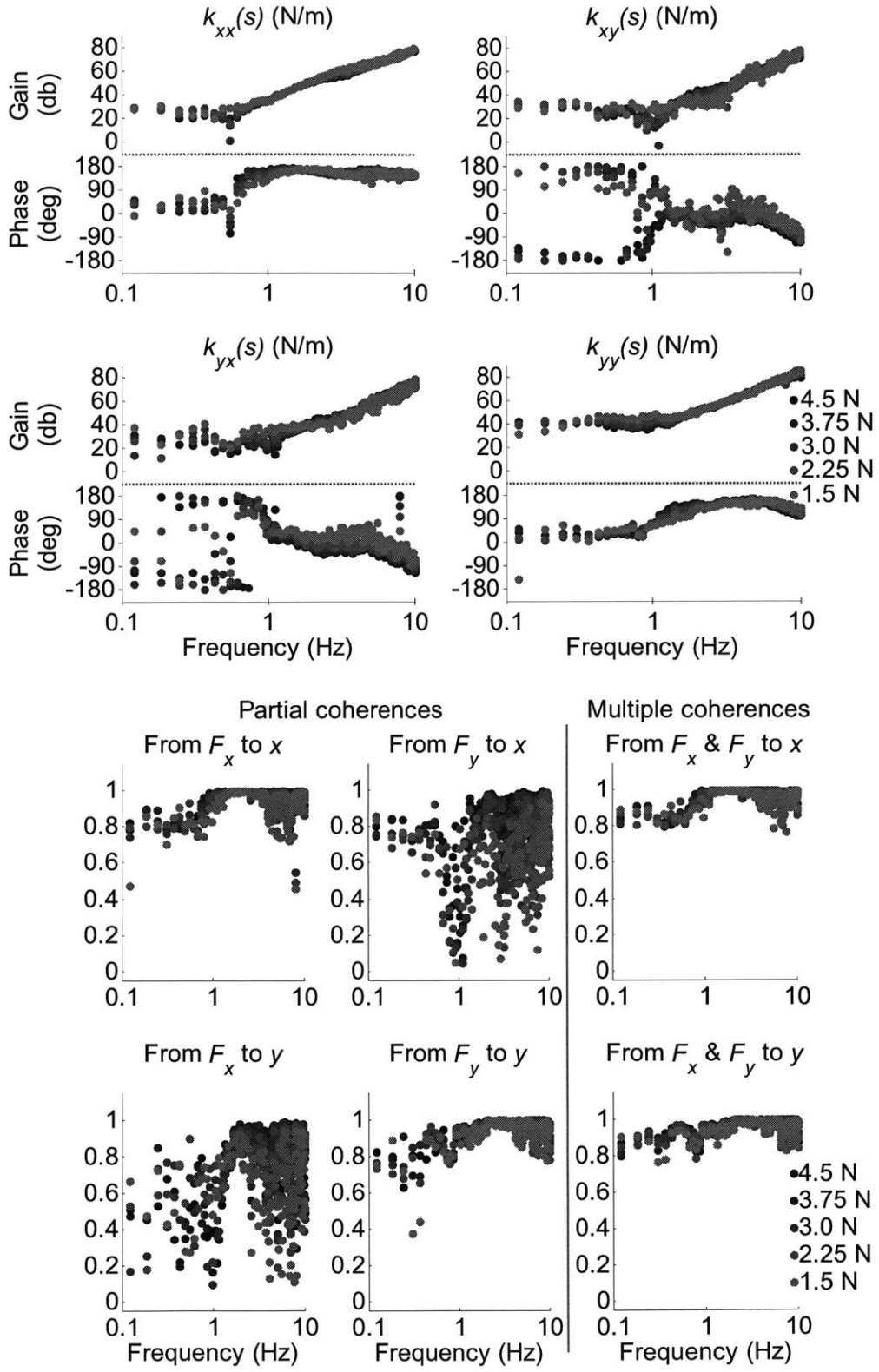

Figure F.37. Subject E, right arm, plastic arm trough, 5 overlaps: dynamic stiffness spectral estimates (top), and partial and multiple coherences (bottom)

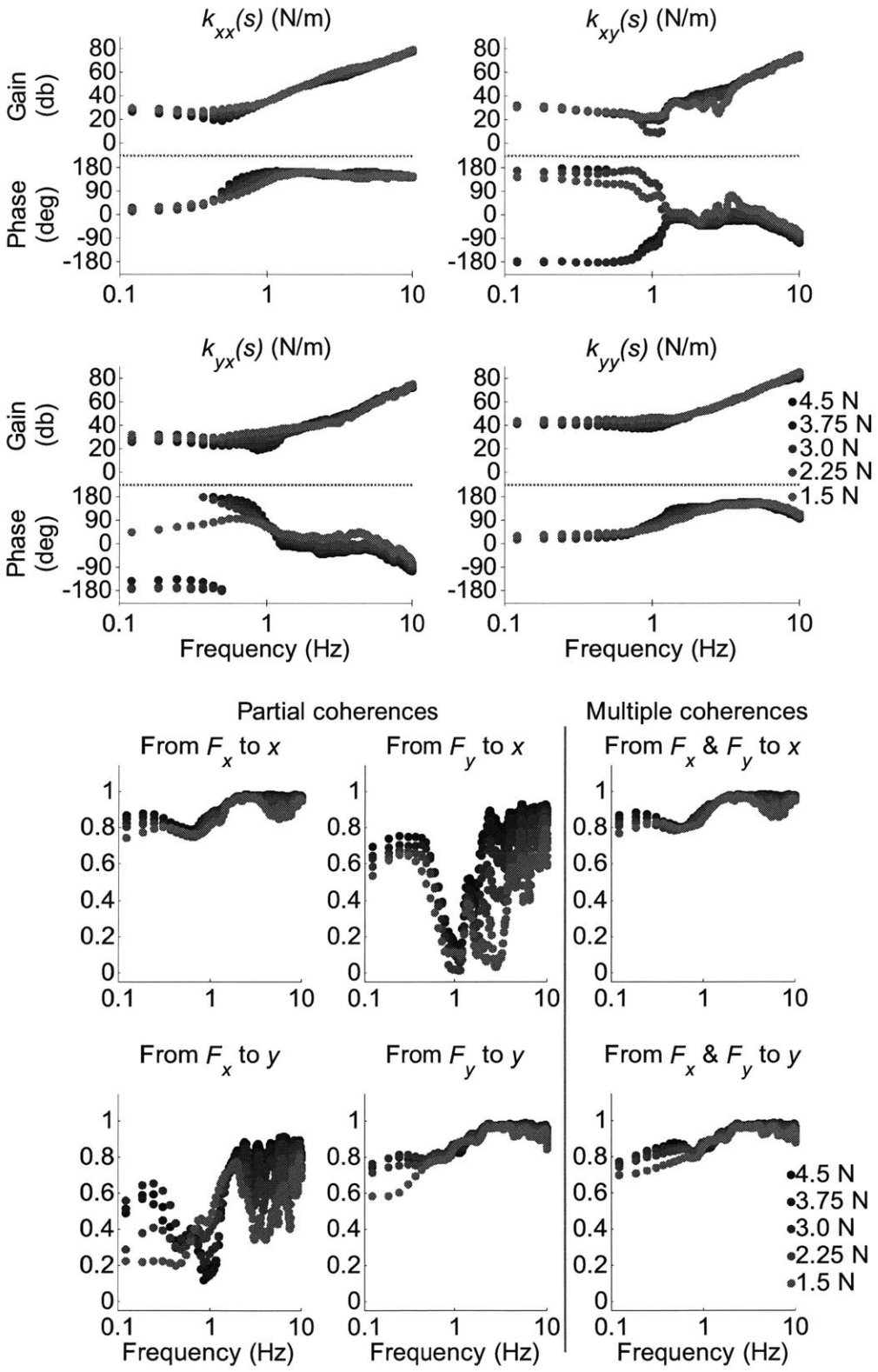

Figure F.38. Subject E, right arm, plastic arm trough, 45 overlaps: dynamic stiffness spectral estimates (top), and partial and multiple coherences (bottom)

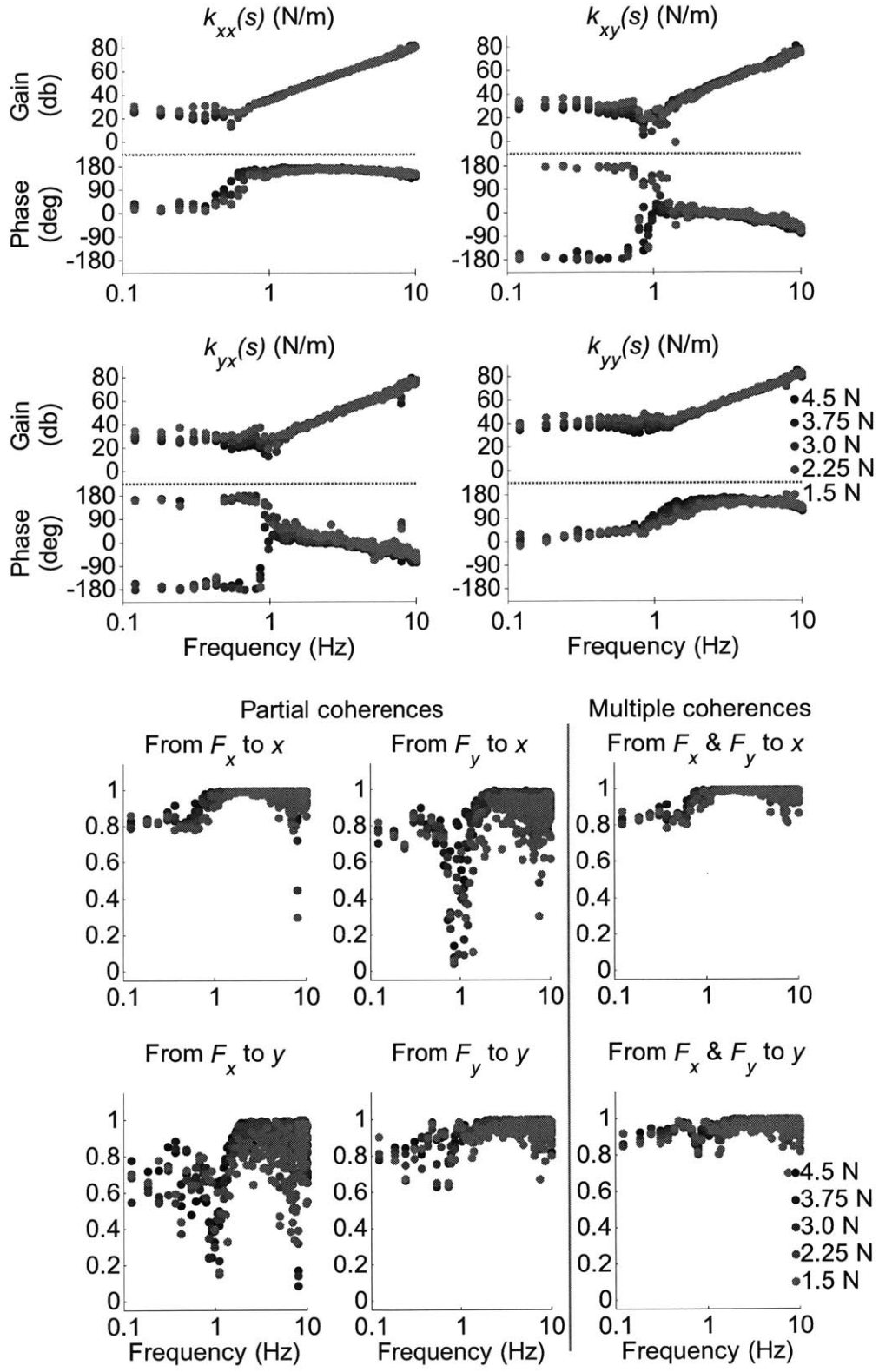

Figure F.39. Subject E, right arm, carbon-fiber arm trough, 5 overlaps: dynamic stiffness spectral estimates (top), and partial and multiple coherences (bottom)

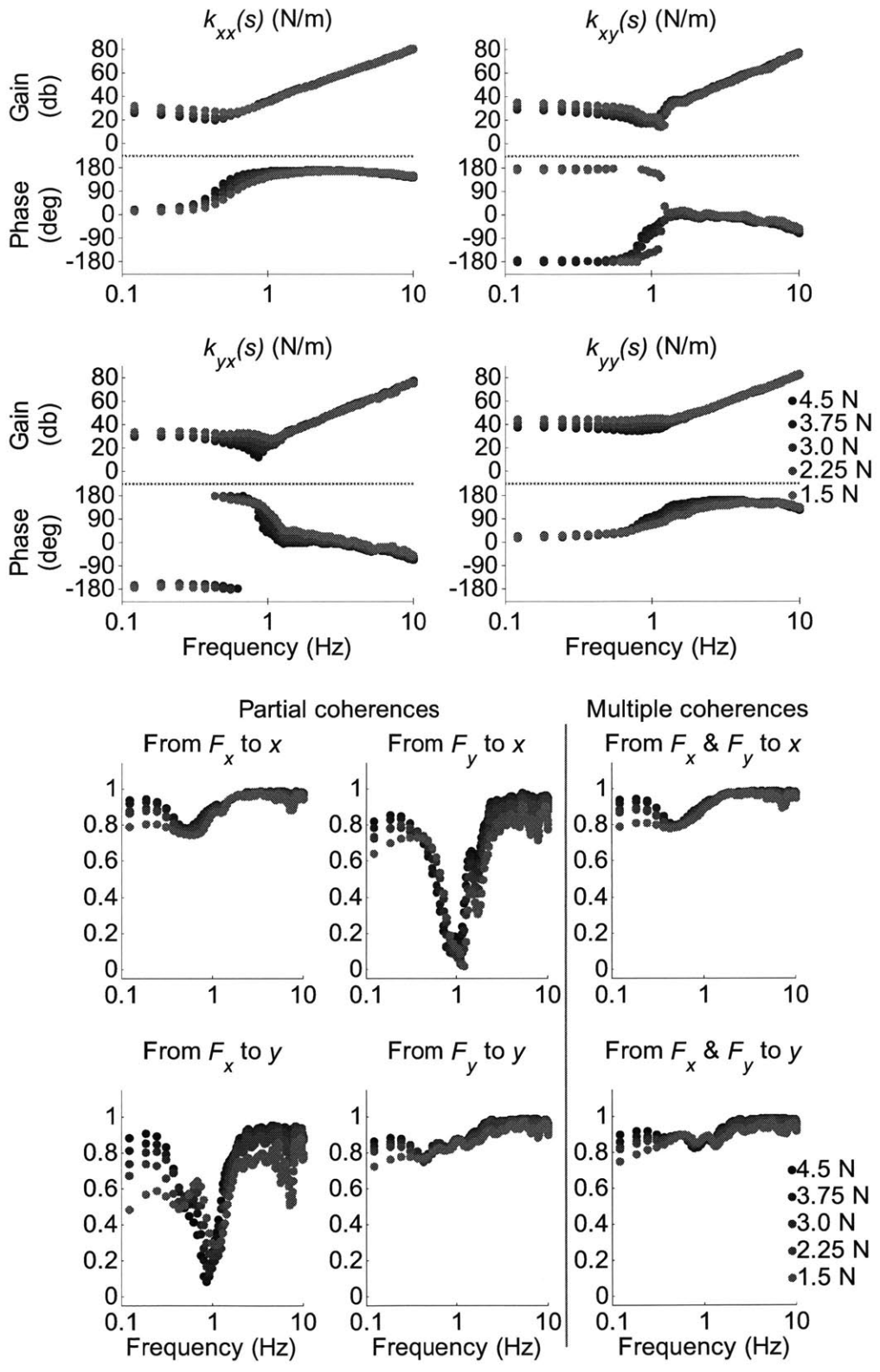

Figure F.40. Subject E, right arm, carbon-fiber arm trough, 45 overlaps: dynamic stiffness spectral estimates (top), and partial and multiple coherences (bottom)

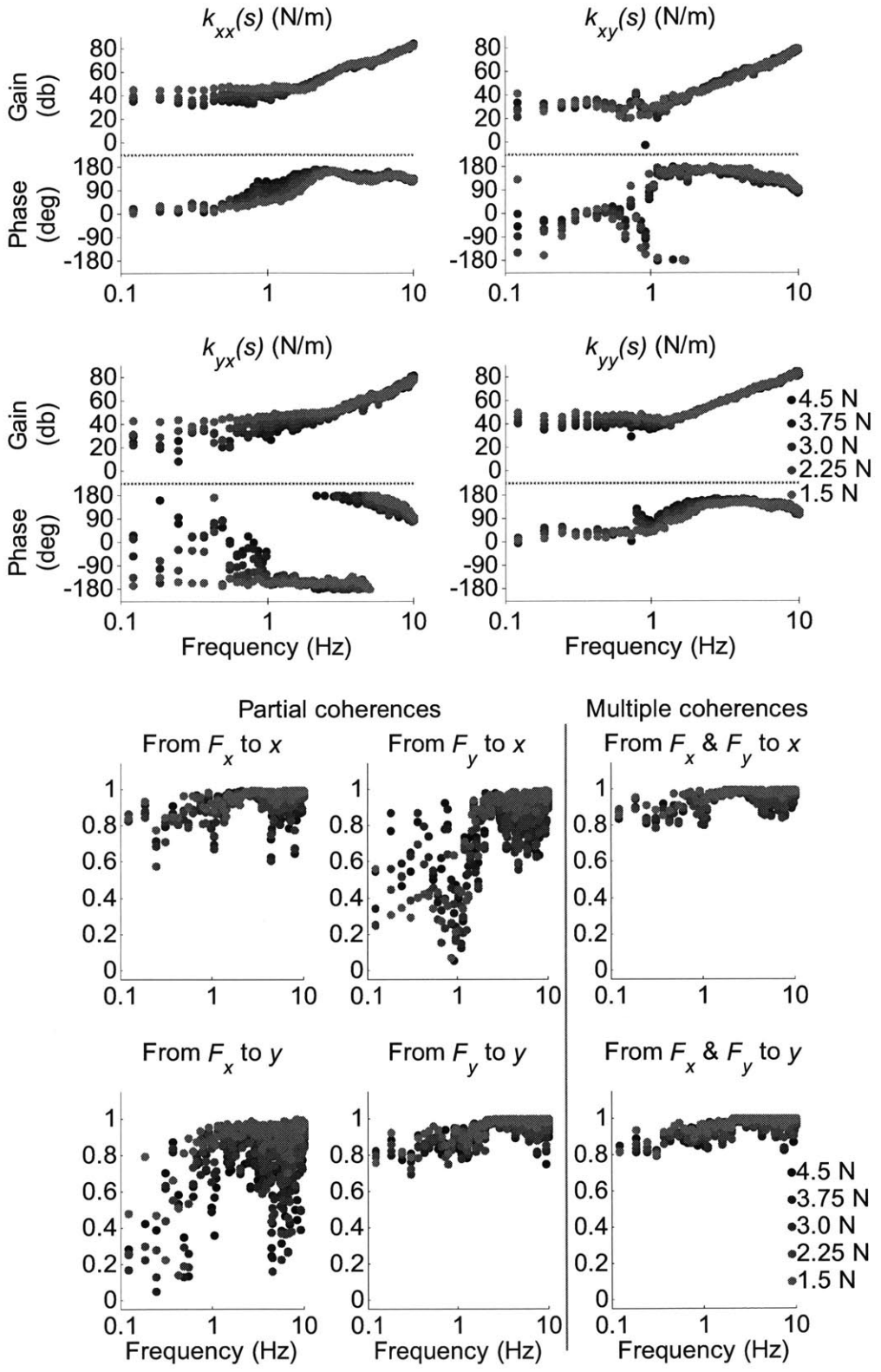

Figure F.41. Subject F, left arm, plastic arm trough, 5 overlaps: dynamic stiffness spectral estimates (top), and partial and multiple coherences (bottom)

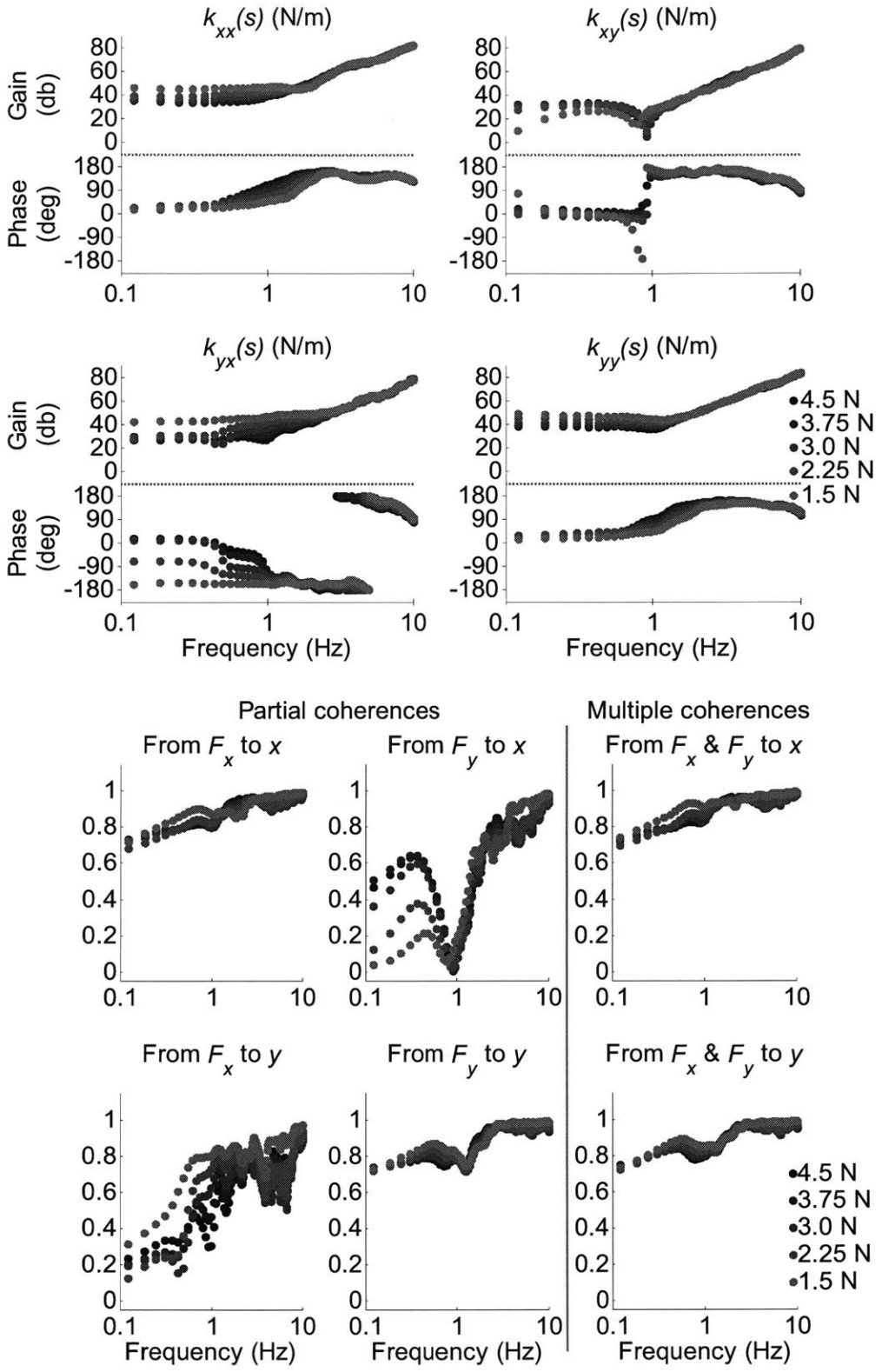

Figure F.42. Subject F, left arm, plastic arm trough, 45 overlaps: dynamic stiffness spectral estimates (top), and partial and multiple coherences (bottom)

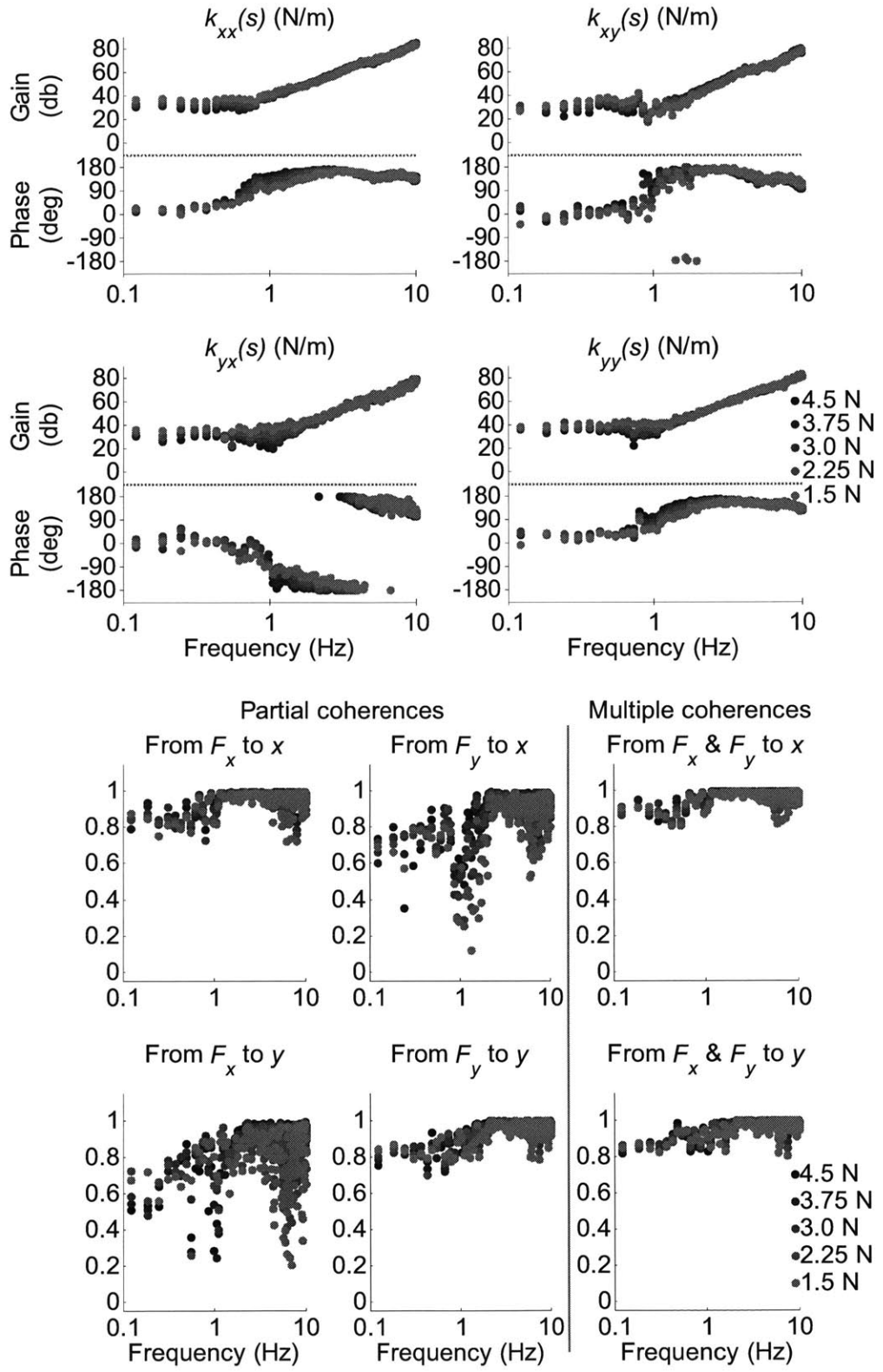

Figure F.43. Subject F, left arm, carbon-fiber arm trough, 5 overlaps: dynamic stiffness spectral estimates (top), and partial and multiple coherences (bottom)

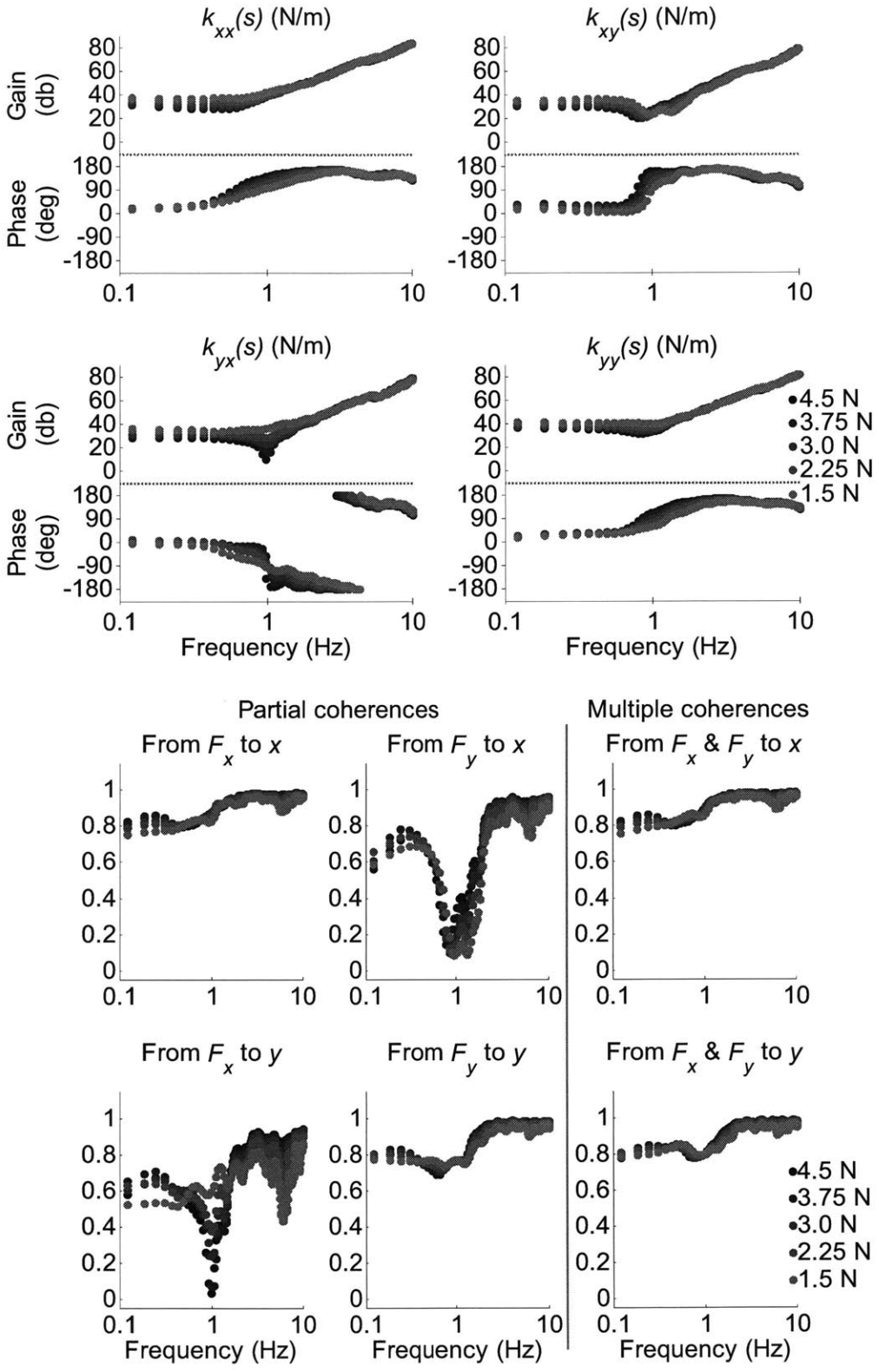

Figure F.44. Subject F, left arm, carbon-fiber arm trough, 45 overlaps: dynamic stiffness spectral estimates (top), and partial and multiple coherences (bottom)

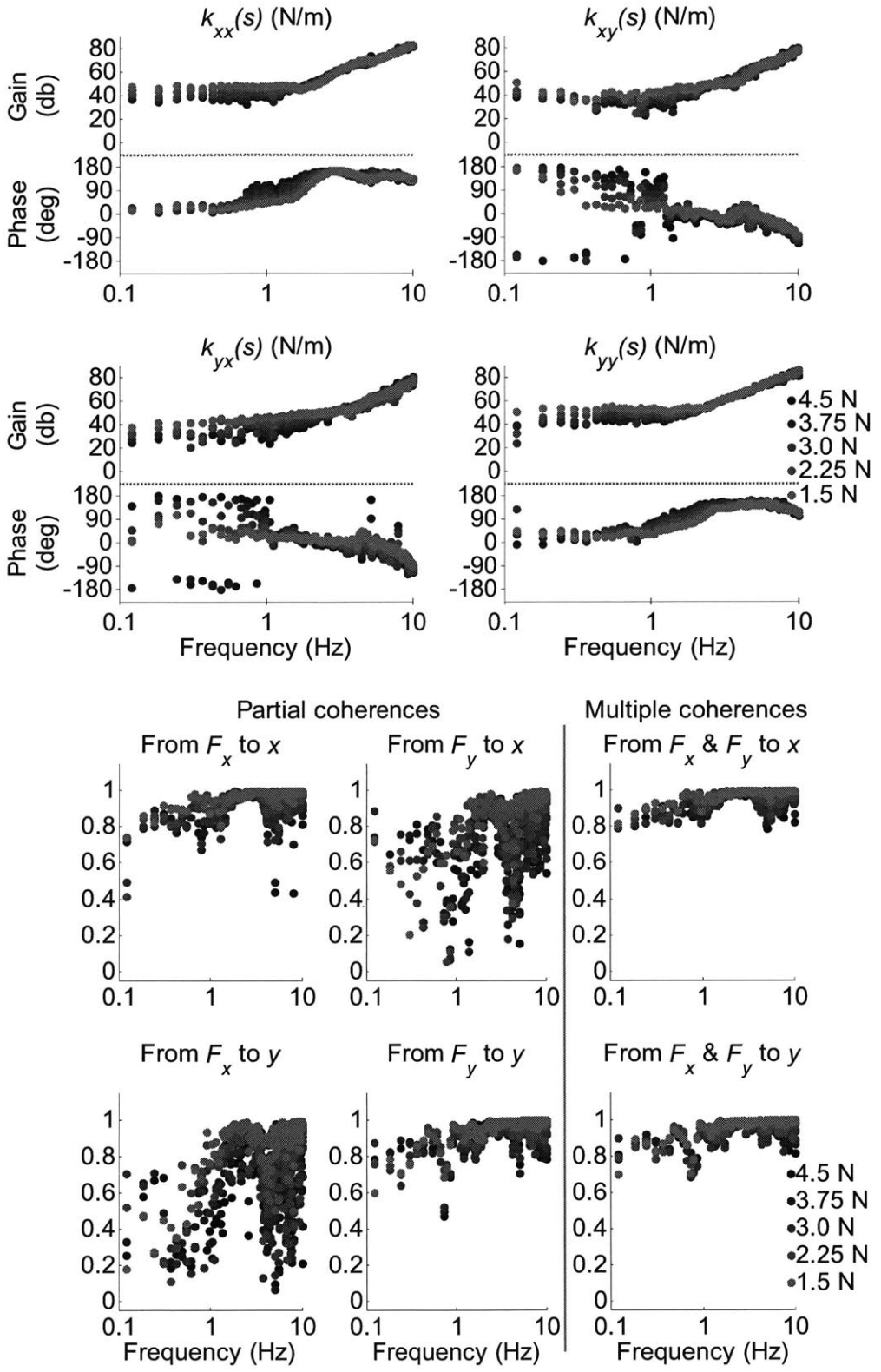

Figure F.45. Subject F, right arm, plastic arm trough, 5 overlaps: dynamic stiffness spectral estimates (top), and partial and multiple coherences (bottom)

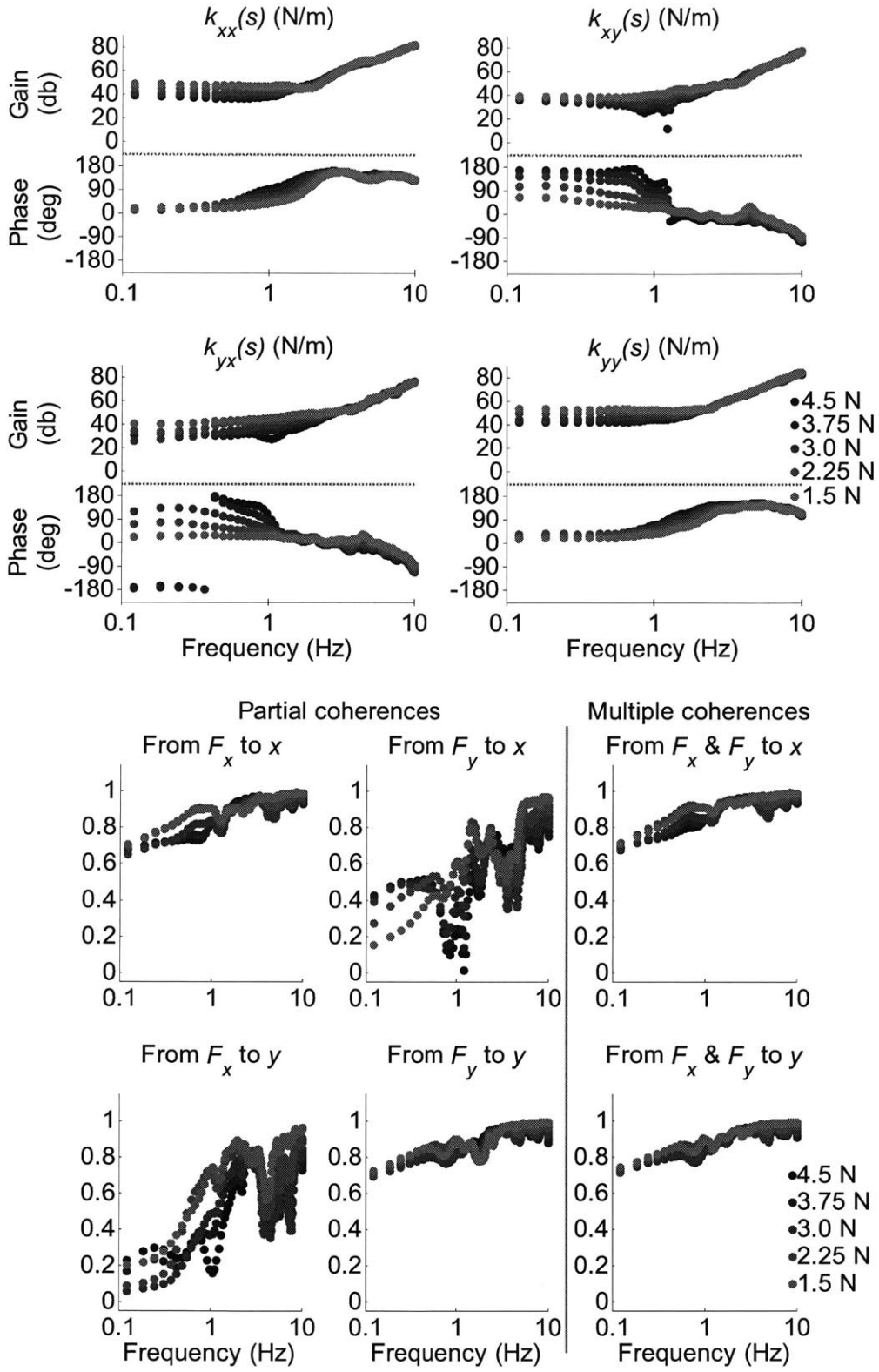

Figure F.46. Subject F, right arm, plastic arm trough, 45 overlaps: dynamic stiffness spectral estimates (top), and partial and multiple coherences (bottom)

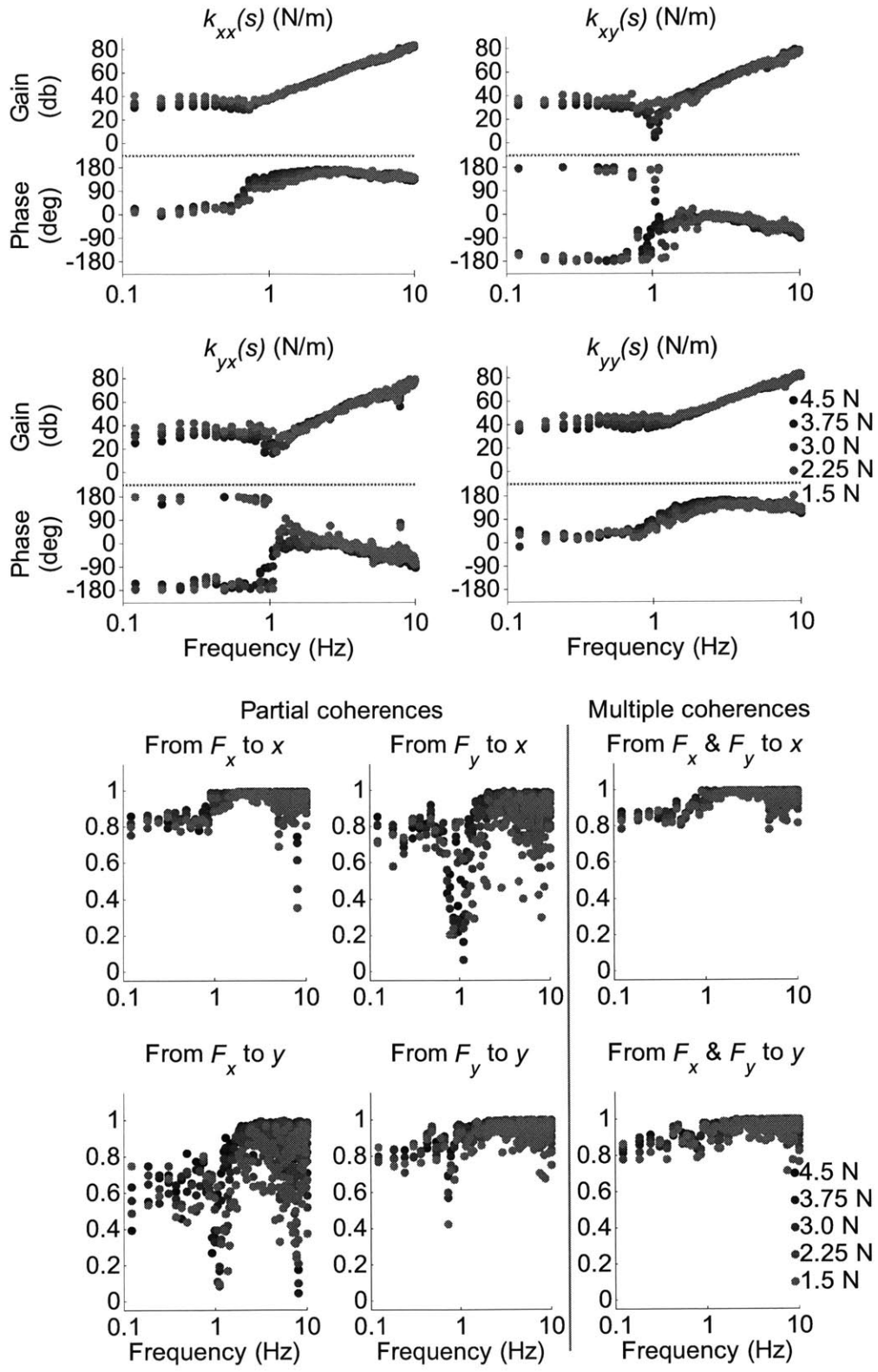

Figure F.47. Subject F, right arm, carbon-fiber arm trough, 5 overlaps: dynamic stiffness spectral estimates (top), and partial and multiple coherences (bottom)

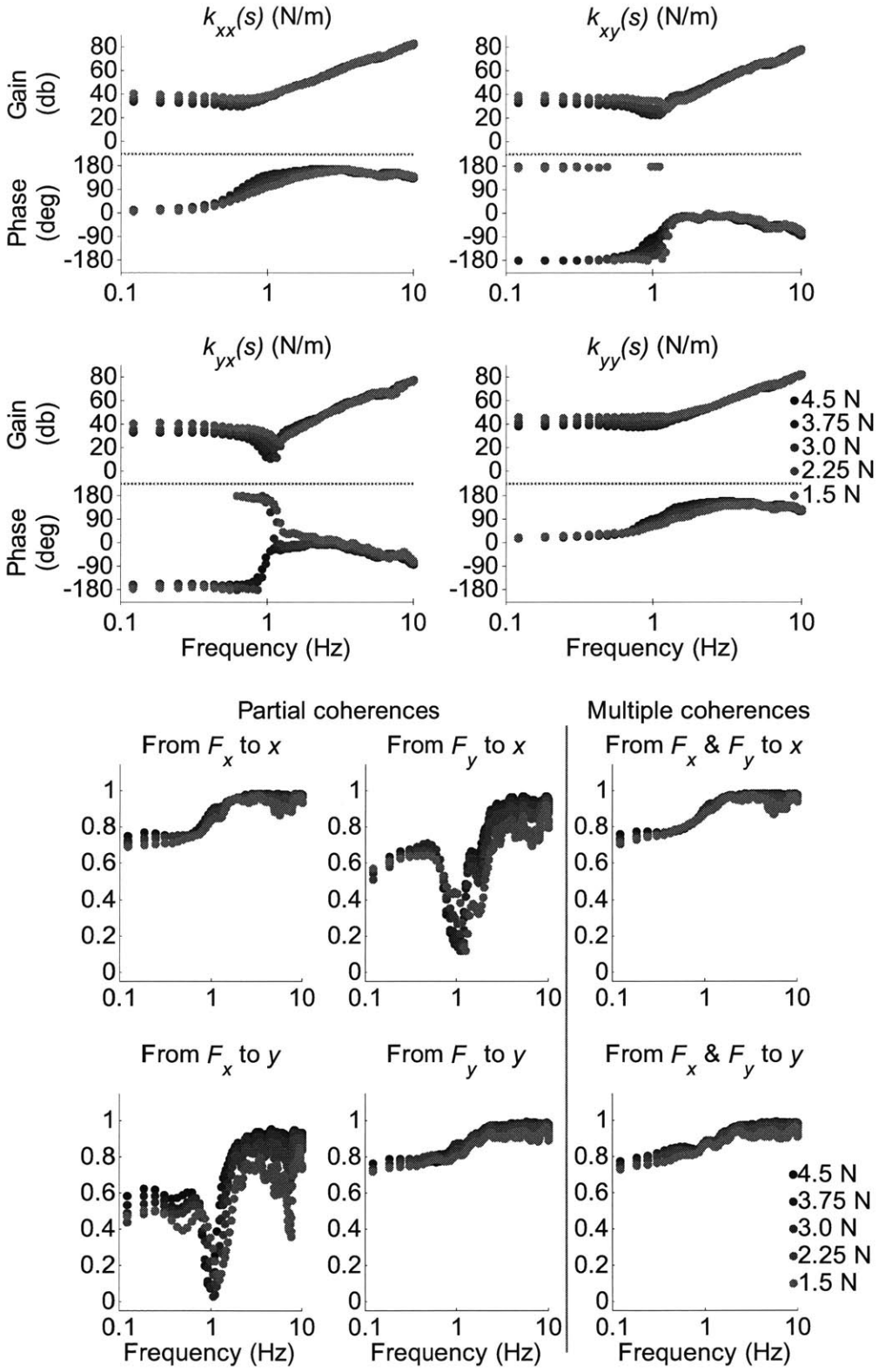

Figure F.48. Subject F, right arm, carbon-fiber arm trough, 45 overlaps: dynamic stiffness spectral estimates (top), and partial and multiple coherences (bottom)

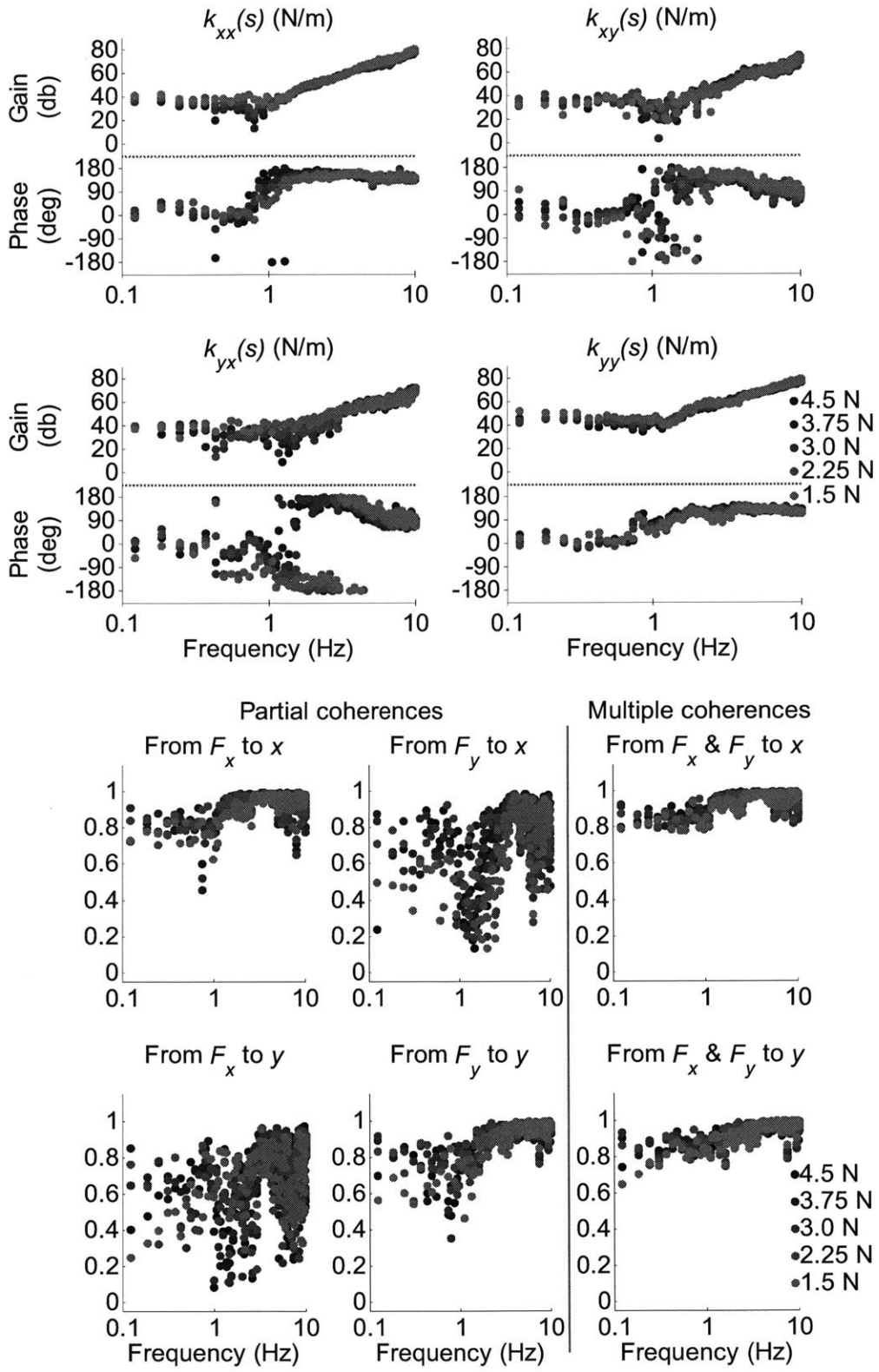

Figure F.49. Subject G, left arm, plastic arm trough, 5 overlaps: dynamic stiffness spectral estimates (top), and partial and multiple coherences (bottom)

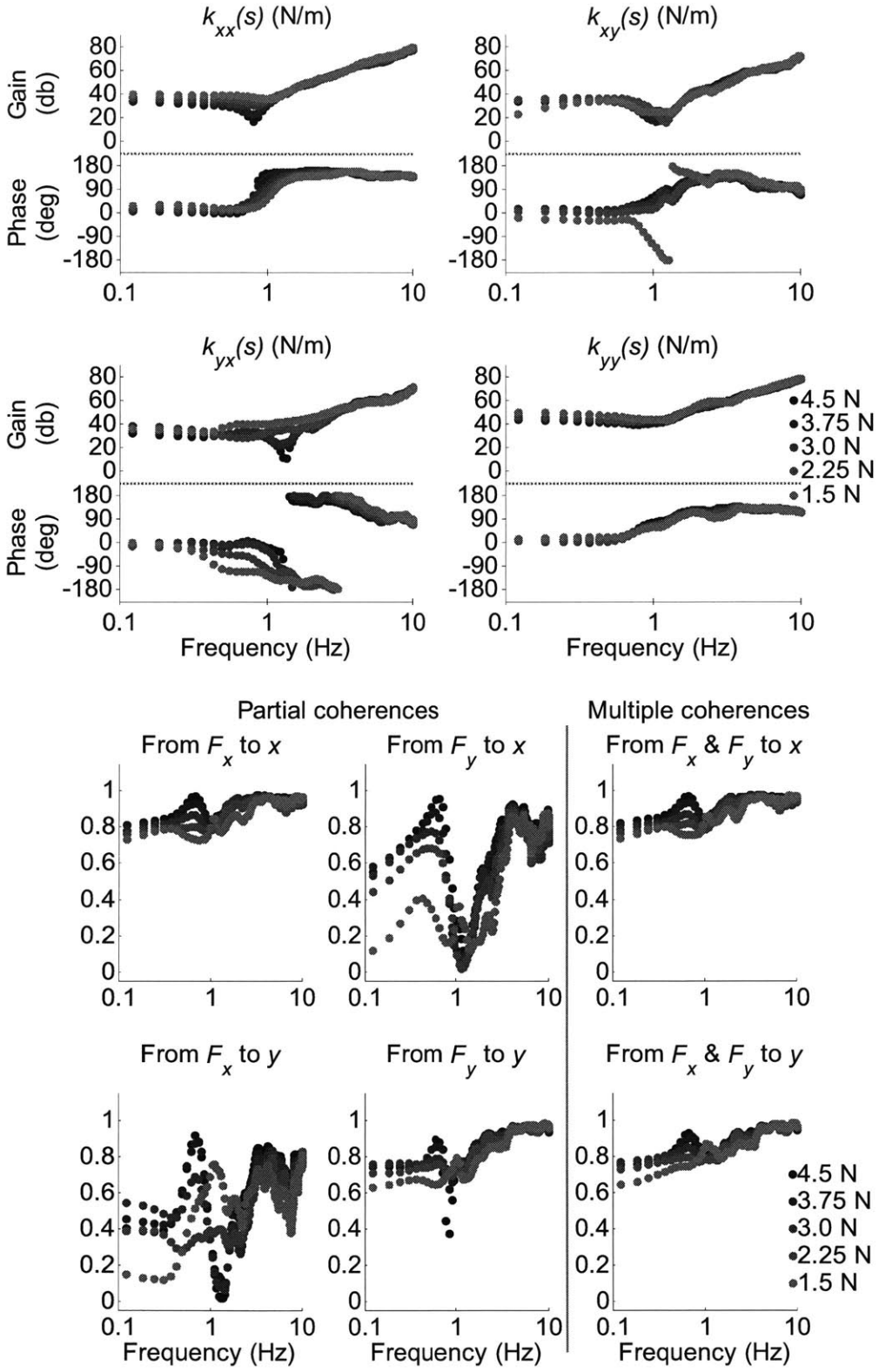

Figure F.50. Subject G, left arm, plastic arm trough, 45 overlaps: dynamic stiffness spectral estimates (top), and partial and multiple coherences (bottom)

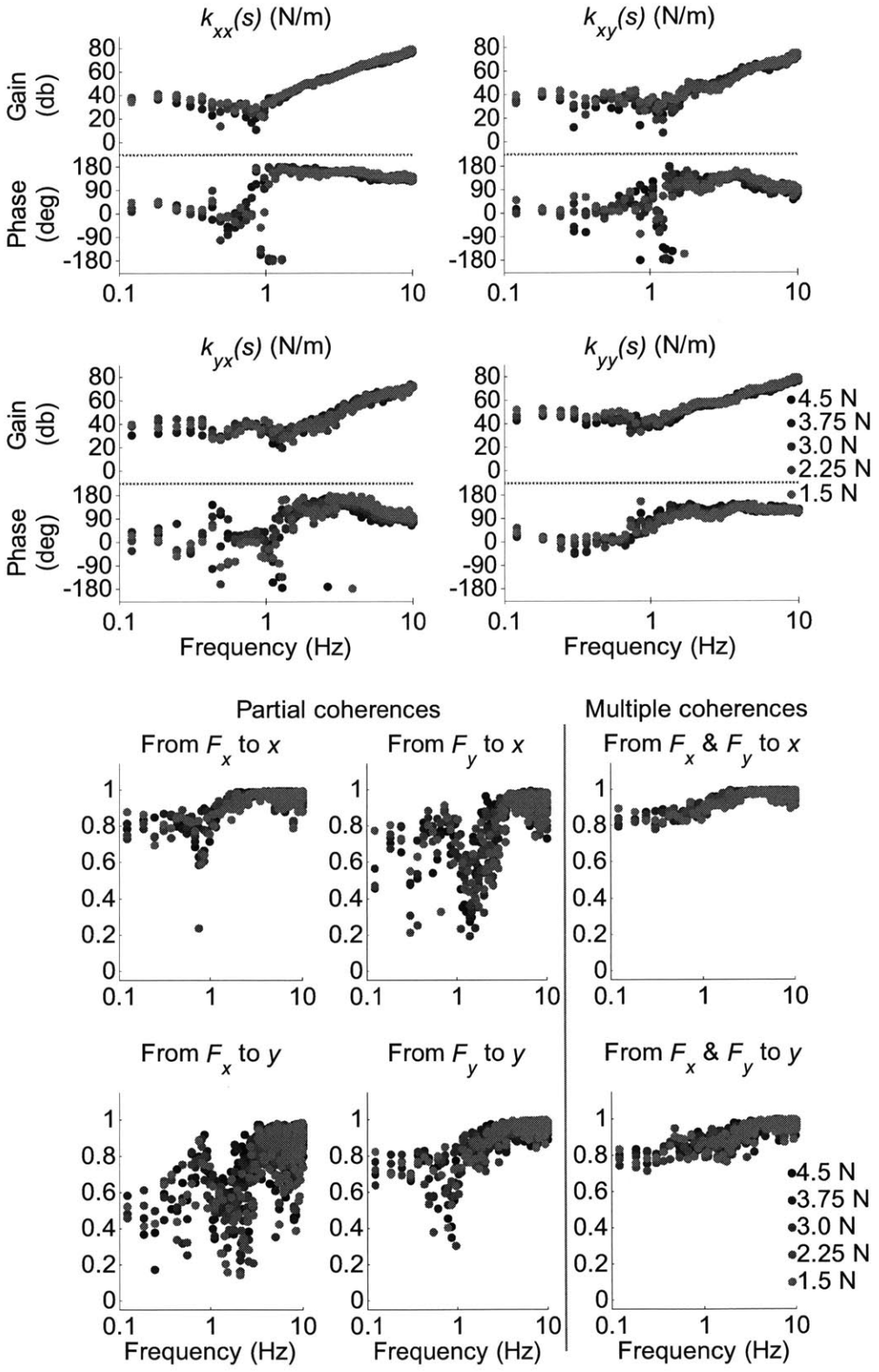

Figure F.51. Subject G, left arm, carbon-fiber arm trough, 5 overlaps: dynamic stiffness spectral estimates (top), and partial and multiple coherences (bottom)

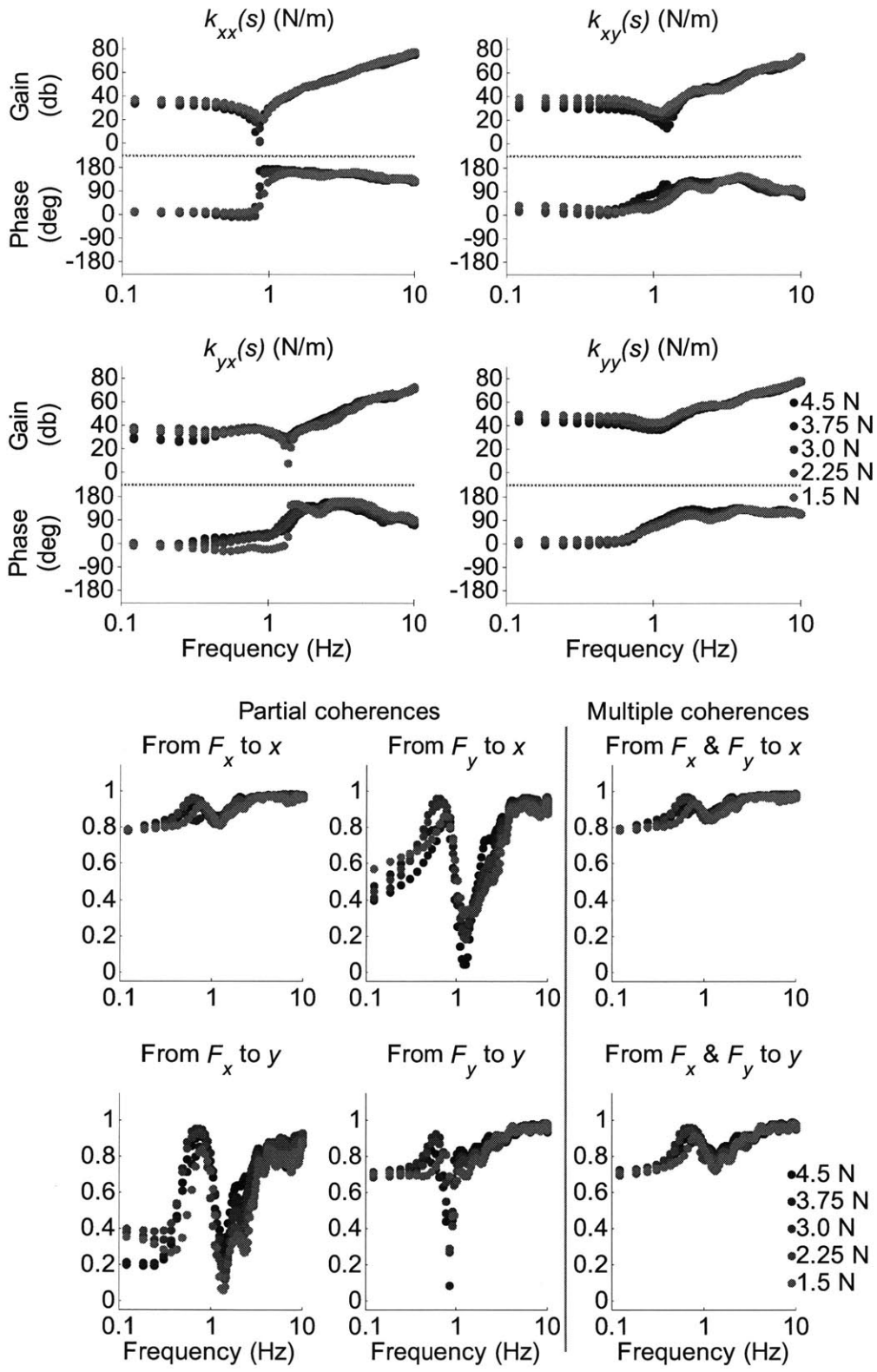

Figure F.52. Subject G, left arm, carbon-fiber arm trough, 45 overlaps: dynamic stiffness spectral estimates (top), and partial and multiple coherences (bottom)

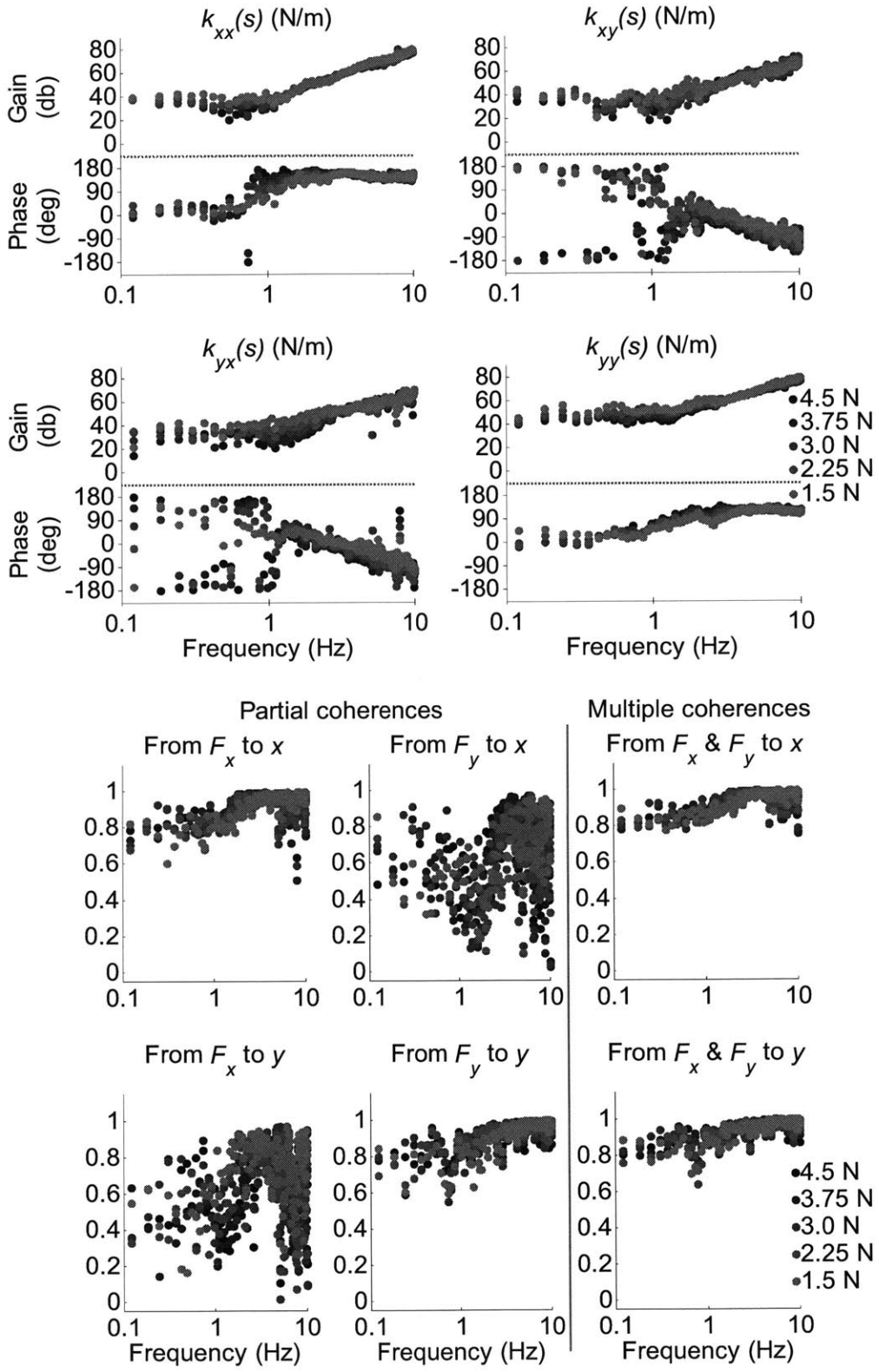

Figure F.53. Subject G, right arm, plastic arm trough, 5 overlaps: dynamic stiffness spectral estimates (top), and partial and multiple coherences (bottom)

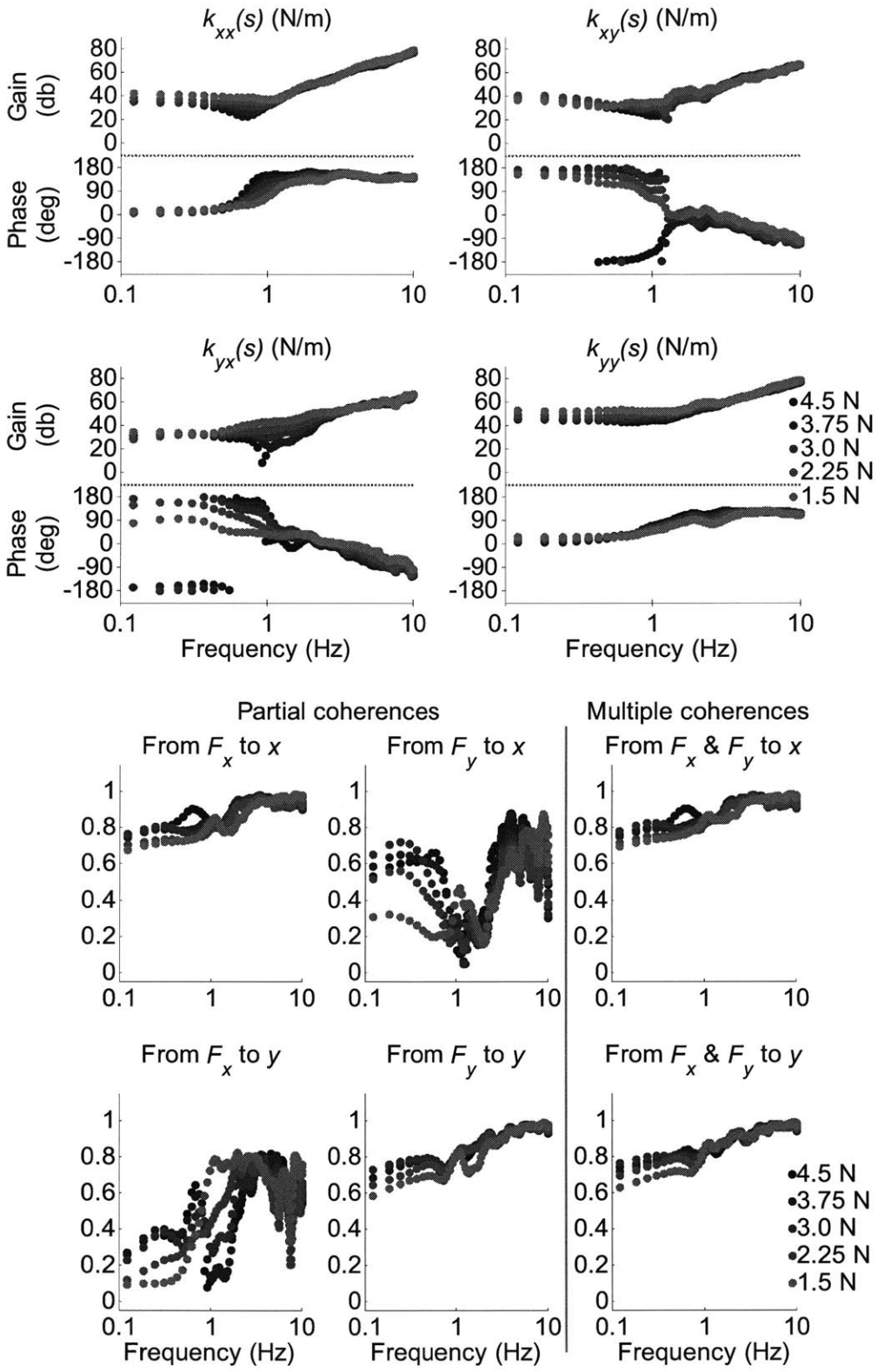

Figure F.54. Subject G, right arm, plastic arm trough, 45 overlaps: dynamic stiffness spectral estimates (top), and partial and multiple coherences (bottom)

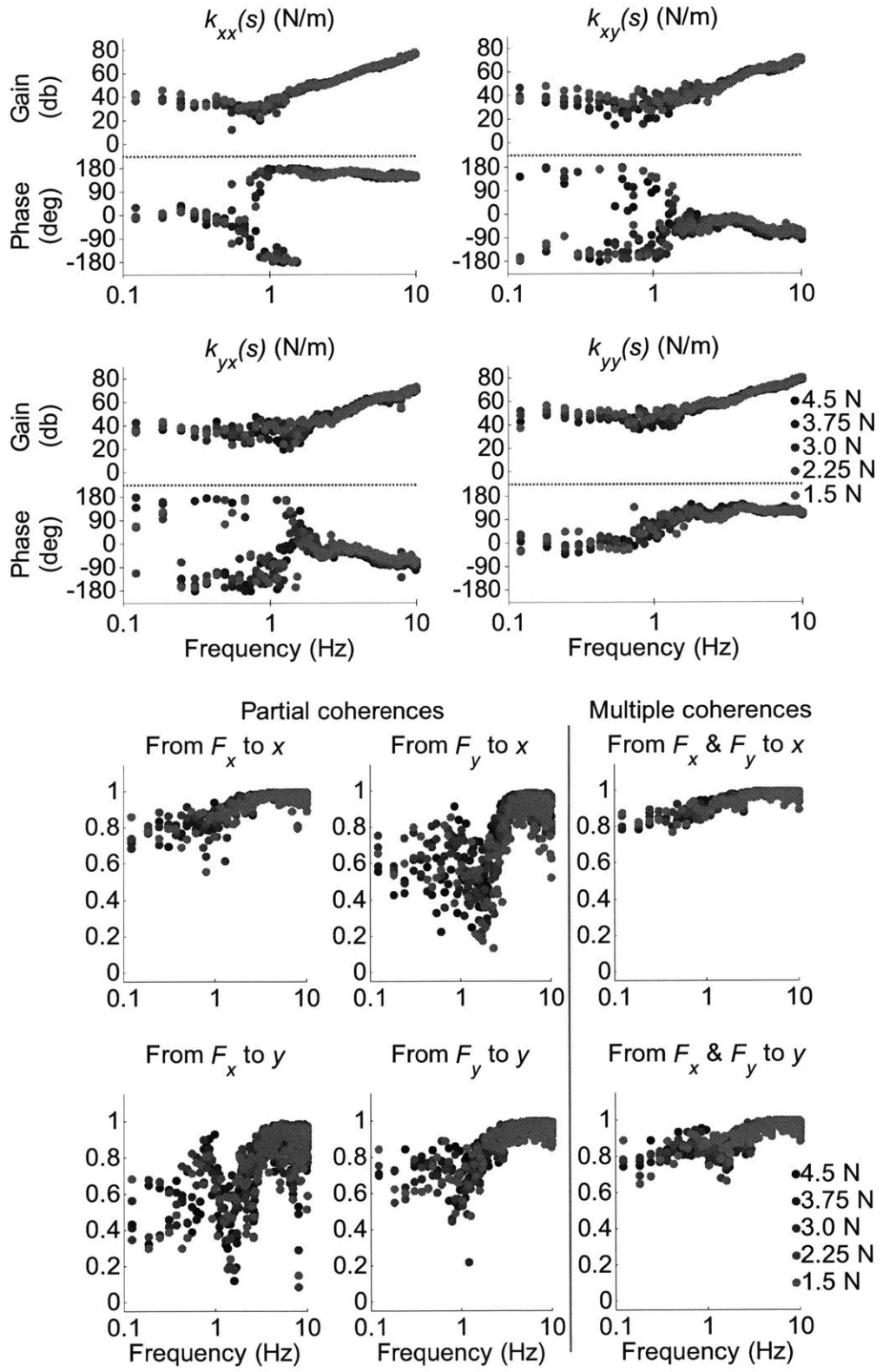

Figure F.55. Subject G, right arm, carbon-fiber arm trough, 5 overlaps: dynamic stiffness spectral estimates (top), and partial and multiple coherences (bottom)

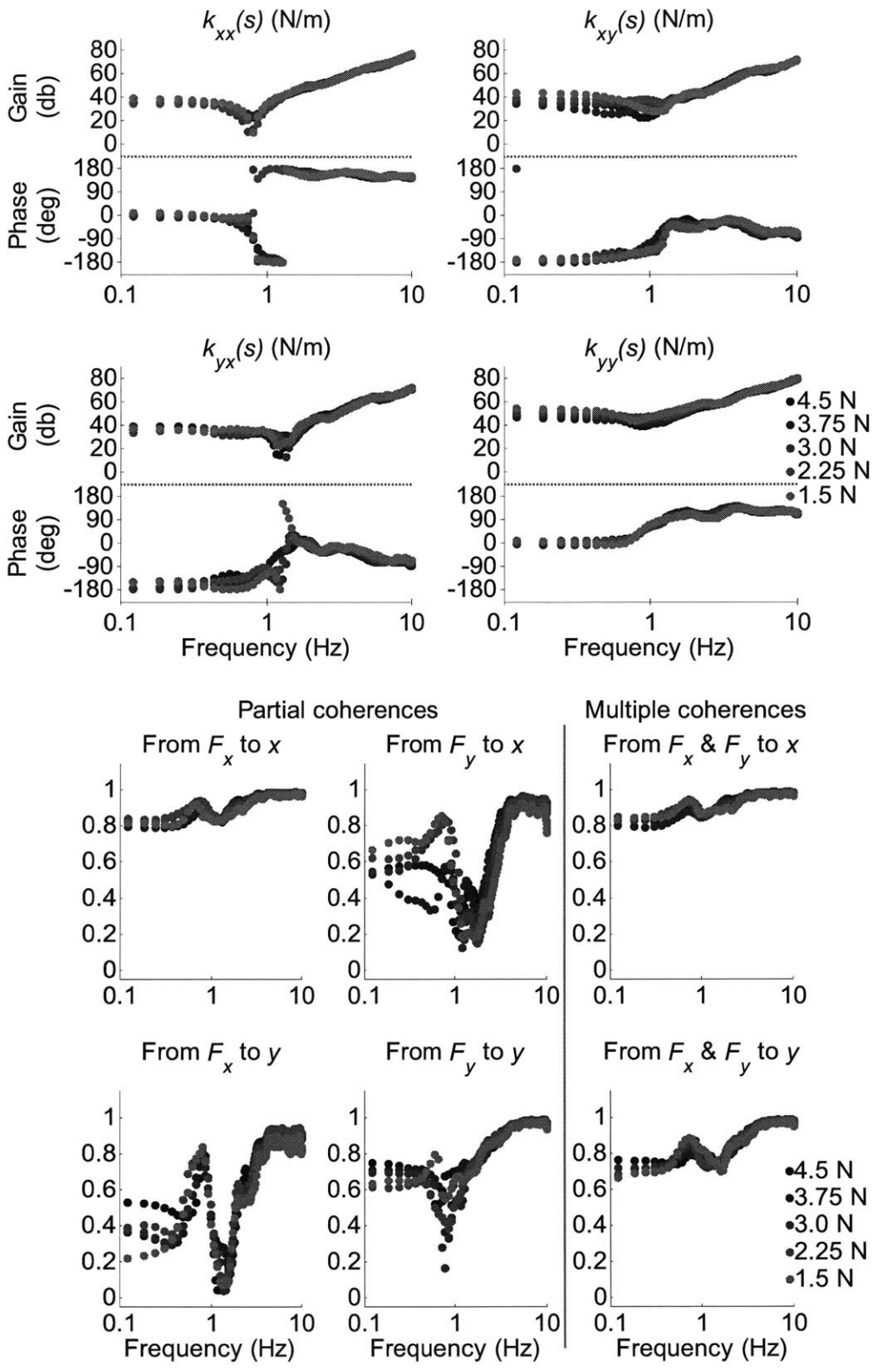

Figure F.56. Subject G, right arm, carbon-fiber arm trough, 45 overlaps: dynamic stiffness spectral estimates (top), and partial and multiple coherences (bottom)

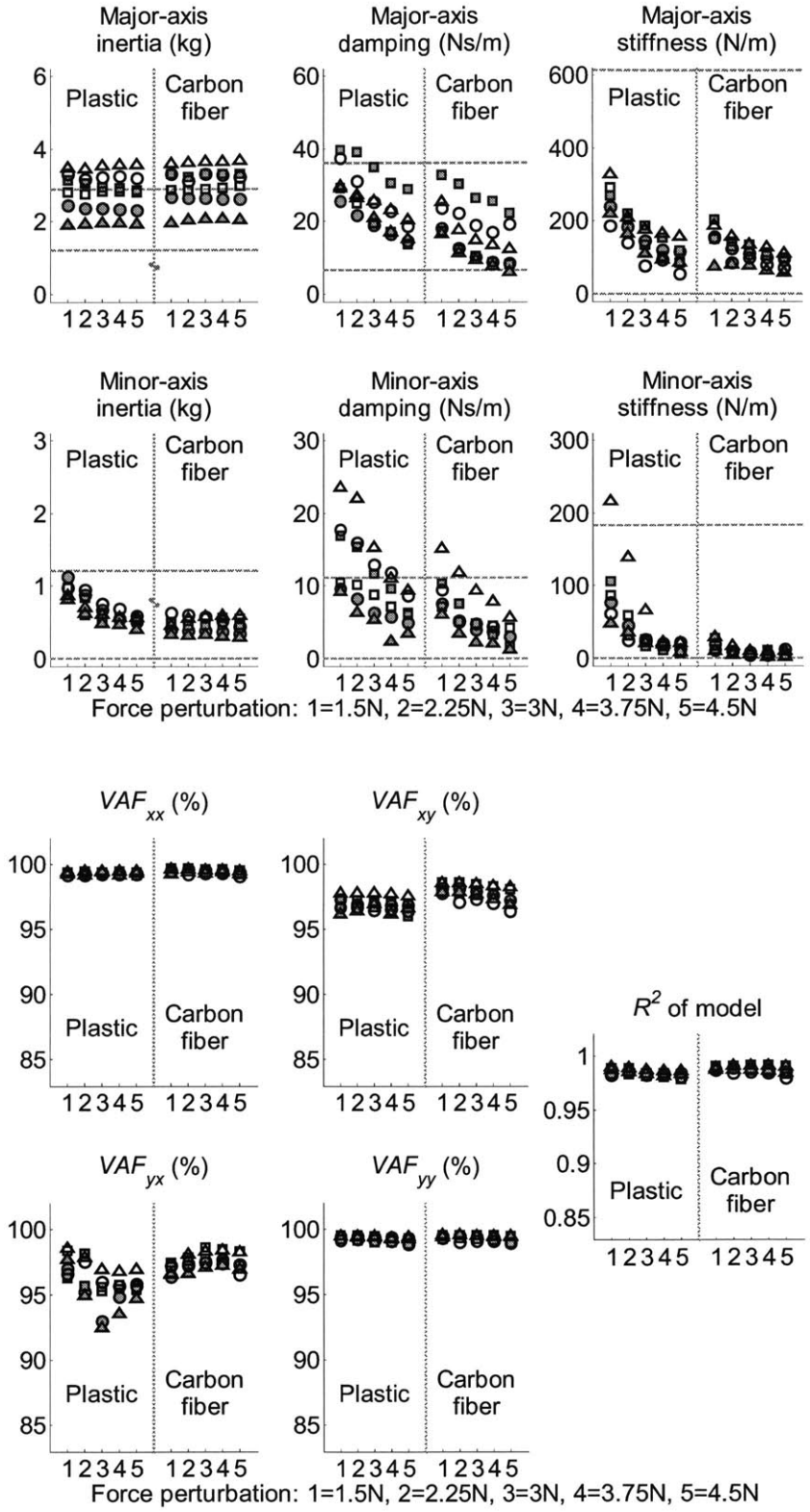

Figure F.57. Left arm, 5 overlaps, asymmetric: inertia, damping, and stiffness matrix major and minor axis properties (top), and *VAF* and R^2 of model (bottom)

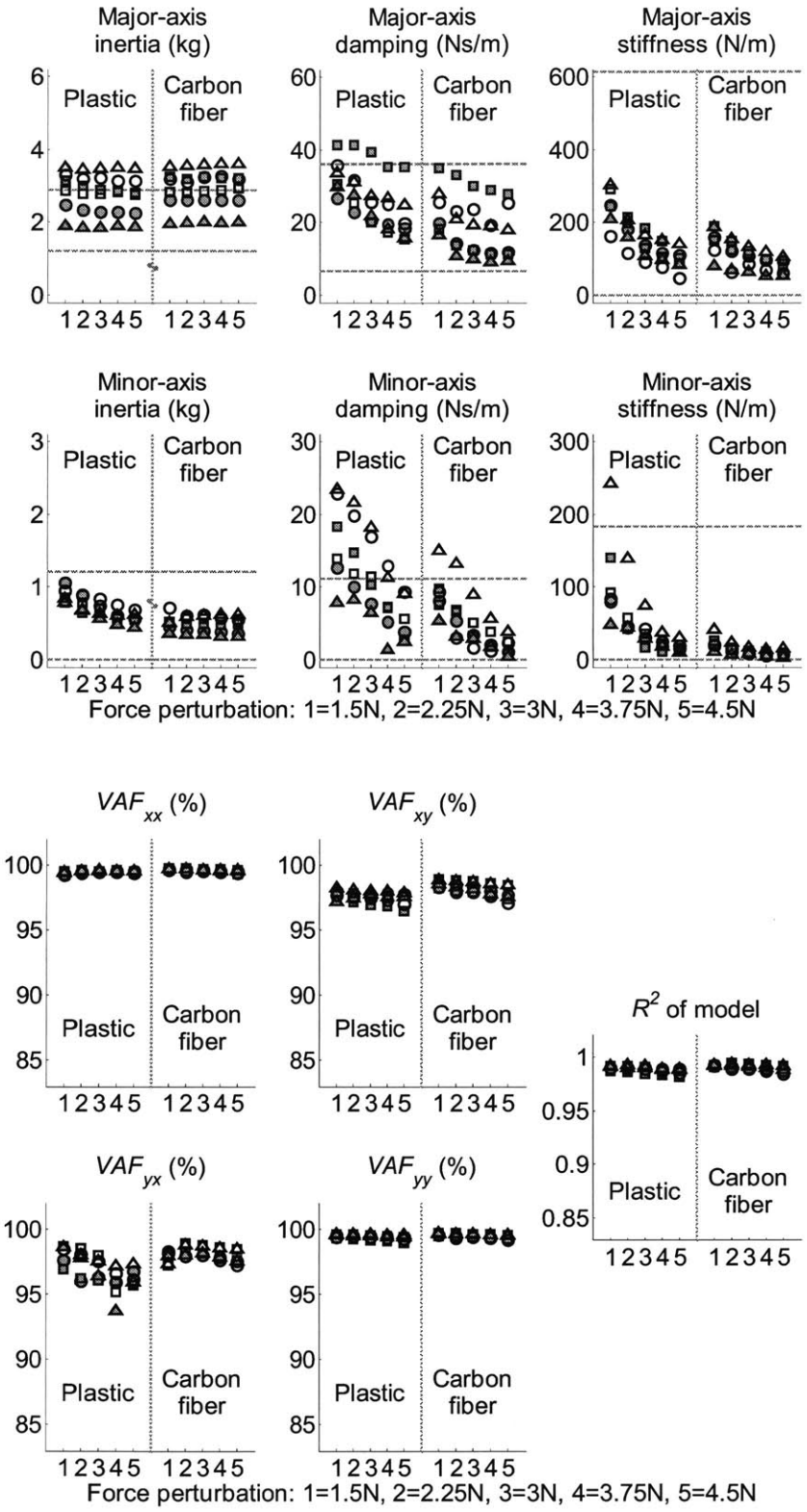

Figure F.58. Left arm, 45 overlaps, asymmetric: inertia, damping, and stiffness matrix major and minor axis properties (top), and *VAF* and R^2 of model (bottom)

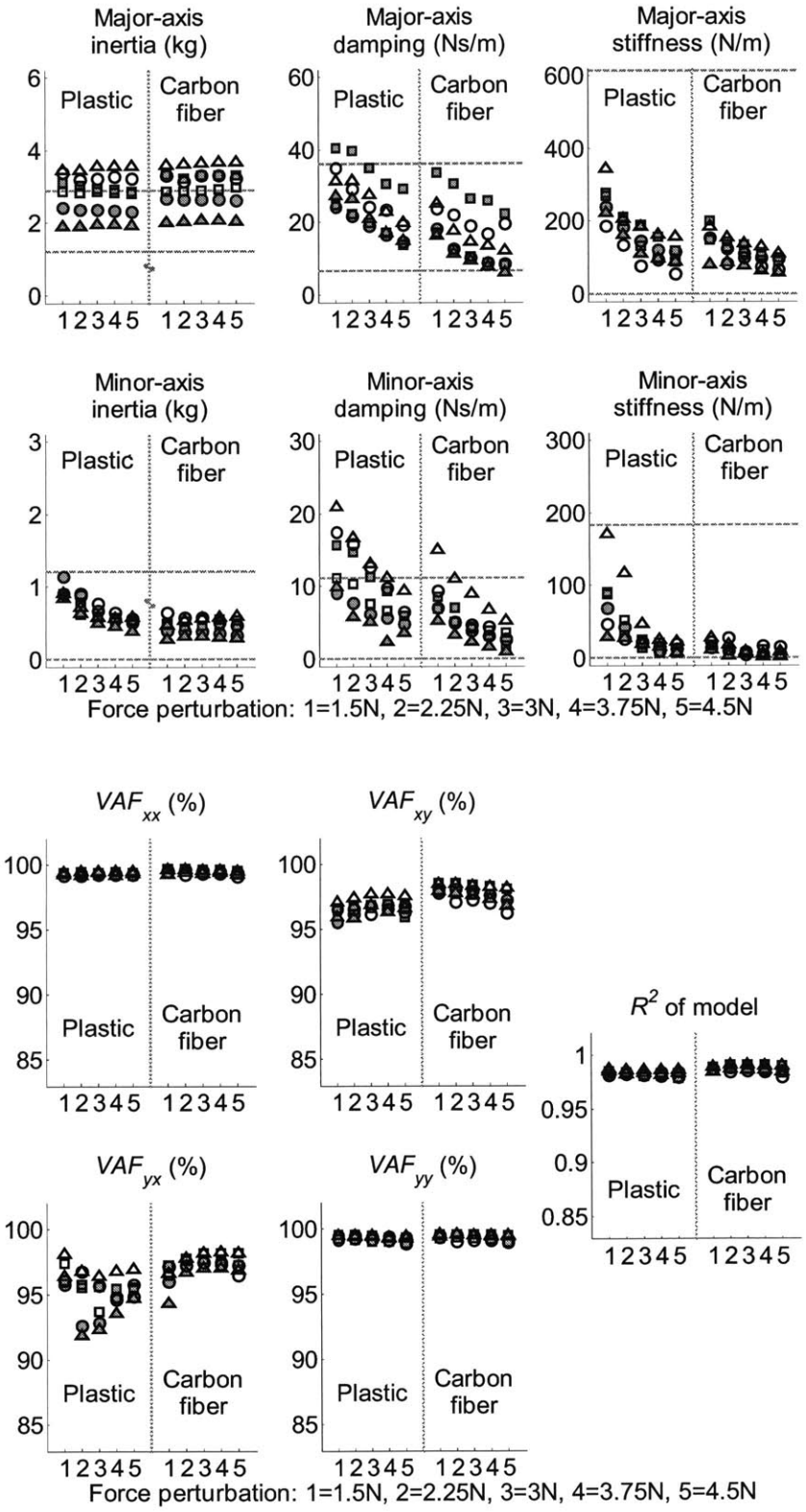

Figure F.59. Left arm, 5 overlaps, symmetric: inertia, damping, and stiffness matrix major and minor axis properties (top), and *VAF* and R^2 of model (bottom)

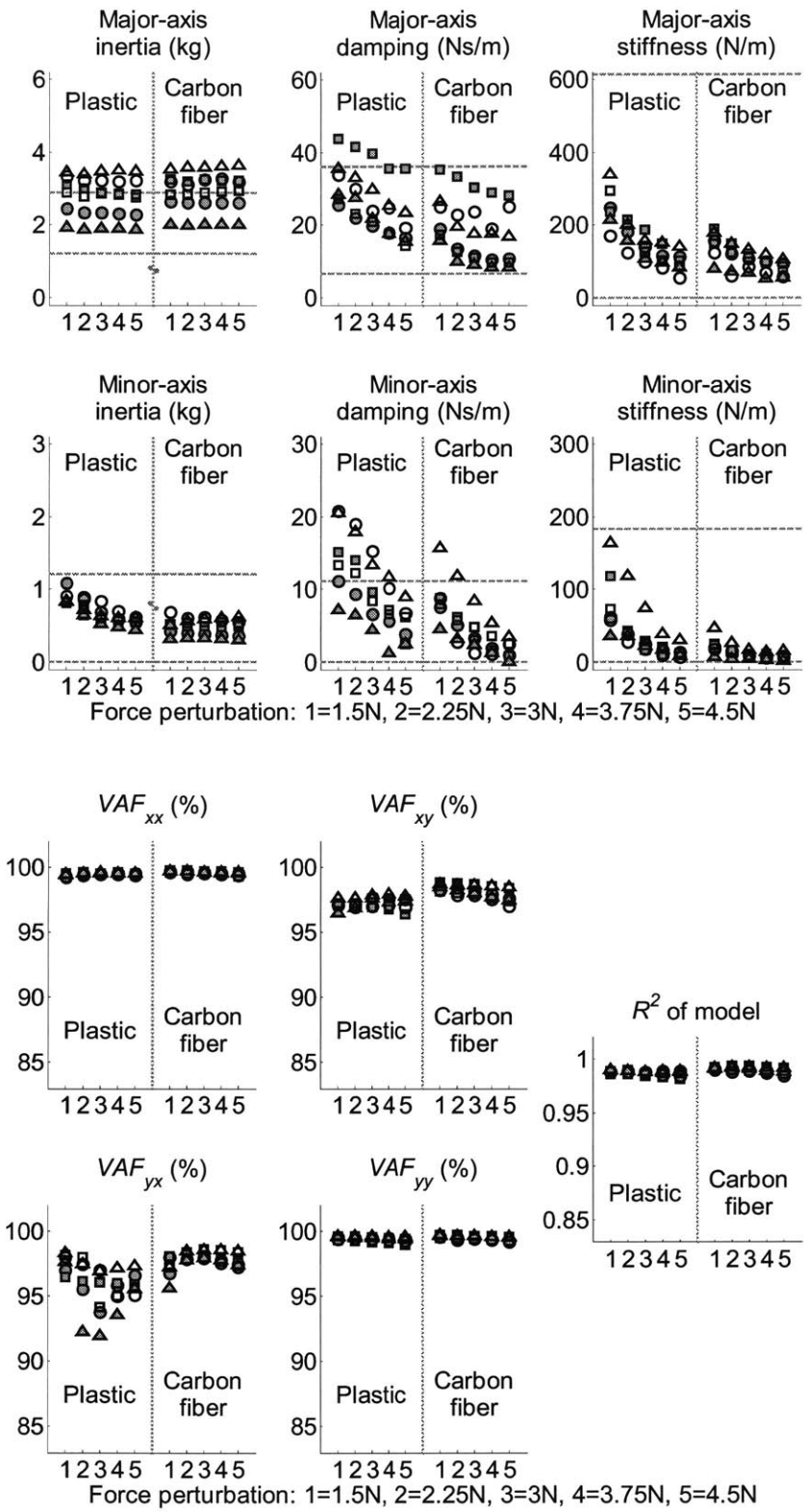

Figure F.60. Left arm, 45 overlaps, symmetric: inertia, damping, and stiffness matrix major and minor axis properties (top), and *VAF* and R^2 of model (bottom)

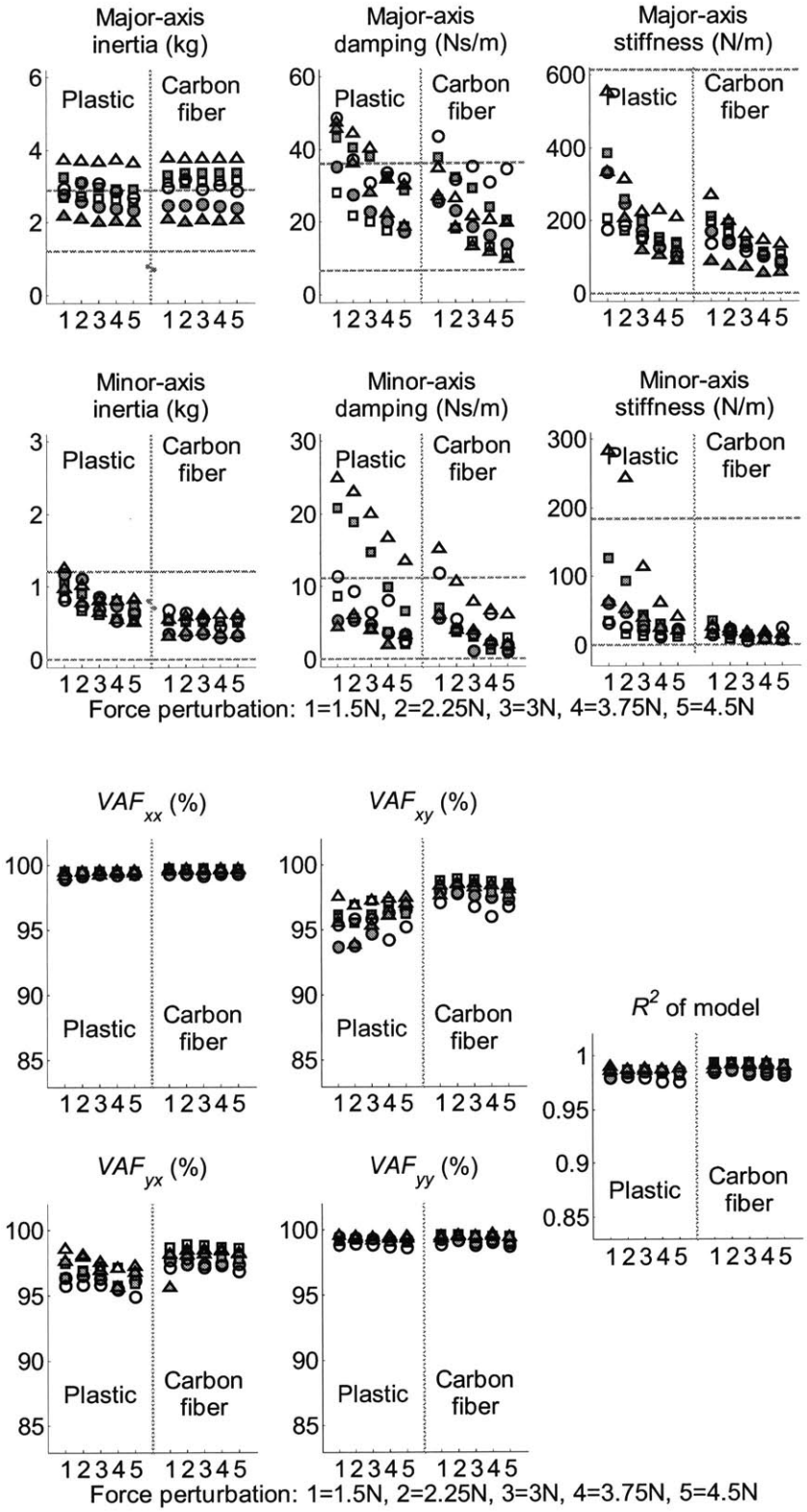

Figure F.61. Right arm, 5 overlaps, asymmetric: inertia, damping, and stiffness matrix major and minor axis properties (top), and *VAF* and R^2 of model (bottom)

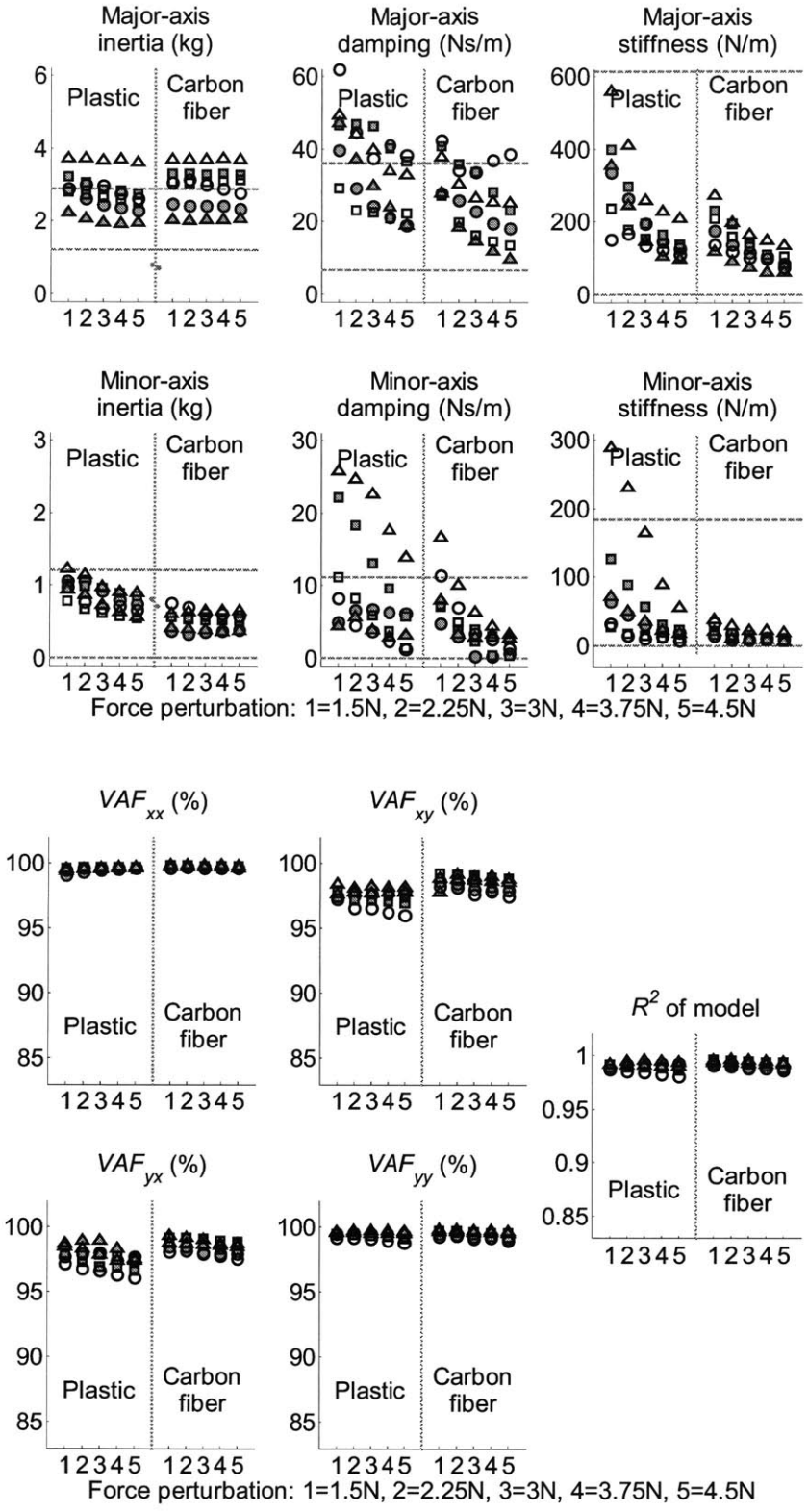

Figure F.62. Right arm, 45 overlaps, asymmetric: inertia, damping, and stiffness matrix major and minor axis properties (top), and *VAF* and R^2 of model (bottom)

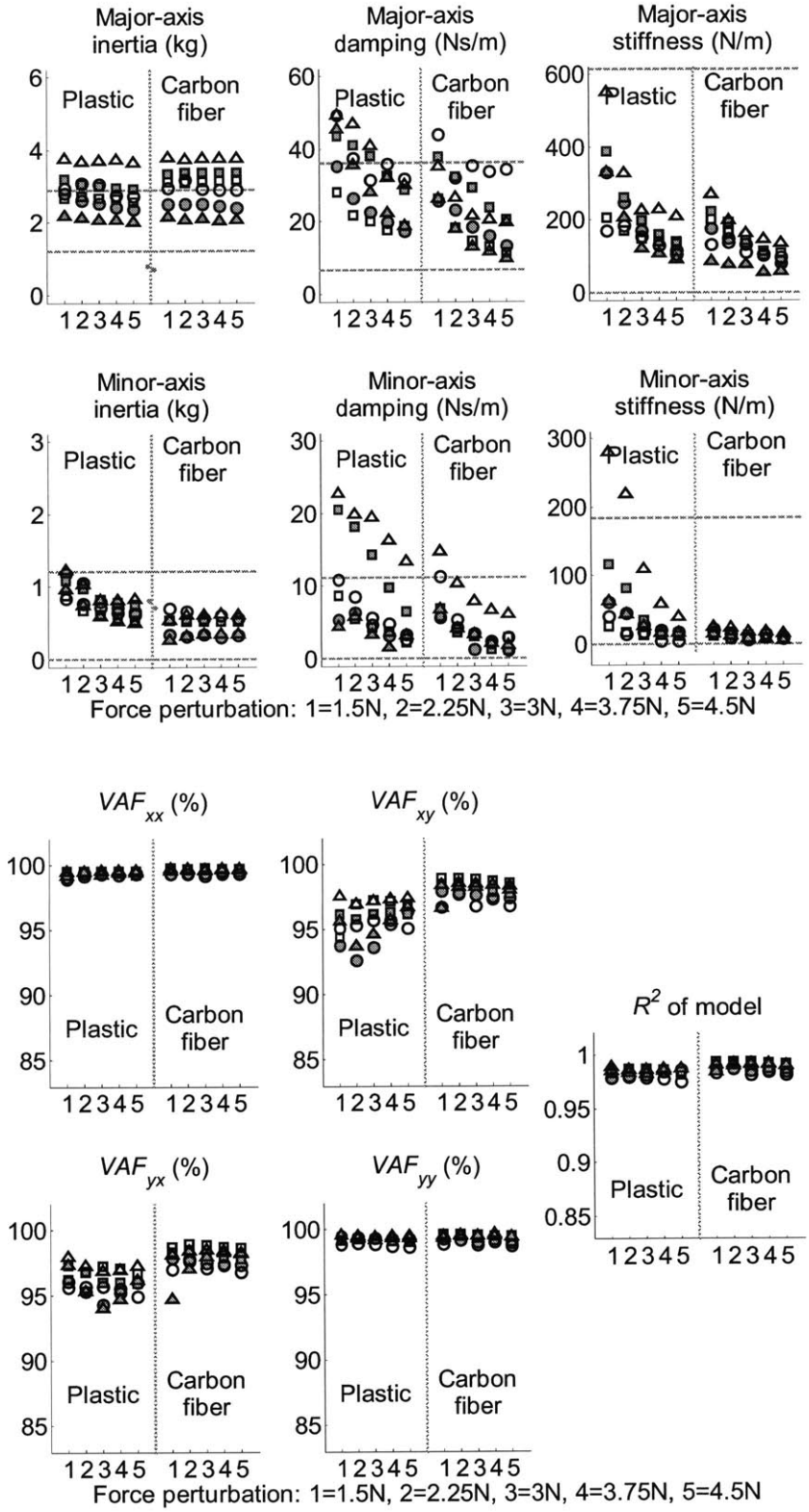

Figure F.63. Right arm, 5 overlaps, symmetric: inertia, damping, and stiffness matrix major and minor axis properties (top), and *VAF* and R^2 of model (bottom)

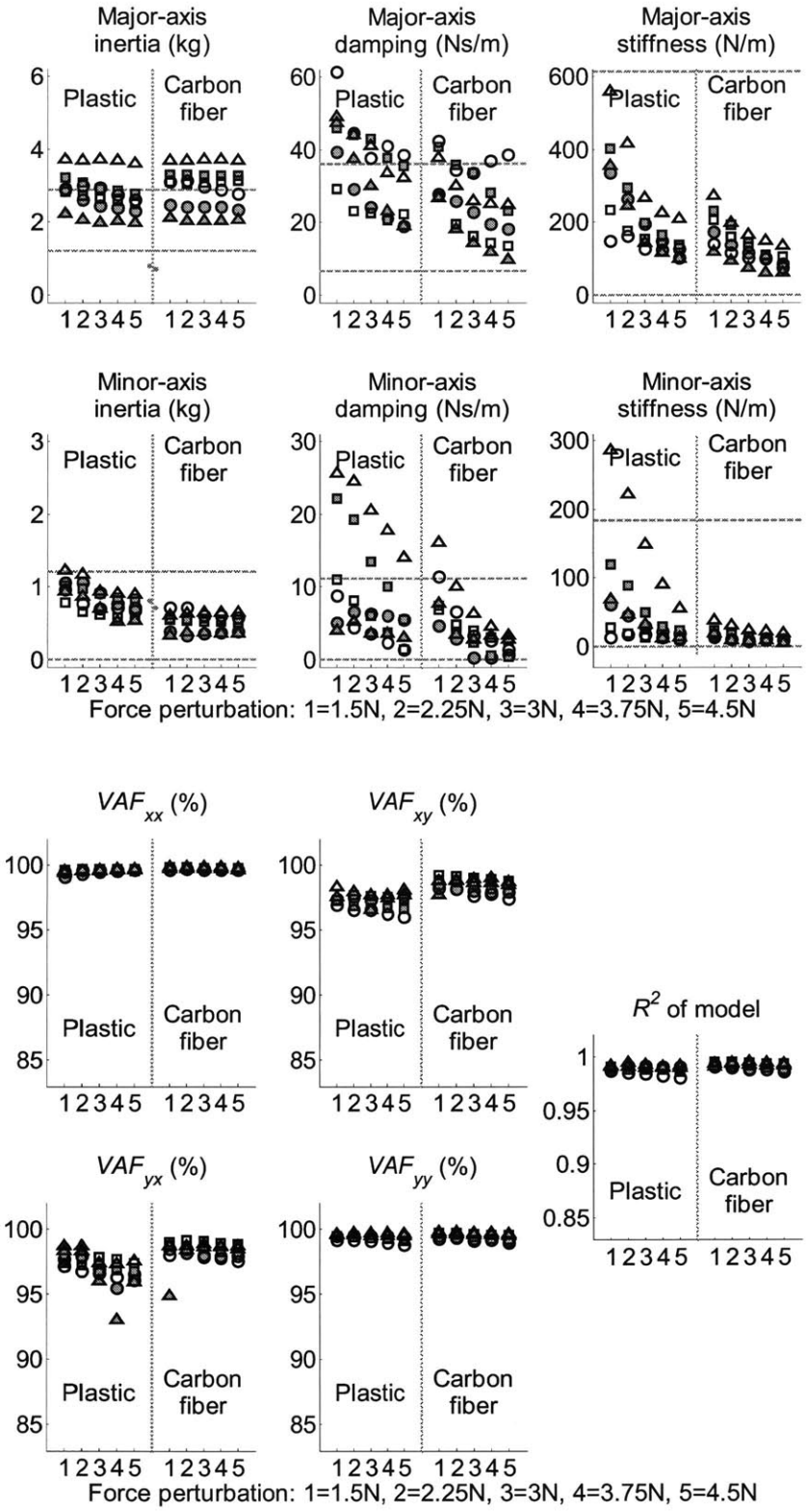

Figure F.64. Right arm, 45 overlaps, symmetric: inertia, damping, and stiffness matrix major and minor axis properties (top), and *VAF* and R^2 of model (bottom)

Appendix G

Experimental results of arm mechanical impedance testing of stroke patients

Spectral analysis results from the hemiplegic and less-impaired arms of six chronic stroke patients are included in this appendix as Figures G.1-G.24. The dynamic stiffness spectral estimates (top graph), and the partial and multiple coherences of the derived dynamic compliance estimate (bottom graph) are included in each figure. Welch's periodogram method was used to estimate the power spectral density and coherence functions [8]. In Chapter 6, the number of data points included in the FFT calculation was defined as N_{FFT}, the length of the Hanning windowing function as N_{WND}, and the number of overlapped samples as N_{OVL}. The odd numbered figures contain the spectral analysis results with $N_{FFT} = 8192$, $N_{WND} = 8192$, and $N_{OVL} = 4096$ ($N_{MNS} = 5$ overlapping data segments), whereas the even numbered figures contain the results with $N_{FFT} = 8192$, $N_{WND} = 2048$, and $N_{OVL} = 1536$ ($N_{MNS} = 45$). Ten tests were conducted on each arm by alternating between the left (L) and right (R) arms (3L, 3R, 4L, 4R, 3L, 3R). The dynamic stiffness spectral estimates depicted in the figures are the mean values of the first block of 3 tests, the second block of 4 tests, and the third block of 3 tests. Nonlinear least-squares optimizations were used to define inertial, damping, and stiffness parameters for a linear second-order model of the dynamic stiffness spectral estimates. Two model structures were considered: 1. symmetric mass matrix, asymmetric damping and stiffness matrices; 2. symmetric mass, damping, and stiffness matrices. The results for both $N_{MNS} = 5$ and $N_{MNS} = 45$ are given in Figures G.25-G.28, which display the major and minor-axis properties (top graph), and the Variance Accounted For and R^2 of the model (bottom graph).

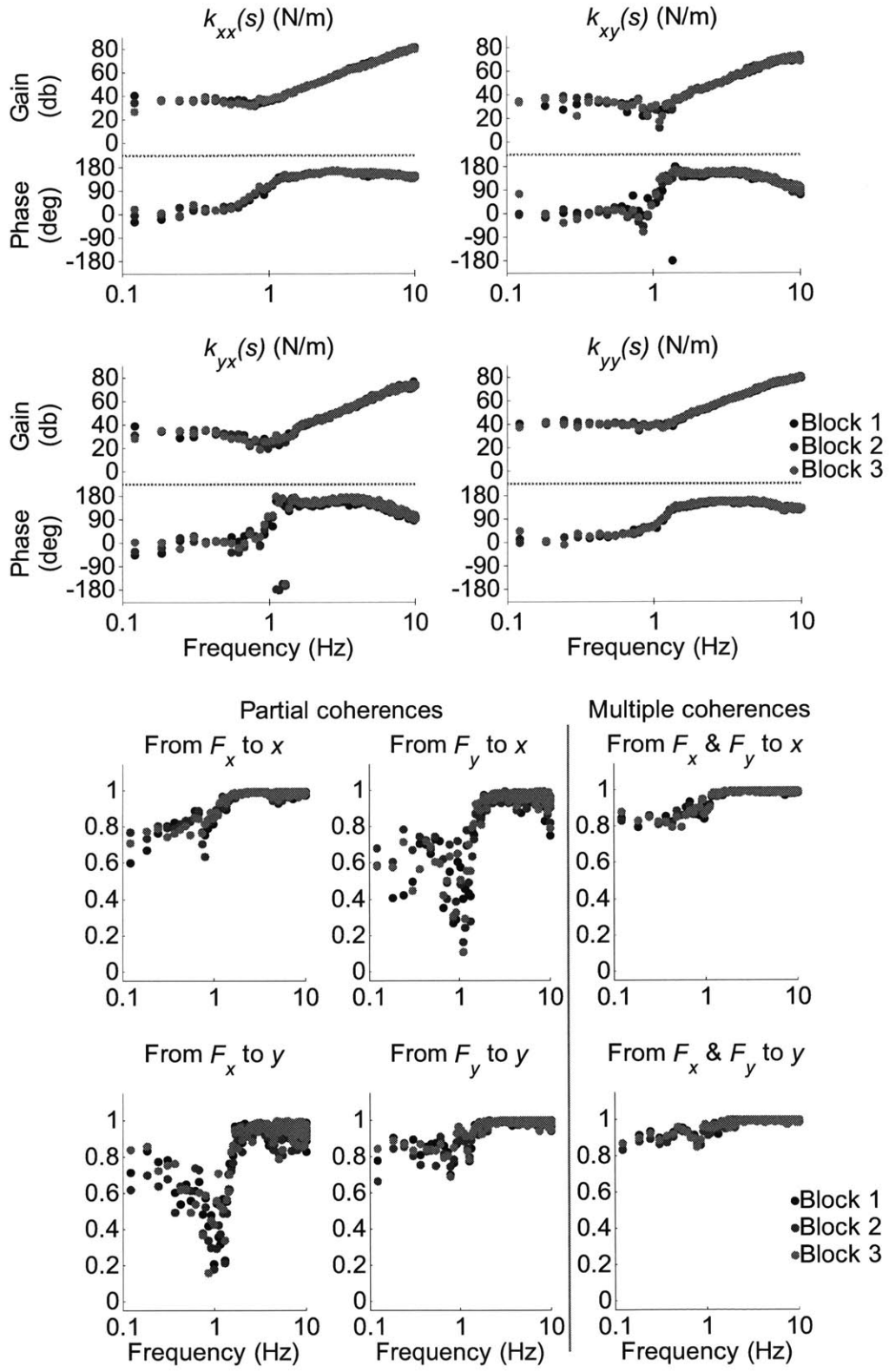

Figure G.1. Patient 1, left hemiplegic, left arm, 5 overlaps: dynamic stiffness spectral estimates (top), and partial and multiple coherences (bottom)

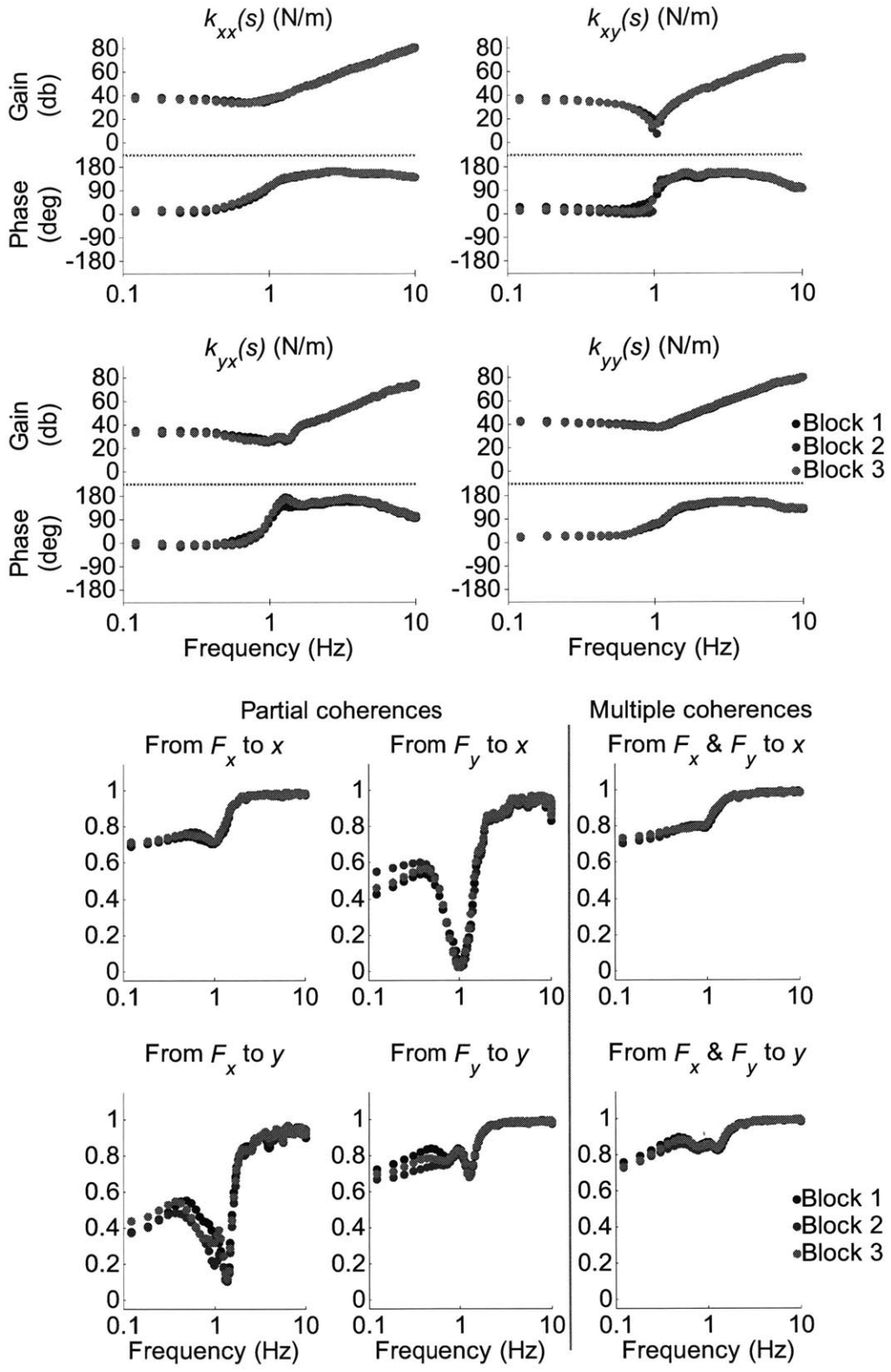

Figure G.2. Patient 1, left hemiplegic, left arm, 45 overlaps: dynamic stiffness spectral estimates (top), and partial and multiple coherences (bottom)

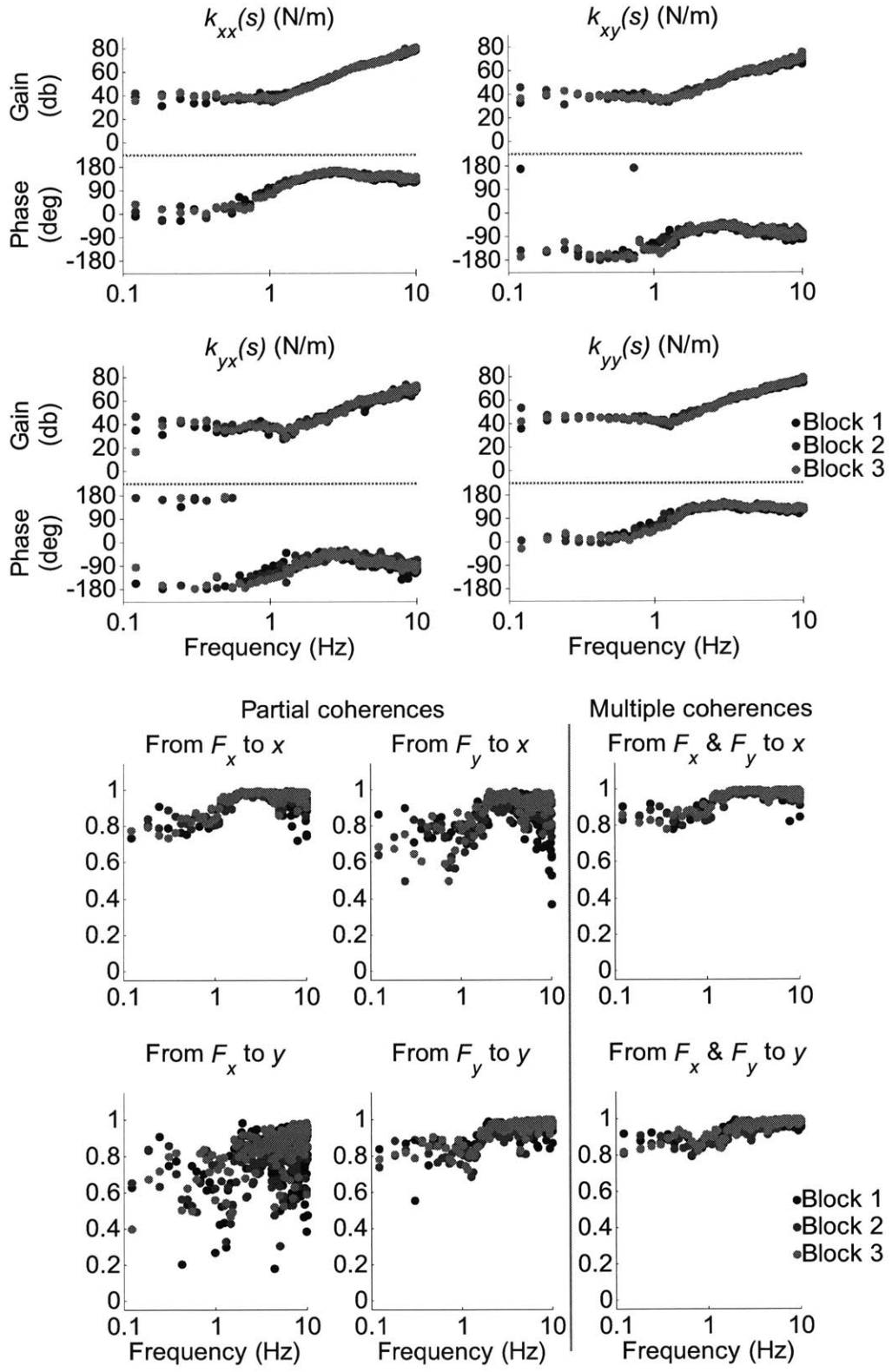

Figure G.3. Patient 1, left hemiplegic, right arm, 5 overlaps: dynamic stiffness spectral estimates (top), and partial and multiple coherences (bottom)

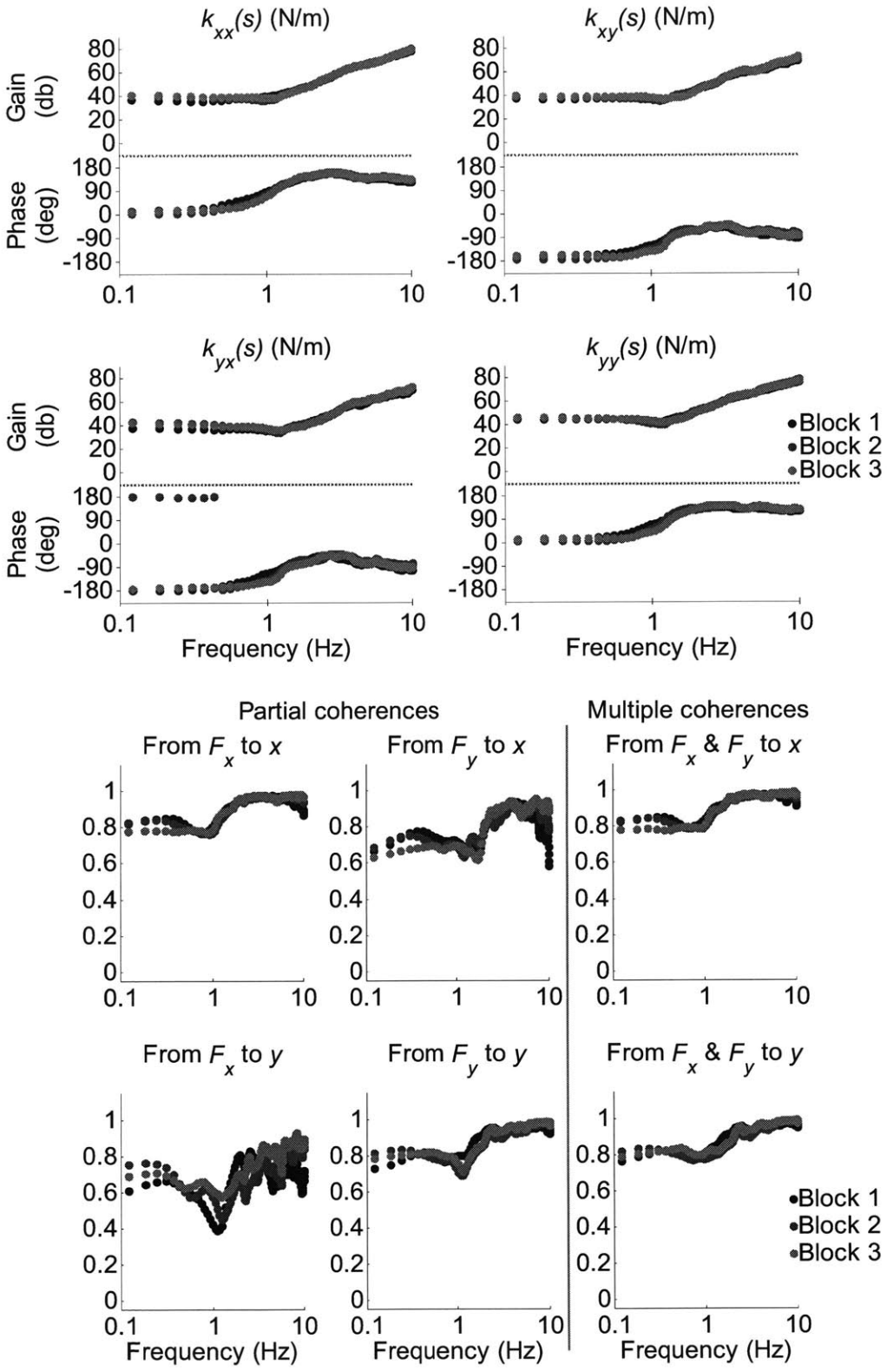

Figure G.4. Patient 1, left hemiplegic, right arm, 45 overlaps: dynamic stiffness spectral estimates (top), and partial and multiple coherences (bottom)

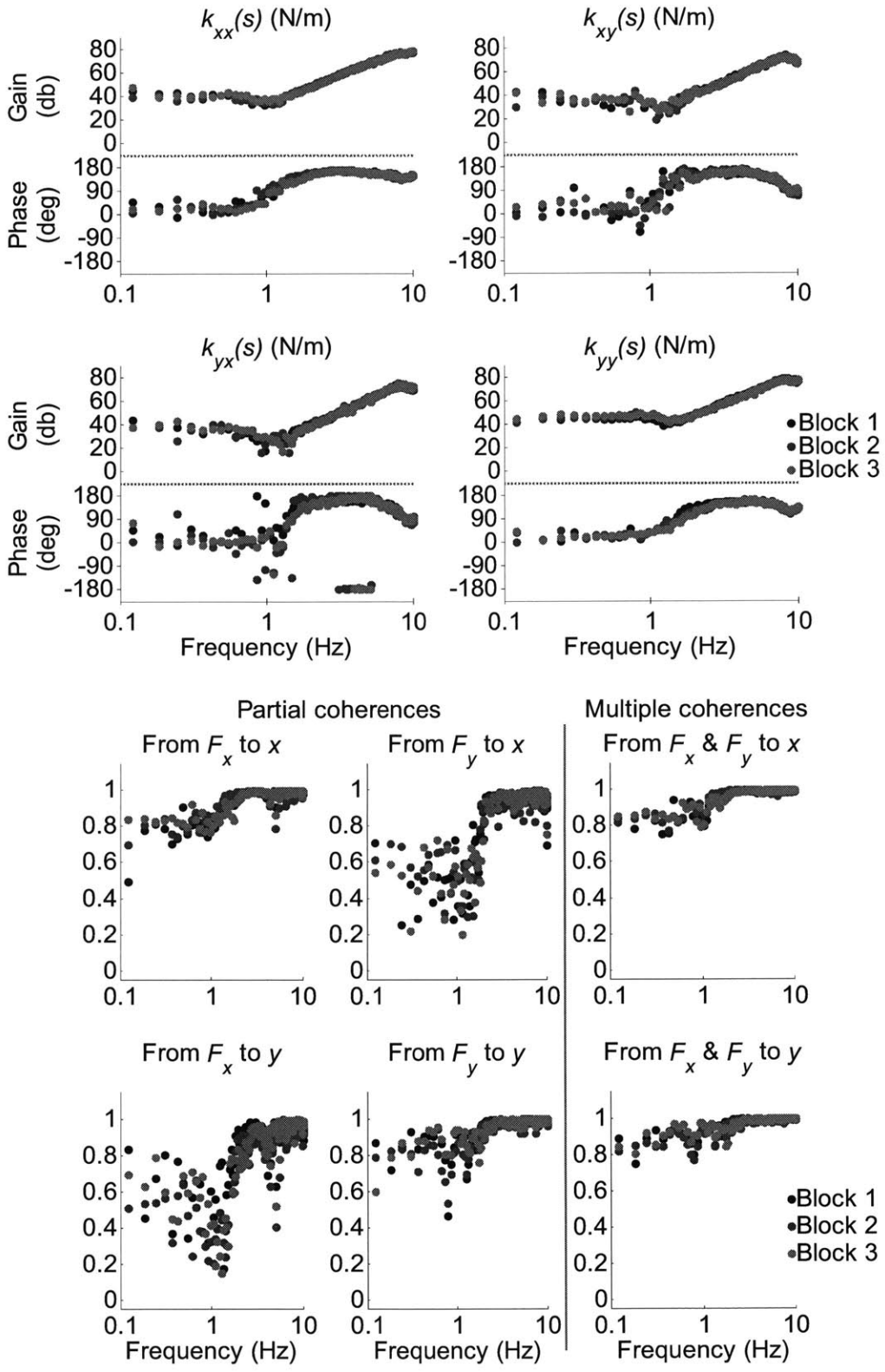

Figure G.5. Patient 2, left hemiplegic, left arm, 5 overlaps: dynamic stiffness spectral estimates (top), and partial and multiple coherences (bottom)

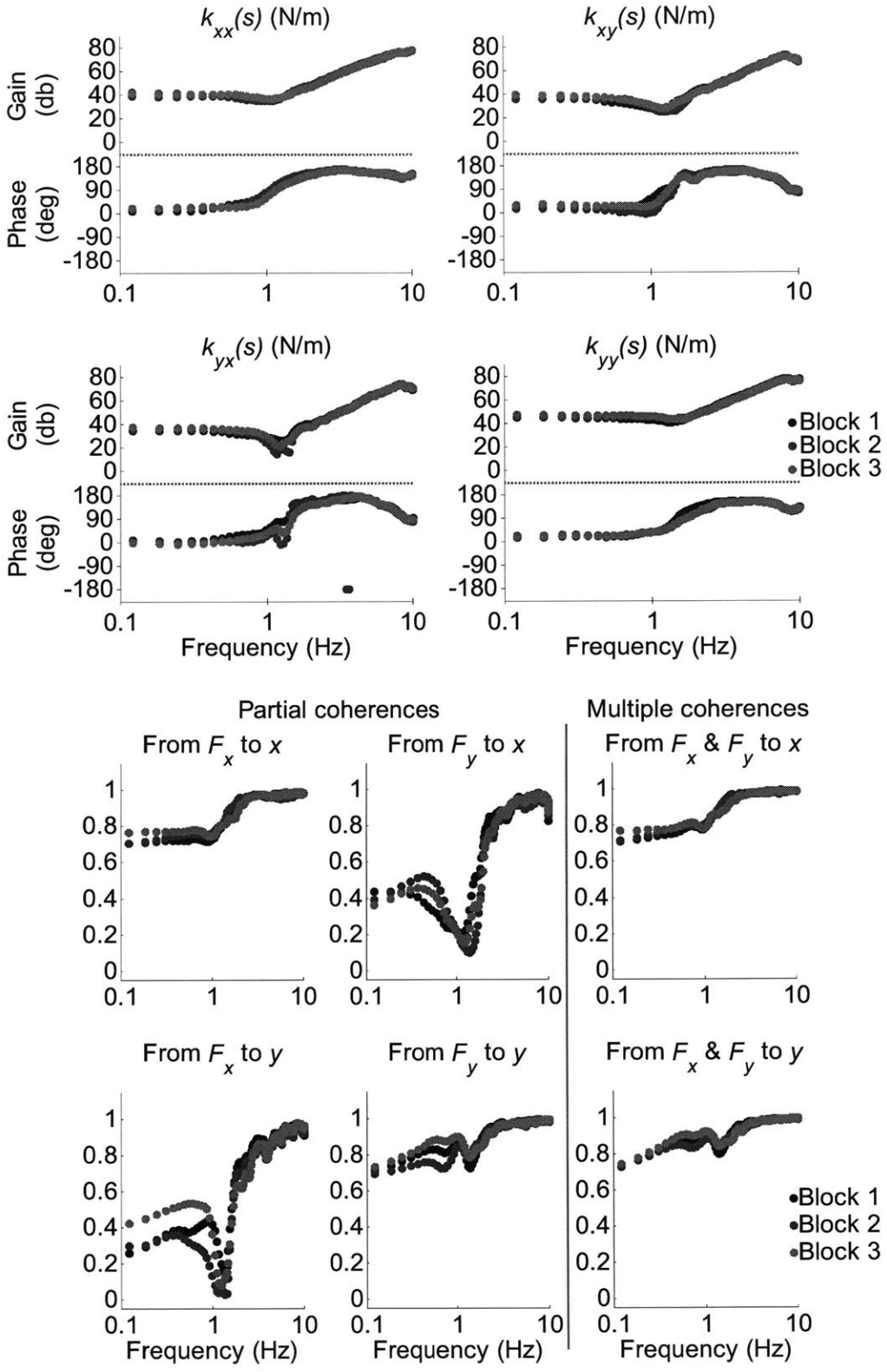

Figure G.6. Patient 2, left hemiplegic, left arm, 45 overlaps: dynamic stiffness spectral estimates (top), and partial and multiple coherences (bottom)

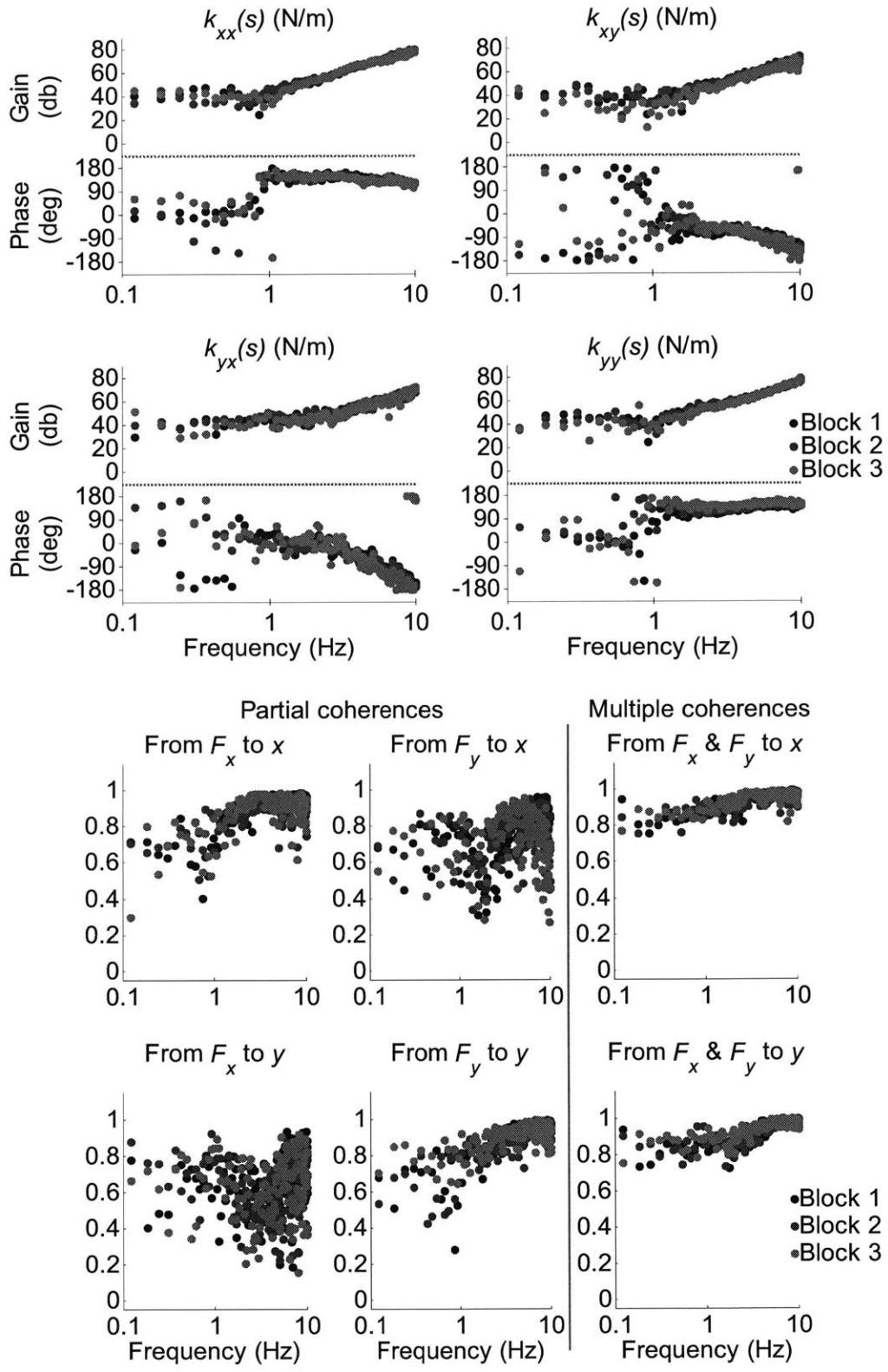

Figure G.7. Patient 2, left hemiplegic, right arm, 5 overlaps: dynamic stiffness spectral estimates (top), and partial and multiple coherences (bottom)

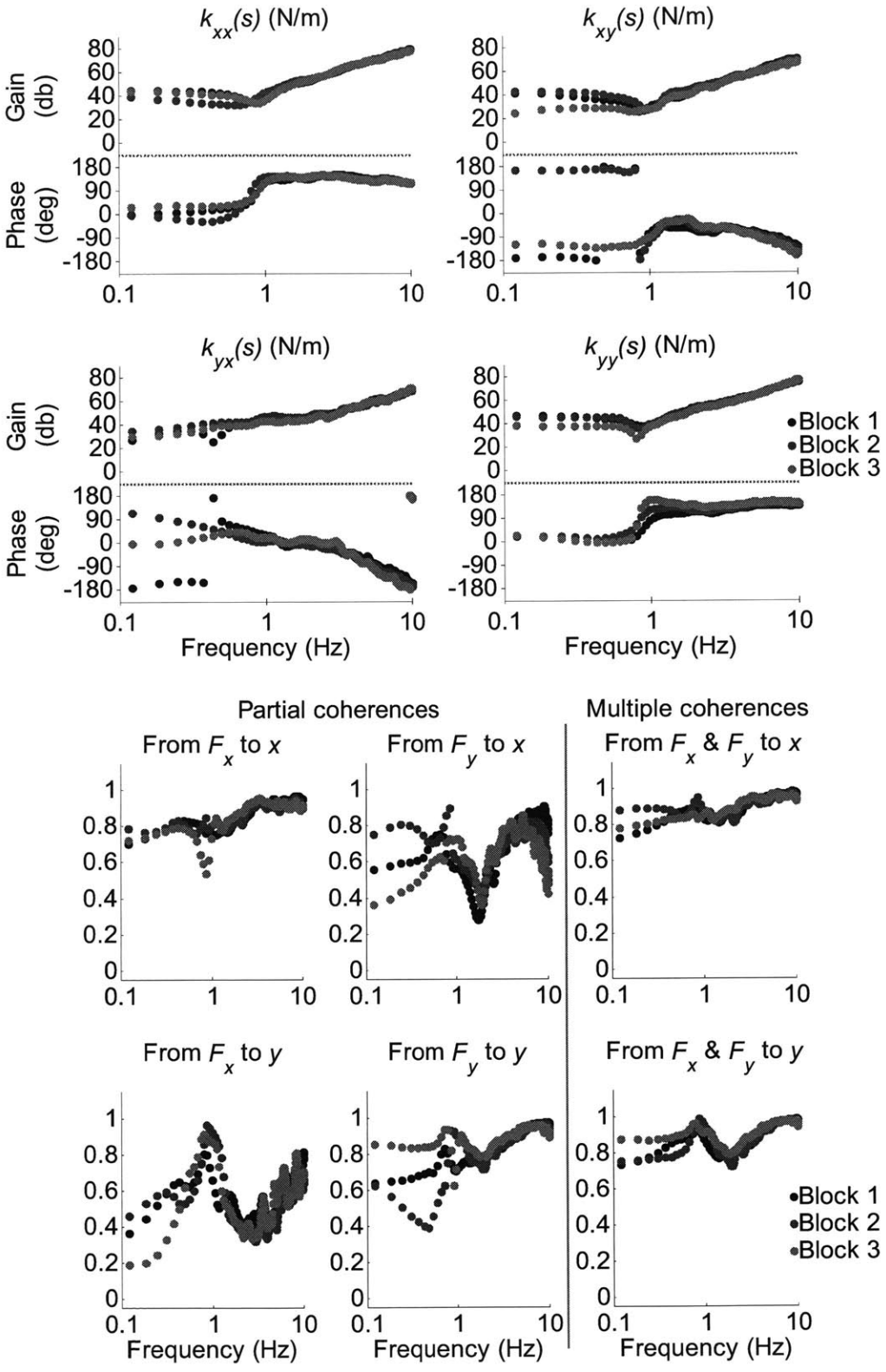

Figure G.8. Patient 2, left hemiplegic, right arm, 45 overlaps: dynamic stiffness spectral estimates (top), and partial and multiple coherences (bottom)

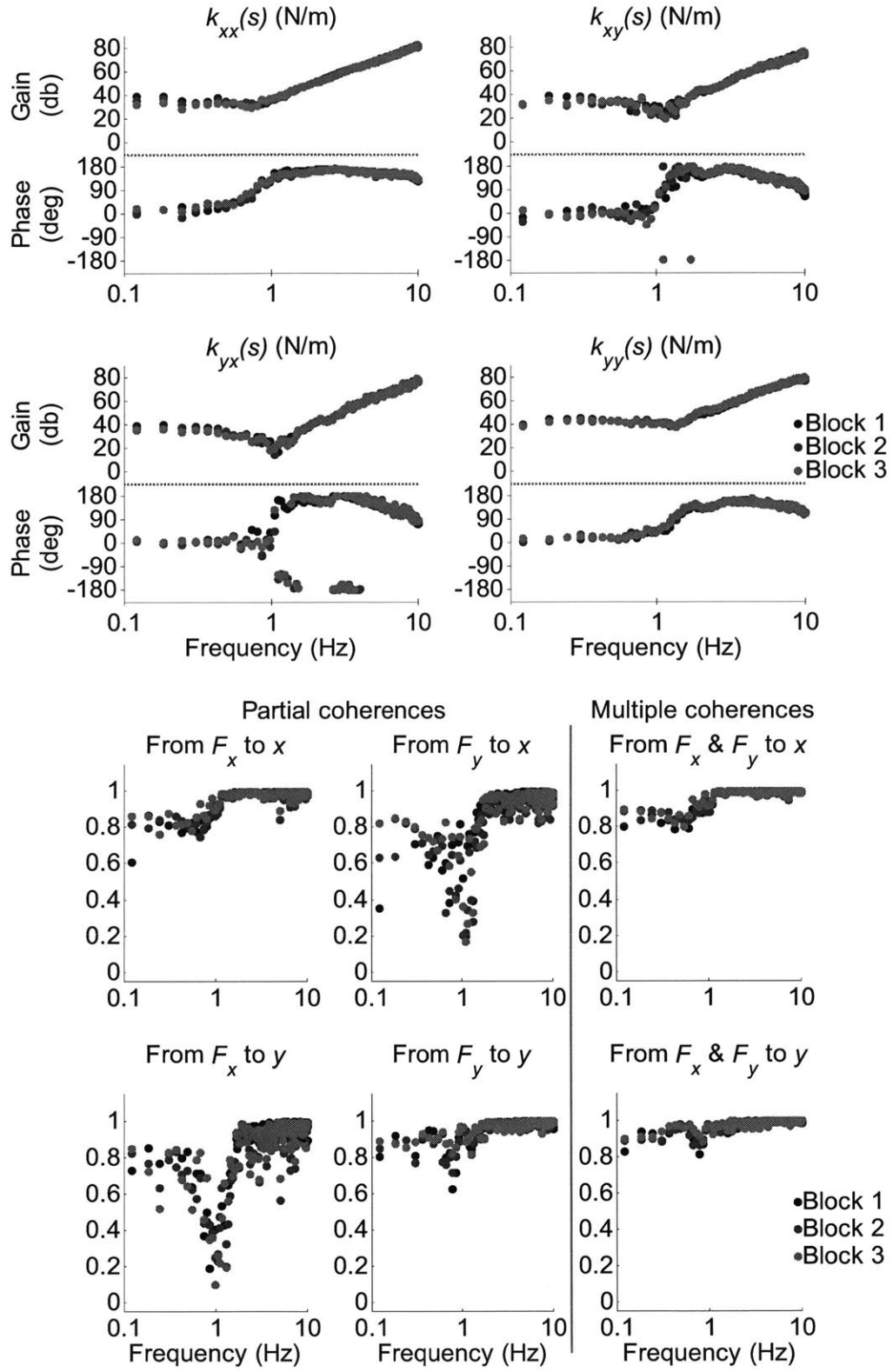

Figure G.9. Patient 3, left hemiplegic, left arm, 5 overlaps: dynamic stiffness spectral estimates (top), and partial and multiple coherences (bottom)

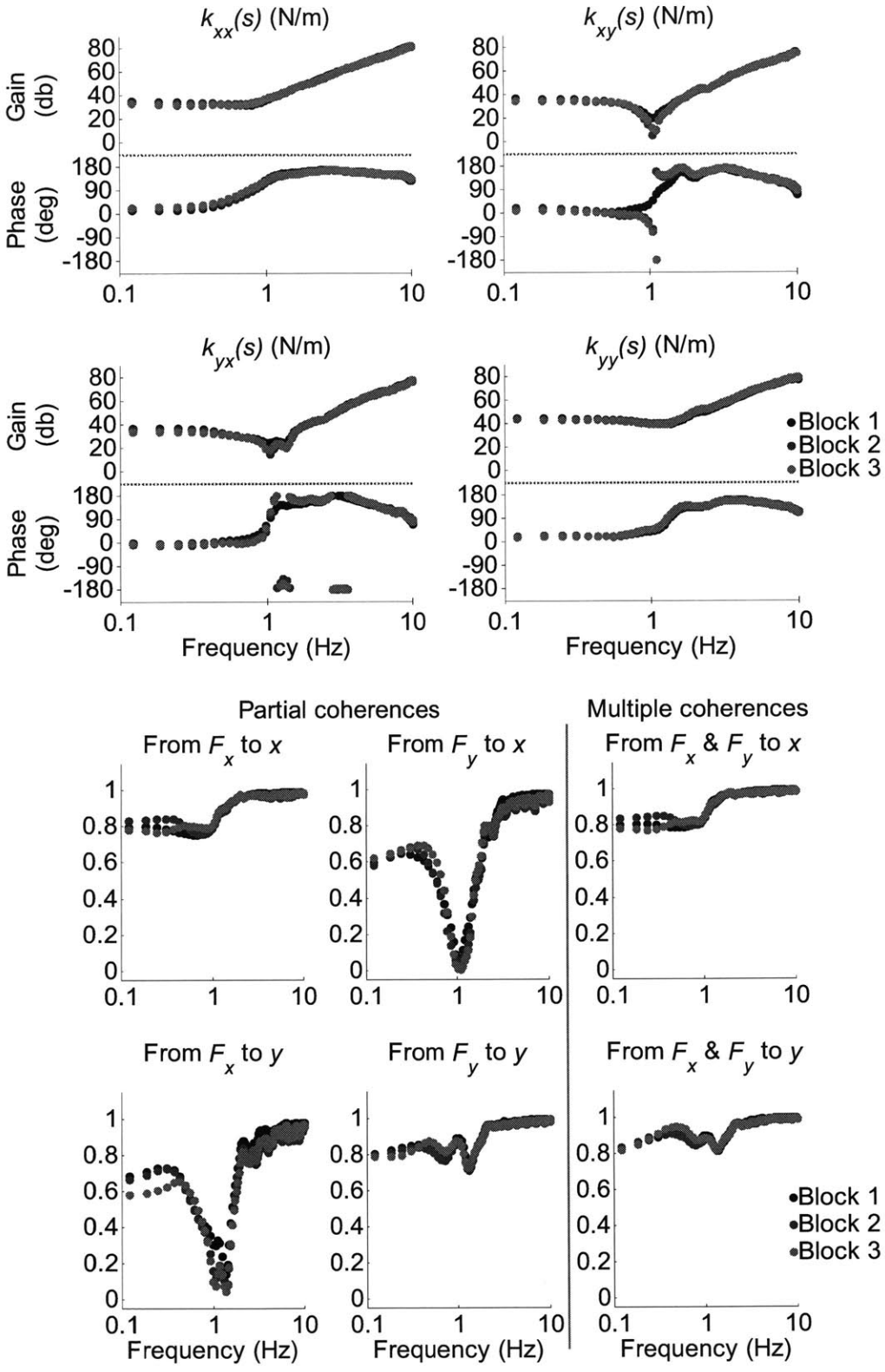

Figure G.10. Patient 3, left hemiplegic, left arm, 45 overlaps: dynamic stiffness spectral estimates (top), and partial and multiple coherences (bottom)

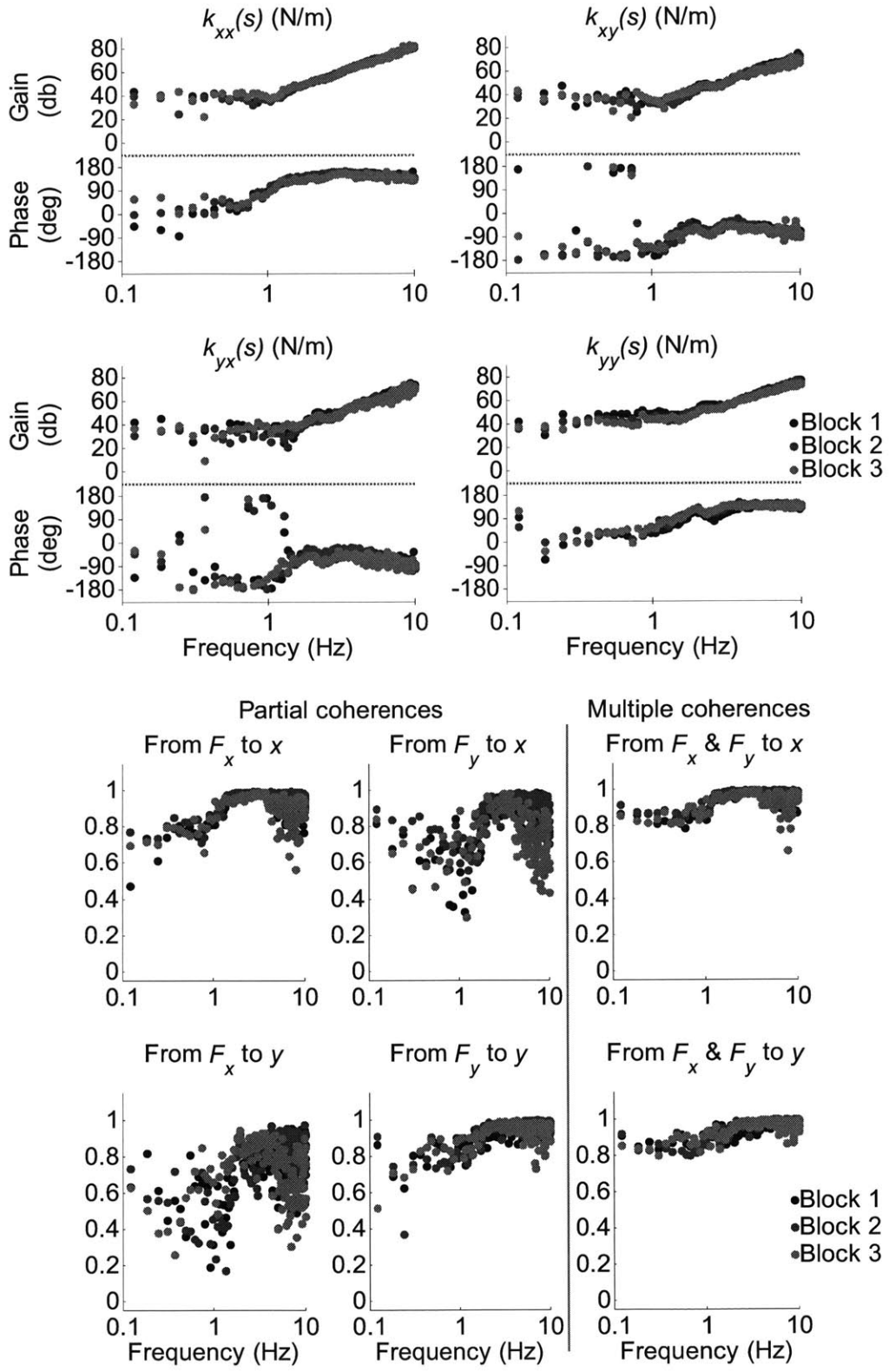

Figure G.11. Patient 3, left hemiplegic, right arm, 5 overlaps: dynamic stiffness spectral estimates (top), and partial and multiple coherences (bottom)

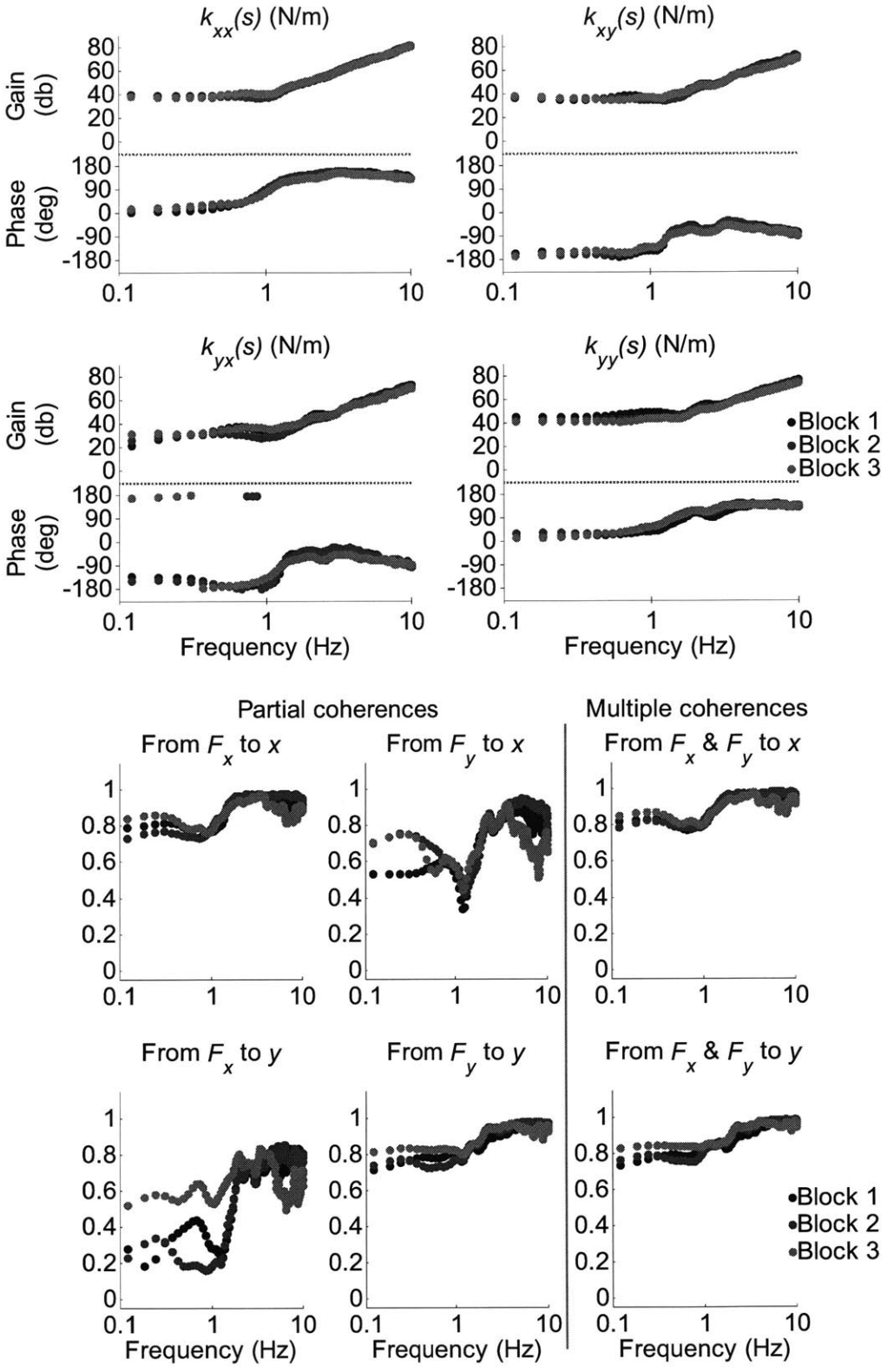

Figure G.12. Patient 3, left hemiplegic, right arm, 45 overlaps: dynamic stiffness spectral estimates (top), and partial and multiple coherences (bottom)

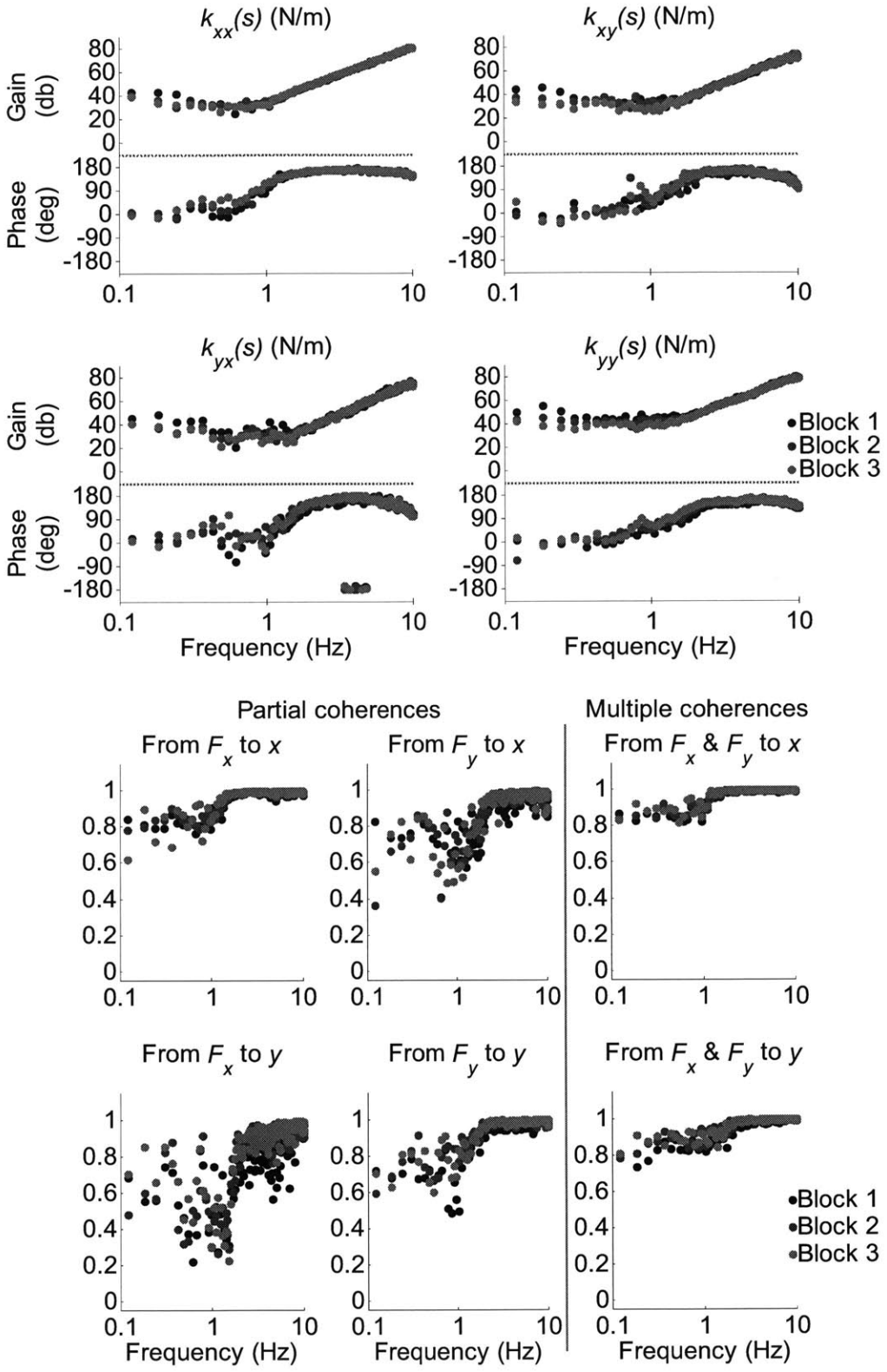

Figure G.13. Patient 4, right hemiplegic, left arm, 5 overlaps: dynamic stiffness spectral estimates (top), and partial and multiple coherences (bottom)

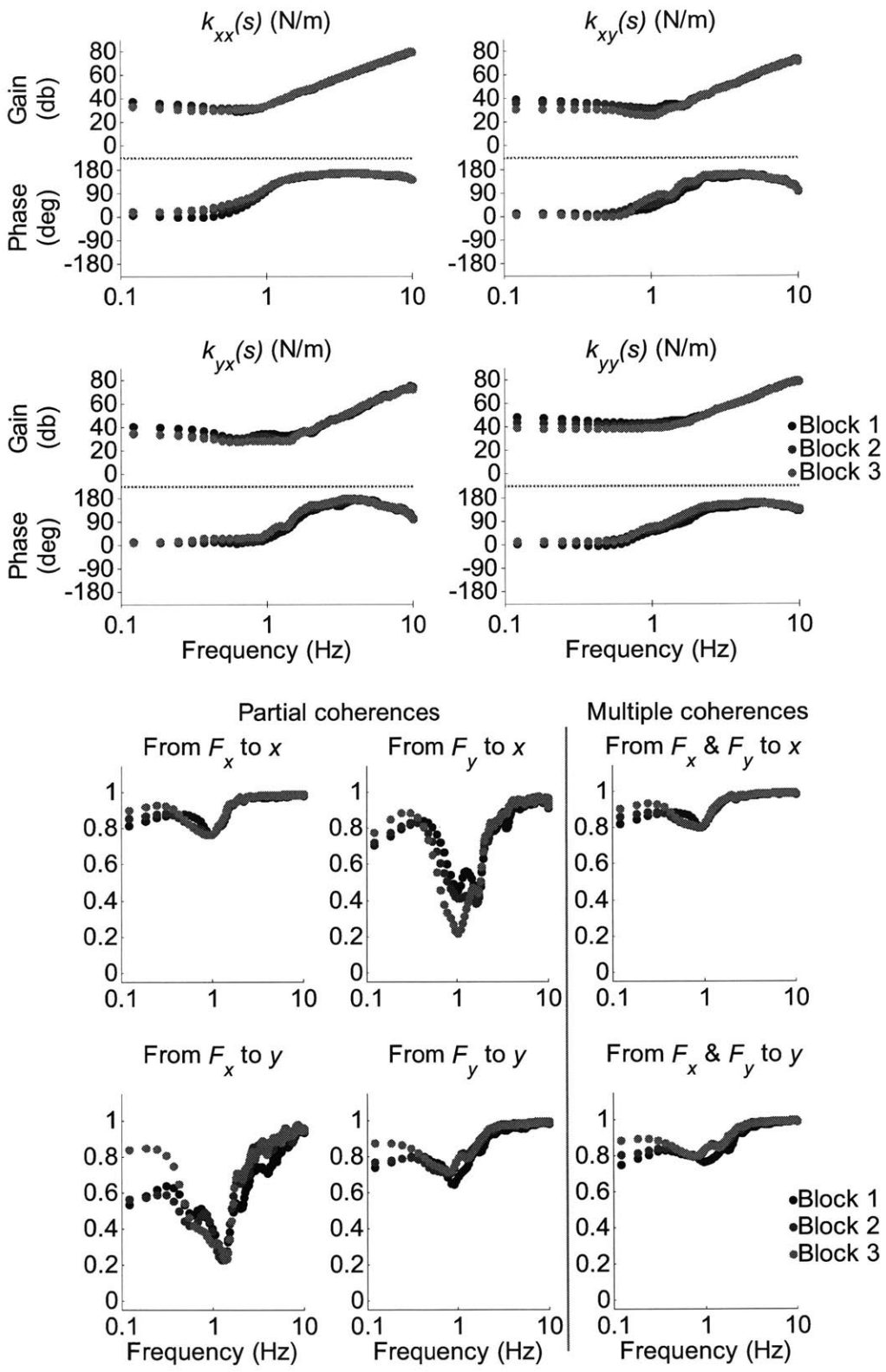

Figure G.14. Patient 4, right hemiplegic, left arm, 45 overlaps: dynamic stiffness spectral estimates (top), and partial and multiple coherences (bottom)

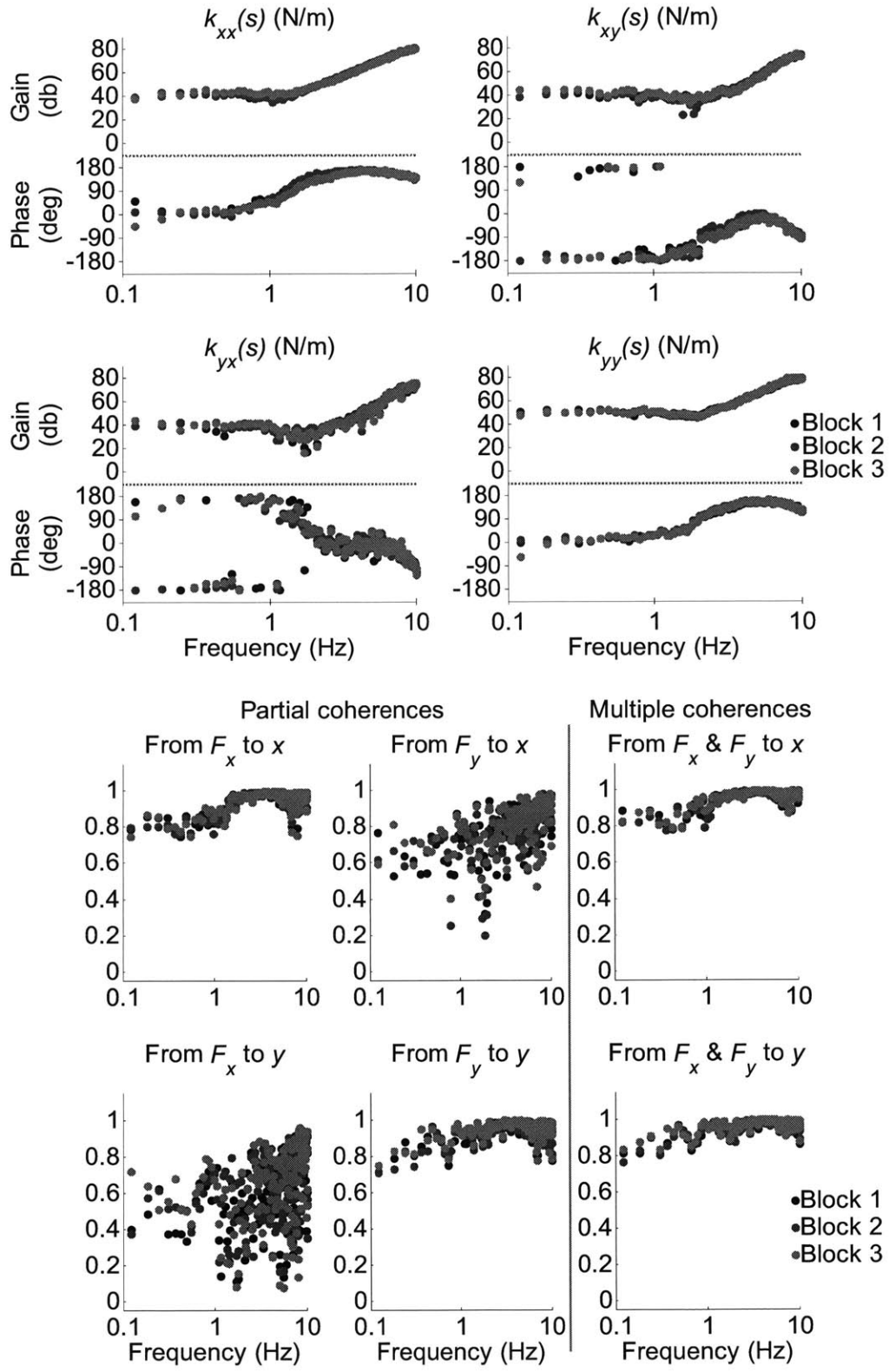

Figure G.15. Patient 4, right hemiplegic, right arm, 5 overlaps: dynamic stiffness spectral estimates (top), and partial and multiple coherences (bottom)

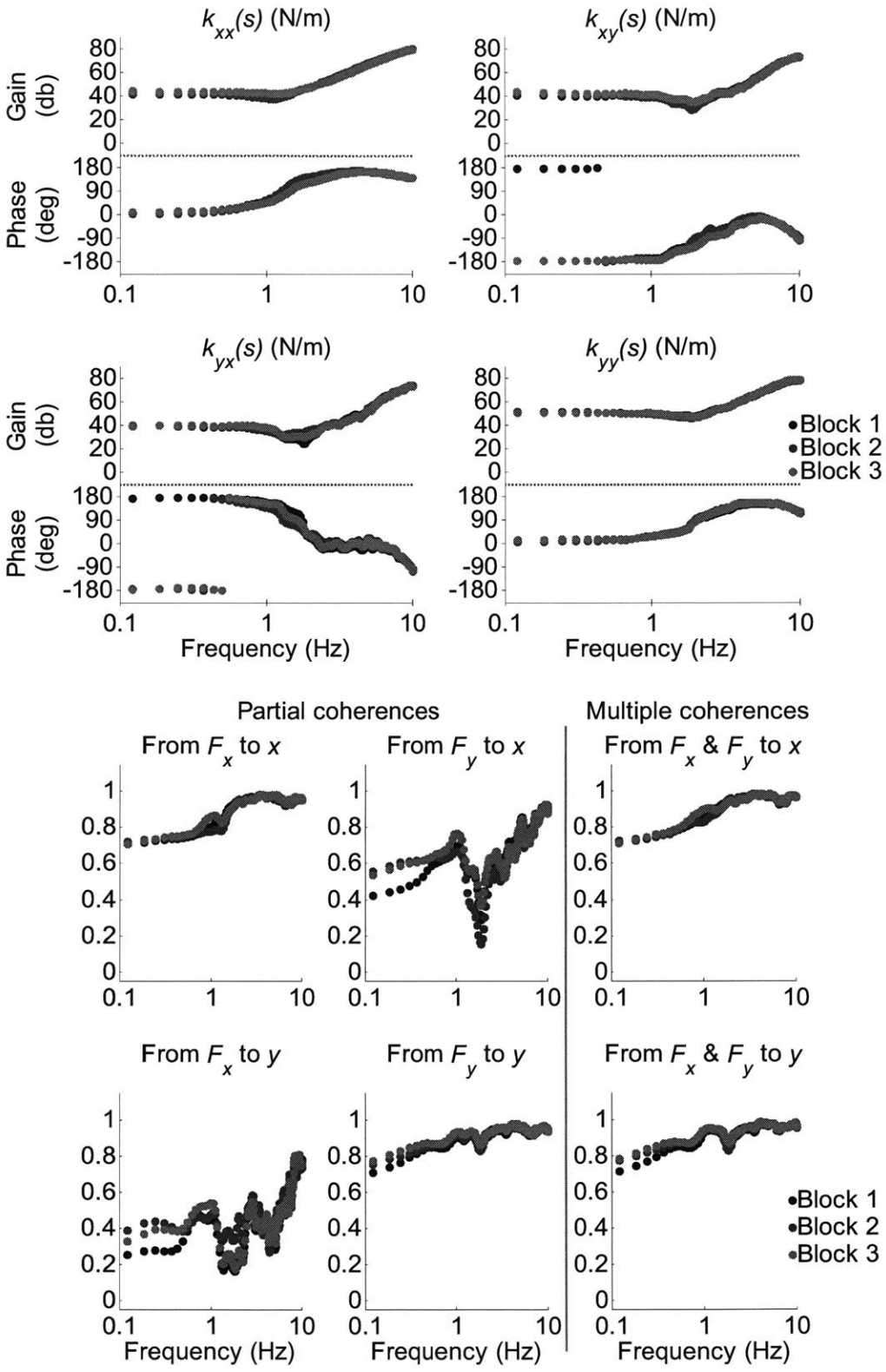

Figure G.16. Patient 4, right hemiplegic, right arm, 45 overlaps: dynamic stiffness spectral estimates (top), and partial and multiple coherences (bottom)

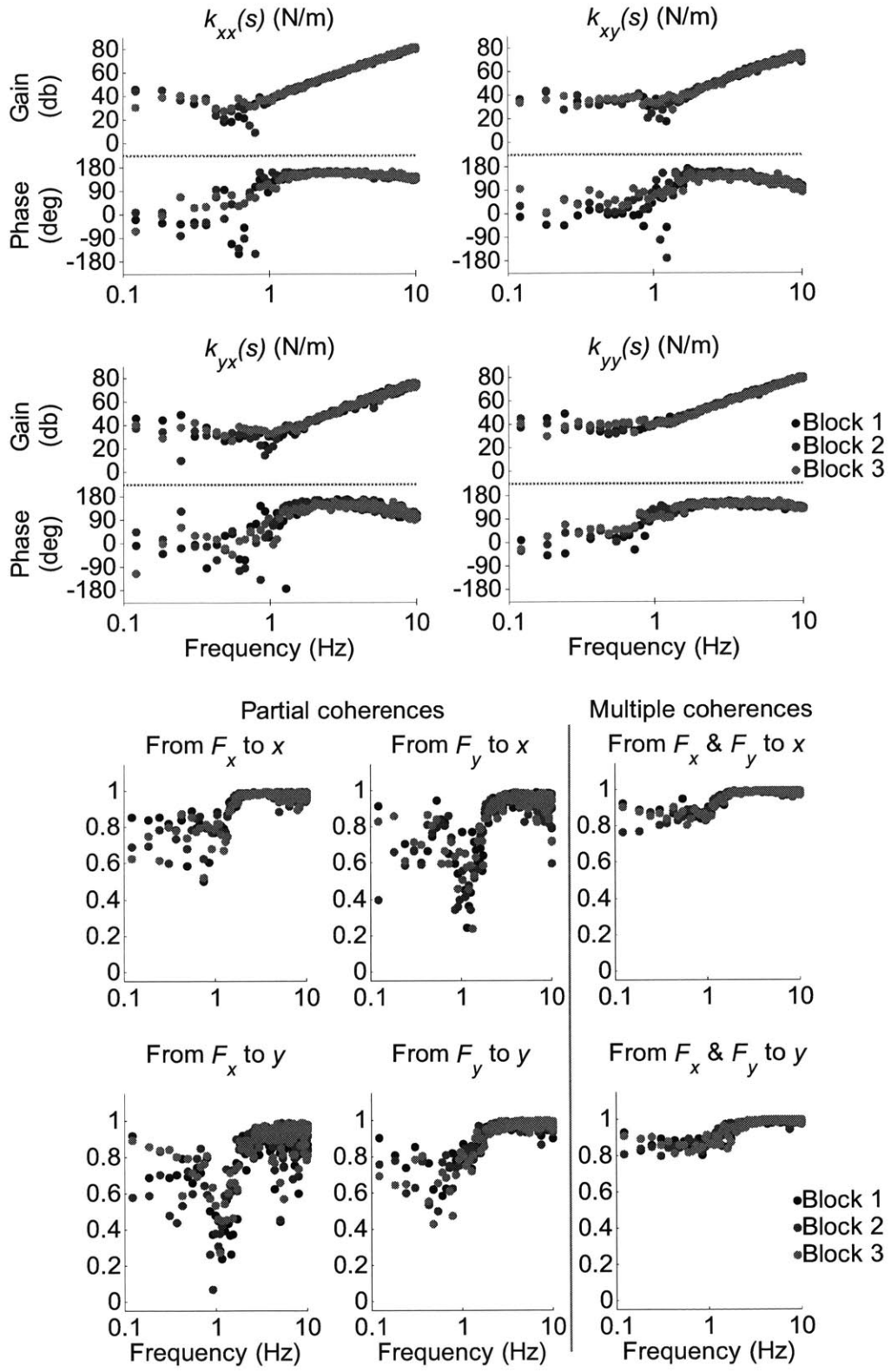

Figure G.17. Patient 5, right hemiplegic, left arm, 5 overlaps: dynamic stiffness spectral estimates (top), and partial and multiple coherences (bottom)

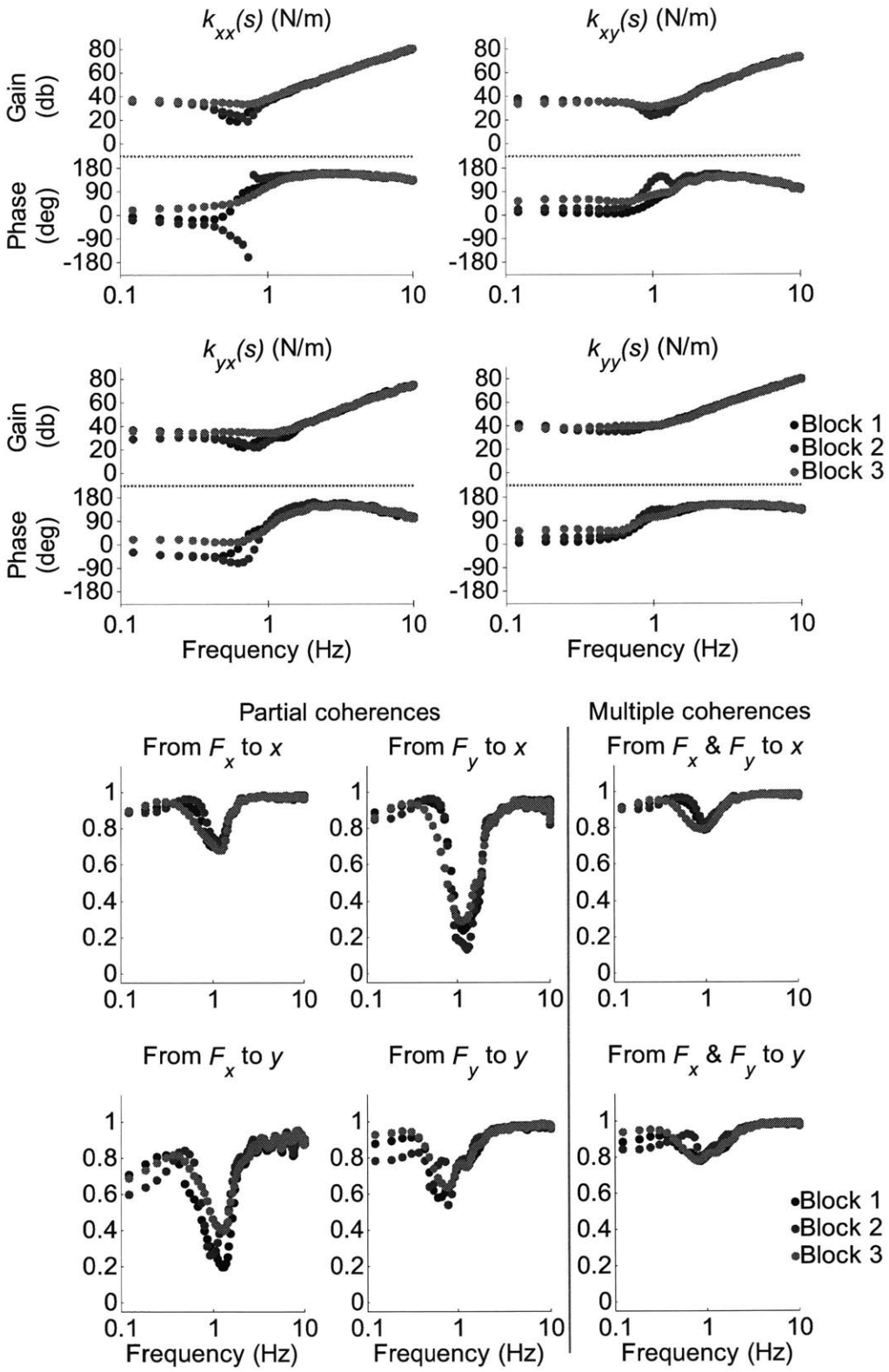

Figure G.18. Patient 5, right hemiplegic, left arm, 45 overlaps: dynamic stiffness spectral estimates (top), and partial and multiple coherences (bottom)

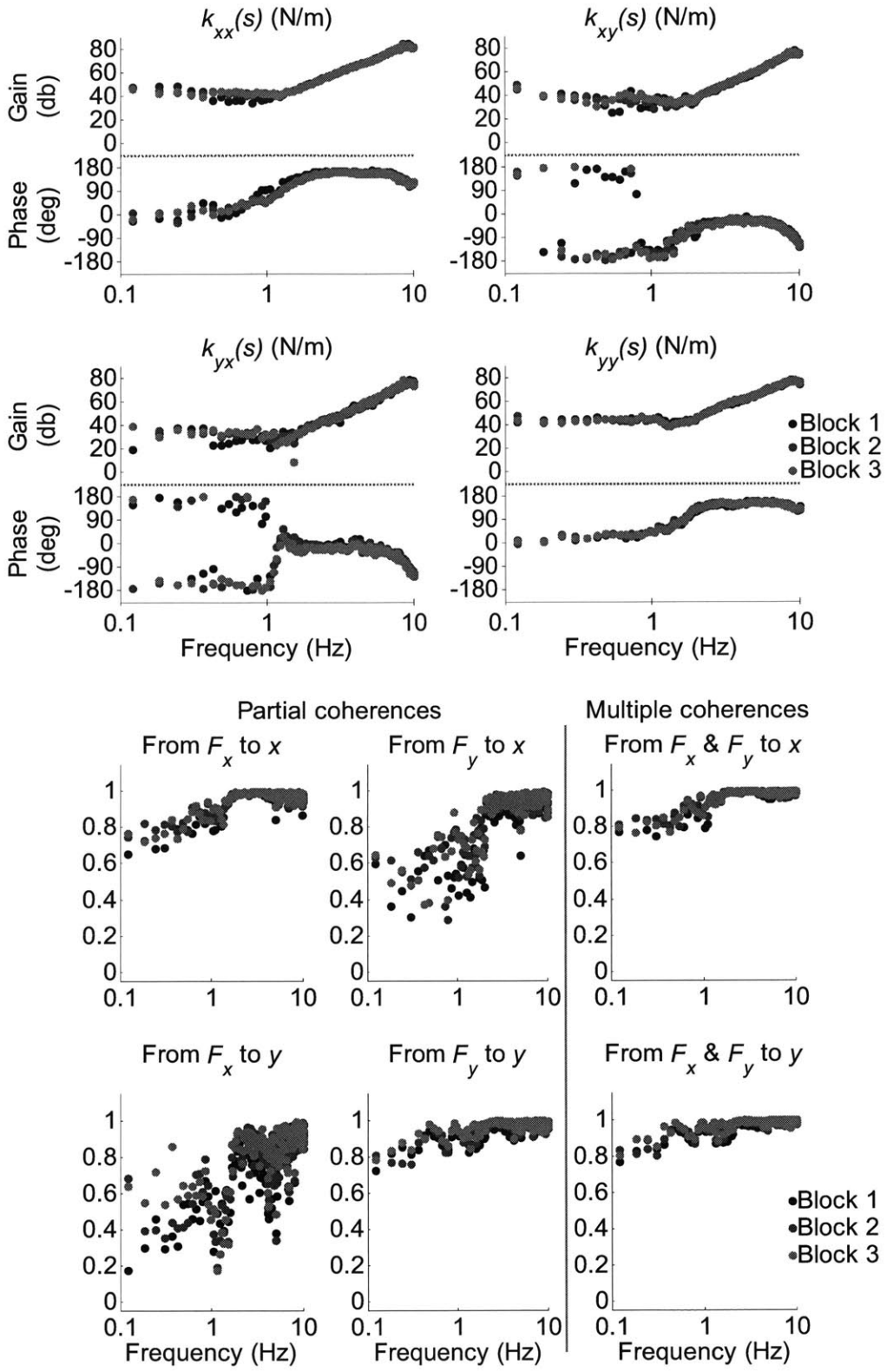

Figure G.19. Patient 5, right hemiplegic, right arm, 5 overlaps: dynamic stiffness spectral estimates (top), and partial and multiple coherences (bottom)

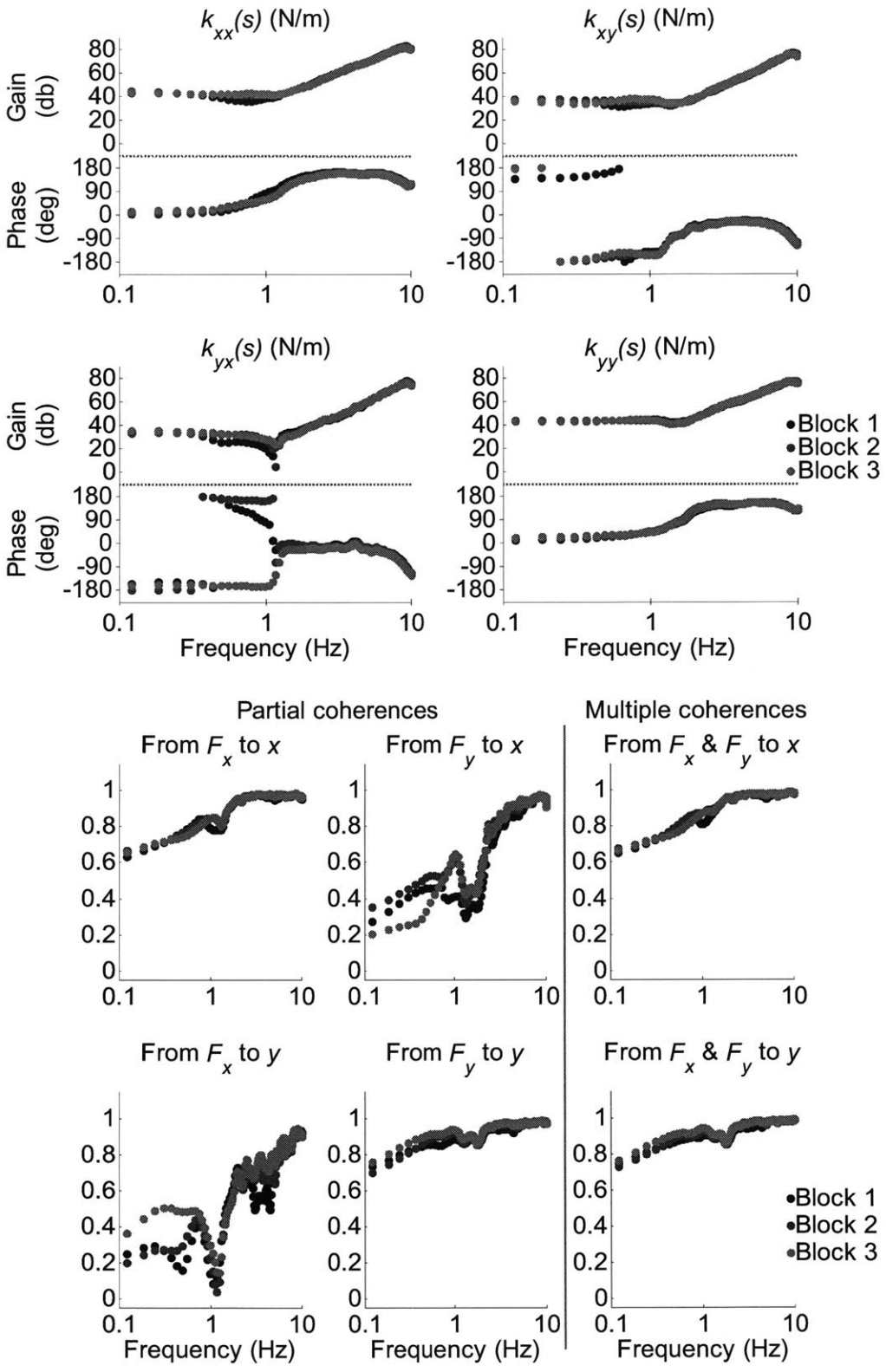

Figure G.20. Patient 5, right hemiplegic, right arm, 45 overlaps: dynamic stiffness spectral estimates (top), and partial and multiple coherences (bottom)

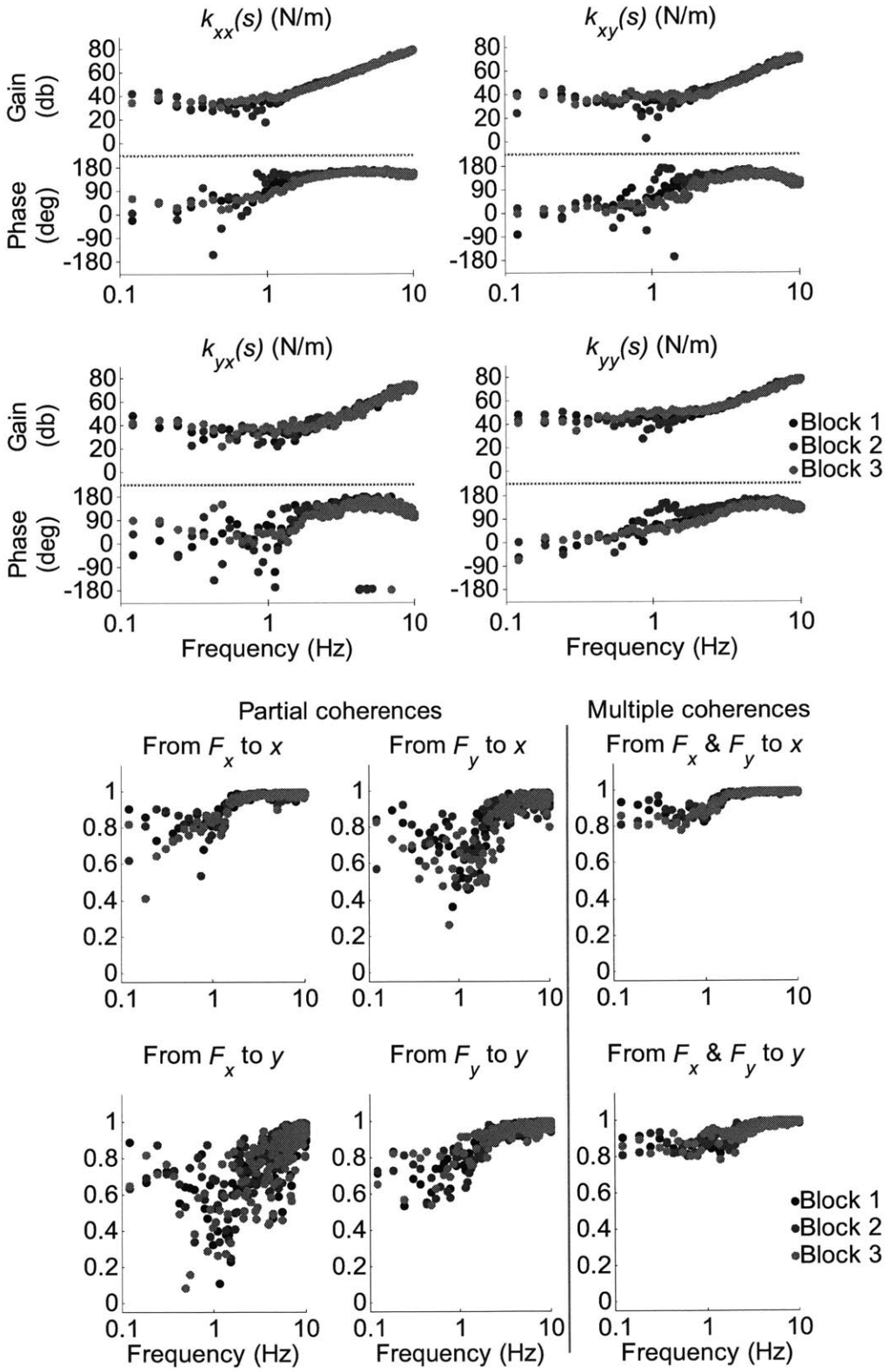

Figure G.21. Patient 6, right hemiplegic, left arm, 5 overlaps: dynamic stiffness spectral estimates (top), and partial and multiple coherences (bottom)

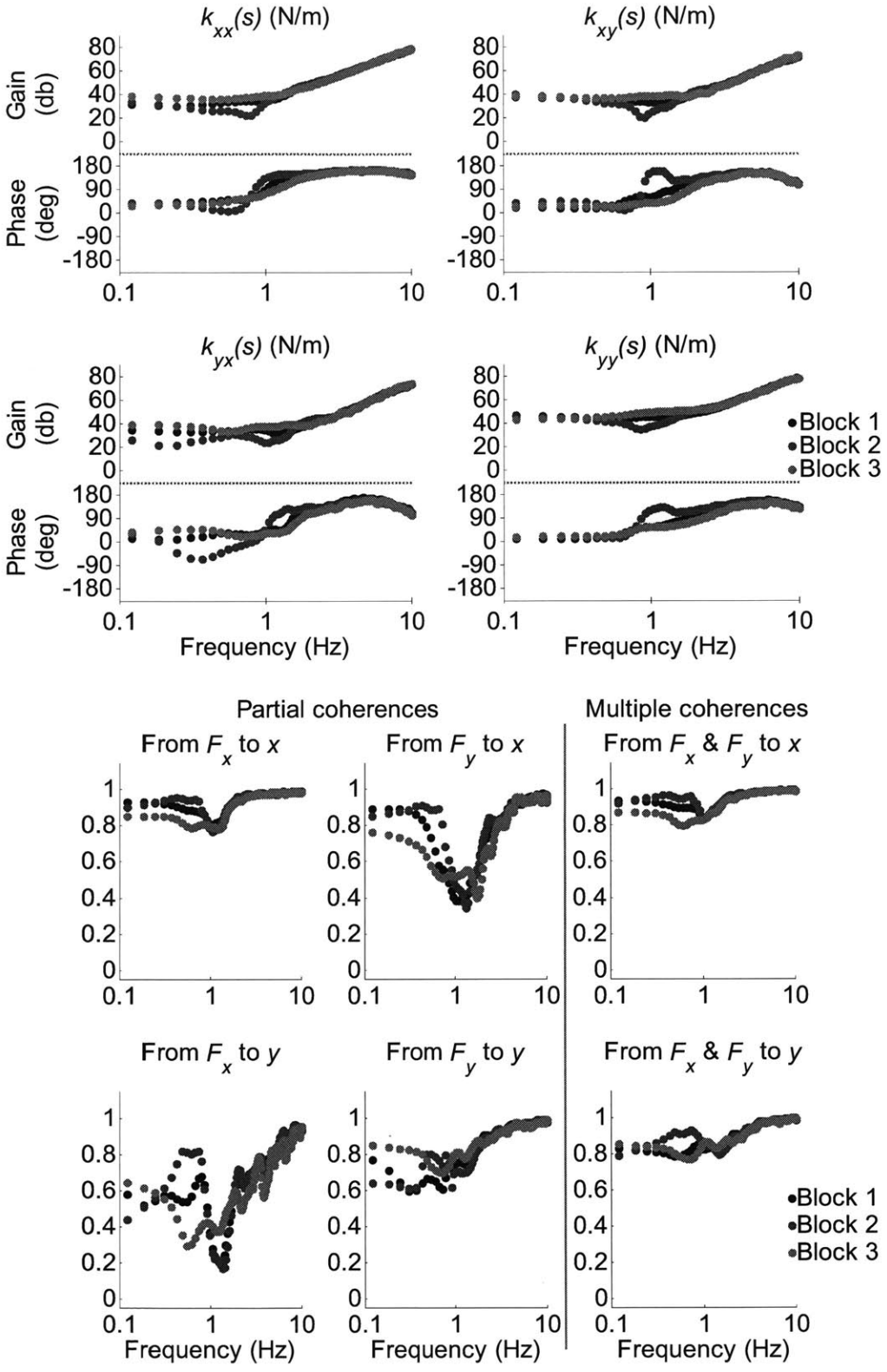

Figure G.22. Patient 6, right hemiplegic, left arm, 45 overlaps: dynamic stiffness spectral estimates (top), and partial and multiple coherences (bottom)

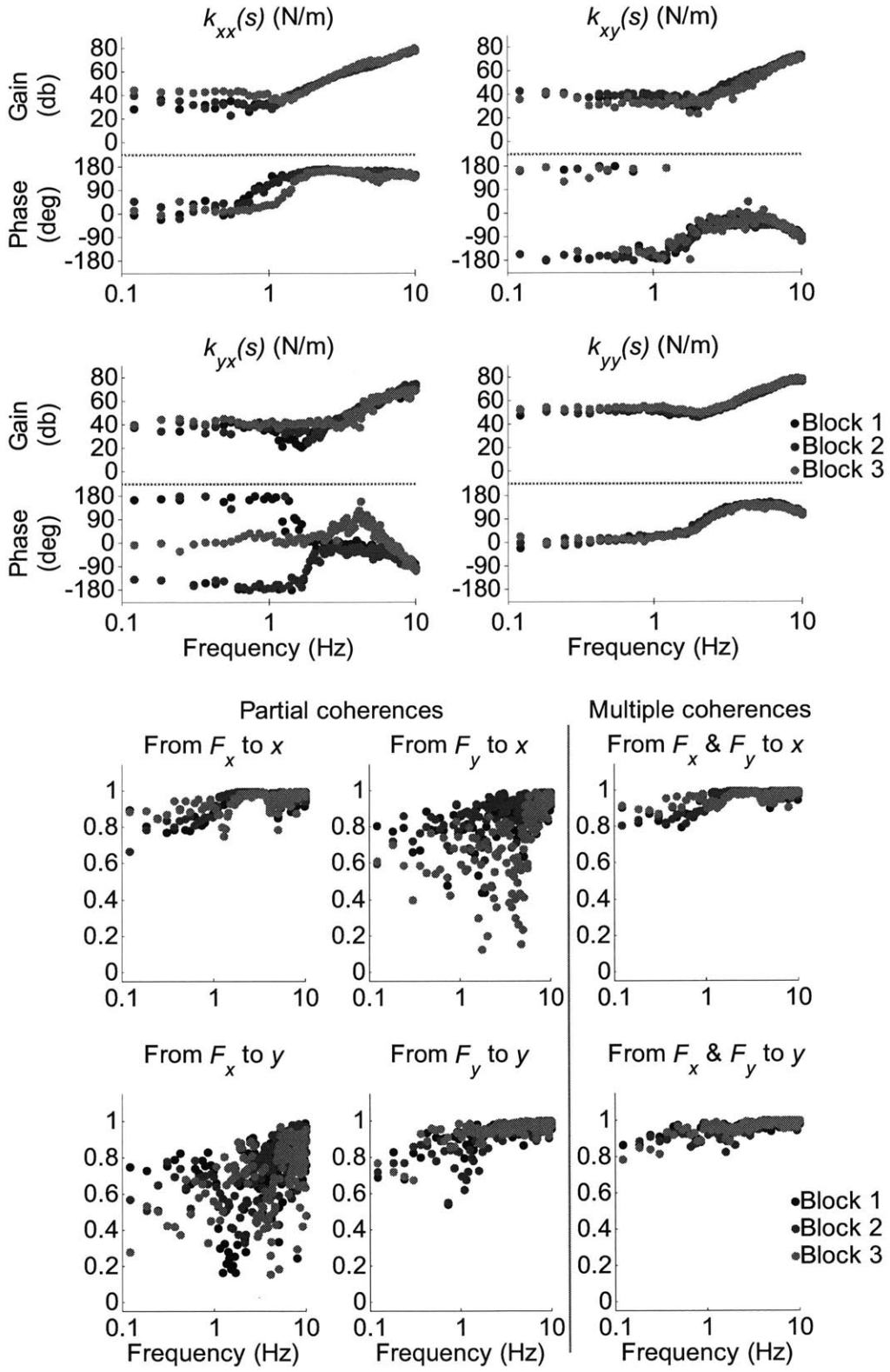

Figure G.23. Patient 6, right hemiplegic, right arm, 5 overlaps: dynamic stiffness spectral estimates (top), and partial and multiple coherences (bottom)

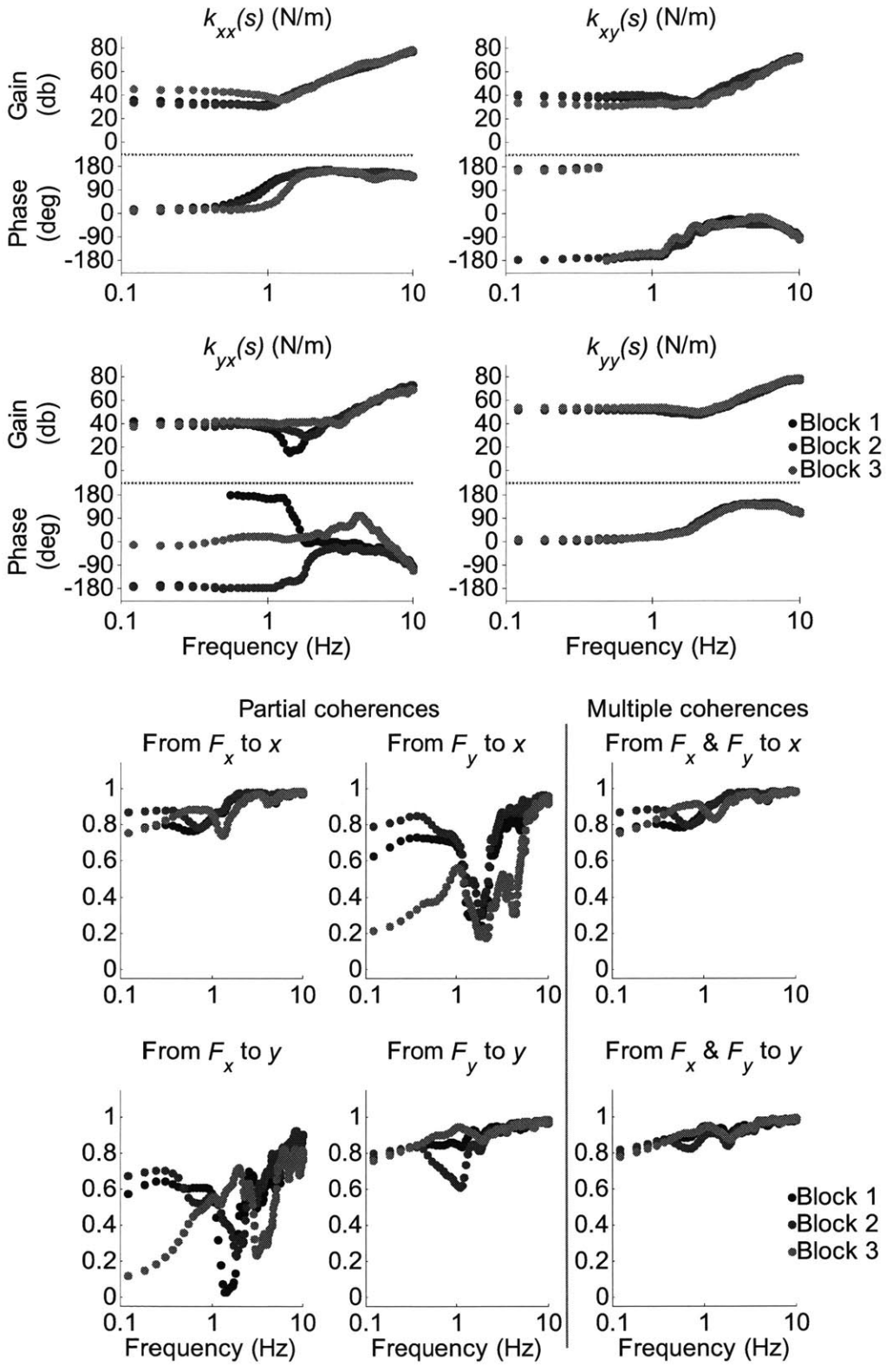

Figure G.24. Patient 6, right hemiplegic, right arm, 45 overlaps: dynamic stiffness spectral estimates (top), and partial and multiple coherences (bottom)

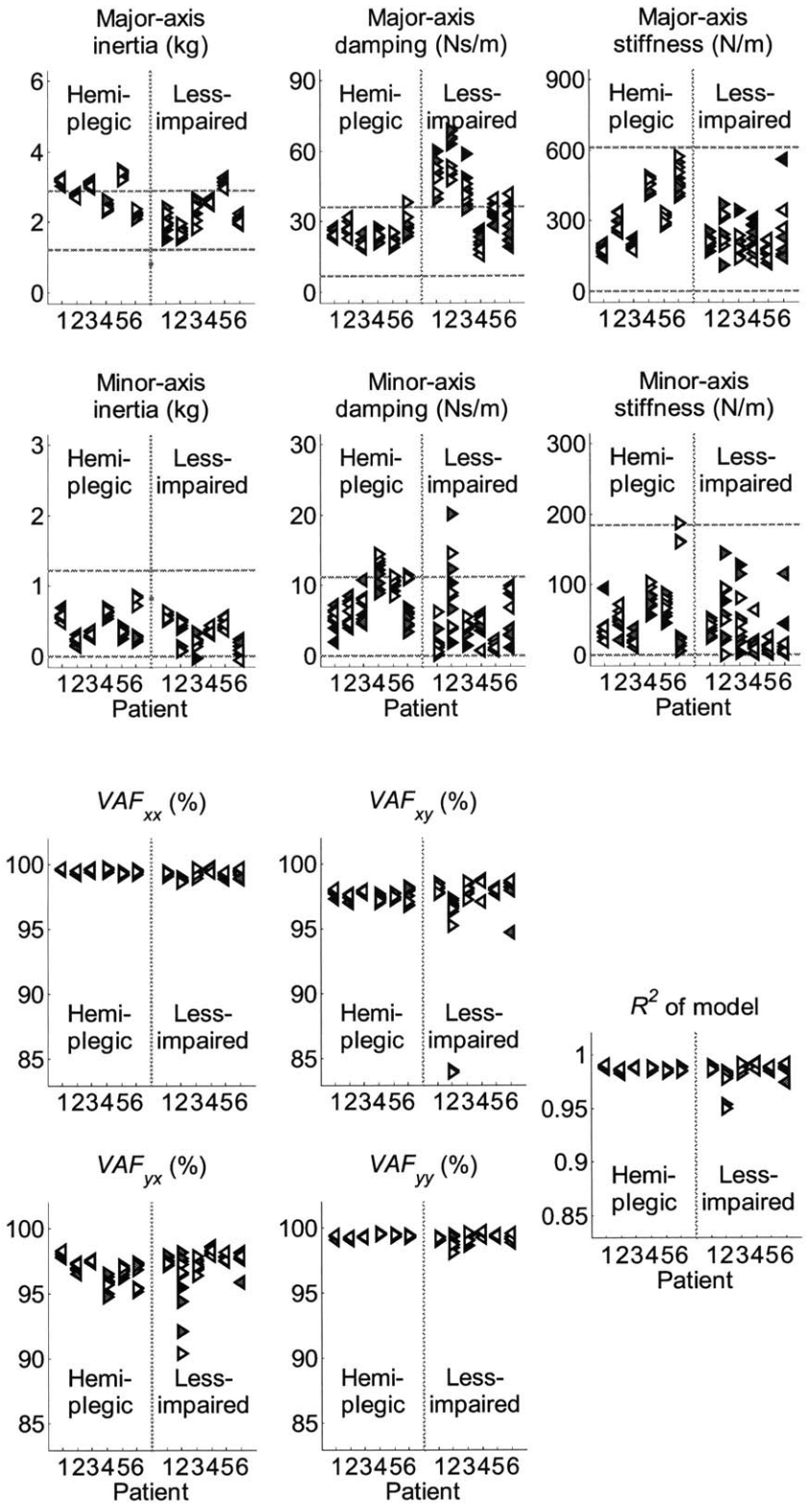

Figure G.25. Both arms, 5 overlaps, asymmetric: inertia, damping, and stiffness matrix major and minor axis properties (top), and *VAF* and R^2 of model (bottom)

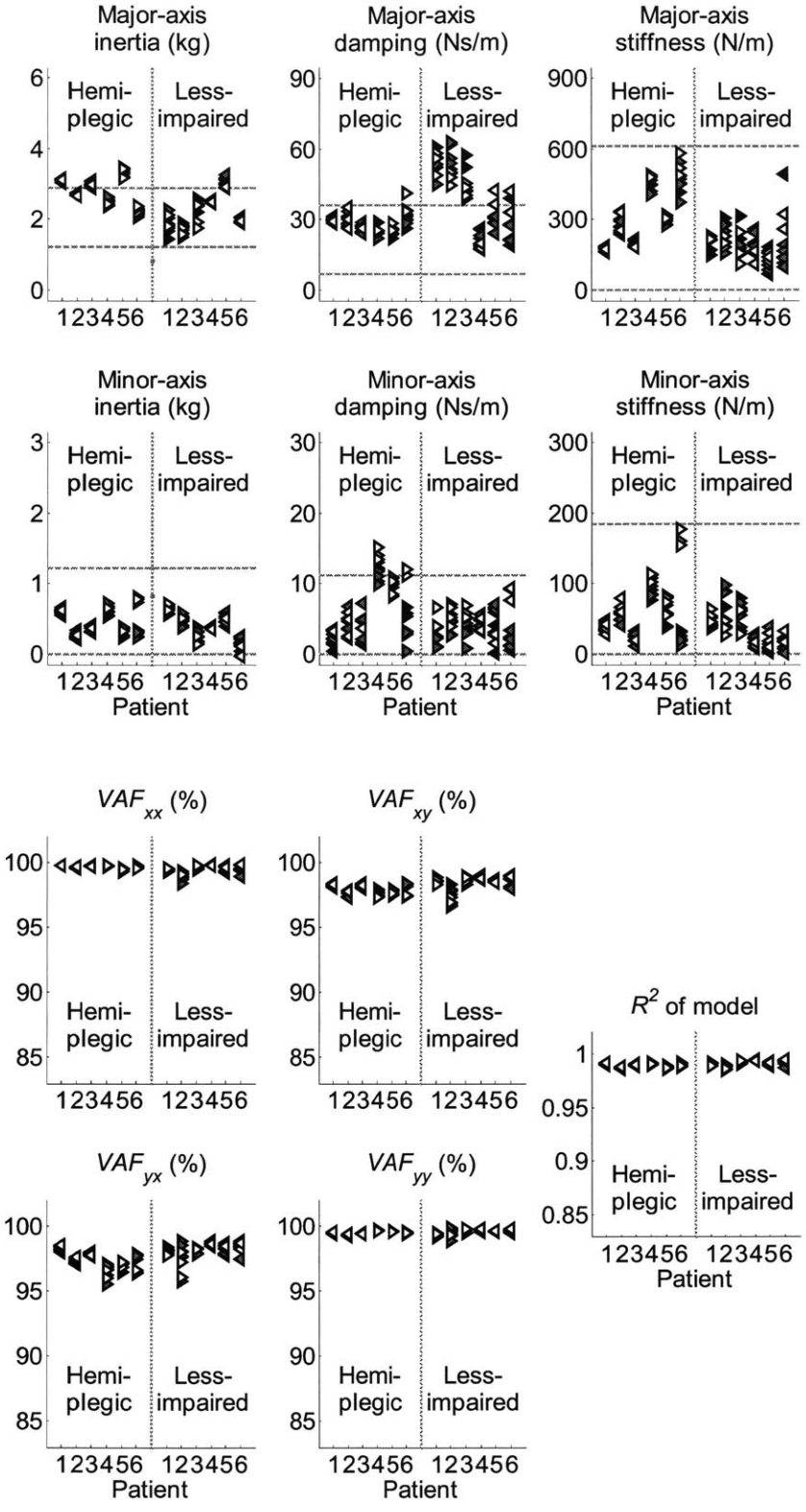

Figure G.26. Both arms, 45 overlaps, asymmetric: inertia, damping, and stiffness matrix major and minor axis properties (top), and *VAF* and R^2 of model (bottom)

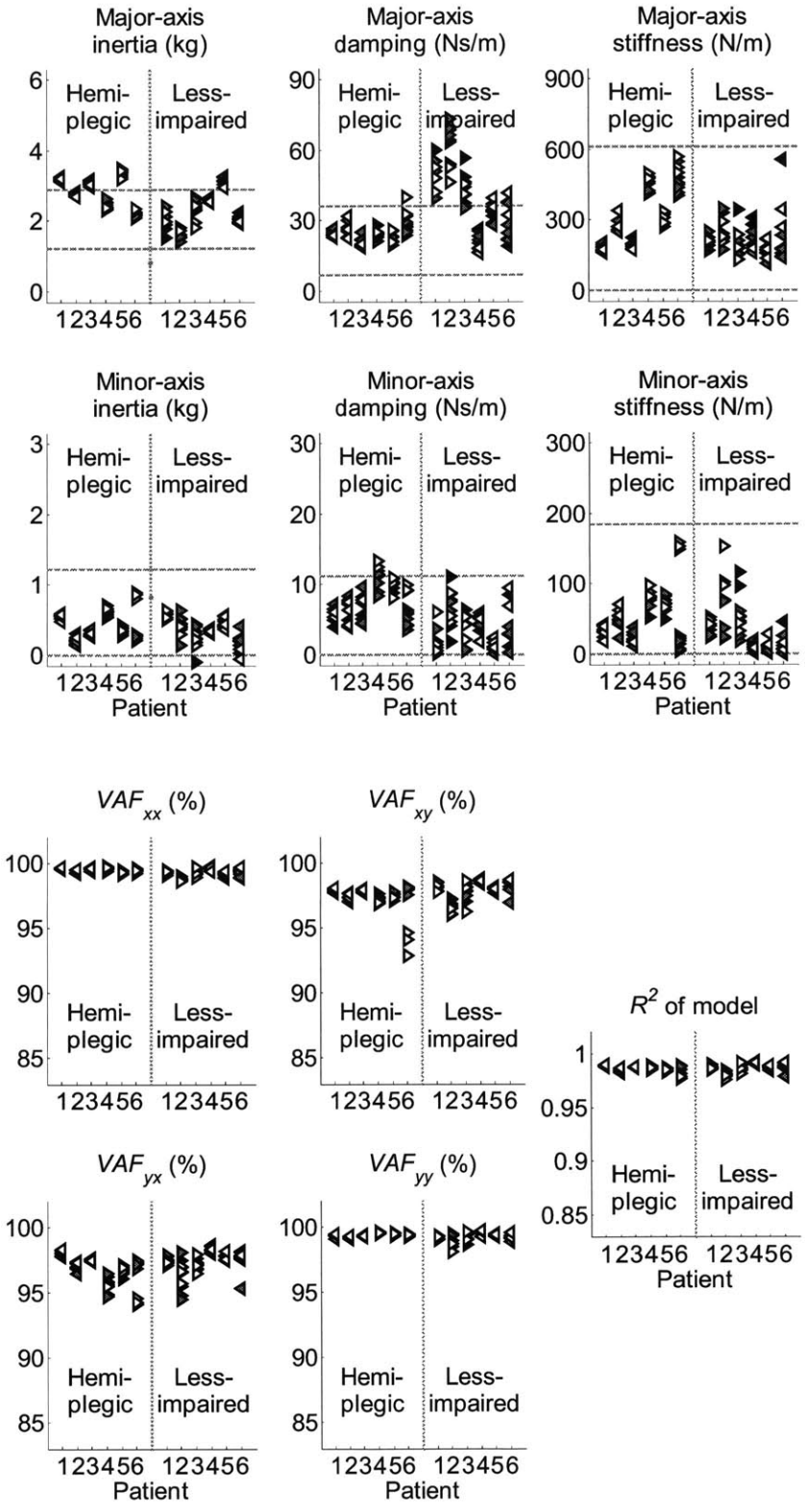

Figure G.27. Both arms, 5 overlaps, symmetric: inertia, damping, and stiffness matrix major and minor axis properties (top), and *VAF* and R^2 of model (bottom)

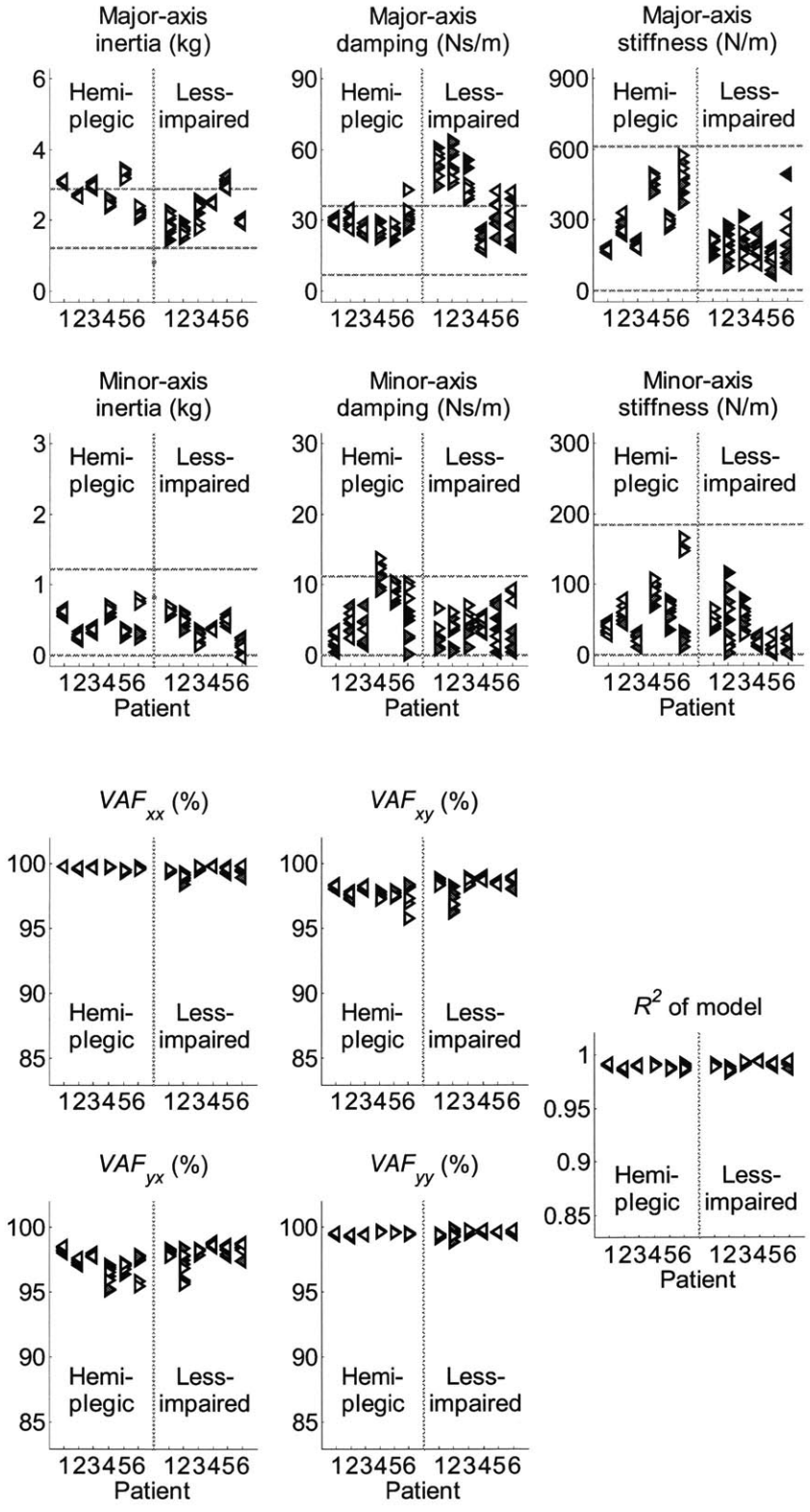

Figure G.28. Both arms, 45 overlaps, symmetric: inertia, damping, and stiffness matrix major and minor axis properties (top), and *VAF* and R^2 of model (bottom)

Bibliography

[1] A. M. Acosta , R. F. Kirsch, and E. J. Perreault, "A robotic manipulator for the characterization of two-dimensional dynamic stiffness using stochastic displacement perturbations," *J Neurosci Meth*, vol. 102, no. 2, pp. 177-186, 2000.

[2] Adams, J. A. , A closed-loop theory of motor learning *J Mot Behav*, vol. 3, pp. 111-150, 1971.

[3] M. L. Aisen, H. I. Krebs, N. Hogan, F. McDowell, and B. T. Volpe, "The effect of robot-assisted therapy and rehabilitative training on motor recovery following stroke," *Arch Neurol*, vol. 54, no. 4, pp. 443-446, 1997.

[4] Al-Ameer, H. and Toole, T., Combinations of blocked and random practice orders: benefits to acquisition and retention *J Hum Mov Stud*, vol. 25, pp. 177-191, 1993.

[5] American Heart Association, *Heart Disease and Stroke Statistics - 2005 Update*, Dallas, TX: American Heart Association, 2004.

[6] Armstrong, T. R., "Training for the production of memorized movement patterns," University of Michigan, Dept. of Psychology, Ann Arbor, MI, Tech. Rep. No. 26, 1970.

[7] J. S. Bendat and A. G. Piersol, *Engineering Applications of Correlation and Spectral Analysis*, New York: J. Wiley, 1993.

[8] J. S. Bendat and A. G. Piersol, *Random Data: Analysis and Measurement Procedures*, New York: Wiley, 2000.

[9] R. W. Bohannon and M. B. Smith , "Interrater reliability of a Modified Ashworth Scale of muscle spasticity," *Phys Ther*, vol. 67, no. 2, pp. 206-207, 1987.

[10] T. Brashers-Krug, R. Shadmehr, and E. Bizzi, "Consolidation in human motor memory," *Nature*, vol. 382, no. 6588, pp. 252-255, 1996.

[11] Bryan, W. L. and Harter, N., Studies in the physiology and psychology of the telegraphic language *Psychol Rev*, vol. 4, pp. 27-53, 1897.

[12] Bryan, W. L. and Harter, N., Studies on the telegraphic language: the acquisition of a hierarchy of habits *Psychol Rev*, vol. 6, pp. 345-375, 1899.

[13] S. P. Buerger, "Stable, High-Force, Low-Impedance Robotic Actuators for Human-Interactive Machines," Ph.D. thesis, Dept. Mech. Eng., Massachusetts Institute of Technology, Cambridge, MA, 2005.

[14] E. Burdet, R. Osu, D. W. Franklin, T. E. Milner, and M. Kawato, "The central nervous system stabilizes unstable dynamics by learning optimal impedance," *Nature*, vol. 414, no. 6862, pp. 446-449, 2001.

[15] E. Burdet, R. Osu, D. W. Franklin, T. Yoshioka, T. E. Milner, and M. Kawato, "A method for measuring endpoint stiffness during multi-joint arm movements," *J Biomech*, vol. 33, no. 12, pp. 1705-1709, 2000.

[16] C. G. Burgar, P. S. Lum, P. C. Shor, and H. F. M. Van der Loos, "Development of robots for rehabilitation therapy: the Palo Alto VA/Stanford experience," *J Rehabil Res Dev*, vol. 37, no. 6, pp. 663-673, 2000.

[17] G. Caithness, R. Osu, P. Bays, H. Chase, J. Klassen, M. Kawato, D. M. Wolpert, and J. R. Flanagan, "Failure to consolidate the consolidation theory of learning for sensorimotor adaptation tasks," *J Neurosci*, vol. 24, no. 40, pp. 8662-8671, 2004.

[18] J. Celestino, H. I. Krebs, and N. Hogan, "A robot for wrist rehabilitation: characterization and initial results," *Proceedings - 8th International Conference on Rehabilitation Robotics (ICORR 2003).*

[19] A. D'Souza, S. Vijayakumar, and S. Schaal, "Learning inverse kinematics," *Proceedings of the IEEE International Conference on Intelligent Robots and Systems (IROS 2001),* Maui, HI, USA, Oct. 2001.

[20] M. C. Diamond, E. R. Greer, A. York, D. Lewis, T. Barton, and J. Lin, "Rat cortical morphology following crowded-enriched living-conditions," *Exp Neurol*, vol. 96, no. 2, pp. 241-247, 1987 .

[21] M. C. Diamond, C. A. Ingham, R. E. Johnson, E. L. Bennett, and M. R. Rosenzweig, "Effects of environment on morphology of rat cerebral-cortex and hippocampus," *J Neurobiol*, vol. 7, no. 1, pp. 75-85, 1976.

[22] M. C. Diamond, R. E. Johnson, A. M. Protti, C. Ott, and L. Kajisa, "Plasticity in the 904-day-old male-rat cerebral-cortex," *Exp Neurol*, vol. 87, no. 2, pp. 309-317, 1985.

[23] M. C. Diamond, F. Law, H. Rhodes, B. Lindner, M. R. Rosenzweig, D. Krech, and E. L. Bennett, "Increases in cortical depth and glia numbers in rats subjected to enriched environment," *J Comp Neurol*, vol. 128, no. 1, pp. 117-26, 1966.

[24] J. M. Dolan , M. B. Friedman, and M. L. Nagurka, "Dynamic and loaded impedance components in the maintenance of human arm posture," *IEEE Trans Syst Man Cybern*, vol. 23, no. 3, pp. 698-709 , 1993.

[25] S. E. Fasoli, H. I. Krebs, J. Stein, W. R. Frontera, and N. Hogan, "Effects of robotic therapy on motor impairment and recovery in chronic stroke," *Arch Phys Med Rehabil*, vol. 84, no. 4, pp. 477-482, 2003.

[26] S. E. Fasoli, H. I. Krebs, J. Stein, R. Hughes, A. Mccarthy-Jacobson, W. Frontera, and N. Hogan, "Effects of robotic therapy on upper limb motor impairments in chronic stroke," *Stroke*, vol. 33, no. 1, pp. 350-351, 2002.

[27] M. Ferraro, J. J. Palazzolo, J. Krol, H. I. Krebs, N. Hogan, and B. T. Volpe, "Robot-aided sensorimotor arm training improves outcome in patients with chronic stroke," *Neurology*, vol. 61, no. 11, pp. 1604-1607, 2003.

[28] P. M. Fitts and M. I. Posner, *Human Performance*, Belmont, CA: Brooks/Cole, 1967.

[29] J. R. Flanagan, E. Nakano, H. Imamizu, R. Osu, T. Yoshioka, and M. Kawato, "Composition and decomposition of internal models in motor learning under altered kinematic and dynamic environments," *J Neurosci*, vol. 19, no. 20, pp. RC34, 1999.

[30] J. R. Flanagan and A. K. Rao, "Trajectory adaptation to a nonlinear visuomotor transformation: evidence of motion planning in visually perceived space," *J Neurophysiol*, vol. 74, no. 5, pp. 2174-2178, 1995.

[31] T. Flash and N. Hogan, "The coordination of arm movements: an experimentally confirmed mathematical model," *J Neurosci*, vol. 5, no. 7, pp. 1688-1703, 1985.

[32] C. A. Foster, "A performance characterization of an interactive robot," S.M. thesis, Dept. Mech. Eng., Massachusetts Institute of Technology, Cambridge, MA, 1999.

[33] A. R. Fugl-Meyer, L. Jaasko, I. Leyman, S. Olsson, and S. Steglind, "The post-stroke hemiplegic patient - Part 1: a method for evaluation of physical performance," *Scand J Rehabil Med*, vol. 7, no. 1, pp. 13-31, 1975.

[34] D. M. Gillard, S. Yakovenko, T. Cameron, and A. Prochazka, "Isometric muscle length-tension curves do not predict angle-torque curves of human wrist in continuous active movements," *J Biomech*, vol. 33, no. 11, pp. 1341-1348, 2000.

[35] H. Gomi and M. Kawato, "Human arm stiffness and equilibrium-point trajectory during multi-joint movement," *Biol Cybern*, vol. 76, no. 3, pp. 163-171 , 1997.

[36] S. J. Goodbody and D. M. Wolpert, "Temporal and amplitude generalization in motor learning," *J Neurophysiol*, vol. 79, no. 4, pp. 1825-1838, 1998.

[37] S. J. Goodbody and D. M. Wolpert, "The effect of visuomotor displacements on arm movement paths," *Exp Brain Res*, vol. 127, no. 2, pp. 213-223, 1999.

[38] E. R. Greer , M. C. Diamond, and G. M. Murphy, "Increased branching of basal dendrites on pyramidal neurons in the occipital cortex of homozygous brattleboro rats in standard and enriched environmental-conditions - A Golgi-study," *Exp Neurol*, vol. 76, no. 2, pp. 254-262 , 1982.

[39] Henry, F. M. and Rogers, D. E., Increased response latency for complicated movements and a 'memory drum' theory of neuromotor reaction *Res Q*, vol. 31, pp. 621-652, 1960.

[40] N. Hogan, "An organizing principle for a class of voluntary movements," *J Neurosci*, vol. 4, no. 11, pp. 2745-2754, 1984.

[41] N. Hogan, "Impedance control - An approach to manipulation - Part I: theory," *J Dyn Syst Meas Contr*, vol. 107, no. 1, pp. 1-7, 1985.

[42] N. Hogan, "Impedance control - An approach to manipulation - Part II: implementation," *J Dyn Syst Meas Contr*, vol. 107, no. 1, pp. 8-16, 1985.

[43] N. Hogan, "Impedance control - An approach to manipulation - Part III: applications," *J Dyn Syst Meas Contr*, vol. 107, no. 1, pp. 17-24, 1985.

[44] N. Hogan, "The mechanics of multi-joint posture and movement control," *Biol Cybern*, vol. 52, no. 5, pp. 315-331, 1985.

[45] N. Hogan, "Skeletal muscle impedance in the control of motor actions," *J Mech Med Biol*, vol. 2, no. 3-4, pp. 359-373, 2002.

[46] N. Hogan, H. I. Krebs, A. Sharon, and J. Charnnarong, "Interactive robotic therapist," U.S. Patent 5 466 213, Massachusetts Institute of Technology, 1995.

[47] W. James, *The Principles of Psychology*, New York: Holt, 1890.

[48] Jordan, M. I. and Rumelhart, D. E., Forward models: supervised learning with a distal teacher *Cognit Sci*, vol. 16, pp. 75-87, 1992.

[49] H. S. Jorgensen, H. Nakayama, H. O. Raaschou, J. Vivelarsen, M. Stoier, and T. S. Olsen, "Outcome and time-course of recovery in stroke. Part II: time-course of recovery - The Copenhagen Stroke Study," *Arch Phys Med Rehabil*, vol. 76, no. 5, pp. 406-412, 1995.

[50] G. C. Joyce , P. M. Rack, and D. R. Westbury, "The mechanical properties of cat soleus muscle during controlled lengthening and shortening movements," *J Physiol*, vol. 204, no. 2, pp. 461-474, 1969.

[51] E. R. Kandel, J. H. Schwartz, and T. M. Jessell, *Principles of Neural Science*, New York: McGraw-Hill, Health Professions Division, 2000.

[52] J. A. S. Kelso, *Dynamic patterns: the self-organization of brain and behavior*, Cambridge, MA: MIT Press, 1995.

[53] H. I. Krebs , M. L. Aisen, B. T. Volpe, and N. Hogan, "Quantization of continuous arm movements in humans with brain injury," *Proc Natl Acad Sci Unit States Am*, vol. 96, no. 8, pp. 4645-4649, 1999.

[54] H. I. Krebs , M. Ferraro, S. P. Buerger, M. J. Newbery, A. Makiyama, M. Sandmann, D. Lynch, B. T. Volpe, and N. Hogan, "Rehabilitation robotics: pilot trial of a spatial extension for MIT-MANUS," *J Neuroengineering Rehabil*, vol. 1, no. 1, 2004.

[55] H. I. Krebs , N. Hogan, M. L. Aisen, and B. T. Volpe, "Robot-aided neuro-rehabilitation," *IEEE Trans Rehabil Eng*, vol. 6, no. 1, pp. 75-87, 1998.

[56] H. I. Krebs , N. Hogan, W. Hening, S. V. Adamovich, and H. Poizner, "Procedural motor learning in Parkinson's disease," *Exp Brain Res*, vol. 141, no. 4, pp. 425-437, 2001.

[57] H. I. Krebs , J. J. Palazzolo, L. Dipietro, M. Ferraro, J. Krol, K. Rannekleiv, B. T. Volpe, and N. Hogan, "Rehabilitation robotics: performance-based progressive robot-assisted therapy," *Auton Robot*, vol. 15, no. 1, pp. 7-20, 2003.

[58] H. I. Krebs , B. T. Volpe, M. L. Aisen, and N. Hogan, "Increasing productivity and quality of care: robot-aided neuro-rehabilitation," *J Rehabil Res Dev*, vol. 37, no. 6, pp. 639-652, 2000.

[59] H. I. Krebs , B. T. Volpe, J. Palazzolo, S. Fasoli, Ferraro M., L. Edelstein, and N. Hogan, "Disturbances of higher level neural control - Robotic applications in stroke," *IEEE Proceedings from the 23rd International Conference of the Engineering in Medicine and Biology Society (EMBS 2001),* Istanbul, Turkey.

[60] H. I. Krebs , B. T. Volpe, J. Palazzolo, B. Rohrer, M. Ferraro, S. Fasoli, L. Edelstein, and N. Hogan, "Robot-aided neuro-rehabilitation in stroke: interim results on the follow-up of 76 patients and on movement performance indices," In: *Integration of Assistive Technology in the Information Age*, M. Mokhtari, Ed., Amsterdam: IOS Press, 2001.

[61] Lashley, K. S., The accuracy of movement in the absence of excitation from the moving organ *Am J Physiol*, vol. 43, pp. 169-194, 1917.

[62] T. D. Lee and R. A. Magill, "The locus of contextual interference in motor-skill acquisition," *J Exp Psychol-Learn Mem Cogn*, vol. 9, no. 4, pp. 730-746, 1983.

[63] C. S. Li, C. Padoa-Schioppa, and E. Bizzi, "Neuronal correlates of motor performance and motor learning in the primary motor cortex of monkeys adapting to an external force field," *Neuron*, vol. 30, no. 2, pp. 593-607, 2001.

[64] E. Marder and R. L. Calabrese , "Principles of rhythmic motor pattern generation," *Physiol Rev*, vol. 76, no. 3, pp. 687-717, 1996.

[65] M. M. Merzenich, W. M. Jenkins, P. Johnston, C. Schreiner, S. L. Miller, and P. Tallal, "Temporal processing deficits of language-learning impaired children ameliorated by training," *Science*, vol. 271, no. 5245, pp. 77-81, 1996.

[66] J. S. Milton and J. C. Arnold, *Introduction to Probability and Statistics: Principles and Applications for Engineering and the Computing Sciences*, New York: McGraw-Hill, 1990.

[67] F. A. Mussa-Ivaldi, "Nonlinear force fields: A distributed system of control primitives for representing and learning movements," *IEEE Proceedings of Computational Intelligence in Robotics and Automation (CIRA),* Monterey, CA, USA, 1997.

[68] F. A. Mussa-Ivaldi, N. Hogan, and E. Bizzi, "Neural, mechanical, and geometric factors subserving arm posture in humans," *J Neurosci*, vol. 5, no. 10, pp. 2732-2743, 1985.

[69] K. M. Newell, "Schema theory (1975): retrospectives and prospectives," *Res Quart Exercise Sport*, vol. 74, no. 4, pp. 383-388, 2003.

[70] R. J. Nudo, B. M. Wise, F. Sifuentes, and G. W. Milliken, "Neural substrates for the effects of rehabilitative training on motor recovery after ischemic infarct," *Science*, vol. 272, no. 5269, pp. 1791-1794, 1996.

[71] Oxford University Press, Oxford English Dictionary, http://dictionary.oed.com/.

[72] J. L. Patton and F. A. Mussa-Ivaldi, "Robotic teaching by exploiting the nervous system's adaptive mechanisms," *7th International Conference on Rehabilitation Robotics (ICORR),* Evry, France, 2001.

[73] J. L. Patton and F. A. Mussa-Ivaldi, "Robot-assisted adaptive training: custom force fields for teaching movement patterns," *IEEE Trans Biomed Eng*, vol. 51, no. 4, pp. 636-646, 2004.

[74] E. J. Perreault, R. F. Kirsch, and A. M. Acosta, "Multiple-input, multiple-output system identification for characterization of limb stiffness dynamics," *Biol Cybern*, vol. 80, no. 5, pp. 327-337, 1999.

[75] A. Polit and E. Bizzi, "Processes controlling arm movements in monkeys," *Science*, vol. 201, no. 4362, pp. 1235-1237, 1978.

[76] A. Polit and E. Bizzi, "Characteristics of motor programs underlying arm movements in monkeys," *J Neurophysiol*, vol. 42, no. 1, pp. 183-194, 1979.

[77] K. A. Provins, "The effect of peripheral nerve block on the appreciation and execution of finger movements," *J Physiol*, vol. 143, no. 1, pp. 55-67, 1958.

[78] P. M. Rack and D. R. Westbury, "The short range stiffness of active mammalian muscle and its effect on mechanical properties," *J Physiol*, vol. 240, no. 2, pp. 331-350, 1974.

[79] D. J. Reinkensmeyer, L. E. Kahn, M. Averbuch, A. McKenna-Cole, B. D. Schmit, and W. Z. Rymer, "Understanding and treating arm movement impairment after chronic brain injury: progress with the ARM Guide," *J Rehabil Res Dev*, vol. 37, no. 6, pp. 653-662, 2000.

[80] D. J. Reinkensmeyer, B. D. Schmit, and W. Z. Rymer, "Assessment of active and passive restraint during guided reaching after chronic brain injury," *Ann Biomed Eng*, vol. 27, no. 6, pp. 805-814, 1999.

[81] J. Sanford, J. Moreland, L. R. Swanson, P. W. Stratford, and C. Gowland, "Reliability of the Fugl-Meyer assessment for testing motor-performance in patients following stroke," *Phys Ther*, vol. 73, no. 7, pp. 447-454, 1993.

[82] R. A. Scheidt, J. B. Dingwell, and F. A. Mussa-Ivaldi, "Learning to move amid uncertainty," *J Neurophysiol*, vol. 86, no. 2, pp. 971-985, 2001.

[83] R. A. Scheidt, D. J. Reinkensmeyer, M. A. Conditt, W. Z. Rymer, and F. A. Mussa-Ivaldi, "Persistence of motor adaptation during constrained, multi-joint, arm movements," *J Neurophysiol*, vol. 84, no. 2, pp. 853-862, 2000.

[84] R. A. Schmidt, "Schema theory of discrete motor skill learning," *Psychol Rev*, vol. 82, no. 4, pp. 225-260 , 1975.

[85] R. A. Schmidt and T. D. Lee, *Motor Control and Learning: A Behavioral Emphasis*, Champaign, IL: Human Kinetics, 1999.

[86] R. A. Schmidt and C. A. Wrisberg, *Motor Learning and Performance*, Champaign, IL: Human Kinetics, 2000.

[87] R. A. Schmidt and G. Wulf, "Continuous concurrent feedback degrades skill learning: implications for training and simulation," *Hum Factors*, vol. 39, no. 4, pp. 509-525, 1997.

[88] B. D. Schmit, J. P. A. Dewald, and W. Z. Rymer, "Stretch reflex adaptation in elbow flexors during repeated passive movements in unilateral brain-injured patients," *Arch Phys Med Rehabil*, vol. 81, no. 3, pp. 269-278, 2000.

[89] R. Shadmehr and H. H. Holcomb , "Neural correlates of motor memory consolidation," *Science*, vol. 277, no. 5327, pp. 821-825, 1997.

[90] R. Shadmehr and F. A. Mussa-Ivaldi, "Adaptive representation of dynamics during learning of a motor task," *J Neurosci*, vol. 14, no. 5, pp. 3208-3224, 1994.

[91] Shea, J. B. and Morgan, R. L., Contextual interference effects on the acquisition, retention, and transfer of a motor skill *J Exp Psychol Hum Learn Mem*, vol. 5, pp. 179-187, 1979.

[92] J. Stein, H. I. Krebs, W. R. Frontera, S. E. Fasoli, R. Hughes, and N. Hogan, "Comparison of two techniques of robot-aided upper limb exercise training after stroke," *Amer J Phys Med Rehabil*, vol. 83, no. 9, pp. 720-728, 2004.

[93] S. P. Swinnen, D. E. Nicholson, R. A. Schmidt, and D. C. Shapiro, "Information feedback for skill acquisition - Instantaneous knowledge of results degrades learning," *J Exp Psychol-Learn Mem Cogn*, vol. 16, no. 4, pp. 706-716 , 1990.

[94] Trowbridge, M. H. and Cason, H., An experimental study of Thorndike's theory of learning *J Gen Psychol*, vol. 7, pp. 245-260, 1932.

[95] T. Tsuji, P. G. Morasso, K. Goto, and K. Ito, "Human hand impedance characteristics during maintained posture," *Biol Cybern*, vol. 72, no. 6, pp. 475-485 , 1995.

[96] B. T. Volpe , H. I. Krebs, N. Hogan, L. Edelstein, C. Diels, and M. Aisen, "A novel approach to stroke rehabilitation: robot-aided sensorimotor stimulation," *Neurology*, vol. 54, no. 10, pp. 1938-1944, 2000.

[97] B. T. Volpe , H. I. Krebs, N. Hogan, L. Edelstein, C. Diels, and M. L. Aisen, "Robot training enhanced motor outcome in patients with stroke maintained in three year follow-up," *Neurology*, vol. 52, no. 6, pp. A16, 1999.

[98] B. T. Volpe , H. I. Krebs, N. Hogan, L. Edelsteinn, C. M. Diels, and M. L. Aisen, "Robot training enhanced motor outcome in patients with stroke maintained over 3 years," *Neurology*, vol. 53, no. 8, pp. 1874-1876, 1999.

[99] D. J. Williams, H. I. Krebs, and N. Hogan, "A robot for wrist rehabilitation," *IEEE Proceedings from the 25th International Conference of the Engineering in Medicine and Biology Society (EMBS 2003),* Cancun, Mexico.

[100] C. J. Winstein, "Knowledge of results and motor learning - Implications for physical therapy," *Phys Ther*, vol. 71, no. 2, pp. 140-149, 1991.

[101] C. J. Winstein, P. S. Pohl, and R. Lewthwaite, "Effects of physical guidance and knowledge of results on motor learning: support for the guidance hypothesis," *Res Q Exerc Sport*, vol. 65, no. 4, pp. 316-23, 1994.

[102] D. M. Wolpert, "Computational approaches to motor control," *Trends Cognit Sci*, vol. 1, no. 6, pp. 209-216, 1997.

[103] D. M. Wolpert, Z. Ghahramani, and M. I. Jordan, "Are arm trajectories planned in kinematic or dynamic coordinates? An adaptation study," *Exp Brain Res*, vol. 103, no. 3, pp. 460-470, 1995.

[104] D. M. Wolpert and M. Kawato, "Multiple paired forward and inverse models for motor control," *Neural Networks*, vol. 11, no. 7-8, pp. 1317-1329, 1998.

[105] G. Wulf and R. A. Schmidt, "Variability of practice and implicit motor learning," *J Exp Psychol-Learn Mem Cogn*, vol. 23, no. 4, pp. 987-1006, 1997.

[106] G. Wulf, R. A. Schmidt, and H. Deubel, "Reduced feedback frequency enhances generalized motor program learning but not parameterization learning," *J Exp Psychol-Learn Mem Cogn*, vol. 19, no. 5, pp. 1134-50, 1993.

[107] W. X. Yao, M. G. Fischman, and Y. T. Wang, "Motor skill acquisition and retention as a function of average feedback, summary feedback, and performance variability," *J Motor Behav*, vol. 26, no. 3, pp. 273-282, 1994.

[108] D. E. Young and R. A. Schmidt, "Augmented kinematic feedback for motor learning," *J Mot Behav*, vol. 24, no. 3, pp. 261-273, 1992.